



HAL
open science

Synthesis of novel bio-sourced surfactants from carbohydrates and their self-assembly in aqueous media and application as emulsifiers

Lea Spitzer

► **To cite this version:**

Lea Spitzer. Synthesis of novel bio-sourced surfactants from carbohydrates and their self-assembly in aqueous media and application as emulsifiers. Organic chemistry. Université de Poitiers, 2021. English. NNT : 2021POIT2261 . tel-03279285

HAL Id: tel-03279285

<https://theses.hal.science/tel-03279285>

Submitted on 6 Jul 2021

HAL is a multi-disciplinary open access archive for the deposit and dissemination of scientific research documents, whether they are published or not. The documents may come from teaching and research institutions in France or abroad, or from public or private research centers.

L'archive ouverte pluridisciplinaire **HAL**, est destinée au dépôt et à la diffusion de documents scientifiques de niveau recherche, publiés ou non, émanant des établissements d'enseignement et de recherche français ou étrangers, des laboratoires publics ou privés.

THESE

Pour l'obtention du Grade de

DOCTEUR DE L'UNIVERSITE DE POITIERS

(ECOLE SUPERIEURE d'INGENIEURS de POITIERS)

(Diplôme National - Arrêté du 25 mai 2016)

Ecole Doctorale :

Chimie Ecologie Géosciences Agrosociétés « *Théodore Monod* »

Secteur de Recherche : Chimie organique, minérale, industrielle

Présentée par :

Lea Spitzer

Synthesis of biobased surfactants from carbohydrates and their self-assembly in aqueous media: from micelles to bioactive emulsions

Directeur de thèse : JÉRÔME François

Co-directeurs de thèse : LECOMMANDOUX Sébastien and
CRAMAIL Henri

Soutenue le 22.03.2021
devant la Commission d'Examen

JURY

Rapporteurs :

BENVEGNI Thierry
METAY Estelle

Professeur, Université de Rennes, ENSCR
Directrice de recherche CNRS, Université de Lyon, ICBMS

Examineurs :

CÖLFEN Helmut
CAPRON Isabelle
LECOMMANDOUX Sébastien
CRAMAIL Henri
JÉRÔME François

Professeur, Universität Konstanz, Konstanz
Directrice de recherche, INRAE, Nantes
Université de Bordeaux, LCPO
Professeur, Université de Bordeaux, LCPO
Directeur de recherche CNRS, Université de Poitiers, IC2MP

"Dans la vie, rien n'est à craindre, tout est à comprendre."

Marie Curie

Acknowledgments

I would like to gratefully acknowledge the University of Poitiers, University of Bordeaux and the Région Nouvelle Aquitaine for the financial support towards my PhD.

I am sincerely thankful to my supervisor Dr. François Jérôme, Prof. Henri Cramail and Prof. Sébastien Lecommandoux for their continuous support during the three years of my PhD study. Their patience and motivation helped and guided me during the time of research and writing of this thesis.

I would like to express my sincere gratitude to Prof. Thierry Benvegna and Dr. Estelle Metay, who accepted to review my manuscript. I would also like to thank the rest of my thesis committee: Prof. Helmut Cölfen, Dr. Isabelle Capron, Prof. Sébastien Lecommandoux, Prof. Henri Cramail and Dr. François Jérôme.

Moreover, I would like to thank all the people from the LCPO in Bordeaux, especially from Team 2, Team 3 and the permanent staff for their help during the laboratory work. Many thanks also to all the members of Team IC2MP from the University of Poitiers for their warm welcome and support during my stay in Poitiers.

I would like to address a very special thanks to Dr. Pablo Gómez Argudo, who joint me during my third year of PhD in ‘our Team 5’. I learned a lot of his spanish philosophy and I am very grateful for all his support, motivation and endless discussions about science and life in general.

Invaluable thanks to my “sauveurs” Dr. Fiona Magliozzi, Dr. Pauline Vincent, Dr. Nicolas Longhitano, Dr. Cédric Cabral Almada and Péroline Helbling, without whom I could not have imagined finishing this PhD. I consider myself very lucky to have had them as good colleagues and good friends next to my side.

Finally, I would like to thank my family and all my relatives for their support throughout my whole studies in chemistry. I would not have been able to reach this far without their backup. I want to admit a special thanks to my father, who saved me with his knowledge in informatics during the redaction of this thesis.

Résumé

Ce travail de thèse a été consacré à la synthèse d'oligosaccharides fonctionnalisés pour préparer de nouveaux tensioactifs biosourcés. Partant de monosaccharides non protégés (mannose et glucose), ou d'oligosaccharides (dérivés de cellulose), la réaction de Fischer-glycosylation, utilisant l'alcool propargylique comme accepteur de motif glycosyle, a été utilisée pour fonctionnaliser l'extrémité réductrice du sucre avec un groupe alcyne. Une optimisation du procédé de synthèse en deux étapes a permis d'obtenir de façon quantitative des oligosaccharides fonctionnalisés de degré de polymérisation moyen (\overline{DP}_n) allant jusqu'à 8. Le couplage par réaction de Huisgen, avec différents acides gras porteurs de fonctions alcyne a ensuite permis de préparer une série de tensioactifs bio-sourcés. Les propriétés tensioactives et d'auto-assemblage de quatre dérivés amphiphiles de type oligomannose et présentant des parties hydrophobes de taille variable (acide oléique et ricinoléique) ont été étudiées en milieu aqueux par diffusion de la lumière et des rayons X, ainsi que par cryo-microscopie électronique en transmission. Des études des relations structure-propriétés ont pu être avancées permettant d'expliquer les différents comportements d'auto-assemblage observés. Dans une dernière étude, les tensioactifs dérivés du mannose ont été exploités pour stabiliser des émulsions O/W avec différentes huiles végétales. Ces émulsions ont montré une excellente stabilité colloïdale sur plusieurs mois et une interaction spécifique avec une lectine (ConA) se liant au mannose.

Abstract

This work was dedicated to the synthesis of end-functional oligosaccharides to prepare new biobased surfactants. Starting from unprotected monosaccharides (mannose and glucose) or oligosaccharides (derived from cellulose), Fischer-Glycosylation reaction with propargyl alcohol as glycosyl acceptor was utilized to functionalize the reducing-end of the sugars with an alkyne group. With the optimization of the synthesis process in two-steps, functionalized oligosaccharides could be obtained quantitatively with average degree of polymerization (DP_n) up to 8. The Huisgen cyclo-coupling with azide functionalized long chain fatty acids afforded subsequent a series of bio-based surfactants. The surfactant properties and the self-assembly of four oligomannose-derived amphiphiles with different hydrophobic tails (oleate and ricinoleate) have been studied *via* dynamic light- and X-ray scattering, as well as by cryo-transmission electron microscopy. The study of structure-property relationships could be realized explaining the different self-assembling behavior. In a final study, the mannose-derived surfactants were exploited to stabilize O/W emulsions with different vegetable oils. The emulsions showed an excellent colloidal stability over several months and a specific interaction with lectin (ConA), binding to mannose.

Abbreviations

Chemicals

PGA	Propargyl alcohol
PMan	Propargyl mannopyranoside
(PMan) _n	Propargyl-(oligo)-mannopyranoside
MeRic	Methyl ricinoleate
MeOI	Methyl oleate
TBD	1,5,7-triazabicyclo[4.4.0]dec-5-ene
BSTFA	<i>N,O</i> Bis(trimethylsilyl)trifluoroacetamide
FAE	Fatty acid ester
N ₃ OI	3-azido-1-propyl oleate
N ₃ Ric	3-azido-1-propyl ricinoleate
N ₃ Pric; N ₃ (Ric) _n	3-azido-1-propyl-(oligo)-ricinoleate
(PMan) ₃ - <i>b</i> -OI	Propargyl manno-(tri)-pyranoside- <i>block</i> -oleate
(PMan) ₈ - <i>b</i> -OI	Propargyl manno-(okta)-pyranoside- <i>block</i> -oleate
(PMan) ₃ - <i>b</i> -Ric	Propargyl manno-(tri)-pyranoside- <i>block</i> -ricinoleate
(PMan) ₈ - <i>b</i> -Ric	Propargyl manno-(okta)-pyranoside- <i>block</i> -ricinoleate
MCC	Microcrystalline Cellulose
COS	Cellulose-Oligosaccharides
PGA-COS	(Propargyl)-Cellulose-Oligosaccharides
ConA	Concanavalin A
RCA ₁₂₀	Ricinus Communis Agglutinin
PBS	Phosphate Buffered Saline

Techniques

NMR	Nuclear Magnetic Resonance Spectroscopy
COSY	Homonuclear Correlation Spectroscopy
HSQC	Heteronuclear Single-Quantum Correlation Spectroscopy
HMBC	Heteronuclear Multiple Bond Correlation Spectroscopy
NOESY	Nuclear Overhauser Enhancement Spectroscopy
MALDI-TOF	Matrix Assisted Laser Desorption/Ionisation-Time of flight
ATR-IR	Attenuated Total Reflectance Infrared Spectroscopy
SEC	Size Exclusion Chromatography
GC-FID	Gas Chromatography with Flame-Ionization Detection
ITC	Isothermal Titration Calorimetry
DLS	Dynamic light scattering
SAXs	Small Angle X-ray Diffraction
Cryo-TEM	Cryo-Transmission Electron Microscopy

Characteristics

\overline{M}_n	number average molar mass
\overline{DP}_n	Average degree of polymerization
PDI or Đ	Polydispersity index or Dispersity
HLB	Hydrophilic-Lipophilic-Balance
R_H	Hydrodynamic radius
R_g	Radius of gyration

γ	Interfacial Tension
CAC	Critical Aggregation Concentration
CMC	Critical Micelle Concentration
ΔG^o	Gibbs Energy
A_{min}	Minimum Surface Area

General Table of Contents

Resumé/Abstract	
Abbreviations	
General Introduction	i

Chapter I: Bibliography

Contents

1 Carbohydrates	5
1.1 Historical introduction to sugar chemistry	5
1.2 Monosaccharides	6
1.2.1 Nomenclature and Structures	6
1.2.2 Mutarotation	10
1.2.3 Conformational Analysis	11
1.2.4 Anomeric Effect	11
1.3 Disaccharides	14
1.3.1 Formation of Glycosidic Linkage	14
1.4 Polysaccharides	14
1.4.1 Cellulose	14
2 Oligosaccharide Synthesis	16
2.1 O-Glycosylation	17
2.1.1 Reaction	17
2.1.2 Historical development and concepts	17
2.1.3 Mechanism	21
2.1.4 Protecting Group Free approaches	23
2.1.5 Alkynyl Glycosides: Propargyl glycosides	26
2.2 General methods for oligosaccharide synthesis	29
2.2.1 A) Chemical Oligomerization strategies	29
2.2.2 B) Depolymerization methods	37
3 Sugar based surfactants	41
3.1 Introduction bio-based surfactants	41

3.2	Sugar based surfactants.....	43
3.3	Alkyl polyglycosides (APG)	44
3.4	End-functionalization of oligosaccharides to prepare amphiphilic conjugates.....	50
3.5	Azide-alkyne Huisgen cycloaddition (CuAAC).....	55
4	Self-assembly of amphiphilic molecules and polymers	57
4.1	Principles of Self-Assembly of amphiphilic molecules.....	57
4.2	Critical micelle concentration (CMC).....	60
4.3	Self-assembly of amphiphilic molecules to micelles and vesicles	62
4.4	Principles of Self-Assembly of amphiphilic copolymers	64
4.5	HLB of Surfactants.....	68
5	O/W - Emulsions.....	69
5.1	Definition and Basics.....	69
5.2	Colloidal Stability.....	70
5.3	Preparation of Emulsions	75
7	Conclusion.....	77
8	Bibliography.....	79

Chapter II A: Sequential acid-catalyzed alkyl glycosylation and oligomerization of unprotected carbohydrates

Contents

1	Introduction	86
2	Step 1: Propargylation.....	87
2.1	First screen of reaction conditions.....	87
2.2	Analysis of PMan by NMR spectroscopy	92
2.3	Kinetic study by NMR	97
2.4	Kinetic study by GC and ESI-MS.....	102
3	Step 2: Oligomerization.....	108
3.1	Kinetic study	108
3.2	Discussion on the reaction mechanism	115

3.3	Optimization of the oligomerization reaction	119
4	Structural elucidation of (PMan) _n	123
5	Application to other Monosaccharides: Glucose	129
6	Conclusion	130
7	Appendix	132
8	Bibliography	152

Chapter II B: Depolymerization and functionalization of cellulose by ball-milling

Contents

1	Introduction	156
2	Depolymerization and functionalization of cellulose	157
2.1	Mechanocatalytic depolymerization	157
2.2	End-functionalization with propargyl alcohol	161
3	Conclusion	166
4	Appendix	168
	Bibliography	172

Chapter III: Self-assembly and surfactant properties

Contents

1	Introduction	179
2	Preparation of the amphiphiles	180
2.1	Functionalization of fatty acid methyl esters (FAME)	180
2.2	Huisgen Click reaction	188
3	Self-assembly	193
3.1	Critical aggregation concentration (CAC)	193
3.1.1	Tensiometry: Pendant Drop (PD)	193
3.1.2	Isothermal Titration Calorimetry (ITC)	199
3.2	Direct Solubilization	201
3.2.1	Dynamic light scattering (DLS)	202

3.2.2	SAXS.....	207
4	Conclusion.....	214
5	Appendix.....	216
	Bibliography.....	220

Chapter IV: Emulsions and molecular targeting

Contents

1	Introduction	227
2	O/W Emulsion: Castor oil	228
2.1	Surfactant/Castor oil/water	228
2.2	Surfactant/Castor oil/PBS.....	230
3	O/W Emulsion with different oils	234
3.1	Emulsions with different oils in water	234
3.1.1	Mineral Oil.....	235
3.1.2	Sunflower Oil	236
3.1.3	Olive Oil.....	237
3.1.4	Soybean Oil.....	238
3.2	Surfactant/PBS/Sunflower, - Soybean, - or Olive oil 37°C	240
3.3	Emulsions with mixtures of mannose- and glucose-based surfactants	241
3.3.1	Emulsions with glucose-based surfactants.....	242
3.3.2	Emulsion with mixtures of mannose- and glucose-based surfactants	243
4	Molecular targeting: Concanavalin A (ConA).....	243
5	Conclusion.....	250
6	Appendix.....	251
	Bibliography.....	254

	General Conclusion and Perspectives.....	256
--	------------------------------------------	-----

Chapter V: Experimental Section

Contents

1	Methods and Chemicals	264
1.1	Chemicals	264
1.2	Methods	264
2	Glycosylation of Sugars.....	277
3	Functionalization of Fatty Acids.....	278
4	Huisgen-Cycloaddition	281
5	Ball-milling protocol	283
6	Self-Assembly protocols	283
7	Emulsion protocols and molecular targeting	284
8	Calibration and Kinetic study.....	284
8.1	GC-Chromatography	284
8.1.1	Calibration of Mannose	286
8.1.2	Calibration of PMan	287
8.2	Size-exclusion-chromatography.....	288
8.2.1	Calibration of Mannose	288
8.2.2	Calibration of PMan	290
9	Calculation of <i>DP_n</i> and <i>M_n</i> by ¹ H-NMR spectroscopy.....	292
10	Calculation of MW and DP by Mass spectroscopy	294
11	Appendix.....	297
	Bibliography.....	311

General Introduction:



“Meeting the needs of the present without compromising the ability of future generations to meet their own needs...”^[1] The probably most quoted definition of sustainability from the United Nations World Commission on Environment and Development outlines the collective task of our society, especially during the ecological crisis of the 21. century. Already for over 50 years, scientists have sounded alarms regarding climate change caused by burning of fossil fuels and indicated the devastating consequences if the CO₂ emissions continues to climb.^[2] The Intergovernmental Panel on Climate Change (IPCC) concluded 2014 that the dominate cause of the observed warming has been the human influence.^[3] Besides, there was a long-held scientific consensus blaming humans to affect the earth climate by their carbon emission reported by Cook et al. in 2016.^[4] In 2012, green-house-gas emissions (GHG) associated with the production and disposal of plastic was accounted to the emission of 390 million tons CO₂ globally^[5]. This presents to date only 1 % of the global annual carbon budget but is predicted to increase importantly if the plastic usage keeps continuing in the speed it does actually. Here, it needs to be mentioned that today only 6 % of the total oil produced worldwide are utilized to manufacture polymers. Not only the emissions of GHG arising from polymers, but also the great number of waste generated each year presents a big hurdle since the begin of commercial synthetic chemistry in the mid-19th century. There was about 275 million metrictons (MT) of plastic waste provoked in 192 coastal countries in 2010. Among them, 4.8 to 12.7 million MT entered the ocean. There are suspected calculations of about 150 million tons of total plastic accumulation in our world ocean systems today.^[6] Deadly effects on marine organism through physical entanglement, ingestion of microplastic and coral reef destruction are just few consequences to name.

The group around J. B. Zimmermann^[7] illustrated the ‘characteristics of today’s and tomorrow’s chemical sector’ in their review based on the design for a green chemistry future published in 2020. Thereby, they addressed on the development from a singular focus-based design of a chemical product to a more broaden and sustainable approach.

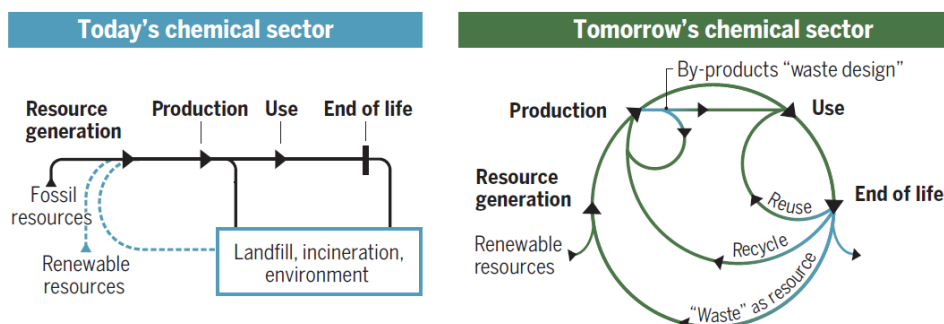
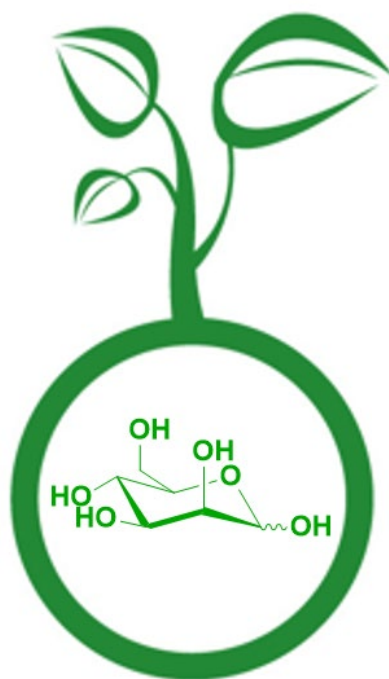


Figure 1. Schema of today’s and tomorrow’s chemical sector.^[7]

Indeed, the early aim of a chemical product was defined mainly by one definition of function: “performance”. The function of sustainability seemed not to be relevant, resulting in a linear path for chemical production. They were mainly based on fossil fuels going through a production chain with the only target of high reactivity. Products being toxic, unintentionally

persistent or generating waste at rates higher than their intended production (25 to 100 times for pharmaceutical products e.g.) mainly ended up on landfill or incineration and damaged consecutively our environment. The past could demonstrate the failed efforts attempting recycling of polymeric material. Only 2 %^[8] out of the total plastic produced is recycled globally. Moving the chemical sectors to circular processes, where not only conditions and circumstance during the production, but also the inherent nature of the product and their end-of-life perspectives are taken into account, are crucial nowadays. A closed carbon cycle and the “defossilisation” might be achieved within the transition from fossil- to renewable-based chemistry. Lignocellulosic biomass^[9] among with CO₂^[10] are the most promising feedstocks, since they are available in sufficient amount. Not only the tons of lignocellulose produced each year makes it an abundant feedstock of renewable carbon world wide. The photosynthetic carbon capture by plant biomass is an effective strategy to fight against climate change. Forest restoration, together with exploitation of underutilized biomass can be one key-factor to finally decouple chemical production from fossil fuels (besides the energy needed to synthesize chemicals). Surely, the production of chemicals from renewable resources needs to be at least as sufficient, bearing comparable or improved properties and showing better life-cycle assessments as petroleum-based ones. However, this transition is inexcusable to every scientist and close to nature, where waste does not exist.

Chapter I: Bibliography



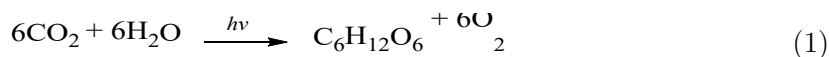
Contents

1	Carbohydrates	5
1.1	Historical introduction to sugar chemistry	5
1.2	Monosaccharides	6
1.2.1	Nomenclature and Structures	6
1.2.2	Mutarotation	10
1.2.3	Conformational Analysis	11
1.2.4	Anomeric Effect	11
1.3	Disaccharides	14
1.3.1	Formation of Glycosidic Linkage	14
1.4	Polysaccharides	14
1.4.1	Cellulose	14
2	Oligosaccharide Synthesis	16
2.1	O-Glycosylation	17
2.1.1	Reaction	17
2.1.2	Historical development and concepts	17
2.1.3	Mechanism	21
2.1.4	Protecting Group Free approaches	23
2.1.5	Alkynyl Glycosides: Propargyl glycosides	26
2.2	General methods for oligosaccharide synthesis	29
2.2.1	A) Chemical Oligomerization strategies	29
2.2.2	B) Depolymerization methods	37
3	Sugar based surfactants	41
3.1	Introduction bio-based surfactants	41
3.2	Sugar based surfactants	43
3.3	Alkyl polyglycosides (APG)	44
3.4	End-functionalization of oligosaccharides to prepare amphiphilic conjugates	50
3.5	Azide-alkyne Huisgen cycloaddition (CuAAC)	55
4	Self-assembly of amphiphilic molecules and polymers	57
4.1	Principles of Self-Assembly of amphiphilic molecules	57
4.2	Critical micelle concentration (CMC)	60

4.3	Self-assembly of amphiphilic molecules to micelles and vesicles	62
4.4	Principles of Self-Assembly of amphiphilic copolymers.....	64
4.5	HLB of Surfactants.....	68
5	O/W - Emulsions	69
5.1	Definition and Basics.....	69
5.2	Colloidal Stability.....	70
5.3	Preparation of Emulsions.....	74
7	Conclusion.....	77
8	Bibliography.....	79

1 Carbohydrates

From all the classes of organic compounds occurring in nature, carbohydrates can be seen as one of the largest abundant and divers' ones. They are produced during the most important reaction assuring life on earth by employing sunlight: photosynthesis.



They are found distributed in animal and plant tissues, where they fulfil different functions as energy reserves (starch, glycogens), structural materials (cellulose, chitin, mannans), cell recognition derivatives (oligoproteins and glycolipids), information transfer agents (nucleid acid) and more.^[11] Due to their waste availability and versatility, they found applications in foods, nutraceuticals, pharmaceuticals, textiles, papers and biodegradable packaging materials.^[12]

1.1 Historical introduction to sugar chemistry

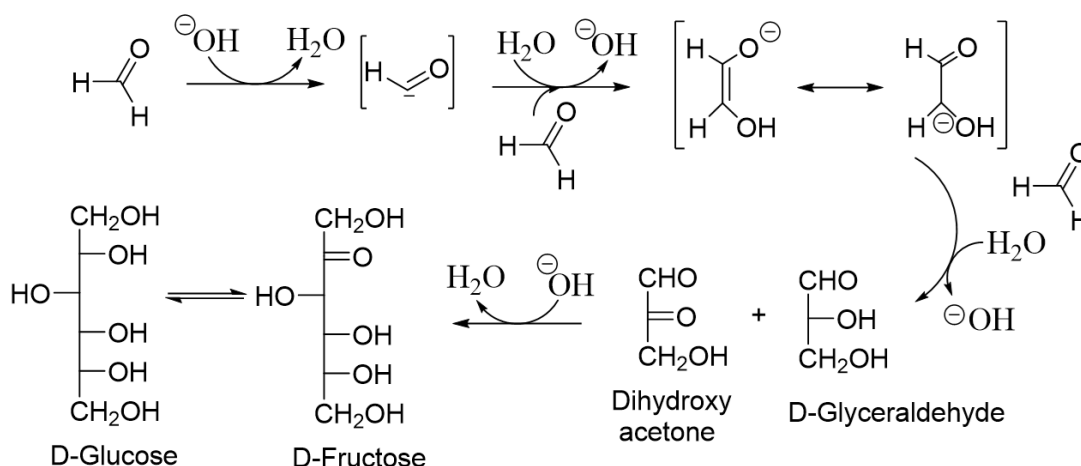


Figure 2. The Formose reaction.^[13]

The beginning of the utilization of sugars dates back to the eight century before Christ were sugars were already famous as sweetener (sucrose) though only affordable by the very wealthy.^[13] The first observation of the formation of a sugar came along with Alexander Butlerov's discovery of the formose reaction in 1861 (Figure 2).^[14] It could be shown that glucose was the major product formed out of simple formaldehyde. But what is exactly a sugar, respective a carbohydrate? Pioneer works of the "father of carbohydrate chemistry" Emil Fischer gave them - the hydrates of carbon - a simple empirical formula: $\text{C} \cdot \text{H}_2\text{O}$ (or CH_2O), hence $\text{C}_5\text{H}_{10}\text{O}_5$ and $\text{C}_6\text{H}_{12}\text{O}_6$ as molecular formulae.^[15] The evidence of the presence of an aldehyde or ketone group referred them with terms like aldopentose/aldohexose or

ketopentoses/ketohexoses, respectively. Nowadays, the term ‘carbohydrates’ has a much larger definition including simple mono- to polymeric forms, oxidized or reduced sugars and/or other types of atoms (nitrogen, sulfur...).[16] The elucidation of the structure and relative conformation of monosaccharides were accomplished with combination of polarimetry and chemical techniques by Fischer *et al.* in 1891. To the starting point of his analysis in 1870, only two aldohexoses (glucose and galactose), one ketose (fructose) and three disaccharides (lactose, maltose and sucrose) were noted. Sugars were known to be composed of 6 carbons, 6 oxygens and 12 hydrogens and to be able to reduce Tollens’ reagent ($[\text{Ag}(\text{NH}_3)_2]^+$). Together with the work of Kiliani, they reported that glucose and fructose share the same configuration at C-3, C-4 and C-5 due to the formation of identical osazones upon the reaction of phenylhydrazine. The additional results for glucose and mannose, showing likewise the formation of the same (Figure 3), led consequently to the conclusion that the latter are C-2 epimers.

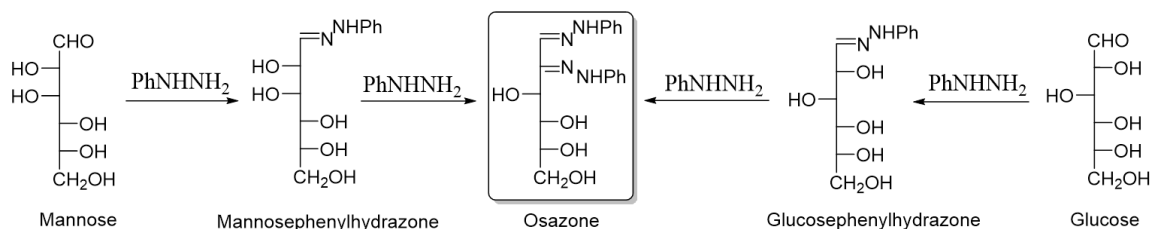


Figure 3. Reaction of mannose and glucose resulting in the formation of the same osazone.[13]

The next breakthrough was the discovery of the reduction of sugar lactones to their corresponding aldoses. It was proved, that the D-enantiomers of arabinose, glucose, mannose and fructose exhibit all the same configuration at the chiral centres of C-1 - C-3. With the help of polarimetry, the correlations of the configuration and optical activities could be assigned. This provided the final piece to determine the configuration of the aldopentoses.[13] At that time, Fischer published his famous ‘Fischer Projection’ that became a universal way to present the two-dimensional form of sugars in a linear form.[17] The position of the hydroxyl group of the lowest chiral centre (C-5) of D-glucose on the right side was initially a hazardous decision of Fischer, confirmed 60 years later by X-ray crystallography.[18] Altogether, Fischer provided the foundation of organic and bioorganic chemistry of carbohydrates and could transfer his inspiration to over 300 doctoral students.

1.2 Monosaccharides

1.2.1 Nomenclature and Structures

Prior to the systematization thanks to the work of Emil Fischer (see below), the names of the carbohydrates found commonly their origins in their source. Fructose as the ‘fruit sugar’, glucose as the ‘grape sugar’ and lactose as the ‘milk sugar’. By time, a systematic

nomenclature was developed. Sugars are generally defined as polyhydroxy- aldehydes and ketones with a general formula of $C_n(H_2O)_n$. They are separated into mono- and more complex oligo- and polysaccharides, whereas the monosaccharides are the building blocks of the latter. There are two major groups of monosaccharides, differentiated whether their acyclic form possesses an aldehyde- (aldose) or a keto (ketose) group. The prefix added at the end is used to distinguish between these two forms: -ose is used for the group of aldoses and -ulose for the group of ketose, respectively. According to the number of carbons in their skeleton they are counted via the IUPAC rules^[19]: triose (C_3), tetrose (C_4), pentose (C_5), hexose (C_6), heptose (C_7), octose (C_8), nonose (C_9) etc.^[11] As every second carbon atom of the sugar alcohol is sp^3 hybridized, it contains consequently a chiral centre. This geometry is visualized within the uniform Fischer-projection. Thereby, the carbon chain is drawn vertically having the carbonyl group placed at the top and the last carbon atom at the bottom. Here, all vertical lines present the chain lying below an imaginary plane and all horizontal lines above it. The carbon atoms are counted starting from the carbonyl atom. For a better illustration, the manipulation of the Fischer-projection of the simplest monosaccharide, glyceraldehyde, is shown in Figure 4.^[13]

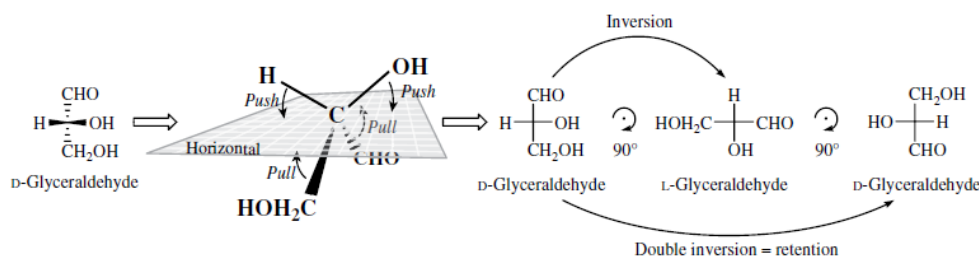
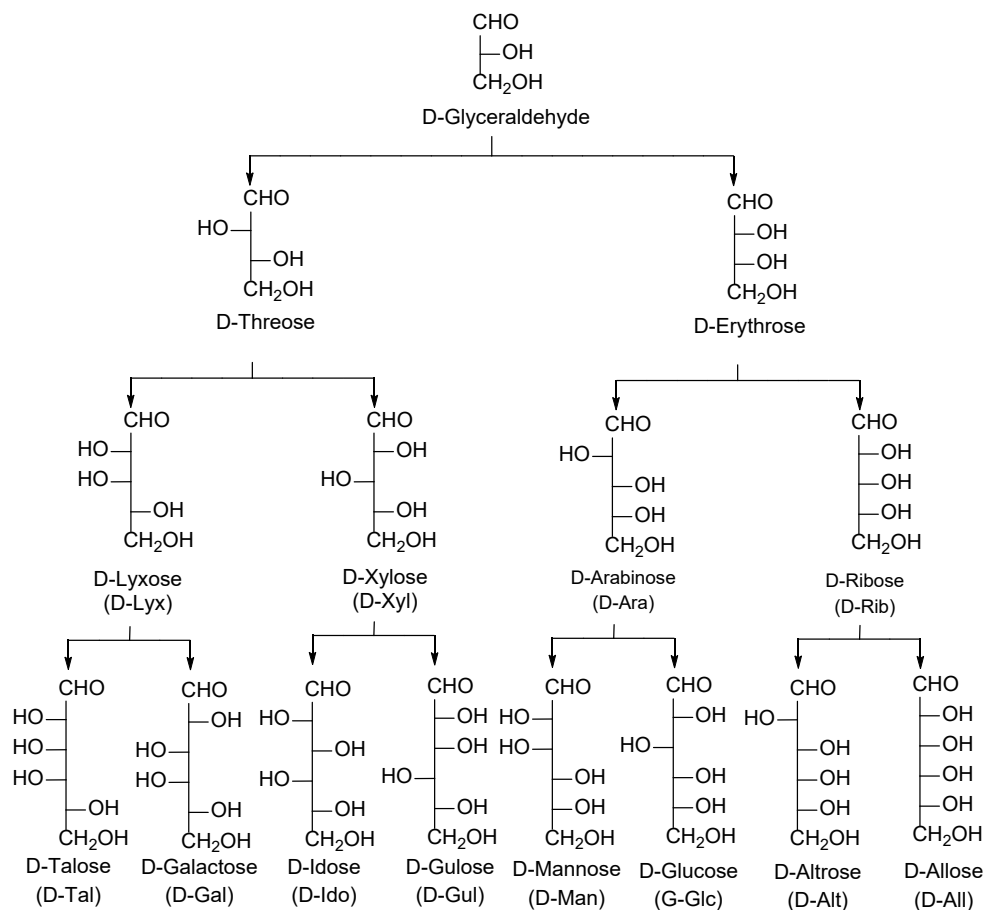
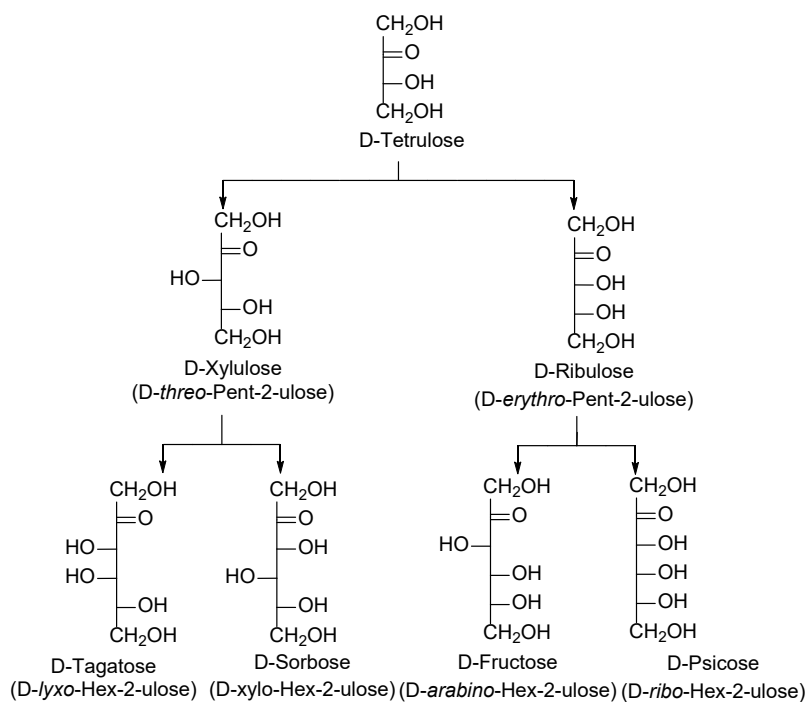


Figure 4. Manipulation of the Fischer-projection of D-Glyceraldehyde.^[13]

The prefix *D* and *L* in the example of Figure 4 distinguish between the two enantiomeric forms of the monosaccharides. If the OH group at the highest numbered chiral atom is at the right side, the prefix D- and if it is at the left side, prefix L is assigned. Enantiomers are characterized by the fact, that their mirror images are nonsuperposable to each other. Each of them inhibits a series of diastereomers by changing the configuration of another (but only one) stereocentre. Since every chiral carbon atom has a mirror image and the number of those atoms determines the number of possible isomers n , there are 2^n possibilities. The series of the D-aldoses, respectively D-ketoses are illustrated in the following figures.

Figure 5. Family tree of D-aldoses.^[13]Figure 6. Family tree of D-ketoses.^[13]

These open-ring structures, however, are not the favoured configuration of sugars. Intramolecular nucleophilic attack by the hydroxyl group at C-4 or C-5 on the carbonyl group

leads to the consequent formation of a five-membered furanose- or a six-membered pyranose hemiacetal (Figure 7).

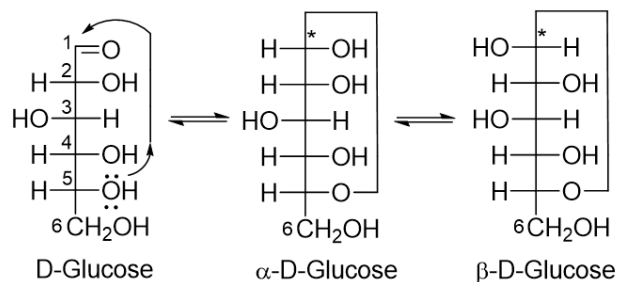


Figure 7. Intramolecular nucleophilic attack by the OH atom at C-5 on the carbonyl group leading to pyranose hemiacetal ring in its two anomeric form.^[11]

The cyclization affords a new chiral centre at the C-1 atom which is termed the anomeric position. This results to the formation of two new diastereomers named α - and β -anomer. In the Fischer-projection, the anomeric exocyclic substituent and the oxygen of the ether bond are *cis* for the α -anomer and *trans* for the β -anomer (Figure 8, (b)). Haworth developed another projection to simplify the anomeric configuration in a three-dimensional perspective. In its projection, the anomeric OH group is on the bottom face for the α -anomer and on the top for the β -anomer (Figure 8, (c) and (d)).

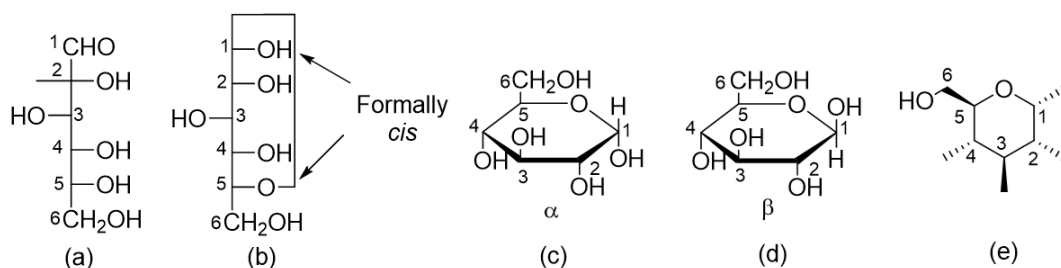


Figure 8. Different projections of α -D-glucose. (a) linear Fischer projection, (b) cyclic Fischer, (c) & (d) Haworth, (e) Mills projection.^[13]

1.2.2 Mutarotation

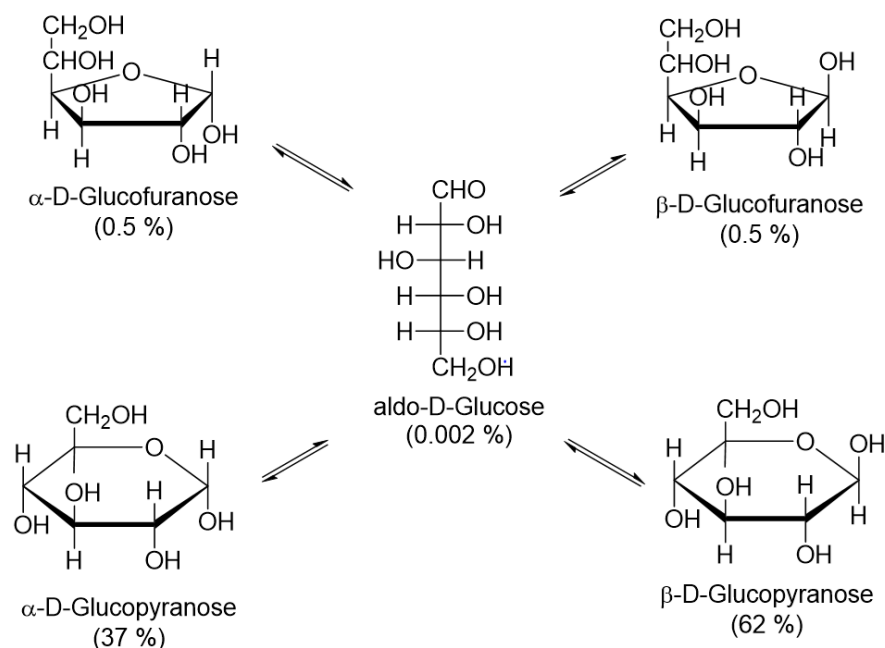


Figure 9. Tautomeric forms resulting of the mutarotation of D-glucose.^[11]

The anomeric forms of sugars are tent to transform into one another if they are dissolved in an aqueous solution. The two isomers are also called ‘epimers’. The isomerization process is called mutarotation^[20] and is characterized with the change in optical rotation of polarized light. Here, α -D-glucose has a value of specific rotation of $+112^\circ$, whereas its β -anomer provokes only a value of $+19^\circ$. Upon equilibration, these two species show a value of $+52^\circ$. There are five different forms within this equilibrium mixture: α -D-glucopyranose, β -D-glucopyranose, α -D-glucofuranose, β -D-glucofuranose and one open ring form aldo-D-glucose (Figure 9). The transformation into each other can be either base- or acid-catalyzed (Figure 10, respectively Figure 11) and is in general a very slow process. It is affected by temperature, polarity of the solvent and some enzymes that are capable to promote this reaction. In general, the six-membered ring- (pyranoside) is preferred to the five-membered ring form (furanoside), whereas for the α - and β -anomers, the preference differs drastically depending on the sugar species (D-Glucose: 36.4 % for α and 63.6 % for β , D-Mannose: 76.4 % for α and 32.6 % for β).

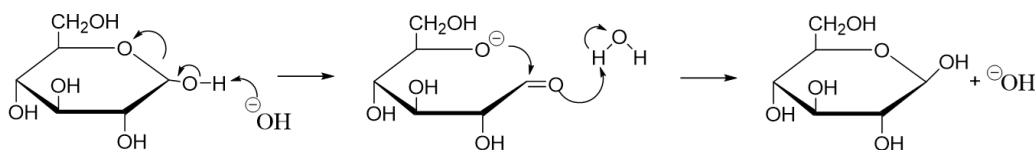
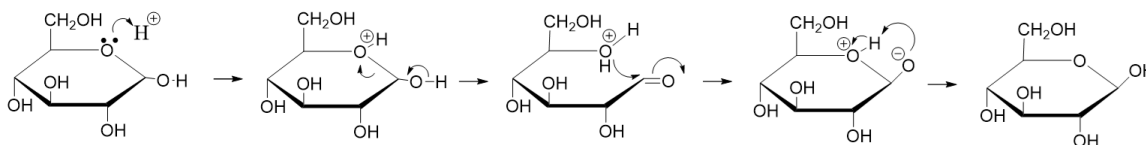


Figure 10. Mutarotation catalyzed by a base.^[11]

Figure 11. Mutarotation catalyzed by an acid.^[11]

1.2.3 Conformational Analysis

To get more insights to the real structures of sugars, three-dimensional modelling that uses correct bond lengths and angles of the sp^3 -hybridized carbons were elaborated. They showed that the sugar rings are not flat but form numerous of different shapes. The term ‘conformation’ is referring the relative position of the proton atoms and hydroxyl groups to the ring. The different shapes are called conformers and since they are convertible to each other, they create another group of isomers. Their nomenclature contains one big letter indicating the form (for example C for chair) with a superscripted number for the atom located above the plane of the ring and a subscripted number for the atom located below the plane of the ring (see Figure 12).^[11]

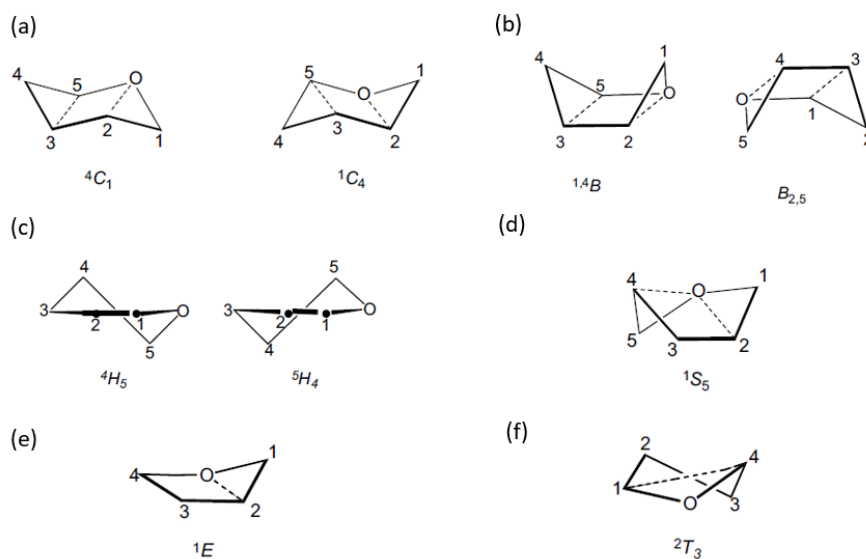


Figure 12. Conformation of the pyranose ring (a) chair, (b) boat, (c) half chair, (d) skew; conformation of the furanose ring (e) envelope, (f) twist; for (b)-(f) only the most common are depicted (total number for (b) = 6, (c) = 12, (d) = 6, (e) = 10, (f) = 10.^[11]

1.2.4 Anomeric Effect

Among these various possibilities, the conformer which possesses the minimum of free energy is the most stable and common one. The free energy is calculated based on the attractive and repulsive interactions like the van-der-Waals forces (vdW), polar and hydrophobic interactions, hydrogen-bridges, steric interactions, solvation effects and tensions due to the

bond's length and angles. A demonstration is given by the favoured conformer of D-glucose, β -D-Glucopyranose, shown in Figure 13. In general, equatorial substituents are less sterically demanding than axial substituents and though energetically preferred. The 4C_1 conformation of glucose presents the most stable one, having all bulky hydroxyl groups in the equatorial plane and all protons in the axial plane. To this, Hassel and Ottar presented 1947^[21] the 'Hassel-Ottar effect', pointing out the unfavourable 1,3-diaxial interactions between the axial substituents at C-1, C-3 and C-5 ((c), Figure 13). The most instable situation in a pyranose ring is the so-called 'delta 2' ((b) and (d), Figure 13). The instability arises from the unfavorable position of the hydroxy group at C-2, which cuts the angle formed by the ring oxygen and the OH group of C-1 into two. β -D-mannopyranose is one of the natural sugars that have the OH-2 in the axial position so that the 'delta 2' conformation is possible.^[11]

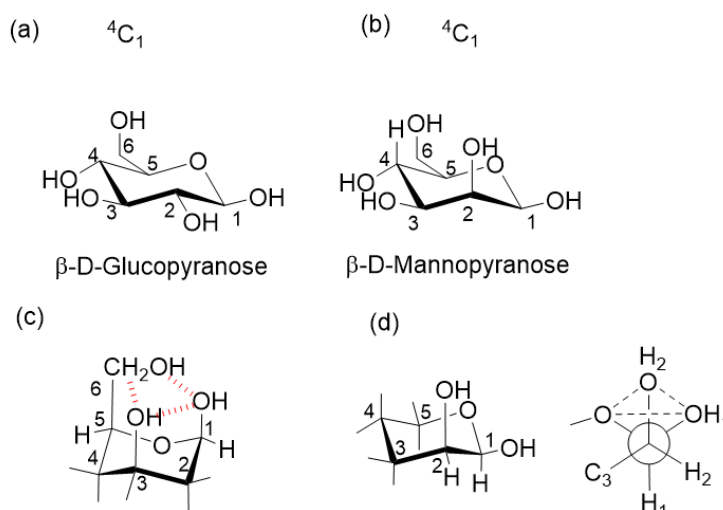


Figure 13. (a) β -D-glucopyranose, (b) β -D-mannopyranose, (c) 1,3-diaxial interactions referred to the 'Hassel-Ottar' effect, (d) delta-2 effect.^[11]

Later, John Edward^[22] analyzed the effect of the substituents at the anomeric centre. He assigned a general higher stability for α -D- 4C_1 -anomers than for their β -counterparts. This phenomena was later defined by Lemieux^[23] as the 'anomeric effect'. Even though there are numerous of theories to explain this special behaviour of sugars, all of them are based on hyperconjugative- and electrostatic effects. The nonbonding electron pair of O-5 has thereby the most important role. The substituent R at the anomeric position is effected of the lone pair electrons from O-5, if it is in the axial position. Then, it has an antiperiplanar position towards the C1-X antibonding orbital. The electrons of the lone pair get delocalized and stabilizes the empty orbital of the C1-X through hyperconjugation ($n-\sigma$). This effect gets even more important, if the substituent R is electronegative ($X = O, S, N, F, Cl, Br$ or I). Then, the combination of electronic suction of the adjacent ring oxygen and the substituent afford an electron deficient at the anomeric position. In the case of an equatorial substituent at the

anomeric centre, the distance of the orbitals gets too large and the stabilization described above can't occur. Therefore, the α -anomer is generally preferred over its β -counterpart.

The stabilization through hyperconjugation is not the only explanation for this preference. There is an electrostatic effect arising from the dipole-dipole interaction of the ring oxygen and the substituent at the anomeric carbon atom. If X is in an equatorial position (β -anomer), its lone pairs interacts strongly with the ring oxygen. In addition, the Newman-projection demonstrates the repulsion effects in the C-5–O-5–C-1–X system (Figure 14, c), showing the preference of synclinal (*gauche*, α) over antiperiplanar (*anti*, β) conformation. The anti-conformer has the electronegative substituent X placed between two lone pairs, which results in higher repulsion and lower stability. Besides the two effects just described, there can be other factors that contribute to the anomeric preference such as solvent and sterically hindrance. Water, e.g. as it is a very polar solvent, weakens the anomeric effect. That is why in an aqueous solution both conformers are still present with a free energy difference of only 1.5 kJ mol^{-1} (expected upon theoretical calculations would be 3.8 kJ mol^{-1}).

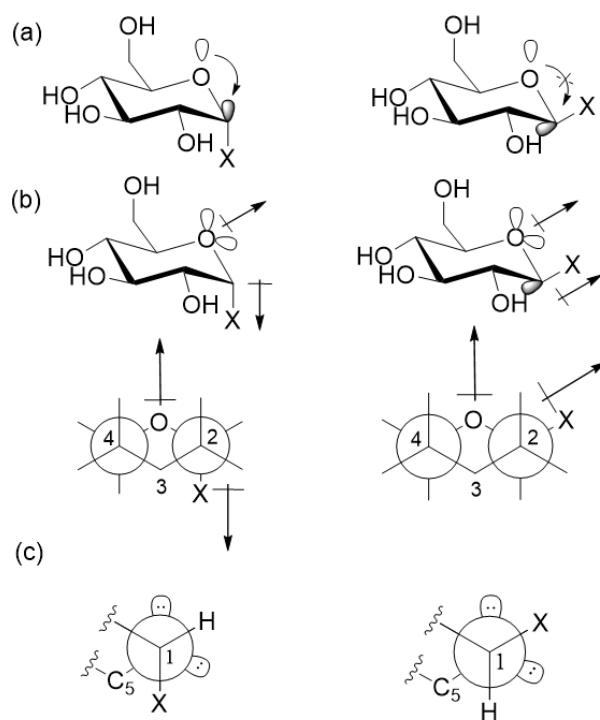


Figure 14. (a) $n-\sigma^*$ interaction = hyperconjugation, (b) dipole-dipole interaction, (c) electrostatic repulsion between lone-pair electrons of the ring oxygen and the anomeric substituent X.^[13]

1.3 Disaccharides

1.3.1 Formation of Glycosidic Linkage

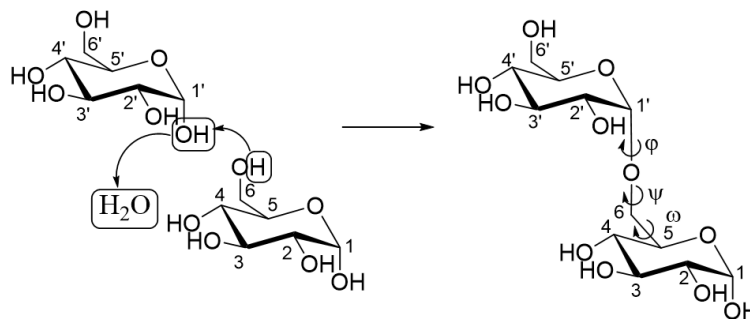


Figure 15. Condensation reaction of two D-glucopyranosides with the degrees of freedom (angles) of the α -(1,6) glycosidic linkage.

Disaccharides are formed by the condensation reaction of two monosaccharide units. Thereby, any nonanomeric hydroxyl atom of one sugar reacts with the anomeric atom of another sugar to form a new ether bond, the so-called glycosidic linkage. Taking into account that both sugar parts can react either with their anomeric centre in α - or β -position, or with any alcohol group at C-2, C-3, C-4 and C-5, there are 11 different possibilities for a binding. For a simple description, the glycosidic linkages are general reported in parenthesis with an arrow referring their position. The simplified nomenclature of disaccharides consists of the atom of the linkage, followed by the abbreviated name of sugar part and its ring size. The disaccharide maltose (two glucose molecules α -1,4 linked to each other) e.g., is written in its short form as the following: O- α -D-Gl p -(1 \rightarrow 4)D-Gl c p . Another classification for the linkage of two monosaccharides is their conformation, described through the three torsion angles φ , Ψ and ω (see Figure 15). The glycosidic bond has in general a very dynamic character and can therefore occupy various conformations with different energies.

1.4 Polysaccharides

1.4.1 Cellulose

According to the International Union of Pure and Applied Chemistry (IUPAC), carbohydrates containing 3 to 10 sugar units are called oligosaccharides and polysaccharides from 11 and more sugar units. They are usually complex biopolymers with possible branching points within the chain and intramolecular cross linking through glycosidic linkages. They are separated in homo- and heteropolysaccharides and possess, except for cyclic rings, a defined chain character from the nonreducing to the reducing end. As for disaccharides, polysaccharides also may have either α - or β - configuration and glycosidic linkages between the sugar units at position 1, 2, 3, 4 or 6. Polysaccharides can be either only composed of sugar units (neutral polysaccharides

such as amylose and cellulose) or contain sugar acids (anionic polysaccharides such as pectins) or cationic groups (cationic polysaccharides, chitosan).

Among them, cellulose is the most abundant polysaccharide on earth. It is produced by nature to 50 - 100 billion tons per year and finds various applications in personal care, paper, textiles, heat insulators, packaging etc. Besides, there are many chemicals and fuels that are produced by cellulose such as ethanol, carboxy- or hydroxyethyl cellulose, cellulose acetate, hydrocarbons, sorbitol, γ -valerolactone and alkyl glycosides to name some of them.^[24] Cellulose was first discovered and isolated by Anselme Payen^[25] in 1838, with a structural elucidation 82 years later by Herman Staudinger^[26]. It is a polymer of varying molar mass and repeating units (DP) ranging from 800 up to 10 000, depending on its extraction method^[24a]. It is composed of cellobiose units (β -D-glucopyranoside β -(1,4) linked to each other), while each glucose unit is rotated 180 ° in the plane to its neighbour, giving cellulose its linear structure. Besides, it has a ‘twisted ribbon’ structure due to the hydrogen bonding between the chains in a parallel or antiparallel sense. The presence of hydroxyl groups at the C-2, C-3 and C-6 position leads to a strong network, so that cellulose is semi-crystalline at a supramolecular level. There, the polysaccharide chains are packed to ‘microfibrils’ with diameters around 10 up to 30 nm, comprising amorphous areas around them. This leads to important rigidity, explaining their application as the most copious building material for cell wall of plants.^[15]

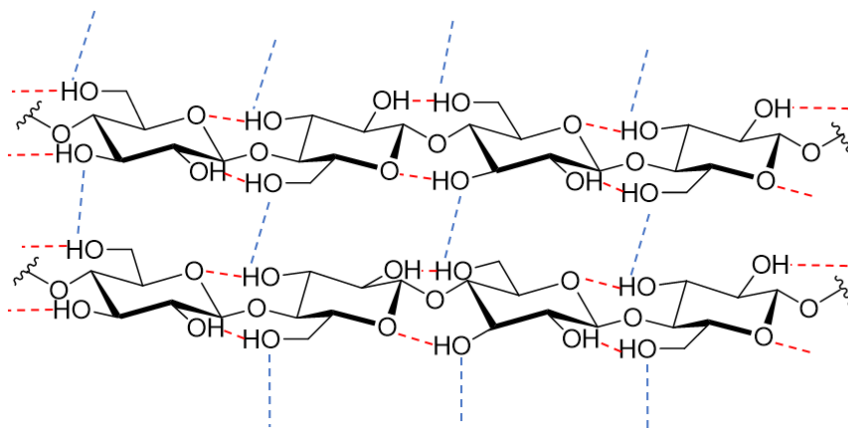


Figure 16. Inter- and intramolecular hydrogen bond network of cellulose.^[27]

This condensed assembling is likewise the reason of the insolubility of cellulose in water and common organic solvents. Researchers applied aqueous acid solutions or mechanical forces and succeed to solubilize the amorphous part and could isolate cellulose-particles (e.g. microcrystalline cellulose (MCC)) that are treatable for laboratory work.

2 Oligosaccharide Synthesis

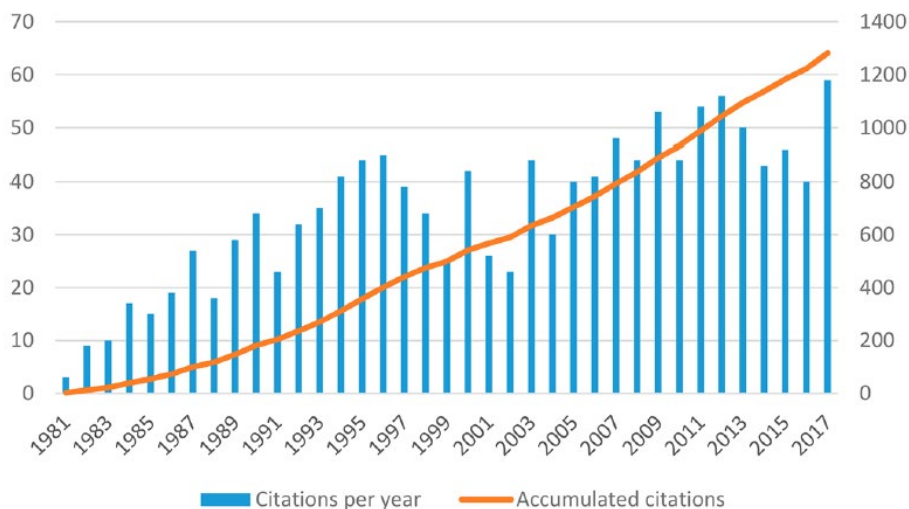


Figure 17. References of Glycosylation reactions during the past forty years.^[28]

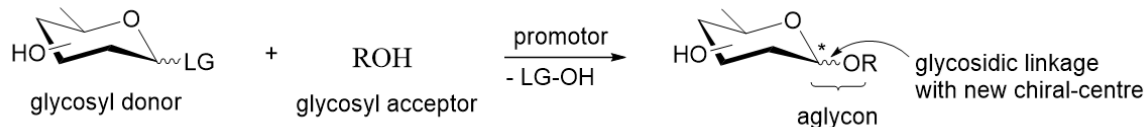
Oligosaccharide-, or glycan^a sequences are found numerous in Nature and notably the human body: over half of all of our proteins are N- or O-glycosylated compounds.^[29] The cell-surface contributes various glycolipids, glycosaminoglycans and free oligosaccharides.^[30] These biomolecules present a lot of potential informations that led to diverse biological and medical applications. Specially in terms of biomarkers, oligosaccharides showed promising features. They could be applied as markers for breast-, colon-, and lung cancer and also as mediation of AIDS, Alzheimer etc.^[31] In general, there are two ways to obtain oligosaccharides, either by isolation of natural products, or chemical synthesis using enzymatic- and/or organic-chemical approaches. Until today, none of these methods could really beat the other so that oligosaccharide synthesis presents still the biggest challenge for glycoscientists.

The main hurdle in their preparation presents the stereo- and regiochemical control of the reaction. A lot of expeditious strategies have been established over the last few decades trying to overcome this challenge.^[32] From the invention of novel glycosyl donors towards the employment of one-pot strategies, the development went up to combinatorial and finally automated approaches. Researchers tried to simplify the preparation by decreasing either purification- or protecting-deprotecting steps. Recently, the invention of automated solid-phase synthesis based on modified peptide synthesizer invented by Seeberger *et al.*^[33] caused high attraction. For any of these strategies, the sugar units are combined by glycosylation, the central-reaction in glycoscience. In order to optimize the oligosaccharide synthesis, this reaction was extensively studied over the past forty years (Figure 17) and will be discussed in the following chapter.

a) glycan is the general term describing any 'compound consisting of a large number of monosaccharides linked glycosidically'^[34]

2.1 O-Glycosylation

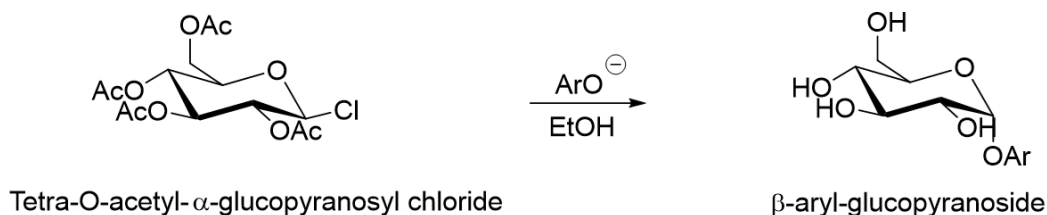
2.1.1 Reaction



Scheme 1. General scheme of the glycosylation reaction.

Typically, a glycosylation reaction presents the coupling of a glycosyl donor with a glycosyl acceptor through the formation of a glycosidic linkage. The glycosyl donor is usually a monomeric sugar, whereas one distinguishes between a carbohydrate based- (glycon or glycosyl unit) and a non-carbohydrate based acceptor (aglycon, ROH, Scheme 1). The new linkage affords an acetal, bearing a chiral centre (*) which again provokes the similar synthesis of two anomers (α - and β -configuration). There are different types of glycosidic linkages, depending on the heteroatom of the glycosyl acceptor, but usually linkages between O, C, S and N-atoms are formed. More precisely, glycosylation can be described as nucleophilic displacement of the leaving group at the anomeric position of the donor by a hydroxyl group of the acceptor.^[16, 32] The full reaction mechanism is a very complex process and, to date, still not fully understood. The recent mechanistic pathways, aspects and factors are discussed in subsection 2.1.3.

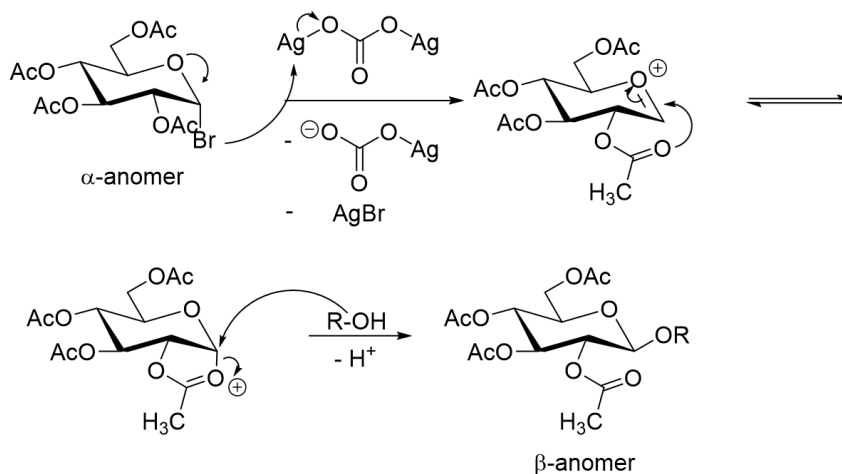
2.1.2 Historical development and concepts



Scheme 2. Synthesis of aryl glycoside by A. Michael.^[35]

The very first report of a synthetic route towards glycosides was already in 1870 when M.A. Colley observed the formation of acetochlorhydrose from glucose upon the reaction with acetyl chloride. Arthur Michael^[36] reported 9 years later the synthesis of pure alkyl glycosides by applying Colley's intermediate to present the first stereoselective glycosylation. He prepared aryl glycosides from tetra-O-acetyl-glucopyranosyl chloride (Scheme 2). Around the same time, A. Gautier synthesized the first ethyl glycoside from the acid catalysed reaction of glucose with ethanol. He falsely assigned his product to be 'Diglucose', which was corrected

by Emil Fischer^[37] in 1893 to provide the basis of the nowadays well-known ‘Fischer-Glycosylation’. It was W. Koenigs and E. Knorr^[38], who could later apply the synthesis of Michael for the preparation of a broad range of different aglycons in 1901. They reported a general glycosylation of acetyl-glucopyranosyl halides with alcohols to exclusively β -alkyl glycosides (Scheme 3) using silver carbonate. The S_N2 character of the substitution step was the key factor to insure the stereoselective outcome of their reaction by inversion of the configuration.



Scheme 3. Koenigs-Knorr reaction mechanism.

At this stage, the utilization of carbohydrate-based glycons instead of alcohols to prepare oligosaccharides was very complicated. The poor nucleophilicity of the hydroxyl groups of the sugars were tried to improve with different catalytic systems. While Koenigs and Knorr worked with Ag_2CO_3 or Ag_2O , Thus, Zemple, Gerecs and later Helferich and Wedermeyer proved that heavy metal catalyst such as mercury (II) salts could improve the reactivity.^[39] But as the reactivity increases, the stereoselectivity got lost, which is a common problem in organic chemistry. Here, Lemieux and Fletcher provided the breakthrough with their work of the relation between the reactivity of glycosyl halides and the nature of various protecting groups at the sugar ring. They reported that the **participating effect** of the acyl group in the C-2 position was responsible for the formation of only 1,2-trans glycoside (see Koenigs-Knorr mechanism, Scheme 3). Consequently, to obtain the 1,2-cis anomer, non-participating groups at the C-2 position were necessary, which lead them to the conclusion, that the conformational outcome was mainly directed by the anomeric effect (see subsection 1.2.4) and the nature of the group at C-2.

For carbohydrates, the choice of a protecting group is generally limited to an ether- or ester compound and can be classified in terms of their influence on the glycosylation reaction. It was found that ether-groups are inert, impeding the nucleophilic attack due to steric hindrance, while ester-groups participate to glycosylation and influence the stereoselectivity of the glycosidic linkage.^[16] Within these new insights, a wave of different glycosyl donors was

reported between 1970 and 1980. To name only the most important, there were thioglycosides^[40], cyanoethylidene^[41], orthoesters^[42], O-imidates^[43], thioimidates^[44], S-benzothiazolyl derivatives^[45], thiopyridyl derivatives^[46] and glycosyl fluorides^[47]. Altogether, the most successful and though widely used today are trichloroacetimidates^[48], thioglycosides^[49] and fluorides.^[50]

Apart from the investigation of different leaving groups, Hashimoto^[51] and Fraser-Reid^[52] reported the **'armed-disarmed' concept** based on Lemieux observations of protecting groups (see below). They postulated, that in general ether linkages at the C-2 position are 'arming', meaning non-participating and leading to 1,2-*cis* glycosides, whereas acyl linkages at the C-2 position are 'armed', showing neighbouring group participation and leading to 1,2-*trans* glycosides. Subsequently, Paulsen noted the difference in stability of benzyl- and acetyl substituted bromide glycosides (Figure 18), which are directly correlated to this concept. He explained that acetyl groups, as they are electron withdrawing, disfavour a positive charge at the C-1 position and though disarm the ring. Ether groups, contrarily, do not hinder the development of a positive charge in the ring, resulting in an armed pyranose. The 'armed-disarmed' concept can be furthermore applied to control the nucleophilicity of the hydroxyl groups of the glycosyl acceptor and slow down the glycosylation reaction if needed.

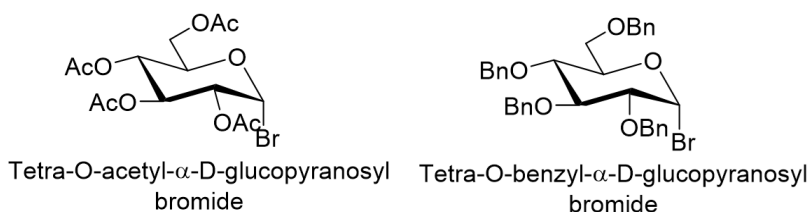
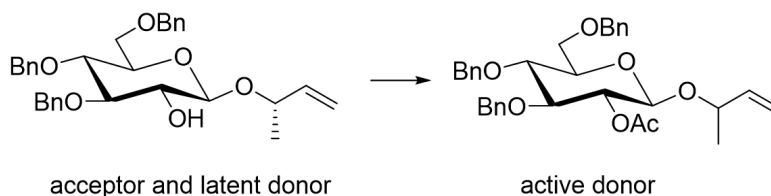


Figure 18. Left = 'disarmed' Acetyl and right = 'armed' benzyl-protected glycoside.

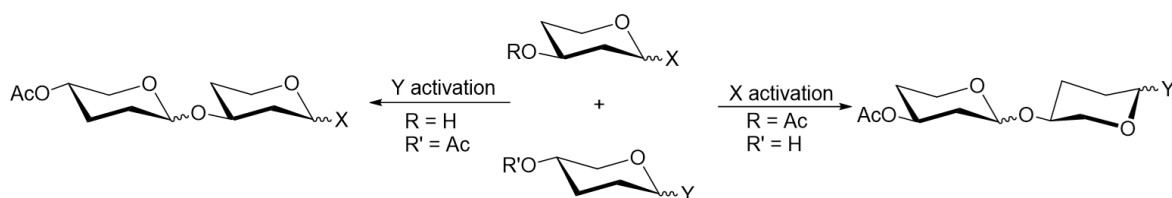
In 1992, Roy *et al.*^[53] laid the foundation for selective anomeric reactivity with the report of the **'latent-active glycosylation' concept**. Here, the 'latent' glycosyl donors possess a stable group at the anomeric position, that remains intact during the corresponding glycosylation reaction. But, by later chemical modifications, it can be turned into an 'active' donor that can be then glycosylated. Scheme 4 shows one famous example for such transformation.



Scheme 4. Transform of a 'latent'- to an 'active' glycosyl donor.^[16]

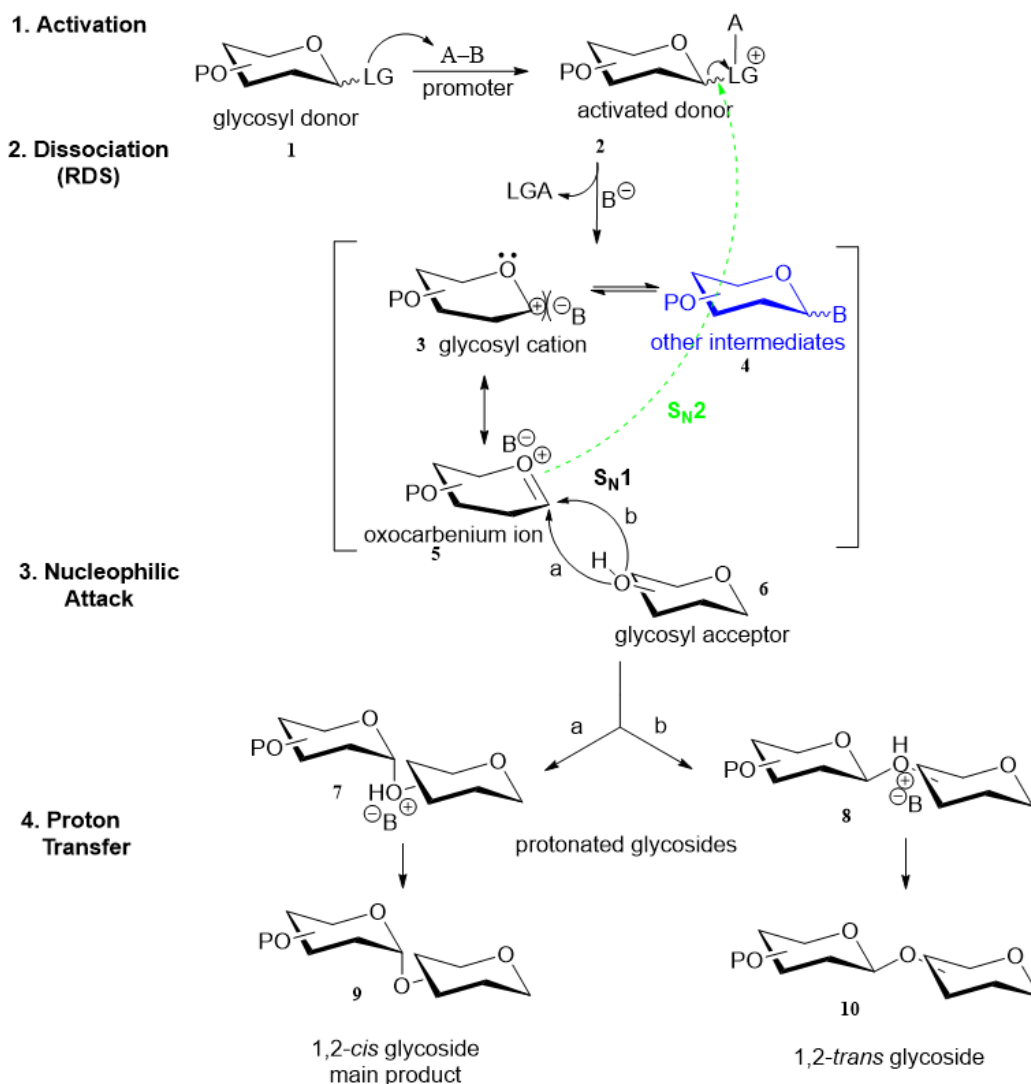
The 'latent/active' concept was at the same time exploited for the synthesis of trisaccharide libraries^[54], employing vinyl- and allyl donors. Finally, Ogawa *et al.* described the **'concept of**

orthogonality', which should revolutionize the oligosaccharide synthesis.^[55] Their aim was to prepare two different glycosidic linkages out of the same product mixture using separate activation strategies. They proposed a reaction of two sugar units with a different leaving group (X and Y), which was activated in a unique manner (demonstrated in Scheme 5). Within this, they could prepare two different disaccharides depending on the applied activation strategy.



Scheme 5. Formation of two different glycosides *via* the principle of orthogonality.^[16]

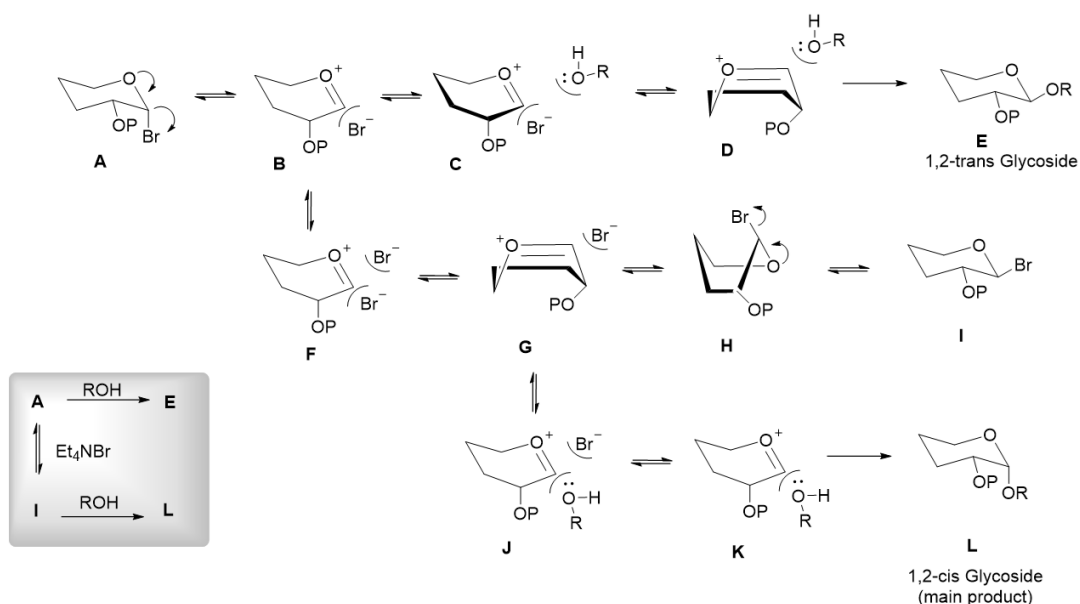
2.1.3 Mechanism

Scheme 6. General assumed reaction mechanism of the chemical glycosylation.^[16, 32]

The glycosylation mechanism can be explained within four main steps as shown in Scheme 6. Initially, glycosyl donor **1** is activated by a promoter or catalyst to give donor **2**. It is worth mentioning, that this step can be either reversible or irreversible, depending on the type of leaving group and activation method.^[56] Then, the leaving group is cleaved leading to the formation of the glycosyl cation **3**. This step is also called ‘dissociation’ and is typically irreversible and though the rate determining step (RDS) of the overall reaction. The formed glycosyl cation is stabilized via resonance from O-5, affording oxocarbenium ion **5**. Both types persist a flattened half-chair conformation with sp² hybridization of the anomeric atom. This combination is responsible for the stereoselectivity of the obtained glycosides. Then, the glycosyl acceptor (**6**) can either attack the anomeric centre from the bottom face (*a*) or the top face (*b*) of the ring. The nucleophilic attack leads to the 1,2-*cis*-, respectively 1,2-*trans* glycosides **7** and **8**, which are finally deprotonated in the terminal step of the reaction. The

1,2-*cis*, or α -anomer **9** is the thermodynamically favoured product that is obtained together with its counterpart **10** (kinetic products). Some reports mentioned the formation of other intermediates (compound **4**) during step-2 due to competing reactions like elimination-, substitution-, cyclization- (inter-, and intramolecular orthoesterification), migration- and redox reaction.^[57] However, they were usually underestimated and ignored and should not be further discussed here.

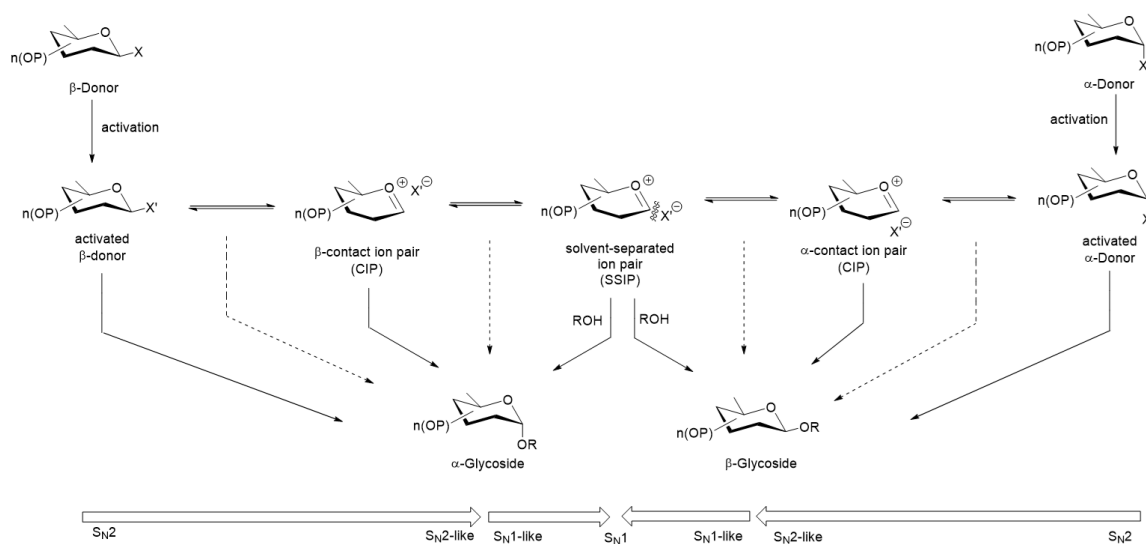
More importantly is the still occurring debate, whether the nucleophilic displacement at the anomeric position occurs in a unimolecular (S_N1) or a bimolecular (S_N2) fashion. Towards this, the seminal work of Lemieux^[58] could bring more details, helping to understand this complex reaction. Scheme **7** shows his postulated detailed mechanism, that was intended to demonstrate the role of the different ion-pair complexes.



Scheme 7. Seminal work of Lemieux regarding S_N1/S_N2 character of the Glycosylation.^[59]

Briefly, he found a rapid adjusting equilibrium between the relative stable compound **A** and its more reactive counterpart **I** upon the addition of Et_4NBr to the reaction. It led to the preferred reaction of the glycosyl acceptor ROH with **I** to form glycoside **L**. This was reported to proceed through a S_N2 mechanism via a tight ion-pair complex **K**. Lemieux and coworkers supposed that the energy barrier for the nucleophilic substitution for **I** \rightarrow **L** (formation of α -glycoside) was lower than for **A** \rightarrow **E** (formation of β -glycoside). This opened up the possibility to control the outcome of the reaction, if the difference of the energy barrier was sufficient. Then, the formation of only α -glycoside could be controlled. Therefore, the reaction needed to be carried out using a very mild catalyst (R_4NBr), very reactive substrates and prolonged reaction times.^[16] Recently, the group around D. Crich and L. Bohé^[56] published a complete study about the debate of the glycosylation mechanism at the S_N1 - S_N2 interface. They defined the chemical glycosylation in general as “nucleophile substitution at sp^3 carbon with emphasis

on the subset of electrophiles carrying an ether oxygen at the electrophilic site". They described the two mechanistic pathways of the nucleophile substitution as ‘two limiting mechanism’ or ‘extremes’. The unimolecular, dissociative case (S_N1), that goes through the formation of a carbenium ion intermediate and the bimolecular case (S_N2), that goes through an associative transition state. The divergence between them is illustrated in Scheme 8 with a focus on the different ion-pairs, dominating in the relevant mechanistic pathway.



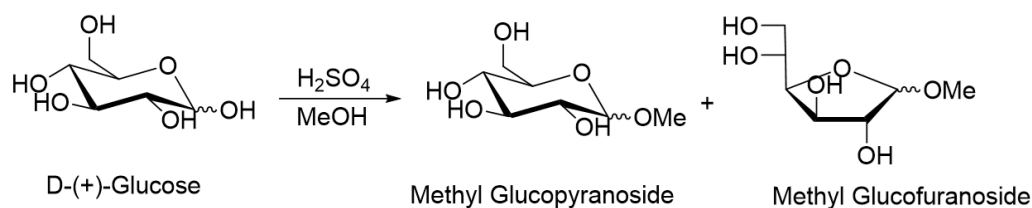
Scheme 8. Glycosylation reaction between the two limiting mechanism.^[56]

Regardless the stereoselective outcome of the reaction, the extreme unimolecular S_N2 and bimolecular S_N1 mechanism are separated by different sets of diastereomeric ion pairs. From covalently bond activated donor (‘extreme’ S_N2) through contact ion pairs (CIP) towards solvent separated ion pair (SSIP, ‘extreme’ S_N1). The focus on the mechanistic studies was the determination of the reaction kinetic and stereoselectivity with the aim to detect important reaction intermediates to explain the ‘switch’ between the two limiting mechanisms. Crich and Bohé are convinced, that the general trend of a particular glycosylation reaction (S_N1 or S_N2 fashion), can only be judged by kinetic studies. Early works showed the preference of the S_N2 mechanism for the substitution of several glycoside halides with strong anionic nucleophiles, but preferences for S_N1 mechanism if the nucleophile was an alcohol and the reaction occurred under pseudo-first-order solvolytic conditions. Altogether, a unique reaction mechanism for chemical glycosylation can still not be defined and it will need more profound studies, for a complete mechanistic understanding.

2.1.4 Protecting Group Free approaches

Most of the previous discussed glycosylation strategies/concepts employ protecting groups in order to control the stereoselectivity. The utilization of unprotected glycosyl donors affords

indeed various additional challenges, but can also simplify the overall reaction. To bring a benefit, the glycosyl donor must be easily accessible and the relevant reaction should be applicable for many different alcohols and sugars. Furthermore, the glycosylation must be very effective and occurs with reasonable amounts of catalyst and reaction times. The missing directing group at C-2 and the possible reaction of all free hydroxyl groups in the sugar ring complicates the stereocontrol. But, once these conditions are fulfilled, there are numerous advantages that outweigh the efforts, making this strategy so attractive. To name some, there are first of all the overall reaction steps, that are drastically reduced since no protecting-deprotecting manipulations are necessary. Iterative glycosylation gets possible, which can be extended to oligosaccharide synthesis. In addition, the unprotected hydroxyl groups are more reactive than their acyl-protected counterparts, so that the resulting glycosides can be directly applied to antibody- and other therapeutic issues.^[32a, 60] The most popular reaction applying unprotected carbohydrates is still the 100 year old Fischer-Glycosylation (Scheme 9), an alkylation of sugars by alcohols under acid conditions, which is discussed in more details in subchapter 3.^[37]



Scheme 9. Fischer-Glycosylation.

It is therefore not surprising, that the main attempts towards protecting group free glycosylation are based on Fischer's method. Over the past decades, various promising methods dealing with modified Fischer reaction and different catalytic systems have been reported, while the most promising ones should be mentioned here. In 2007, Mukhopadhyay *et al.* exploited the catalytic system of sulphuric acid immobilized on silica to couple unprotected sugars with different alcohols.^[61] They reported successful glycosylation within 2 hours using an excess of 5 molar equivalents of alcohol. In a different study, Pfaffe and Marwald^[62] developed the glycosylation of unprotected functionalized alcohols with free D-ribose in the presence of 10 mol % titanium(IV)-tert-butoxide and 50 mol % of D-mandelic acid at room temperature. Interestingly, they observed only the formation of ribose furanoside. The same group reported subsequently the organo-catalyzed glycosylation of unprotected and unactivated glycosides with LiClO_4 as a catalyst. In addition of traces of PPh_3 and CBr_3 , they obtained exclusively β -anomers as products.^[63]

Another catalytic system was investigated by Bhattacharay, using bismuth-based nitrates^[64] and later sulfamic acid.^[65] The glycosylation of unprotected unactivated sugars was likely

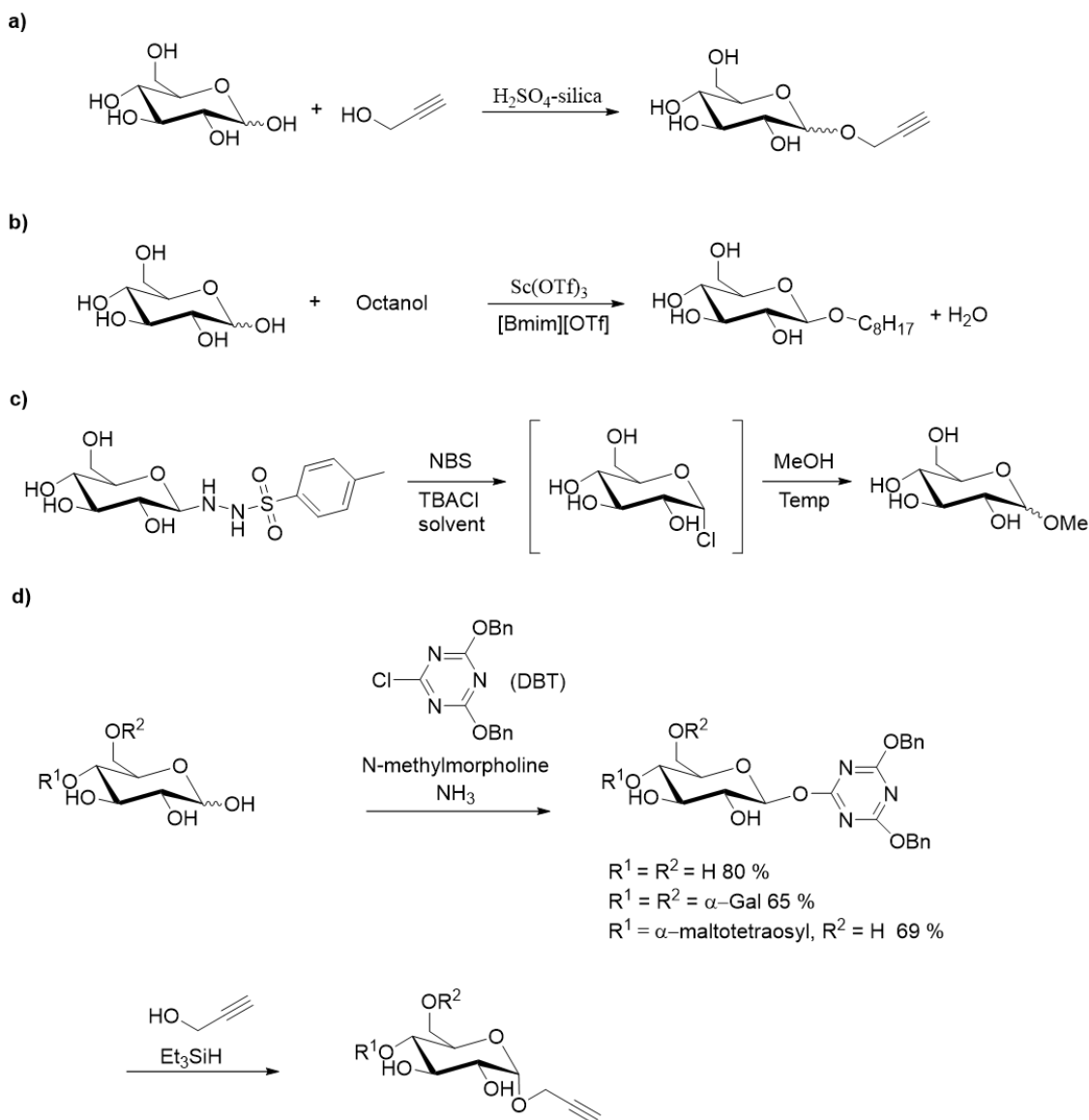
studied with NH_4Cl and could show better results than with standard catalyst such as Amberlite IR-120 (H^+) resin, InCl_3 , $\text{In}(\text{OTf})_3$, $\text{Sc}(\text{OTf})_3$ and HCl .^[66]

Ionic liquids (ILs) were evenly tested to improve the protecting free approaches. As it resulted, 1-ethyl-3-methylimidazolium benzoate ($[\text{emIm}][\text{ba}]$) in presence of Amberlite-IR-120 or p-tolouensulfate acid (TsOH) showed successful glycosylation reactions. Auge and Sizun reported an increase in yield and stereoselectivity of the glycosylation with $\text{Sc}(\text{OTf})_3$ by adding an ionic liquid and attributed the success to the presence of the latter. Under optimized conditions, they needed only 1 mol% of the ionic liquid $[\text{bmim}][\text{OTf}]$ and could successfully glycosylate unprotected sugars with octanol in α -selectivity.^[61]

A different strategy was reported by Toshima *et al.*, who developed a photoinduced activation of unactivated deoxy thioglycosyl donors. They used boronic acid as temporary 1,3-diol protection group, so that self-coupling and the formation of anhydro sugars could be prevented, but the primary OH group was still available for the glycosylation.^[67]

A promising strategy, using an anomeric protecting group for unprotected carbohydrates was developed by Nitz and co-workers. Therefore, they first synthesized N'-Glycosyltoluenesulfonohydrazides (GSHs) glycosides that serve as glycosyl donor. The activation with NBS in DMF gave the in situ formation of an unprotected glycosyl chloride, that could be coupled with various alcohols to prepare alkyl glycosides. However, this reaction was not stereoselective, which limited the scope of the anomeric leaving group.^[68]

Another protecting-free approach was developed by Ishihara *et al.*, where they synthesized 4,6-dibenzyloxy-1,3,5-triazin-2-yl (DBT) glycosides as 'activated glycosyl donors' to be converted into alkyl glycosides through alcoholysis. The glycosylation with various alcohols was carried out under hydrogenolytic conditions using palladium/carbon or triethylsilane as reducing agent. Their protocol could be applied to acid-labile oligosaccharides as well as acid-labile aglycon alcohols.^[69]

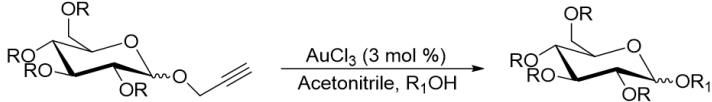
Scheme 10. Selected examples of protection-free glycosylation approaches.^[61, 68-70]

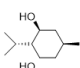
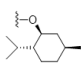
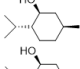
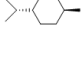
2.1.5 Alkynyl Glycosides: Propargyl glycosides

Propargyl glycosides are among the alkynyl glycosides the most popular and widespread ones and should be discussed in more detail in the following chapter. They are easy to synthesize from aldoses through modified Fischer glycosylation reactions, stable to diverse chemical manipulations and can be directly used for saccharide couplings. They are hence attractive glycons for oligosaccharide synthesis and their chemoselective anomeric activation was consequently studied by a lot of researchers. It was found, that the alkynophilicity of gold salts can be used to selectively activate propargyl glycosides. Hota *et al.* explored the transition metal mediated activation using AuCl_3 , PtCl_2 , $\text{Co}_2(\text{CO})_8$ and RuCl_3 . To this, they performed the reaction between propargyl 2,3,4,6-tetra-*o*-benzyl- α/β -glucoside and water with 3 mol % AuCl_3 in acetonitrile. They observed complete hydrolysis to per-*O*-benzylated lactol upon 12 h of reaction at room temperature. The reaction could then be successfully applied

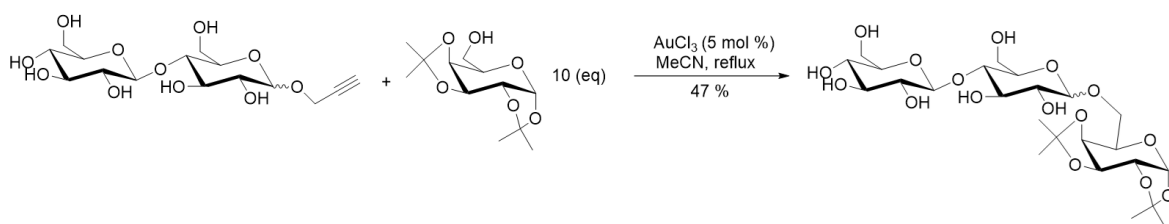
to other aglycons to give mixtures of α/β glycosides and disaccharides in good yields.^[71] Interestingly, the other metal catalyst led only to the decomposition of the donors, affording no products.

Table 1. Hota's glycosylation of propargyl glycosides with different alcohols.^[71]



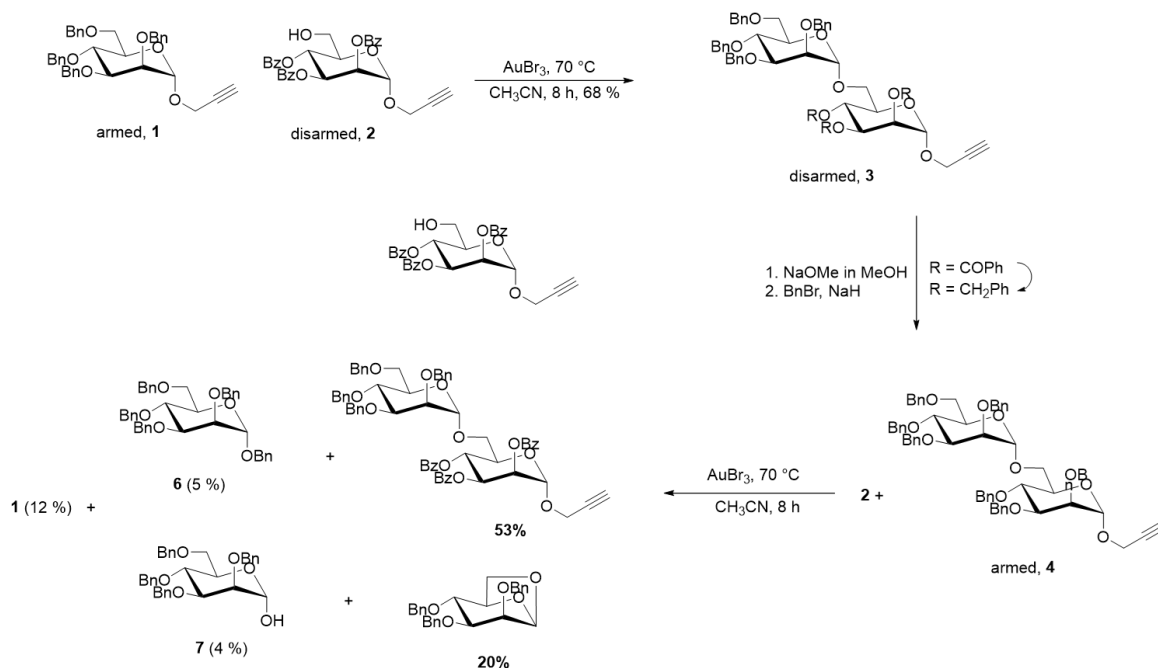
R	Aglycone (R ₁ OH)	Time/Temp./yield	R ₁
Bn	H ₂ O	12 h/ RT/ 70 %	H
Bn	Menthol 	6 h /60 °C/ 68 %	
Ac	Menthol 	48 h/ 60 °C/ 0 %	No reaction
Bz	menthol 	48 h/ 60 °C/ 0 %	No reaction

Inspired by their work, Mamidyala and Finn^[72] explored the activation of unprotected propargyl- galactoside,- glucoside and mannosides with different aglycons under the typical Au^(III) catalyzed conditions. They concluded, that it was required to provide the aglycone in high excess and to reflux the reaction mixture to obtain good yield. Secondary or sterically demanding alcohols retarded the glycosylation reaction, as well as insufficient excess of the latter. The same group tried to apply the developed method towards the preparation of larger oligosaccharides. They reported the successful synthesis of a 1,6-linked trisaccharide in 47 % yield due to the reaction of propargylated lactosyl donor and diacetone-D-galactose (Scheme 11).



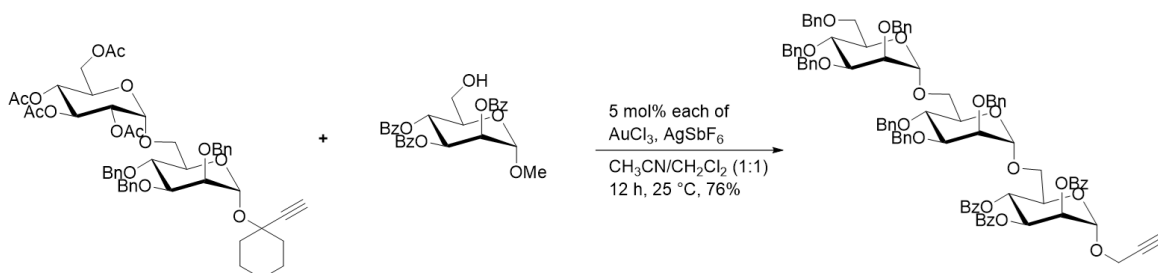
Scheme 11. Synthesis of a trisaccharide *via* the glycosylation of propargyl lactose with diacetone-D-galactose.^[72]

Later in 2013, Kayastha and Hota expanded their gold-catalyzed glycosylation by the application of the 'armed-disarmed' strategy. They aimed to obtain higher oligosaccharides (DP > 2) *via* a three step protocol, shown in Scheme 12.^[73]



Scheme 12. 'armed-disarmed' method during gold-catalyzed glycosylation.^[73b]

They first reacted the 'armed' per-benzylated propargyl mannopyranoside (**1**) with its 'disarmed' per-benzoylated counterpart (**2**) to obtain disaccharide (**3**) in 68 % yield. Their attempts to form higher oligosaccharides by sequential glycosylation failed due to the double activation of two 'armed' anomeric centres in the disaccharides. When they 'rearmed' the disaccharide (**3**) and react it with another disarmed glucoside (**2**), they obtained disaccharide (**3**), 1,6-anhydro sugar (**5**), propargyl mannosides (**1**), benzyl glycoside (**6**) and lactol (**7**), but not the desired trisaccharide. The high reaction temperature and the oxophilicity of gold was blamed to retain the formation of higher oligosaccharides and the as-described double activation led in addition to the cleavage of the glycosidic linkage of the disaccharide. Finally, with the addition of AgSbF_6 , the reaction temperature could be decreased to 25 °C and the screening of different leaving groups gave one combination leading to the succeed formation of a *1,2-trans* trisaccharide in 76 % yield (Scheme 13).^[73b]



Scheme 13. Succeed preparation of a trisaccharide by gold-catalyzed glycosylation in the presence of AgSbF_6 .^[73b]

2.2 General methods for oligosaccharide synthesis

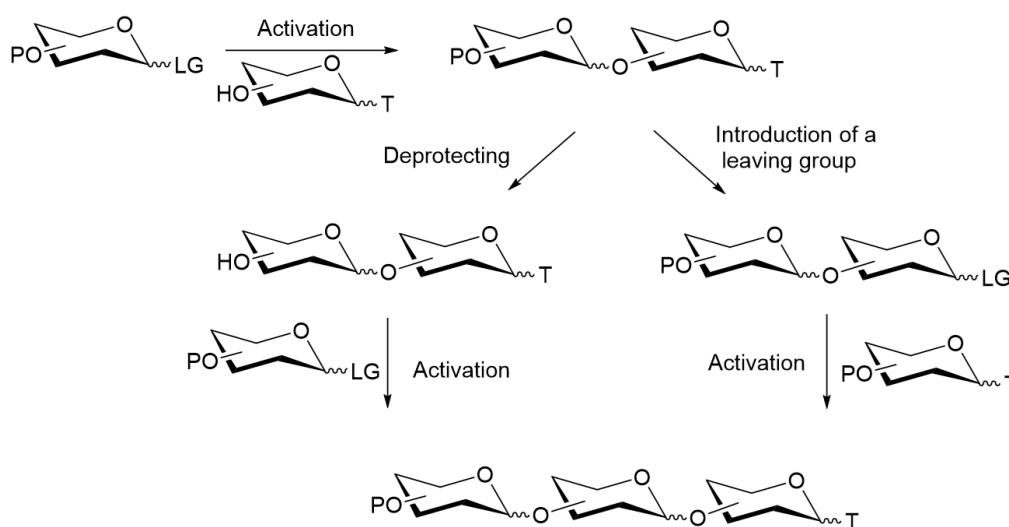
2.2.1 A) Chemical Oligomerization strategies

“Although we have now learned to synthesize oligosaccharides, it should be emphasized that each oligosaccharide synthesis remains an independent problem, whose resolution requires considerable systematic research and a good deal of know-how. There is no universal reaction condition for oligosaccharide synthesis” – Hans Paulsen.

As the famous citation of Paulsen mention, there is not one ‘ideal method’ to prepare oligosaccharides following a general and reliable glycosylation reaction strategy. In fact, the optimized conditions for different glycosylation reactions can vary from microwave heating to frozen temperatures and is very dependent on the substrates, catalyst and the aimed application. Today, oligosaccharides are either isolated from natural sources or prepared enzymatically and/or chemically. A brief review about the progress in chemical synthesis is given in the following.

2.2.1.1 Conventional linear method

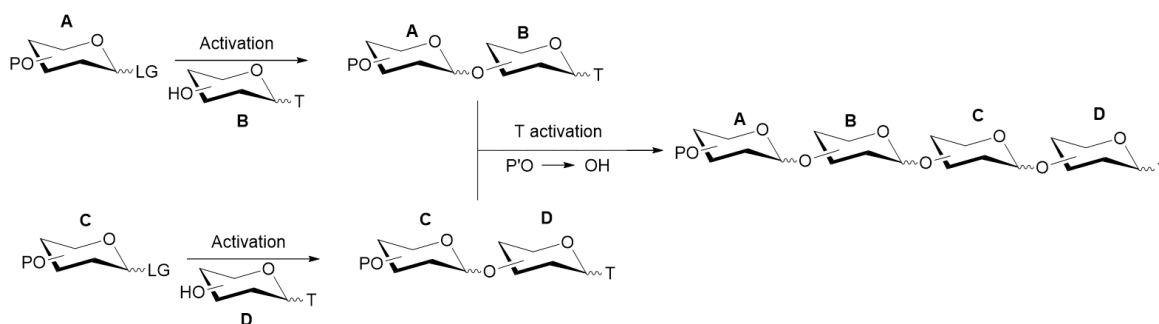
This conventional linear method presents the oldest strategy for the preparation of oligosaccharides. Here, a protected glycosyl donor is reacted with a glycosyl acceptor to afford a disaccharide in a first step. The disaccharide is then converted into a second-generation glycosyl acceptor- or donor, which in turn reacts with another donor or acceptor to form a trisaccharide. This sequence is then repeated until the desired length of oligosaccharide is obtained.



Scheme 14. Conventional linear oligosaccharide synthesis.^[16, 74]

2.2.1.2 Convergent method

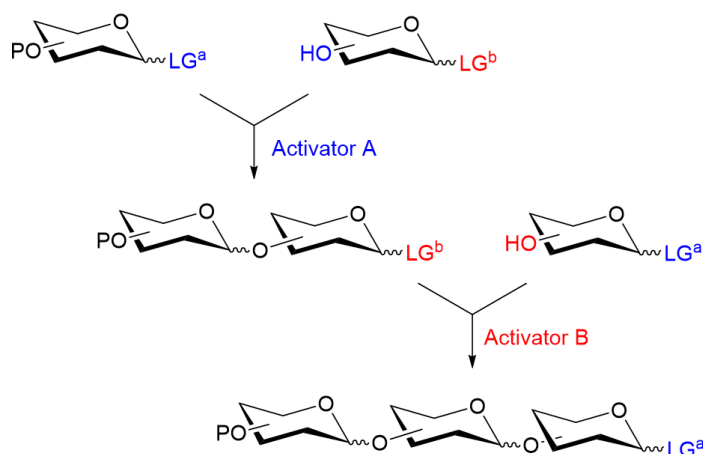
This strategy presents a simplified version of the linear approach, where pre-formed oligosaccharide-fragments are assembled together. It is a faster method with fewer overall linear steps and the possibility to utilize readily available disaccharides. It is compatible with glycosylation concepts such as ‘latent-active’, selective-chemoselective, orthogonal and two-stage approaches.^[16]



Scheme 15. Convergent linear oligosaccharide synthesis.^[16]

2.2.1.3 Leaving group based: selective or orthogonal

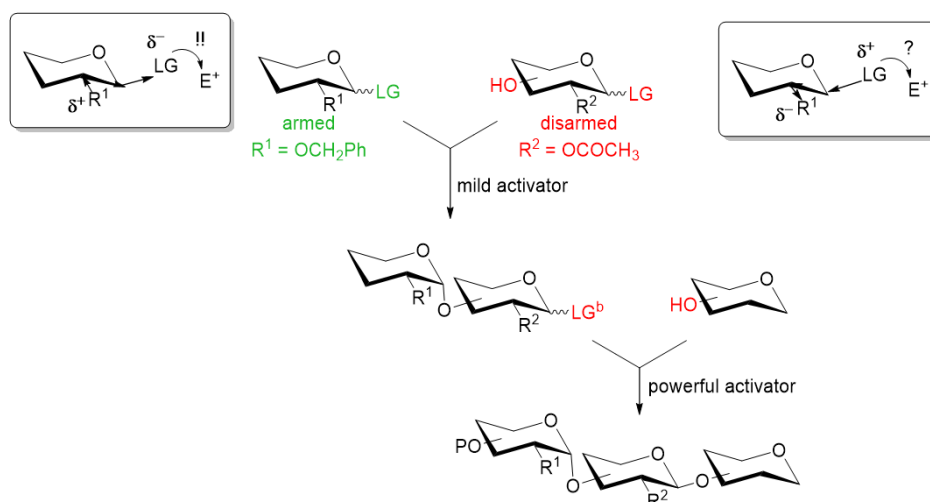
In this method, the glycosyl donor (LG^a) as well as the glycosyl acceptor (LG^b) are bearing a leaving group. They can be selectively activated with a suitable activator affording a disaccharide bearing the ‘non-activated’ leaving group (LG^b) of the acceptor on the anomeric centre. Then, a second activator is needed to selectively activate leaving-group b to combine the disaccharide with a third sugar to a trisaccharide. The orthogonal character of this reaction is described by the exclusive activation of one LG within two chemically distinct glycosylation reactions. It is one of the most advanced technique used for oligosaccharide synthesis.^[75] It is mainly used for the activation of phenyl thioglycosides over glycosyl fluorides with S-ethyl and S-thiazolinyl.^[76]



Scheme 16. Leaving group based oligosaccharide Synthesis shown for orthogonal method.^[32b]

2.2.1.4 Protecting group based: chemoselective ‘armed-disarmed’ concept

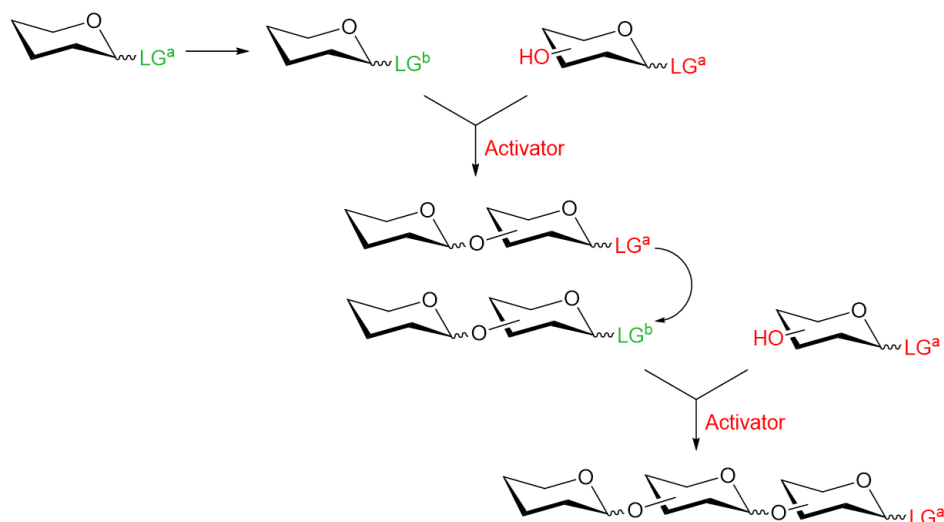
This method has its origins in the armed-disarmed approach of Fraser-Reid developed in 1992.^[77] Towards this, a benzylated building block (electronically activated, armed) is chemoselectively activated over its acylated counterpart (electronically deactivated, disarmed). Both derivatives have the same type of leaving group, of which only one gets activated by a mild promoter. A more powerful activator is then needed to afford a trisaccharide in a second step. It is worth mentioning, that the same leaving groups can be utilized for all the building blocks of the sequence. Furthermore, the protecting group at C-2 influences the stereochemical outcome, so that exclusively a series of cis-trans- oligosaccharides is obtained (see chapter 2.1.2). This method has become the basis of programmable multistep approaches like highly efficient one-pot oligosaccharide synthesis.^[78]



Scheme 17. Protecting group based oligosaccharide synthesis based on the ‘armed-disarmed’ concept.^[74]

2.2.1.5 Preactivation method: two-step activation

This method is presenting a two-step activation sequence with the possibility of reiteration. Initially, the glycosyl acceptor, as well as its donor are charged with the same type of leaving group. Prior to the coupling by glycosylation, the leaving group of the donor (LG^a) is converted to LG^b , that can be selectively activated by activator A. After succeed coupling, leaving group LG^a can be again converted to its active counterpart LG^b and the disaccharide can be coupled with another building block to afford a trisaccharide (and so on).



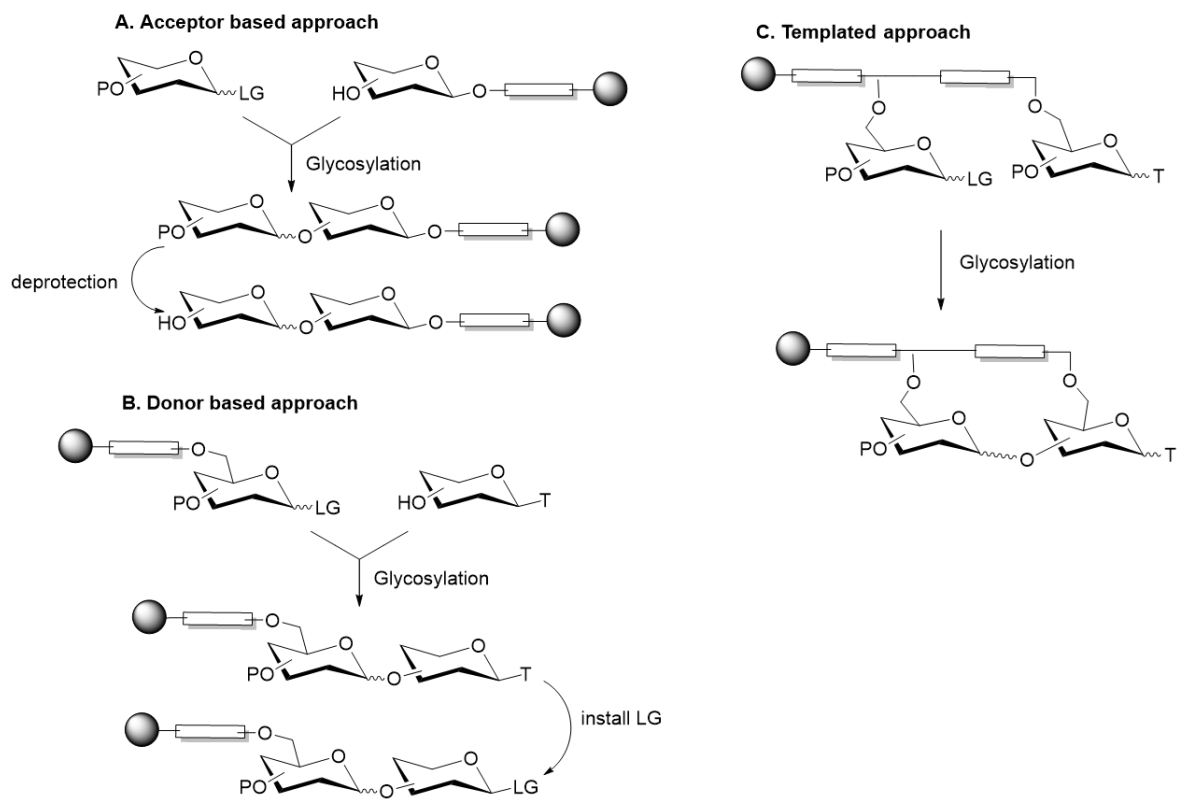
Scheme 18. Two-step activation method for oligosaccharide synthesis.^[74]

2.2.1.6 One-pot method

The advantage of this strategy is the ability to prepare oligosaccharides in a step-wise fashion, without the requirement of any purification steps of intermediates, since all the glycosylations are performed in ‘one pot’. Hence, this concept desires fine-tuning and the control of all the compounds presented in the batch. Normally, the respective reactants are added sequentially upon their consumption, so that the most reactive hydroxyl group reacts with the most reactive leaving group etc. The first approaches were based on the ‘armed-disarmed’ principle up to ‘superarming protecting groups’ by Bols *et al.*^[79] The second exploited chemoselective activation, differentiating the reactivity of donor and acceptor by the electronic properties of the respective protecting group. Another strategy presents a subsequent, selective activation of one leaving group after another. The limitation of this method lies clearly in the number of available leaving groups for a multistep reaction. Other concepts are dealing with preactivation strategies of the building blocks or exploits different activities of the various hydroxyl groups in the sugar ring.^[32b]

2.2.1.7 Supported and tagged method

The next development of oligosaccharide synthesis was the application of the solid-phase method, initially invented for oligopeptides by Merrifield in 1985.^[80] The numerous advantages like the easy work-up (no purification of intermediates necessary) and the rapidity of the overall reaction, make this strategy very attractive. The main approaches are based on solid-phase polymer supports (= beads). The first solid supports were invented by Fréchet and Schuerch^[81], whereas there was a lot of progress and investigation the past decades.

Scheme 19. Glycosylation methods on polymer support.^[32b]

In general, there are two main strategies to be mentioned. Either, the acceptor is bond to the support having its donor in the liquid phase (acceptor-based, A, Scheme 19), or vice-versa (donor-based, B, Scheme 19). In the case of the donor-based solid support, the temporary protecting group of the acceptor needs to be converted into a leaving group upon each glycosylation step in order to continue the chain elongation.

The acceptor-based method will always possess a liquid phase that is predominated by the highly active donor. By that, even at advance stage of assembly (high degree of oligomerization), good yields are still attained. The third approach, called template method, combines the two just described strategies. Here, the donor as well as the acceptor are bound on the solid-support and one needs two-directional activation methods. The solid-supports that are used are mainly based on polystyrene (PS) bead crosslinked with 1 % divinylbenzene. Over time, also other beads were investigated like polystyrene grafted with different length of poly ethyleneglycol (PEG) to develop tentagels, hypogels and argogels with good swelling properties in polar and non-polar solvents. Apart from those, other beads like PS grafted with PEG and crosslinked with tetrahydrofuran-derived bridges (JandaJel^[82]), controlled-pore class^[83]- and nanoporous gold-based^[84] supports were reported. In order to attach the corresponding sugar to the solid-support, glycoscientists usually uses linkers in between, since they can reach higher activities. The most recent developed linkers are given in Figure 19, with Reichardt's spacer^[85], Seebergers Lenz linker^[33b], safety catch linker^[86] and the photocleavable linker.^[87] Besides them, Seeberger *et al.* reported in 2016 a photocleavable linker with whom he was able to prepare oligosaccharides with the free reducing end.^[32b, 88]

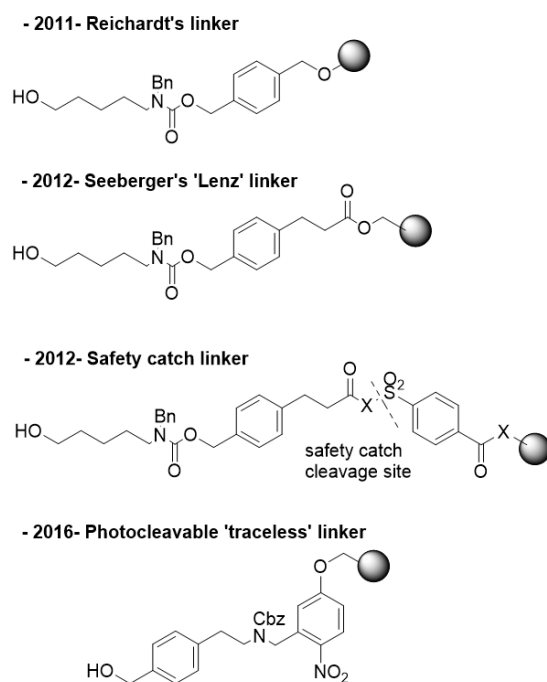


Figure 19. Recent linkers in polymer-support oligosaccharide synthesis.^[32b]

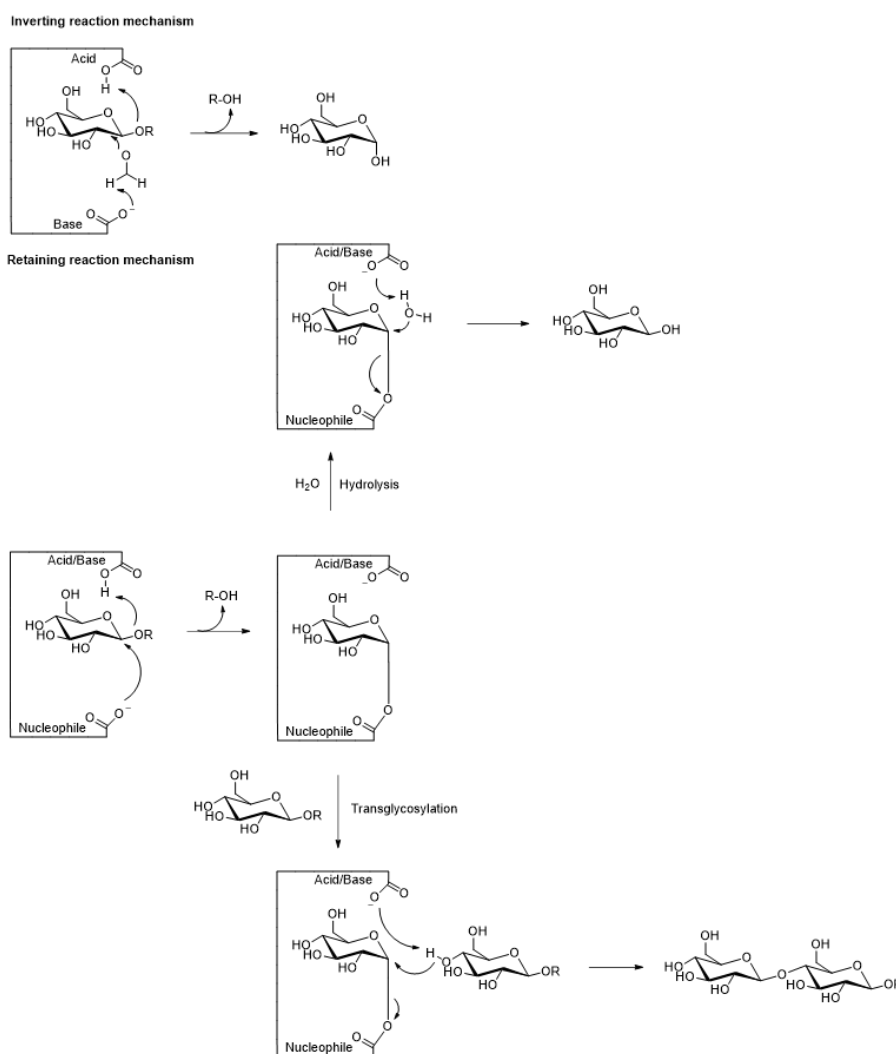
2.2.1.8 Automated oligosaccharide synthesis

The breakthrough of solid-support strategies enabled stream-line and combinatorial approaches to finally adapt the traditional oligosaccharide synthesis towards an automated, computer-based setup. Within this, the human error factor could be eliminated, good reproducibility attained and the real-time reaction monitored by using computers. The most automated platforms are using a computer interfaces in combination with a liquid handling equipment. The main goal is to find a successful automated sequence and to record it with the help of a computer, to be able to reproduce exactly the same product as often as desired. Another benefit is the realisation of a real-time reaction monitoring in order to reduce the reaction time and the amount of reagents and solvents.

As for the solid-phase method, Seeberger was the main driving force, notably with his invention of the 'first fully automated solid-phase oligosaccharide synthesis in 2012'^[33b], later marked as Gyconeer 2.2. Seeberger mainly used octenediol linker and cleaved the oligosaccharides by olefin cross-metathesis to obtain pentenyl (oligo) glycosides.^[32b] With his first solid-phase OS synthesizer, he obtained 42 % overall yield of a heptasaccharide in 24 h, compared to 9 % in 14 days with manual synthesis methods. The high costs of the synthesizer and the time to train the personal motivated researchers to investigate in less expensive and more accessible platforms that can be found in common laboratories (e.g. parallel synthesizers syringe pumps, micro reactors or HPLC setups). However, most of the automated methods are still in progress and a lot of improvement will need to be done in order to scale-up the process for industrial purposes.^[32b]

2.2.1.9 Chemo-enzymatic methods

Complete regio- and stereoselectivity in glycosylation reactions without the need of protecting groups can be achieved using various enzymes. For the oligosaccharide synthesis, glycosyl transferase and glycosidase turned out to be suitable. Especially mutated glycosidases, so-called glycosynthases, can efficiently synthesize oligosaccharides without hydrolysing them at the same time. The amino acid residues in the active site of these enzymes causes a steric hindrance, so that only one anomer is formed selectively. β -glycosidases, for instance, lead only to the formation of β -glycosidic bonds through the attack of the hydroxyl group from the β -face. Glycosidases have in general two complementary activities: dehydrative condensation and hydrolysis. Their biological role is the hydrolysis of the glycosidic bonds of polysaccharides, but under special condition, they can perform the reverse reaction and catalyse the formation of glycosidic bonds. To this, however, it is absolutely needed to introduce an appropriate leaving group at the anomeric position to prepare a suitable glycosyl donor. To name some examples, there are the *p*-nitrophenyl glycosides, glycosyl fluorides or oxazolines.^[89]

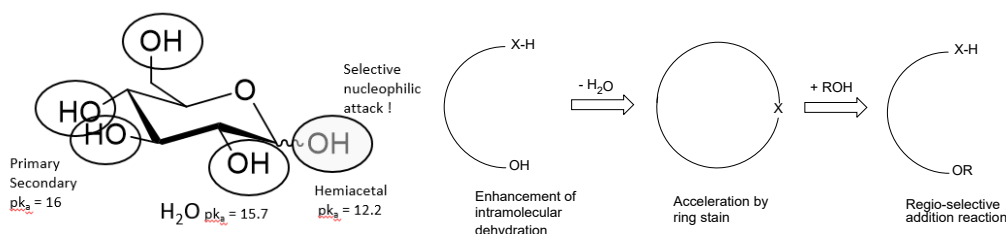


Scheme 20. Reaction mechanism of glycosidases: ‘inverting’ and ‘retaining’.^[90]

The glycosidases are classified as ‘retaining’ or ‘inverting’, as they retain or invert the stereochemistry of the glycosidic bond that is cleaved by hydrolysis. Scheme 20 shows the mechanism for each type of enzyme. Regardless the type of enzyme, they have two active-sites that contain each a carboxylic acid residue. During the inverting reaction, one of them acts as an acid-, and the other one as a base catalyst, while the reaction proceeds *via* a single-displacement mechanism. In the retaining reaction, the active-sites act as nucleophile and acid/base catalyst and the reaction proceeds *via* a double-displacement mechanism, going through the formation of a covalent glycosyl enzyme intermediate and an oxocarbenium-ion like transition state (not shown in scheme). There are two possible pathways, either hydrolysis or transglycosylation.

By using enzymatic approaches, a direct anomeric activation in aqueous media has become possible. Shoda *et al.* developed thereby various methods, where he exploited the differences in acidity (pK_a -values) of the three kinds of hydroxyl groups in the sugar ring and the surrounding water molecules. With a pK_a of 12.2, the hemiacetal OH-group differs from the primary and secondary OH-groups ($pK_a = 16$) and even from water-molecules ($pK_a = 15.7$), so that a selective nucleophilic attack to an appropriate electrophile gets possible. By using 4,6-dimethoxy-1,3,5-triazine-2-yl (DMT), they prepared active glycosides that could be recognized by various glycosidases and were suitable for enzymatic catalysed transglycosylation reactions. The DMT-glycosides are easy to prepare in aqueous media without the need of any protecting groups. They are stable and can be stored at room temperature and showed good transglycosylation activities.

Another strategy of direct anomeric activation was the preparation of 1,2-anhydro-sugars *via* intramolecular dehydration. Here, the strategy was to enhance the dehydration when going through a cyclic ring intermediate, since the intramolecular dehydration is entropic favoured over the intermolecular reaction. The second step was a subsequent addition of a nucleophile affording 1,6-anhydro sugars, S-glycosides, N-glycosides or glycosyl halides, whereas the reaction was driven by ring-strain. The 1,2-anhydro sugars were prepared by the reaction of unprotected sugars with 2-chloro-dimethylimidazolium chloride (DMC) in water.



Scheme 21. Left = different acidities of the hydroxyl groups in a sugar ring; right = concept of direct anomeric activation via dehydration in water.^[89]

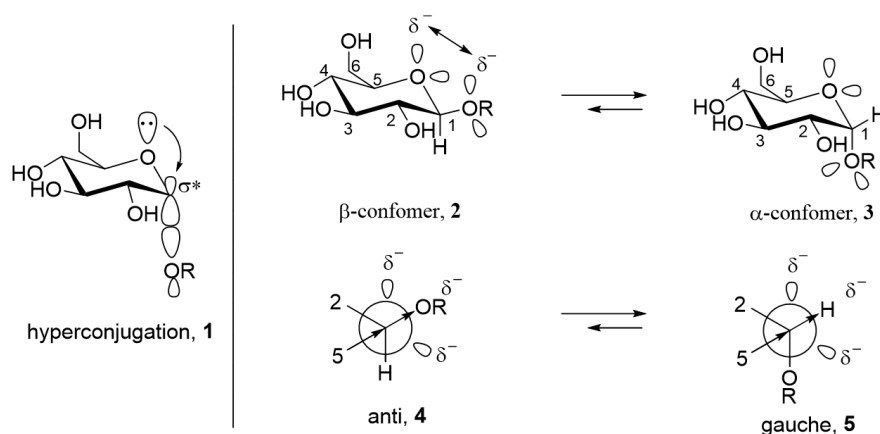
One can divide the chemo-enzymatic process into four steps: 1) the transformation of a polysaccharide biomass to a refined raw material, 2) the anomeric activation of the latter, 3)

the enzymatic catalyzed glycosylation towards functionalized oligosaccharides and 4) the degradation of the products by glycosidases. Altogether, chemo-enzymatic catalyzed glycosylation reactions to prepare oligosaccharides show several advantages compared to classical chemical approaches. In contrast to the time consuming preparation of an activated glycosyl donor, enzymatic catalyst enables the possibilities of a direct anomeric activation in aqueous media. The high regio- and stereoselectivity, abstention of any protecting group and low-environment impacts making them very attractive for glycoscientists. However, the high costs of the substrates and the poor yields still hampers an industrial scale up and limits further applications.^[89]

2.2.2 B) Depolymerization methods

Another strategy to obtain well-defined oligosaccharides is the depolymerization of biomolecules like cellulose, chitin and starch etc. To this, the cleavage of the glycosidic bonds between the sugar units of these polysaccharides is the pre-requisite step, which is in general a very complex and challenging task.

Cellulose, for instance, is a very robust polymer, possessing a strong hydrogen bond network at the supramolecular level which hinders its hydrolysis and though the depolymerization. The chains are kept together by the van der Waals interactions, so that water is excluded from the glycosidic bond. The protonation of the anomeric oxygen of the β -(1,4)-glycosidic linkage is hampered due to the higher basicity of the surrounding oxygen atoms and the ‘exo-anomeric effect’ shortens the glycosidic bonds, which locks the conformation and leads to an additional stabilization. This effect is due to the hyperconjugative delocalization of the lone-pair density of the exocyclic oxygen atom at the C-1 into the σ^* orbital of the C-1–O-5 bond. The stabilization afforded by this hyperconjugation is maximized, when the glycosidic substituent OR at C-1 is oriented gauche to the C-1–O-5 bond. In that case, the C-1–O-5 bond is lengthened, the C-1–O bond shortened and the O-C-O angle widened, which stabilizes and favours the gauche conformer. In addition, this conformation avoids the interactions between the orbitals of the lone pair of the aglycon OR and those of the ring oxygen (**2 + 4**, Scheme **22**), giving further stabilization.^[91]



Scheme 22. Explanation and origin of the exo-anomeric effect.^[91b, 91d]

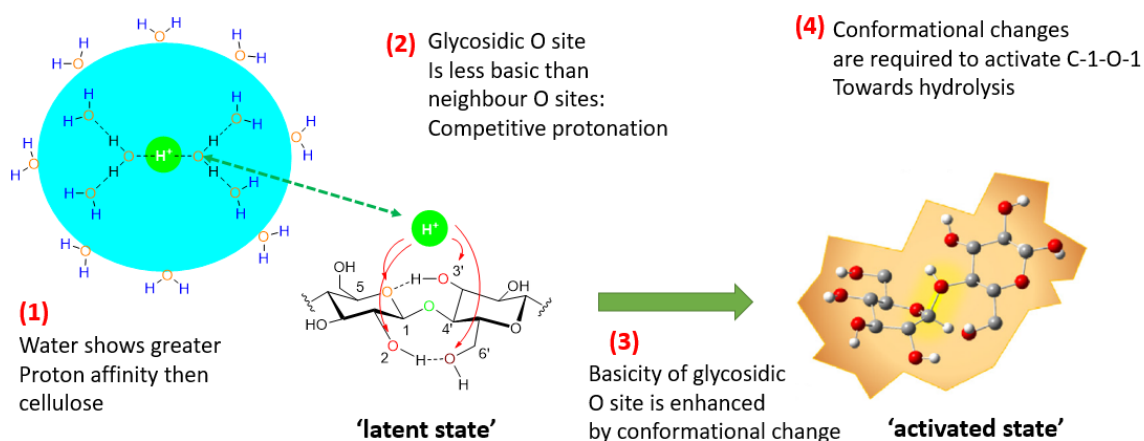
Altogether, the β -(1,4) glycosidic bond possesses an energy barrier of 125 - 167 kcal/mol that needs to be overcome in order to cleave the linkages between the anhydroglucose units.^[92] Today, many different methods have been developed to break down cellulose. Several of these methods have been commercialised, such as the prosea process^[93] based on steam explosion or the enzymatic hydrolysis process of POET-DSM^[94] and Abengoa.^[95] Other strategies, that showed promising results are the supercritical solvolysis of cellulose in water or polar aprotic solvents. The most prominent among them is the Plantrose^[96] process. Here, cellulose is depolymerized in supercritical water without the use of any enzymes, which decreases importantly the overall costs. Alternative routes are the acid hydrolysis of cellulose in γ -valerolactone (GVL)^[97], or the extrusion of biomass under basic conditions followed by depolymerization *via* enzymatic hydrolysis.^[98]

Recent studies reported the breaking down of cellulose by using *non-thermal technologies*. The so obtained low molecular weight glucans have a degree of polymerization (DP) between 5 - 120 and show all possible glycosidic linkage positions (α/β -1,4, -1,3, -1,6, -1,2). They therefore differ from cellodextrins, which are exclusively linked via the β -1,4 position. The new branching patterns brought a higher solubility of the molecules in water or organic solvents and facilitates following chemical modifications. Hence, the soluble glucans found applications as surfactants, thickening agents, glues and absorbents. *Non-thermal technologies* are defined as techniques, that do not depend on an external source of heating, while the chemical reaction is activated by pressure, electric or magnetic field, waves, light or *in situ* generated heat. Since these methods enable a downstream processing below 100 °C, they offer notable advantages regarding the degradation and though the purity of the sugars. Furthermore, the absence of solvents greatly facilitates the subsequent isolation of the glucans. To name the three most popular non-thermal technologies, there are mechanocatalysis, non-thermal atmospheric plasma and sonochemistry, while the following chapter will focus on the mechanocatalytic depolymerization of cellulose.

2.2.2.1 Mechanocatalytic depolymerization of cellulose: Ball-milling

Milling processes and the effect of mechanical grinding to alter the cellulose structure is a well-known old technique. The mechanical forces provide the energy to alter the crystalline structure and reduce the particle size of cellulose. There are many different mills that can be applied such as planetary mills, shaker mills, attrition mills and rolling mills. In a mechanocatalytic approach, the contact that is afforded between the catalyst and the cellulose during the milling process is crucial, since it is the synergistic effect between mechanical forces and catalysis, which finally attains the depolymerization. Compared to either the classical acidic catalysed depolymerization or ball-milling process of cellulose, their combination could reduce the activation energy barrier to 66 % and furthermore shortens the reaction times from 24 - 48 to 2 - 6 hours.^[99]

As already described in detail, the depolymerization of cellulose is a challenging task, where the most of the activation energy for the hydrolysis is encountered for the protonation of the anomeric atom. The strong affinity of H^+ to water is hampering the protonation of the glycosidic atom as well as the proximity of the more basic oxygen atoms O-2, O-3, O-4, O-5 and O-6. In addition, the oxygen atom O-6 is even capable to scavenge the proton from the glycosidic site, de-protonating again the desired O-1 position. Since every protonation of another neighbored hydroxyl O-atom is protecting the glycosidic linkage from hydrolysis, a very strong acid is needed to ensure the protonation of all sites including the targeted O-1. But even if the glycosidic position is successfully protonated, conformational changes are required to activate the C-1–O-1 bond for an effective hydrolysis. The fully protonated form of cellulose is presenting only a ‘latent state’, that needs to be activated with mechanical forces to initiate the hydrolysis. This activation step presents a conformational change of the cellulose chains, enabling the access of water molecules towards the glycosidic linkage.



Scheme 23. Barriers to overcome to hydrolyse cellulose (inspired by Schüth *et al.*^[100]).

It was shown experimentally that only the combination of mechanical strength and acid catalysis led to high percentages of water-soluble glucans in moderate reaction times. By impregnation of cellulose with an acid, 10 - 20 % of water-soluble products are formed instantaneously. Further depolymerization could not be achieved within longer impregnation steps or aging of the acidified cellulose. On the contrary, the altering of an H₂SO₄-impregnated cellulose in a closed vial at room temperature afforded a black solid, that is no longer soluble in water (carbonization of sugar). Mechanical forces were therefore needed to complete the hydrolysis and to obtain higher yields of water soluble products. The latter brings the glycosidic linkages into a suitable conformation that can be protonated in order to initiate the hydrolysis. Since during the mechanocatalytical process, depolymerization and recombination of the *in-situ* formed oligosaccharides proceed analogous, 70 % of the obtained products possesses other glycosidic linkages than the initial β -1,4 from the cellulose.

The first mechanocatalytic depolymerization of cellulose was reported by Blair and co-workers^[101] in 2010. They used a layered mineral kaolinite as acid catalyst with a surface acidity of $H_0 < -3$. The latter is defined by the Hammett acidity function H_0 through the following equation

$$H_0 = pK_{BH^+} + \log \frac{[B]}{[BH^+]} \quad (2)$$

where pK_{BH^+} is the negative logarithm for the dissociation of the conjugated acid of a very weak base B. Within this, they could hydrolyse 84 % of the introduced cellulose into a water-soluble fraction upon three hours of reaction in a shaker mill. The main products were levoglucosan, fructose and glucose. An improvement was attained by impregnation of cellulose with catalytic amounts of strong acids (0.4 - 0.9 mmol/g cellulose H₂SO₄ or HCl) prior to the milling step. Thereby, cellulose was completely converted after two hours to low molecular weight glucans (DP 2 - 7).^[102] By impregnation of the cellulose particles, the acid interacts with the surface of the glucan chains and prevents them from agglomeration, since they hinder the formation of an intermolecular hydrogen bond network. Besides, the non-stereospecific re-oligomerization of the *in situ* oligosaccharides leads to the formation of α -(1,6) linkages, which inhibits the recrystallization of the glucans.

It was suggested, that the sulphuric acid was physically and not chemically adsorbed, since no sulfonation was found of the obtained glucans.^[92] The applied acid catalyst, however, needs to be mechanically robust and possess physically accessible and chemically active sites. One of the main hurdles of employing liquid acids such as H₂SO₄ or HCl is their removal at the end of the reaction. Karam *et al.*^[99] reported in 2018 the mechanocatalytic depolymerization with Aquivion PW98, a strongly acidic perfluorinated sulfonic acid ionomer ($H_0 = -12$). Using this solid catalyst, they obtained 90 - 97 % of water soluble sugars under optimized conditions. The complete characterization of the glucans showed the formation of oligosaccharides with

DP up to 11 and glycosidic linkages in all possible positions (α/β -1,4, -1,3, -1,6, -1,2). This could prove the simultaneous depolymerization and reverse random glycosylation during the mechanocatalytic process. They also analysed the effect of the milling-speed/duration and water content of the acid catalyst. They concluded, that the depolymerization rate and the kinetic of the reaction is mostly governed by mechanical forces and is not catalytically controlled. Longer milling times and faster rotations can in some case increase the amount of soluble product. At too long reaction times, or rotation speed above 500 rpm, however, the cellulose molecules were degraded to coloured tar-like insoluble products. Especially the content of water of the acid catalyst turned out to have a great impact on the mechanocatalytical process. It was suggested that the water is buffering the mechanical forces and lowers the depolymerization rate. This effect was referred to the liquid-assisted grinding and its influence was proved by remarkably higher depolymerization rates with freeze-dried cellulose samples. Altogether, these data confirmed that the kinetic of the mechanocatalytic process is controlled by the mechanical forces and that the reaction rate can be tuned by the content of water, catalyst and the rotational speed of the miller.

3 Sugar based surfactants

Among the various applications of sugars (see in previous chapters), the interest in sugar-based surfactants is strongly motivated by their favourable properties for consumer products and technical applications, mostly related to their low toxicity. Compared to the well-known petrol-based alkyl-polyethyleneglycol-ethers, they also show very low sensitivity towards temperature changes and promising degradation properties.^[103] Despite the decrease in cost for petroleum based surfactants, the manufacturing of sugar-based amphiphiles has increasing over the past years, showing the importance and interest of the industry for those precious biomolecules.^[104]

3.1 Introduction bio-based surfactants

Generally speaking, one understands by a surfactant a molecule capable to adhere to any interface (liquid-gas, solid-liquid, solid-gas or water-oil) and consequently to lower their surface energy. This effect is caused by its molecular structure that is separated into a hydrophilic and a lipophilic part linked to each other. The hydrophilic part can either be neutral (nonionic surfactants) or charged (cationic, anionic and amphoteric surfactants). The surfactant gets adsorbed at the interface, subsequently lowering their surface energy until saturation is attained (= critical micelle concentration CMC). At this point, the interfacial tension stays constant and the surfactants start to self-assemble to energetically preferred structures like micelles or vesicles. The balance between the hydrophilic and the lipophilic domain (called hydrophilic to lyophilic balance, HLB) indicates whether the amphiphile is

more likely to be soluble in polar/aqueous- or non-polar solutions. For instant a surfactant with a high HLB value, is highly water-soluble and suitable to dissolve oil into water and vice-versa.^[105] Bio-based surfactants need to be derived totally or to a large part from biological products, agricultural or forestry resources (plant, animal and marina).^[106] The European Commission of Standardization (CEN) classified them into four categories: wholly biobased (> 95 %), majority biobased (50 % - 94 %), minority biobased (5 % - 49 %) and non-biobased (< 5 %). Another separation was made between ‘bio-based’ surfactants and ‘biosurfactants’. While the definition of the former was just described, the term ‘biosurfactant’ signifies that the molecules are directly produced by microorganism. The same rules are applied for bio-based polymers and biopolymers, respectively.

Surfactants have a general high demand worldwide. Their global market was estimated to 30.64 billion dollar in 2016 and predicted to reach 39.86 billion by 2021.^[107] With the trend to more sustainable chemical products and stronger regulations on greener process, bio-based surfactants will form a permanent part of the global surfactant market. Ester bonds are the major linkage used to connect the two parts of the amphiphiles, often consisting of fatty acids for the lipophilic and polysaccharides and proteins for the hydrophilic part. The fatty acids are derived either from oilseeds as triglycerides or recovered from oleochemical coproducts as free fatty acids (FFA) during refining processes. The ester bonds are preferable due to their biodegradability and biocompatibility but shows stability problems and lack of performance in applications such as detergents during washing processes. Therefore, other linkages have been developed such as ether, amides and carbonates, which then again lead to less biodegradability. There is though always a compromise between performance and biodegradability.^[108]

3.2 Sugar based surfactants

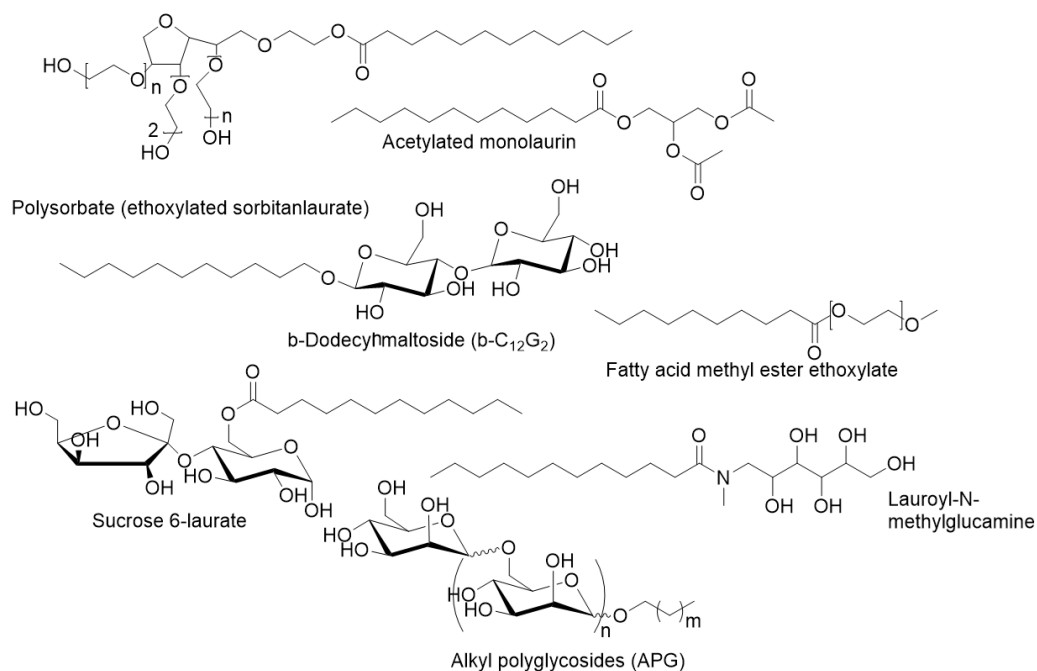


Figure 20. sugar based nonionic surfactants.^[108]

Carbohydrates present one of the main resources to obtain the hydrophilic part for bio-based surfactants. They are categorized as nonionic surfactants, with the sugar part linked through an ester, ether or amide bond to a fatty acid residue (some examples are shown in Figure 20). Among them, fatty acid esters with bio-based glycerol, glycol and other sugar derivate count the highest number and find various applications in food (margarine, ice cream, bread, chewing gum), pharmaceuticals (drug delivery and emulsifier) and cosmetics (emulsifier, viscosity builder).

Some other important sugar-based surfactants are glycolipids such as rhamnolipids, mannosylerythritol or sugar esters derived from mono-, or disaccharides coupled with fatty acyl donors (FFA or FAME). These esters could show good biodegradability and antimicrobial activities. Sugar alcohol ester, precisely sorbitan-, and ethoxylated sorbitan ester, known under the names Span and Tween respectively, are frequently applied as emulsifiers. Fatty acid ester of ethylene and propylene glycol, as well as polyglycerol, form another important group. Polyglycerol polyricinoleate^[109], for example, shows good properties as emulsifier for salad dressings or chocolate.

Sugars conjugates with short and long-chain alkyl groups *via* acetal linkages are known as alkyl polyglycosides (APG) and will be the focus of the following subchapter. They are industrially produced through the acid-catalyzed Fischer glycosylation reaction. This reaction couples unprotected monomeric sugars with long chain alkyl alcohols (C₅-C₁₈). Finally, there are glucose amides that showed higher stabilities than their ester homologues and N-alkyl and N-methyl glucamides, which have similar properties as alkyl glucosides.^[108]

3.3 Alkyl polyglycosides (APG)

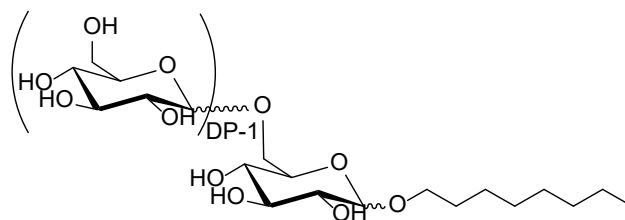
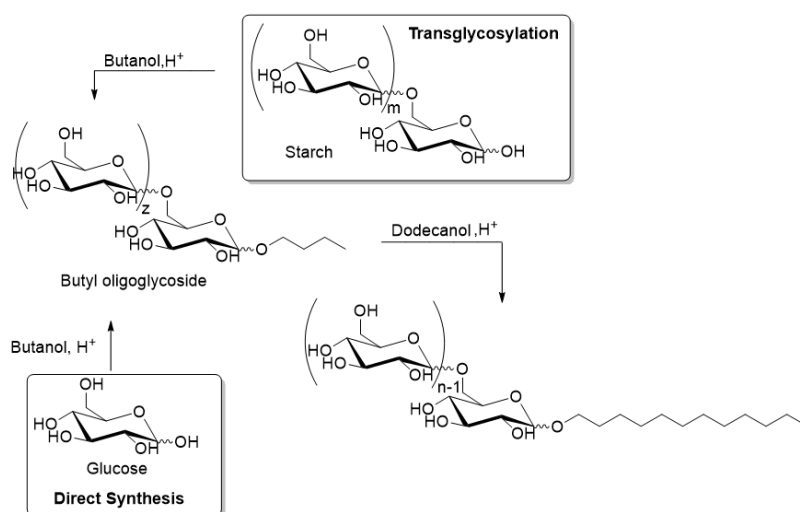


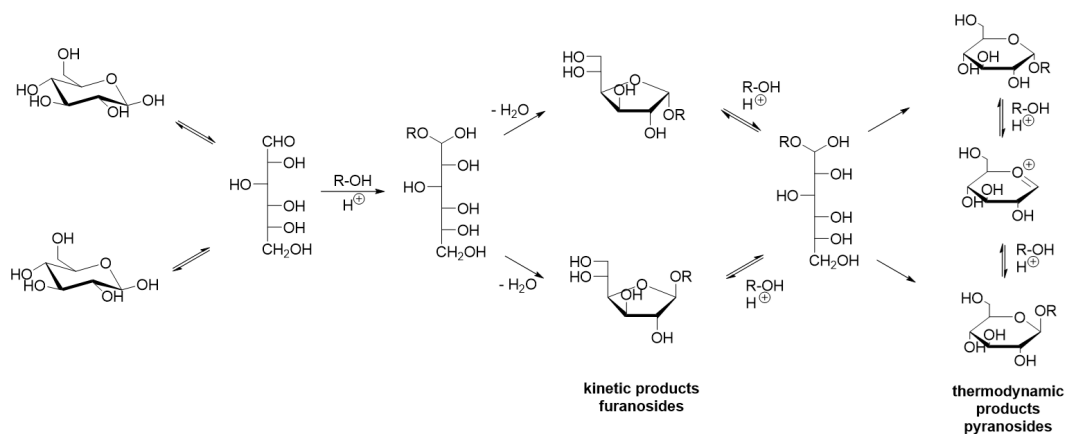
Figure 21. Molecular structure of alkyl polyglycosides (here = octyl glycoside); typical DP = 1-2.

Alkyl polyglycosides (APG) are alkylated carbohydrates, that present a complex mixture of α - and β - pyrano-, and furanoside isomers of mono- and randomly linked polyglycosides. Since their first discovery in the late 1890s^[36-37], they were produced on an industrial scale one century later by Henkel. Today, they find a lot of applications in food, detergents, cosmetic, agrochemicals and pharmaceutical issues^[110] and could show excellent ecotoxicological profiles since they are claimed to be ready biodegradable.^[111] They are prepared through Fischer glycosylation reaction of carbohydrates with fatty alcohols under acid conditions. The carbohydrates are obtained (monomeric or polymeric form) from corn, wheat and potatoes, while the fatty alcohols are usually based on vegetable oils such as coconut, palm or rapeseed.^[35] The first APGs were prepared with fatty alcohols of C₈-C₁₀, whereas nowadays also longer chain alkyl polyglycosides ($\geq C_{18}$) are synthesized. The short chain APGs can be obtained by the ‘direct synthesis’, whereas for their long chain analogues, an intermediate step is needed going through transglycosylation of butyl or propyl glycoside by longer alkyl alcohols (e.g. dodecanol). Scheme 24 shows the industrial pathways of APGs demonstrating both strategies.



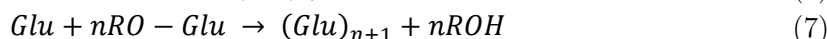
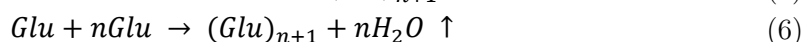
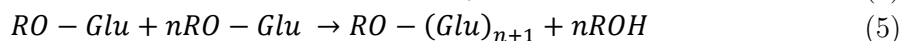
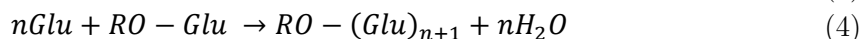
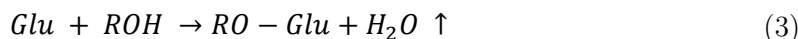
Scheme 24. Industrial pathways of alkyl polyglycoside synthesis.^[35]

The high temperatures (120 - 150 °C) that are needed for the depolymerization of starch or other polysaccharide sources and the complex procedure lead to high plant costs.^[111] That is why it remains challenging to prepare these bio-based surfactants in a comparable fashion to petroleum-based ones. Another hurdle presents the enlargement of the hydrophilic part, which is still a current challenge for glycoscientists. Thereby, exhaustive studies have been carried out to obtain a better understanding of the reaction mechanism. Hill and Ribinsky^[35] were the first to present a complete study of APGs in 1997 which still holds true and is cited in recent reviews of bio-based surfactants^[108] and alkyl polyglycosides.^[111] Scheme 25 shows the proposed reaction mechanism, where a reducing sugar (glycosyl donor) is reacting with an excess of alcohol (glycosyl acceptor). It could be shown, that the reaction proceeds through acetalization of the open-ring form of the sugar, forming first α/β -furanosides (kinetic products), which are slowly converted to α/β -pyranosides (thermodynamic products).^[112]



Scheme 25. Reaction mechanism of Fischer glycosylation.^[113]

The glycosylated sugars can then further react with each other or other alcohol molecules. A complex equilibrium is established between the various competing reactions, that determines the composition of the final product mixture. Geetha *et al.*^[111] summed up in their review of alkyl polyglycosides published in 2012 all the possible reaction pathways.



In a first step (Equation (3)), the relevant sugar (here glucose = Glu), reacts with a fatty alcohol (ROH) to the alkyl glycoside (RO-Glu) under the loss of water. The fatty alcohol acts here as glycosyl acceptor and attacks the activated sugar (glycosyl donor) via nucleophilic

substitution. The formed alkyl glycoside can then react with another activated sugar to form an alkylated disaccharide (Equation (4)). Either this reaction is repeated, resulting in a prolongation of the chain, or the alkylated monoglycoside of reaction (3) reacts with another alkyl monoglycoside under the cleavage of the fatty alcohol (Equation (5)). In a similar fashion, the glucose molecules can react with each other, affording nonalkylated oligosaccharides (Equation (6)). These glucose oligosaccharides can equally be obtained by the reaction of an alkylated glycoside with an activated sugar under the cleavage of the fatty alcohol (Equation (7)). Altogether, these reactions demonstrate the complexity of the Fischer glycosylation, making a prediction of the product mixture very challenging. Nevertheless, with the help of the modified statistic model of P.J. Flory^[35], one can approximately describe the distribution of the obtained oligomers.

$$DP = \frac{p_1}{100} \times 1 + \frac{p_2}{100} \times 2 + \dots = \sum_{i=1}^{\infty} \frac{p_i}{100} \times i \quad (8)$$

More precisely, this description concerns a statistic distribution of the average degree of polymerization (DP), that is calculated from the mole percent (p_i) of the respective oligomer “ i ” in the corresponding product mixture. The various studies of alkyl polyglycosides showed, that the DP can be controlled by adjusting the amount of sugar to alcohol. In a general setup, a molar excess of alcohol between 1 and 6 leads to average DPs between 1.4 and 2.2.^[113] However, the main product remains the monoalkylated glycoside (constituted to 50 % or more) as shown in Figure 22.

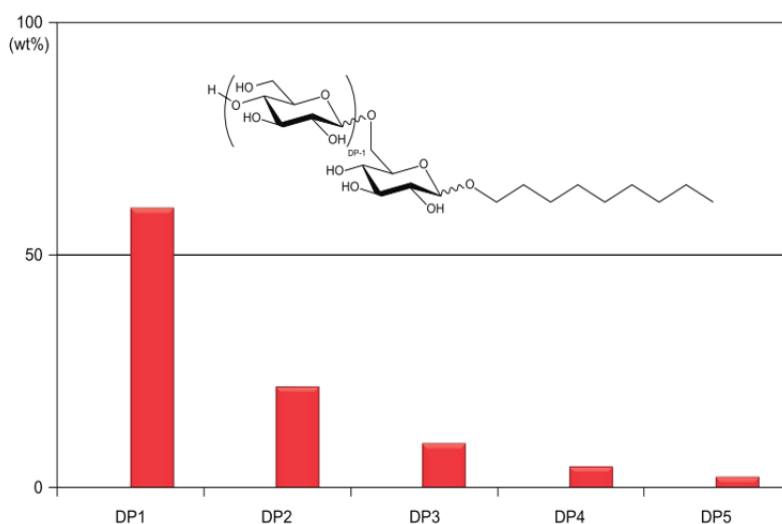


Figure 22. Distribution of dodecyl glycoside oligomers with a DP = 1.3.^[113]

One of the most reported problems that is hampering an enlargement of the DP is the uncontrolled polymerization of glucose. It was found that such side-reaction occurs more frequently at higher temperatures, forming randomly linked ‘polydextrose’. In order to find a

way to improve the DP to higher molar mass, Hins and Ribinsky^[35] analyzed the mass balance between the target alkyl oligomers and polydextrose.

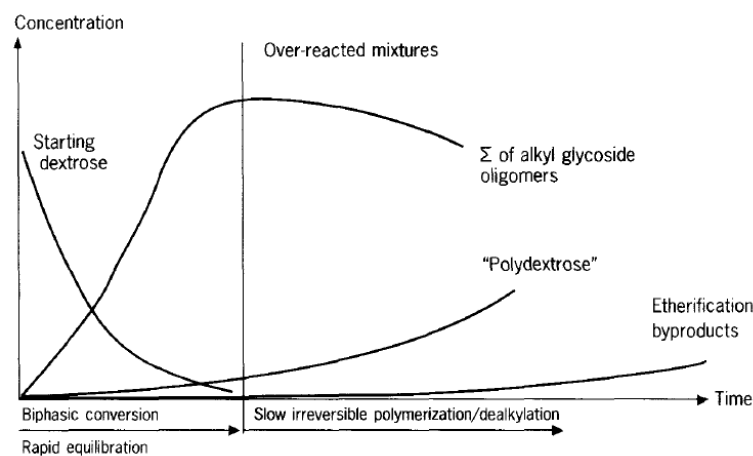


Figure 23. Mass balance between alkyl glycosides and polydextrose during glycosylation.^[35]

As the diagram in Figure 23 shows, the reaction between glucose and fatty alcohol reaches very fast its equilibrium, followed by a slow degradation of the alkyl glycosides (dealkylation and polymerization). Polydextrose presents the thermodynamically most stable product and is formed irreversible. A vertical line in the diagram gives the maximal concentration of oligosaccharides and defines the reaction afterwards as ‘over-reacted’. From this point, polymerization and etherification are dominating the reaction, affording different by-products. The vertical line gives likewise the maximum conversion rate, which they proved by the presence of free glucose molecules in the product mixture, when they stopped the reaction before reaching that point. As it resulted, the Fischer glycosylation between sugars and alcohol is very sensitive to the reaction conditions, which should be discussed separately.

Molar ratio between sugar to alcohol

All present studies of APGs claimed the molar ratio between sugar to alcohol as the main influence factor for the DP. In fact, by adjusting the amount of sugar to fatty alcohol, scientist could precisely control the DP of the obtained alkyl polyglycosides. The higher the excess of fatty alcohol, the lower the resulting DP, consequently. However, due to the prevention of any solvent, they were restricted to work at least with an excess of alcohol of two molar equivalents, since the solution was too viscous and proper stirring/mixing of sugar and alcohol could not be assured.

Temperature and nature of sugar

The operating temperature for the Fischer glycosylation is usually between 80 and 120 °C. The minimal temperate needed strongly depends on the nature of the applied sugar. ‘C5’ sugars like fructose could be glycosylated under milder conditions at 80 °C, since they don’t compose a primary alcohol (like OH-6 for ‘C6’ sugars), that favours self-etherification. Glucose based APGs need in contrast temperatures of 120 °C and show side-reactions like polymerization, degradation and etherification. The formation of coloured tar-like materials

(humin like) could be found for all kind of monosaccharides, when the reaction was carried out at higher temperatures.

Time

As the graph in Figure 23 is demonstrating, longer reaction times shift the reaction mixture to the thermodynamically favoured products. The formed alkyl oligosaccharides start to dealkylate and degrade, affording randomly polymerized sugars and alkyl monoglycosides. With the fine control of the reaction time, one can therefore tune the product composition and find the point, where the maximum of sugar is converted without already important degradation processes.

Pressure

The degradation and polymerization processes are strongly assigned to the released water during the glycosylation. That's why, in industrial processes, the reaction is usually carried out at low pressures of 20 to 100 mbar to remove the water.

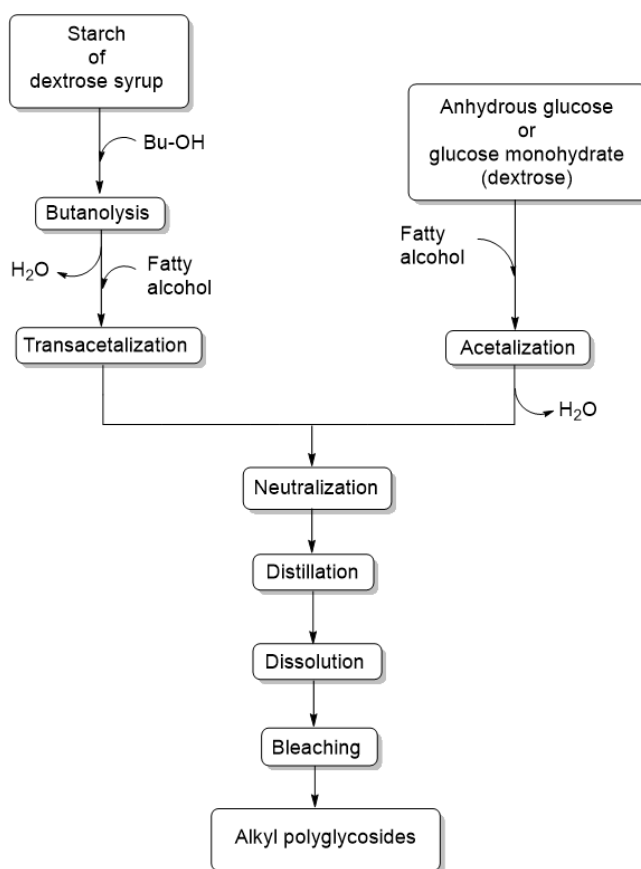
Catalyst

In general, any acid catalyst with sufficient strength can be used to activate the sugars to form a carbocation and initiate the glycosylation reaction. The catalyst that are mainly used are H_2SO_4 , HCl , H_3PO_4 , BF_3 and sulfonic acids. The nature of the catalyst can lower the unwanted polymerization of glucose. It was shown that the glycosylation of glucose with H_2SO_4 led to 20 % polydextrose, whereas sterically hindered sulfonic acid afforded only 2 % of the undesired side product.^[114] Of all the catalytic system tested, the best results were obtained using a binary catalyst comprised of a strong organic acid and a weak base. This setup and a molar ratio of sugar to alcohol of 1 to 5, could reduce the formation of polydextrose to 0.7 %.^[111] The utilization of an organic acid was suggested to be advantageous, since the side reactions are known to take place in the polar phase (traces of water).^[115] The same results were obtained with the employment of hydrophobic acids like alkyl benzene sulfonic acids.

Another promising pathway was the glycosylation under emulsion conditions performed by Karam *et al.*^[116] with the help of the solid superacid PFSA (Aquivion perfluorosulfonic acid). With Aquivion as the acid catalyst, it was possible to successfully alkylate glucose and glucose syrup (H_2SO_4 is not capable to convert glucose syrup) to APGs with 85 % yield and a DP of 1.2. These results were ascribed to a 'pickering-like' emulsification of the biphasic reaction media due to the amphiphilic character of Aquivion.

Van Es *et al.*^[117] presented a method, where they utilized a cocatalyst in order to reduce the amount of the main acid. As cocatalyst, they took 5-furandicarboxylic acid or its *n*-decyl ester to assist the reaction initially catalyzed by sulfuric acid. The co-catalyst could add phase transfer properties and reduce unwanted side-reactions. Finally, the glycosylation reaction was tested with a system using sulfoxides and sulfones, that act as solvent and catalyst at the same time. These organic compounds could glycosylate glucose with high efficiency and were recovered and recycled after the reaction by liquid-liquid separation. Also here, the improvement was assigned to the biphasic reaction medium.^[118]

Industrial process of the preparation of APGs

Figure 24. Industrial process of APG production.^[113]

At an industrial scale, APGs are prepared *via* two different procedures, summarized in Figure 24. Due to the difficulties discussed previously, this process demands elaborated techniques and finely balanced parameters. The high amounts of corrosive or toxic catalyst, the large quantities of fatty alcohol and high temperatures are problems for an industrial scale up. Henkel was the first company that started with the production of two plants in the United States and Germany in the end of the 1990s. Today, the capacity has increased enormously and is estimated to 100.000 tons per year. The main resources for the industrial production of APGs are sugar cane in Brazil or sugar beet in Europe.

However, as described earlier, the production of APGs is either carried out by the direct synthesis or by transacetalization. In each case, the corresponding sugar is thoroughly suspended in an excess of fatty alcohol to maintain a heterogeneous solid/liquid reaction. The non-solubility of the sugar in the alcohol presents one of the main hurdles during the preparation of APGs. A modified direct synthesis discusses the use of degraded glucose syrup or a second solvent and/or emulsifiers to obtain fine-droplet dispersion that promotes the conversion rate. The APG can be generally separated in water-soluble ($C_{8/10}$, $C_{12/14}$) and water insoluble products (C_{16-18}), depending on their DP and the chain length of the fatty alcohol used. Regardless the method applied, the glycosylation is carried out in a first step by using

an acid catalyst and operating temperatures above 120 °C for pyranosides and lower temperatures around 80 °C for “C5” sugars. The excess of fatty alcohol is mainly between 2 and 6 equivalents of the employed sugar. After the reaction, the acid solution is neutralized using standard bases (mostly NaOH or MgO), affording a yellowish solution composed of 50 up to 80 % of non-reacted fatty alcohol. The remaining excess of alcohol is then removed by vacuum distillation. For this step, it is important to keep the thermal stress as low as possible, in order to prevent the formation of pyrolysis products. Therefore, multistage distillations, thin-layer or short-path evaporators are necessary. The obtained crude powder is then dissolved in water to obtain a high concentrated paste of 50 to 70 % of alkyl polyglycosides. The final work-up steps include bleaching, adjusting of the pH and microbial stabilization, before the product reaches a satisfying quality for the market.^[35, 113]

Another strategy that might pave the way to APGs with high DP is the exploitation of chemo-enzymatic approaches. β -Glycosidases are hydrolytic enzymes that could be successfully applied for the synthesis of alkyl-glycosides, reported by the Rather and Mishra in 2013.^[119] They are available from natural- (microorganism and plants) or commercial sources (almond seeds) and work either in a retaining or inverting reaction mechanism as already described in subsection 2.2.1. Compared to the classical chemical synthesis method for APGs, the enzymatic route bears a lot of advantages such as mild reaction conditions (neutral pH-value, ambient reaction temperature, atmospheric pressure) and high enantio- and stereospecific selectivity. However, even if these methods can improve the APG production for many aspects, they are still too costly to become industrially and economically viable (market price of APG is around 1.5 €/kg). Besides, for long chain fatty alcohols above C₈, the miscibility for the sugar becomes very low, which drastically decreases the yield. Higher temperatures would indeed increase the solubility of the long chain alkyl alcohols, but also denature the enzymes. Altogether, further studies are necessary to develop thermophilic and organic-solvent-tolerant enzymes, to commercialize the enzymatic route in bioreactors.^[119]

3.4 End-functionalization of oligosaccharides to prepare amphiphilic conjugates

Another strategy for the preparation of amphiphilic carbohydrates is the end-functionalization of poly-, respectively oligosaccharides at their terminal end (anomeric position, reducing end). Frequently, oligosaccharides are applied to prepare amphiphilic block copolymers (oligosaccharide-based block copolymers = OBCPs), which tend to self-assemble to nanoparticles or sub-nanopatterned thin-films^[120] in aqueous solution due to the high incompatibility between the two blocks. They are highly attractive due to their biocompatibility for nanomedicine^[121] and nanoelectronic^[122] applications. The incorporation of the oligosaccharide block as natural compound allows a valorization of the respective

biomass, which is getting more and more important nowadays. Since the first reported preparation of a linear block copolymer from polysaccharides in 1961 from Ceresa^[123], various strategies have been developed to obtain these conjugated structures.

There are mainly three methods to be named, such as the *in vitro* enzymatic polymerization of a PS chain from end-functionalized synthetic polymer blocks, the polymerization of a synthetic block from a polysaccharide ('grafting from'), or the coupling between two previous prepared blocks bearing antagonist functions at their ends ('grafting on'). This chapter will be focusing on the grafting on strategy. To this, regio- and stereoselective functionalization of the anomeric position (reducing-end) of the oligosaccharides are carried out. The different chemical behaviour of the hemiacetal group at the reducing-end compared to the remaining OH group of the sugar ring is exploited to modify the latter with various nucleophiles. One of the most common method is the one-pot reductive amination by ring-opening at the chain end of the respective saccharide. This method occurs within two-steps as demonstrated in Figure 25.

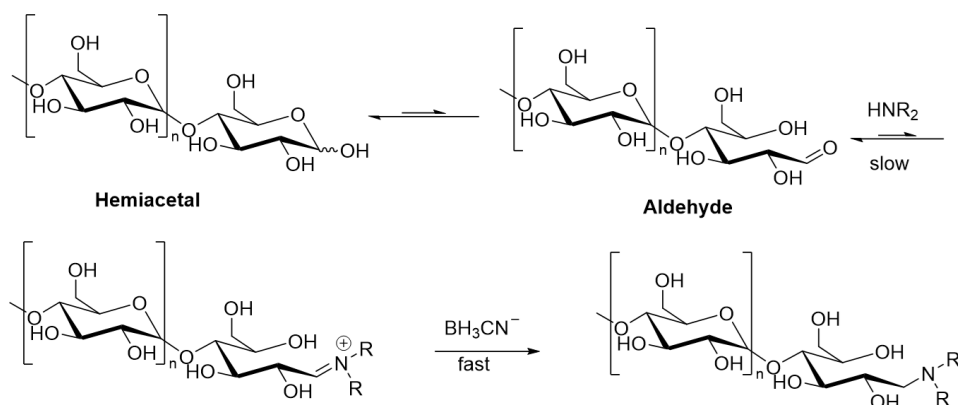


Figure 25. Reductive amination at the reducing end of a sugar-derivative to introduce an amine function.^[124]

In this reaction, the aldehyde form of the sugar reacts with an amine to form an iminium ion, which is then reduced by a suitable reducing agent (sodium cyanoborohydride is widely used^[125]). Since the amount of the free aldehyde-form in the equilibrium of the sugar isomers is very low compared to the cyclic hemiacetal (see subsection 1.2), this reaction takes usually days to proceed. Nevertheless, it was applied for the direct synthesis of oligosaccharide-based amphiphiles such as the block copolymers of hyaluronan (DP 5) and PEO (DP 47)^[126] and aminoalditols (XGO- C_n) of branched xylo-oligosaccharides bearing alkyl chains of 8 to 18 carbon atoms.^[127] The reaction could be improved if the reducing end was oxidized to an aldonic acid lactone. This was shown by Loss and Stadler^[128], who reported the successful synthesis of a hybrid block copolymer employing maltoheptaonolactone. Other groups mentioned the utilization of amine groups at the reducing-end of polysaccharides to couple them with synthetic polymers. Therefore, the polysaccharides were first protected by acetyl-,

or trimethylsilyl groups. Kamitakahara *et al.*^[129] reported the preparation of cellulose triacetate-*block*-oligoamide-15 copolymers using cellulose triacetate (CTA) with a primary amine at the anomeric position and Liu and Zhang^[130] the coupling of an amino end-functionalized dextran with an acryloyl end-capped PCL block. However, the most widespread method to couple another polymer/molecule to the saccharide block is the copper (I)-catalyzed azide-alkyne cycloaddition (CuAAC). To proceed this reaction, the sugar part needs to be functionalized with an alkyne-, or an azide function, respectively. Many reported studies mentioned the introduction of propargylamine followed by N-acetylation to supply the oligosaccharide with an alkyne function (Figure 26).

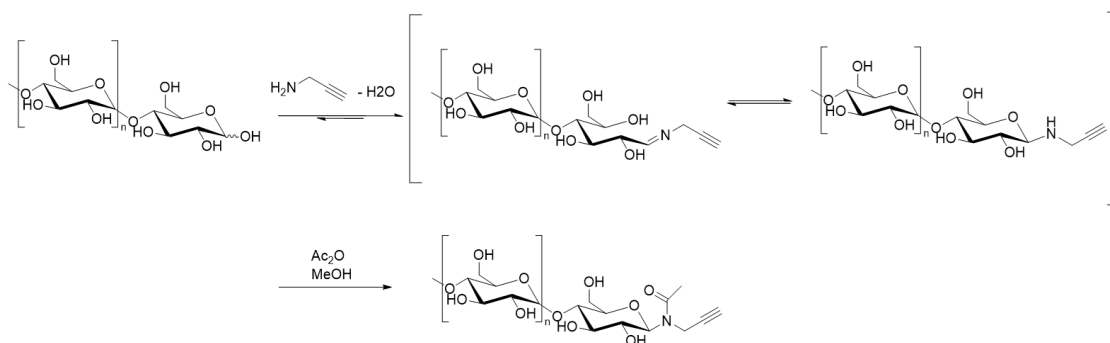


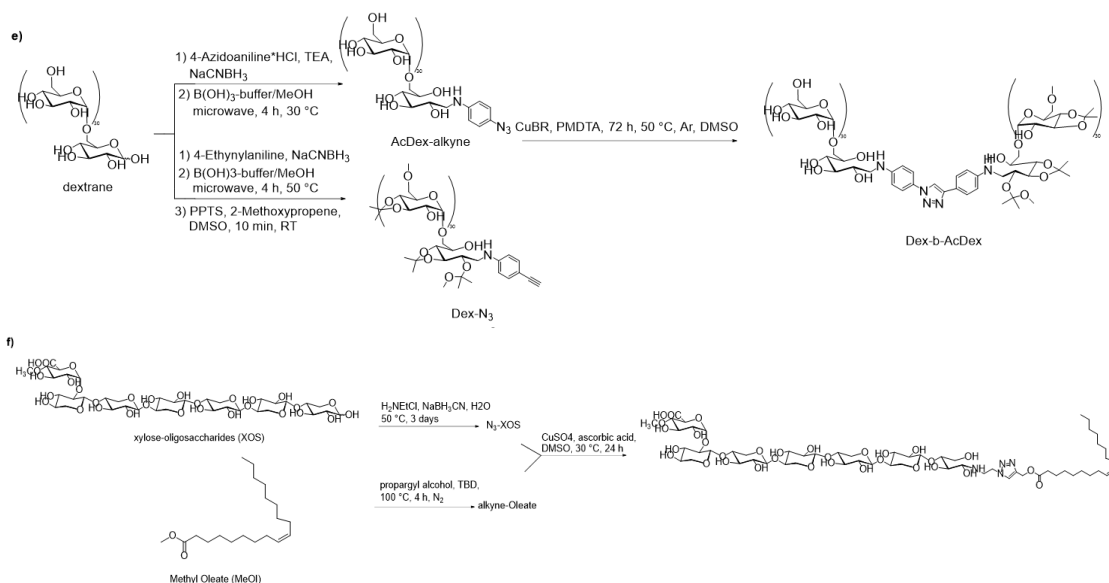
Figure 26. General scheme for the chemoselective functionalization of terminal free oligosaccharides with propargylamine to give N-acetyl propargyl glycosylamides.^[131]

Within this method, the synthesis of polysaccharide-, respectively oligosaccharide based block copolymers such as glycol-polyorganosiloxanes^[131], hybrid oligosaccharide-*block*-poly(N-isopropylacrylamide) based on propargyl-functionalized maltoheptaose^[121b] and fully maltose based block copolymers^[121a] were reported. The reductive amination (utilizing NaBH_3CN as reducing agent) was evenly considered for the introduction of an alkyne function at the terminal end of the oligosaccharides. Here, hyaluronan-*b*-poly(γ -benzyl L-glutamate)^[132], dextran-*block*-poly(γ -benzyl L-glutamate)^[133], amylose-*block*-polystyrene copolymers^[128], chondroitin sulfate-*block*-poly(lactic acid)^[134] and the preparation of a fully polysaccharide based block copolymer composed of a hydrophilic dextran and a hydrophobic acetylated dextran block^[135] have been reported. The last example named was published by Breitenbach *et al.*, where they introduced the alkyne-, as well as the azide group *via* reductive amination, varying only the applied amine. They utilized either 4-azidoaniline hydrochloride for the introduction of the azide-, or 4-ethynylaniline for the alkyne group.

The introduction of an azide group was equally reported by Modolon *et al.* in 2012^[121a] and more recently by Chemin in 2018.^[136] Modolon took advantage of the ‘Shoda Method’^[137] to functionalize unprotected sugars with an azide using 2-chloro-1,3-dimethylimidazolium chloride (DMC) as activating agent. This method is known for its efficiency in functionalization of unprotected mono- and oligosaccharides at their reducing-end (see subsection 2.1.4). Within this, the authors prepared oligosaccharide-based amphiphilic block

co-oligomers composed of a hydrophilic maltoheptaosyl block and a hydrophobic peracetylated maltoheptaosyl block. Rosselgong *et al.* introduced an azide function at the terminal end of unprotected xylo-oligosaccharides *via* reductive amination, which they coupled in a following click reaction with alkyne functionalized fatty acids. Some of the aforementioned amphiphilic conjugates are listed in Scheme 26.

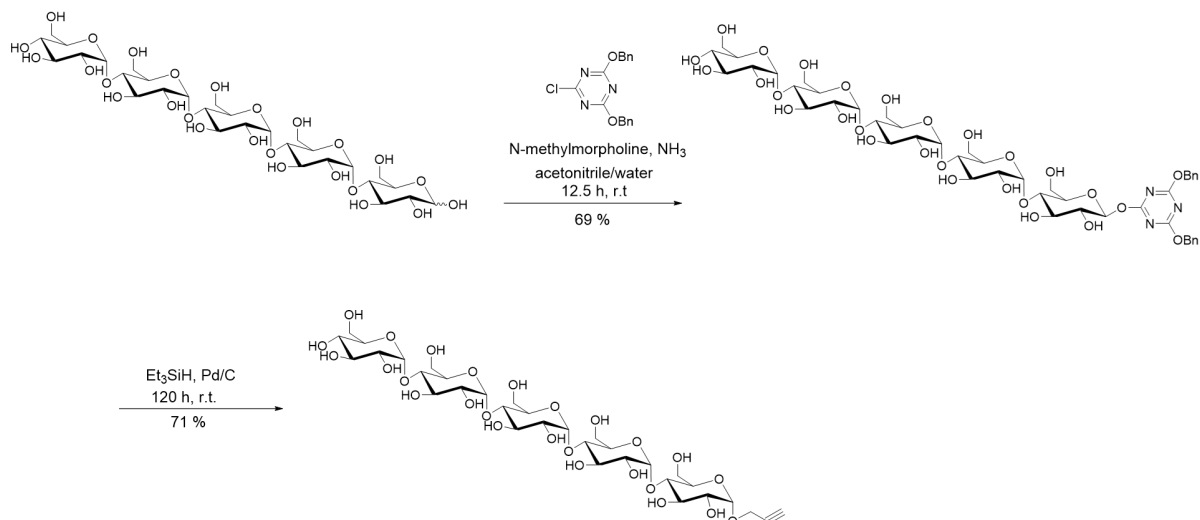




Scheme 26. Selected examples of end-functionalized oligosaccharides and preparation of amphiphilic conjugates.^{[132],[121a],[138],[139],[135],[136]}

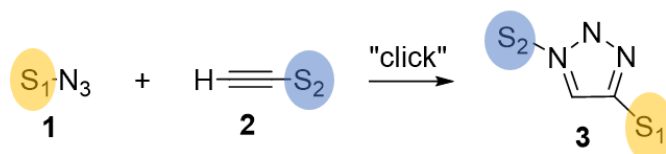
There is a huge interest for alternative routes to functionalize the reducing end of unprotected oligosaccharides. The reductive amination needs to go through the ring-open aldehyde form of the sugar, which causes long reaction durations of several days. The simplest and direct route to functionalize the anomeric position of unprotected sugars is still the glycosylation reaction developed by Emil Fischer (chapter 2.1.5). However, the acid conditions of the Fischer-glycosylation hamper its application on oligo- and polysaccharides, since it leads to depolymerization afforded by the protonation of the inner glycosidic linkages. The key to solve this problem would be a site-specific intramolecular activation at the reducing end. Shoda *et al.*^[69] developed 2013 a protection-free synthesis of alkyl glycosides without the need of any acid promoter, that could be successfully applied to oligosaccharides. At first, DAT-glycosides (4,6-dibenzyloxy-1,3,5-triazin-2-yl (DBT) glycosides), were prepared as glycosyl-donors. The conversion to alkyl glycosides followed then by nucleophilic substitution with alkyl alcohols under palladium/carbon catalyzed hydrogenolytic conditions. Within this, the authors could introduce primary and secondary alcohols with different alkyl chain lengths (C₁ - C₈) and also double and triple bonds to the reducing end of the sugars. They applied their method to a pentasaccharide by introducing an alkyne function at the terminal end of the sugars using propargyl alcohol. They observed no depolymerization during both reaction steps, indicating the regioselective activation of the anomeric position. Once the DBT group was introduced, triethylsilane was used as reductant to selectively debenzylate the benzyl groups on the triazine ring. The so deliberated hydroxyl groups led to an efficient side-specific activation of the anomeric centre of the oligosaccharides, allowing a selective substitution with propargyl

alcohol (Scheme 27). However, the presented method is very costly and deals with non-environmentally friendly catalyst.



Scheme 27. Protection-free functionalization of oligosaccharides without acid promoter by Shoda et. al.^[69]

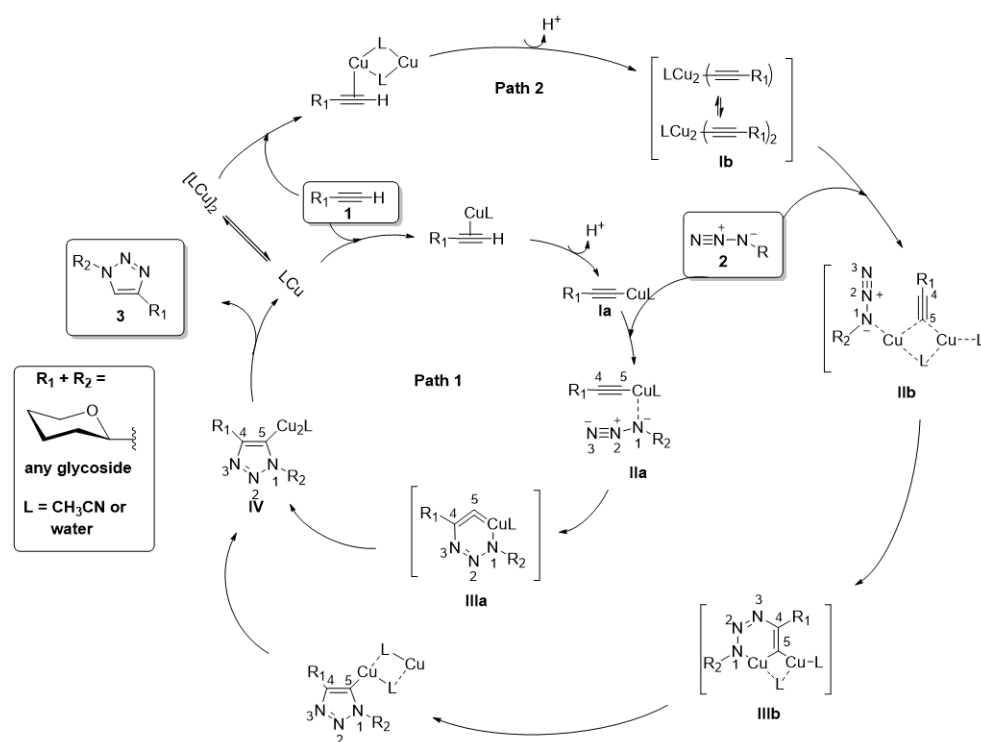
3.5 Azide-alkyne Huisgen cycloaddition (CuAAC)



Scheme 28. Cu(I) catalyzed azide-alkyne 1,3-dipolar cycloaddition (CuAAC). (i) S_1 = sugar, S_2 = sugar; (ii) S_1 = sugar, S_2 = non sugar; (iii) S_1 = non sugar; S_2 = sugar.

The copper(I)-catalyzed azide-alkyne 1,3-dipolar cycloaddition (CuAAC), explored by Huisgen in 1960^[140], is one of the most popular and highly efficient reaction for chemists to combine completely different molecular entities. In the field of glycoscience, this reaction has gained a lot of attention in the past 15 years and was applied to prepare various glycoconjugates and glycopolymers for biological and pharmaceutical applications. The CuAAC falls into the categorization of the ‘click chemistry’ defined by Sharpless in 1999. He defined a set of ‘stringent criteria’ for a reaction to be defined as “click”. Accordingly, the respective reaction must be modular, broad in scope, high yielding, creating no or only inoffensive side-products, that can be removed without chromatographic methods, stereospecific and effected under mild conditions in easily removable solvents (e.g. water). The Cu-catalyzed click chemistry combines terminal alkynes (**2**) with organic azides (**1**) to obtain exclusively 1,4-disubstituted 1,2,3-triazoles (**3**). In carbohydrate chemistry, this method was exploited to prepare glycoconjugates in a rapid and efficient manner. The heterocyclic triazolyl

ring joins thereby the sugar moiety to another sugar or biomolecule (Scheme 28). Within this, numerous glycoconjugates such as glycoproteins, oligomers, glycopolymers, glycoclusters, glycolipid conjugates, sugar-based macrocycles, glycopeptides and oligonucleotides have been synthesized with widespread applications in labeling, microarray constructions, sensing, promising enzyme inhibitors and drug discovery. Another important application of this reaction is found for the preparation of sugar based amphiphilic compounds as described in the previous chapter. There are mainly three different protocols for the copper catalyst, (i) direct utilization of copper(I) source, (ii) creation of Cu(I) throughout the reaction by reduction of Cu(II) salts or (iii) oxidation of copper from its elemental form. The most widespread method is the *in-situ* formation of Cu(I) by reduction of copper(II) salts such as CuSO_4 or $\text{Cu}(\text{OAc})_2$, since it is unaffected under oxidizing and aqueous conditions. The mechanism of this reaction was extensively studied and resulted to be very complex due to the tendency of copper to form complexes with the various additives of the reaction (ligands, reactants, solvents, etc.). However, the studies could provide two plausible pathways (I and II, Scheme 29), which are described in the following.



Scheme 29. Mechanism of the copper(I)-catalyzed azide-alkyne cycloaddition.

The ligand for copper(L) that is often used is acetonitrile, but similar results were also obtained with water or other solvents. In the first step, Cu(I) coordinates to the terminal alkyne by displacing one of its ligands. The so afforded μ -coordinated aggregate deprotonates to give copper acetylides **Ia** and **Ib** in a protic medium. Then, the C-2 carbon of **Ia**, resp. **Ib** accepts an electron from N-3 of an azide to form the complexes **IIa** and **IIb**. These complexes rearrange to **IIIa** and **IIIb** due to the nucleophilic attack of the terminal N-3 to the C-4 atom.

The lone pair (N-1) of the six-membered ring (metallacycle **IIIa** and **IIIb**) attacks C-5 to give the intermediate **IV** (via ring contraction). Finally, the latter is protonated either by a base or a solvent and the copper complex is dissociated to give the 1,4-disubstituted 1,2,3-triazole **3**.

The incorporation of an alkyne- or azide function onto sugar components is largely reported in the literature by well-established reaction procedures. The anomeric centre of the carbohydrates was shown to be the preferred position for their introduction. The CuAAC can be considered as one of the most successful protocols used to prepare multivalent carbohydrate-based molecules.

4 Self-assembly of amphiphilic molecules and polymers

4.1 Principles of Self-Assembly of amphiphilic molecules

Amphiphilic molecules like surfactants tends to self-association, when they are dissolved in a selective solvent. This causes a spontaneous formation of ordered structures, a phenomenon called self-assembly. One very popular example is the formation of micelles from surfactants in aqueous solution. The assembly process is fundamental in our living cells and exploited for the preparation of various nanostructured materials. The intermolecular forces that hold the amphiphilic molecules together are based on van der Waals-, hydrophobic-, hydrogen-bonding- and electrostatic interactions. Since these forces are not as strong as the covalent or ionic bonds in solid particles, the whole colloidal object is soft and flexible and adapt its environmental structure by flowing. That is why self-assembled structures are also characterized as 'fluid-like complexes'. The change of the solution conditions, such as pH-value and ionic strength, affect the intermolecular forces between the molecules of one aggregate and modify their size and shape. Some of the structures formed by amphiphilic molecules in aqueous solution are given in Figure **27** and will be discussed in the following.^[141]

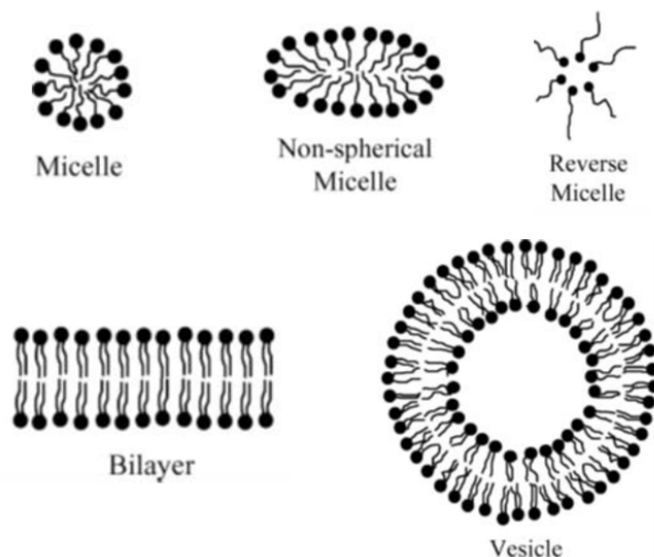


Figure 27. Associated structures of amphiphiles: micelle, non-spherical micelle, reverse micelle, vesicles and bilayer.^[142]

The self-assembly process is governed by a thermodynamic equilibrium between free amphiphilic molecules and their aggregated structures. In such equilibrium, the chemical potential μ of identical molecules in different aggregates must be the same.

$$\mu = \mu_N = \mu_N^\circ + \frac{1}{N} k_B T \log \frac{1}{N} x_N = \text{const.} \quad N = 1, 2, 3, \dots \quad (9)$$

Equation (9) describes the chemical potential, where μ_N is the mean chemical potential of a molecule in an aggregate, N the aggregation number, μ_N° the corresponding standard part of the chemical potential (mean interaction free energy/molecule) and X_N the concentration of the molecules in the aggregates. For isolated monomers in solution, the aggregate number N is 1 and consequently $\mu_1^\circ = \mu_1^\circ$ and $X_1 = X_1$. Equation (9) is derived from the *law of mass action*, that describes the rate of association as $k_1 X_1^N$ and the rate of dissociation as $K_N (X_N/N)$, where $K = K_1/K_N = \exp[-N(\mu_N^\circ - \mu_1^\circ/KT)]$, while K is the equilibrium constant. Within this, Equation (9) can be described in a more equivalent form:

$$X_N = N(X_1 e^{\left[\frac{(\mu_1^\circ - \mu_N^\circ)}{KT}\right]})^N \quad (10)$$

In order to completely describe the system, Equation (11), giving the total solute concentration C , is needed.

$$C = x_1 + x_2 + x_3 + \dots = \sum_{N=1}^{\infty} x_N \quad (11)$$

It needs to be mentioned, that these equations assume ideal mixing conditions and exclude the effects of any interaggregate interactions.

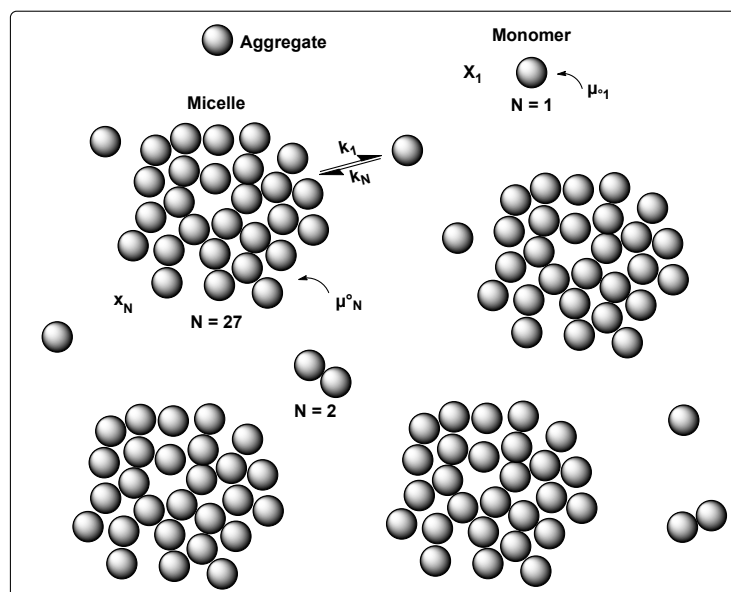


Figure 28. Association of N monomers into an aggregate (here = micelle; mean lifetime of one amphiphile in micelle: $10^{-5} - 10^{-3}$ sec)^[141]

Aggregates are only formed, if there is a difference in the cohesive energies between the molecules in the monomer- and aggregated (dispersed) state. If the intermolecular interactions with the surroundings of all molecules in the mixture (monomer and aggregates) are the same, μ_N° stays constant in different aggregates and Equation (9) becomes

$$X_N = NX_1^N \quad \text{for } \mu_1^\circ = \mu_2^\circ = \mu_3^\circ = \dots = \mu_N^\circ \quad (12)$$

From $X_i < 1$, it follows that $X_N \ll 1$ and though most of the molecules are in the monomer state. Respectively, the formation of larger aggregates is even less probable as μ_N° increases with a higher number of N (can be shown by Equation (9)). The condition for a succeed formation of stable larger aggregates is $\mu_N^\circ < \mu_1^\circ$ for at least some values of N . Either μ_N° decreases with higher numbers of N , or shows a minimum for a finite value of N . The functional variation of μ_N° with N is an indicator for many physical properties, such as the mean size and polydispersity of the aggregates. Consequently, X_N in Equation (9) presents a distribution function, since there are a number of different structurally populations that coexist in one single phase in a thermodynamically equilibrium. For each of these structures, a different functional form of μ_N° is determined, depending on the geometrical shape of the aggregate. The geometry of the aggregate shall also determine the dependence of μ_N° from N and as aforementioned, aggregation is only possible if μ_N° decreases with N . For the simplest structure, one-dimensional rod-like aggregates, the interaction force between two monomers

can be expressed as multiplicative of the thermal energy $-\alpha k_B T$ ('monomer-monomer-bond energy'). The total free energy of this interaction is then given by,

$$N\mu_N^\circ = -(N-1)\alpha k_B T \quad (13)$$

where α is a positive constant, depending on the strength of the intermolecular interactions. For an infinitely long chain (μ_∞°), Equation (12) can be ascribed as

$$\mu_N^\circ = -\left(1 - \frac{1}{N}\right)\alpha k_B T = \mu_\infty^\circ + \frac{\alpha k_B T}{N}. \quad (14)$$

The bulk energy of a molecule in an infinite aggregate is described by μ_∞° and as N increases, μ_N° decreases asymptotically towards μ_∞° . This form can be adapted and gets more complicated for other structures and shapes like two-dimensional discs or three-dimensional spheres. However, a general equation can be assigned considering the dimensionality (p) of the corresponding aggregate.

$$\mu_N^\circ = \mu_\infty^\circ + \frac{\alpha k_B T}{N^p} \quad (15)$$

For one dimensional structures p is 1, for two-dimensional p gets $\frac{1}{2}$ and $\frac{1}{3}$ for three dimensional structures, respectively.^[141]

4.2 Critical micelle concentration (CMC)

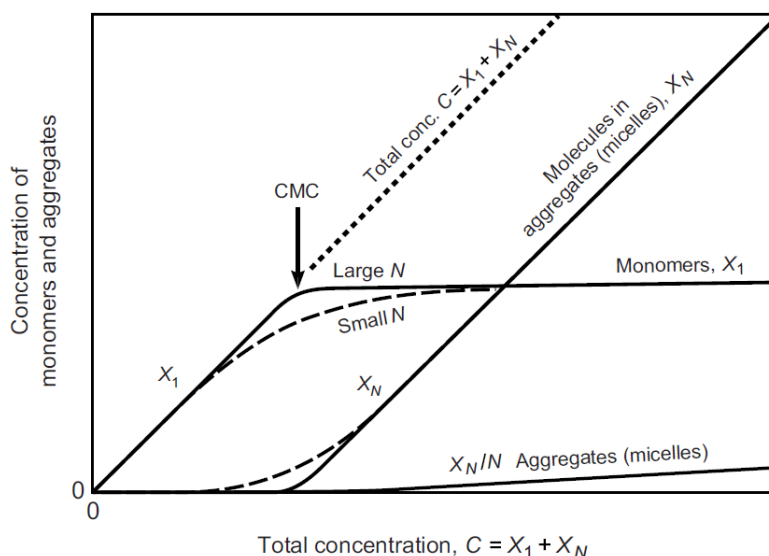


Figure 29. Relation of the unimer concentration to the formation of micelles.^[141]

Aggregates start to form when the unimer concentration reaches a certain number. By incorporating Equation (15) into the fundamental equation for self-assembly, we find that

$$\begin{aligned} x_N &= N(x_1 e^{\left[\frac{(\mu_1^\circ - \mu_N^\circ)}{k_B T}\right]})^N \\ &= N(x_1 e^{\left[\alpha \left(1 - \frac{1}{N^p}\right)\right]})^N \approx N[x_1 e^\alpha]^N \end{aligned} \quad (16)$$

As depicted in Figure 29, at low unimer concentration (x_1), the unimers are mainly presented as isolated molecules. By increasing the amount of unimers to the system, the concentration in the solution will increase until it reaches a critical point. Since x_N can never reach infinity, Equation (15) shows that once x_1 approaches $e^{-\alpha}$, it can no further increase. This critical point is called critical aggregation concentration (CAC) or more common critical micelle concentration (CMC). From Equation (15), it follows that

$$(x_1)_{crit} = e^{-\frac{(\mu_1^\circ - \mu_N^\circ)}{k_B T}} = e^{-\alpha}. \quad (17)$$

Once the CMC is reached, further addition of unimers results in the formation of more aggregates, while keeping the unimer concentration constant.^[141] In more simple words, the CMC is the concentration of surfactants in a solution above which micelles are formed and upon which all further addition of surfactants will only continue to form micelles. When a surfactant is added to an aqueous solution, the hydrophilic part will be oriented to- and the lipophilic part away from the water phase. This orientation results in a reduced surface tension between the water and air interphase. By subsequent addition of surfactants, they will cover all the surface, which further decrease the surface tension and start to aggregate into micelles, when the surface is saturated. At that point, any further addition of a surfactant will only increase the number of micelles, since the surface of water is already completely covered.

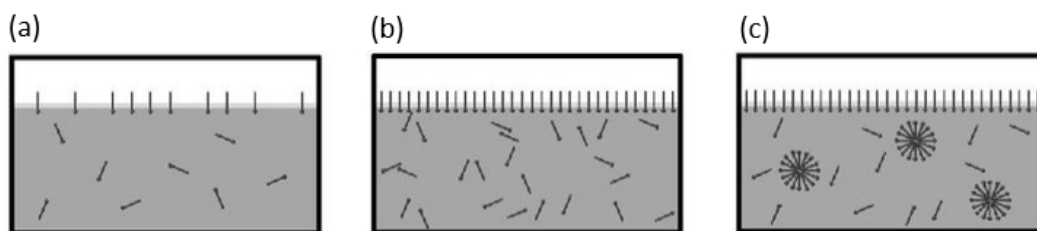


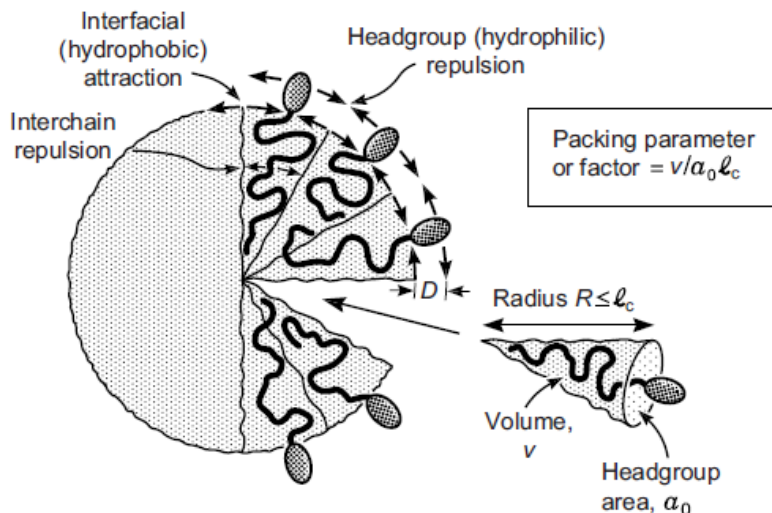
Figure 30. Subsequent addition of surfactants to a solution until CMC is reached. (a) surfactants start to cover the water surface, (b) surface is saturated by surfactants, (c) start of aggregation of the surfactants to micelles = cmc.^[143]

4.3 Self-assembly of amphiphilic molecules to micelles and vesicles

Self-assembly occurs, when the loss of entropy by aggregation is compensated by the gain of cohesive energy. Hydrocarbons in water show phase separation and no stable colloidal spheres. The hydrophobic energy of transferring the alkyl chains from the water phase into the bulk hydrocarbon phase determines their solubility. Since amphiphilic molecules are able to assemble in a way, that μ°_N reaches a minimum or a constant value, their aggregation is not infinite (phase separation) but end up with defined structures of finite sizes (micelles). These micelles show a Gaussian size distribution in solution with a mean aggregation number $M = \langle N \rangle$ and a polydispersity σ (= standard deviation of the distribution of aggregation).

$$\sigma^2 \approx \frac{\partial \log \langle N \rangle}{\partial \log C} \quad (18)$$

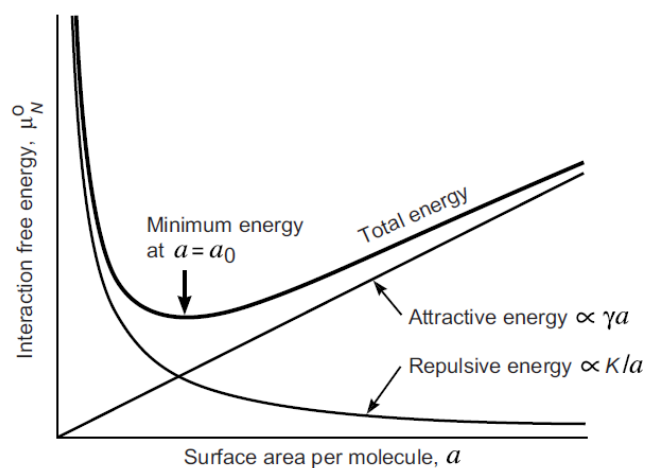
There are various structures that can be formed of amphiphiles (see Figure 27), depending on the molecular architecture. Solvent parameters can afford the transformation of one into another initiated by the interactions between (inter-aggregation forces) and within (intra-aggregation forces) the aggregates. In general, there are two competitive forces, the hydrophobic attractions between the nonpolar alkyl chain and the hydrophilic, ionic or sterically repulsions of the polar head group. These forces lead to the orientation of the head groups towards the water side and the chain ends facing away. Both forces are competitive and tend to increase or decrease the interfacial area per molecule exposed to the water phase. The main influence derives from the “hydrophobic effect”, that prevent entropic unfavourable interactions of the hydrophobic chain with water. The attractive forces among the nonpolar chains and the head groups with water, stabilize further the assembled structures. Figure 31 shows a schematic description of a micelle. Their form can be described within the surface size of the head group a_0 , the volume v of the nonpolar chain, the molecular length of the chains l_c and the radius R .

Figure 31. Schematic representation of a micelle.^[141]

Due to the attractive interactions between the hydrophobic chains, there is an interfacial tension force at the fluid hydrocarbon-water interface. This causes a positive interfacial free energy of around 50 mJ/m^2 , which is reduced in the presence of polar headgroups to $\approx 20 \text{ mJ/m}^2$. The interfacial free energy contributes to μ_N° and can be expressed as

$$\mu_N^\circ = \gamma a + \frac{k}{a}, \quad (19)$$

where k is a constant. Hence, the minimum energy can be found at $\mu_N^\circ(\text{min}) = 2\gamma a_0$ with a_0 being the optimal surface area per molecule at the hydrocarbon-water interface. For this finite value of a , the interamphiphilic interactions in micelles (attractive and repulsive forces) shows a minimum for the free energy.

Figure 32. Plot of free energy as a function of a .^[141]

As well as for the surface area of the headgroup, there are optimal values for the remaining parts of the amphiphilic molecule packed in a micelle. The final assembled structure depends

on the geometry of these “packing parameters”, for which the minimum of interfacial free energy is reached. These are defined by the already mentioned surface area of the head group a_0 , the volume of the hydrocarbon chain v and the length of these chains l . For the length, a critical value l_{crit} can be found, which limits their extension so that $l_c \leq l_{max}$ (l_{max} is the length of the fully extended chain). The most favourable structure can then be predicted on the basis of the range of the dimensionless “packing parameter” P , also referred as “Israelachvili packing parameter”, shown in Table 2.

Table 2. Packing parameters and their corresponding structures.

Packing parameter ' P '	Structure-type
$v/a_0l_c = 1/3$	Spherical micelle
$1/3 < v/a_0l_c < 1/2$	Non spherical micelle
$1/2 < v/a_0l_c < 1$	Vesicle or double layer
$v/a_0l_c > 1$	Inverted structure

It has to be mentioned, that the given structure-types present the limiting shapes of the aggregates. There is a large number of different structures, that can be formed, fulfilling the same critical packing parameters. Since for all of them, a_0 is the same (and so is μ°_N), the preferred structure will be the one with the smallest aggregation number (entropically favoured). A spherical micelle is therefore formed, when a_0 is overweighting v_0 of the hydrocarbon chain. The radius of the micelle R will thus not exceed the critical chain length l_c .^[141]

4.4 Principles of Self-Assembly of amphiphilic copolymers

Similar to amphiphilic molecules, polymers contributed of a hydrophilic and a hydrophobic part show self-assembly to minimize energetically unfavourable hydrophobic-water interactions in aqueous solution. With modern polymer synthesis, the preparation of well-defined block-, graft-, dendritic-, star-like-, or cyclic copolymers got feasible, allowing the control of the self-organized morphologies. However, linear block copolymers (BCPs) are the most extensively studied ones, which again are classified as AB diblock, ABA triblock, alternating-, or tapered block copolymers. They form aggregates of various morphologies, which are determined by the inherent molecular curvature. This, in turn, influences the packing of the copolymer chains and the specific nanostructures can be estimated by the calculation of its packing parameter.

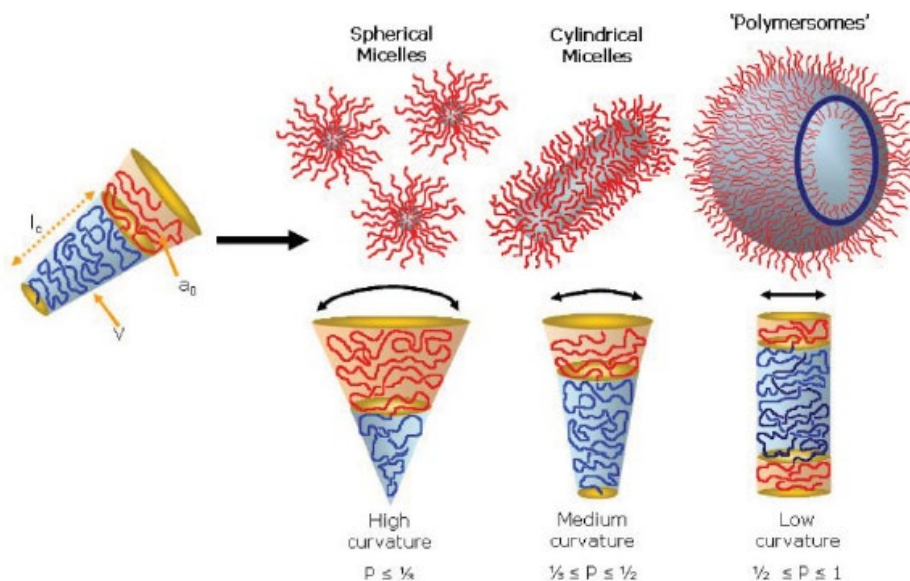


Figure 33. Self-assembled structures of amphiphilic block copolymers dependent on the respective inherent molecular curvature and packing parameter.^[144]

The calculation of P and the assignment of the corresponding morphology is similar to the one of amphiphilic molecules (see above). The principals of self-assembly are as well very similar to those of small molecules, whereas aggregates of polymers show higher stability and durability due to their improved physical properties. The self-organization process is driven by the combination of unfavourable mixing enthalpy and small mixing entropy, together with the prevention of phase separation due to the covalent bonding between the hydrophobic and hydrophilic part of the polymer blocks. These polymers afford more precisely a microphase separation, that depends on three parameters: 1) the volume fraction of block A and B (with $f_A + f_B = 1$), 2) the total degree of polymerization (with $N = N_A + N_B$) and 3) the Flory-Huggins parameter X_{AB} (a parameter indicating the degree of incompatibility between the two blocks A and B). This parameter can be described by following formula,

$$X_{AB} = \left(\frac{z}{k_B T} \right) \left[\varepsilon_{AB} - \frac{1}{2} (\varepsilon_{AA} + \varepsilon_{BB}) \right] \quad (20)$$

where z is the number of nearest neighbours per repeating unit in the polymer, k_B the Boltzmann constant, $k_B T$ the thermal energy and ε_{AB} , ε_{AA} and ε_{BB} the interaction energies between the repeat units of A-B, A-A and B-B. The just described equation is only valid for a system of copolymers in bulk. For the self-assembly process in solution, the situation gets more complex, so that for an AB block copolymer, six Flory-Huggins parameters need to be accounted: ε_{AB} , ε_{AS} , ε_{AN} , ε_{BS} , ε_{BN} and ε_{SN} , with S = good solvent for both blocks and N = poor solvent (selected solvent, most commonly water) for one of the blocks. For amphiphilic diblock copolymers, more than twenty different morphologies have been identified. Some examples from the diblock PS-*b*-PAA are illustrated in Figure 34, including spherical micelles, rods,

bicontinuous rods, lamellae, vesicles, hexagonally packed hollow hoops (HHHs) and large compound micelles (LCMs).

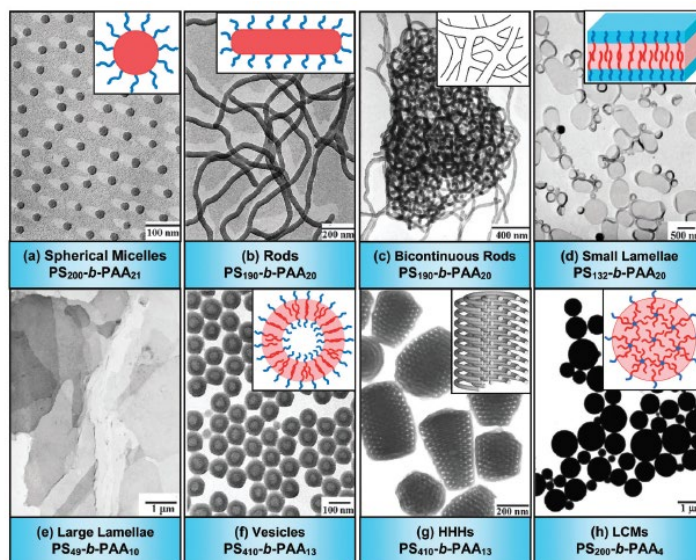


Figure 34. TEM-images of different morphologies from polystyrene-*block*-poly(acrylic acid) ($\text{PS}_m\text{-}b\text{-PAA}_n$).^[145]

The simple, spherical micelles can be considered as the starting morphology, since they are usually the first aggregates that are formed. Rods are typically composed of a cylindrical core, surrounded by the hydrophilic corona with diameters of the same order as those of primary spheres. The bilayers (lamella and vesicles) are then the next step of arrangements of the copolymer chains, while the closed bilayers (=vesicles) are in general more stable. Hexagonally packed hollow hoop aggregates present the phase-inverted counterpart of rods and the large compound micelles the aggregation of inverse micelles. There are several methods for the preparation of block copolymer aggregates in solution. The most popular is the co-solvent (or solvent switch) method^[146], where the amphiphilic BCPs are dissolved in a good solvent for both blocks (DMF, THF, DMSO), followed by the slow addition of a selective solvent (e.g. water, a nonsolvent for the hydrophobic block). The addition is continued, until the percentage of the selective solvent is above the amount where aggregation starts. By this, the kinetic is quenched and the morphologies are frozen, especially in the case of high T_g hydrophobic segment such as PS. In a last step, the common solvent is then removed by dialysis. Another widely used method is the direct hydration technique^[147], where usually a thin film of the BCP is rehydrated in a selective solvent using different approaches, such as mechanical mixing, sonication, extrusion or electrical fields. Other methods include electroformation^[148], layer-by-layer preparation^[149], microfluidic techniques^[150] or the formation of aggregates directly during the synthesis of BCPs.^[151] The different morphologies are mainly influenced by three contributions to the free energy during the aggregate formation. At first, the degree of stretching of the core-forming blocks, second, the interfacial tension between the

core of the micelle and solvent outside the core and, finally, the repulsive interaction between the corona forming chains. Altogether, the different structures are controllable by variations in the copolymer composition, the concentration of the water content in solution, the nature of the common solvent and additives such as ions, etc. Water plays a special role, enabling the transformation of different morphologies, called the ‘morphogenic effect’. Figure 35 shows the different structures of the aggregates depending on the water content in a second solvent. Initially formed micelles are transformed to rods and vesicles by increasing amount of water.

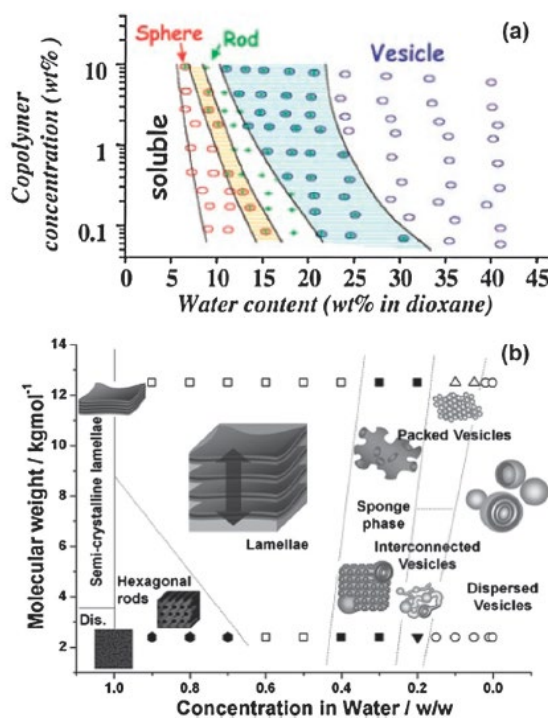


Figure 35. (a) Phase diagram of (polystyrene)₃₁₀-*block*-(poly(acrylic acid))₅₂ (PS₃₁₀-*b*-PAA₅₂) in dioxane-water (water content vs copolymer concentration). (b) Phase diagram poly(*n*-butylene oxide)-*block*-poly(ethylene oxide) (PBO-*b*-PEO) in water (molecular weight vs copolymer concentration).^[145]

In the early stage of micellization, the degree of segregation is small and the copolymer chains have just started to form micelles during the addition of water. The degree of stretching of the chains in the core is not high, since only a small number of polymer chains are present. Spherical micelles are formed with any common solvent at the start of the addition of water. By increasing the amount of water to the system, the mobility of the polymer chains in the core decreases. Consequently, there are less aggregates present and the total interfacial energy between the core and the water decreases, while the stretching of the chains in the core increases. At a critical amount of water, the spheres change to rods and then to vesicles, to minimize the free energy by reducing the stretching penalty of the polymer chains.^[144-145]

4.5 HLB of Surfactants

W. C. Griffin proposed in 1954^[152] a system to categorize surfactants by their hydrophilic-lipophilic balance, the so called HLB-value. Thereby, the molecular weight fraction of the hydrophilic part is calculated and multiplied by 20 to give HLB values ranging from 1 (oleic acid) to 40 (sodium dodecyl sulphate) (eq. 21). For oxyethylated surfactants, the HLB value do not exceed 20.

$$HLB = 20 \times \frac{M_h}{M} \quad (21)$$

M_h ...molecular mass of the hydrophilic portion

M ...molecular mass of the whole molecule

By this method, the surfactants were classified for different applications such as emulsifiers, detergents, wetting agents etc. as given in Table 3.

Table 3. List of HLB values by the Griffin-method.

State of the surfactant in water	HLB number range	Corresponding application
Non-dispersible	1.5 - 3	Anti-foaming agent
	1 - 4	Emulsifier for W/O emulsions
Poorly dispersible	2 - 6	
Turbid unstable dispersion	6 - 8	Wetting agent
Turbid stable dispersion	8 - 10	
Semi-transparent dispersion	10 - 13	Emulsifier for O/W emulsions
Transparent solution	13 and more	
	13 - 15	Detergent
	15 - 18	Solubiliser

Griffin argued, that the HLB value reflects the strength and efficiency of the hydrophilic and lipophilic part of the surfactant. The weight fraction was therefore calculated by simply counting the polar and nonpolar “region” of the molecule. Another strategy was reported by Davies in 1957^[153] based on chemical functional groups in the molecule. Here, each hydrophilic and hydrophobic group was assigned with a specific number (values) and the HLB value was calculated by $HLB = 7 + m \times H_h - n \times H_l$, where m is the number of hydrophilic groups, n the number of lipophilic groups, H_h the specific value of the hydrophilic groups and H_l the specific value of the lipophilic groups. By this method, the effects of stronger and weaker hydrophilic groups can be taken into account. However, the classification of Griffin is today the most reported and popular one, mainly used to predict the amphiphilic behaviour of a

surfactant. Moreover, not only surfactants are categorized within a HLB value. Researchers determined the HLB values of various oils, helping to find the suitable surfactant to prepare a stable emulsion. If the number of the emulsifier fits the one of the oil, there is a great chance that the emulsion will be stable. Emulsifiers with a low HLB number do expose a lipophilic character and are used in water-in-oil (W/O) emulsion, whereas emulsifiers with a high HLB number are hydrophilic and are suitable for oil-in-water (O/W) emulsions. By blending two or more emulsifiers, the HLB value can be tuned by a simply addition of their values, helping to approach the best to the target number.^[143]

5 O/W - Emulsions

5.1 Definition and Basics

An emulsion can be defined as a biphasic system of two immiscible liquids, where one liquid (dispersed phase) is dispersed as small droplets in another liquid (continuous phase).^[154] These systems are in general thermodynamically unstable and require an emulsifying agent that forms a thin film around the droplets to keep them in the dispersion. They are categorized upon their morphology and spatial arrangement of the phases. The main commons are either water-in-oil (W/O), or oil-in-water (O/W) emulsions. More complex systems are presented by emulsions with more than one dispersed phase such as $(O_1 + O_2)/W$ or $(W_1 + W_2)/O$, or multiple mixtures like W/O/W or O/W/O emulsions.^[155]

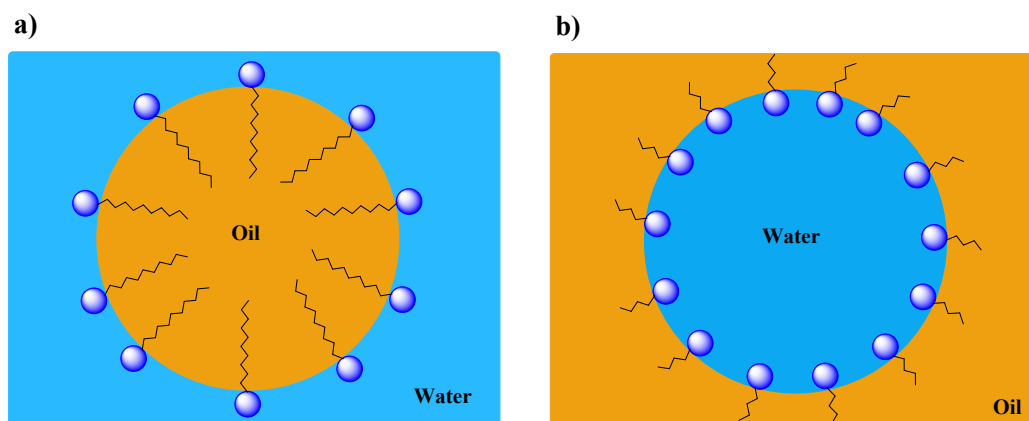


Figure 36. Schema of a) oil-in-water (O/W) and b) water-in-oil (W/O) emulsion.

A further categorization is presented by the size of the dispersed droplets in macro- and nano-emulsions. In macroemulsions, the size of the droplets is in the range of 0.1 to 0.5 μm . These systems are only kinetically stable and usually milky due to the large size of the droplets. Nano-emulsions are thermodynamically unstable dispersions of particles with the size of 20 to 100 nm. Depending on the size of the droplets, they can be either transparent, translucent or opaque.^[156] Another category of emulsions is formed by micelles with the size of 5 to 50 nm,

whereas these systems are more likely described as ‘swollen micelles’ than emulsions and are thermodynamically stable.

5.2 Colloidal Stability

Colloidal stability defines the status of a dispersion that stays in solution and resists against any aging-processes. The interparticle pair potential between the droplet surfaces need to overcome the combined effects of gravity, convection, Brownian motion and short-range attractive forces that lead the system to inevitable phase-separation and breakdown of the dispersion. There are two forms of interaction potentials, attractive and repulsive, that can be measured in units of the thermal energy (kT) and plotted in a potential diagram as a function of surface-to-surface separation. The resulting curve presents the potential $U(d)$ (with d = distance of the surface separation), whose shape gives information about the strength and nature of the interaction force between the surfaces. Derjaguin, Landau^[157], Verwey and Overbeek^[158] developed to this a quantitative theory to define the colloidal stability, the so-called DLVO theory.

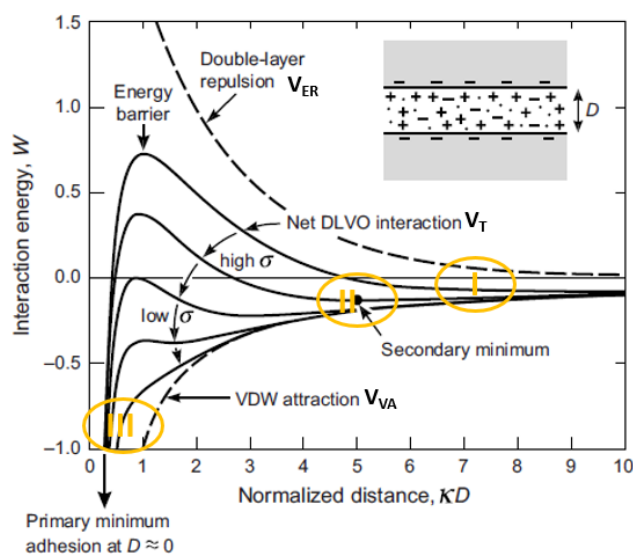


Figure 37. DLVO theory depicting the Van-Der-Waals interaction Energy (V_{VA} dashed line), repulsive Energy (V_{ER} , dashed line) and the total interaction Energy (V_T continuous line) as a functions of the particle distance (r).^[141]

The DLVO theory is ‘the’ classical theory of electrostatic stability of colloids based on kinetic arguments. The dispersion stability is thereby determined by kinetic *and* thermodynamic observations. The DLVO potential is composed of two essential interaction terms, the electrical repulsive forces (Gouy-Chapman electric double layer) V_{ER} and the attractive London-van-der-Waals forces V_{VA} . The electrical repulsion has its origin in the overlap of the electrical double-layer that surrounds the spheres of the charged particles. In the case of very small distances between the colloids, they are referred to the Born repulsion, whereas at larger

distance, to the Coulomb repulsive forces. The attractive forces occur at close separation of the colloids and arises from fluctuations in the electron density distributions of the particles. This attraction is called ‘London dispersion force’ and is a short-range force, inversely proportional to the inter-molecular distance ($W \propto -1/r^6$). It is one of the three Van-Der-Waals interactions, forming the group of attractive forces between polar and non-polar particles. To name the other ones, there are the Keesom- (dipole-dipole interaction) and Debye forces (dipole-induced dipole interaction), which should not be described further. With the DLVO theory, the change in the potential energy, when two particles approach to each other is calculated. Hence, the total interaction energy V_T is determined by estimating the potential energies of attraction (London dispersion, V_A) and repulsion (electrostatic including Born, V_R) in relation to the inter-particle distance.

$$V_T = V_R + V_A \quad (22)$$

Figure 37 shows the exponential decrease of V_R with increasing distance of the colloids, whereas V_A inversely decreases for larger distances. At very short distance, V_T has a primary minimum (III) passing through a shallow minimum (secondary minimum, II) with increasing distances, to end up approximating to zero energy at very large distances (I). In general, a dispersion is stable, if there is a strong long-range repulsion, so that the particles are kept in large distances to each other. The energy barrier (E_A) is too high to overcome, so that the particles stay in dispersion ($V \gg KT$). In that primary minimum, the colloidal system is in its thermodynamically stable state. There is an intermediate state, where the energy barrier to reach contact between the particles is still too high, so that the particles may sit in the weaker secondary minimum (II) or stay dispersed in solution (I). Both cases are referred as kinetically stable. When there is only a very low charge density or potential, the energy barrier will be very low, so the particles can reach each other and aggregate. Below the *critical coagulation concentration* of electrolytes, the energy barrier will be so small, that coagulation of the particles occurs immediately. This is shown in Figure 37, where the energy barrier falls below the $W = 0$ axis. This state is referred as an unstable colloidal dispersion, while its curve approaches more and more the pure van der Waals curve of attraction.

The DLVO theory was initially postulated for ionic colloids containing charged surfaces. In the case of non-ionic colloids and therefore lacking electrostatic effects, the stabilization of the dispersion can be provided by steric and electro-steric repulsions. Both can be obtained by covering the surface of the colloids with polymers. If two colloids, with a surface charged of polymeric compounds, approach each other, the polymer chains overlap and get compressed at the droplet surface. The high concentration of polymeric chains at the droplet surface leads to an increase osmotic pressure, affording repulsion and kinetic stability of the dispersion. Furthermore, there is a volume restriction, more precisely a decrease in entropy, since the

chains lose possible conformations due to the overlapping. If the polymers at the droplet surface are charged, they afford an additional electro-steric repulsion. It is worth mentioning, that the effect of stabilization is strongly dependent on the amount of polymer added. At very low polymer concentration, bridging flocculation occurs, whereas at very high concentration, the droplets are immobilized in an entangled polymer network, that can afford depleting flocculation (see Figure 38).^[141, 159]

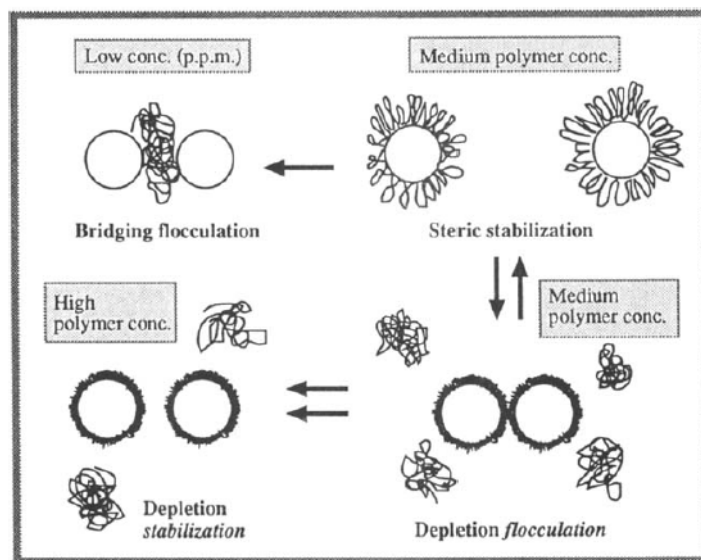
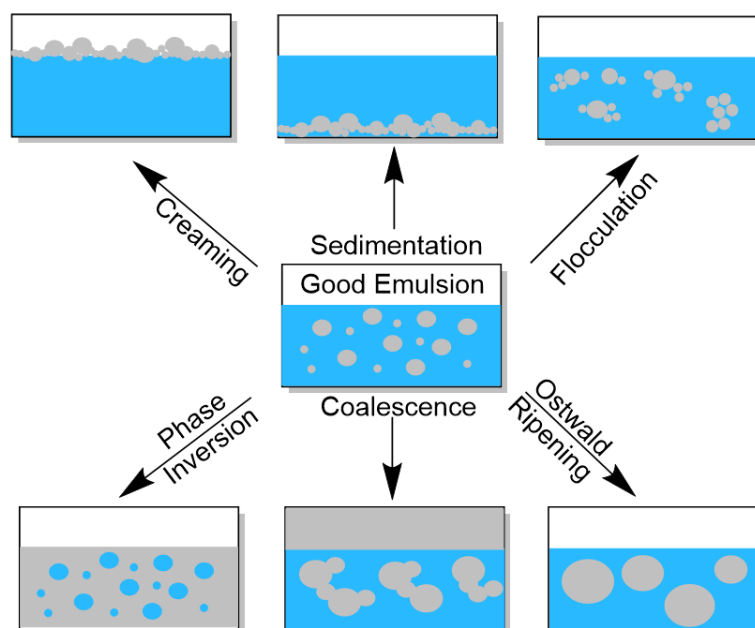


Figure 38. Polymer induced colloidal stability by steric stabilization.^[160]

Emulsification, as previous described, is a non-spontaneous process resulting in small droplets with large surface areas dispersed in a media. The droplets will always tend to approach each other to end up in their thermodynamically stable state of adhesion ($D = 0$, Figure 37). Accordingly, if there is no emulsifying agent that prevents the aggregation, the emulsion will breakdown. There are various aging process leading to the breakdown of an emulsion, illustrated in Scheme 30.

Scheme 30. Destabilization process of emulsions.^[154]

Flocculation

Flocculation presents the most common process of emulsion altering. During flocculation, the droplets of an emulsion approach each other without changing their identities and primary sizes. Depending on the strength of the attractive forces, these phenomena can be either reversible (weak flocculation $U(d) \sim kT$) or irreversible (strong flocculation $U(d) > kT$). It is provoked by the attractive van der Waals interactions between the surface of the droplets.

Coalescence

Coalescence is an advanced aging process, where the droplets are changing their size distribution by the fusion of two or more of them into larger ones. This can occur between the droplets in a creamed or sedimented layer, in a floc, or simple by the contact of droplets during collision. If this process pursues, the emulsion will end up within two distinct liquid phases.

Ostwald-ripening

The diffusion of the droplets into the continuous phase and therefore the production of larger particles over time is called Ostwald-ripening. Even in immiscible liquids, there is a small percentages of solubility, especially for smaller droplets due to effects of curvatures. This causes a diffusion of the smaller droplets to the bulk and the deposition on larger ones. Hence, small droplets disappear and larger ones are taking over until complete phase separation. The diffusion from small, polydisperse particles to bigger monodispersed ones is thermodynamically favoured. The solubility of larger particles is higher than for smaller ones and since the ripening is related to the difference in the droplet size, a narrower size distribution is afforded.

Sedimentation and Creaming

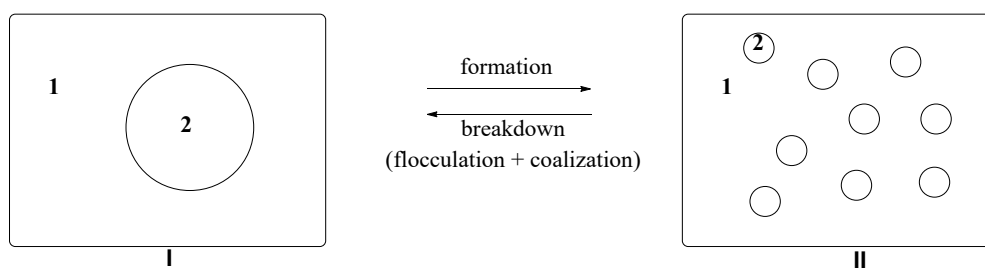
Both processes result from external forces such as gravitation or centrifugation. When the Brownian motion of the particles are exceeded by these forces, the larger droplets will move to the bottom (sedimentation, for the case that their density is lower than that of the medium)

or to the top (creaming, for the case that their density is higher than that of the medium) of the cotenant. The particles may form a closed-packed array, but they keep their initial size and can be re-dispersed by shaking.

Phase inversion

Phase inversion is occurring at a critical volume fraction of the dispersed phase, where it comes to an exchange between the disperse phase and the medium. This process often undergoes a transition state through multiple emulsions. In an O/W emulsion, the continuous aqueous phase can be emulsified in the oil droplets and form a W/O/W emulsion. When this process continues, the entire aqueous phase will be emulsified in the oil, so that the oil becomes the continuous phase, resulting in a W/O emulsion.^[156]

5.3 Preparation of Emulsions



Scheme 31. General scheme of the formation of an emulsion.^[154]

The process of the formation of an emulsion is demonstrated in Scheme 31. During emulsification (represented here for an O/W emulsion), a large droplet of oil (2) with a surface A_1 is divided in smaller droplets of A_2 , where $A_2 \ll A_1$. The interfacial tension $\gamma_{1,2}$ is the same for the large and the small droplets, whereas the surface energy term $\Delta A\gamma_{1,2}$ and the entropy of dispersion $T\Delta S^{conf}$ (configurational entropy) are both positive. This leads to a positive Gibbs free energy ΔG for the formation of the emulsions. With the second law of thermodynamics, it follows:

$$\Delta G^{form} = \Delta A\gamma_{1,2} - T\Delta S^{conf} \quad (23)$$

Emulsification is therefore in the most cases a non-spontaneous process, presenting a thermodynamically unstable system. The expansion of the interface, when the bulk oil with the surface area A_1 is separated into droplets of surface Area A_2 , affords energy. Once the required energy could be applied and the emulsion is formed, emulsifier agents are required to kinetically stabilize the droplets from coagulation. The stabilizer provides an energy barrier between the droplets, hampering the reversion from state II to I (Scheme 31). The surfactant can be either an ionic or a neutral compound, that adsorbs to the freshly formed interfacial film and decreases the interfacial tension γ (IFT). The volume fraction of the dispersed phase

and the droplet size distribution are determined by the emulsification process and the nature of the emulsifier.

In a classical protocol (agent-in-water method), the emulsifying agent is first dissolved into the continuous phase, followed by the addition of the dispersing phase under vigorous agitation. The applied shear is crucial to obtain small droplets. Frequently applied methods are employing paddle, propeller, turbines or ultrasound to achieve high mechanical forces. Other popular strategies are going through phase inversion mechanism to reduce mechanical forces needed (e.g. the formation of butter). However, the traditional methods lead to uncontrolled polydisperse size distributions of the droplets in the emulsion. Advanced methods, using extrusion strategies to pass the dispersed phase through a pipette into a continuous phase, showed improvements to reach monodispersed emulsions (membranes, microfluidic, nanofluidic etc.). The ability of different surfactants to stabilize an emulsion is given as emulsifying activity index (EAI), or emulsifying capacity (EC). The EAI is referred to the area covered per amount of surfactant, whereas the EC is referred to the amount of oil, that can be emulsified by a specific amount of the surfactant. In order to choose the optimal emulsifier for the targeted oil-water, respectively water-oil system, the concept of HLB is the most useful approach. The HLB-value, described in chapter 4.5, can give a good reference for the choice of the emulsifier. It was used to categorize the emulsifier in oil soluble or water soluble, showing their tendency to either promote a W/O or O/W emulsion. It needs to be mentioned, that in many cases, the emulsification technique shows a greater importance than the HLB value. The latter should be rather seen as indicator and not as promise for a succeed emulsification.^[161] Pseudoternary phase diagrams can help finding the optimized ratio between oil, surfactant and aqueous phase. A system consisting of these three compounds can be depicted on a phase tetrahedron with its apexes presenting the pure components (Figure 39). Upon testing the stabilities of emulsions with different ratios, the emerging triangle gives hindrance of the phase behaviour and can be used to find the optimal composition for the desired emulsion.^[162]

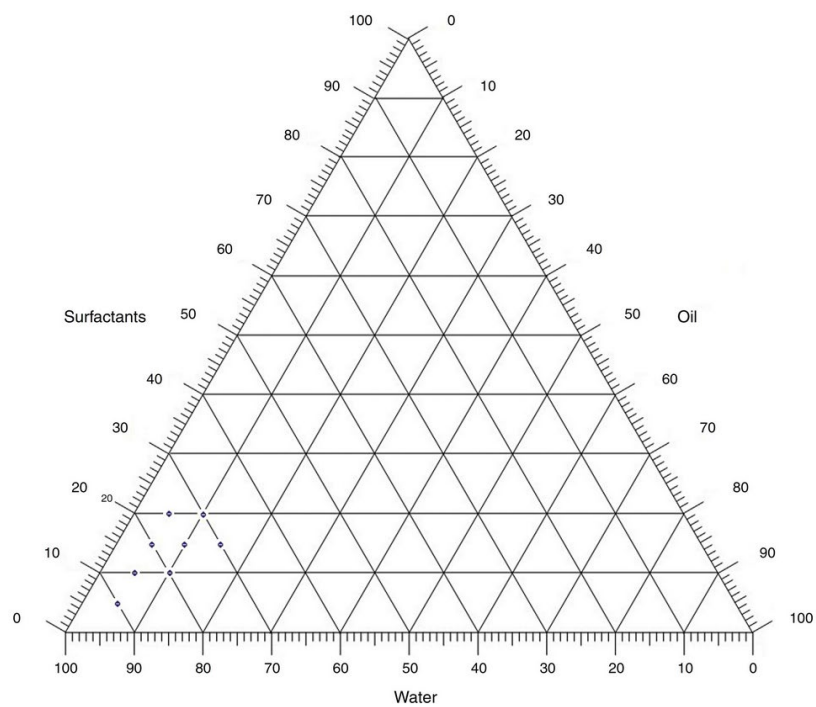


Figure 39. Pseudo-ternary phase diagram for a O/W emulsion.^[163]

7 Conclusion

The versatility and the unique properties of carbohydrates, especially oligosaccharide structures, make them one of the most valuable renewable resources in nature. Therefore, there is a high interest in cheap and industrially scalable synthesis methods to produce and isolate these bio-macromolecules. For glycoscientists it remains until today one of the most difficult task.

Regardless of whether researchers start from simple monosaccharide- or larger polysaccharide structures, the main hurdle of glycan preparation is the stereo- and regiochemical control of the reaction. This is achieved by using various protecting methods, different leaving groups creating 'activated glycosides' and numerous activation strategies. Consequently, these methods afford additional manipulations after each glycosylation step, which lead to a line-up of complex reactions. Simplification is pursued *via* one-pot or combinatorial approaches, where the purification and protecting-deprotecting steps are reduced. Finally, automated setups and/or enzymatic strategies could remarkably improve the oligosaccharide synthesis in terms of reaction time, stereo-control and yield. These methods, however, still need to be improved since are to date too expensive for an industrial scale-up.

Another promising pathway is the utilization of unprotected, non-activated carbohydrates, excluding any protection groups. Whereas this method could reduce drastically the overall reaction steps, it faces different challenges regarding the stereoselectivity. A feature, which is more or less accepted, depending on the type of application. The most popular reaction in this field, the Fischer glycosylation, is today industrially applied to prepare sugar-based surfactants. Among them, alkyl polyglycosides (APGs) are forming the most important and widespread group. They show average degree of polymerization ranging from 1.4 to 2.1. The attempts to reach higher DP is hamper due to the *in situ* release of water during the synthesis and the subsequent depolymerization of the formed oligosaccharides. One of the main hurdle is the poor solubility of the sugars in longer chain fatty alcohols (C₁₂ - C₁₈).

Consequently, there are to date less available data of the impact of the DP towards sugar-based surfactants. The main studies related to structure-property trends of sugar based amphiphiles focus on the impact of the alkyl chain. More analyses would be beneficial to provide predictive models for the development of new and improved bio-based surfactants. The synthesis of amphiphiles with high DP sugar groups is therefore needed to fill the remaining gaps of the structural influence to surfactant properties.

During the work of this thesis we explored synthetic strategies to obtain oligosaccharides from unprotected sugars, focusing on the expand and control the DP. The prepared oligomers should be readily functionalized to couple them with a hydrophobic segment. This objective

faces the challenge of a controlled functionalization of sugars and an improved oligomerization at the same time. The so-prepared amphiphilic compounds should be exploitable to study their surfactant properties and further applications.

8 Bibliography

- [1] Report of the World Commission on Environment and Development: Our common future
- [2] M. J. Hornsey, K. S. Fielding, *Social Issues and Policy Review* **2019**, *14*, 3-35.
- [3] R. K. Pachauri, M. R. Allen, V. R. Barros, J. Broome, W. Cramer, R. Christ, J. A. Church, L. Clarke, Q. Dahe, P. Dasgupta, *Climate change 2014: synthesis report. Contribution of Working Groups I, II and III to the fifth assessment report of the Intergovernmental Panel on Climate Change*, Ipcc, **2014**.
- [4] J. Cook, N. Oreskes, P. T. Doran, W. R. Anderegg, B. Verheggen, E. W. Maibach, J. S. Carlton, S. Lewandowsky, A. G. Skuce, S. A. Green, *Environmental Research Letters* **2016**, *11*, 048002.
- [5] aD. E. MacArthur, D. Waughray, M. Stuchtey, in *World Economic Forum*, **2016**; bJ. Candela, D. Carlson, *WMO Bulletin* **2017**, *66*.
- [6] aJ. Jambeck, R. W. Geyer, TR, Perryman, M., Andrady, A., Narayan, R., and Law, KL, **2015**; bH. G. Dam, M. Eriksen, L. C. M. Lebreton, H. S. Carson, M. Thiel, C. J. Moore, J. C. Borerro, F. Galgani, P. G. Ryan, J. Reisser, *PLoS ONE* **2014**, *9*, e111913.
- [7] P. T. A. Julie B. Zimmermann, Hanno C. Erythropel, Walter LEitner, *Science* **2020**, *367*, 397-400.
- [8] www.plasticeurope.org/en/resources/publications/619-plastic-facts-2018.
- [9] C. Somerville, H. Youngs, C. Taylor, S. C. Davis, S. P. Long, *science* **2010**, *329*, 790-792.
- [10] Q. Liu, L. Wu, R. Jackstell, M. Beller, *Nature communications* **2015**, *6*, 5933.
- [11] R. E. Wrolstad, *Food carbohydrate chemistry, Vol. 48*, John Wiley & Sons, **2012**.
- [12] F. Lichtenthaler, **2002**.
- [13] S.-C. Hung, M. M. L. Zulueta, *Glycochemical synthesis: strategies and applications*, Wiley Online Library, **2016**.
- [14] A. Boutlerow, *Liebigs Ann. Chem.* **1861**, *120*, 295–298
- [15] R. V. Stick, *Carbohydrates: the sweet molecules of life*, Elsevier, **2001**.
- [16] R. V. Stick, S. Williams, *Carbohydrates: the essential molecules of life*, Elsevier, **2010**.
- [17] H. Maehr, *Tetrahedron: Asymmetry* **1992**, *3*, 735-748.
- [18] J. Bijvoet, A. Peerdeman, A. Van Bommel, *Nature* **1951**, *168*, 271-272.
- [19] A. D. McNaught, *Pure and Applied Chemistry* **1996**, *68*, 1919-2008.
- [20] R. S. Shallenberger, **1982**.
- [21] O. a. O. Hassel, B. , *Acta Chemistry Scandinavia* **1947**, *1*, 929.
- [22] J. Edward, *Chemistry and industry* **1955**, *3*, 1102-1104.
- [23] R. Lemieux, in *Molecular rearrangements, Vol. 2*, Interscience New York, **1964**, pp. 719-723.
- [24] aD. Klemm, B. Heublein, H. P. Fink, A. Bohn, *Angewandte chemie international edition* **2005**, *44*, 3358-3393; bD. Klemm, F. Kramer, S. Moritz, T. Lindström, M. Ankerfors, D. Gray, A. Dorris, *Angewandte Chemie International Edition* **2011**, *50*, 5438-5466.
- [25] A. Payen, *Comptes rendus* **1838**, *7*, 1052-1056.
- [26] H. Staudinger, *Berichte der deutschen chemischen Gesellschaft* **1920**, *53*, 1073 - 1085.
- [27] W. Flauzino Neto, **2017**.
- [28] M. M. Nielsen, C. M. Pedersen, *Chem Rev* **2018**, *118*, 8285-8358.
- [29] A. C. Varki, R. D.; Esko, J. D.; Freeze, H. H.; Bertozzi, C., P. H. R.; Stanley, G. W.; Etzler, M. E., *Essentials of glycobiology*, CSH Laboratory Press, New York, **2009**.
- [30] D. S. Alonzi, D. C. Neville, R. H. Lachmann, R. A. Dwek, T. D. Butters, *Biochemical Journal* **2008**, *409*, 571-580.
- [31] aC. A. Reis, H. Osorio, L. Silva, C. Gomes, L. David, *Journal of clinical pathology* **2010**, *63*, 322-329; bB. Adamczyk, T. Tharmalingam, P. M. Rudd, *Biochimica et Biophysica Acta (BBA)-General Subjects* **2012**, *1820*, 1347-1353; cL. R. Ruhaak, S. Miyamoto, C. B. Lebrilla, *Molecular & Cellular Proteomics* **2013**, *12*, 846-855; dC. B. Lebrilla, H. J. An, *Molecular*

- bioSystems* **2009**, *5*, 17-20; eS. Futakawa, K. Nara, M. Miyajima, A. Kuno, H. Ito, H. Kaji, K. Shirotani, T. Honda, Y. Tohyama, K. Hoshi, *Neurobiology of aging* **2012**, *33*, 1807-1815.
- [32] aR. Das, B. Mukhopadhyay, *ChemistryOpen* **2016**, *5*, 401-433; bM. Panza, S. G. Pistorio, K. J. Stine, A. V. Demchenko, *Chemical Reviews* **2018**, *118*, 8105-8150.
- [33] aM. Hurevich, P. H. Seeberger, *Chemical communications* **2014**, *50*, 1851-1853; bL. Kröck, D. Esposito, B. Castagner, C.-C. Wang, P. Bindschädler, P. H. Seeberger, *Chemical Science* **2012**, *3*, 1617-1622.
- [34] G. P. Moss, P. A. S. Smith, D. Tavernier, **1995**, *67*, 1307.
- [35] K. Hill, W. Von Rybinski, G. Stoll, *Alkyl polyglycosides*, Wiley Online Library, **1997**.
- [36] A. Michael, *Am. Chem. J.* **1879**, *1*, 305-312.
- [37] E. Fischer, *Ber. Dtsch. Chem. Ges.* **1893**, *26*, 2400-2412.
- [38] W. Koenigs, E. Knorr, *Berichte der deutschen chemischen Gesellschaft* **1901**, *34*, 957-981.
- [39] aK. Igarashi, in *Advances in Carbohydrate Chemistry and Biochemistry*, Vol. 34, Elsevier, **1977**, pp. 243-283; bG. Zemplén, A. Gerecs, *Berichte der deutschen chemischen Gesellschaft (A and B Series)* **1930**, *63*, 2720-2729.
- [40] aR. Ferrier, R. Hay, N. Vethaviasar, *Carbohydrate Research* **1973**, *27*, 55-61; bK. Nicolaou, S. Seitz, D. Papahatjis, *Journal of the American Chemical Society* **1983**, *105*, 2430-2434.
- [41] A. F. Bochkov, N. K. Kochetkov, *Carbohydrate Research* **1975**, *39*, 355-357.
- [42] N. Kochetkov, L. Backinowsky, Y. E. Tsvetkov, *Tetrahedron Letters* **1977**, *18*, 3681-3684.
- [43] J. R. Pougny, J. C. Jacquinet, M. Nassr, D. Duchet, M. L. Milat, P. Sinay, *Journal of the American Chemical Society* **1977**, *99*, 6762-6763.
- [44] W. Zhong, G.-J. Boons, *Edited by* **2008**, *4*, 261.
- [45] S. Hanessian, **1980**.
- [46] R. Woodward, E. Logusch, K. Nambiar, K. Sakan, D. Ward, B. Au-Yeung, P. Balaram, L. Browne, P. Card, C. Chen, *Journal of the American Chemical Society* **1981**, *103*, 3215-3217.
- [47] T. Mukaiyama, Y. Murai, S.-i. Shoda, *Chemistry Letters* **1981**, *10*, 431-432.
- [48] R. R. Schmidt, J. C. Castro-Palomino, O. Retz, *Pure and applied chemistry* **1999**, *71*, 729-744.
- [49] aG. W. Hart, P. Sinaÿ, B. Ernst, *Carbohydrates in chemistry and biology: Biology of saccharides. Lectins and saccharide biology*, Vol. 4, Wiley-VCH, **2000**; bJ. D. Codée, R. E. Litjens, L. J. van den Bos, H. S. Overkleeft, G. A. van der Marel, *Chemical Society Reviews* **2005**, *34*, 769-782.
- [50] T. Mukaiyama, *Angewandte Chemie International Edition* **2004**, *43*, 5590-5614.
- [51] S.-i. Hashimoto, H. Sakamoto, T. Honda, H. Abe, S.-i. Nakamura, S. Ikegami, *Tetrahedron letters* **1997**, *38*, 8969-8972.
- [52] B. Fraser-Reid, U. E. Udodong, Z. Wu, H. Ottosson, J. R. Merritt, C. S. Rao, C. Roberts, R. Madsen, *Synlett* **1992**, *1992*, 927-942.
- [53] R. Roy, F. O. Andersson, M. Letellier, *Tetrahedron letters* **1992**, *33*, 6053-6056.
- [54] G.-J. Boons, S. Isles, *The Journal of organic chemistry* **1996**, *61*, 4262-4271.
- [55] aO. Kanie, Y. Ito, T. Ogawa, *Tetrahedron letters* **1996**, *37*, 4551-4554; bY. Ito, T. Ogawa, *Journal of the American Chemical Society* **1997**, *119*, 5562-5566.
- [56] P. O. Adero, H. Amarasekara, P. Wen, L. Bohe, D. Crich, *Chem Rev* **2018**, *118*, 8242-8284.
- [57] A. F. e. Bochkov, G. E. Zaikov, *Chemistry of the O-glycosidic bond: formation and cleavage*, Elsevier, **2016**.
- [58] R. U. Lemieux, K. B. Hendriks, R. V. Stick, K. James, *Journal of the American Chemical Society* **1975**, *97*, 4056-4062.
- [59] A. V. Demchenko, *Handbook of Chemical Glycosylation* **2008**, *9*, 1-27.
- [60] B. L. Stephen Hanessian, *Chem Rev* **2000**.
- [61] T.-J. Park, M. Weïwer, X. Yuan, S. N. Baytas, E. M. Munoz, S. Murugesan, R. J. Linhardt, *Carbohydrate Research* **2007**, *342*, 614-620.
- [62] M. Pfaffe, R. Mahrwald, *Organic Letters* **2012**, *14*, 792-795.
- [63] S. Schmalisch, R. Mahrwald, *Organic Letters* **2013**, *15*, 5854-5857.

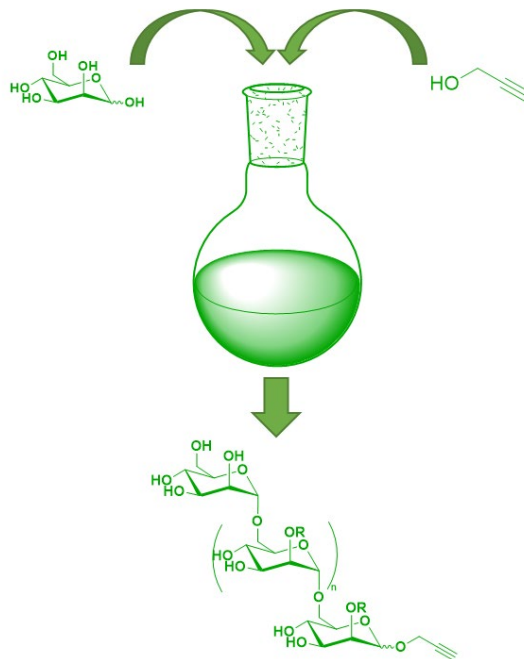
- [64] I. K. Polanki, S. H. Kurma, A. K. Bhattacharya, *Journal of Carbohydrate Chemistry* **2015**, *34*, 196-205.
- [65] G. Guchhait, A. K. Misra, *Catalysis Communications* **2011**, *14*, 52-57.
- [66] D. K. Sharma, M. R. Lambu, T. Sidiq, A. Khajuria, A. K. Tripathi, S. K. Yousuf, D. Mukherjee, *RSC Advances* **2013**, *3*, 11450-11455.
- [67] M. Nakanishi, D. Takahashi, K. Toshima, *Organic & Biomolecular Chemistry* **2013**, *11*, 5079-5082.
- [68] L. J. G. Edgar, S. Dasgupta, M. Nitz, *Organic letters* **2012**, *14*, 4226-4229.
- [69] M. Ishihara, Y. Takagi, G. Li, M. Noguchi, S.-i. Shoda, *Chemistry Letters* **2013**, *42*, 1235-1237.
- [70] B. Roy, B. Mukhopadhyay, *Tetrahedron Letters* **2007**, *48*, 3783-3787.
- [71] S. Hotha, S. Kashyap, *Journal of the American Chemical Society* **2006**, *128*, 9620-9621.
- [72] S. K. Mamidyala, M. G. Finn, *The Journal of Organic Chemistry* **2009**, *74*, 8417-8420.
- [73] aA. K. Kayastha, S. Hotha, *Chemical Communications* **2012**, *48*, 7161-7163; bA. K. Kayastha, S. Hotha, *Beilstein Journal of Organic Chemistry* **2013**, *9*, 2147-2155.
- [74] A. V. Demchenko, *Handbook of chemical glycosylation: advances in stereoselectivity and therapeutic relevance*, John Wiley & Sons, **2008**.
- [75] O. Kanie, Y. Ito, T. Ogawa, *Journal of the American Chemical Society* **1994**, *116*, 12073-12074.
- [76] P. Pornsuriyasak, A. V. Demchenko, *Chemistry – A European Journal* **2006**, *12*, 6630-6646.
- [77] U. E. U. B. Fraser-Reid, Z. F. Wu, Z. H. Ottoson, J. R. Merritt, C.S. Rao, Roberts, R. Madsen, *Synlett* **1992**, 927-942.
- [78] S. S. Kulkarni, C. C. Wang, N. M. Sabbavarapu, A. R. Podilapu, P. H. Liao, S. C. Hung, *Chem Rev* **2018**, *118*, 8025-8104.
- [79] M. Heuckendorff, C. M. Pedersen, M. Bols, *Chemistry–A European Journal* **2010**, *16*, 13982-13994.
- [80] B. Merrifield, *Bioscience Reports* **1985**, *5*, 353-376.
- [81] C. Schuerch, J. M. Frechet, *Journal of the American Chemical Society* **1971**, *93*, 492-496.
- [82] P. H. Toy, K. D. Janda, *Tetrahedron letters* **1999**, *40*, 6329-6332.
- [83] A. Heckel, E. Mross, K.-H. Jung, J. Rademann, R. R. Schmidt, *Synlett* **1998**, *1998*, 171-173.
- [84] N. V. Ganesh, K. Fujikawa, Y. H. Tan, S. S. Nigudkar, K. J. Stine, A. V. Demchenko, *The Journal of organic chemistry* **2013**, *78*, 6849-6857.
- [85] P. Czechura, N. Guedes, S. Kopitzki, N. Vazquez, M. Martin-Lomas, N.-C. Reichardt, *Chemical communications* **2011**, *47*, 2390-2392.
- [86] J. Yin, S. Eller, M. Collot, P. H. Seeberger, *Beilstein journal of organic chemistry* **2012**, *8*, 2067-2071.
- [87] S. Eller, M. Collot, J. Yin, H. S. Hahm, P. H. Seeberger, *Angewandte Chemie International Edition* **2013**, *52*, 5858-5861.
- [88] M. Wilsdorf, D. Schmidt, M. Bartetzko, P. Dallabernardina, F. Schuhmacher, P. Seeberger, F. Pfrenge, *Chemical Communications* **2016**, *52*, 10187-10189.
- [89] S.-i. Shoda, *Proceedings of the Japan Academy, Series B* **2017**, *93*, 125-145.
- [90] G. Perugini, A. Trincone, M. Rossi, M. Moracci, *Trends Biotechnol* **2004**, *22*, 31-37.
- [91] aH. Thøgersen, R. U. Lemieux, K. Bock, B. Meyer, *Canadian Journal of Chemistry* **1982**, *60*, 44-57; bR. Lemieux, *Pure and Applied Chemistry* **1971**, *25*, 527-548; cG. Jeffrey, J. Pople, J. t. Binkley, S. Vishveshwara, *Journal of the American Chemical Society* **1978**, *100*, 373-379; dC. J. Cramer, D. G. Truhlar, A. D. French, *Carbohydrate research* **1997**, *298*, 1-14.
- [92] F. Jérôme, G. Chatel, K. De Oliveira Vigier, *Green Chemistry* **2016**, *18*, 3903-3913.
- [93] <http://www.betarenables.com>.
- [94] <http://poet-dsm.com>.
- [95] <http://www.abengoa.com/web/en/index3.html>.
- [96] <http://renmatix.com/technology/plantrose-technology/how-itworks>.
- [97] J. S. Luterbacher, J. M. Rand, D. M. Alonso, J. Han, J. T. Youngquist, C. T. Maravelias, B. F. Pfleger, J. A. Dumesic, *Science* **2014**, *343*, 277-280.

- [98] <http://www.ecoethanol.fr/>.
- [99] A. Karam, P. N. Amaniampong, J. M. Garcia Fernandez, C. Oldani, S. Marinkovic, B. Estrine, K. De Oliveira Vigier, F. Jerome, *Front Chem* **2018**, *6*, 74.
- [100] F. Schüth, R. Rinaldi, N. Meine, M. Käldestrom, J. Hilgert, M. D. K. Rechulski, *Catalysis Today* **2014**, *234*, 24-30.
- [101] S. M. Hick, C. Griebel, D. T. Restrepo, J. H. Truitt, E. J. Buker, C. Bylda, R. G. Blair, *Green Chemistry* **2010**, *12*, 468-474.
- [102] N. Meine, R. Rinaldi, F. Schüth, *ChemSusChem* **2012**, *5*, 1449-1454.
- [103] C. Stubenrauch, *Current Opinion in Colloid & Interface Science* **2001**, *6*, 160-170.
- [104] D. G. Hayes, D. K. Solaiman, R. D. Ashby, *Biobased Surfactants: Synthesis, Properties, and Applications*, Elsevier, **2019**.
- [105] J. Scheibel, Samuel Rosen Memorial Award Lecture, 98th AOCs Annual Meeting and Expo, Quebec, **2007**.
- [106] US Senate Committee on Agriculture Nutrition and Forestry.
- [107] pp. Markets and Markets (2016) Available at <https://www.marketsandmarkets.com/Market-Reports/biosurfactants-market-2493.html>.
- [108] M. Henkel, R. Hausmann, in *Biobased Surfactants (Second Edition)* (Eds.: D. G. Hayes, D. K. Y. Solaiman, R. D. Ashby), AOCs Press, **2019**.
- [109] A. Bódalo, J. Bastida, M. F. Máximo, M. C. Montiel, M. Gómez, S. Ortega, *Biochemical Engineering Journal* **2009**, *46*, 217-222.
- [110] J. Steber, W. Guhl, N. Stelter, F. Schröder, *Tenside, surfactants, detergents* **1995**, *32*, 515-521.
- [111] D. Geetha, R. Tyagi, *Tenside surfactants detergents* **2012**, *49*, 417-427.
- [112] B. Capon, *Chemical Reviews* **1969**, *69*, 407-498.
- [113] B. Estrine, S. Marinkovic, F. Jérôme, **2019**, 365-385.
- [114] G. Borsotti, T. Pellizzon, Google Patents, **1996**.
- [115] W. v. R. K. Hill, *Ang. Chem. Int. Ed.* **1998**, *37*, 1328-1345.
- [116] F. Jérôme, K. De Oliveira Vigier, A. Karam, B. Estrine, S. Marinkovic, C. Oldani, *ChemSusChem* **2017**.
- [117] D. S. van Es, S. Marinkovic, X. Oduber, B. Estrine, *Journal of Surfactants and Detergents* **2013**, *16*, 147-154.
- [118] C. Ludot, B. Estrine, J. Le Bras, N. Hoffmann, S. Marinkovic, J. Muzart, *Green Chemistry* **2013**, *15*, 3027-3030.
- [119] M. Y. Rather, S. Mishra, *Sustainable Chemical Processes* **2013**, *1*, 7.
- [120] J. K. Kim, S. Y. Yang, Y. Lee, Y. Kim, *Progress in Polymer Science* **2010**, *35*, 1325-1349.
- [121] aS. de Medeiros Modolon, I. Otsuka, S. b. Fort, E. Minatti, R. Borsali, S. Halila, *Biomacromolecules* **2012**, *13*, 1129-1135; bl. Otsuka, K. Fuchise, S. Halila, S. Fort, K. Aissou, I. Pignot-Paintrand, Y. Chen, A. Narumi, T. Kakuchi, R. Borsali, *Langmuir* **2010**, *26*, 2325-2332.
- [122] I. Otsuka, S. Tallegas, Y. Sakai, C. Rochas, S. Halila, S. Fort, A. Bsiesy, T. Baron, R. Borsali, *Nanoscale* **2013**, *5*, 2637-2641.
- [123] R. Ceresa, *Polymer* **1961**, *2*, 213-219.
- [124] C. Schatz, S. Lecommandoux, *Macromol Rapid Commun* **2010**, *31*, 1664-1684.
- [125] R. F. Borch, M. D. Bernstein, H. D. Durst, *Journal of the American Chemical Society* **1971**, *93*, 2897-2904.
- [126] Y. Yang, K. Kataoka, F. M. Winnik, *Macromolecules* **2005**, *38*, 2043-2046.
- [127] L. Greffe, L. Bessueille, V. Bulone, H. Brumer, *Glycobiology* **2004**, *15*, 437-445.
- [128] K. Loos, R. Stadler, *Macromolecules* **1997**, *30*, 7641-7643.
- [129] H. Kamitakahara, Y. Enomoto, C. Hasegawa, F. Nakatsubo, *Cellulose* **2005**, *12*, 527-541.
- [130] J. Yang, Y. S. Zhang, K. Yue, A. Khademhosseini, *Acta biomaterialia* **2017**, *57*, 1-25.

- [131] S. Halila, M. Manguian, S. Fort, S. Cottaz, T. Hamaide, E. Fleury, H. Driguez, *Macromolecular Chemistry and Physics* **2008**, *209*, 1282-1290.
- [132] K. K. Upadhyay, J.-F. L. Meins, A. Misra, P. Voisin, V. Bouchaud, E. Ibarboure, C. Schatz, S. Lecommandoux, *Biomacromolecules* **2009**, *10*, 2802-2808.
- [133] C. Schatz, S. Louguet, J. F. Le Meins, S. Lecommandoux, *Angewandte Chemie International Edition* **2009**, *48*, 2572-2575.
- [134] A. R. Fajardo, A. Guerry, E. A. Britta, C. V. Nakamura, E. C. Muniz, R. Borsali, S. Halila, *Biomacromolecules* **2014**, *15*, 2691-2700.
- [135] B. B. Breitenbach, I. Schmid, P. R. Wich, *Biomacromolecules* **2017**, *18*, 2839-2848.
- [136] J. Rosselgong, M. Chemin, C. C. Almada, G. Hemery, J. M. Guigner, G. Chollet, G. Labat, D. Da Silva Perez, F. Ham-Pichavant, E. Grau, S. Grelier, S. Lecommandoux, H. Cramail, *Biomacromolecules* **2018**.
- [137] N. Yoshida, M. Noguchi, T. Tanaka, T. Matsumoto, N. Aida, M. Ishihara, A. Kobayashi, S. Shoda, *Chem Asian J* **2011**, *6*, 1876-1885.
- [138] Y. Liao, L. J. Goujon, E. Reynaud, S. Halila, A. Gibaud, B. Wei, R. Borsali, *Carbohydr Polym* **2019**, *212*, 222-228.
- [139] O. S. Hernandez, G. M. Soliman, F. M. Winnik, *Polymer* **2007**, *48*, 921-930.
- [140] R. Huisgen, *Angewandte Chemie International Edition in English* **1963**, *2*, 565-598.
- [141] J. N. Israelachvili, *Intermolecular and surface forces*, Academic press, **2011**.
- [142] P. Nikam, S. Uprit, S. Ranvir, **2018**.
- [143] <https://de.wikipedia.org/wiki/Datei:CMC.pdf>.
- [144] A. Blanz, S. P. Armes, A. J. Ryan, *Macromol Rapid Commun* **2009**, *30*, 267-277.
- [145] Y. Mai, A. Eisenberg, *Chem Soc Rev* **2012**, *41*, 5969-5985.
- [146] L. Zhang, A. Eisenberg, *Polymers for Advanced Technologies* **1998**, *9*, 677-699.
- [147] S. Jain, F. S. Bates, *Science* **2003**, *300*, 460-464.
- [148] F. M. Menger, M. I. Angelova, *Accounts of chemical research* **1998**, *31*, 789-797.
- [149] R. A. Caruso, A. Susha, F. Caruso, *Chemistry of Materials* **2001**, *13*, 400-409.
- [150] H. C. Shum, J.-W. Kim, D. A. Weitz, *Journal of the American Chemical Society* **2008**, *130*, 9543-9549.
- [151] W.-D. He, X.-L. Sun, W.-M. Wan, C.-Y. Pan, *Macromolecules* **2011**, *44*, 3358-3365.
- [152] W. C. Griffin, *J. Cosmetic Chem* **1954**, *5*, 249.
- [153] J. Davies, in *Gas/Liquid and Liquid/Liquid Interface. Proceedings of the International Congress of Surface Activity, Vol. 1*, **1957**, pp. 426-438.
- [154] T. Tadros, *Encyclopedia of Colloid and Interface Science*, Springer, **2013**.
- [155] A. S. Kabalnov, E. Schchukin, *Advances in colloid and interface science* **1992**, *38*, 69-97.
- [156] F. Goodarzi, S. Zendejboudi, *The Canadian Journal of Chemical Engineering* **2018**, *97*, 281-309.
- [157] B. Derjaguin, N. Churaev, V. Muller, in *Surface Forces*, Springer, **1987**, pp. 293-310.
- [158] E. J. W. Verwey, J. T. G. Overbeek, K. Van Nes, *Theory of the stability of lyophobic colloids: the interaction of sol particles having an electric double layer*, Elsevier Publishing Company, **1948**.
- [159] P. C. Hiemenz, P. C. Hiemenz, *Principles of colloid and surface chemistry, Vol. 188*, M. Dekker New York, **1986**.
- [160] P. C. Hiemenz, R. Rajagopalan, *Principles of Colloid and Surface Chemistry, revised and expanded*, CRC press, **2016**.
- [161] T. F. Tadros, *Emulsions: Formation, stability, industrial applications*, Walter de Gruyter GmbH & Co KG, **2016**.
- [162] L. L. Schramm, *Emulsions, foams, suspensions, and aerosols: microscience and applications*, John Wiley & Sons, **2014**.
- [163] R. F. Rodrigues, I. C. Costa, F. B. Almeida, R. A. S. Cruz, A. M. Ferreira, J. C. E. Vilhena, A. C. Florentino, J. C. T. Carvalho, C. P. Fernandes, *Revista Brasileira de Farmacognosia* **2015**, *25*, 422-425.

Chapter II A:

Sequential acid-catalyzed alkyl glycosylation and oligomerization of unprotected carbohydrates



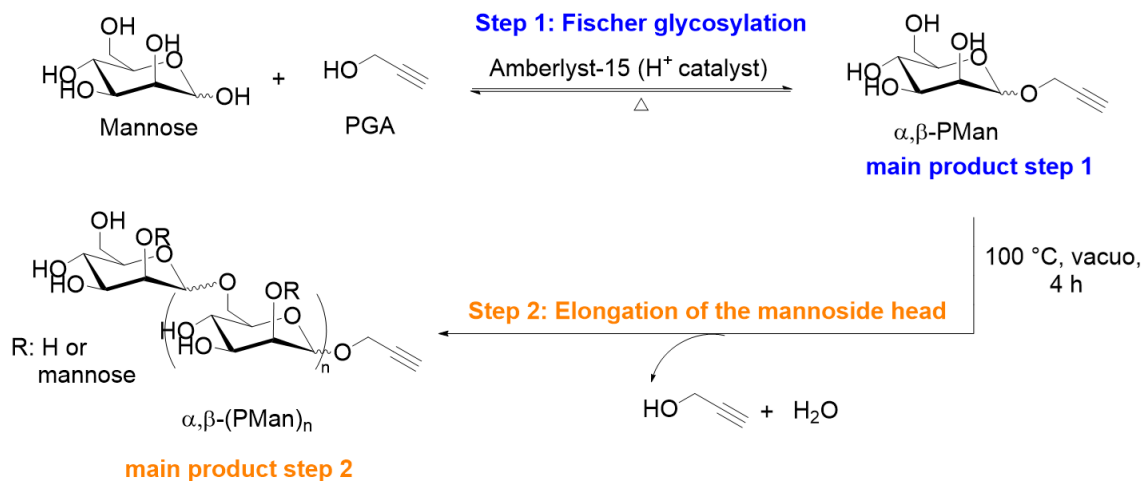
Contents

1	Introduction	86
2	Step 1: Propargylation	87
2.1	First screen of reaction conditions	87
2.2	Analysis of PMan by NMR spectroscopy	92
2.3	Kinetic study by NMR	97
2.4	Kinetic study by GC and ESI-MS	102
3	Step 2: Oligomerization	108
3.1	Kinetic study	108
3.2	Discussion on the reaction mechanism.....	115
3.3	Optimization of the oligomerization reaction.....	119
4	Structural elucidation of (PMan)_n	123
5	Application to other Monosaccharides: Glucose	129
6	Conclusion	130
7	Appendix	132
8	Bibliography	152

1 Introduction

Surfactants are ubiquitous molecules in our daily life with multiple applications in various sectors such as personal care, paint, food, medicine, water treatment, materials, etc.^[1] Because of environmental concerns, the manufacture of bio-based surfactants has become of growing interest.^[1c, 2] Alkylpolyglycosides (APG) are the most wide-spread ones, industrially produced through the acid-catalyzed Fischer glycosylation reaction.^[1a, 3] Due to the release of water during the reaction, all attempts to produce APG with a \overline{DP}_n higher than 2.1 failed.^[3b, 4]

Here, we present another strategy to prepare sugar based surfactants (long chain APG) based on the Fischer glycosylation with propargyl alcohol (PGA). The latter served as a linker to subsequently introduce the lipophilic moiety to the sugar part of the APG by copper-catalyzed Huisgen reaction. In this chapter, we developed the organic synthesis of the propargyl-(oligo)-mannopyranoside ((PMan)_n) through sequential acid catalyzed alkyl glycosylation. The preparation of the amphiphiles by ‘click reaction’ will be discussed later in chapter III. The in-depth study of the glycosylation of mannose (and glucose) with PGA was carried out by NMR, - GC, - SEC and mass spectroscopy. By variation of the experimental conditions (temperature, time and molar ratio between alcohol to sugar) we attempted to (1) extend the \overline{DP}_n and (2) assure complete functionalization of the obtained oligosaccharides. Multidimensional NMR spectroscopy was used to determine the chemical structure and a plausible reaction mechanism was proposed and discussed with the reported ones in the literature.



Scheme 1. Summarized method of the two-step approach for the preparation of the propargyl oligosaccharides (PMan = propargyl mannopyranoside).

The synthesis of (PMan)_n was performed in a two-step process, with the acid-catalyzed glycosylation of monomeric sugars (here = mannose) with propargyl alcohol (PGA) in step 1 (blue), and the elongation of the sugar head in step 2 (orange). The separation of this method in two steps was essential to assure complete propargylation of the obtained oligosaccharides and to tune the degree of polymerization (DP). In order to optimize the reaction, both steps were analyzed separately and the results are discussed in the following. As a case study, mannose was first selected.

2 Step 1: Propargylation

2.1 First screen of reaction conditions

Fischer glycosylation is a well-known method for the preparation of simple propargyl glycosides from free sugars.^[5] To the best of our knowledge, the formation of propargylated oligosaccharides, following this reaction strategy, has not been reported so far.^[6] Inspired by the simple and fast access to alkyne-functionalized glycosides, we exploited the reaction between free monosaccharides (mannose and glucose) and PGA, attempting the synthesis of propargyl-oligosaccharides.

As catalyst we chose Amberlyst-15, which is a strongly acidic sulfonic acid applied in various catalytic reactions such as etherification, olefin hydration, esterification, glycosylation and even industrial processes.^[7] It comprises a macroporous polymer based on a styrene-divinylbenzene crosslinked system (chemical structure in Figure 1).

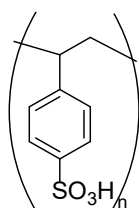


Figure 1. Chemical structure of Amberlyst-15 resin.^[7c]

In a first set of experiments, mannose was suspended in an excess of propargyl alcohol and stirred in the presence of amberlyst-15 at 40 to 50 °C. The catalytic amount and the molar ratio between sugar to alcohol was varied and the reaction was followed over a time period of 1 to 24 h. Table 1 shows the reaction parameters that were tested within the first essays.

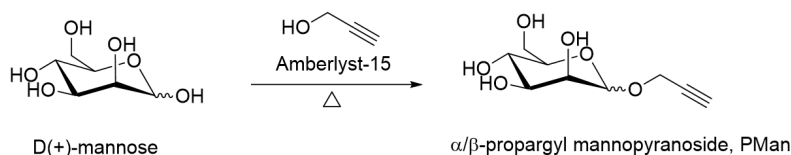


Table 1. Reaction parameters during the first experiments.

Variables	Range
Temperature (°C)	40 - 50
Catalyst (mol%)	4.2 - 33.6
Propargyl alcohol (eq.)	2 - 8.47
Time (h)	1 - 24

Scheme 2. First screen of the reaction by changing the reaction parameters: temperature, amount of the catalyst, weight percentage of mannose in PGA and reaction time.

First, mannose was dispersed in 8.47 equivalent propargyl alcohol at 40 °C with 4.2 mol% (H^+) of amberlyst-15. The obtained heterogeneous reaction mixture required vigorous stirring, since the sugar was not completely solubilized. The conversion of mannose reached only 26 % after 2 h, and 41 % after 7 h of reaction. By doubling the catalytic amount of amberlyst-15 (8.4 mol%), the conversion rate could be increased to 37 % (after 2 h) and 52 % after 7 h. Further increase in the amount of amberlyst-15 (33.6 %) could remarkably improve the reaction rate and gave a conversion of over 70 % after 2 h. On the other hand, when the temperature of the reaction was increased by 10 degrees (keeping 4.2 mol% of catalyst), the conversion reached already 53 % after 2 h and 89 % after 7 h.

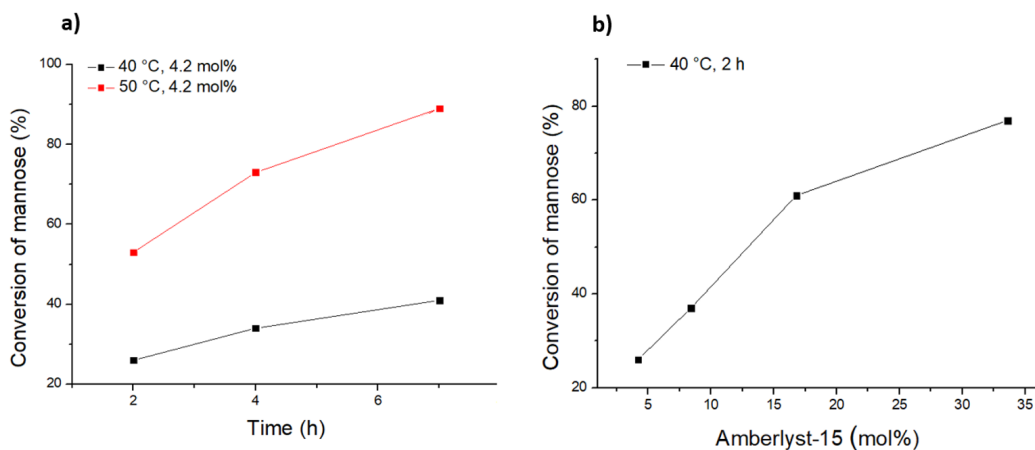


Figure 2. Plot of the conversion rate of mannose comparing (A) different temperatures 40- and 50 °C and (B) different amounts of amberlyst-15 from 4.2 - 33.6 mol%.

Figure 2 summarizes the conversion rates of mannose at 40, and 50 °C with different mol% of catalyst in relation to the reaction time. The diagram shows that higher temperatures improve the reaction more efficiently than larger amounts of amberlyst-15. The increase of the temperature by only 10 degrees could triple the conversion rate. The amount of amberlyst-15, however, needed to be increased 8 times to obtain significant higher reaction rates. We suggested, that the higher solubility of mannose in PGA at 50 °C was the main factor for the faster reaction.

Finally, we analyzed the influence of the molar ratio of alcohol to sugar by varying the excess of PGA to mannose. The high amount of PGA (8.47 eq.) could ensure a proper stirring in the previous experiments. In the literature with respect to the synthesis of alkyl polyglycosides (APG), it could be shown that the molar ratio between 1:2 and 1:6 enables controlling the DP of the oligomer so-formed.^[1a, 3b, 8] In order to improve the DP, we lower the excess of PGA from ~ 8 to 1 equivalent. Unfortunately, low ratio of PGA/mannose hampered the stirring of the mixture and the reaction could not proceed, consequently. Seeking for a compromise between low amounts of PGA and a proper stirring, the ratio PGA/mannose was fixed to 5 in the following experiments.

We next determined the temperature needed to dissolve mannose in PGA without the presence of amberlyst-15. Therefore, mannose was dispersed in 5 eq. PGA and stirred vigorously for 30 minutes at temperatures between 60 - 120 °C. The boiling point of PGA (115 °C) limited a further increase in the reaction temperature since the utilization of an autoclave was not considered. Figure 3 shows the resulting solutions at different temperatures. We observed, that complete dissolution of mannose was only reached at temperatures above 100 °C. The color of the solution changed from bright yellow (60 °C) to dark orange (120 °C).

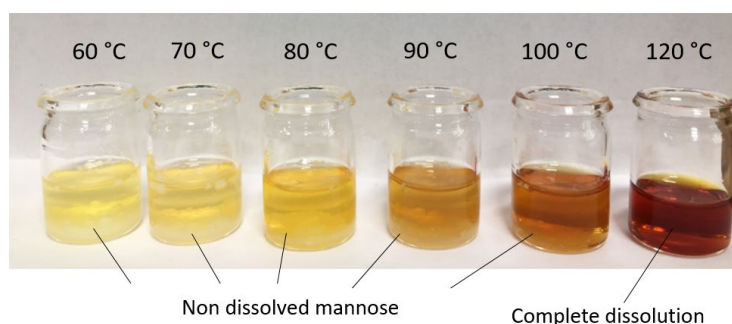


Figure 3. Solubility tests of mannose (1 eq.) in propargyl alcohol (5 eq.), stirred for 30 minutes at temperatures between 60 - 120 °C.

The colorization of the solution was suggested to arise from degradation reactions. Untreated PGA is a colorless to slightly yellowish liquid that is known to polymerize with the contact of heat, light or oxidizing agents.^[9] In a reference reaction, we heated PGA with- and without the presence of amberlyst-15 to study the promotion of the polymerization by the acidic catalyst.

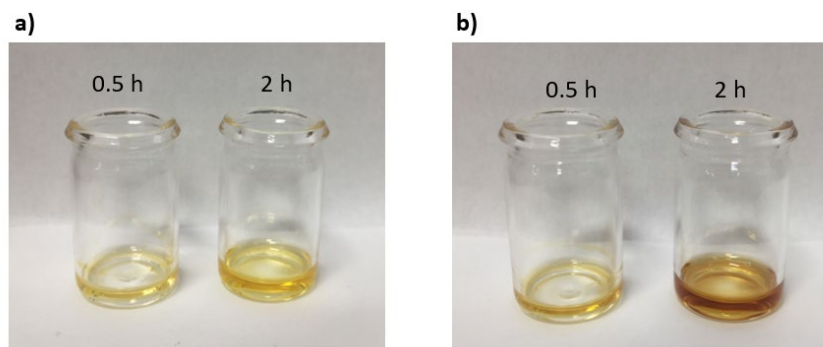


Figure 4. **a)** propargyl alcohol at 80 °C; **b)** propargyl alcohol + amberlyst-15 at 80 °C.

As shown in Figure 4, PGA changed its color from bright yellow to orange upon heating at 80 °C. In the presence of the acidic catalyst (image **b**)), a distinct colorization could be observed and the obtained liquid was less soluble in water. We dissolved the obtained orange solution in DMSO and analyzed it by NMR spectroscopy. The obtained spectrum (Figure 5) supported the polymerization of propargyl alcohol due to the broad series of resonance between 5 and 3.5 ppm. According to the literature^[9a], these signals were attributed to hydroxyl (OH) and methylene (CH₂) protons of the random configured polymer. Clearly, the polymerization of PGA was promoted by amberlyst-15 and was one of the reasons for the coloration of the glycosylation reaction of mannose and PGA.

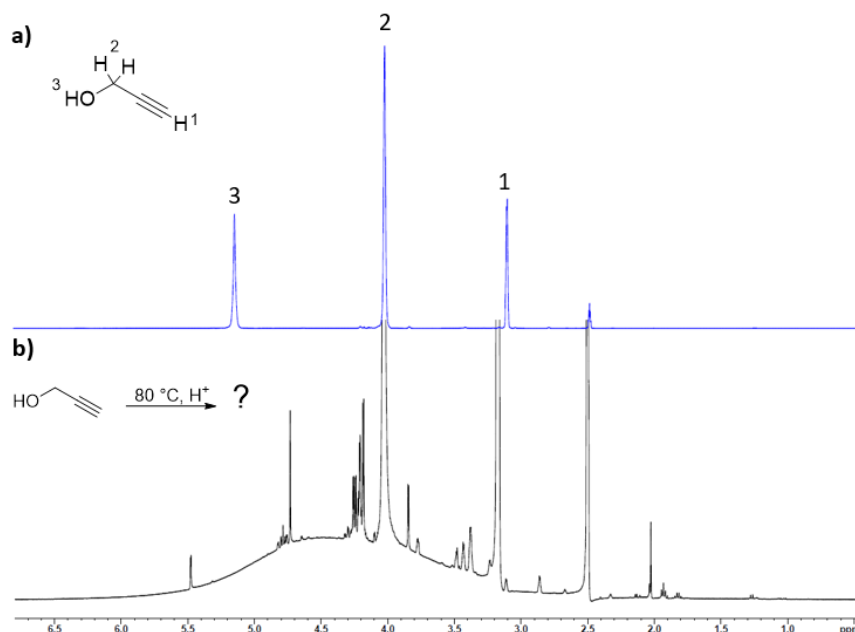


Figure 5. ¹H-NMR (400 MHz, d₆-DMSO) spectrum of **a)** propargyl alcohol and **b)** propargyl alcohol after stirring at 80 °C with amberlyst-15 for 2 h.

The solutions of mannose in PGA at 60 - 120 °C in the absence of amberlyst-15 were then analyzed by ¹H-NMR spectroscopy to study the reaction of PGA with mannose. The obtained data (Figure 6) showed no signals that might indicate a glycosylation reaction. Besides the appearance of the peaks from propargyl alcohol (4.20 ppm and 2.79 ppm), only the signals of

pure mannose were detected. In line with the literature of Fischer Glycosylation^[3b, 6, 10], we confirmed the requirement of the acid catalyst for a reaction between mannose and PGA.

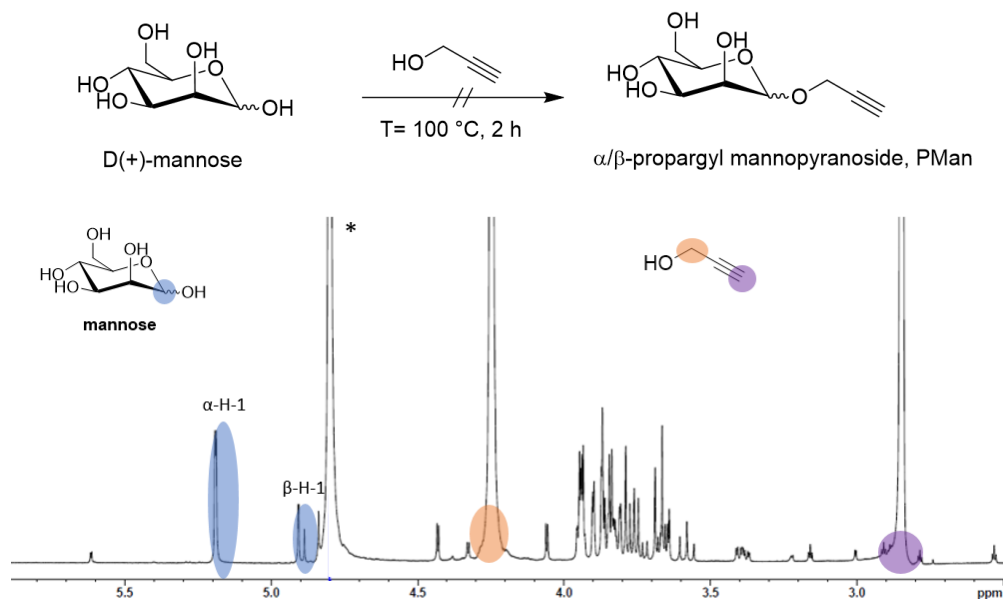


Figure 6. ¹H-NMR (400 MHz, D₂O) spectrum of the reference reaction between mannose and propargyl alcohol in the absence of amberlyst-15 catalyst.

Mannose was then again dispersed in PGA and 4.2 mol% of amberlyst-15 was added to initiate the glycosylation reaction. The mixtures were heated at temperatures from 60 up to 120 °C.

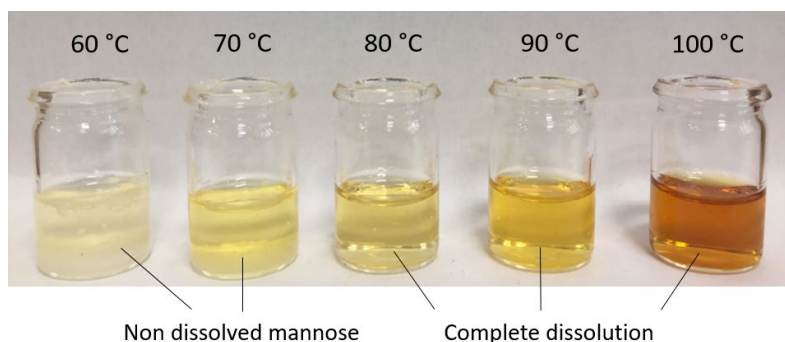


Figure 7. Reaction conditions: mannose (1 eq.) + propargyl alcohol (5 eq.) + amberly-15 (4.2 mol%) stirred at temperatures between 60 - 100 °C for 30 minutes.

In the presence of the amberlyst-15, mannose was completely dissolved in PGA already at 80 °C after 10 minutes (Figure 7). At 100 °C, a homogeneous solution was obtained instantaneously after the start of the reaction. The same change in the color was observed as for the solutions without amberlyst-15, from yellow at 60 °C to orange at 120 °C. We suggested that the colorization arises from the formation of black tar-like materials due to degradation of mannose.^[3b] Frequently observed byproducts of any acid catalyzed reaction of carbohydrates at high temperatures are general described as *humins*.^[11] Recent studies showed that *humins*

are chemical networks mainly composed of furan motives with different functional groups (Figure 8).^[12] Their formation depend strongly on the type of carbohydrate, acid catalyst, temperature and time of the reaction. Analysis on the acid-catalyzed dehydration of C-6 sugars to 5-hydroxymethylfurfural (HMF) and levulinic acid (LA), report an important content of *humins* between 5 to 50 wt.% in their product mixtures.^[11] During the development of our glycosylation/oligomerization strategy, we tried therefore to keep the reaction times as short-, and the temperature as low as possible. For the following experiments, we fixed the temperature to **60 - 100 °C**, the amount of amberlyst-15 to **4.2 mol%** and the PGA/mannose ratio to **3 - 5**.

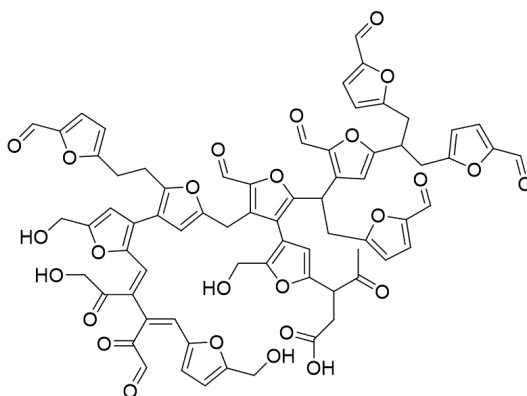


Figure 8. Model of a fragment of a glucose-derived humin.^[12c]

2.2 Analysis of PMan by NMR spectroscopy

Propargyl mannopyranoside (PMan) was isolated and fully characterized by 2D NMR spectroscopy. The analysis provided reference spectra for the subsequent study of the glycosylation reaction and the obtained propargyl-(oligo)-mannopyranosides.

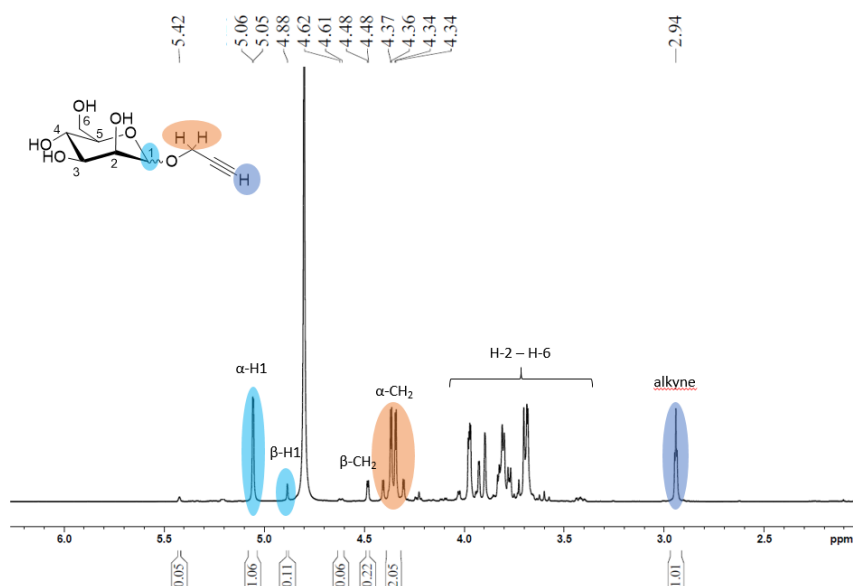


Figure 9. ¹H-NMR (400 MHz, D₂O) spectrum of propargyl mannopyranoside.

Figure 9 shows the $^1\text{H-NMR}$ spectra of PMan (obtained upon glycosylation of mannose with PGA and isolated by column chromatography, EE/MeOH 10:1). The signals corresponding to the propargylated anomeric protons (blue) can be easily assigned due to their large shift to high field ($\alpha\text{-H-1} = 5.06$ ppm, $\beta\text{-H-1} = 4.88$ ppm) compared to pure mannose ($\alpha\text{-H-1} = 5.20$ ppm, $\beta\text{-H-1} = 4.92$ ppm). The methylene protons from the propargyl group gave a doublet for the β -anomer ($\beta\text{-CH}_2$, orange, 4.48 ppm) and a doublet of a doublet for the α -anomer ($\alpha\text{-CH}_2$, orange) at 4.37 - 4.34 ppm. The signal at 2.95 - 2.94 ppm supported the coupling of mannose with PGA with a chemical shift to downfield compared to pure PGA (2.80 ppm ($\text{HC}\equiv\text{C}$) and 4.20 ppm (CH_2)). The analysis showed a predominant character of the α -anomer, with a ratio of α/β : 88/12. The small doublet at 5.42 ppm was assigned to the anomeric proton of levomannosane (LVM), that is a known side-product in Fischer type glycosylation reactions.^[3b, 8] A summary of the anomeric protons is given in Table 2, together with the signals of mannose and levomannosane.

Table 2. Chemical shift of the relevant anomeric protons for PMan.

Chemical shift (ppm)	Compound
5.43	Levomannosane
5.20	α -Mannose
5.06	α -propargyl-mannopyranoside
4.92	β -Mannose
4.88	β -propargyl-mannopyranoside

2D NMR spectroscopy was carried out to determine the signals of H-2 to H-6 and the corresponding carbon frequencies. First, correlation spectroscopy (COSY) was measured to identify the homonuclear spins (proton-proton) that are coupled together. COSY NMR spectroscopy gives information of the direct J-coupling (germinal and vicinal) of cross-peaks, connecting the protons of the sugar ring. The spectrum shows the frequencies of the protons along both axes, so that the diagonal peaks correspond to the 1D-NMR experiment and the cross peaks indicate the couplings, respectively.

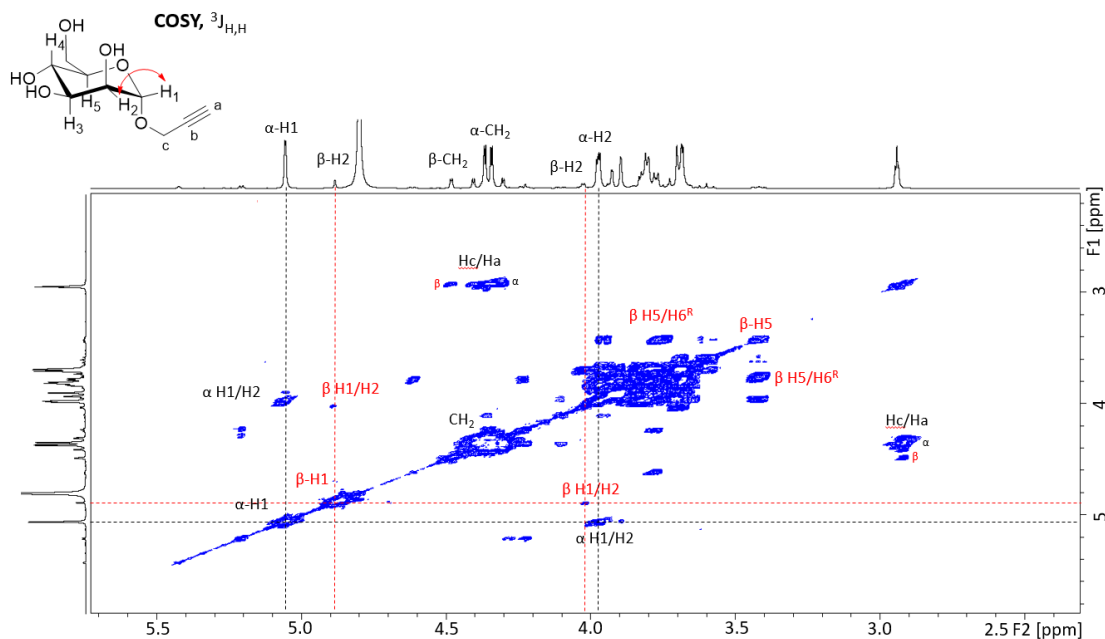


Figure 10. ^1H - ^1H COSY NMR spectrum of propargyl mannopyranoside, PMan.

Figure 10 shows the obtained COSY NMR spectrum with the assignments of the α -anomer in black and the β -anomer in red. The data shows the coupling of the anomeric proton (H-1) to H-2 (α : $^3J_{\text{H-1,H-2}} = 1.6$ Hz, β : $^3J_{\text{H-1,H-2}} = 0.83$ Hz) and the coupling between the methylene protons (CH_2) and the alkyne proton ($\text{HC}\equiv\text{C}$) of the propargyl group (α/β : $^4J_{\text{-CH}_2\text{-H-alkyne}} = 2.4$ Hz). The signal for β -H-6 could be determined due to the coupling with the β -C-5 proton (β -H-5/H-6, red). The signal of β -H-5 is known for its shift to upfield^[13], differentiating it from the remaining protons of the sugar ring. The signal of the β -H-4 was then determined with the coupling to β -H-5.

Heteronuclear single-quantum correlation spectroscopy (HSQC, Figure 11) was carried out to give the direct correlation between proton- and carbon atoms (separated by one bond). The spectrum shows the ^1H -NMR in the horizontal- and the ^{13}C -NMR in the vertical axis. Furthermore, HSQC NMR experiments distinguishes between the CH_3/CH and the CH_2 group, depending on the pulse angle θ , affording positive signals for even numbers of protons and negative signals for uneven numbers.

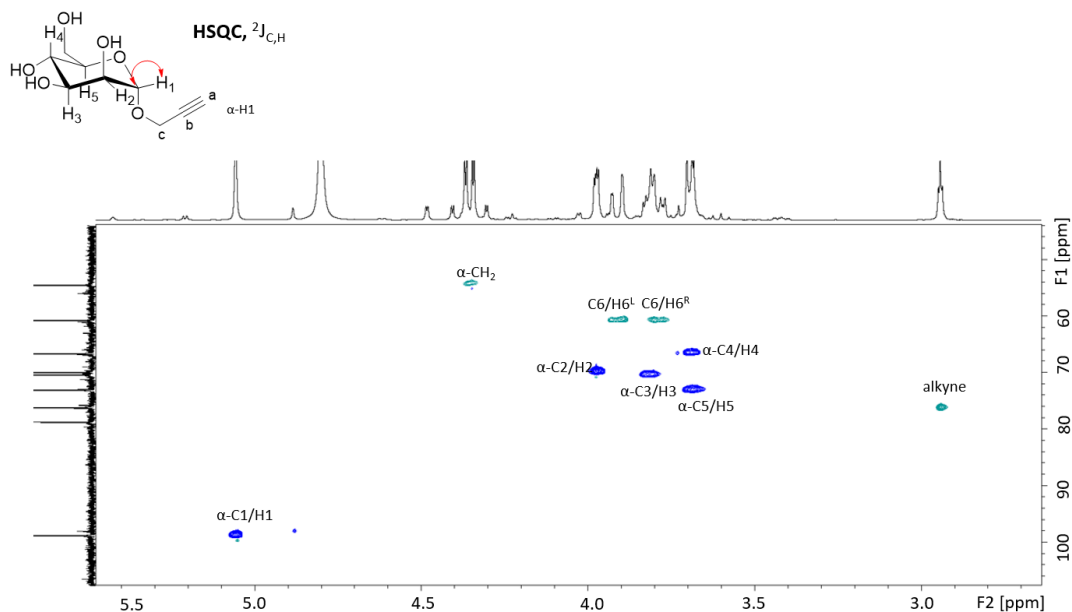


Figure 11. ^1H - ^{13}C HSQC NMR spectrum of propargyl mannopyranoside.

In the HSQC spectra in Figure 11, the CH_2 and CH peaks are given in green and the CH_3 in blue, respectively. The signals for the methylene protons (CH_2), the alkyne ($\text{HC}\equiv\text{C}$) and the protons at C-6 could be determined.

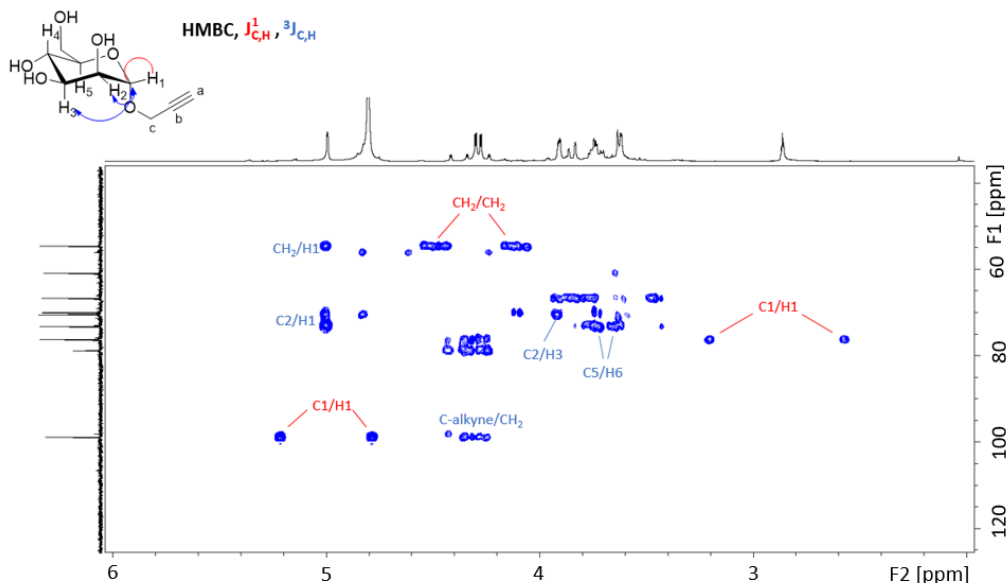


Figure 12. ^1H - ^{13}C HMBC NMR spectrum of propargyl mannopyranoside.

The HMBC (heteronuclear Multiple Bond Correlation) NMR spectra give the correlation between carbons and protons that are separated over long distance (two, three, up to four bonds for conjugated system). With the data obtained from the spectra in Figure 12, the remaining signals for H-3, H-4 and H-5 could be determined. After the assignment of H-3 and H-5 by the coupling of C-5/H-6 and C-2/H-3, H-4 could be determined subsequently. The signals of all protons are again summarized in Table 3 and the carbon atoms in Table 4, along with pure mannose as reference.

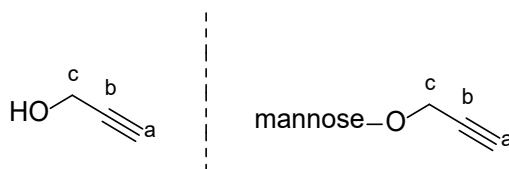
Table 3. ^1H -NMR shift of mannose and propargyl mannopyranoside in D_2O (400 MHz).

Sugar	H-1	H-2	H-3	H-4	H-5	H-6 ^L	H-6 ^R
α -mannose	5.19	3.95	3.85	3.67	3.81	3.87	3.75
β -mannose	4.91	3.96	3.65	3.61-3.56	3.42-3.37	3.90	3.76
α -PMan	5.06-5.05	3.98-3.97	3.81	3.69	3.68	3.93-3.90	3.78
β -PMan	4.88	3.98	3.68	3.61-3.57	3.42-3.39	3.90	3.78

Table 4. ^{13}C -NMR shift of mannose and propargyl mannopyranoside in D_2O (100.4 MHz).

Sugar	C-1	C-2	C-3	C-4	C-5	C-6
α -mannose	94	70.7	70.2	66.8	72.4	60.9
β -mannose	93.6	71.2	73.0	66.6	76.1	60.9
α -PMan	98.8	69.8	70.4	66.6	73.1	60.7
β -PMan	97.9	70.1	61.6	66.8	76.3	60.7

Finally, to confirm the succeed glycosylation reaction, the signals of pure propargyl alcohol and PGA bound to mannose are compared and summarized in Table 5.

Table 5. ^1H and ^{13}C -NMR shift of propargyl alcohol and propargyl mannopyranoside in D_2O .

Compound	a	a	b	c	c
	^1H -NMR	^{13}C -NMR	^{13}C -NMR	^1H -NMR	^{13}C -NMR
Propargyl alcohol	2.80-2.78	74.24	81.9	4.20	49.3
α -PMan	2.95-2.94	76.04	78.6	4.37-4.34	54.5
β -PMan	2.95-2.94	76.04	78.7	4.48	55.9

2.3 Kinetic study by NMR

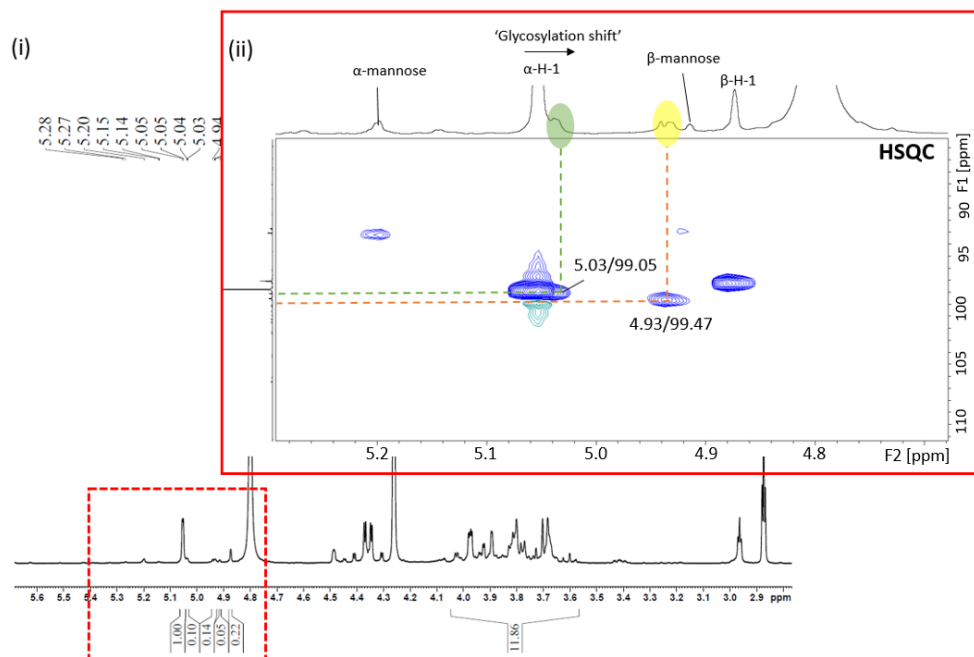


Figure 13. (i) ^1H -NMR (400 MHz, D_2O) spectrum of the reaction of mannose (1 eq.) with propargyl alcohol (5 eq.) and amberlyst-15 (4.2 mol%) at 80 °C after 12 h; (ii) zoom of the corresponding ^1H - ^{13}C HSQC NMR spectrum to the anomeric region.

The glycosylation reaction between mannose and PGA was followed over time by NMR spectroscopy. Figure 13 shows the obtained spectrum after 12 h at 80 °C with a molar ratio PGA/mannose of 5. The zoom of the corresponding HSQC NMR spectra in the anomeric region (ii) showed the appearance of a ‘shoulder peak’ (green, 5.03 ppm) at the signal of $\alpha\text{-H-1}$ from pure monomeric PMan (5.05 - 5.06 ppm). Another significant signal was observed at 4.93 ppm (yellow), along with other peaks in the anomeric region that were difficult to define due to their low intensity. The ‘shoulder’ at 5.03 ppm was attributed to the anomeric proton of the propargylated end-group of mannose-oligomers. This claim is supported by the ‘glycosylation shift’^[13-14], generally observed in oligosaccharides. Due to its poor intensity, it was not possible to analyze the signal in more detail.

The multiplet at 4.9 ppm, in contrast, could be extensively studied by multidimensional NMR spectroscopy. The signal was tentatively assigned to the anomeric proton of a $\alpha\text{-(1,6)}$ -glycosidic linkage. We supported this claim by HMBC NMR experiments (Figure 14, (i)), with the carbon-proton long range coupling of the corresponding carbon signal at 99.47 ppm with the H-6^{R} protons of the anhydromannose unit. The α -configuration was further confirmed by a carbon-proton coupling of 171.32 Hz ($^1J_{\text{C-1}^{\text{H-6R}}}$ from HMBC spectrum).

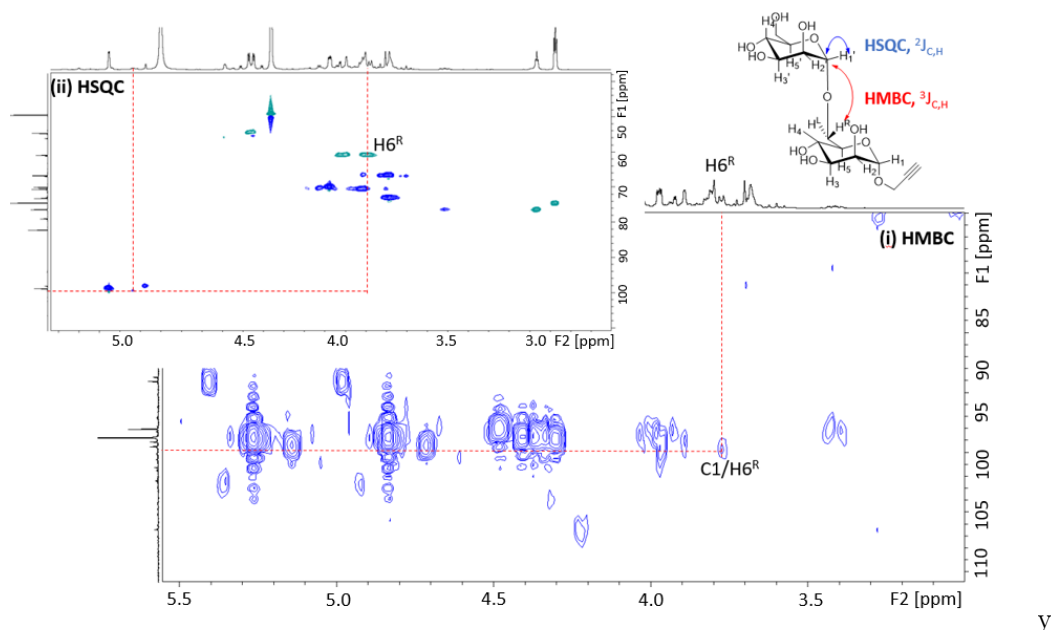
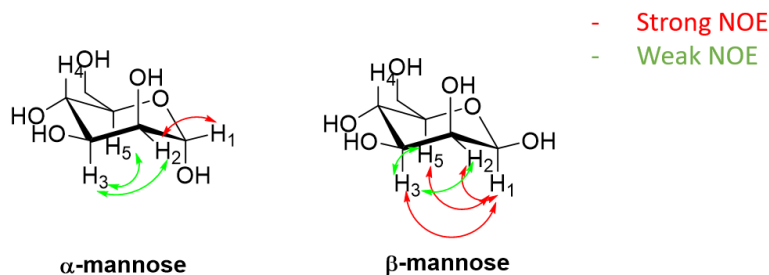


Figure 14. (i) ^1H - ^{13}C HMBC spectrum of the reaction of mannose (1 eq.) with propargyl alcohol (5 eq.) and amberlyst-15 (4.2 mol%) at 80 °C after 12 h; (ii) zoom of the ^1H - ^{13}C HSQC spectrum.

To confirm these findings, a NOESY (Nuclear Overhauser Effect Spectroscopy) NMR experiment was carried out (Figure 15). This method is frequently used to determine the linkage pattern of carbohydrates. It gives long range coupling between two protons in a distance of up to 5 Å. The resulting strong NOE signals for 1,3-diaxial- and low NOE signals for equatorial-axial protons enable to differentiate between the α/β -anomers. For the α -anomer, the experiment shows usually strong couplings between H-1/H-2, and for the β -anomer strong couplings between H-1/H-2, H-1/H-3 and H-1/H-5, respectively (Scheme 3).^[14a] The data from NOESY NMR (Figure 15) supported the assignment of the anomeric proton at 4.93 ppm (yellow, Figure 13) to the α -(1,6) linkage by its proton-proton long range coupling to the H-6^R protons of the anhydromannose unit (H-1/H-6, red).



Scheme 3. Differentiation between α/β -anomer of mannose by NOESY NMR.

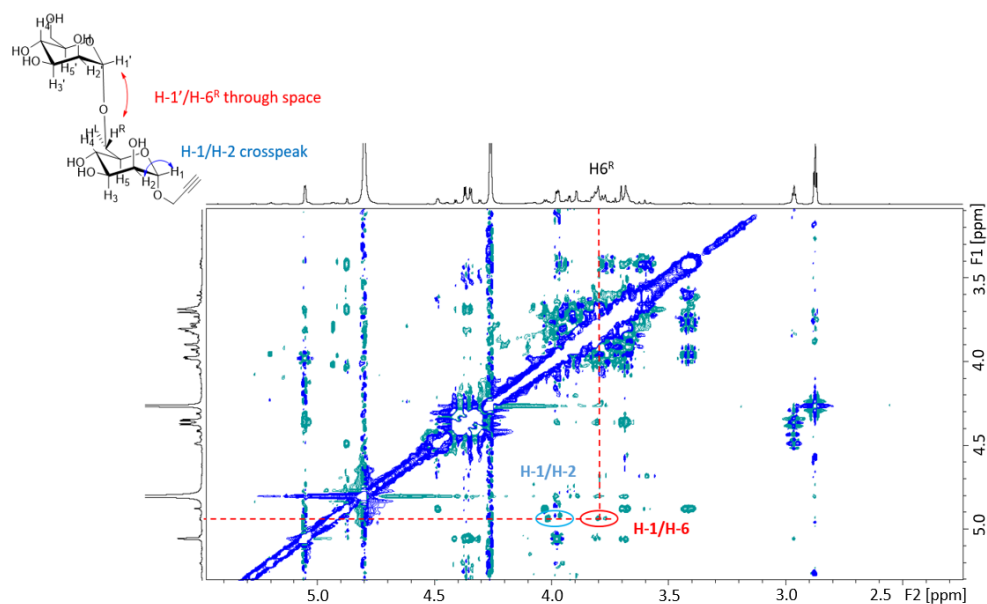


Figure 15. ^1H - ^1H NOESY spectrum of the reaction of mannose (1 eq.) with propargyl alcohol (5 eq.) and amberlyst-15 (4.2 mol%) at 80 °C after 12 h.

Together with the results of the HSQC and HMBC NMR spectra, we concluded the formation of oligomeric molecules linked via α -(1,6)-glycosidic bonds during the glycosylation of mannose with PGA. The attributions of all signals of the anomeric protons are again summarized in the zoom of the proton NMR spectrum in Figure 16.

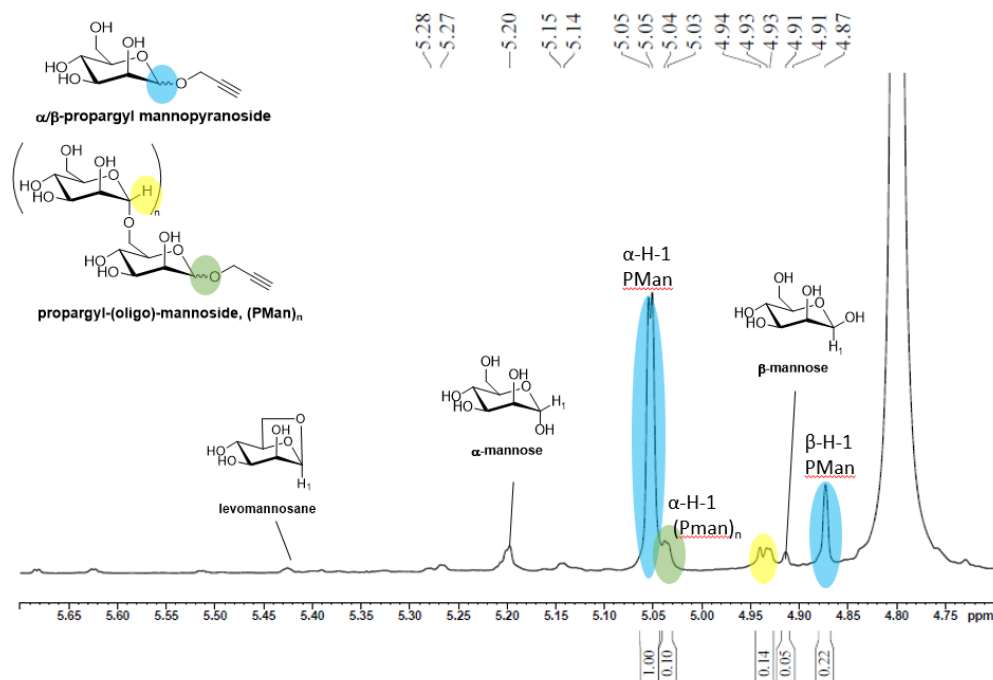


Figure 16. Zoom to the anomeric region of the ^1H -NMR (400 MHz, D_2O) spectrum of the reaction of mannose (1 eq.) with propargyl alcohol (5 eq.) and amberlyst-15 (4.2 mol%) at 80 °C after 12 h; ratio α/β PMan: 83/17; relative proportion of the signals: levomannosane (2 %), α -mannose (5 %), α -PMan (60 %), α -(PMan) $_n$ (19 %), β -mannose (5 %), β -PMan (9 %).

In a following study, we pursued the glycosylation reaction of mannose with PGA over a time period of 48 h by varying the temperature from 60 to 100 °C and the molar ratio PGA/mannose from 3 to 5. The composition of the batches are given in Table 6.

Table 6. Composition of the different Fischer Glycosylation experiments **A - E**.

Experiment	Mannose (eq.)	Propargyl alcohol (eq.)	Amberlyst-15 (mol%)	Temperature (°C)	other
A	1	5	4.2	80	-
B	1	5	4.2	100	-
C	1	5	4.2	60	-
D	1	3	4.2	80	-
E	1	5	4.2	80	MgSO ₄

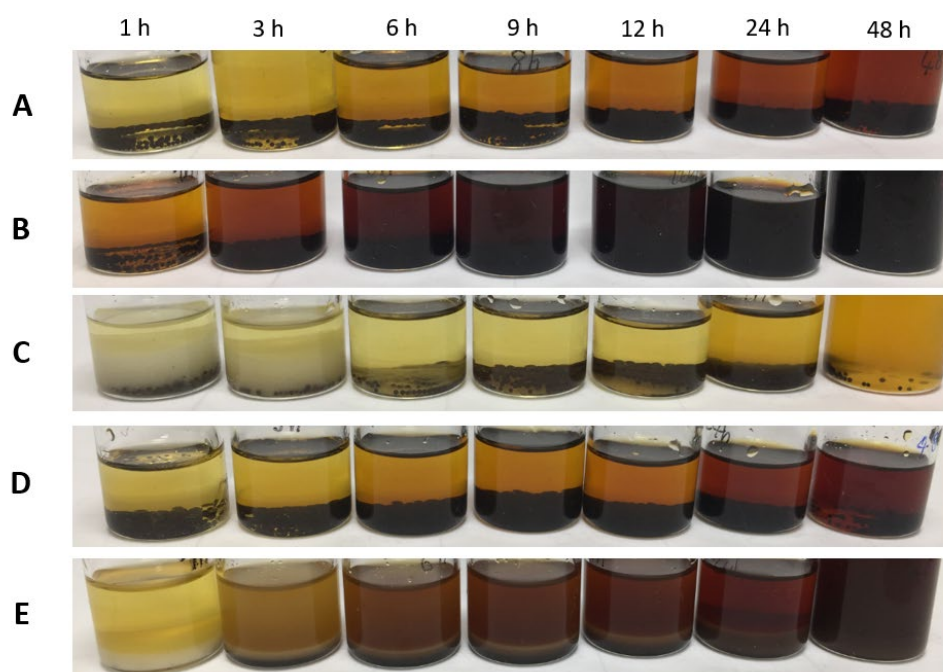


Figure 17. Images of the Fischer Glycosylation **A - E** after different reaction times from 1 h to 48 h.

Figure 17 shows the images of the samples of the glycosylation reactions over a period of 1 - 48 h. Regardless the temperature and molar ratio of PGA/mannose, the color of the samples turned from yellow to orange up to dark brown during the reaction. As already observed and described in this chapter in the subsection 2.1, the color was tentatively assigned to the polymerization of PGA and the formation of tar-like materials (*humins*). At 60 °C, the colorization was less intense, but we faced problems of immiscibility between mannose and PGA. The reaction started only after 6 h, where a complete dissolution of mannose in PGA could be observed.

The glycosylation reaction was followed by ¹H-NMR spectroscopy (see Figure 16). The relative proportions (proton integral) of the anomeric protons of PMan (blue, α-H-1 and β-H-1), pure

mannose (5.20 and 4.91 ppm) and (PMan)_n (green and yellow) were therefore considered. The calculation of the \overline{DP}_n is given in the experimental section and the corresponding NMR spectra are attached in the appendix of this chapter.

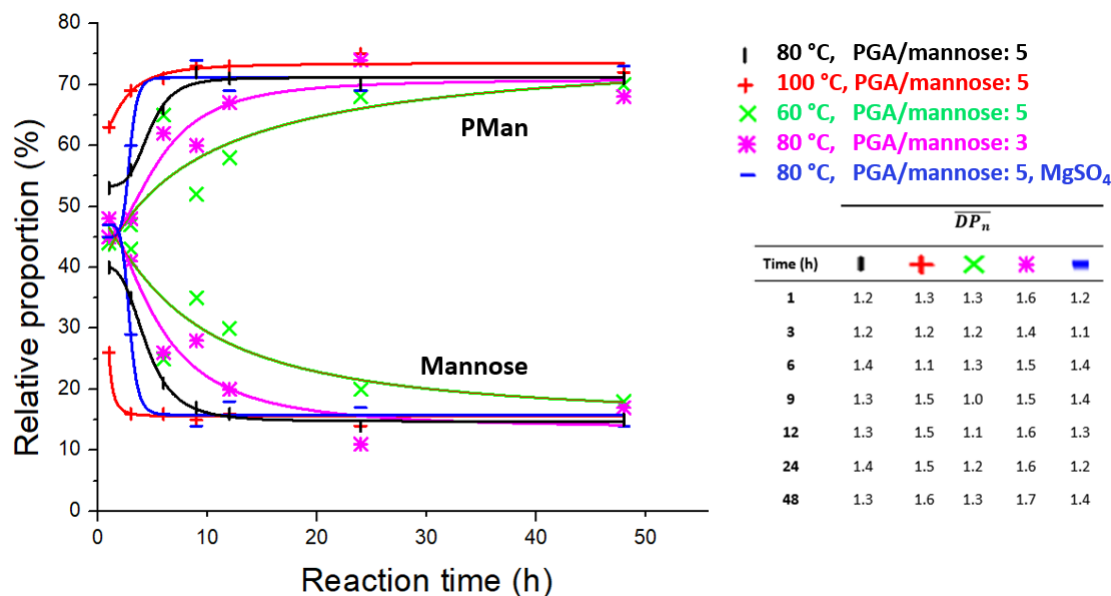


Figure 18. Left: plot of the relative proportions of mannose and PMan as a function of the reaction time over 48 h (shown are the data points with the corresponding trend curves) with the \overline{DP}_n (right table) calculated by ¹H-NMR spectroscopy.

A plot of the relative proportion of PMan and mannose as a function of the reaction time is provided in Figure 18. The obtained data show that the conversion of mannose and the yield of PMan leveled off at around 15 - 20 % and 60 - 75 % after ~ 7 h of reaction. Extending the reaction time from 7 h to 48 h did not result in a complete conversion of mannose, suggesting that the system has reached a thermodynamic equilibrium. The \overline{DP}_n of (PMan)_n was calculated by ¹H-NMR and varied between 1.1 - 1.7. The highest \overline{DP}_n was reached for the lowest ratio of PGA/mannose of 3 (purple). This result was in line to what was observed in previous studies. Lower excess of alcohol leads to higher \overline{DP}_n in the Fischer glycosylation reaction of alkyl polyglycosides (APG).^[3b]

However, the percentage of the oligomers remained very little and did not significantly increase when the reaction time was extended to 48 h. We supposed that the *in situ* released water prevented oligomerization. Also the presence of a drying agent (MgSO₄, blue) could not improve the \overline{DP}_n , capturing not sufficiently the water during the reaction. Longer reaction times only led to the formation of more tar-like materials (see color of the mixture, Figure 17).

2.4 Kinetic study by GC and ESI-MS

Gas-Chromatography (GC)

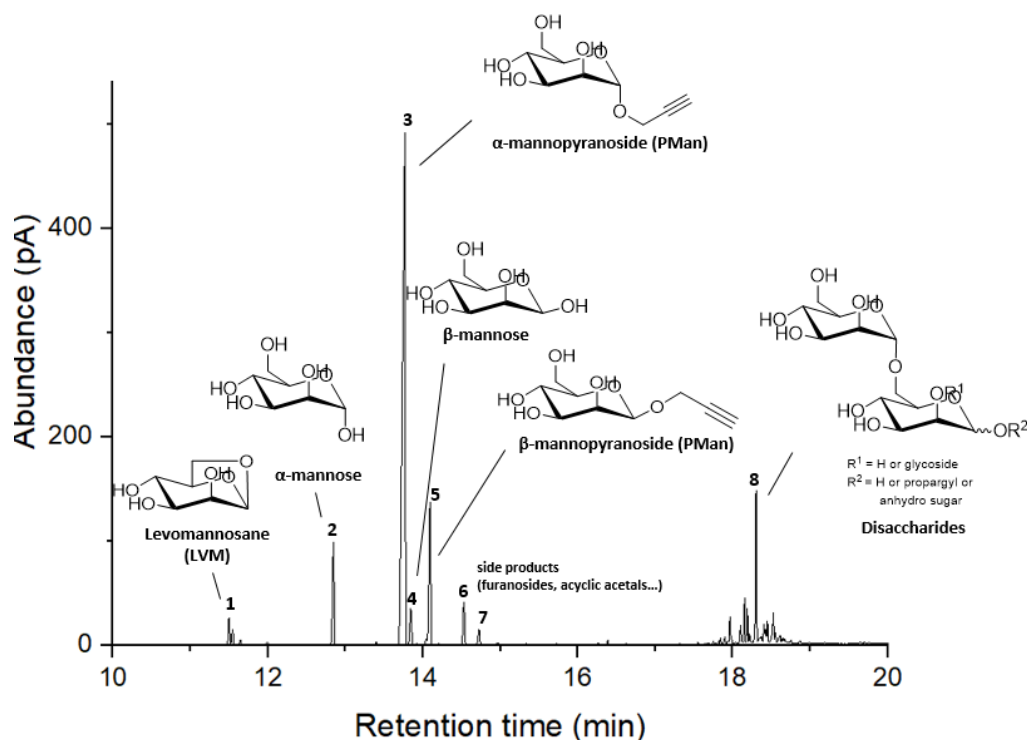
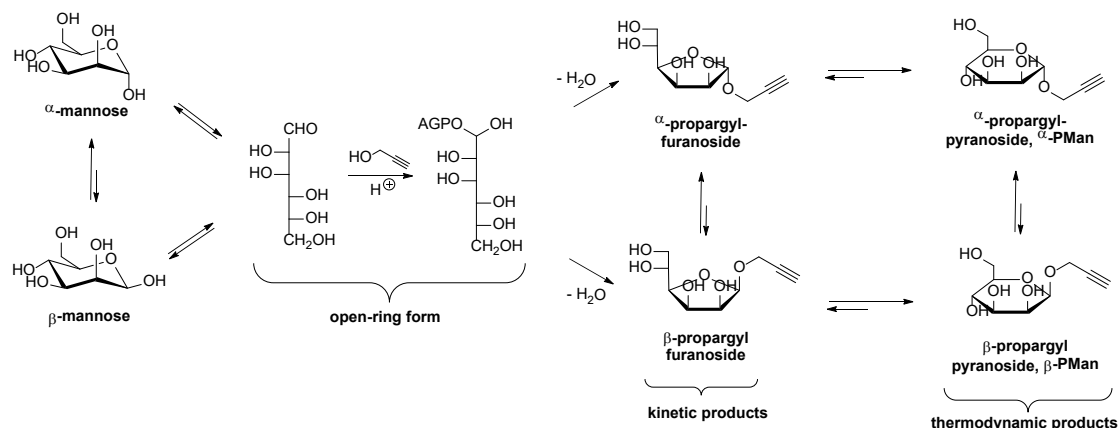


Figure 19. Typical GC-FID spectrum of the glycosylation of mannose with PGA (Reaction conditions: mannose (1 eq.) + propargyl alcohol (5 eq.) + amberlyst-15 (4.2 mol%), 80 °C, 12 h); relative surface area (%): Peak¹ = 2.69, Peak² = 6.11, peak³ = 55.57, peak⁴ = 2.56, peak⁵ = 9.43, peak⁶ = 2.75, peak⁷ = 1.04, peak⁸ = 19.85.

We next analyzed the product mixture of the glycosylation of mannose with PGA by comparison with authentic standards of the gas chromatography (GC). Sequential oximation-trimethylsilylation derivatization procedure was used to quantify the mono- and disaccharide fraction. The retention times of standard chemicals, as well as the protocol of derivatization are given in the experimental section.

Figure 19 shows a typical GC spectrum after 12 h of reaction between mannose and PGA at 80 °C. The data obtained showed the formation of α/β -propargyl-(mono)-mannopyranoside as main product in 79 % yield (PMan, peak 3 and 5) along with a conversion of mannose of 91 % (α -mannose, peak 2, β -mannose, peak 4). Other detected products were disaccharides (peak 8), levomannosane (LVM, peak 1) and also minor products such as furanoside and acyclic acetals (peak 6 and 7) in a relative proportion of 20 %, 3 % and 8 %, respectively. The various signals for peak 8 were tentatively attributed to different glycosidic-linked disaccharides. Since no protecting groups were utilized, each free OH group of mannose could possibly react with another mannose or PMan, leading to numerous different linked mannose-dimers. However, the previous study by NMR spectroscopy supported the preferred connection

through α -(1,6)-glycosidic linkage. The largest signal of peak **8** was therefore assigned to the (1,6) linked dimer.



Scheme 4. Fischer Glycosylation mechanism (inspired by Estrine *et al.*^[15]).

In line with the mechanism for the Fischer glycosylation reported in the literature^[8, 15], PMan was suggested to be formed through acetalization of the open-ring form of the saccharides (Scheme 4). The kinetically favored furanosides (α/β -propargyl furanoside, kinetic products) rearranged then to the more stable pyranosides (α/β -propargyl pyranoside, thermodynamic products), affording in total four different cyclic forms of the glycosides (two α/β -anomers for each sugar cycle). The signals found and assigned to furanosidic compounds in the GC spectrum (peak **6** + **7**, Figure 19), supported the proposed mechanism. They accounted to only 3 % (relative proportion) of the mono- and disaccharide fraction, which proved their poor stability. Furthermore, the data showed a preference of the α -anomers with a α/β -ratio of 85:15 (α -PMan peak **3** vs β -PMan **5**, Figure 19). These results were in accordance with the calculated ratio by $^1\text{H-NMR}$ (α/β : 83/17, Figure 16). Note, that α -anomer presented the thermodynamic product and was preferentially obtained with increasing reaction times and temperatures.

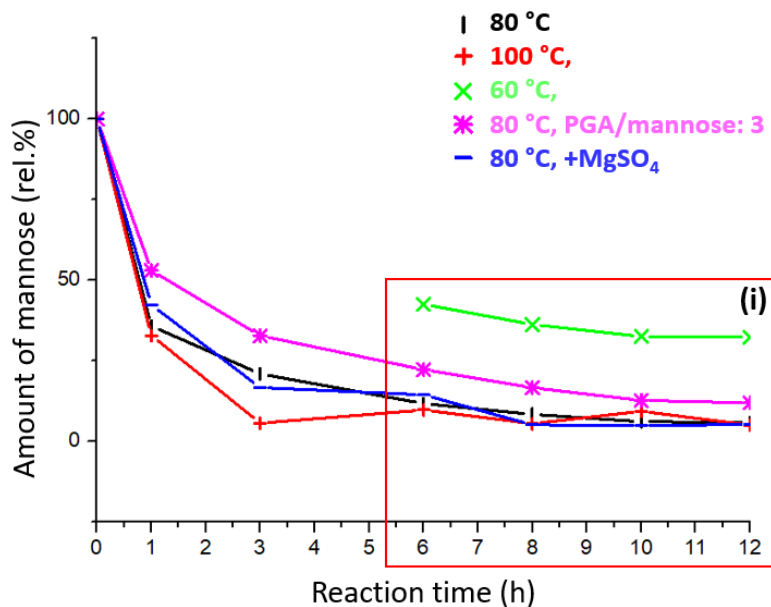


Figure 20. Plot of the conversion rate of mannose during step 1 as a function of time obtained by GC; the ratio PGA/mannose was 5 besides for the purple curve; (i) = claimed thermodynamic equilibrium.

Next, step 1 was followed over time by GC to compare the results to the NMR data. Figure 20 shows a plot of the calculated relative proportions of mannose as a function of the reaction time up to 12 h. The data confirmed the previous observed thermodynamic equilibrium (red box, (i)) that is reached after approximately 7 h of reaction. At that point, the conversion of mannose remained about 90 % and the yield of PMan around 60 - 70 %. The immiscibility problems of the reaction at 60 °C (green) explained the lower conversion rates of mannose (green line), since the reaction started only after 6 h (complete solubilisation of mannose).

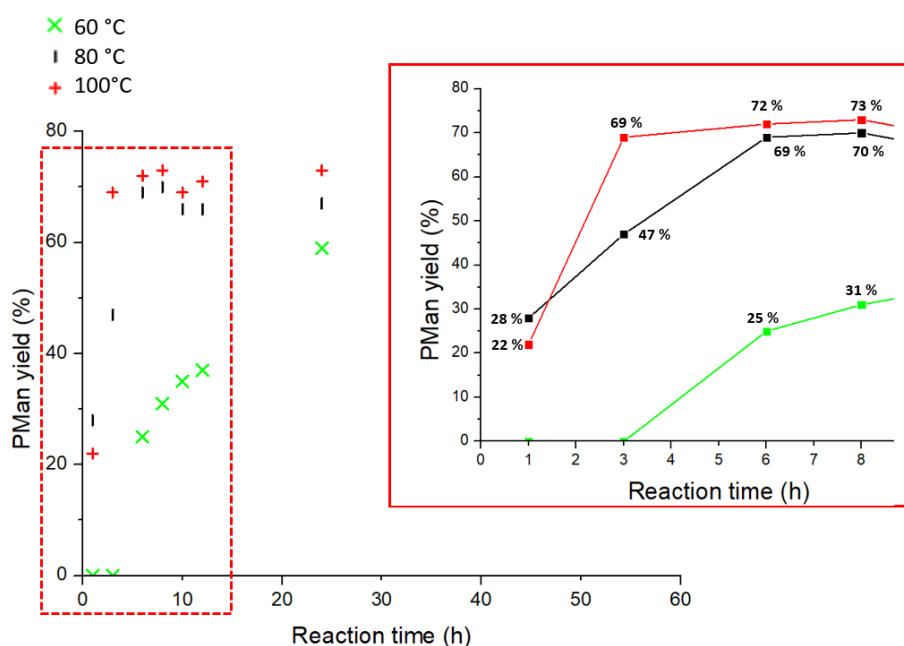


Figure 21. Effect of the reaction temperature on the PMan yield.

The influence of the temperature on the glycosylation reaction was next studied (Figure 21). We denoted that the decrease of reaction temperature from 100 °C to 60 °C decreased the reaction rate from 23 mol/h to 9.5 mol/h. For instance, after 3 h of reaction, PMan was obtained in 47 % and 69 % yield at 80 °C and 100 °C, respectively. When the temperature was further lowered to 60 °C, we faced the already discussed problems of immiscibility between mannose and PGA. The reaction started therefore only after 6 h and a conversion of mannose of about 80 % was observed after 12 h of reaction (reaction rate: 2.5 mol/h).

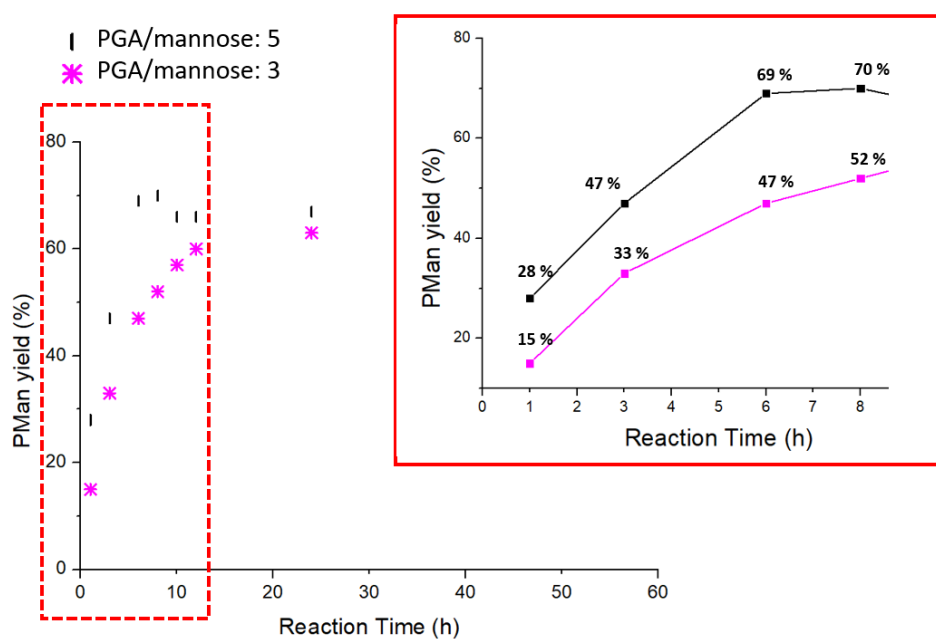


Figure 22. Effect of the PGA/mannose molar ratio on the reaction rate (both reactions are carried out at 80 °C).

For the next experiments, we fixed the temperature at 80 °C to compare only the influence of the PGA/mannose molar ratio. The decrease of the excess of PGA from 5 to 3 (Figure 22) obviously slowed down the reaction rate from 6.2 mol/h to 4.5 mol/h. We tentatively attributed these observations to an increase of the reaction media viscosity. However, this did not significantly impact either the PMan yield or the \overline{DP}_n of (PMan)_n recovered in step 1, further supporting that *in situ* released water prevents oligomerization in a large extend.

Electrospray ionization mass spectroscopy (ESI-MS)

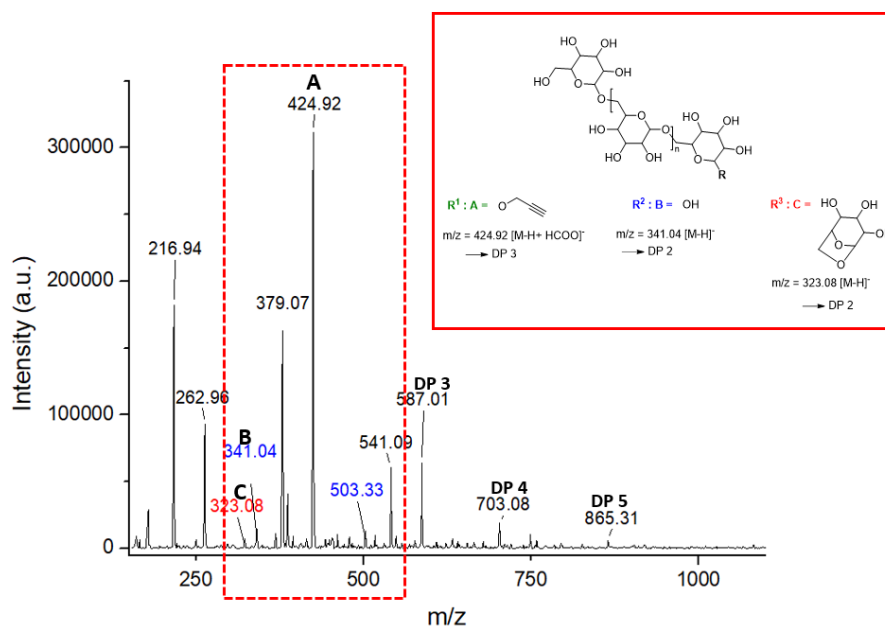


Figure 23. ESI-MS (dist. water with 0.01 % formic acid, negative) spectrum of step 1 (80 °C, PGA/mannose: 5.) after 1 h.

The glycosylation was additionally analyzed by ESI mass spectroscopy. The spectrum of the reaction of mannose and PGA at 80 °C after 1 h is given as illustrative example in Figure 23. (The change in temperature, molar ratio PGA/mannose and reaction time gave no significant change in the ESI-MS spectrum and were therefore not provided). The obtained spectrum (Figure 23) showed a series (A) of monoanionized peaks with sequential increments of $m/z = 162$ u, corresponding to anhydromannose residues as repeating unit. This series was assigned to propargylated oligosaccharides (PMan)_n. Since the samples were dissolved in an aqueous solution with 0.01 % formic acid, the formation of HCOO⁻ adducts could be observed next to monodeprotonated peaks. The calculated value for PMan gave 262.09 u in case of deprotonation ($[PMan]^- = 217.08$ g/mol) and formation of the adduct with HCOO⁻ (= 45.01 g/mol). The mass found in the demonstrated spectrum was in accordance with the calculated values and supported the formation of (PMan)_n with DP up to 5: $m/z = 865.31$ [M-H]⁻. According to previous NMR studies, they correspond to a \overline{DP}_n of 1.3 and proved that these oligomers presented only a very low percentage of the batch.

A second population (**B**) was found with values for m/z of 341.04 and 503.33 u. These peaks were assigned to terminal free oligomannosides $(\text{Man})_n$ with \overline{DP}_n up to 3. Finally, a third series (**C**) was observed having -56 increments in mass units in comparison to the m/z values for $(\text{PMan})_n$. We tentatively attributed them to oligomannoside terminated by a dehydrated anydromannose residue. The formation of this series remained however quasi negligible as it was covered in the noise of the spectra.

Altogether, during step 1, mannose could be glycosylated with PGA exclusively at the anomeric position under mild conditions between 80 and 100 °C. The reaction reached its equilibrium after *ca.* 7 h, while PMan was obtained in 60 - 70 % yield (GC). The glycosylation showed a predominant character of the α -anomer (α/β : 88/12) that increased with higher temperature and longer reaction times. More detailed analysis denoted that next to PMan, also small amounts of $(\text{PMan})_n$ were formed, indicating an oligomerization. However, neither the extension of the reaction duration nor the increase/decrease in temperature or molar ratio between PGA/mannose could significantly increase the amount of $(\text{PMan})_n$. We concluded, that the *in situ* released water during the glycosylation reaction prevented the oligomerization in a large extend. Furthermore, the excess of PGA favored the formation of monomeric PMan. But lower ratio PGA/mannose than 3 could not be effected due to the increased viscosity of the resulting mixture that could then not be stirred anymore.

3 Step 2: Oligomerization

3.1 Kinetic study

The so-formed propargylated mannose (PMan) from step 1 was then self-polymerized to (PMan)_n. We aimed at obtain oligosaccharides, which contain exclusively the propargyl group at their terminal end. Step 1 was utilized to ensure the complete propargylation of mannose and step 2 to extend the \overline{DP}_n . As we denoted from step 1, that \overline{DP}_n could not be increased above 1.7, it was anticipated that the *in situ* released water from the glycosylation reaction hampered the oligomerization. Along with a vacuum distillation of the excess of PGA out of the reaction mixture after step 1, we removed the formed water and initiated finally a polymerization. It was crucial to find a balance between high \overline{DP}_n , complete propargylation and also degradation of mannose. The optimization of this process and the corresponding kinetic studies are presented in the following.

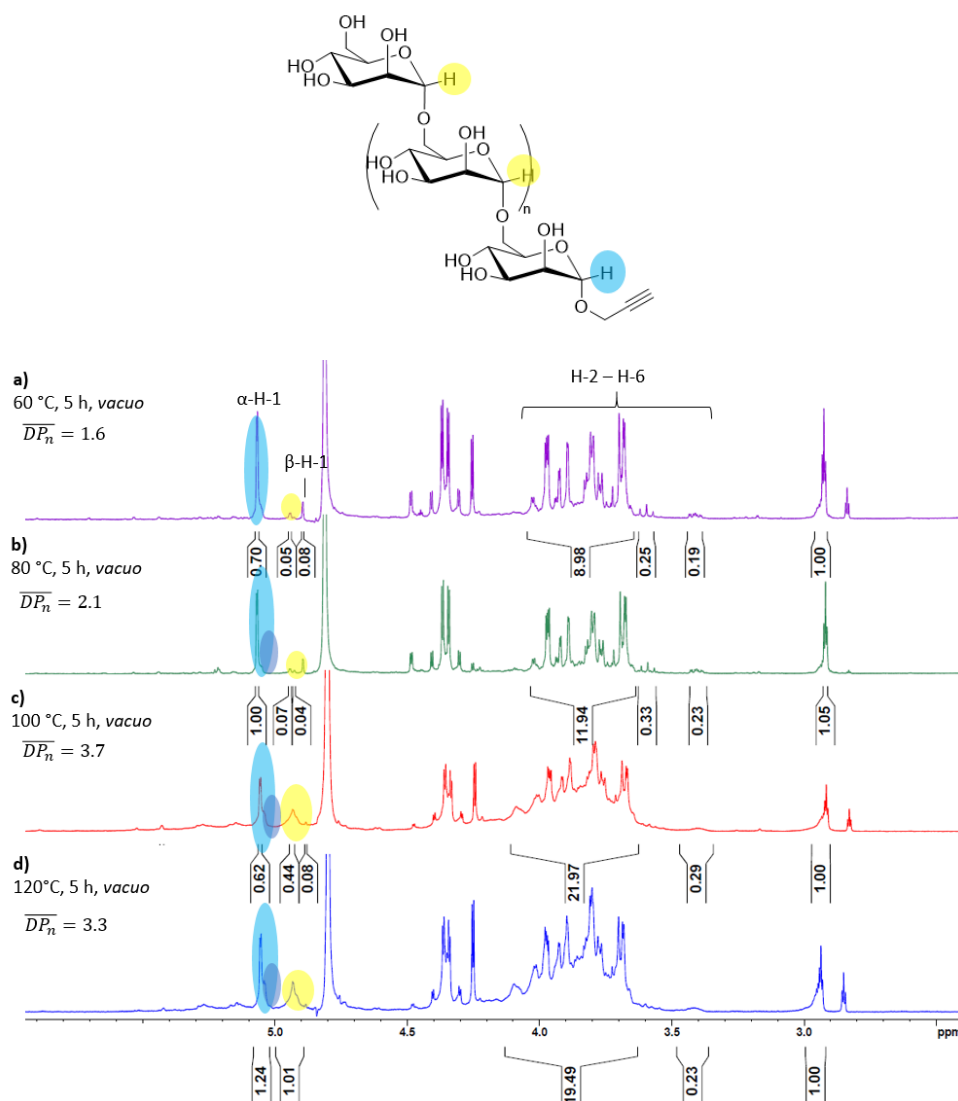


Figure 24. ¹H-NMR (400 MHz, D₂O) spectra after 5 h of polymerization reaction (step 2) under vacuum at different temperatures of the mixture of **step 1** = 12 h (80 °C, PGA/mannose: 5).

In order to increase the \overline{DP}_n , the reaction mixture after step 1 was heated under vacuum (60 - 120 °C, Figure 24) to distil out the excess of PGA and the *in situ* released water. The effect of this treatment was monitored by NMR spectroscopy and SEC. As illustrated in Figure 24, an effective polymerization was only observed at temperatures above 80 °C (reactions c) and d)). The polymerization afforded oligomannosides with a \overline{DP}_n of 3.7 at 100 °C and of 3.3 at 120 °C. Seeking for a compromise between the stability of (PMan)_n and the reaction rate, the temperature of the reaction was fixed at 100 °C in the following experiments. The exposure of (PMan)_n to high temperatures was in general tried to be kept as low as possible.

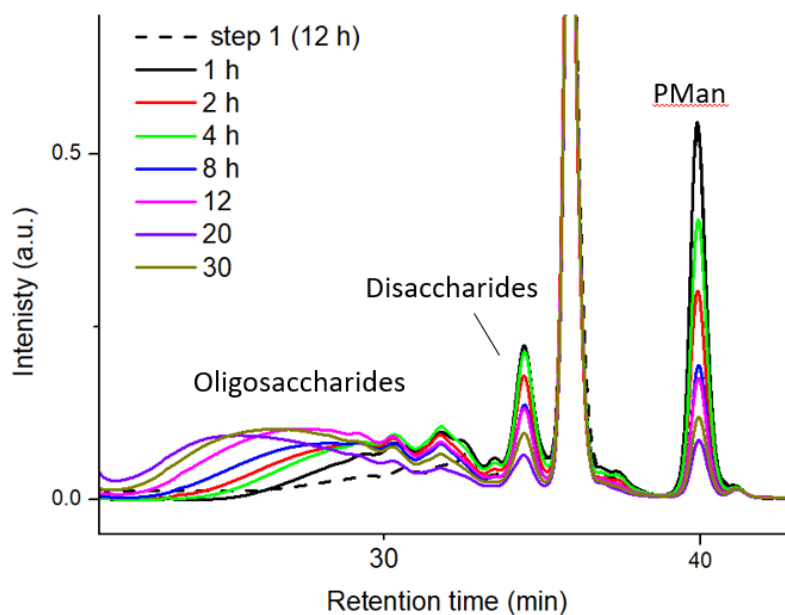


Figure 25. Plot of overlaid SEC (measured against dextran-standards in H₂O at 25 °C) traces of polymerization medium (**P1**) at 100 °C under *magnetically stirring* after **step 1** = 12 h, 80 °C, PGA/mannose: 5).

Table 7. Evaluation of polymerization **P1**.

Time (h)	Conversion (%) [*] of PMan	\overline{M}_n (g/mol) (SEC)	\overline{D} (M_n/M_w) (SEC)	\overline{DP}_n (g/mol) (NMR)
1	20	272	1.44	2.2
2	44	310	1.48	2.9
4	56	343	1.7	3.2
8	72	448	1.76	4.0
12	76	478	1.93	4.2
20	82	587	2.07	4.9
30	87	665	2.07	5.6

^{*}Calculated by the surface area of the refractive index detector of SEC.

The evaluation of the average degree of polymerization (\overline{DP}_n) and the average molar mass (\overline{M}_n) was monitored by ¹H-NMR spectroscopy and SEC over a time period of 1 to 30 h to follow the polymerization process. As illustrated in Figure 25, a clear shift towards larger molar masses was observed during the reaction, supporting the elongation of the

oligosaccharide moiety. After 4 h under vacuum, the \overline{DP}_n reached 3.2. The polymerization reaction was continued for 30 h, while the \overline{DP}_n was only slowly increased to 5.3. The SEC data showed the conversion of PMan under this treatment (up to 87 % after 30 h, Table 7). Since mannose is nearly completely consumed in step 1, it is reasonable to admit that PMan is hydrolysed in step 2 to afford an oxocarbenium ion that further reacts with the (PMan)_n chain (see later for more information).

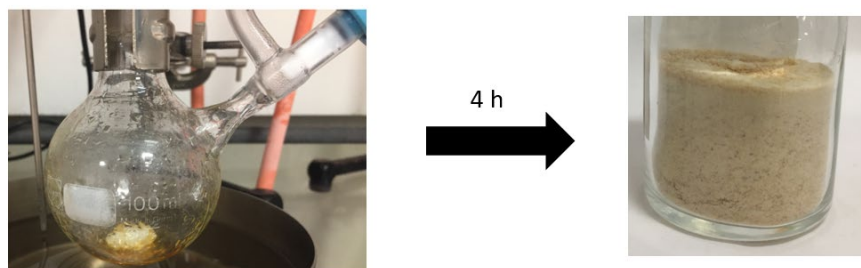


Figure 26. Left: polymerization (image after 20 minutes) reaction under magnetic stirring in a Schlenk-flask; right: obtained crude powder after 4 h of reaction.

The polymerization reaction was carried out in a Schlenk-flask under vigorous agitation using a magnetic stirrer. After only 10 to 20 minutes, the majority of PGA was distilled out, affording a sticky viscous oil (Figure 26, left). When the treatment was continued for another 4 h, a beige-brown powder of the oligomannosides was obtained (Figure 26, right). Note that the viscous oil was difficult to stir, which could explain the slow increase in \overline{DP}_n during this step (see Table 7). The time needed to evaporate the excess of PGA restricted consequently the duration of the reaction. A good stirring during step 2 seemed to be crucial to reach higher DP_n , pushing us to investigate different laboratory set-ups.

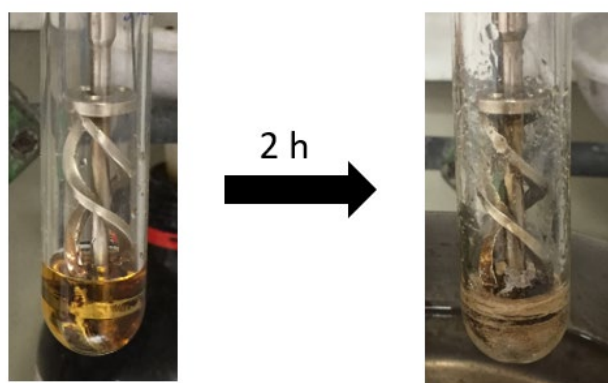


Figure 27. Left: Schlenk-tube with crude solution of step 1; right: Schlenk tube after 2 h at 100 °C under vacuum.

We thus used a mechanical stirrer (Figure 27) to improve the agitating rate. The mechanical forces enabled a permanent stirring all along the evaporation process. The viscous oil that was obtained after the first 10 - 20 minutes, gave a beige-brown powder already after 2 h under

vacuum (Figure 27, right). Consequently, the contact between the mannose molecules was higher.

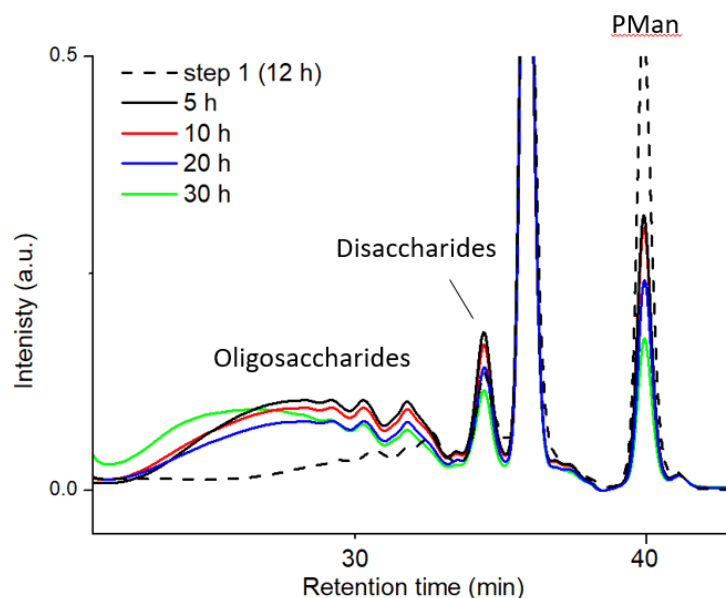


Figure 28. Plot of overlaid SEC (measured against dextran-standards in H₂O at 25 °C) traces of polymerization medium (P2) at 100 °C under *mechanical stirring* after **step 1** = 12 h (80 °C, PGA/mannose: 5)

Table 8. Evaluation of the polymerization P2.

Time (h)	Conversion (%)* of PMan	\overline{M}_n (g/mol) (SEC)	\overline{D} (M_n/M_w) (SEC)	\overline{DP}_n (g/mol) (NMR)
5	64	414	1.92	4.1
10	65	464	1.93	4.2
20	77	562	2.37	4.6
30	83	580	2.21	4.9

*Conversion rate calculated by the surface area of the refractive index detector of SEC.

The employment of a mechanical stirrer (Figure 27) could slightly improve the polymerization rate for short reaction times. The obtained \overline{DP}_n under mechanical stirrer was 3.2 after 4 h and 4.1 after 5 h of reaction. During the following 25 h of reaction, the DP_n increased only by 1.4 to reach 4.9 (see Table 8). The polymerization was slightly faster than with a mechanical stirrer, but also here, the distillation of PGA limits the duration of the reaction. The elongation of the oligosaccharides might proceed faster with a mechanical stirring, but the final DP_n was suggested to depend on the kinetic.

After the distillation of PGA (step 2), the obtained crude powder still needed to be washed with chloroform to get rid of the last remaining traces of PGA. NMR spectroscopy experiments (see appendix) showed that PGA was not completely removed even after 30 h of heating under vacuum at 100 °C. We suggested, that the reversible glycosylation reaction of mannose with PGA released continuously traces of PGA during step 2 (see later for more information). After washing with CHCl₃, the (PMan)_n were obtained in NMR yields of 80 up to 88 %. The

remaining fraction of (PMan) could be further separated from (PMan)_n by column-chromatography (acetonitrile/water 10 - 30 vol.-%) due to their important difference in their retardation factors (R_f). This presented a simple method to (1) ‘purify’ the oligomers, (2) increase the \overline{DP}_n and (3) decrease the dispersity D , consequently. This method of ‘purification’ was utilized for the complete elucidation of the structure of (PMan)_n by NMR (see later in chapter II A, section 4) and the preparation of amphiphiles (see later in Chapter III).

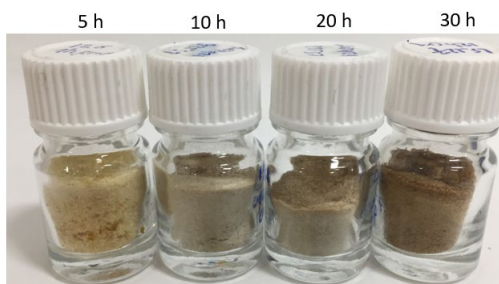


Figure 29. Obtained powder of oligosaccharides after polymerization **P1** (magnetically stirring).

During step 2, the color of the samples turned from light beige to dark brown, suggesting the formation of tar-like materials (humins) as already discussed during step 1. The exposure of the oligosaccharides at 100 °C over a longer time period was proposed to generate these unwanted side products. In order to quantify them, the product was filtrated over active carbon (Figure 30) as it is a known and expedient procedure to remove tar-like materials from sugars.^[8, 16]

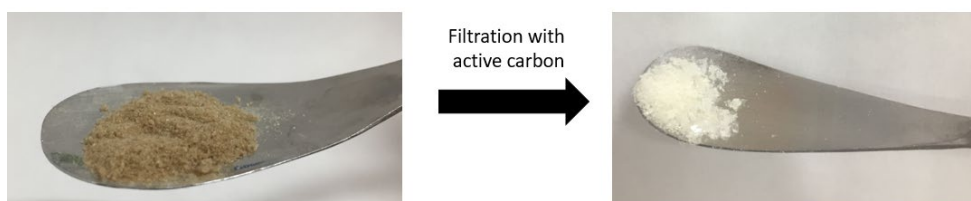


Figure 30. Image of the oligosaccharides before (left) and after (right) filtration with active carbon.

Table 9. Mass loss after the filtration with active carbon of the samples of the polymerization **P1** after different reaction times.

Entry	Time of polymerization (h)	Relative proportion of coloured side-products (%)
1	5	20
2	10	24
3	20	28
4	30	30

(PMan)_n from step 2 were dissolved in a solution of water/ethanol (50:50) and stirred after the addition of a spatula tip of active carbon for 20 minutes (at room temperature). The

obtained black solution was filtrated (cellulose acetate, 0.4 μm) and the solvent was removed under reduced pressure to give a white powder (Figure 30, right). The difference in mass gave approximately the amount of tar-like materials (between 20 and 30 wt.%, Table 9). Note, that some fraction of $(\text{PMan})_n$ could also get stuck on the filter or the active carbon. The exact amount of side-products could thus not be determined following this protocol. However, a general trend to higher amounts of tar-like materials could be observed during longer reaction times of step 2. Even though exact quantitative values could not be provided, the resulting pure white powder supported the successful removal of the unwanted side-products. We calculated the total isolated yield of $(\text{PMan})_n$ after the purification to be at least 56 - 70 %, respectively.

On the basis of all these results, we carried out a third polymerization study (**P3**). The duration of the reaction was set to 4 h, which was demonstrated to be sufficient to remove PGA and to obtain high \overline{DP}_n . The reaction was carried out in a slim Schlenk tube using a mechanical stirrer to optimize the agitation during the evaporation process. Amberlyst-15 was separated from the crude mixture of step 1 by centrifugation and collected. With this protocol, we could obtain $(\text{PMan})_n$ with a DP_n of 5.5 after 4 h of reaction. The obtained mixture contained only 9 % of monomeric PMan (determined by SEC) and the oligosaccharides could be obtained in 88 % NMR yield after washing with chloroform (Table 10).

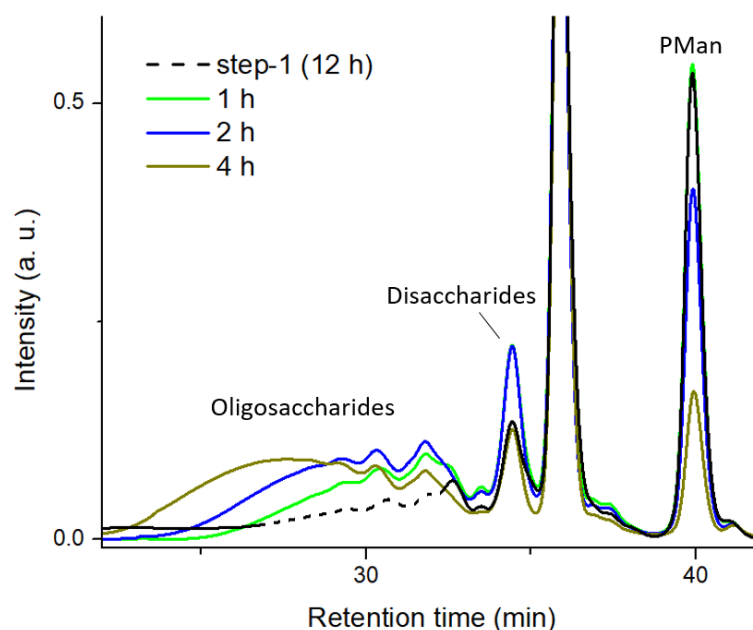


Figure 31. Overlaid SEC (measured against dextran-standards in H_2O at 25 $^\circ\text{C}$) traces of the polymerization mixture (**P3**) at 100 $^\circ\text{C}$ under optimized conditions.

Table 10. Evaluation of polymerization **P3**.

Time (h)	Conversion (%) [*] of PMan	\overline{M}_n (g/mol) (SEC)	\overline{D} (M_n/M_w) (SEC)	\overline{DP}_n (g/mol) (NMR)
1	17	448	1.7	3.2
2	56	665	1.85	4.3
3	88	721	1.87	4.4
4	91	802	1.9	5.5

^{*}Conversion rate calculated by the surface area of the refractive index detector of the signal for PMan by SEC.

The obtained $(PMan)_n$ of **P1**, **P2** and **P3** were next analyzed by MALDI-tof spectroscopy to support the chemical composition. Figure 32 shows one of the obtained spectrum with the series of monoanionized peaks of $(PMan)_n$ (**A**) as $[M-Na]^+$. The m/z of $(PMan)_n$ was calculated by the addition of the molar mass of PMan ($M = 218.08$ g/mol) with the mannose repeating unit ($M = 162.06$ g/mol) in the $(PMan)_n$ chain and the Na^+ counterion ($M = 23$ g/mol). The theoretical m/z values gave consequently 241.08 u for PMan, 403.14 u for $(PMan)_2$, etc. (see in more detail in the experimental section). The detected signals in the spectrum were in line with these theoretical values and confirmed the formation of $(PMan)_n$ up to $DP = 12$: $m/z = 2023.74 [M-Na]^+$, corresponding to DP_n of *ca.* 5 due to NMR analysis. Within the noise of the MS spectra, a second series (**B**), with m/z lower than 56 as compared to $(PMan)_n$ was observed. This series corresponds to the already detected (during step 1) mannose molecules terminated by a dehydrated anhydromannose unit ($(LVM)_n$, Figure 23). Since their signals were covered by the noise of the spectrum and could not be further elucidated by NMR investigations (see later for more information), they were considered as quasi-negligible. The series of terminal free $(Man)_n$, as observed in step 1, could not be detected by MALDI-tof MS, confirming the complete propargylation of the oligomannosides.

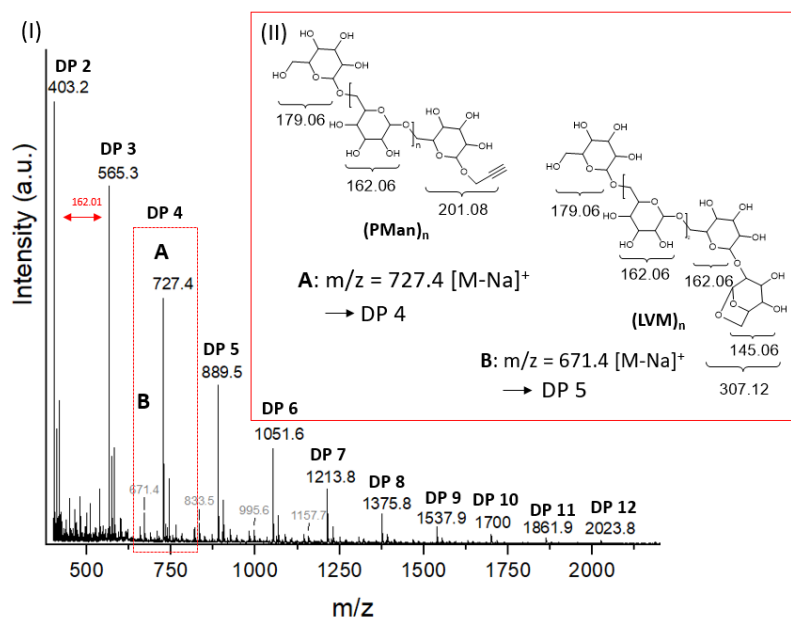
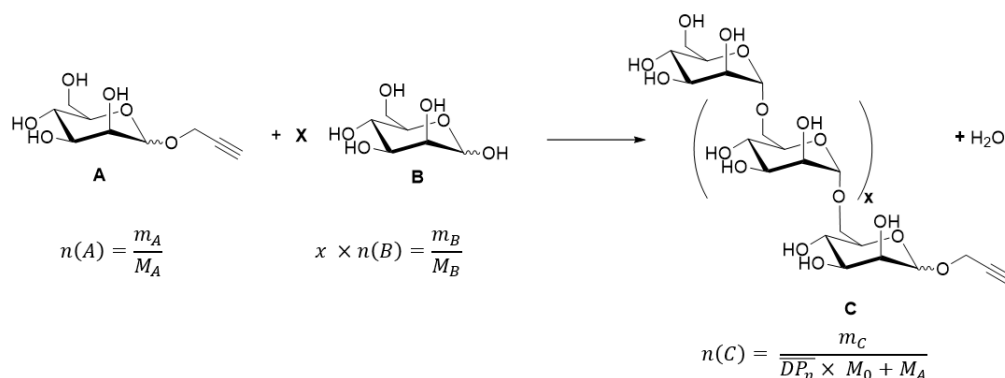


Figure 32. (I) MALDI-TOF spectrum of propargyl-(oligo)-mannopyranoside $(PMan)_n$ (here: after 4 h of polymerization reaction (**P3**)). (II) proposed structure.

3.2 Discussion on the reaction mechanism

To understand the reaction mechanism of the propargylation of mannose and oligomerization thereof, we carried out another set of experiments. As mannose was nearly completely consumed in step 1 (see NMR, GC, SEC and MASS spectroscopy), we suggested that PMan is partly reconverted back to the oxocarbenium ion that is attacked by the (PMan)_n chain, resulting in its propagation. To confirm this hypothesis, we calculated the theoretical yield of (PMan)_n from the amount of mannose and PMan found after step 1 (Scheme 5).

Theoretical yield (%)



Scheme 5. Calculation of the theoretical yield of the polymerization of PMan (**A**) with mannose (**B**).

Table 11. Batch **P4** for the theoretical calculation.

Compound	M (g/mol)	m (g)	V (mL)	n (mmol)	eq.
Mannose	180.16	5		27.75	1
Propargyl alcohol	56.06	7.78	8	138.76	5
Amberlyst-15		0.25			

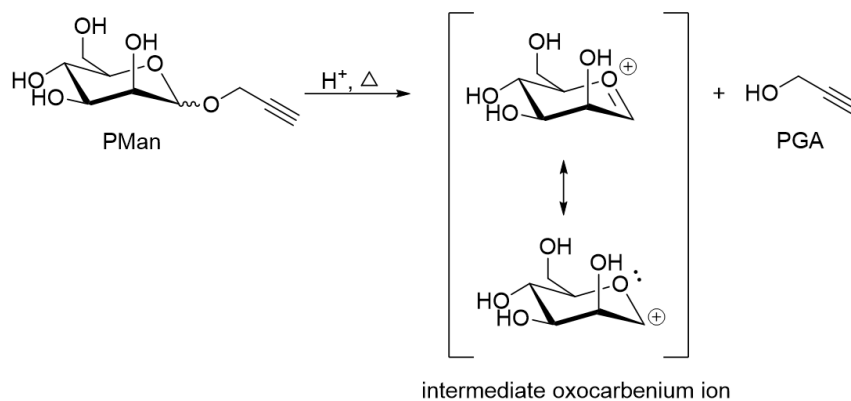
For the reasons of simplification, mannose (**B**) was assumed to be the only ‘source of monomer’ for the polymerization reaction of PMan (**A**) to (PMan)_n (**C**). We carried out a reaction (polymerization **P4**, Table 11) under the typical conditions (**step 1**: 80 °C, 12 h, **step 2**: 100 °C, vacuum, 4 h) and calculated the amount of mannose, that was left upon step 1 by GC. The theoretical yield was calculated using following equation

$$m_C = n(C) \times M_0 + M_A, \quad (1)$$

where m_C is the mass of the oligosaccharides, M_0 the molar mass of the ‘repeating unit’ (corresponding to a mannose unit = 162 g/mol) and M_A the molar mass of PMan (218.21 g/mol). Since mannose is the ‘limiting reagent’ of this reaction, $n(C) = n(B)/4$. Consequently, the theoretical yield of oligosaccharides **C** is calculated with the amount of mannose (n), that is left after step 1 (= composition of the mixture at the start of the polymerization).

After step 1 of reaction **P4**, 0.4 g mannose was found by GC, while step 2 gave 2.45 g (PMan)_n with a \overline{DP}_n of 4 (note that the product contained still 1 g of PMan). However, the maximal

theoretical yield of $(PMan)_n$ with a \overline{DP}_n of 4 gave 1.7 g by using equation (1) and was thus far exceeded in the experiment. This results supported our claim, that mannose was released during step 2 to react with PMan and give a \overline{DP}_n of up to 4. We thus proposed that the glycosylation reaction of mannose with PGA was reversible, so that PMan was reprotonated to give back the oxocarbenium ion (Scheme 6).



Scheme 6. Proposed reaction during the polymerization process: cleavage of the propargyl group under acid conditions to form back the oxocarbenium ion and PGA.

To confirm our hypothesis experimentally, PMan was prepared, isolated by chromatography and freeze dried for one day to remove all traces of water. The purified PMan was dissolved in PGA (5 eq.) and stirred at 80 °C for 1 h (step 1) with Amberlyst-15. The mixture was then heated at 100 °C under vacuum for 4 h (step 2).

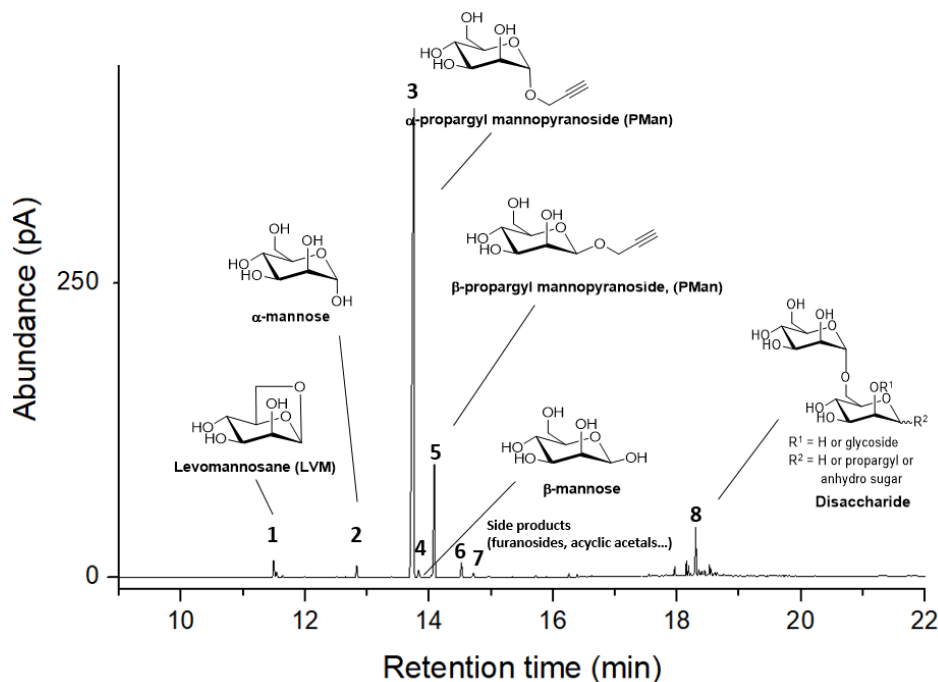


Figure 33. GC-FID spectrum of the reaction of PMan with PGA after step 1. Relative surface area (%): Peak¹ = 1.41, Peak² = 4.5, peak³ = 75.07, peak⁴ = 1.02, peak⁵ = 8.23, peak⁶ = 1.35, peak⁷ = 0.75, peak⁸ = 7.67.

After step 1, the release of free mannose ($\sim 5\%$) was observed by GC (peak **2** and **4**, Figure **33**), along with small amount of oligomers ($\sim 8\%$ disaccharide fraction in GC, peak **8**, Figure **33**). The appeared signals **6** and **7** were assigned to side-products of the glycosylation, as already denoted in this chapter in subsection 2.4 and accounted to $\sim 2\%$. The analysis by NMR spectroscopy supported the formation of mannose with the appearance of a doublet at 5.19 ppm corresponding to the anomeric proton of α -mannose.

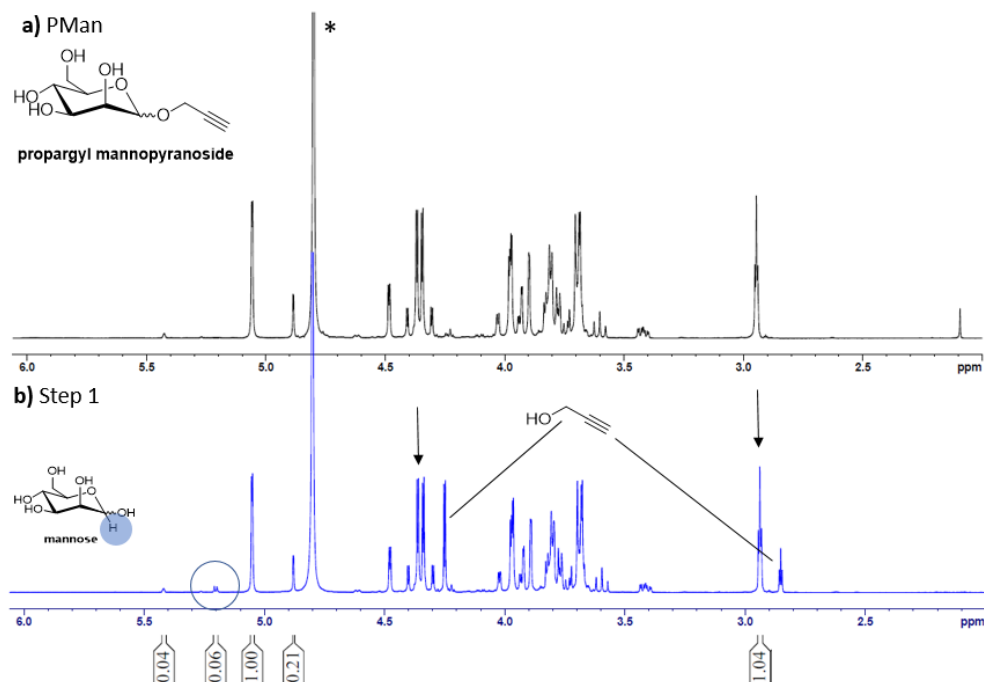


Figure **34**. $^1\text{H-NMR}$ (400 MHz, D_2O) spectra of **a**) pure isolated PMan, **b**) reaction of PMan with PGA after step 1.

After step 2, 75 % of the initial amount of PMan was converted to $(\text{PMan})_n$ with a DP_n of 3.7 in 85 % yield (Figure **35**). When the second step was continued for another 12 h, 82 % of PMan were converted, affording oligosaccharides with a \overline{DP}_n of 5.4. The product was further analyzed by NMR spectroscopy (appendix) and the proposed structure could be confirmed with the assignment of the signals for $(\text{PMan})_n$. In addition, the MALDI-TOF MS showed complete propargylation of the obtained $(\text{PMan})_n$ (see appendix). These findings supported that PMan could be depropargylated to give the oxocarbenium ion back, instantaneously followed by a nucleophile attack of PMan. When this reaction sequence continued, the mannosides chain is elongation to give exclusively $(\text{PMan})_n$, respectively. Note that this oligomerization was only possible due to the solubility of mannose and APG $(\text{PMan})_n$ in PGA. In contrast with fatty alcohols (see literature to APG), this elongation was not observed due to solubility issues, precipitation or degradation problems.

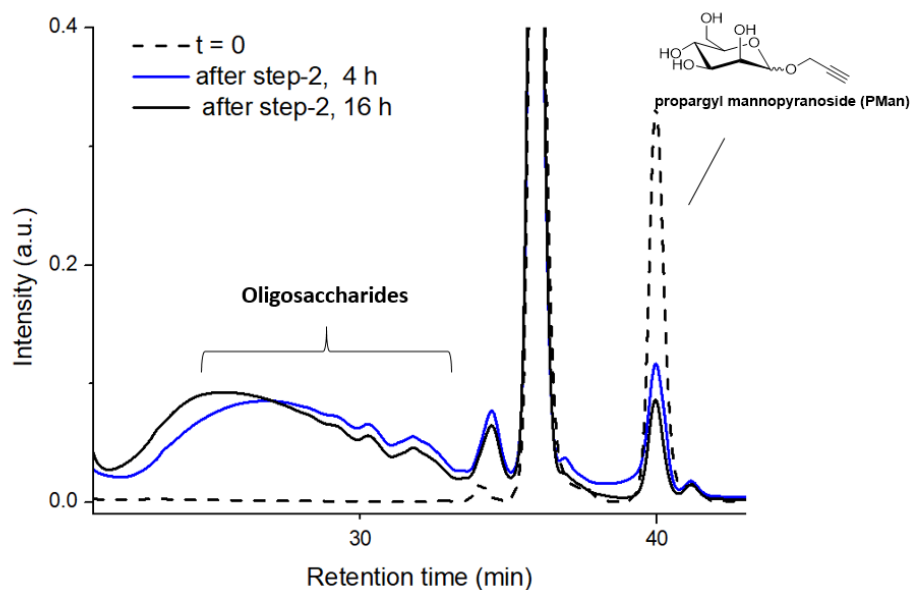
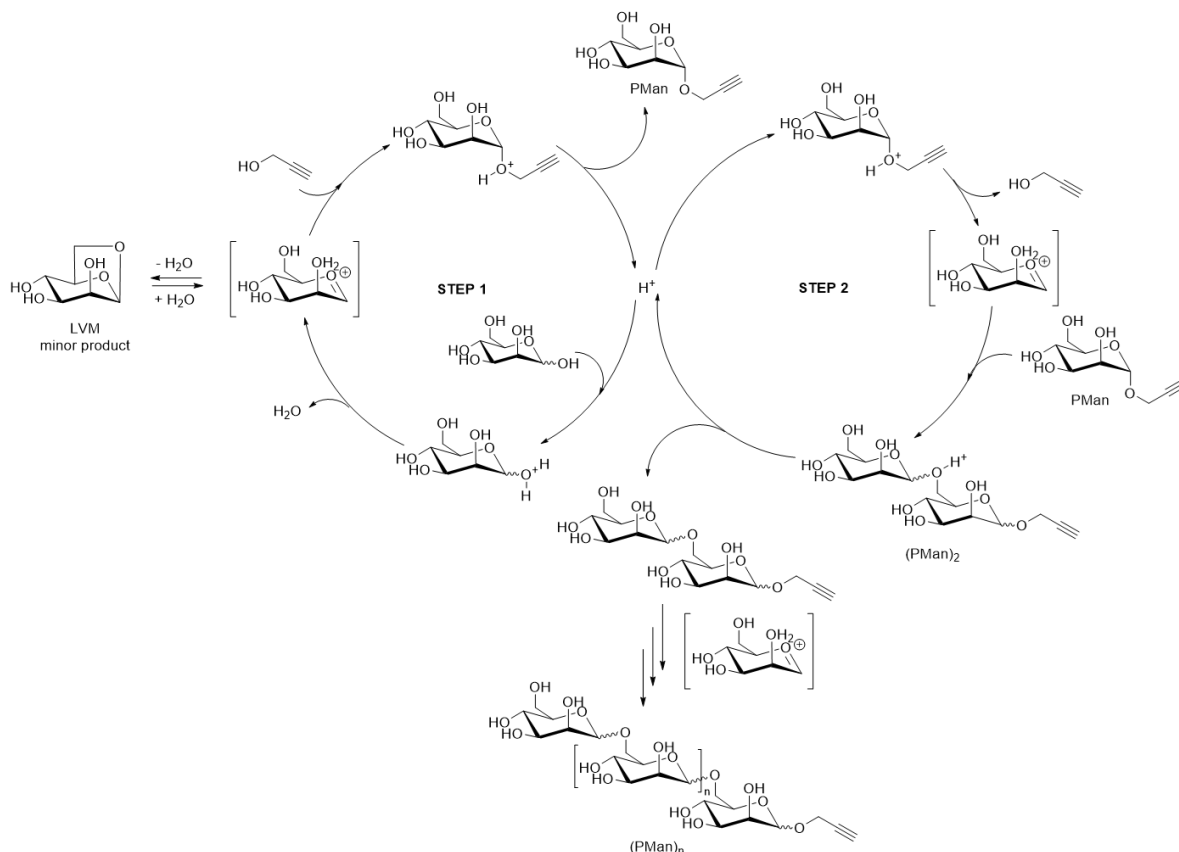


Figure 35. Overlaid SEC (measured against dextran-standards in H₂O at 25 °C) traces of polymerization medium (4 h and 16 h) of PMan (**P5**).

Step 1	Step 2	Conversion of PMan (%)	\overline{M}_n (g/mol) (SEC)	\overline{D} (M_w/M_n) (SEC)	\overline{DP}_n (g/mol) (NMR)
Amberlyst-15, 80 °C, 2 h	100 °C, <i>vacuum</i> , 4 h	75	547	2.0	3.7
	100 °C, <i>vacuum</i> , 16 h	82	673	2.0	5.4

With these last results, we could give a final proposal for the reaction mechanism, including the connection between step 1 and step 2 (Scheme 7). In step 1, mannose was protonated by amberlyst-15 to form the oxocarbenium ion, which was then rapidly trapped by PGA to form PMan. The elongation of the mannose moiety to form APG occurred in a very low extent in step 1, mainly due to the excess of PGA and the *in situ* release of water which prevented oligomerization reaction. We showed that this step was reversible, forming the oxocarbenium ion back from PMan in step 1. Also in step 2, PMan was reprotonated, partly regenerating the oxocarbenium ion. But in this case, the distillation of PGA (and water) under vacuum made the reaction of the oxocarbenium ion with PMan statistically more likely to occur, leading to the formation of (PMan)_n. The reprotonation and the *in situ* formation of the oxocarbenium ion was confirmed with the polymerization of PMan (**P5**). The proposed reaction mechanism also explained the formation of levomannosane (LVM) as a minor product, resulting from the internal cyclization of the oxocarbenium ion.



Scheme 7. Proposed reaction mechanism for step 1 and step 2.

3.3 Optimization of the oligomerization reaction

In a last set of experiments, we tried to improve the oligomerization by changing the conditions of the step 1. To further increase the \overline{DP}_n of $(PMan)_n$, step 1 was stopped before complete conversion of mannose. This should facilitate the reaction of PMan with unreacted mannose and finally lead to higher \overline{DP}_n . When step 1 was stopped after varying the reaction times, different amounts of unreacted mannose were provided to the following polymerization (step 2). The red box (i) in Figure 36 highlights the time range of step 1 before complete conversion of mannose. This range was attributed to the reaction before its thermodynamic equilibrium. At temperatures of 80 °C and for a molar ratio of PGA/mannose of 5 (black and blue), the amount of remaining mannose was around 30 - 40 % after 1 h, 17 - 21 % after 3 h and 12 - 14 % after 6 h of reaction, respectively. At higher temperatures of 100 °C (red), the conversion of mannose reached already its maximum after 3 h. Decreasing the PGA/mannose ratio to 3 (purple), 53 % mannose was left after 1 h and still 17 % after 8 h. At 60 °C (green), unreacted mannose molecules of around 30 to 22 % were found all along step 1.

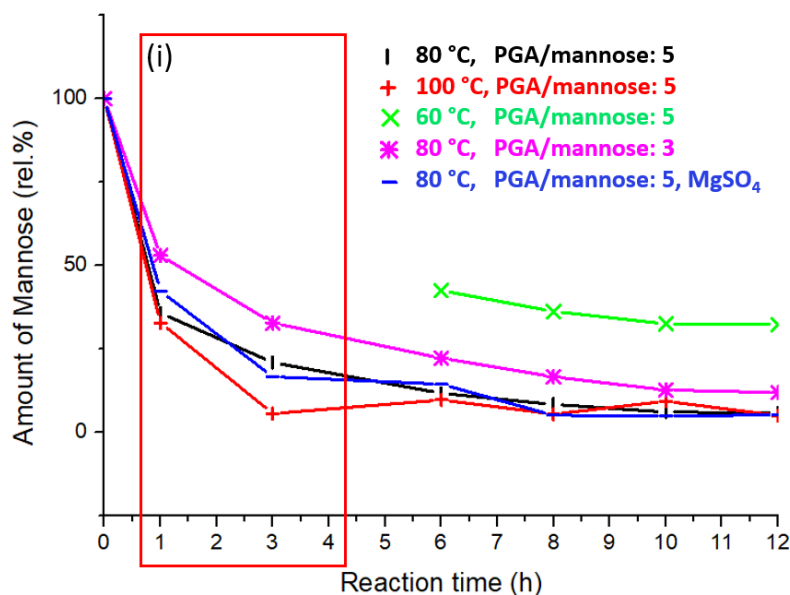


Figure 36. Relative proportion of mannose during step 1 calculated by GC-FID; (i) = reaction before the thermodynamic equilibrium. For the reasons of solubility, at 60 °C (green) the samples could only be considered upon 6 h of reaction.

The mixtures obtained after different durations of step 1 were then heated under vacuum at 100 °C for 4 h (step 2). The obtained oligosaccharides were analyzed by NMR and SEC (see appendix) and summarized in Figure 37.

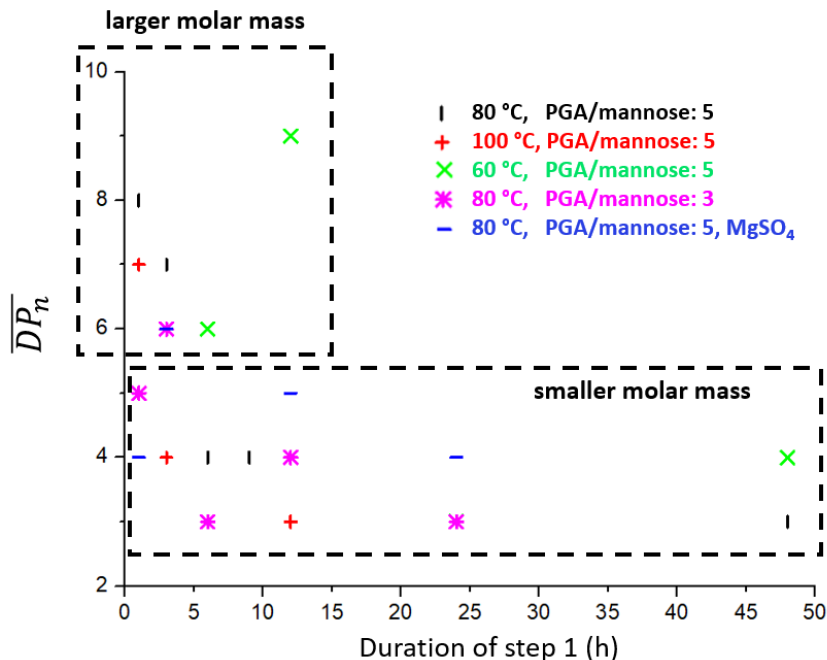


Figure 37. Plot of the average degree of polymerization (\overline{DP}_n) of (PMan)_n as a function of the time of step 1; the dashed box indicates the reaction conditions, which yielded (PMan)_n with larger ($\overline{DP}_n \geq 6$) and smaller molar mass ($\overline{DP}_n \leq 5$).

When vacuum was applied before mannose was completely converted (step 1, (i) = 1 - 4 h, Figure 36), higher \overline{DP}_n could be reached. For instance, when step 1 was stopped after 3 h at

80 °C, 22 % of unreacted mannose were left and gave (PMan)_n with a DP_n of 8 after step 2. The highest DP_n (= 9) was obtained after 12 h at 60 °C (for step 1), denoting 36 % of unreacted mannose in the solution before step 2. The low temperature led to a decreased reaction rate and, consequently, to higher amounts of unreacted mannose. The latter could then randomly polymerize either with PMan or mannose to extend the $\overline{DP_n}$. To our surprise, the decrease of the molar ratio PGA/mannose from 5 to 3 could not remarkably increase the $\overline{DP_n}$. After 3 h of step 1, still 30 % of unreacted mannose were found in the mixture, however, affording (PMan)_n with only DP_n 6 after step 2. Extension of step 1 from 3- to 6- to 48 h, resulted with (PMan)_n with DP_n only between 3 and 4 even though the crude mixture of step 1 contained still up to 20 % of unreacted mannose. We suggested, that the higher concentration of sugar and the resulting higher viscosity hindered a proper stirring and thus the extension of the polymerization reaction. Finally, we showed that the addition of MgSO₄ did not improve the polymerization progress, suggesting that the *in situ* released water could not be sufficiently absorbed.

Altogether, there was a significant increase in the $\overline{DP_n}$, when the polymerization (step 2) was initiated after 1 - 4 h of the primary glycosylation reaction (step 1). The remaining unreacted mannose at that stage of step 1 (20 - 36 %) led to an increased polymerization rate with mannose or PMan molecules. However, a mixture of (PMan)_n (54 - 78 %), terminal free (Man)_n (28 - 14 %) and levomannosanes (LVM) (18 - 4 %) was consequently obtained. The different end-groups were determined by ¹H-NMR spectroscopy (Figure 38).

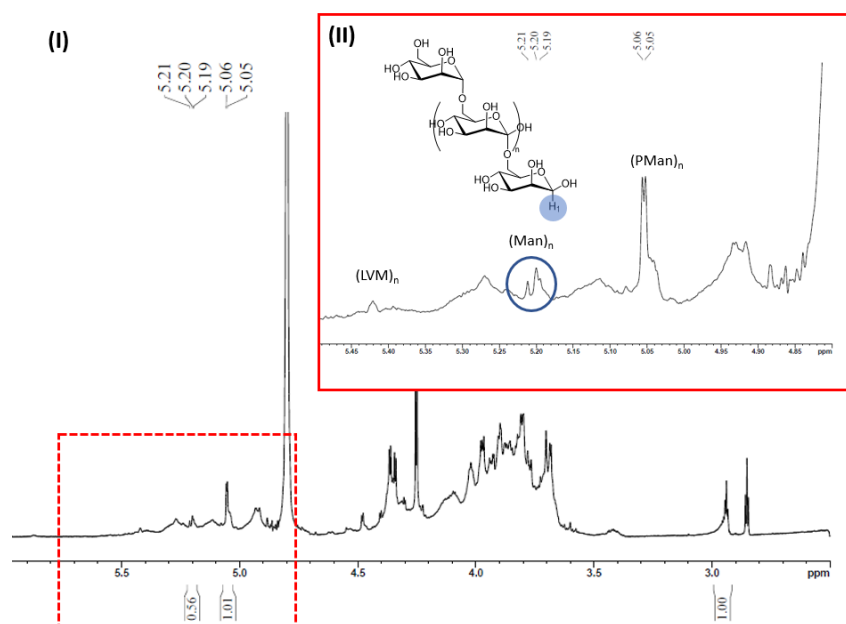


Figure 38. ¹H-NMR (400 MHz, D₂O) spectrum of a mixture of (PMan)_n, (Man)_n and (LVM)_n obtained under following reaction conditions: step (1) = 80 °C, 1 h, PGA/mannose: 5; step (2) = 100 °C, vacuum, 4 h.

$^1\text{H-NMR}$ spectrum in Figure 38 is given as illustrative example to show the mixture of different end-groups obtained for very short times of step 1. The zoom at the anomeric region (II) shows a broad doublet at 5.19 - 5.20 ppm that was assigned to the terminal free $(\text{Man})_n$, the peak at 5.42 ppm to the anhydro sugars $(\text{LVM})_n$ and the peak at 5.06 - 5.05 to $(\text{PMan})_n$. In addition, we denoted intense broad signals in the ppm region between 5.10 - 5.15 and 5.20 - 5.35 ppm. Those were attributed to a high branching degree, supporting an increased random polymerization of mannose.

In conclusion, it was found necessary to achieve nearly complete conversion of mannose in step 1 prior to step 2 to obtain complete functionalized $(\text{PMan})_n$. The minimal reaction times of step 1 are given in Table 12. We found that the highest $DP_n (= 8)$, fulfilling complete propargylation, was obtained after 3 h of step 1 at 80 °C with a PGA/mannose ratio of 5. At higher temperatures (100 °C, 3 h), complete propargylation was still ensured, but with a DP_n of only 3. The reactions at temperature of 60 °C gave no complete propargylation at all. With the decrease of the molar excess of PGA from 5 to 3, 12 h of step 1 were required to give complete propargylated $(\text{PMan})_n$ after step 2.

Table 12. Reaction conditions to obtain complete propargylated $(\text{PMan})_n$.

Experiment	Reaction Conditions	Time of step 1 (h)	Rel. amount of mannose left after step 1 (%)	\overline{DP}_n after step 2
A	80 °C, PGA/Man: 5	3	21	8
B	100 °C, PGA/Man: 5	3	6	3
*C	60 °C, PGA/Man: 5	n.d.	n.d.	n.d.
D	80 °C, PGA/Man: 3	12	12	4
E	80 °C, PGA/Man: 5, MgSO_4	3	17	6

*n.d. = not defined, since complete propargylation was not attained at any time.

4 Structural elucidation of (PMan)_n

The general structure of the oligomannosides could be elaborated *via* 2D NMR spectroscopy such as COSY, HSQC, HMBC, TOCSY and NOESY. With the already evaluated spectra of PMan (Chapter II A, subsection 2.2), the majority of the signals for (PMan)_n could be assigned by superposition of the spectra, according to the glycosylation shift (Figure 39 and Figure 40).

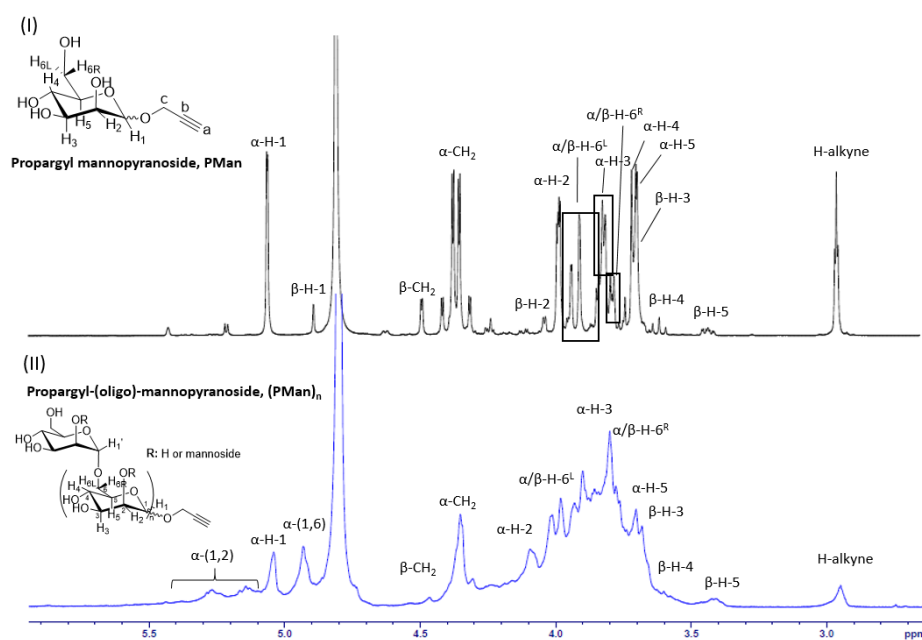


Figure 39. ¹H-NMR (400 MHz, D₂O) spectra of (I) propargyl mannopyranoside and (II) propargyl-(oligo)-mannopyranoside.

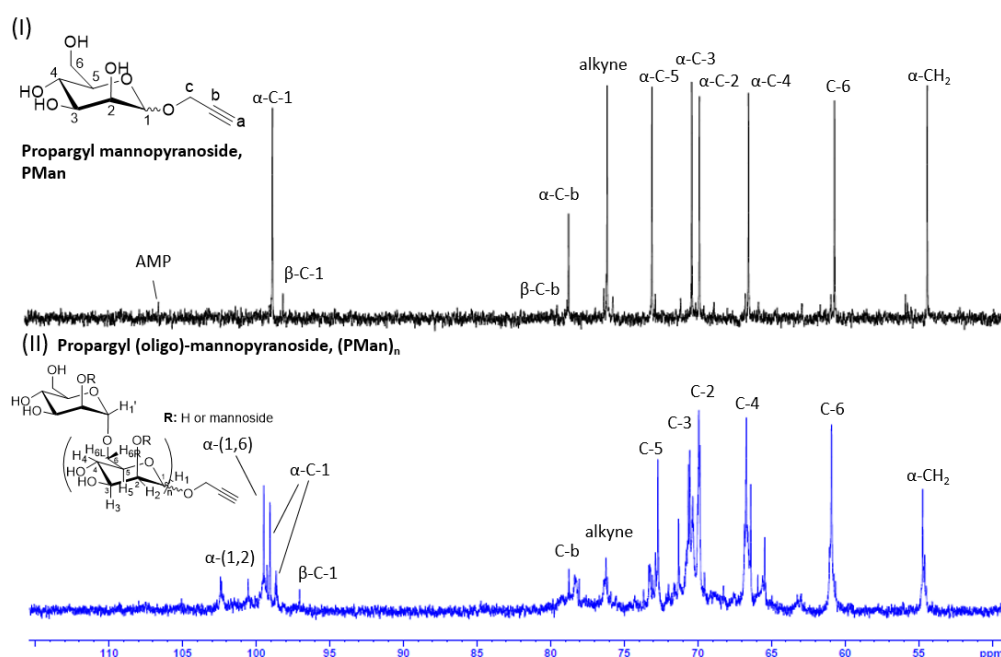


Figure 40. ¹³C-NMR (100.4 MHz, D₂O) spectra of (I) propargyl mannopyranoside and (II) propargyl-(oligo)-mannopyranoside.

The signals, however, which appeared during the polymerization of PMan, could only be determined by multidimensional NMR spectroscopy.

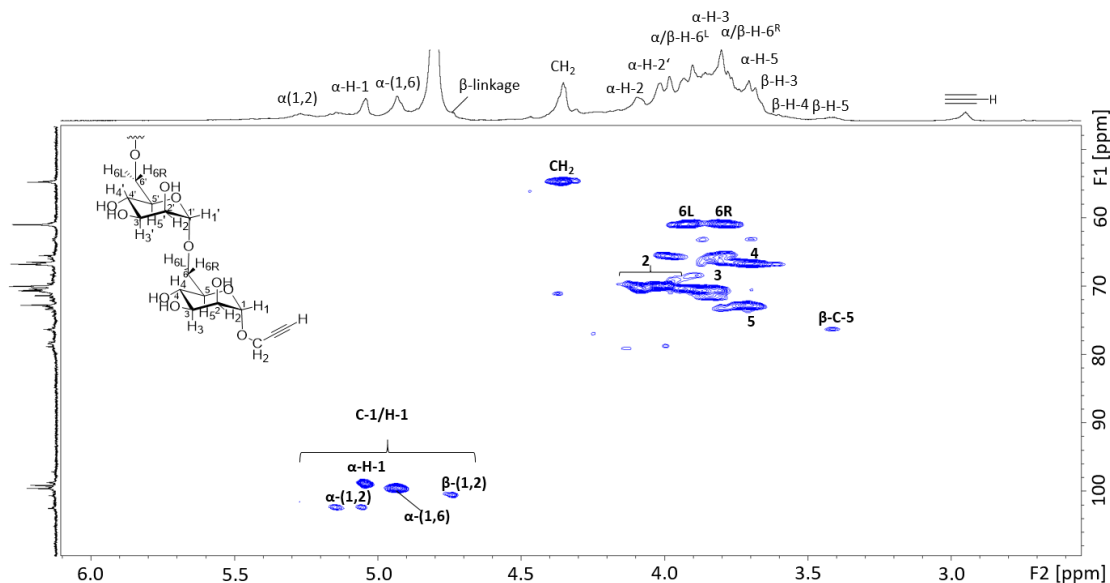


Figure 41. ^1H - ^{13}C HSQC spectrum of propargyl-(oligo)-mannopyranoside.

The ^1H -NMR spectrum of $(\text{PMan})_n$ (Figure 39) showed various broad peaks in the range of 4.90 to 5.32 ppm, region characteristic for the anomeric protons ; these peaks were thus attributed to the glycosidic linkages between the anhydromannose units in the oligomannoside chains. The corresponding signals of the ^{13}C -NMR were consequently assigned from the HSQC NMR spectrum (Figure 41).

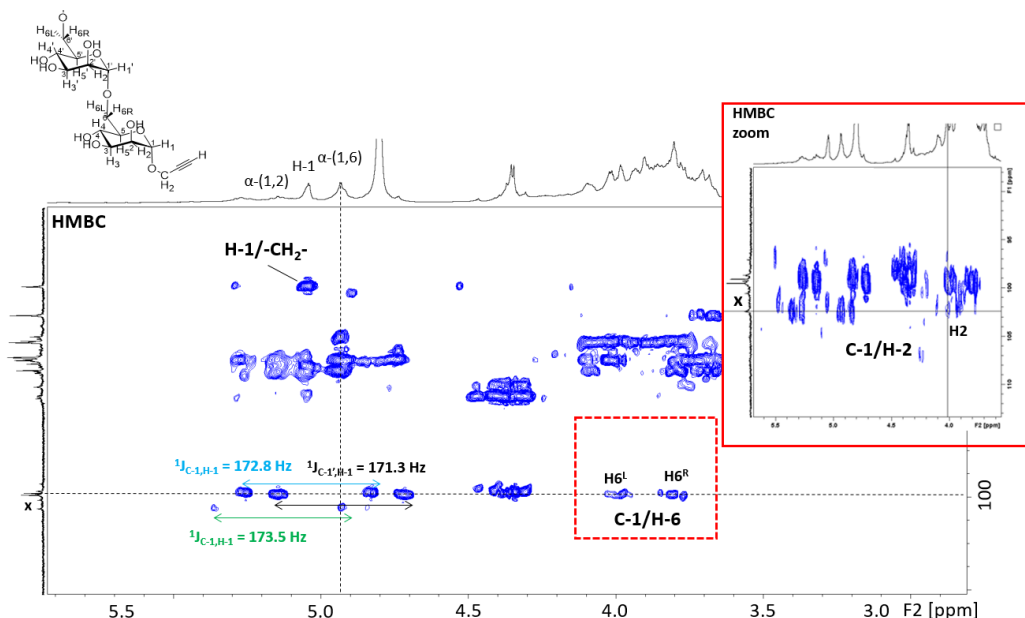


Figure 42. ^1H - ^{13}C HMBC spectrum of propargyl-(oligo)-mannopyranoside.

The broad peak at 5.01 - 5.08 ppm was assigned to the anomeric proton (blue, α -H-1) located in α -position at the chain end of $(\text{PMan})_n$. The assignment of this proton was further

confirmed with a coupling between α -H-1 and $-\text{CH}_2-$ of PGA in the NMR HMBC spectrum (Figure 42). The most significant peak at 4.97 - 4.90 ppm was assigned to the anomeric proton of the α -(1,6) glycosidic linkage, as already described in this chapter in subsection 2.2. This claim is supported by NMR HMBC experiments (Figure 42), showing a proton-carbon long range coupling of the anomeric carbon (**x**) (α -C-1 of (1,6) at 99.25 ppm, Figure 39) with the H-6 protons of the anhydromannose unit. The α -configuration was additionally supported with the short range carbon-proton coupling of 171.32 Hz ($^1J_{\text{C-1/H-1}}$), determined in the same experiment. The zoom of the HMBC NMR spectrum (Figure 42, red box) showed another long range proton-carbon coupling of an anomeric carbon with the H-2 protons of the anhydromannose unit. The short range carbon-proton coupling ($^1J_{\text{C-1/H-1}}$) of this signal gave 173.47 Hz, which indicated again a α -configuration. These results let us to assume, that the mannose-oligomers possess another glycosidic linkages via α -(1,2).

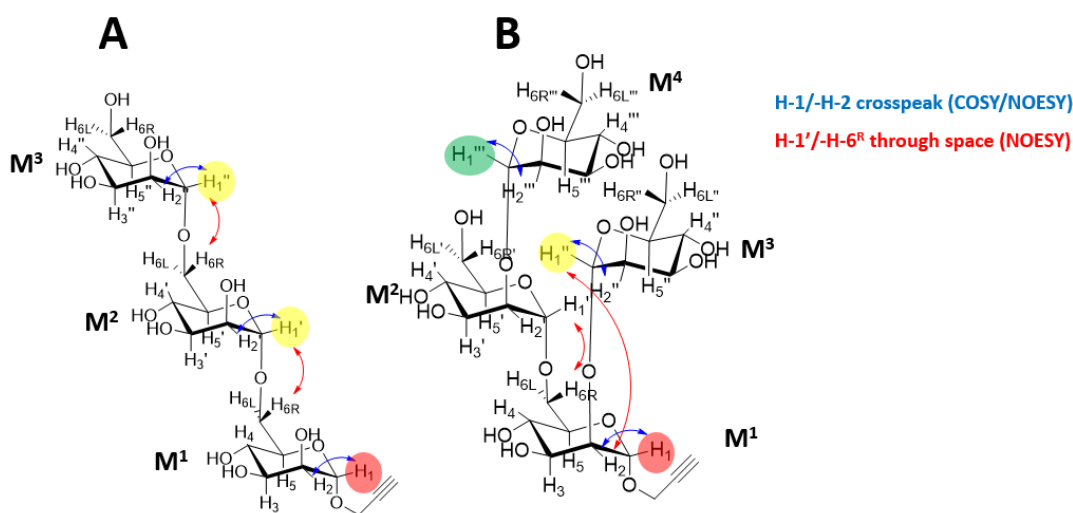


Figure 43. Ideal structures to describe the mannose-oligomers; **A**: linear chain of oligosaccharides linked exclusively via α -(1,6); **B**: branched oligosaccharides linked via α -(1,6) and α -(1,2).

To support this claim, ^1H - ^1H NMR COSY and NOESY experiments were carried out to determine the proton-proton cross- and through space couplings. NOESY NMR spectroscopy is a frequently applied method to determine the linkages in carbohydrates, since it can show the proton-proton coupling through the glycosidic linkage. For the reason of simplification, we considered two ‘ideal’ structures of $(\text{PMan})_n$ for the following evaluations (Figure 43). Structure (**A**) presents a linear mannose-chain with exclusively (1,6) linked units, whereas structure (**B**) shows the (1,6) chain with additional branching at each OH-2.

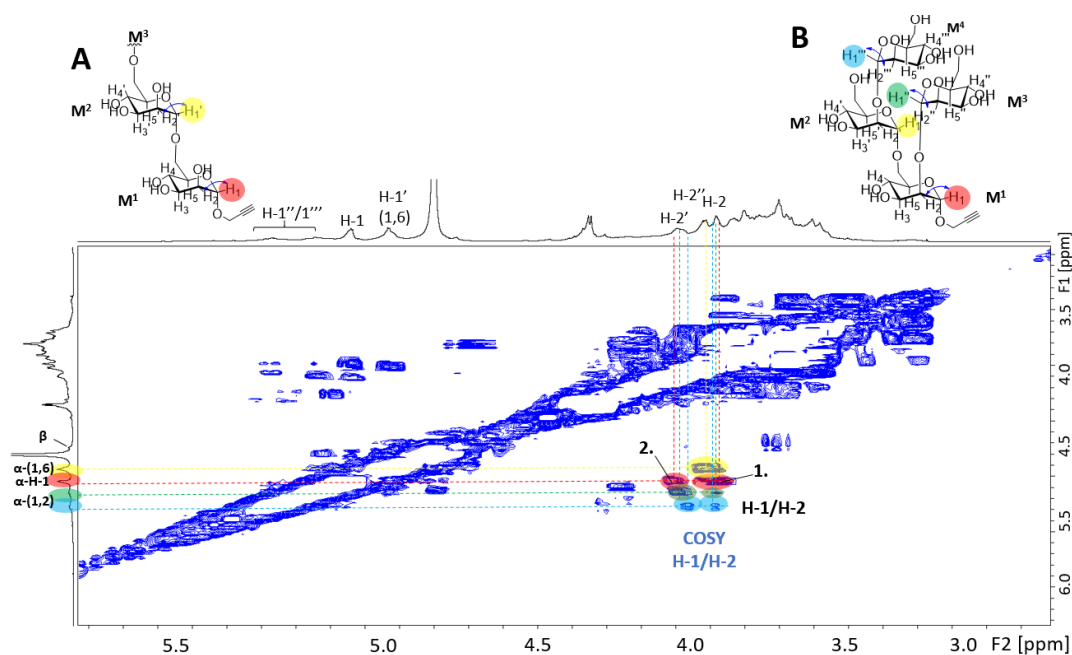


Figure 44. ^1H - ^1H COSY NMR spectrum of propargyl-(oligo)-mannopyranoside.

The COSY spectrum shows the neighbored proton-proton coupling, affording a cross-peak (blue arrow, Figure 43) for all anomeric protons (end-group or glycosidic linkage) with the H-2 of the corresponding sugar ring. Consequently, we assigned the couplings of the anomeric protons (yellow, red, green and blue, Figure 44) in the COSY NMR experiment to H-1/H-2 cross-peaks. The broad signals between 3.98 - 4.10 ppm were attributed to the H-2 protons (H-2, H-2', H-2'', H-2''' structure A and B, Figure 43) of each mannose unit (M^n). We related the ppm values of the H-2 signals to the glycosylation shift of the neighbored proton of glycosidic linkages in oligosaccharides (see Chapter II A, subsection 2.2).

The anomeric proton of the propargylated end (α -H-1, red, 5.01 - 5.08 ppm, Figure 45) shows two H-1/H-2 cross couplings in the COSY NMR spectrum. One of them (1) was strongly suggested to belong to a non-branched terminal end (structure A), supported by comparison to the COSY NMR of pure monomeric PMan (see COSY spectrum, Figure 10). The second proton-proton (H-1/H-2) coupling (2) was attributed to structure B, where OH-2 is glycosylated to mannose unit M^3 (branching), leading to a shift of H-2. The anomeric protons labelled in green and blue, assigned to (1,2) glycosidic linkages (see later in NOESY), gave two proton-proton couplings in the COSY NMR experiment. They were attributed to the two broad peaks at 5.08 - 5.28 ppm, arising from the different branching position to M^3 or M^4 etc.

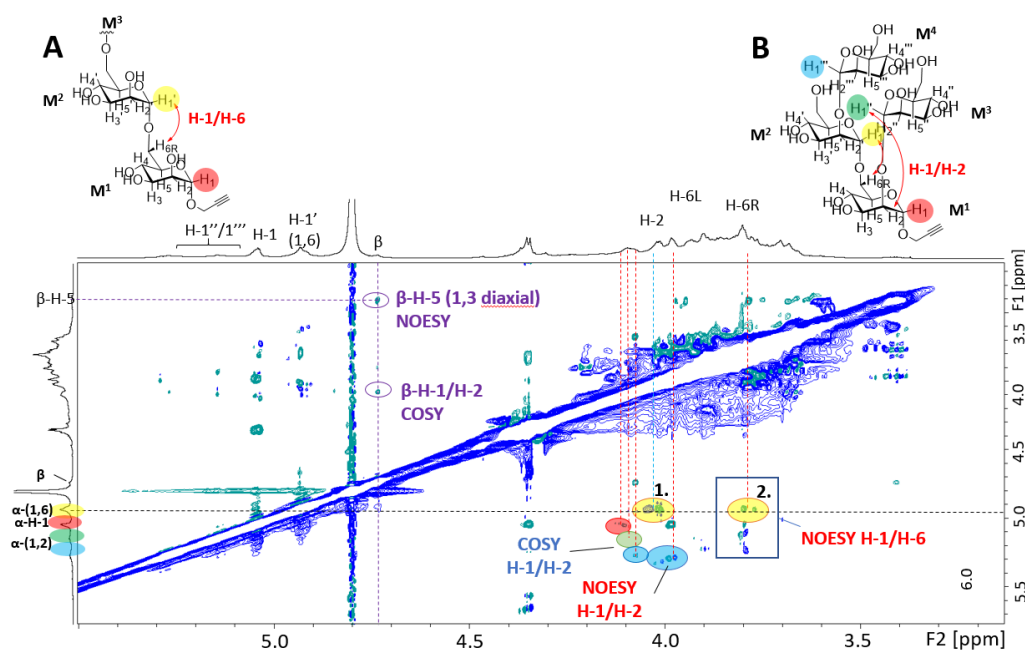


Figure 45. ^1H - ^1H NOESY spectrum of propargyl-(oligo)-mannopyranoside.

The NOESY NMR experiment of the mannose-oligomers (Figure 45) gave two couplings for the anomeric proton at 4.93 ppm (yellow, 1. and 2.). The first signal (1.) presents the already observed H-1/H-2 cross-peak in the COSY NMR experiment and the second (2.) arises from the long-range proton-proton coupling to the H-6 of the sugar ring. The remaining peaks of the glycosidic linkages (green and blue, 5.08 - 5.28 ppm), were attributed to the (1,2) linkages, as COSY and NOESY NMR spectroscopy showed an exclusive H,H-coupling with H-2 protons of the mannose ring (4.1 - 3.98 ppm). One should note, that the additional peak at 4.73 ppm suggests the existence of β -glycosidic linkage. This was supported by the proton-proton long range coupling to β -H-5 (3.41 ppm) in the NMR NOESY experiment (purple). However, due to the poor intensity in the 2D-NMR spectra, they were accounted to very low percentages. Altogether, the combined multidimensional NMR spectroscopy supported the assumed structure of the oligomannoside chain, dominantly assembled through α -(1,6) glycosidic bonds and, in a lower extent branched through α -(1,2) glycosidic linkages.

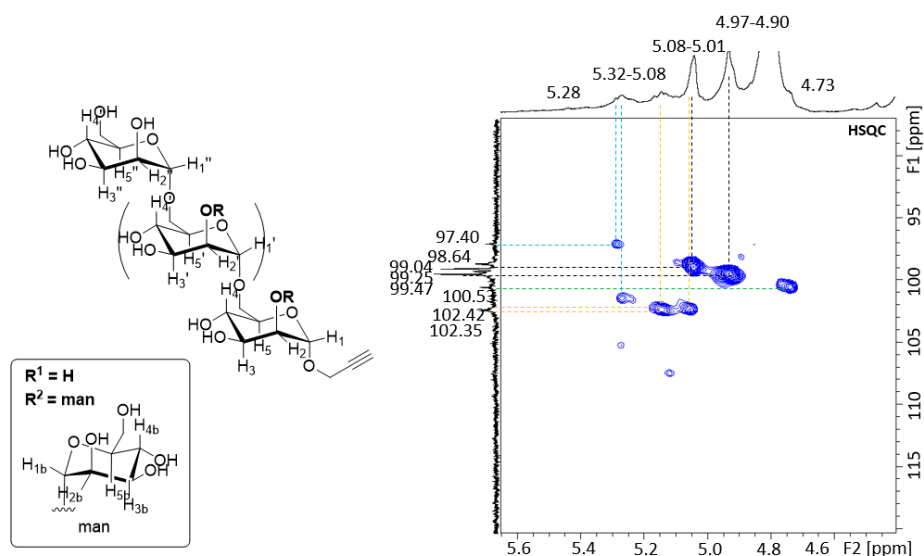


Figure 46. Proposed structure of propargyl-(oligo)-mannopyranoside.

Table 13. Values of the anomeric peaks of proton and carbon NMR spectroscopy. TMS was used as external standard.

$^1\text{H-NMR}$ (ppm)	$^{13}\text{C-NMR}$ (ppm)	anomeric position
5.28	97.04	β -linkage
5.32-5.08	102.35	H-1b « α -(1,2) linkage » / $\text{R}^2 = \text{man}$
5.32-5.08	102.42	H-1b « α -(1,2) linkage » / $\text{R}^2 = \text{man}$
5.08-5.01	98.64	H-1 « propargyl-endgroup » / $\text{R}^1 = \text{H}$
5.08-5.01	99.04	H-1 « propargyl-endgroup » / $\text{R}^2 = \text{man}$
4.97-4.90	99.25	H-1' « α -(1,6) linkage » / $\text{R}^1 = \text{H}$
4.97-4.90	99.47	H-1' « α -(1,6) linkage » / $\text{R}^2 = \text{man}$
4.73	100.53	β -linkage

We summarized the attributions of the corresponding anomeric signals in a zoom of the HSQC spectrum in Figure 46 (right) with a general scheme of the oligomers (left). The chemical shift of the proton and carbon signals are summarized in Table 13. With the integration of the signals in the $^1\text{H-NMR}$ spectrum, the relative proportion of each linkage could be calculated, affording the branching pattern. The results gave 60 % α -(1,6)-, 32 % α -(1,2)- and 8 % β -linkages. Another small doublet found at 5.44 ppm, accounted to 5 % relative to all anomeric protons, was assigned to the anomeric proton of levomannosane (LVM).

5 Application to other Monosaccharides: Glucose

The acid catalyzed reaction of PGA and mannose was transported to glucose, which is attractive, since it is a product potentially derived from lignocellulosic biomass. Therefore, the same conditions as those described for step 1 and 2 were applied. $^1\text{H-NMR}$ spectroscopy (Figure 47) and SEC analysis (see appendix) confirmed the formation of propargyl-(oligo)-glucosides (PGluc_n) with a \overline{M}_n of 542 g/mol ($\overline{DP}_n = 3$) and a dispersity \overline{D} of 2.1 in 83 % yield.

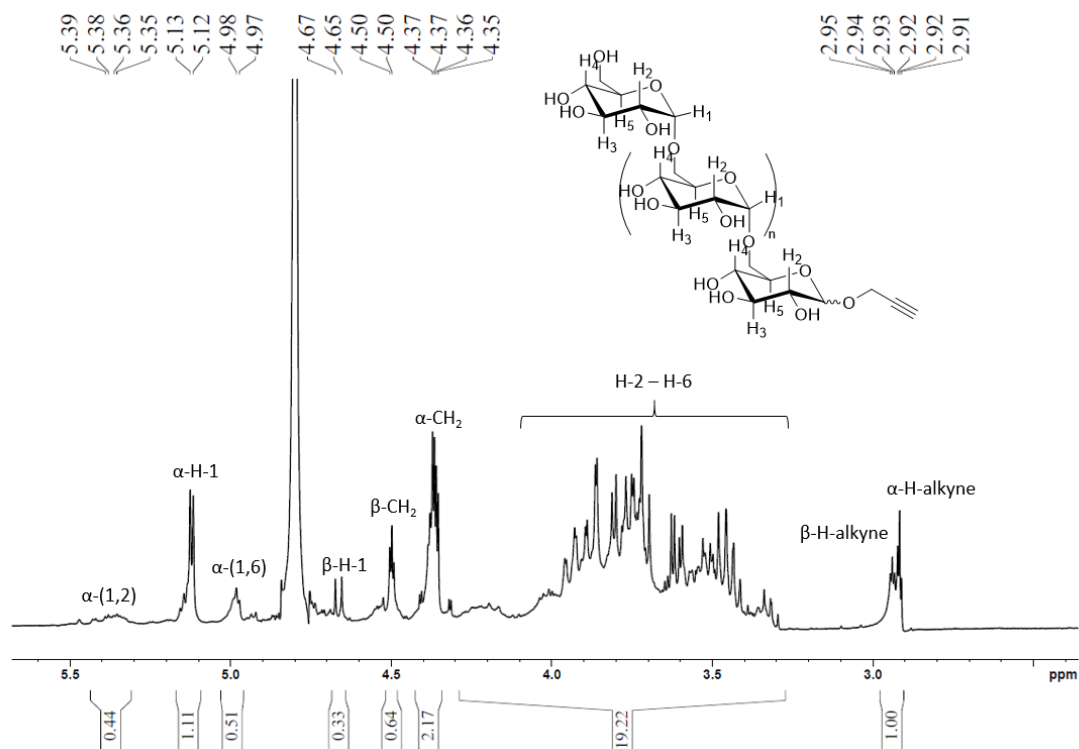
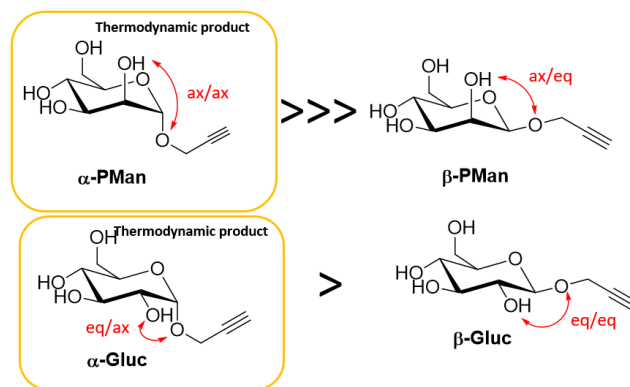


Figure 47. $^1\text{H-NMR}$ (400 MHz, D_2O) of propargyl-(oligo)-glucopyranosides (PGluc_n).

$^1\text{H-NMR}$ investigations clearly evidenced the presence of propargylated α - and β -glucosides with the appearance of two signals for the alkyne protons (2.95 - 2.91 ppm) and two signals corresponding to the anomeric protons of the propargylated terminal positions (α : 5.12 ppm, β : 4.67 ppm). Compared to mannose, the glycosylation with PGA is less stereoselective, which was attributed to the equatorial position of the OH-2 group. Mannose, contrarily, possesses the OH-2 group in the axial position, which leads to a preference of the α -anomer (the α/β ratio of $(\text{PMan})_n$ could not be calculated due to the low signal of β -H-1 in $^1\text{H-NMR}$, Figure 39). This configuration could avoid the 1,3-axial/equatorial (ax./eq.) repulsion between OH-2 and the oxygen atom of the propargyl group (Scheme 8). The equatorial OH-2 in the case of glucose, has not the same influence, affording a α/β ratio of 77:22, calculated by $^1\text{H-NMR}$ spectroscopy. The equatorial position of OH-2 was supposed to lead to strong eq./ax. repulsion for the α -anomer and even stronger eq./eq. repulsion for the β -anomer. Besides the lower stereoselectivity, the reaction rate of glucose was lower than for mannose and the obtained oligomers had a lower \overline{DP}_n .



Scheme 8. Proposed repulsive interactions in the different anomers of PMan and PGluc showing the tendency/preference for the formed products.

6 Conclusion

We could show that the acid catalyzed glycosylation of unprotected monosaccharides (mannose and glucose) with propargyl alcohol led to propargylated oligosaccharides. The separation of the reaction into two steps allowed to glycosylate the monomeric sugar with PGA in a first place, and to elongate the sugar moieties in a following step. The remove of the *in situ* released water of the glycosylation reaction during the distillation of PGA in step 2, resulted to initiate the polymerization. In addition, since the excess of PGA was removed, the reaction of PMan with mannose or other PMan was then more likely to occur. The combined NMR-mass analysis led us to conclude that the as-obtained oligomannosides were (1) fully propargylated at their terminal end, (2) mainly linked through α -(1,6)-glycosidic linkages and (3) exhibited an average \overline{DP}_n up to 8.

Mechanistic studies supported, that the glycosylation reaction of PGA and mannose was reversible under vacuum. The latter was exploited to extend the \overline{DP}_n by the formation of the oxonium carbocation back from PMan, which could then react with another molecule of PMan, resulting in an elongation of the mannoside chains. However, it was mandatory to achieve nearly complete conversion of mannose in step 1 to ensure full propargylated (PMan)_n upon the subsequent polymerization during step 2. One should note that this oligomerization reaction was possible thanks to the solubility of mannose in PGA. In contrast, with fatty alcohols, this elongation was not observed in the literature due to solubility issue, i.e. precipitation (and/or degradation) of APG and sugars upon evaporation.

To our understanding, a further improvement of the presented method was limited by the time needed to evaporate PGA. The latter restricted the duration of the polymerization reaction. Also a lower PGA/mannose ratio led not to higher \overline{DP}_n due to the increased viscosity. In this contribution, an additional solvent might be beneficial, however, this was not intended during this work.

The alkyne group at the chain-end of the prepared oligosaccharides (mannose and glucose) enables the direct access to amphiphiles. To this purpose, the well-known ‘azide-alkyne

Huisgen cyclo-addition' presents an attractive method to prepare long chain fatty APGs, circumventing the transglycosylation step. The *in situ* depolymerization of oligosaccharides, as commonly observed with other functionalization methods, might be thereby avoided. We show in Chapter III the addition of long chain fatty acids via click chemistry to (PMan)_n to prepare mannose-based amphiphiles.

7 Appendix

First screen of reaction conditions: kinetic of the glycosylation reaction of mannose and PGA at 40- and 50 °C.

Table 14. Surface Area of the mannose signal of the SEC after different reaction times. Reaction Conditions: 40 °C, 4.2 mol% catalyst, 8.4 eq. propargyl alcohol.

Time (h)	Surface Area
1	427146.09
2	416124.20
4	373645.79
5	341730.66
6	365792.64
7	335257.95

Table 15. Surface Area of the mannose signal of the SEC after different reaction times. Reaction Conditions: 40 °C, 8.4 - 33.6 mol% catalyst, 8.4 eq. propargyl alcohol, 2 h.

Time (h)	Surface Area
1	n.d.
2	356687.77
7	271086.94

Table 16. Surface Area of the mannose signal of the SEC from the glycosylation reaction using different amounts of amberlyst-15. Reaction Conditions: 40 °C, 8.4 - 33.6 mol% catalyst, 8.4 eq. propargyl alcohol, 2 h.

Amberlyts-15 (mol%)	Surface Area
8.4	292360.73
16.8	223838.28
33.6	132786.75

Table 17. Surface Area of the mannose signal of the SEC after different reaction times. Reaction Conditions: 50 °C, 4.2 mol% catalyst, 8.4 eq. propargyl alcohol.

Time (h)	Surface Area
1	320365.1
2	266823.82
4	160090.02
7	67944.95

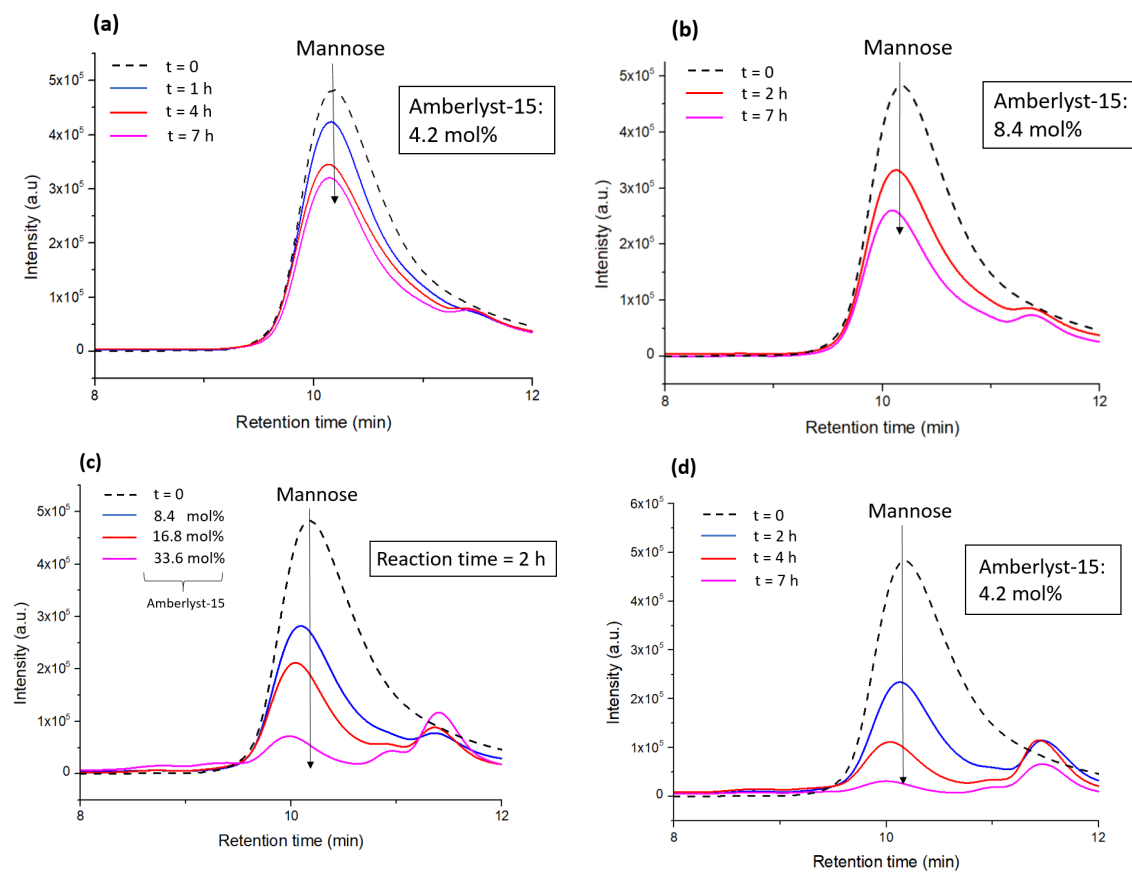


Figure 48. SEC traces (H_2O) of the non-reacted residue after filtration; reaction condition: **a)** 40 °C, 4.2 mol% catalyst, 8.4 eq. propargyl alcohol, **b)** 40 °C, 8.4 mol% catalyst, 8.4 eq. propargyl alcohol, **c)** 40 °C, 8.4 - 33.6 mol% catalyst, 8.4 eq. propargyl alcohol, 2 h, **d)** 50 °C, 4.2 mol% catalyst, 8.4 eq. propargyl alcohol.

Kinetic step 1: NMR.

❖ A: 80 °C, PGA/mannose: 5

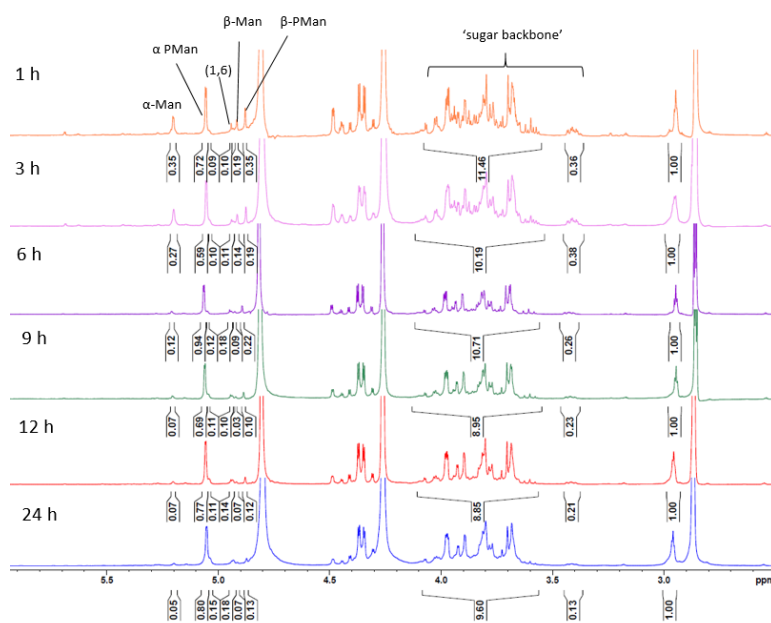
Figure 49. $^1\text{H-NMR}$ (400 MHz, D_2O) spectra of step 1 at 80 °C and a PGA/mannose ratio of 5.

Table 18. Evaluation of the kinetic study of step 1.

Time (h)	Mannose (%)	PMan (%)	Oligomers (%)	\overline{DP}_n
1	41	53	6	1.2
3	35	56	8	1.2
6	22	66	12	1.4
9	17	73	10	1.3
12	16	72	12	1.3
24	15	71	15	1.4
48	16	71	13	1.3

❖ B: 100 °C, PGA/mannose: 5

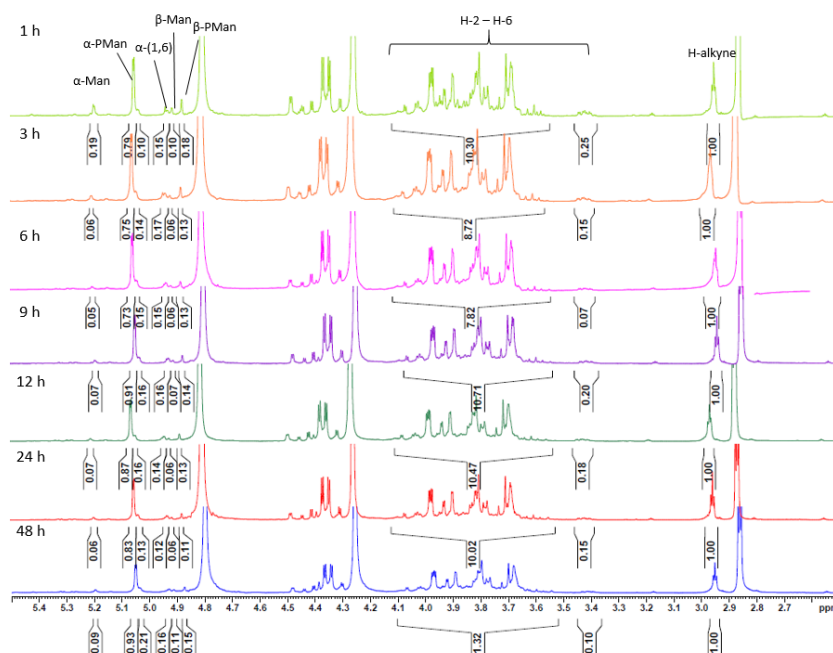


Figure 50. $^1\text{H-NMR}$ (400 MHz, D_2O) spectra of step 1 at 100 °C and a PGA/mannose ratio of 5.

Table 19. Evaluation of the kinetic study of step 1.

Time (h)	Mannose (%)	PMan (%)	Oligomers (%)	\overline{DP}_n
1	26	63	11	1.3
3	16	69	15	1.2
6	16	71	13	1.1
9	15	73	12	1.5
12	16	73	11	1.5
24	14	75	10	1.5
48	17	72	11	1.6

❖ FG-C: 60 °C, PGA/mannose: 5

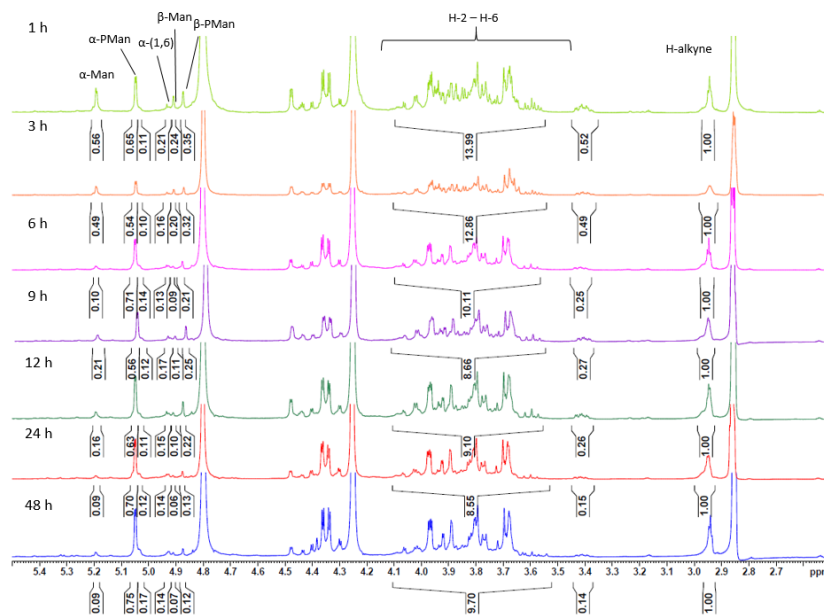
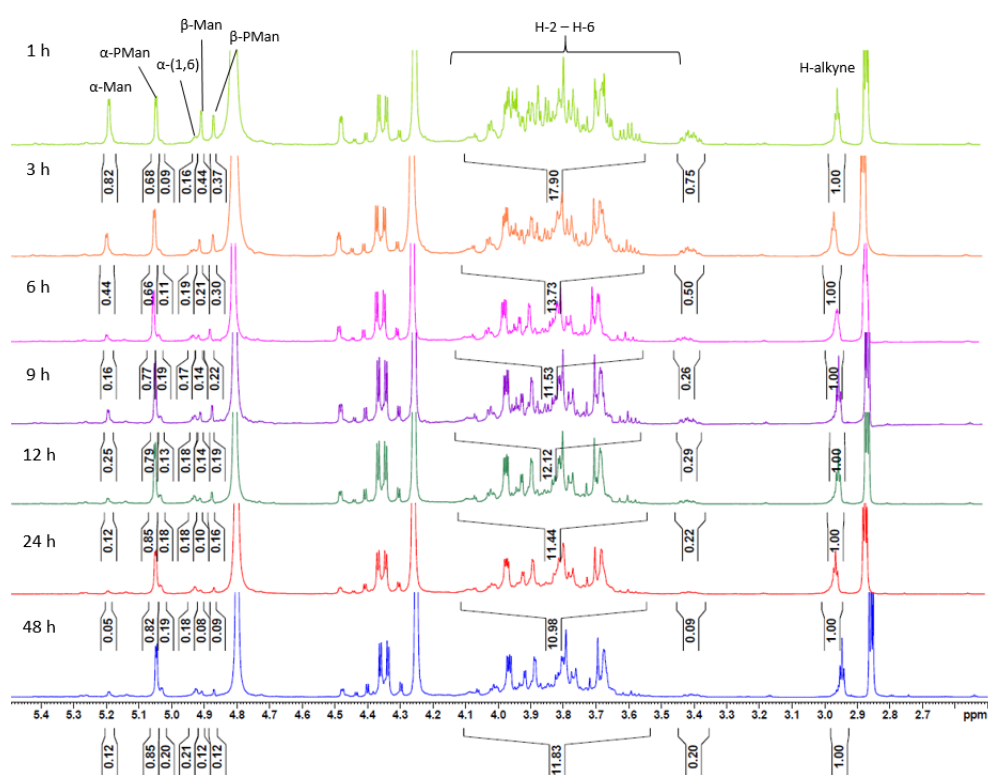
Figure 51. $^1\text{H-NMR}$ (400 MHz, D_2O) spectra of step 1 at 60 °C and a PGA/mannose ratio of 5.

Table 20. Evaluation of the kinetic study of step 1.

Time (h)	Mannose (%)	PMan (%)	Oligomers (%)	\overline{DP}_n
1	45	44	10	1.3
3	47	43	9	1.2
6	25	65	10	1.3
9	35	52	13	1.0
12	30	58	12	1.1
24	20	68	13	1.2
48	18	70	12	1.3

❖ FG-D: 80 °C, PGA/mannose: 3

Figure 52. $^1\text{H-NMR}$ (400 MHz, D_2O) spectra of step 1 at 80 °C and a PGA/mannose ratio of 3.Table 21. Evaluation of the kinetic study of **FG-D** (step 1).

Time (h)	Mannose (%)	PMan (%)	Oligomers (%)	\overline{DP}_n
1	48	45	6	1.6
3	41	48	11	1.4
6	26	62	12	1.5
9	28	60	12	1.5
12	20	67	13	1.6
24	11	74	15	1.6
48	17	68	15	1.7

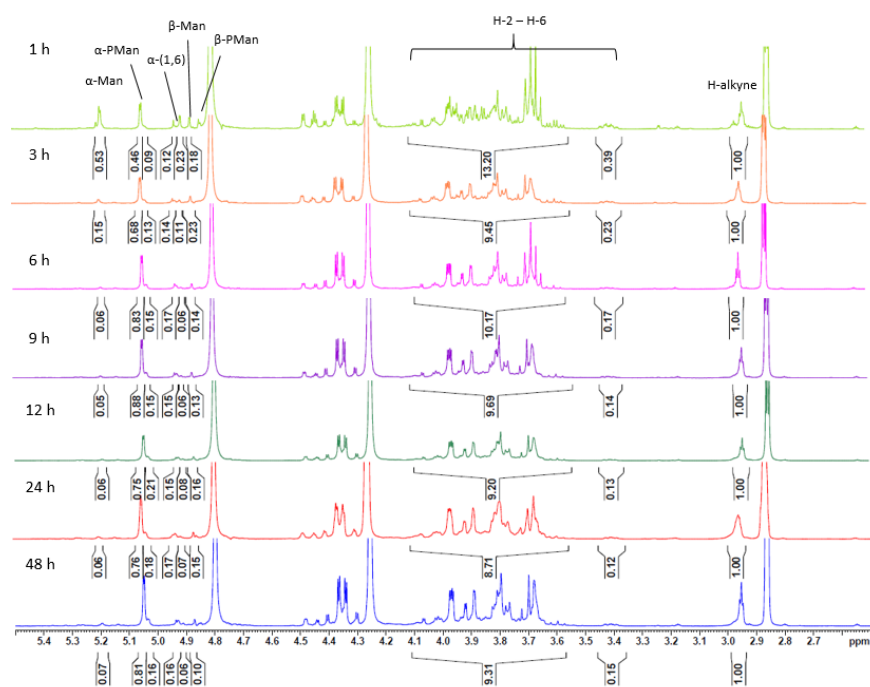
❖ FG-E: 80 °C, PGA/mannose: 5 + MgSO₄

Figure 53. ¹H-NMR (400 MHz, D₂O) spectra of step 1 at 80 °C and a PGA/mannose ratio of 5 + MgSO₄.

Table 22. Evaluation of the kinetic study of step 1.

Time (h)	Mannose (%)	PMan (%)	Oligomers (%)	\overline{DP}_n
1	47	45	8	1.2
3	29	60	11	1.1
6	16	71	13	1.4
9	14	74	12	1.4
12	18	69	13	1.3
24	17	69	14	1.2
48	14	73	13	1.4

Kinetic step 1: GC-FID

Relative surface area of the GC spectra

❖ A: 80 °C, PGA/mannose: 5

Table 23. Surface area after step 1 determined by GC.

Time (h)	A (levomannosane)	A (α -Man)	A (α -PMan)	A (β -Man)	A (β -PMan)	A (Sorbitol)
1 h	0.4211	5.7177	4.4616	1.9216	1.5915	2.7482
3 h	0.6695	4.4259	10.1924	1.4145	2.9026	2.5511
6 h	0.3724	1.557	10.3207	0.5204	1.9652	2.5169
8 h	0.4147	1.6423	15.572	0.496	2.5522	2.4605
10 h	0.2815	0.9589	12.784	0.2435	1.8031	2.5167
12 h	0.2627	0.9319	13.1559	0.2431	1.7586	2.5835
24 h	0.1251	0.3984	8.2464	0.1476	0.7831	2.802
48 h	0.1789	0.594	11.7303	0.177	1.1895	2.7911

❖ B: 100 °C, PGA/mannose: 5

Table 24. Surface area after step 1 determined by GC.

Time (h)	A (levomannosane)	A (α -Man)	A (α -PMan)	A (β -Man)	A (β -PMan)	A (Sorbitol)
1 h	0.1426	2.3706	1.4839	0.8587	0.6978	2.6441
3 h	0.4258	0.9619	13.8146	0.2916	1.7677	2.3525
6 h	0.2394	0.5544	9.0146	0.1898	0.9848	2.396
8 h	0.2418	0.5667	9.2034	0.1891	0.9953	2.7319
10 h	0.2658	0.6142	10.4224	0.2069	1.1277	2.6338
12 h	0.1876	0.4221	7.4401	0.1515	0.7792	2.6485
24 h	0.1696	0.3869	6.6164	0.1467	0.6747	2.7415
48 h	0.3288	0.7603	12.5322	0.2564	1.3468	2.6478

❖ C: 60 °C, PGA/mannose: 5

Table 25. Surface area after step 1 determined by GC.

Time (h)	A (levomannosane)	A (α -Man)	A (α -PMan)	A (β -Man)	A (β -PMan)	A (Sorbitol)
1 h	0.2909	0.8577	5.5136	0.3062	1.044	2.7325
3 h	0.2568	4.4008	2.5677	1.5184	1.1782	2.7165
6 h	0.358	6.8699	3.7881	2.4788	1.6769	2.4599
8 h	0.284	3.9666	3.1813	1.402	1.3547	2.4745
10 h	0.4305	5.048	5.2411	1.8144	2.1561	2.6273
12 h	0.4224	4.554	5.0433	1.646	2.0462	2.6603
24 h	0.3048	2.1506	7.4799	0.7392	2.157	2.6481
48 h	0.3347	2.716	6.639	0.9801	2.1914	2.7596

❖ D: 80 °C, PGA/mannose: 3

Table 26. Surface area after step 1 determined by GC.

Time (h)	A (levomannosane)	A (α -Man)	A (α -PMan)	A (β -Man)	A (β -PMan)	A (Sorbitol)
1 h	0.2901	10.0307	2.9407	3.6086	0.9645	2.4134
3 h	0.6657	7.5162	7.6553	2.4681	2.384	2.5179
6 h	0.4781	3.7481	8.6018	1.3184	2.0583	2.5149
8 h	0.6358	4.0574	13.8835	1.3102	2.9473	2.3136
10 h	0.6932	3.9967	19.7217	1.235	3.6642	2.4588
12 h	0.3683	1.9577	11.1475	0.6408	1.924	2.5112
24 h	0.2161	0.7422	12.3968	0.2131	1.2405	2.5023
48 h	0.2426	1.1392	12.901	0.3708	1.3915	2.6235

❖ E: 80 °C, PGA/mannose: 5, MgSO₄

Table 27. Surface area after step 1 determined by GC.

Time (h)	A (levomannosane)	A (α -Man)	A (α -PMan)	A (β -Man)	A (β -PMan)	A (Sorbitol)
1 h	0.2602	6.0321	3.1744	2.0381	1.0135	2.804
3 h	0.3431	1.8781	7.022	0.6917	1.6254	2.1725
6 h	n.d.	n.d.	n.d.	n.d.	n.d.	n.d.
8 h	0.1828	0.6594	11.1947	0.1853	1.1828	2.0652
10 h	0.3015	1.0762	18.9324	0.2927	1.834	2.2885
12 h	n.d.	n.d.	n.d.	n.d.	n.d.	n.d.
24 h	0.1786	0.786	10.4586	0.2727	0.9708	2.6426
48 h	0.2624	0.9075	16.085	0.2858	1.5397	3.1897

Kinetic step 2: NMR.

❖ Polymerization P1: magnetically stirring

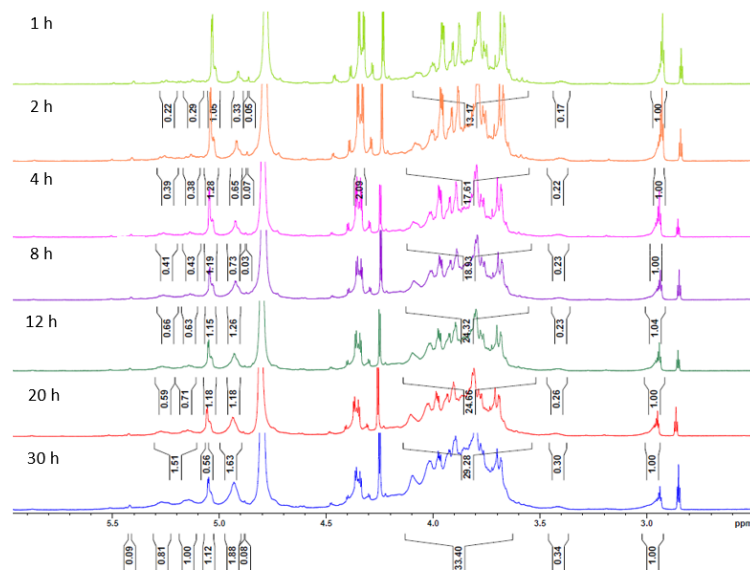
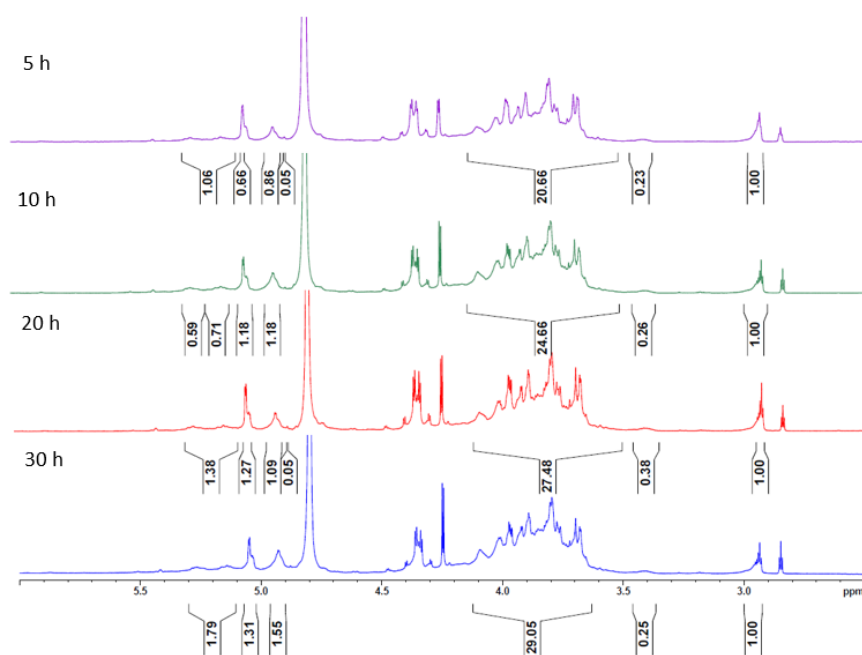
Figure 54. Plot of overlaid ^1H -NMR (400 MHz, D_2O) spectra of the polymerization P1.

Table 28. Surface area of the PMan peak from the SEC spectra and the corresponding calculated conversion rate of PMan of polymerization P1.

Time (h)	Surface Area	Conversion of PMan (%)
t = 0	1.50E-04	--
1	1.19E-04	20
2	8.41E-05	44
4	6.53E-05	56
8	4.22E-05	72
10	3.87E-05	76
20	2.66E-05	82
30	1.89E-05	87

❖ Polymerization **P2**: mechanical stirringFigure 55. Plot of overlaid ¹H-NMR (400 MHz, D₂O) spectra of the polymerization **P2**.Table 29. Surface area of the PMan peak from the SEC spectra and the corresponding calculated conversion rate of PMan of polymerization **P2**.

Time (h)	Surface Area	Conversion of PMan (%)
t = 0	1.50E-04	--
5	5.41E-05	64
10	5.45E-05	65
20	3.39E-05	77
30	4.99E-05	67

❖ Polymerization **P3**: optimized conditions.

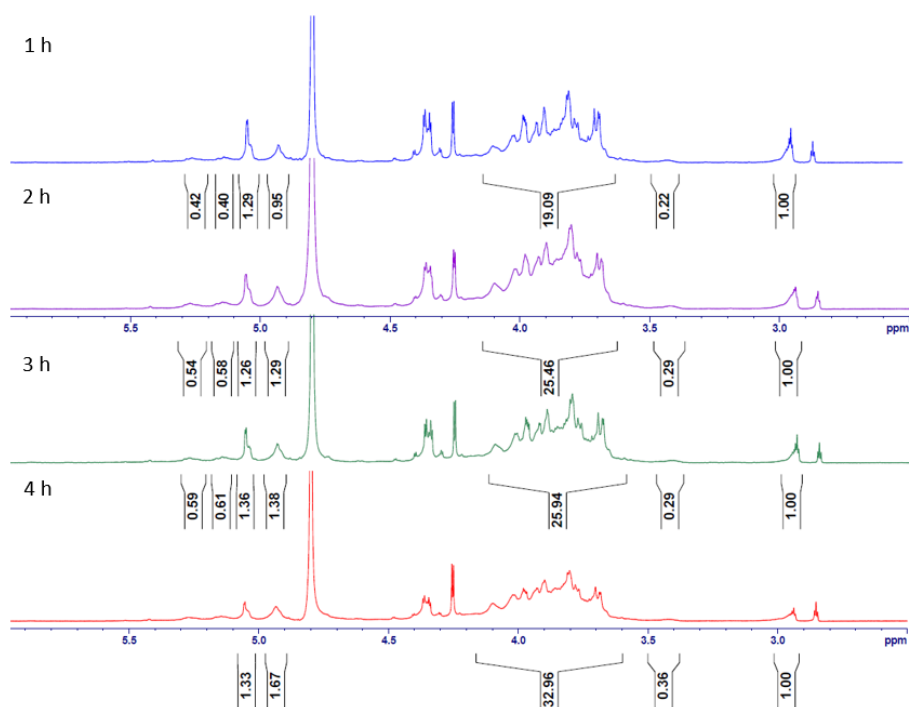


Figure 56. Plot of overlaid ¹H-NMR (400 MHz, D₂O) spectra of the polymerization **P3**.

Table 30. Surface area of the PMan peak from the SEC spectra and the corresponding calculated conversion rate of PMan of polymerization **P3**.

Time (h)	Surface Area	Conversion of PMan (%)
t = 0	1.39E-04	--
1	1.15E-04	17.36
3	6.12E-05	56.23
2	1.67E-05	88
4	1.25E-05	91

❖ Polymerization **P5**: reference polymerization of isolated PMan.

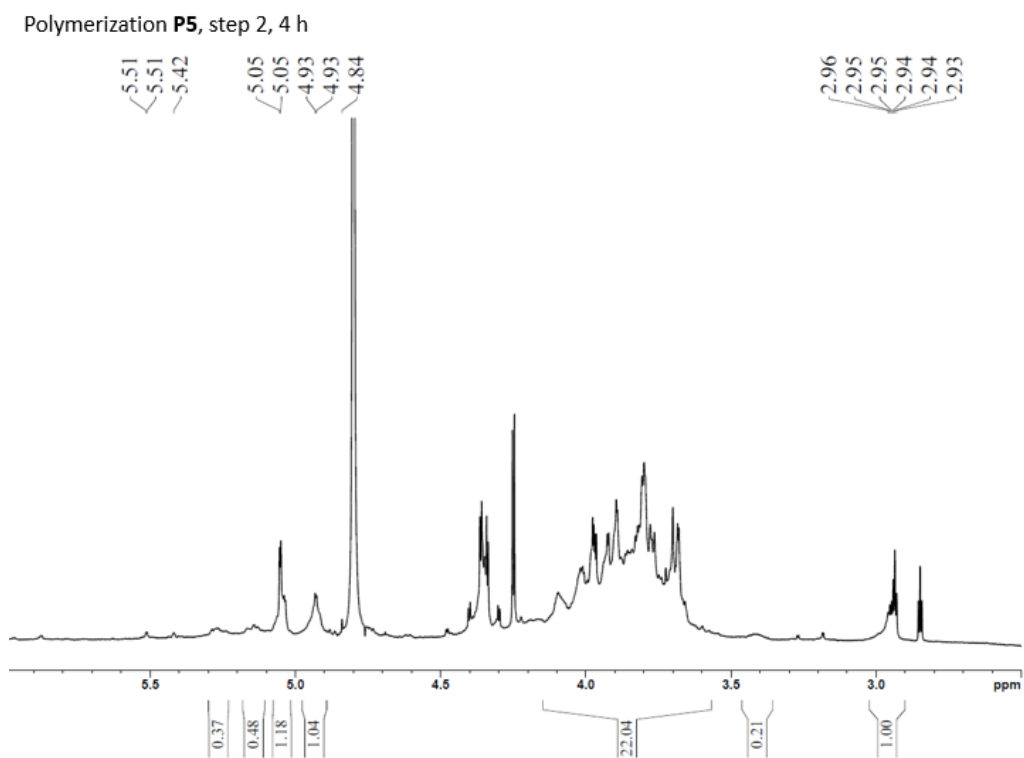


Figure 57. $^1\text{H-NMR}$ (400 MHz, D_2O) spectrum of polymerization of PMan (**P5**) after step 2 = 100 °C, vacuum, 4 h.

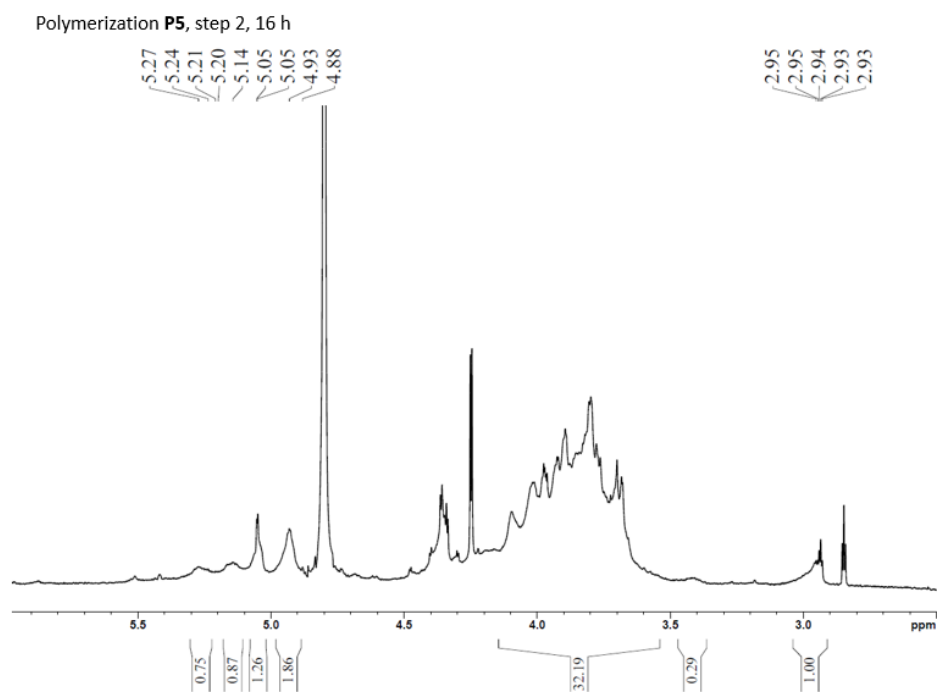


Figure 58. $^1\text{H-NMR}$ (400 MHz, D_2O) spectrum of polymerization of PMan (**P5**) after **step 2** = 100 °C, vacuum, 16 h.

Table 31. Surface area of the PMan peak from the SEC spectra and the corresponding calculated conversion rate of PMan of polymerization **P5**.

Time (h)	Surface Area	Conversion of PMan (%)
t = 0	9.30E-5	--
4	2.28E-5	75

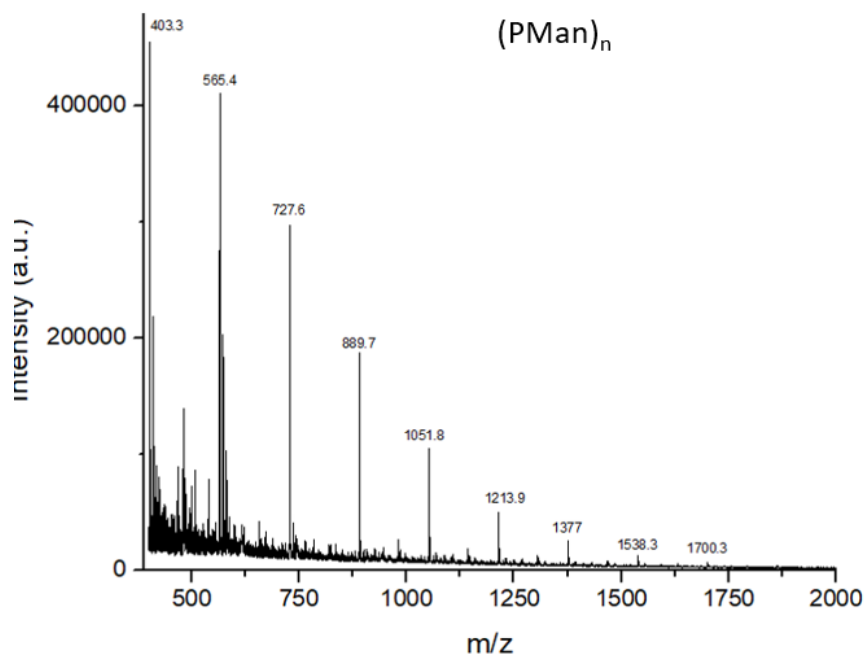


Figure 59. MALDI-tof spectrum of (PMan)_n obtained of the polymerization reaction of PMan (**P5**).

Optimization of the oligomerization reaction.
SEC spectra.

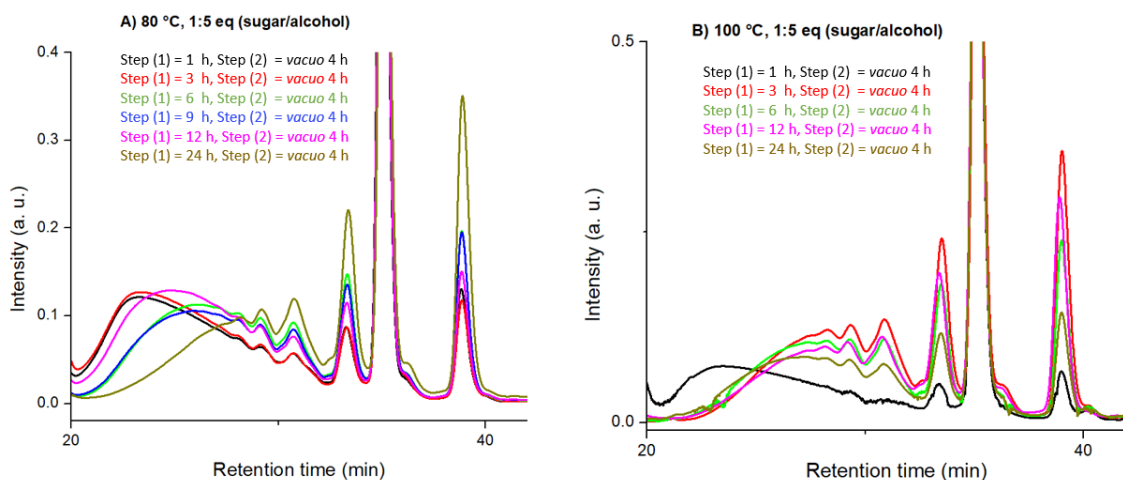


Figure 60. Plot of overlaid SEC (measured against dextran-standard in H₂O at 25 °C) traces after step 2 starting from different conditions of step 1. Left: step 1 = 80 °C, PGA/mannose: 5; right: step 1 = 100 °C, PGA/mannose: 5.

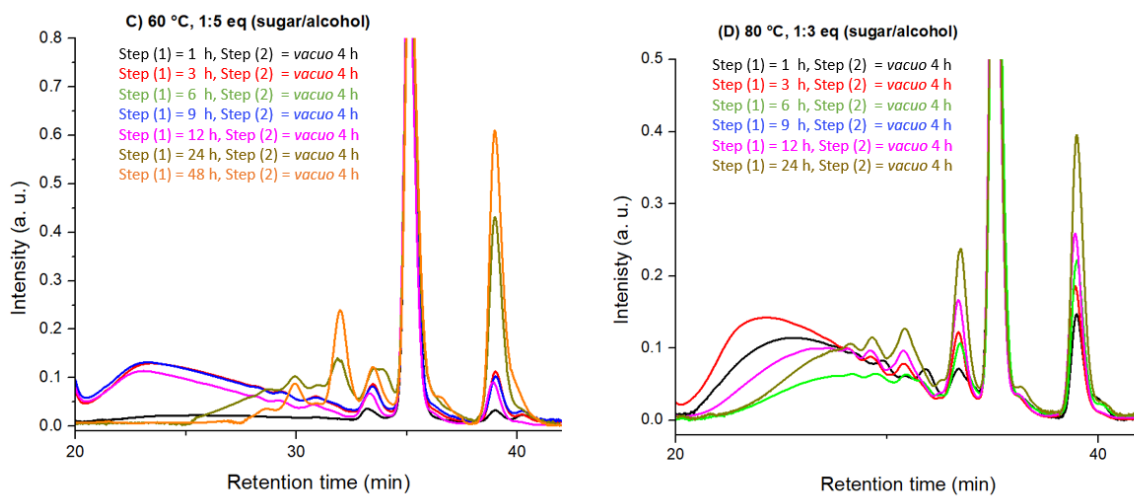


Figure 61. Plot of overlaid SEC (measured against dextran-standard in H₂O at 25 °C) traces after step 2 starting from different conditions of step 1. Left: step 1 = 60 °C, PGA/mannose: 5; right: step 1 = 100 °C, PGA/mannose: 3.

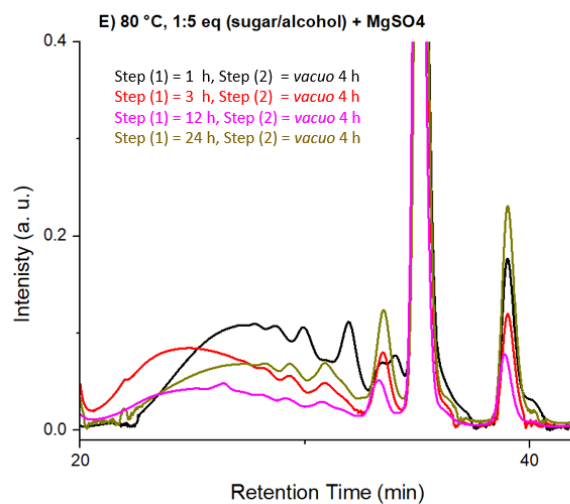


Figure 62. Plot of overlaid SEC (measured against dextran-standard in H₂O at 25 °C) traces after step 2 starting from different conditions of step 1. step 1 = 80 °C, PGA/mannose: 5, MgSO₄.

NMR spectra

❖ A: 80 °C, PGA/mannose: 5

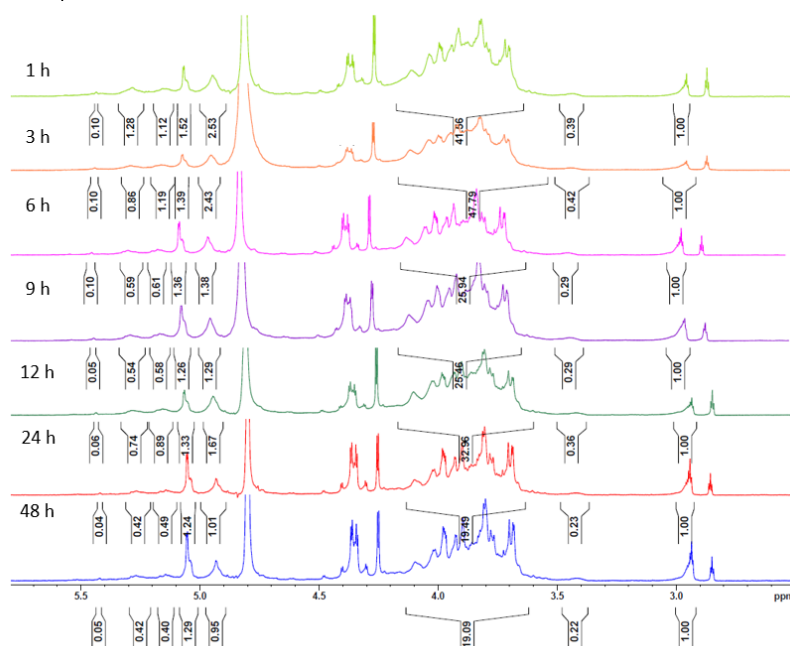


Figure 63. Plot of overlaid ¹H-NMR (400 MHz, D₂O) spectra after step 2 starting from different times of step 1 (= 80 °C, PGA/mannose: 5).

Table 32. Evaluation of the oligosaccharides obtained after step 2.

Time step 1	\overline{M}_n (SEC)	\overline{D} (M_w/M_n)	\overline{M}_n (NMR)	\overline{DP}_n (NMR)
1 h	911.8	2.03	1191	7
3 h	918.2	1.97	1353	8
6 h	671.6	1.82	705	4
9 h	690.6	1.86	705	4
12 h	801.3	1.9	867	5
24 h	503.8	1.62	543	3
48 h	521.4	1.7	543	3

❖ B: 100 °C, PGA/mannose: 5

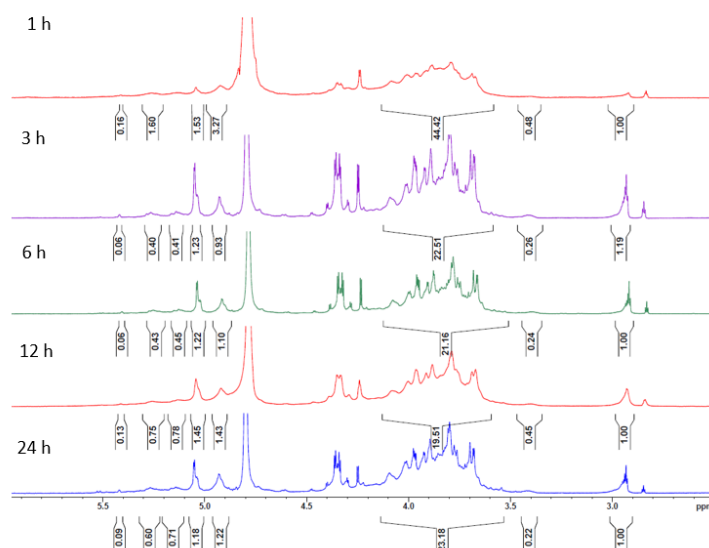


Figure 64. Plot of overlaid ^1H -NMR (400 MHz, D_2O) spectra after step 2 starting from different times of step 1 (= 100 °C, PGA/mannose: 5).

Table 33. Evaluation of the oligosaccharides obtained after step 2.

Time step 1	\overline{M}_n (SEC)	\overline{D} (M_w/M_n)	\overline{M}_n (NMR)	\overline{DP}_n (NMR)
1 h	997.6	1.84	1191	7
3 h	509.7	1.55	705	4
6 h	551.8	1.61	705	4
12 h	508.5	1.55	543	3
24 h	603.4	1.65	705	4

❖ C: 60 °C, PGA/mannose: 5

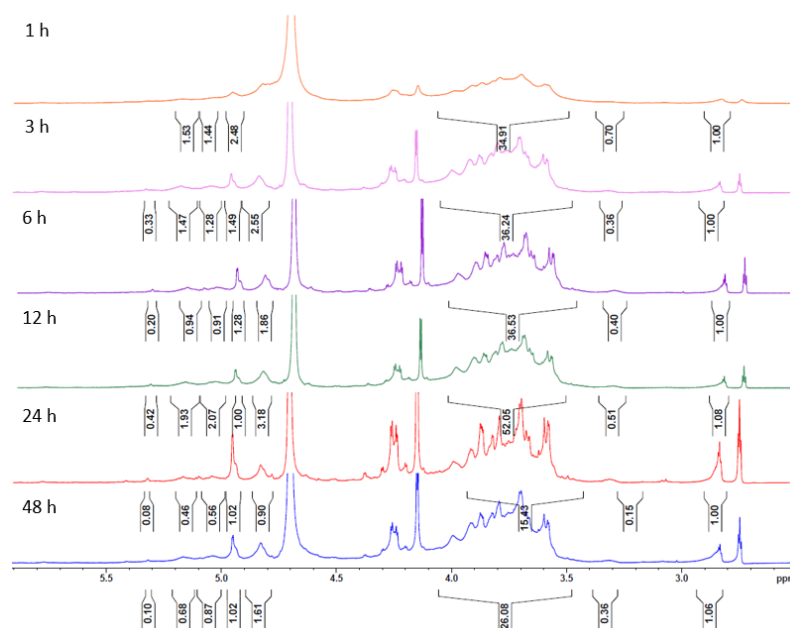


Figure 65. Plot of overlaid ¹H-NMR (400 MHz, D₂O) spectra after step 2 starting from different times of step 1 (= 60 °C, PGA/mannose: 5).

Table 34. Evaluation of the oligosaccharides obtained after step 2.

Time step 1	\overline{M}_n (SEC)	\overline{D} (M_w/M_n)	\overline{M}_n (NMR)	\overline{DP}_n (NMR)
1 h	833.5	1.83	1029	6
3 h	937.6	2.02	1029	6
6 h	n.d.	n.d.	1029	6
12 h	987.6	2.04	1515	9
24 h	395.8	1.27	543	3
48 h	337.7	1.14	705	4

❖ FG-D: 80 °C, PGA/mannose: 3

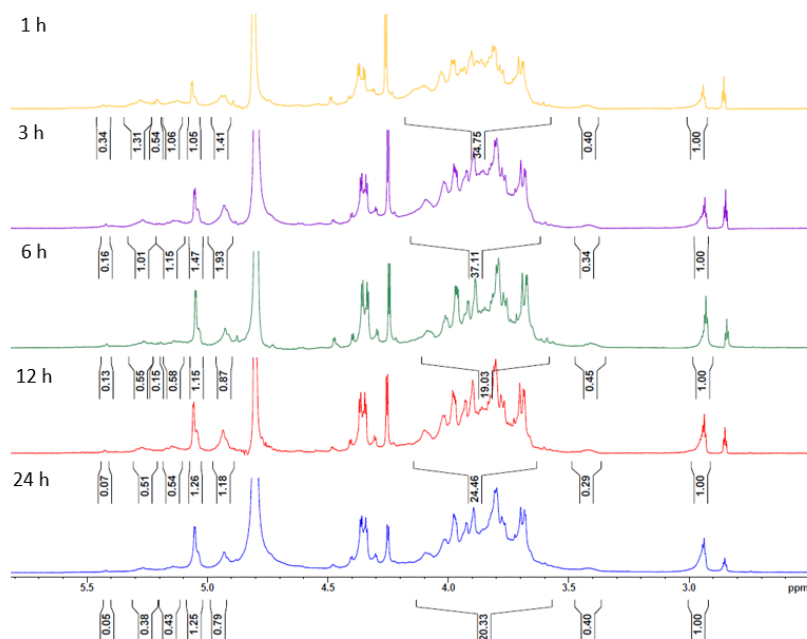


Figure 66. Plot of overlaid ¹H-NMR (400 MHz, D₂O) spectra after step 2 starting from different times of step 1 (= 80 °C, PGA/mannose: 3).

Table 35. Evaluation of the oligosaccharides obtained after step 2.

Time step 1	\overline{M}_n (SEC)	\overline{D} (M_w/M_n)	\overline{M}_n (NMR)	\overline{DP}_n (NMR)
1 h	747.7	1.84	867	5
3 h	839.5	1.93	1029	6
6 h	517.8	1.51	543	3
12 h	614.6	1.77	705	4
24 h	490.4	1.56	543	3

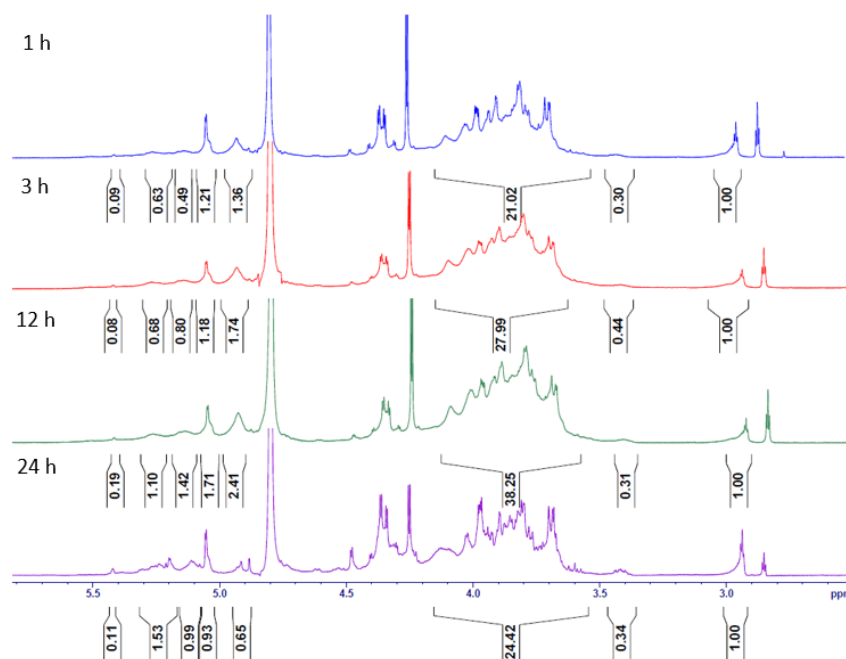
❖ FG-E: 80 °C, PGA/mannose: 5 + MgSO₄

Figure 67. Plot of overlaid ¹H-NMR (400 MHz, D₂O) spectra after step 2 starting from different times of step 1 (= 80 °C, PGA/mannose: 5, MgSO₄).

Table 36. Evaluation of the oligosaccharides obtained after step 2.

Time Step 1	\overline{M}_n (SEC)	\overline{D} (M_w/M_n)	\overline{M}_n (NMR)	\overline{DP}_n (NMR)
1 h	579.00	1.54	705	4
3 h	836.8	1.99	1029	6
12 h	727.6	1.78	867	5
24 h	585.3	1.69	705	4

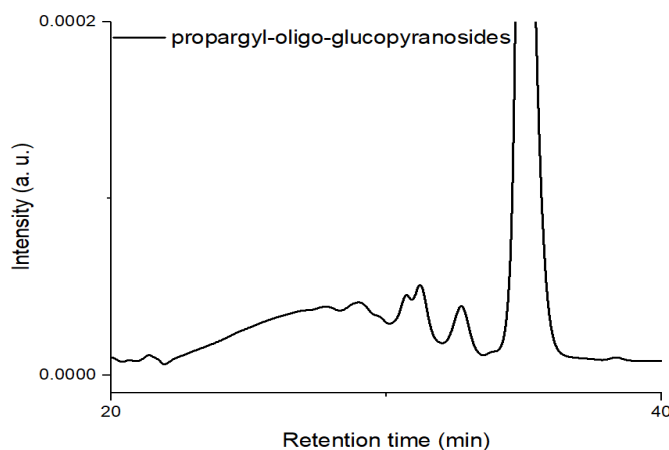


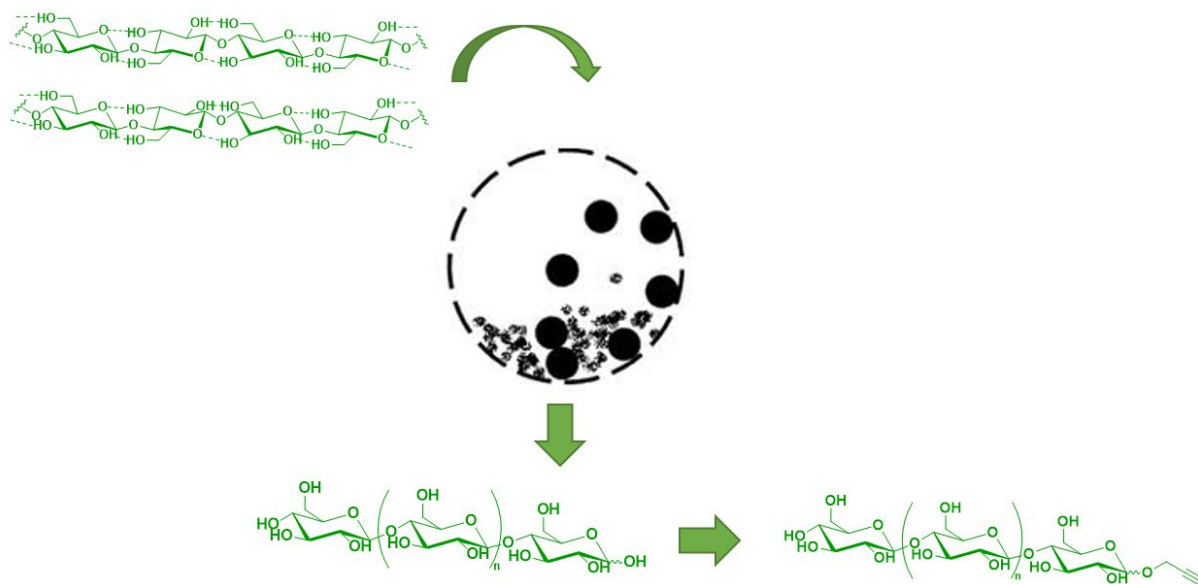
Figure 68. SEC (measured against dextran-standard in H₂O at 25 °C) of propargyl-(oligo)-glucoside.

8 Bibliography

- [1] aD. G. Hayes, D. K. Solaiman, R. D. Ashby, *Biobased Surfactants: Synthesis, Properties, and Applications*, Elsevier, **2019**; bC. Stubenrauch, *Current Opinion in Colloid & Interface Science* **2001**, *6*, 160-170; cM. Henkel, R. Hausmann, in *Biobased Surfactants (Second Edition)* (Eds.: D. G. Hayes, D. K. Y. Solaiman, R. D. Ashby), AOCs Press, **2019**.
- [2] aC. Schatz, S. Lecommandoux, *Macromol Rapid Commun* **2010**, *31*, 1664-1684; bS. de Medeiros Modolon, I. Otsuka, S. b. Fort, E. Minatti, R. Borsali, S. Halila, *Biomacromolecules* **2012**, *13*, 1129-1135; cI. Otsuka, K. Fuchise, S. Halila, S. Fort, K. Aissou, I. Pignot-Paintrand, Y. Chen, A. Narumi, T. Kakuchi, R. Borsali, *Langmuir* **2010**, *26*, 2325-2332; dJ. Scheibel, Samuel Rosen Memorial Award Lecture, 98th AOCs Annual Meeting and Expo, Quebec, **2007**; eC. Schatz, S. Louguet, J. F. Le Meins, S. Lecommandoux, *Angewandte Chemie International Edition* **2009**, *48*, 2572-2575.
- [3] aE. Fischer, *Berichte der deutschen chemischen Gesellschaft* **1893**, *26*, 2400-2412; bK. Hill, W. Von Rybinski, G. Stoll, *Alkyl polyglycosides*, Wiley Online Library, **1997**.
- [4] aF. Jérôme, S. Marinkovic, B. Estrine, *ChemSusChem* **2018**, *11*, 1395-1409; bW. von Rybinski, K. Hill, *Angewandte Chemie International Edition* **1998**, *37*, 1328-1345.
- [5] B. Roy, B. Mukhopadhyay, *Tetrahedron Letters* **2007**, *48*, 3783-3787.
- [6] R. Das, B. Mukhopadhyay, *ChemistryOpen* **2016**, *5*, 401-433.
- [7] aN. Boz, N. Degirmenbasi, D. M. Kalyon, *Applied Catalysis B: Environmental* **2015**, *165*, 723-730; bS. Jetti, N. Babu, G. Paliwal, A. Bhatwra, T. Kadre, S. Jain, *Der Pharma Chem* **2012**, *4*, 417-427; cR. Pal, T. Sarkar, S. Khasnobis, *ARKIVOC: Online Journal of Organic Chemistry* **2012**; dA. Palmieri, S. Gabrielli, R. Ballini, *Chemical communications* **2010**, *46*, 6165-6167; eQ. Tian, S. Zhang, Q. Yu, M.-B. He, J.-S. Yang, *Tetrahedron* **2007**, *63*, 2142-2147.
- [8] D. Geetha, R. Tyagi, *Tenside surfactants detergents* **2012**, *49*, 417-427.
- [9] aA. Furlani, M. V. Russo, A. Longo, M. Yang, *Polymer* **1997**, *38*, 183-189; bK. Yoshimura, T. Kitade, K. Kitamura, K. Hozumi, *Journal of applied polymer science* **1989**, *38*, 1011-1024; cA. Abdel-Fattah, Y. S. Soliman, M. M. Ghobashy, *Journal of Polymer Research* **2018**, *25*.
- [10] E. Fischer, *Ber. Dtsch. Chem. Ges.* **1893**, *26*, 2400-2412.
- [11] S. Agarwal, D. van Es, H. J. Heeres, *Journal of Analytical and Applied Pyrolysis* **2017**, *123*, 134-143.
- [12] aC. B. Rasrendra, M. Windt, Y. Wang, S. Adisasmito, I. G. B. N. Makertihartha, E. R. H. van Eck, D. Meier, H. J. Heeres, *Journal of Analytical and Applied Pyrolysis* **2013**, *104*, 299-307; bJ. Horvat, B. Klaić, B. Metelko, V. Šunjić, *Tetrahedron Letters* **1985**, *26*, 2111-2114; cI. van Zandvoort, Y. Wang, C. B. Rasrendra, E. R. van Eck, P. C. Bruijninx, H. J. Heeres, B. M. Weckhuysen, *ChemSusChem* **2013**, *6*, 1745-1758.
- [13] P. K. Agrawal, *Phytochemistry* **1992**, *31*, 3307-3330.
- [14] aW. A. Bubb, *Concepts in Magnetic Resonance* **2003**, *19A*, 1-19; bJ. Ø. Duus, C. H. Gotfredsen, K. Bock, *Chemical Reviews* **2000**, *100*, 4589-4614.
- [15] B. Estrine, S. Marinkovic, F. Jérôme, **2019**, 365-385.
- [16] K. Böge, L. F. Tietze, *Lipid/Fett* **1998**, *100*, 36-41.

Chapter II B:

Depolymerization and functionalization of cellulose by ball-milling



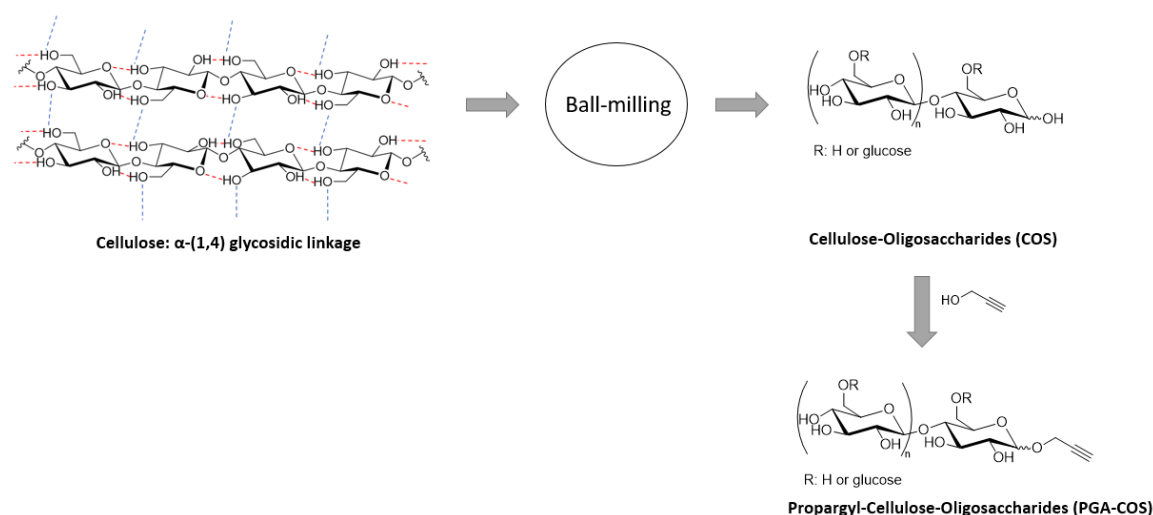
Contents

1	Introduction	156
2	Depolymerization and functionalization of cellulose	157
2.1	Mechanocatalytic depolymerization	157
2.2	End-functionalization with propargyl alcohol	161
3	Conclusion.....	166
4	Appendix.....	168
	Bibliography	172

1 Introduction

Frequently, oligosaccharides are applied to synthesize amphiphilic block copolymers. They are used to prepare self-assembled structures and are attractive for biomedical and pharmaceutical applications due to their non-toxicity and biocompatibility.^[1] These biomolecules are mainly obtained *via* the functionalization of the oligosaccharides at their terminal end.^[2] The subsequent coupling to a hydrophobic segment afford then the amphiphilic structure. The corresponding synthetic strategies exploit the different chemical behaviour of the hemiacetal group at the reducing-end of the sugar ring. The most common methods proceed within several steps such as the reductive amination or the chemo selective incorporation of a propargylamine group (for more details see Chapter I, subsection 4.4). However, these methods afford several reaction and purification steps, limiting an industrial scale-up.

Here, we present another strategy to prepare end-functional oligosaccharides starting from microcrystalline cellulose (MCC). The latter was given to a ball-milling system combined with an acid catalyst (mechanocatalytical depolymerization). The so-obtained cellulose-oligosaccharides (COS) were further glycosylated with propargyl alcohol to bring an alkyne function to their terminal end. We focused on the selective glycosylation of the reducing end of the COS, trying to prevent a cleavage of their intramolecular glycosidic linkages. Compared to the previous prepared propargyl-(oligo)-mannopyranoside ((PMan)_n), this method presents a strategy to prepare alkyne-functional oligosaccharides with a different architecture. While (PMan)_n are mainly linked *via* the α -(1,6)-glycosidic linkage, COS consists of a linear chain of glucose units linked *via* the β -(1,4) position. In this chapter, we discuss the ball-milling process, the in-depth characterization of the obtained COS and the subsequent functionalization with PGA.



Scheme 1. Procedure of the preparation of alkyne functionalized cellulose-oligosaccharides (PGA-COS) starting from MCC *via* ball-milling.

2 Depolymerization and functionalization of cellulose

Water soluble cellulose-oligosaccharides (COS) can be obtained by mechanocatalytic depolymerization. This method utilizes the mechanical forces to alter the cellulose structure and an acid catalyst to protonate and cleave the glycosidic linkages. The associated conformational change of the cellulose chain makes the glycosidic bond more reactive, facilitating the depolymerization. We describe here the procedure of the ball-milling and the detailed analysis of the obtained COS. In a subsequent step, the oligosaccharides were glycosylated with PGA.

2.1 Mechanocatalytic depolymerization

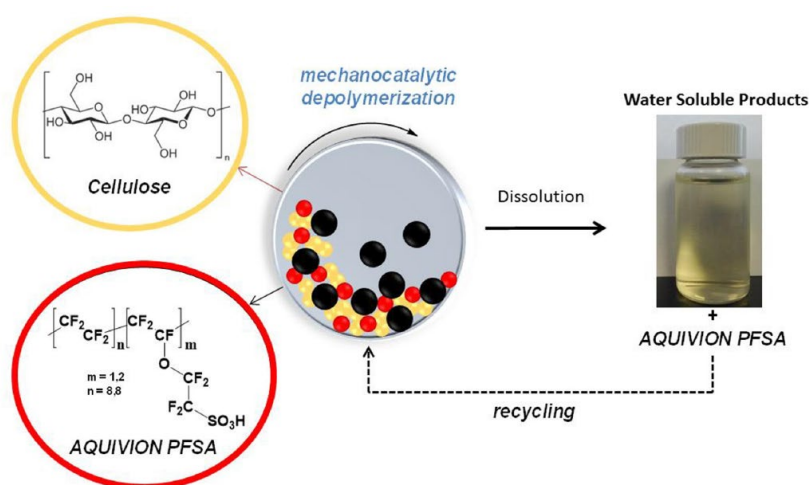


Figure 1. Mechanocatalytic depolymerization of cellulose by Karam, A. *et al.*^[3]

The mechanocatalytic depolymerization of cellulose (Figure 1) was carried out following the protocol of A. Karam *et al.* developed in 2018.^[3] Therefore, we mixed cellulose with Aquivion® PW98, an acid catalyst based on a copolymer of tetrafluoroethylene and sulfonyl fluoride vinyl ether ($CF_2=CF-O-(CF_2)_2-SO_2F$) produced by Solvay Specialty Polymers. This super acid resin showed a good performance during the ball-milling process, yielding water soluble sugars in 90 - 97 %. By applying the same conditions as A. Karam (see more details in the experimental section), we recovered water soluble sugars in 90 % yield after 24 h at a stirring rate of 400 rpm. The as-obtained COS are listed in Table 1.

Table 1. Cellulose-Oligosaccharides **15-18** obtained by ball-milling.

Compound	Milling-time (h)	\overline{M}_n (g/mol) (SEC)	$\overline{D} (\overline{M}_w/\overline{M}_n)$ (SEC)	\overline{DP}_n (NMR)	\overline{M}_n (g/mol)(NMR)
15	32	630	2.28	3.8	634
16	24	575	2.01	4.3	719
17	24	544	1.96	4.0	666
18	24	611	2.12	5	828

The previous analysis of the COS by A. Karam showed that the water-soluble fraction accounted to 13 % monosaccharides, 21 % disaccharides and 65 % to oligosaccharides. Glucose made the main part of the monosaccharides with minor proportions of 1,6-anhydro-D-glucopyranoside (levoglucosan, 3 %) and 1,5-anhydro-D-glucopyranose (1 %). They observed no oxidation or degradation and could determine the branching pattern by sequential oximation-acetylation reaction. All types of α/β -glycosidic linkages were found from (1 \rightarrow 1),- (1 \rightarrow 2),- (1 \rightarrow 3),- (1 \rightarrow 4),- and (1 \rightarrow 6). The initial β -(1,4) linkage of the cellulose units remained still the dominant bond with *ca.* 80 %, followed by the linkage between (1 \rightarrow 6) with 13 %. The same chemical composition was also found by A. Shrotri *et al.*^[4], which supported that during the mechanocatalytical process, self-glycosylation (reversion) reactions proceed at the same time, leading to these branching pattern. The *in situ* obtained COS can thereby react either with each other (branching) or the reaction among free glucose molecules can lead to cross-glycosylations. The final branching pattern is given in Table 2. We assumed that by following the protocol of A. Karam *et al.*, our COS denoted approximately the same structure.

Table 2. Branching pattern of the cellulose-oligosaccharides obtained by ball-milling by A. Karam *et al.*^[3]

Glycosidic bond (%)										Branching pattern (%)
1 \rightarrow 4		1 \rightarrow 2		1 \rightarrow 3		1 \rightarrow 6		1 \rightarrow 1'		1 \rightarrow 4 \rightarrow 6
79,5		3		3		13		1.5		6
α	β	α	β	α	β	α	β	α,α'	α,β'	-
6.5 ^a	73 ^b	1.7 ^c	1.3 ^d	2.3 ^e	0.7 ^f	6.5 ^g	6.6 ^h	1 ⁱ	0,5 ^j	-

^a maltose; ^b cellobiose; ^c kojibiose; ^d laminarabiose; ^e nigerose; ^f soforose; ^g isomaltose; ^h gentiobiose; ⁱ trehalose; ^j neotrehalose

Next, we further analysed the obtained COS (compound **15-18**) by NMR- and MALDI-TOF mass spectroscopy.

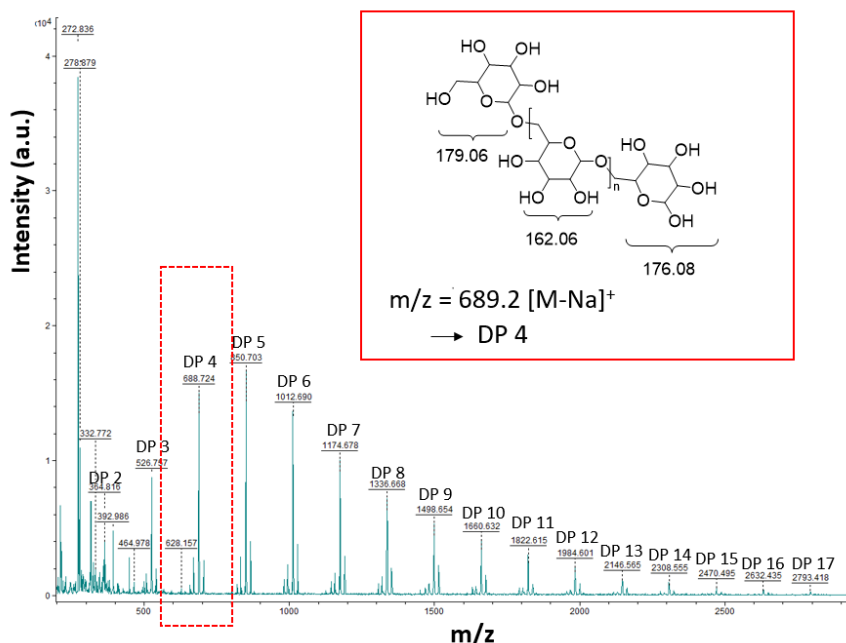


Figure 2. Typical MALDI-TOF spectrum of cellulose-oligosaccharides obtained by ball-milling.

The obtained MALDI-TOF spectrum (Figure 2) showed the series of mono-anionized peaks of COS as $[M-Na]^+$. The detected signals were in line with the theoretical values calculated with the repeating unit ($M = 162.06$ g/mol) and glucose ($M = 176.06$ g/mol). The formation of COS up to DP 17 could be confirmed with a m/z of 2793.41 u $[M-Na]^+$. More information about the average DP and the structure of the COS could be obtained from NMR (Figure 3).

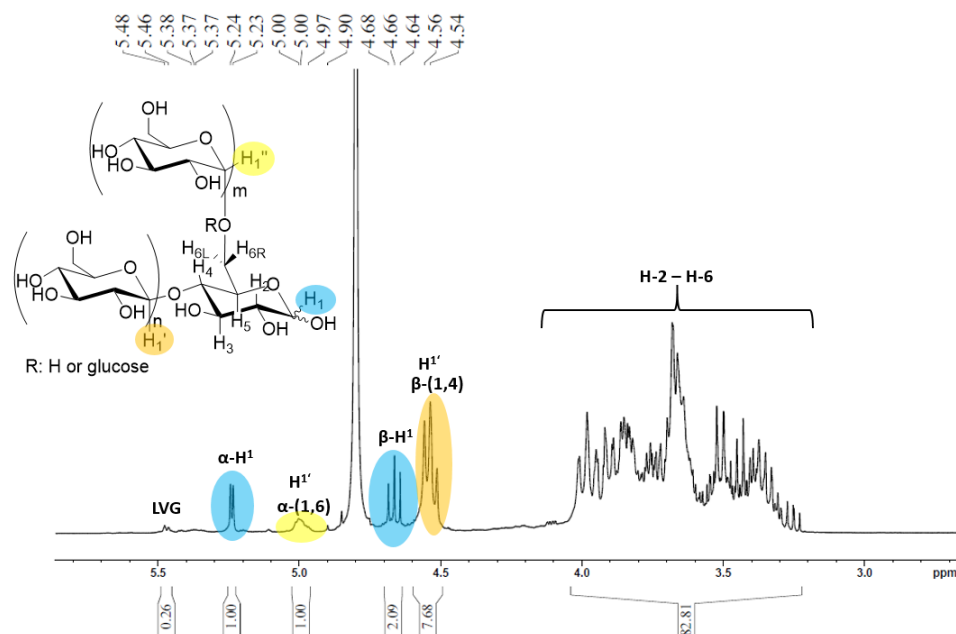


Figure 3. $^1\text{H-NMR}$ (400 MHz, D_2O) spectrum of COS obtained by ball-milling.

The $^1\text{H-NMR}$ spectra (Figure 3) showed the characteristic signals of the cellobiose repeating units (α -(1,4)- glycosidic linked glucose molecules) in cellulose. The α - and β - anomeric

protons could be clearly distinguished due to the difference in their frequency with 5.24 ppm for α -H-1 and 4.66 ppm for β -H-1, respectively. Furthermore, the broad signal at 4.55 ppm was attributed to the anomeric proton at the β -(1,4)-glycosidic linkage (H-1') between the glucose units. Its high intensity supported that the COS were still mainly linked *via* the β -(1 \rightarrow 4) position after the ball-milling. Another linkage was determined with the appearance of the peak at 5.0 ppm. The latter was tentatively assigned to the anomeric proton of the α -(1,6)-glycosidic linkage (H-1''). To further support this claim, multidimensional NMR spectroscopy was carried out.

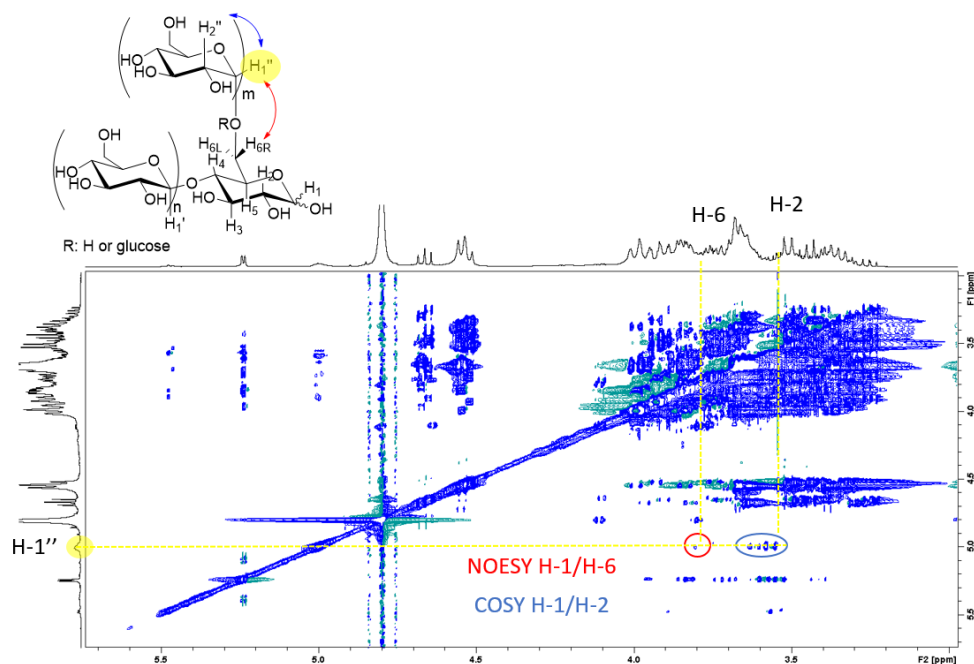


Figure 4. NOESY NMR spectrum of COS obtained by ball-milling.

The deep analysis of the branching pattern by GC of ball-milled COS^[3] showed already the preference for the (1,6) position. NOESY NMR experiment could further support this linkage with the proton-proton long range coupling between H-1'' and H-6 of the sugar ring (Figure 4, red). With a simplified structure of the COS, assuming their connection exclusively *via* the β -(1,4) and α -(1,6) position, we could calculate approximatively the average degree of polymerization (\overline{DP}_n) *via* the following equation:

$$\overline{DP}_n = \frac{(H\alpha + H\beta + H1)}{(H\alpha + H\beta)} \quad (1)$$

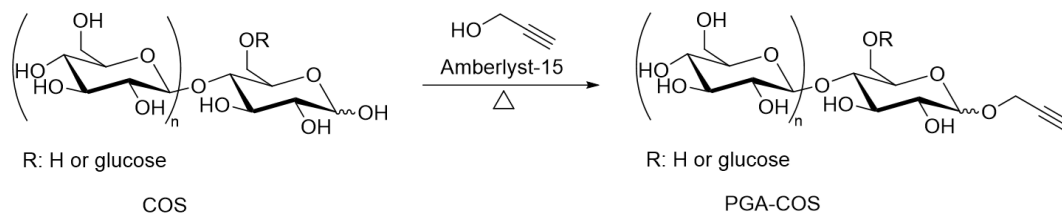
And the average molecular mass through

$$\overline{M}_n = \overline{DP}_n \times M_0 + 18 \quad (2)$$

where H1 presents the anomeric protons of the glycosidic linkage β -(1,4) and α -(1,6), M_0 the mass of the repeating unit (= 162 g/mol) and 18 the loss of water from the glycosidic linkage.

Thereby, we determined the \overline{DP}_n of the COS **15-18** (Table 1) and obtained values between *ca.* 4 to 5, which were in line with previous reported mechanocatalytic depolymerizations^[5]. In the following, the reducing end of the COS was glycosylated with PGA to introduce the alkyne function.

2.2 End-functionalization with propargyl alcohol



Scheme 2. General scheme of the glycosylation of cellulose-oligosaccharides (**COS**) with propargyl alcohol under acid catalysis (amberlyst-15) to give propargyl-cellulose-oligosaccharides (**PGA-COS**).

The COS obtained from the ball-milling were dispersed in an excess of PGA (10 up to 20 eq.) and stirred under the presence of the acidic catalyst, amberlyst-15 (4.2 mol% H⁺), at 100 °C. Since the chains of the COS are known to be acid-labile, we applied vacuum after 20 minutes of the reaction to prevent a depolymerization. Thereby, the excess of PGA was distilled out of the reaction medium as well as the *in situ* released water from the glycosylation. The so-obtained brown colored powder of COS was then analyzed by ¹H-NMR spectroscopy and the spectra of COS before and after the reaction are given in Figure 5.

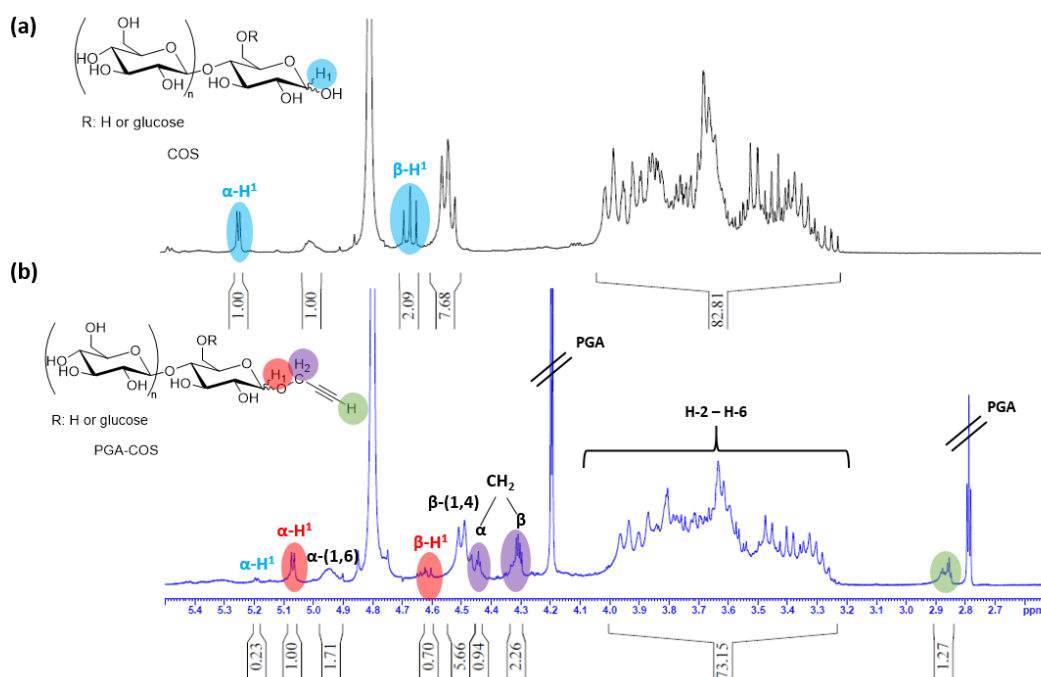


Figure 5. ¹H-NMR (400 MHz, D₂O) spectrum of (a) COS (**15**) and (b) propargyl-cellulose-oligosaccharides (PGA-COS).

$^1\text{H-NMR}$ spectroscopy experiment (Figure 5) showed the successful propargylation of COS with the shift of the anomeric protons (blue to red) from 5.20 ppm to 5.06 ppm for $\alpha\text{-H-1}$ and from 4.64 ppm to 4.60 ppm for $\beta\text{-H-1}$, respectively. In addition, the appearance of the multiplet from the methylene protons of the propargyl group (purple, 4.44 ppm for $\alpha\text{-CH}_2$ and 4.31 ppm for $\beta\text{-CH}_2$) and the signal at 2.88-2.85 ppm from the alkyne proton (green) supported the coupling of COS with PGA. The assignment of these signals was confirmed with the comparison of the spectrum of pure propargyl-glucopyranoside (PGLuc, see appendix). The spectrum showed still the presence of terminal free, non propargylated COS with the signal of the $\alpha\text{-H-1}$ at 5.20 ppm (blue). The integration of the anomeric signals showed, that the latter consists to *ca.* 19 % of the total amount of $\alpha\text{-H-1}$ protons. The functionalization rate was therefore calculated to *ca.* 80 %, including only the α anomeric protons. This assumption was justified due to the overlay of the signals from the $\beta\text{-H-1}$ protons of COS (blue) and PGA-COS (red), hampering their consideration. Equation (1) was then applied to determine the \overline{DP}_n from the spectra, taking only into account the anomeric protons of PGA-COS (in red). From the initial COS with a \overline{DP}_n of *ca.* 4 (sample 15), the \overline{DP}_n increased to 5 for the PGA-COS. Note that this calculation was not “exact” since the amount of COS was not taken into account.

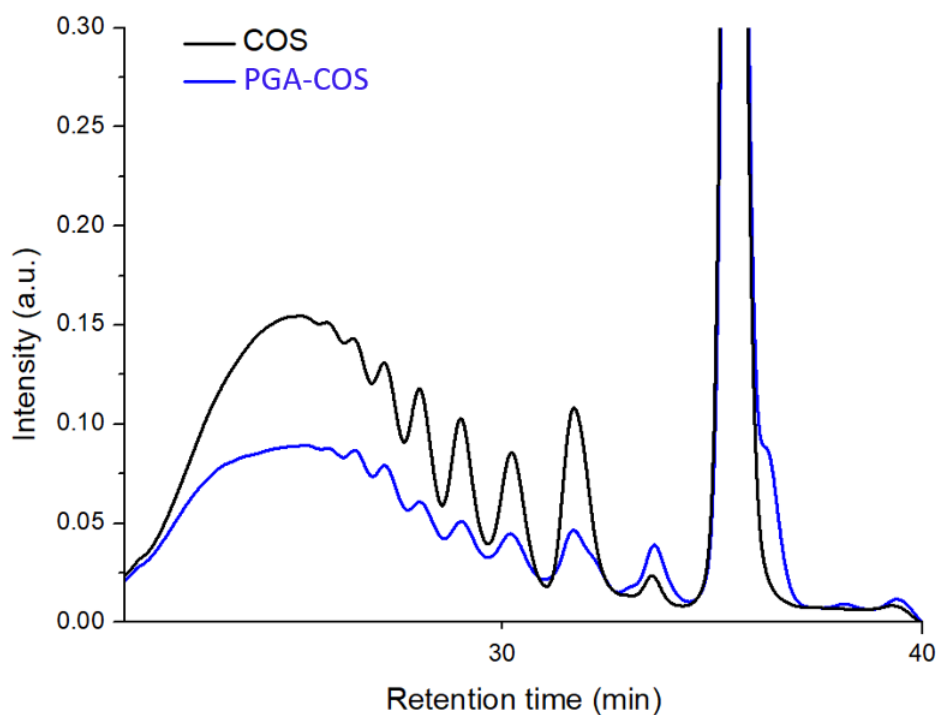


Figure 6. Overlaid SEC (measured against dextran-standards in H_2O at 25 °C) spectra of COS after ball-milling (black) and PGA-COS (blue) after glycosylation with PGA.

The analysis by size-exclusion-chromatography (Figure 6) showed the loss in molar mass of COS after the reaction with PGA. After the glycosylation, \overline{M}_n decreased from 807.3 g/mol for COS to 593.4 g/mol for PGA-COS. In contrast to the NMR analysis, the SEC results denoted a clear decrease in the average molar mass by 26 %.

We could show that a short reaction time of PGA with COS (1 h in total) could propargylate *ca.* 80 % of the terminal end groups. The subsequent application of vacuum could prevent the sugars from depolymerization as demonstrated in the NMR- and SEC spectra. To attain complete functionalized PGA-COS, we explored different reaction conditions (molar ratio PGA/COS, reaction time, vacuum) and the results are summarized in Table 3.

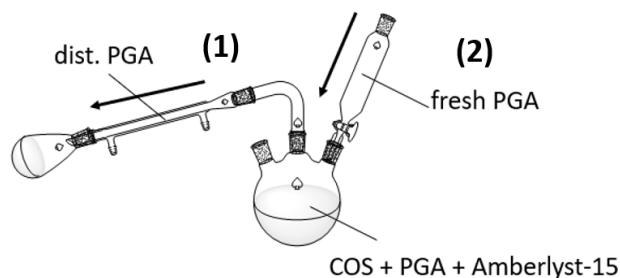
Table 3. Propargylation of COS (batch 16, \overline{DP}_n : 4) with PGA under different conditions.

Experiment t	COS (eq.)	PGA (eq.)	Temp. (°C)	Time (h)	other	Propargylation n (%)	\overline{DP}_n (NMR)
1	1	10	100	2	-	73	3
2	1	20	100	2	-	94	2
3 ^{a)}	1	10	100	1	vacuum	80	5
4 ^{a)}	1	20	100	1	vacuum	80	3
5	1	20	100	1	mol. sieves ^{b)}	34	4
6	1	20	100	12	mol. sieves ^{b)}	77	4
7	1	excess	115	2	distillation ^{c)}	72	4

^{a)} small batch (*ca.* 0.5 g COS), note: 20 min. atm. pressure, then 40 min. under vacuum.

^{b)} molecular sieve = sodium aluminium silicate, 4 Å

^{c)} Distillation set-up see Scheme 3



Scheme 3. Distillation set-up containing (a) the distillation of PGA and (2) the continuous addition of fresh PGA during the reaction.

When the glycosylation of COS with PGA was carried out under atmospheric pressure (experiments 1 and 2, Table 3), 94 % functionalization could be reached. The reaction was completed within 2 h, but the \overline{DP}_n decreased from 4 to 2, denoting the depolymerization of the oligosaccharide chains. We observed that the increase of PGA concentration from 10 eq. (exp. 1) to 20 eq. (exp. 2) improved the glycosylation. While with 20 eq. (exp. 1), almost 100 % of the COS chains were functionalized, with 10 eq., however, only up to 73 % functionalized PGA-COS were obtained. Note that the almost functionalized PGA-COS in exp. 2, however, were partly depolymerized and the \overline{DP}_n decreased to 2.

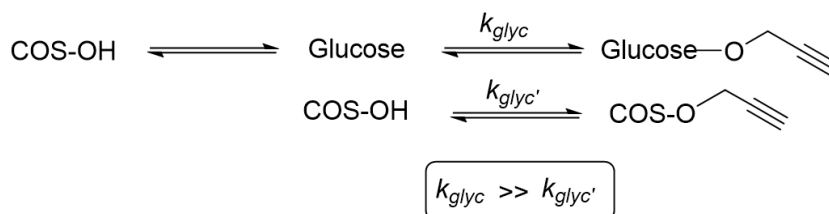
To prevent the depolymerization of COS during the glycosylation with PGA, the reaction was carried out under vacuum. The *in situ* released water from the glycosylation was thereby distilled out from the reaction mixture. We suggested that the water cleaved the glycosidic linkages of COS under the acidic conditions, leading to their depolymerization. With the simultaneous removal of water during the reaction, the COS should be preserved from the hydrolytic cleavage. However, the application of vacuum at reaction temperatures of 100 °C

led consequently also to the distillation of PGA. This stopped the reaction and explained the decrease in functionalization from 100 % to 80 % from exp. **2** to exp. **4**.

Since the application of vacuum limits the duration of the reaction and thereby the effective functionalization, other methods were considered to remove water from the reaction mixture. We first explored the utilization of molecular sieves (sodium aluminium silicate, 4 Å). The latter was added to the reaction mixture and should absorb the released water to protect the COS. We denoted no depolymerization and obtained PGA-COS consisting of the same \overline{DP}_n as the initial COS. Unfortunately, the beads of the molecular sieve somewhat stacked together with the COS during the reaction. We suggested that this hampered the contact between PGA and COS, which led to the low functionalization ratio of 34 % after 1 h of reaction. Expansion of the reaction time to 12 h could reach 77 % of functionalization. However, the glycosylation ratio was 2 to 3 times lower than without molecular sieves under vacuum and atmospheric pressure, respectively. The time to reach comparable degree of functionalization needed to be increased by 10 when molecular sieves were utilized.

In another set of experiments, we installed a distillation bridge and a dropping funnel (see image below Table **3**) to the reaction flask. The continuous addition of fresh PGA through the dropping funnel compensated the amount of alcohol that was distilled. Thereby, the water could be removed keeping always the same amount of PGA in the reaction flask. This distillation set-up could prevent the depolymerization of the COS. The degree of functionalization, however, decreased. After 2 h of reaction, we obtained 72 % functionalized PGA-COS. Within this setup, it was very difficult to control the feeding rate of PGA, which had to be equal to the distillation rate. Due to the time delay to heat the freshly added PGA to the same temperature as the PGA in the reaction flask, the distillation and the addition of PGA were not aligned. Due to the usage of large amounts of PGA and the increasing effort due to the complex setup, we did not continue with this strategy. However, the process might be optimizable outside laboratory capabilities.

Altogether, for the glycosylation of COS with PGA, there was a compromise between complete functionalization and depolymerization. We suggested that the glycosylation of monomeric glucose (k_{glyc}) was much faster than the reaction of the terminal OH group of the COS ($k_{glyc'}$).



Scheme **4**. Competition between the glycosylation reaction between PGA and Glucose (k_{glyc}) and the end group of COS ($k_{glyc'}$).

When the COS are depolymerized to glucose monosaccharides, they are more reactive for the glycosylation with PGA. Besides, PGA might cleave the glycosidic linkage between the sugar-units in the COS chain to give lower molar mass PGA-COS. This claim was supported with

the extension of the reaction, which led to almost 100 % PGA-COS with a decreased \overline{DP}_n . In Figure 7, this process is illustrated following the glycosylation of COS with PGA over a time period of 2 h.

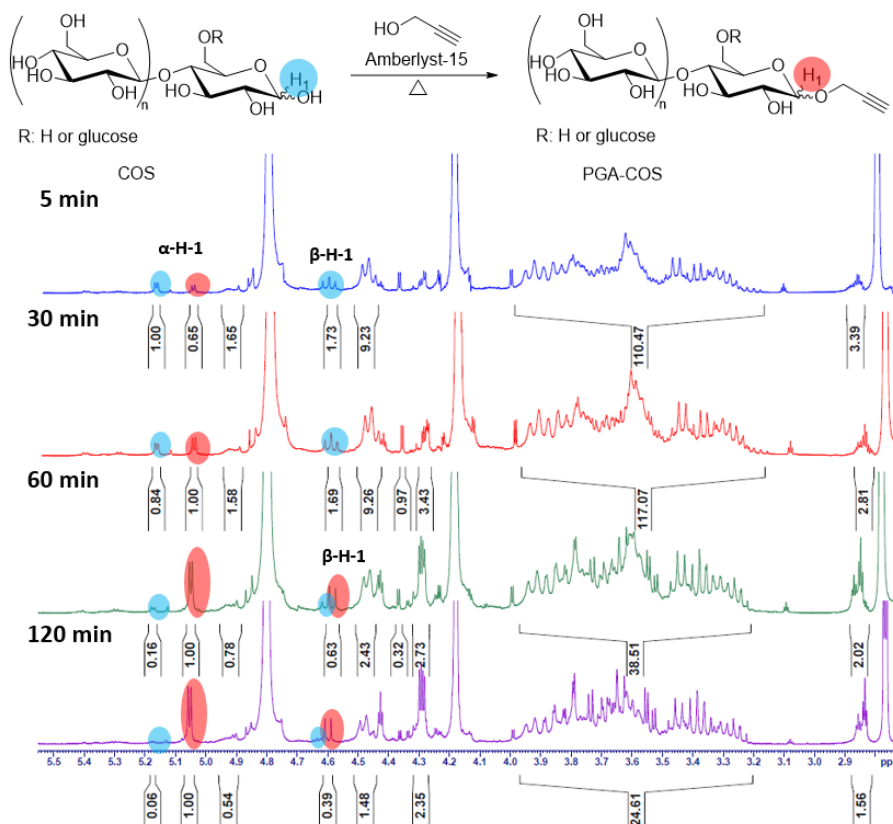


Figure 7. Overlaid plot of the $^1\text{H-NMR}$ (400 MHz, D_2O) spectra of the glycosylation reaction of COS (1 eq.) with PGA (20 eq.) over a time period of 2 h at 100 °C under atmospheric pressure.

The depicted NMR spectra show the anomeric protons of COS in blue and of PGA-COS in red, respectively. The reaction was carried out at 100 °C under atmospheric pressure with an excess of PGA of 20 eq. The data obtained showed, that after 30 minutes of reaction, already 54 % of the COS were functionalized. When the reaction was continued for another 30 minutes, 86 %- and after 2 h finally up to 94 % of the COS chains were propargylated. The \overline{DP}_n , however, decreased from 4 after 30 minutes to *ca.* 2 after 2 h of reaction. We concluded that within this method, whether the COS are completely propargylated but depolymerized, or not depolymerized but functionalized to only maximum 80 %.

3 Conclusion

Altogether, we could present another method to prepare end-functionalized glycosides starting from microcrystalline cellulose. The mechanocatalytic depolymerization of cellulose gave water soluble oligosaccharides, mainly linked *via* the β -(1,4)-glycosidic position with \overline{DP}_n from *ca.* 4 up to 5 after 24 h of stirring at 400 rpm. Elucidation of the structure by multidimensional NMR spectroscopy supported that the COS consisted of additional branching mainly at the OH-6 position. The glycosylation of COS with PGA showed that the OH group at the reducing end of the sugars could be propargylated using an excess of PGA. We denoted that there was a competitive depolymerization under the acid conditions of the reaction, induced either by the *in situ* released water or PGA. With the application of vacuum subsequent after the glycosylation reaction, the depolymerization could be prevented to certain extents. Under optimized conditions, COS were functionalized with PGA to *ca.* 80 %, whereas the \overline{DP}_n decreased from 4 (COS) to 3 (PGA-COS) in the final product. Complete functionalization could only be obtained with an important depolymerization of the COS to $\overline{DP}_n = 2$. We consequently only obtained functionalized di- up to tetrasaccharides, but no larger oligosaccharides.

The glycosylation of the reducing end of oligosaccharides without a cleavage of their intramolecular glycosidic linkages is a very challenging task. Due to the acid conditions of the glycosylation reaction with PGA, a sequential depolymerization could not be provided using unprotected COS. The glycosylation of monosaccharides with PGA and a subsequent oligomerization showed to be a more promising strategy (see Chapter II A). Not only the \overline{DP}_n could be controlled with a fine tuning of the reaction conditions, but also different monosaccharides could be applied, as so far supported for mannose and glucose. Starting from an oligosaccharide requires the utilization of protecting groups to provide depolymerization. The employment of monosaccharides, however, avoided complex protecting-deprotecting steps as they were utilized in our approach without any modification.

The key for the succeed oligomerization of PMan and PGluc was the distillation of the excess of PGA. This step initiated the polymerization reaction and reduced the contact with the *in situ* formed (PMan)_n and (PGluc)_n with PGA and/or water. Thereby, the \overline{DP}_n increased until PGA was distilled (stop of the reaction), while (PMan)_n and (PGluc)_n showed complete propargylation at their reducing end. However, the distillation of PGA after the glycosylation of the COS showed not the same polymerizing effect. We suggested that there were not sufficient free glucose molecules available to form an oxocarbenium ion, that could react with PGA-COS and elongate the chain. It might be considerable in a further work to first completely propargylate the COS and accept their depolymerization, and then re-polymerize them by distilling PGA. However, this approach will change the architecture of the obtained PGA-COS and might lead to the same propargylated gluco-(oligo)-pyranosides as (PGluc)_n from method A. In Figure 8 and Table 4 the main results for both methods A and B are summarized and set against each other.

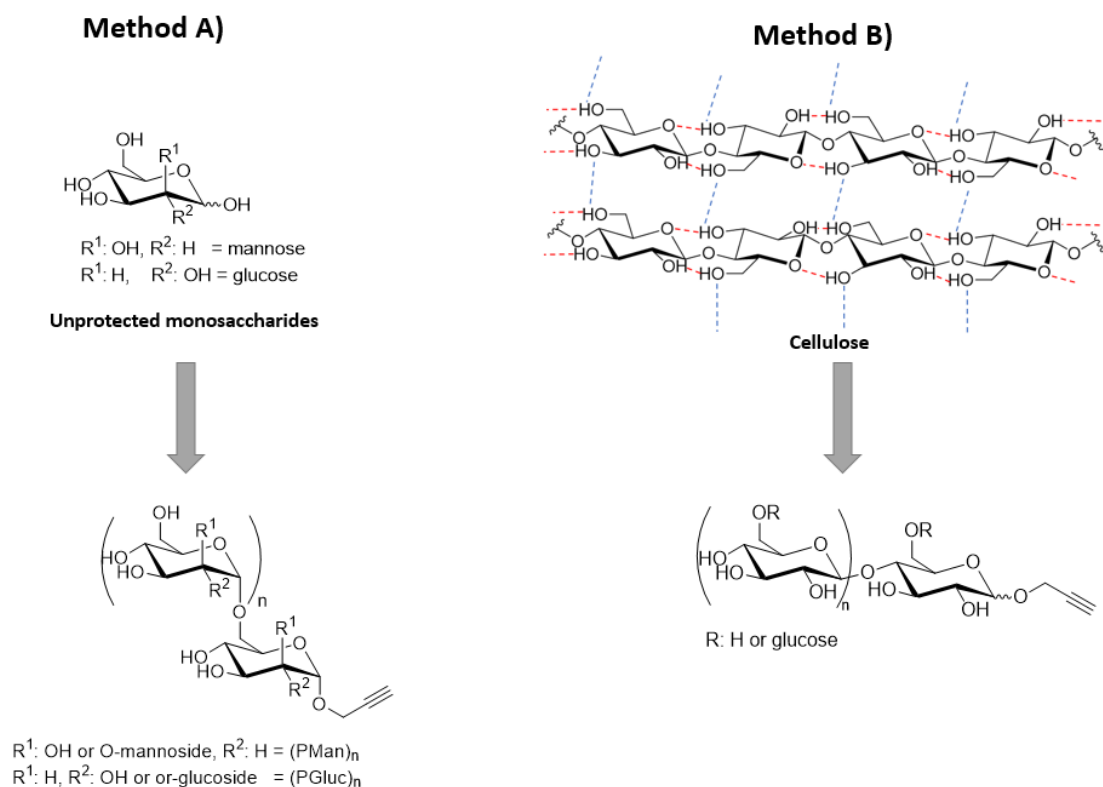
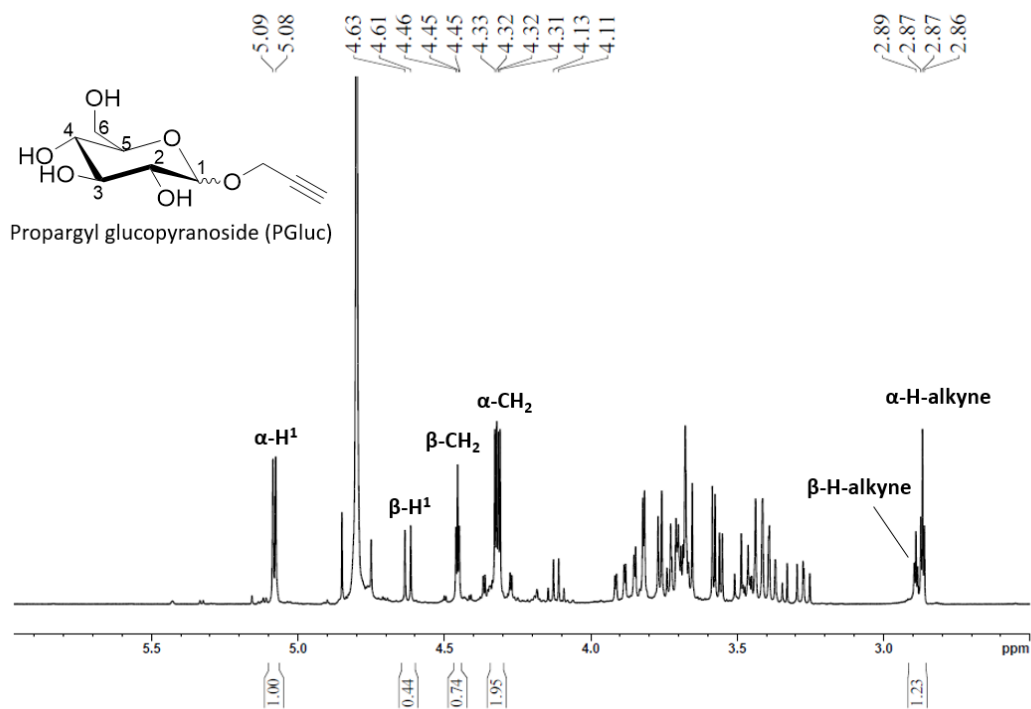
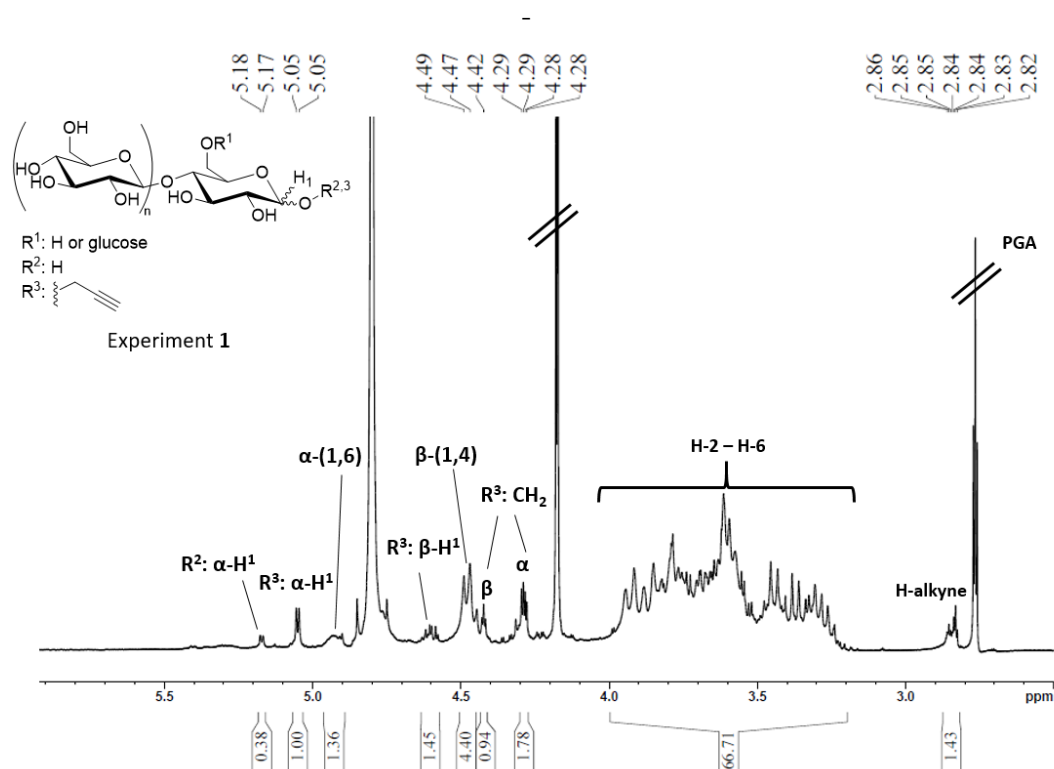


Figure 8. Illustrative comparison of both strategies to prepare end-functionalized oligosaccharides developed during this thesis.

Table 4. Comparison of both strategies to prepare end-functionalized oligosaccharides developed during this thesis.

	Method A)	Method B)
Amount of reactions	one	two
\overline{DP}_n reached	3 - 8	2 - 4
Reagents	Mannose, Glucose, (other monosaccharide imaginable)	COS from ball-milling
Main glycosidic linkages	α -(1,6)	β -(1,4)
Reaction temperature	80 - 100 °C	100 °C
Reaction duration	minimum 8 h	24 h (ball-milling) + 1 - 2 h glycosylation <i>rect.</i> with PGA

4 Appendix

Figure 9. $^1\text{H-NMR}$ (400 MHz, D_2O) spectrum of propargyl glucopyranoside (PGLuc).Figure 10. $^1\text{H-NMR}$ (400 MHz, D_2O) spectrum of propargyl-cellulose-oligosaccharides (PGA-COS) of experiment 1.

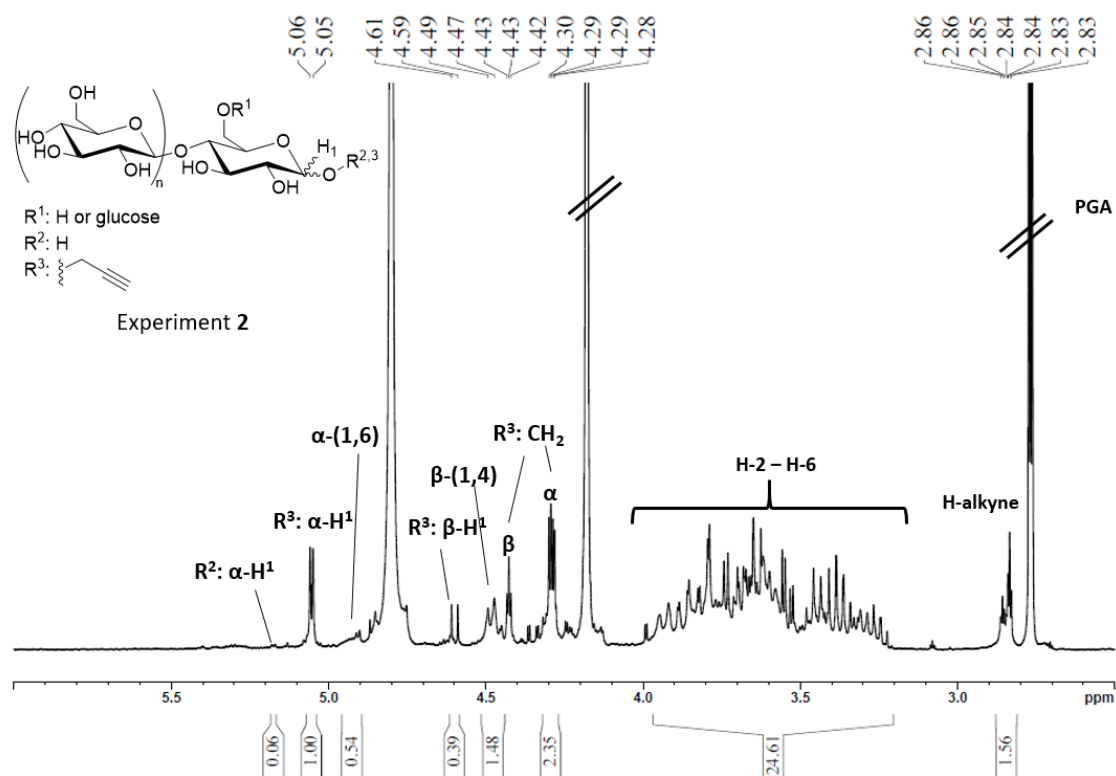


Figure 11. $^1\text{H-NMR}$ (400 MHz, D_2O) spectrum of propargyl-cellulose-oligosaccharides (PGA-COS) of experiment 2.

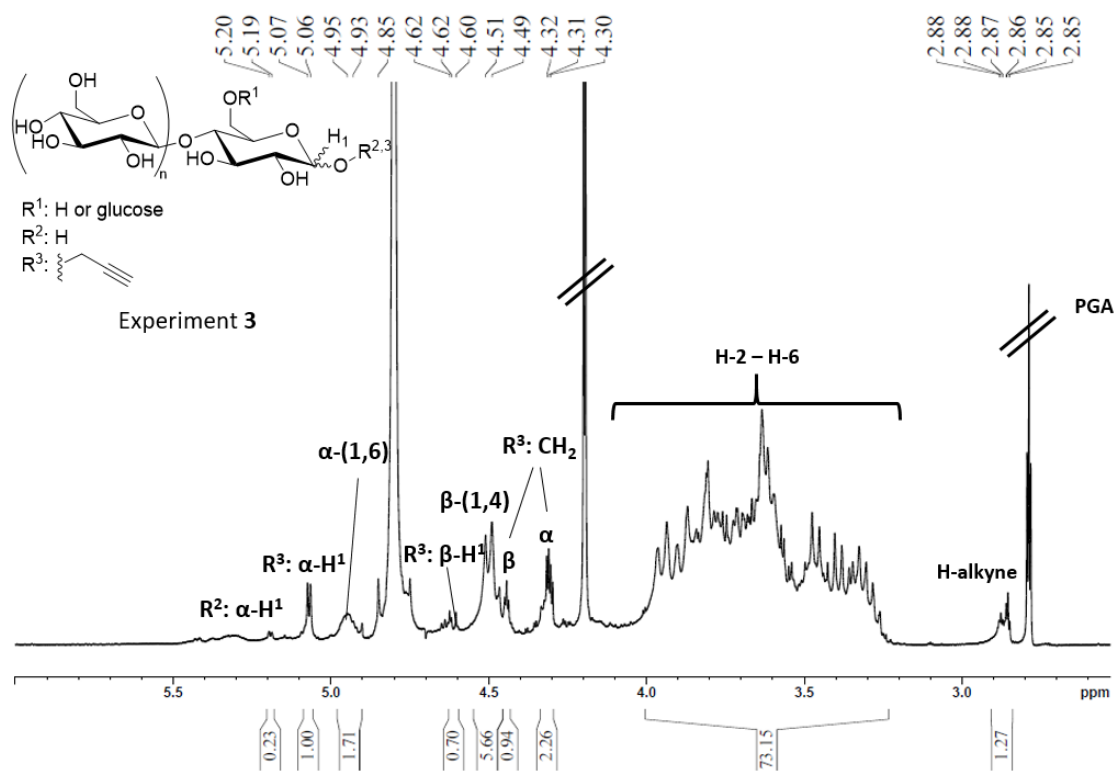


Figure 12. $^1\text{H-NMR}$ (400 MHz, D_2O) spectrum of propargyl-cellulose-oligosaccharides (PGA-COS) of experiment 3.

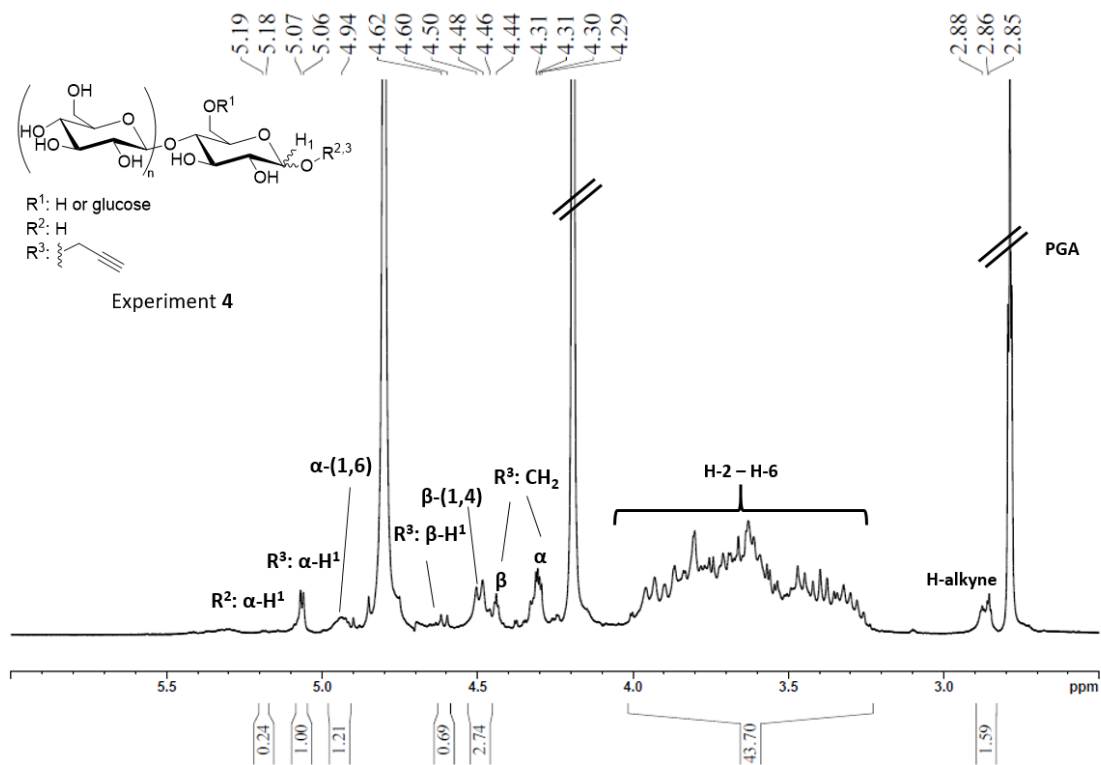


Figure 13. $^1\text{H-NMR}$ (400 MHz, D_2O) spectrum of propargyl-cellulose-oligosaccharides (PGA-COS) of experiment 4.

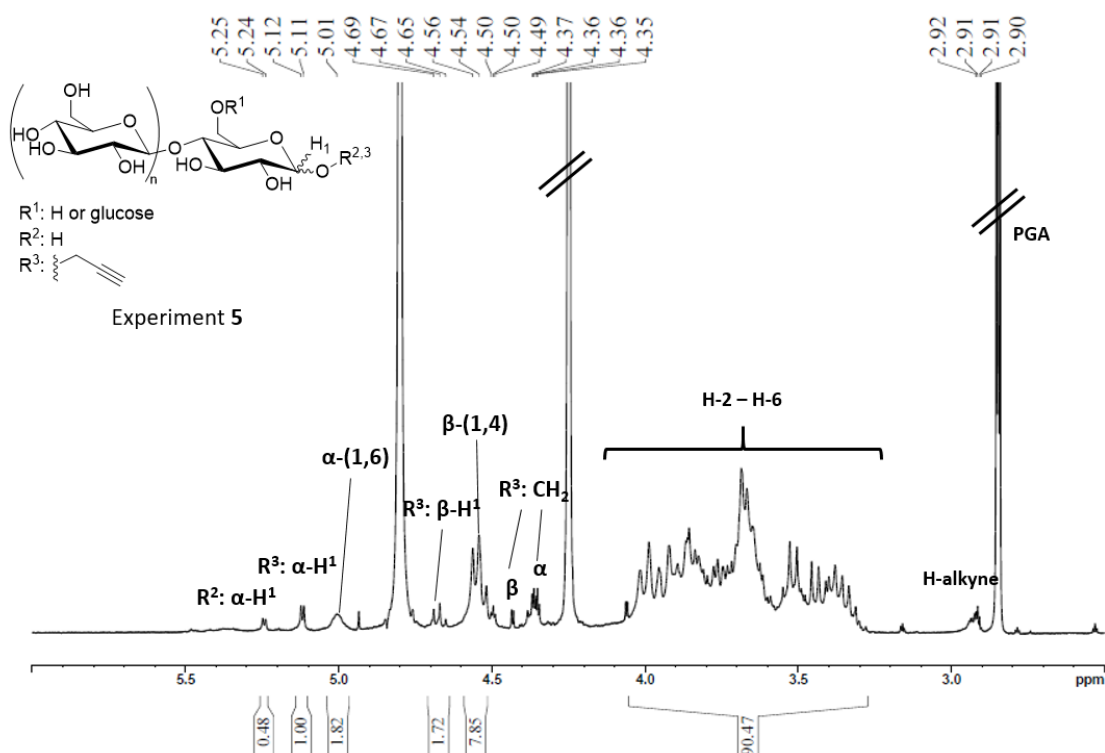


Figure 14. $^1\text{H-NMR}$ (400 MHz, D_2O) spectrum of propargyl-cellulose-oligosaccharides (PGA-COS) of experiment 5.

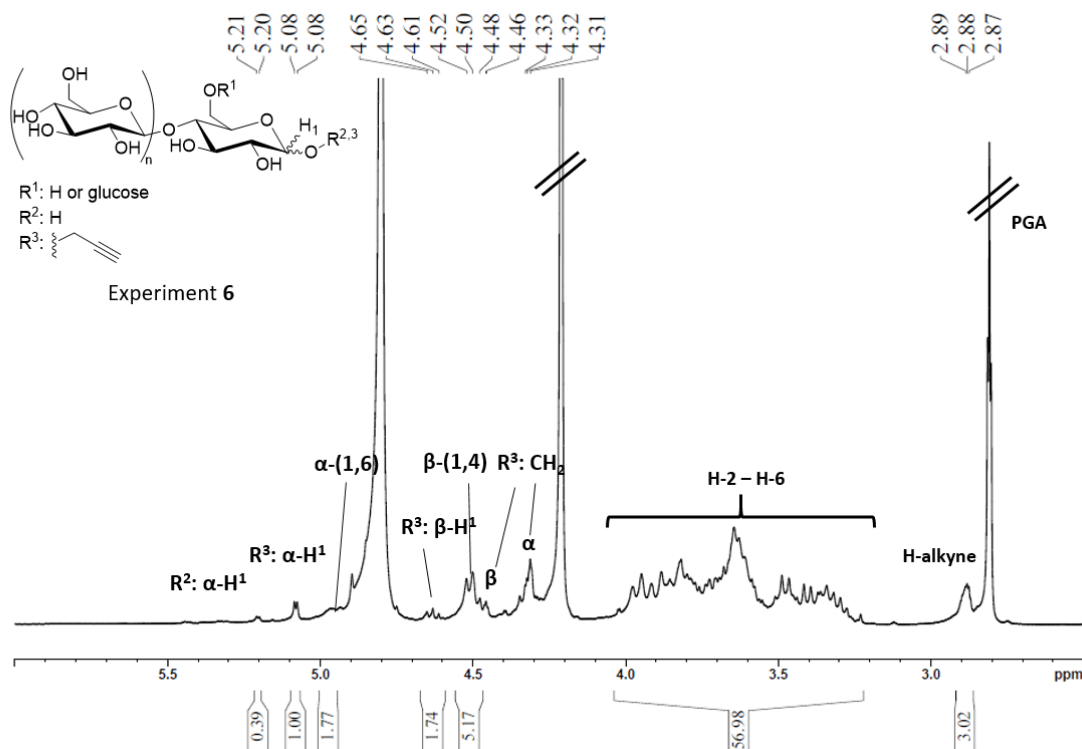


Figure 15. $^1\text{H-NMR}$ (400 MHz, D_2O) spectrum of propargyl-cellulose-oligosaccharides (PGA-COS) of experiment 6.

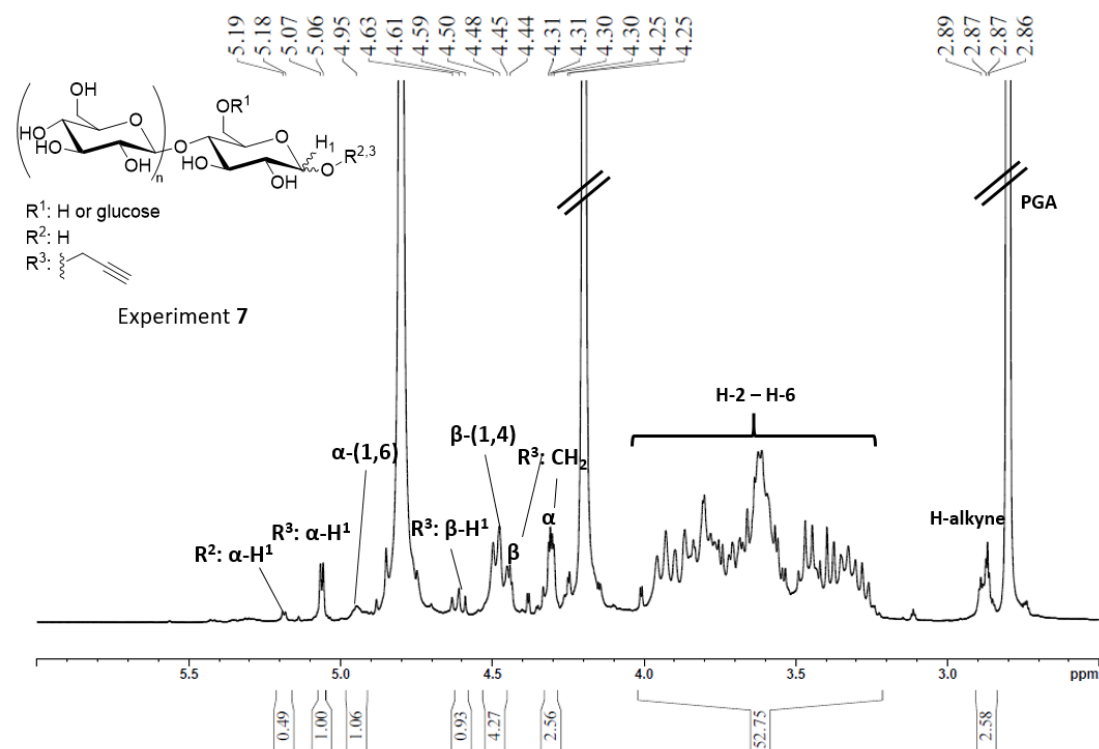
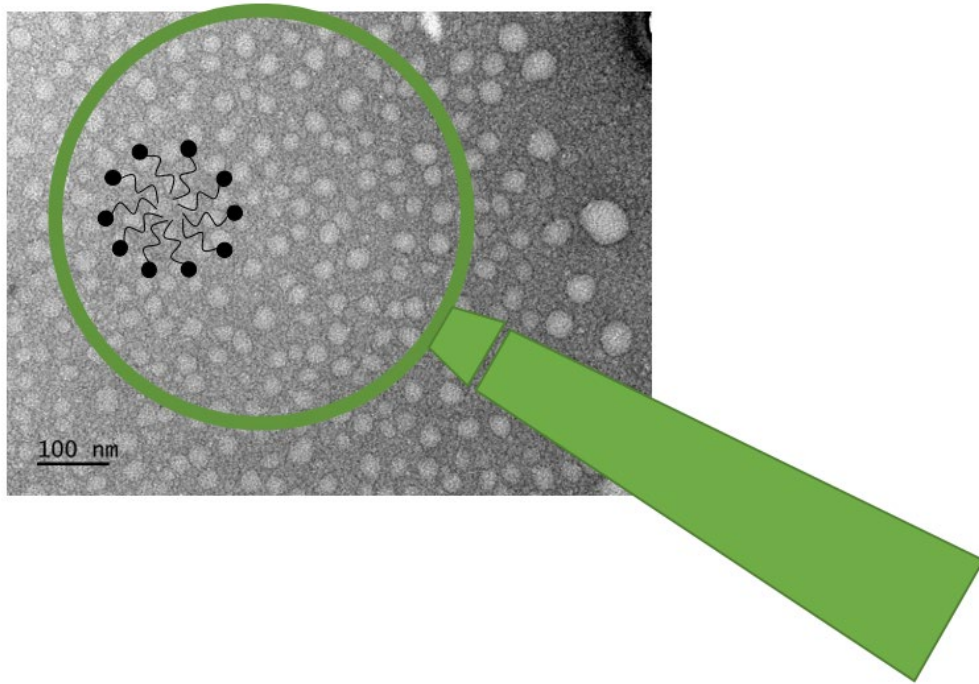


Figure 16. $^1\text{H-NMR}$ (400 MHz, D_2O) spectrum of propargyl-cellulose-oligosaccharides (PGA-COS) of experiment 7.

Bibliography

- [1] aJ. K. Kim, S. Y. Yang, Y. Lee, Y. Kim, *Progress in Polymer Science* **2010**, *35*, 1325-1349; bS. de Medeiros Modolon, I. Otsuka, S. b. Fort, E. Minatti, R. Borsali, S. Halila, *Biomacromolecules* **2012**, *13*, 1129-1135; cI. Otsuka, K. Fuchise, S. Halila, S. Fort, K. Aissou, I. Pignot-Paintrand, Y. Chen, A. Narumi, T. Kakuchi, R. Borsali, *Langmuir* **2010**, *26*, 2325-2332.
- [2] aC. Schatz, S. Louguet, J. F. Le Meins, S. Lecommandoux, *Angewandte Chemie International Edition* **2009**, *48*, 2572-2575; bC. Schatz, S. Lecommandoux, *Macromol Rapid Commun* **2010**, *31*, 1664-1684.
- [3] A. Karam, P. N. Amaniampong, J. M. Garcia Fernandez, C. Oldani, S. Marinkovic, B. Estrine, K. De Oliveira Vigier, F. Jerome, *Front Chem* **2018**, *6*, 74.
- [4] A. Shrotri, L. K. Lambert, A. Tanksale, J. Beltramini, *Green Chemistry* **2013**, *15*, 2761.
- [5] J. Hilgert, N. Meine, R. Rinaldi, F. Schüth, *Energy Environ. Sci.* **2013**, *6*, 92-96.

Chapter III: Self-assembly and surfactant properties



This work was carried out in collaboration with Dr. Pablo Gómez Argudo, to whom I want to address my grateful acknowledgement.

Contents

1	Introduction	179
2	Preparation of the amphiphiles	180
2.1	Functionalization of fatty acid methyl esters (FAME)	180
2.2	Huisgen Click reaction	188
3	Self-assembly	193
3.1	Critical aggregation concentration (CAC)	193
3.1.1	Tensiometry: Pendant Drop (PD)	193
3.1.2	Isothermal Titration Calorimetry (ITC)	199
3.2	Direct Solubilization	201
3.2.1	Dynamic light scattering (DLS)	202
3.2.2	SAXS	207
4	Conclusion	214
5	Appendix	216
	Bibliography	220

1 Introduction

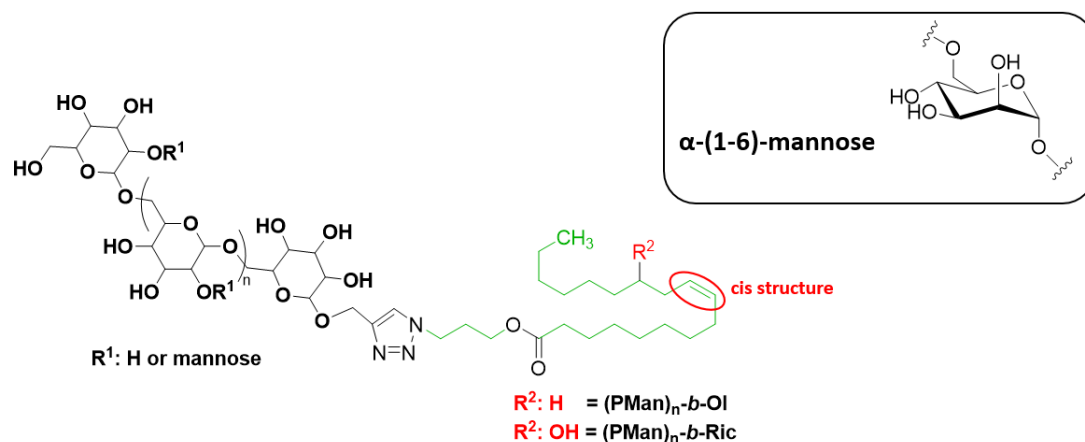


Figure 1. Amphiphilic structure; in black: hydrophilic block, in green: lipophilic block.

Table 1. Library of selected amphiphiles for the following study.

Compound number	Structure	\overline{M}_n (g/mol) (NMR)	HLB
10	PMan ₃ -b-OI	909	11.94
11	PMan ₈ -b-OI	1719	15.75
12	PMan ₃ -b-Ric	924	11.74
13	PMan ₈ -b-Ric	1735	15.60

In this chapter, we describe the synthesis and self-assembly of sugar-based amphiphiles (Figure 1). Thereby, the previously prepared propargylated mannose-oligomers were coupled with long-chain fatty acid ester derivatives by azide-alkyne Huisgen cyclo-addition. The latter were obtained after the transesterification of fatty acid methyl esters (FAME) by azide-functionalized propyl alcohol. For the physical-chemical study of the amphiphiles, we chose a library of four different derivatives (Table 1), changing the size of the polar head (degree of polymerization, $\overline{DP}_n = 3$ to $\overline{DP}_n = 8$) and the type of fatty acid (oleate or ricinoleate, respectively). For the first time, structure-property trends of mannose-oligosaccharide based amphiphiles with average \overline{DP}_n between 3 and 8 are studied. To the best of our knowledge, there are no reports in the literature concerning mannose-based amphiphiles with such high \overline{DP}_n , besides polysaccharide-containing block copolymers.^[1] For other type of sugars, first comprehensive studies on the surfactant properties and self-assembly behavior has been carried out, such as the study on xylan-oligosaccharides derived amphiphiles.^[2]

The influence of an OH group on the hydrophobic chain (in the case of ricinoleate) is also studied, by keeping the sugar block constant and changing only the hydrophobic segment. We systematically analyzed the variations in the CMC and γCMC and their relation to the \overline{DP}_n . In addition, we carried out a deep study in their final structure after their self-assembly in aqueous media by DLS, SAXS and cryo-TEM.

2 Preparation of the amphiphiles

The amphiphiles were prepared by Cu(I) catalyzed azide-alkyne 1,3-dipolar cycloaddition (CuAAC)^[3] between alkyne-terminated mannose-oligomers (PMan)₃ (**8**) and (PMan)₈ (**9**) and azide-functionalized fatty acid ester N₃OI (**5**) and N₃Ric (**6**) (see Scheme 1).

2.1 Functionalization of fatty acid methyl esters (FAME)

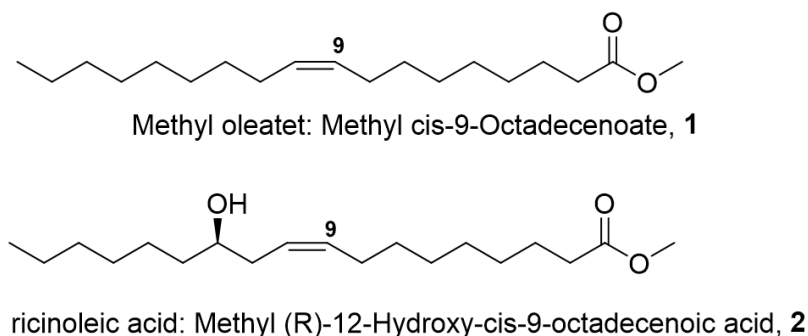
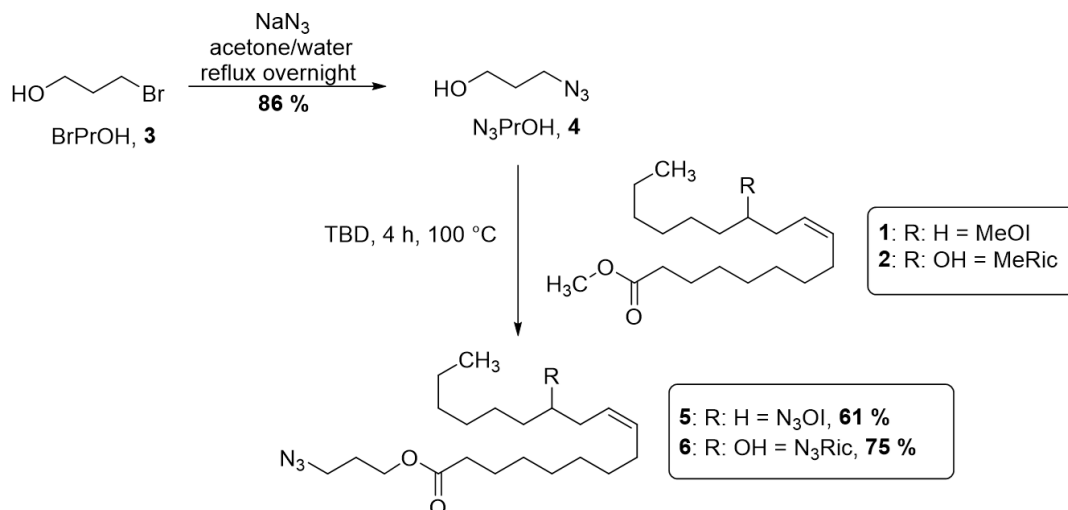


Figure 2. Fatty acid methyl esters (FAME) starting materials (**1**) methyl oleate, (**2**) methyl ricinoleate.

For the hydrophobic tail, we chose the methyl esters of oleate (MeOI) and ricinoleate (MeRic) (Figure 2), originated from vegetable oils, which were functionalized by transesterification reaction with azide-functionalized propyl alcohol (Scheme 1). Oleic acid (cis-9-octadecenoic acid) is one of the most common monounsaturated fatty acid (18:1) found in triglycerides of natural oils like olive-, pecan-, canola-, peanut-, macadamia-, sunflower oil, etc.^[4] Ricinoleic acid (R-12-hydroxy-cis-9-octadecenoic acid), also a 18:1 monounsaturated fatty acid, is obtained from castor plant (*Ricinus communis L.*, Euphorbiaceae).^[5] Today, vegetable oils are one of the most important renewable raw materials in the chemical industry, famous for their sustainability and biodegradability. They are mainly used for the manufacture of surfactants, cosmetic products and lubricants, but also for paint formulations, flooring materials or for coatings and resin applications.^[6] Furthermore, the presence of ester functions and double bonds make them attractive as building blocks in polymer synthesis and enables functionalization *via* epoxidation-, hydroformylation-, ozonolysis-, click- and metathesis reactions.^[7] Their methyl esters (FAME) are derived by transesterification reaction with methanol and are mainly applied in detergents and biodiesel (less corrosive as the ester form). Both, methyl oleate and methyl ricinoleate possess a double bond in cis-configuration, while methyl ricinoleate bears an additional hydroxyl group (OH) at C-12 in R-configuration.



Scheme 1. Synthesis of azide-functionalized fatty acids (**5**, **6**) by transglycosylation of methyl oleate (MeOI, **1**) and methyl ricinoleate (MeRic, **2**) with azide-functionalized propyl alcohol (**4**).

Prior to the transesterification reaction, 3-bromo-1-propanol (**3**) was functionalized with sodium azide (NaN_3) *via* nucleophile substitution ($\text{S}_{\text{N}}2$)^[8] and gave 3-azido-1-propanol (**4**) in 86 % yield. The short azide-functionalized alcohol was then exploited to bring the functionality to the methyl fatty ester of oleate (**1**) and ricinoleate (**2**). The transesterification was carried out in bulk, using TBD (1,5,7-Triazabicyclo(4.4.0)dec-5-en) as a catalyst (0.1 eq.) and an excess of 3-azido-1-propanol (10 eq.) at 100 °C (4 h).^[2, 7] Usually, transesterifications of fatty ester are carried out in bulk at rather high temperatures of around 120 °C. The low boiling point of azido-1-propanol, however, allowed us (1) to decrease the temperature by 20 degrees and (2) to remove the excess of alcohol by distillation under vacuum.^[9] Finally, the pure azide-functionalized oils were obtained after column chromatography on silica (petrol ether/acetyl acetate 9:1) in up to 61 % and 75 % yield for oleate and ricinoleate, respectively.

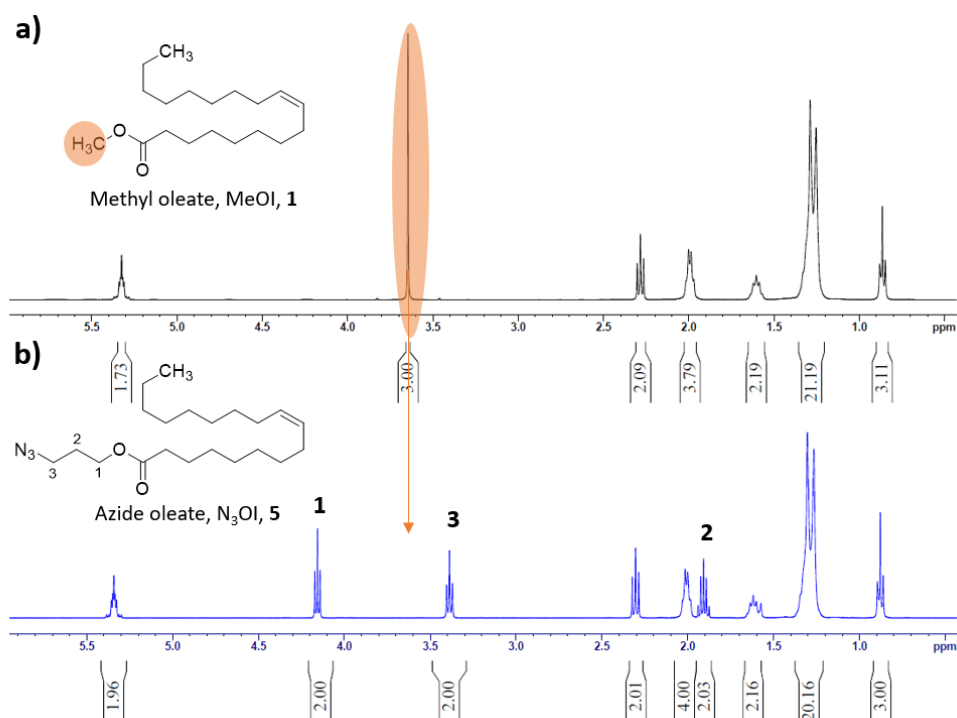


Figure 3. $^1\text{H-NMR}$ (400 MHz, CDCl_3) spectra of **a)** methyl oleate (**1**), **b)** 3-azido-1-propyl-oleate (**5**).

In the case of methyl oleate, $^1\text{H-NMR}$ analysis (Figure 3) showed the complete conversion of MeOI (**1**) with the disappearance of the signal from $-\text{CH}_3$ (orange) of the ester at 3.62 ppm. The new signals arising at 4.14 ppm (**1**, $\text{CH}_2\text{-O}$), 3.37 ppm (**3**, $\text{N}_3\text{-CH}_2$) and 1.98 ppm (**2**, $-\text{CH}_2-$), supported the successful functionalization of the fatty ester.

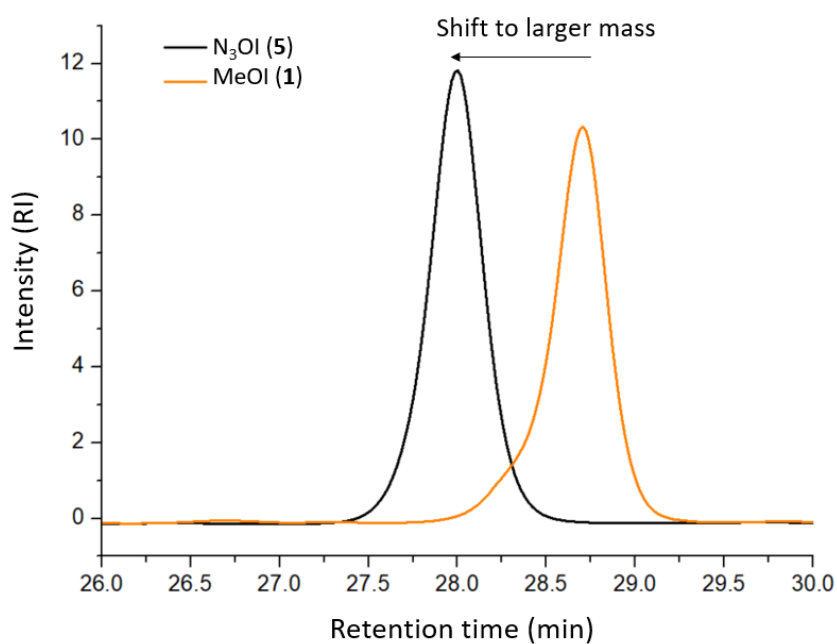


Figure 4. Plot of the overlaid SEC (measured against polystyrene standard in THF at 40 °C) traces of methyl oleate MeOI (orange) and azide-oleate N₃OI (black).

The data obtained from the SEC experiment confirmed the successful transesterification with an increase in relative molar mass from 292 g/mol for MeOI to 507 g/mol for N₃OI with a PDI of 1.01. The characteristic signal for the alkyne stretching bond (N₃) at 2089 cm⁻¹ (ATR-IR, (Figure 5)) confirmed further the successful incorporation of the azide function.

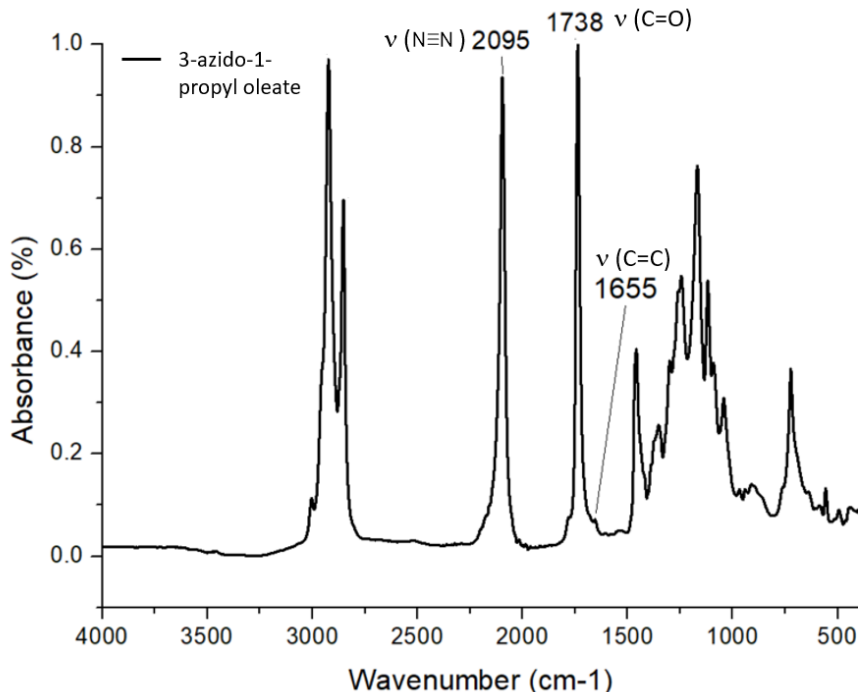
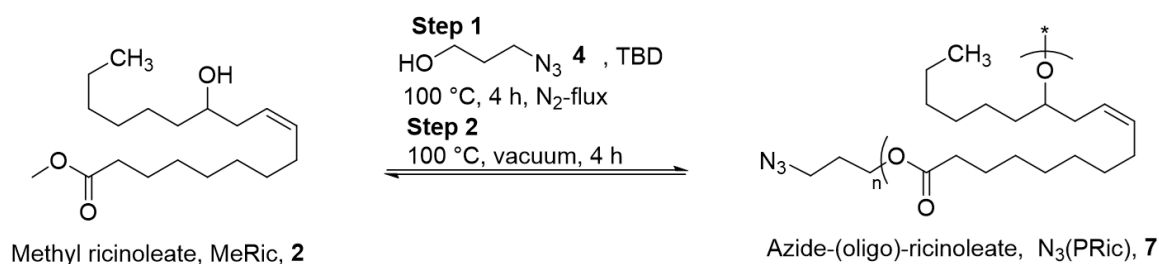


Figure 5. ATR-IR spectrum of 3-azido-1-propyl oleate (5).



Scheme 2. Transesterification of methyl ricinoleate (2) with azide-propanol, along with the simultaneous auto-condensation reaction to 3-azido-1-propyl-(oligo)-ricinoleate (7).

In contrast, during transesterification of methyl ricinoleate we denoted its self-condensation due to the additional hydroxyl group in the alkene chain (C-12) (Scheme 2). While for methyl oleate, the distillation of the excess of alcohol (4) was one purification step, for ricinoleate, however, it initiated the auto-condensation. Therefore, we separated the functionalization of methyl ricinoleate in two steps, with the first presenting the transesterification with azide-propanol (4) and the second the oligomerization reaction initiated with the distillation of the alcohol. The analysis of both steps by size-exclusion chromatography (Figure 6) showed the clear formation of oligomers (orange to black line). We could already find the formation of a

second product after step 1 (orange plot, peak **2**, \overline{M}_n : 994 g/mol), which was assigned to the dimer of $N_3\text{Ric}$, according to the *ca.* double molar mass of 549 g/mol (SEC). $N_3(\text{Ric})_n$ denoted an average molar mass of 1727 g/mol (SEC) with a dispersity D of 1.3. Altogether, we could show that the self-condensation (= oligomerization) was initiated by the distillation of azide-propanol.

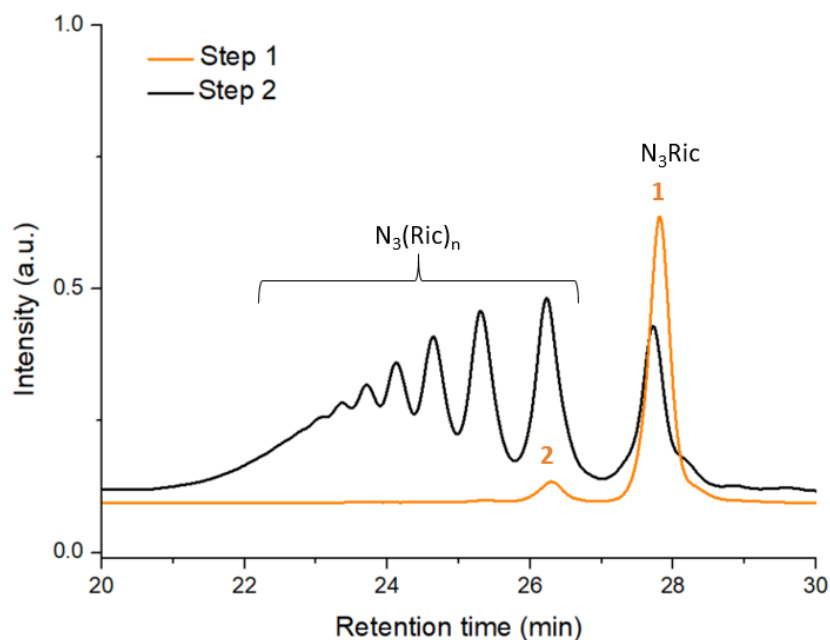


Figure 6. Plot of the overlaid SEC (measured against polystyrene standard in THF at 40 °C) traces of the transesterification of methyl ricinoleate after step 1 (orange) and step 2 (black).

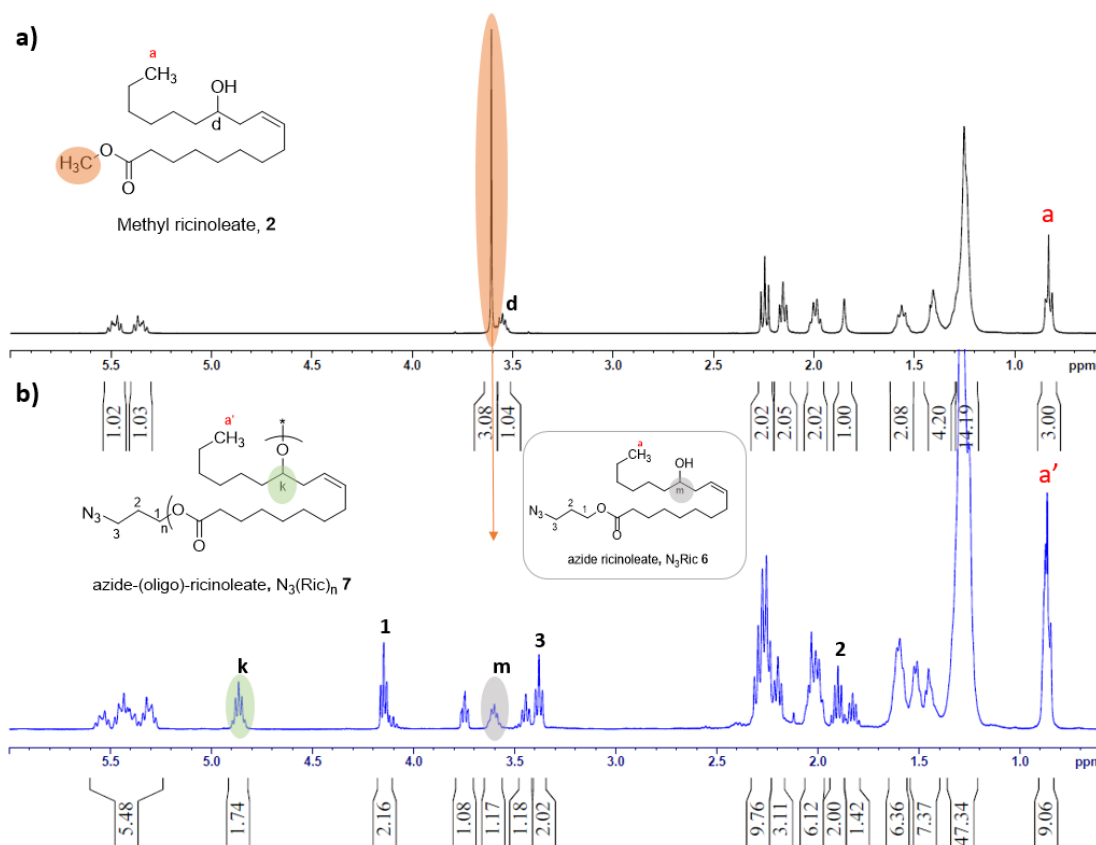


Figure 7. ¹H-NMR (400 MHz, CDCl₃) spectra of **a**) methyl ricinoleate (**6**) and **b**) azide-(oligo)-ricinoleate, N₃(Ric)_n (**7**).

To support this claim, we isolated azide ricinoleate (**6**) after step 1 and performed ¹H-NMR spectra of **6**, methyl ricinoleate (**2**) and oligoricinoleate (**7**) (Figure 7). The obtained data show, that the transesterification was complete, as confirmed by the disappearance of the alkyl group signal **d** (Figure 7 **a**), 3.61 ppm, orange) and by the appearance of the signals from the azide-propyl group at 4.15-4.12 ppm (**1**, CH₂-O), 3.39-3.35 ppm (**3**, N₃-CH₂) and 1.92-1.86 ppm (**2**, -CH₂). Moreover, the characteristic peak of the methine proton -CH- (**d**) at 3.55 ppm in methyl ricinoleate (**2**) (spectrum **a**) is shifted downfield to 4.87 ppm (**k**)^[10], confirming the formation of ester linkages. However, the remaining peak for the methine proton (**m**) in the spectrum of the oligomers (spectrum **b**)), supported a mixture of azide-(*mono*) and (*oligo*)-ricinoleate.

By the application of the end-group method, we could calculate the average degree of polymerization (\overline{DP}_n) and the corresponding molecular weight (\overline{M}_n), respectively. Therefore, the signal for the alkyl peak at 3.39-3.35 ppm (N₃-CH₂) was calibrated and the integral of the methyl protons (CH₃, **a'**) was divided by three protons to give an \overline{DP}_n of 3. The molar mass was then calculated using following equation

$$\overline{M}_n = (289 \times \overline{DP}_n) - (18 \times (n - \overline{DP}_n)) \quad (1)$$

where 289 is the molar mass of the repeating unit, 83 the mass of the azide-propyl group and 18 the loss of water due to the esterification. Using eq. (1), the average molar mass of the azide-(oligo)-ricinoleate was calculated to 942 g/mol.

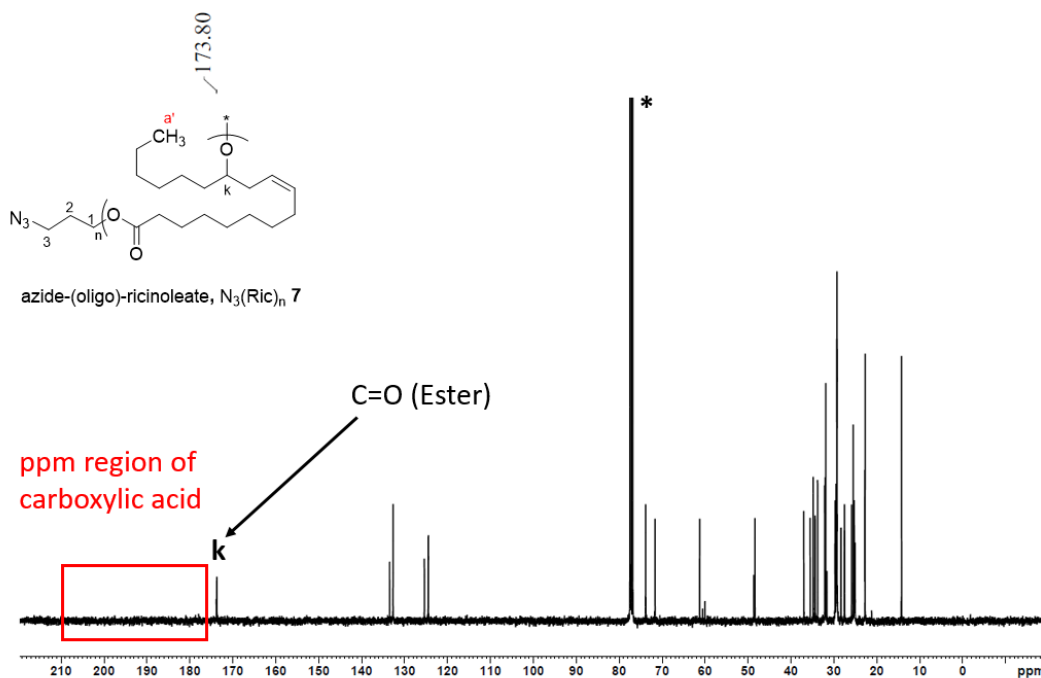


Figure 8. ^{13}C -NMR (100.13 MHz, CDCl_3) spectrum of 3-azido-1-propyl-(oligo)-ricinoleate (7).

The analysis of oligoricinoleate (7) by ^{13}C -NMR- and ATR-IR spectroscopy, could confirm the complete transesterification. No signal belonging to remaining methyl ester MeRic (2) (usually around 174 ppm) or to carboxylic acid (usually around 179 ppm for ricinoleate acid)^[10], were found in the carbon spectrum (Figure 8). The assigned peak in the low field at 173 ppm corresponds to the carbon atom of the ester linkage (k) from the auto-condensation. The remaining signals of the proton- and carbon atoms were determined by multidimensional NMR spectroscopy and are given in the experimental section. The infrared spectrum (Figure 9) shows the characteristic vibrational bond for N_3 at 2096 cm^{-1} and the carbonyl stretching bond ($\text{C}=\text{O}$) at 1731 cm^{-1} of the ester group. The comparison of the IR spectrum of free ricinoleate acid (black plot) proved, that the azide-propyl group was not cleaved during the reaction, supporting complete functionalization of the oligoricinoleate (7).

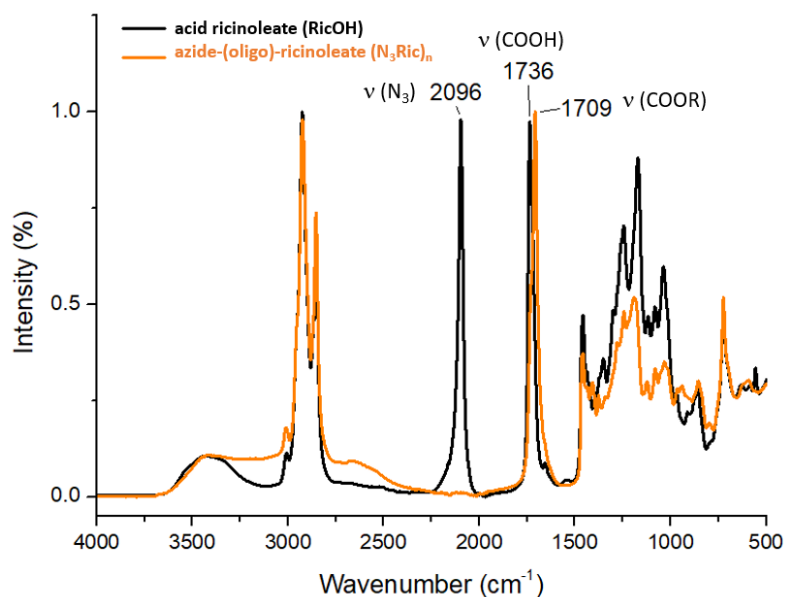


Figure 9. Plot of overlaid ATR-IR spectra of ricinoleate acid (black line) and 3-azido-1-propyl-(oligo)-ricinoleate (orange line).

We next followed the evaluation of the transesterification by NMR spectroscopy in time (Figure 10) with the decrease of the integral of CH_3 from the methyl ricinoleate (**2**) (see appendix for the spectra). The obtained data showed the almost complete conversion of methyl ricinoleate (98 %) after 1 h of reaction. Extending the reaction time from 1 h to 2 h gave then complete conversion and, moreover, the increase of the signal of the methine proton $-\text{CH}-$ (d). This was assigned to the auto-condensation reaction, that proceeded simultaneously to the transesterification, albeit in small extents.

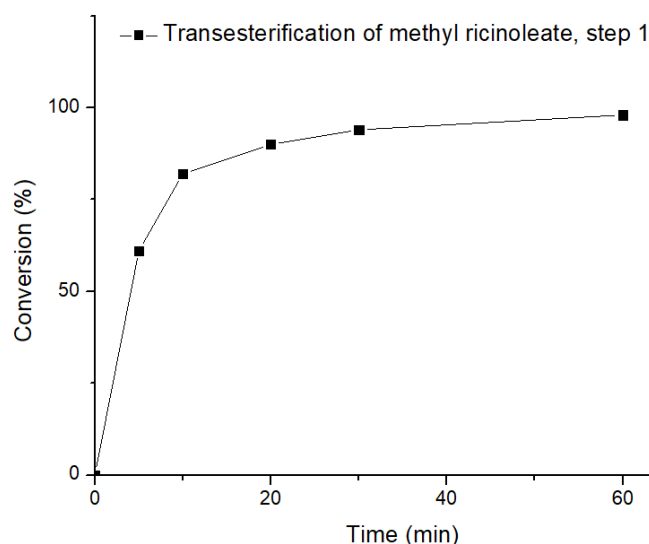


Figure 10. Plot of the conversion of methyl ricinoleate during the transesterification with azide-propanol (step 1: methyl ricinoleate (1 eq.) + 3-azido-1-propanol (10 eq.) + TBD (0.1 eq.)).

Since for the synthesis of the amphiphiles, only azide-(mono)-ricinoleate (**6**) was targeted, we adapted the protocol of the transesterification reaction. The larger azide-(oligo)-ricinoleate

could also be exploited adding other values to the amphiphile. However, this strategy was not further pursued during this work. After step 1, the obtained mixture was next separated from the catalyst TBD (by washing with water) to prevent the oligomerization during the following distillation of the alcohol (**4**). Since we observed already a small percentage of auto-condensation during step 1, we could not completely prevent the formation of some ricinoleate-dimers, leading to a final product of azide-(mono)-ricinoleate, containing 5 % dimers (Figure **11**). Furthermore, the polarity of both compounds was very similar, hampering their separation by column-chromatography.

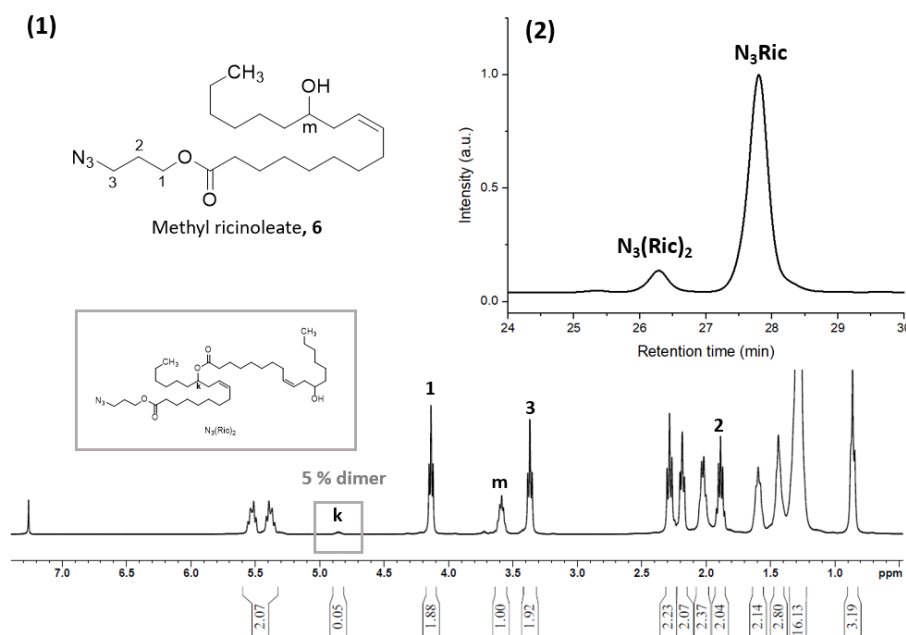
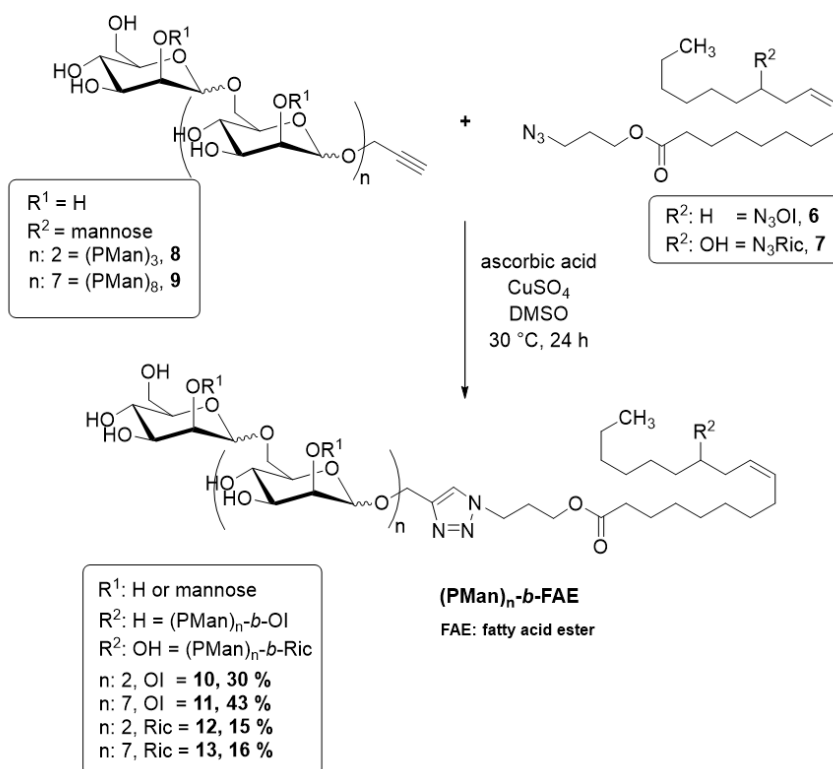


Figure 11. (1) ¹H-NMR spectrum of isolated 3-azido-1-propyl ricinoleate (**6**) with 5 % azide-diclinoleate and (2) corresponding SEC (measured against polystyrene standard in THF at 40 °C) traces.

2.2 Huisgen Click reaction

The just described fatty acid ester (FAE) derivatives were then coupled to the oligomannosides of Chapter 2 by Click Chemistry (Scheme **3**). We chose DMSO as reaction solvent, since it dissolves properly the hydrophilic and the hydrophobic segments as well as the resulting amphiphile. As catalytic system, CuSO₄/sodium ascorbate was selected following a previously reported protocol.^[2] The amount of all compounds was 1 eq. to each other, besides for the fatty acid ester, where a slight excess of 1.2 eq. was utilized. Thereby, the excess of FAE could be easily separated by precipitation of the amphiphiles in ethyl acetate (EtOAc). Copper was removed from the product with Cuprisorb, a well-known powerful specific absorbant for this metal.^[11] The final purification was then carried out by dialysis against pure water to remove sodium ascorbate.



Scheme 3. Cu(I) catalyzed azide-alkyne Huisgen cycloaddition between oligo-mannosides (**8, 9**) and fatty acid ester (**6, 7**) to give amphiphiles **10 - 13**.

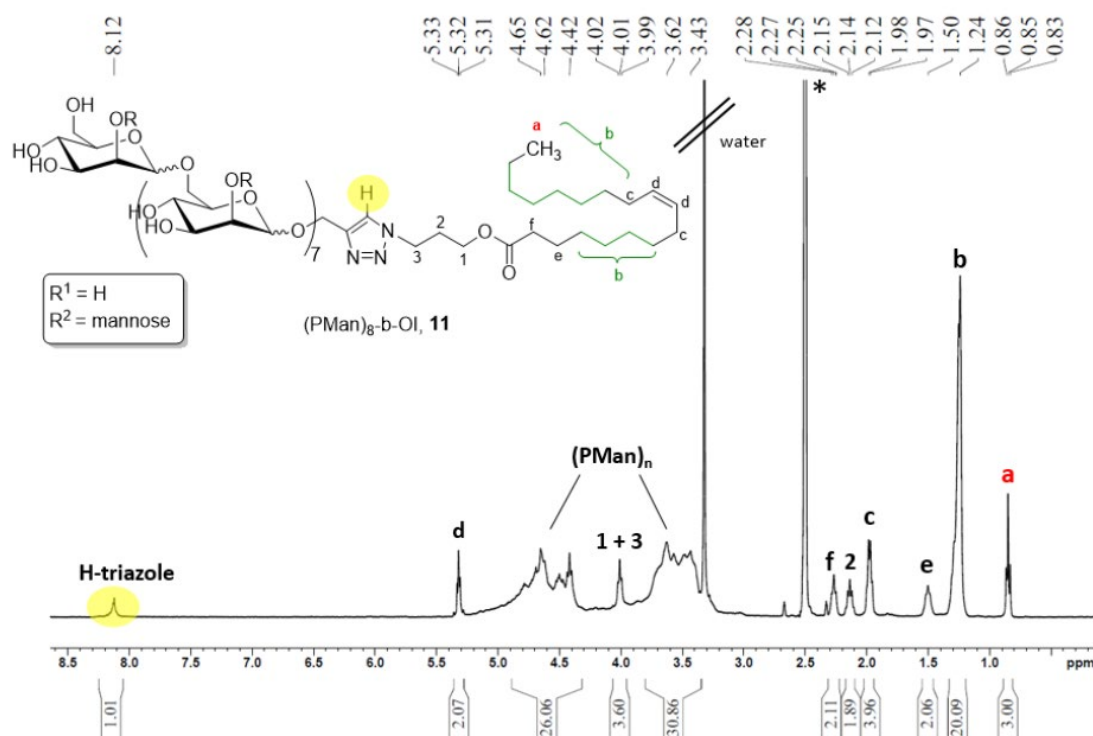


Figure 12. $^1\text{H-NMR}$ (400 MHz, DMSO-d_6) spectrum of amphiphile $(\text{PMan})_8\text{-b-OI}$ (**11**) after cyclo-Huisgen click reaction.

The $^1\text{H-NMR}$ spectra (Figure 12) of the obtained amphiphiles supported their structure with the appearance of the characteristic peaks of FAE at 0.8 - 5.3 ppm, oligo-mannosides at 3.4 -

5 ppm and the triazole peak at 8.1 ppm. The comparison of the proton spectra of the fatty acid ester derivatives and the oligomannosides in DMSO-d₆ enabled the complete assignment of each peak (spectra can be found in the experimental section). The calibration of the alkyl protons (a) confirmed the proposed structure with the integral of the triazole peak being 1, respectively. Moreover, the total number of protons from the signals of the oligosaccharides (3.43 - 3.62 ppm + 4.42 - 4.65 ppm) with $H = 56$, were identical to the initial oligomers prior to click reaction. We concluded, that there was no depolymerization during the cycloaddition of the sugar segments.

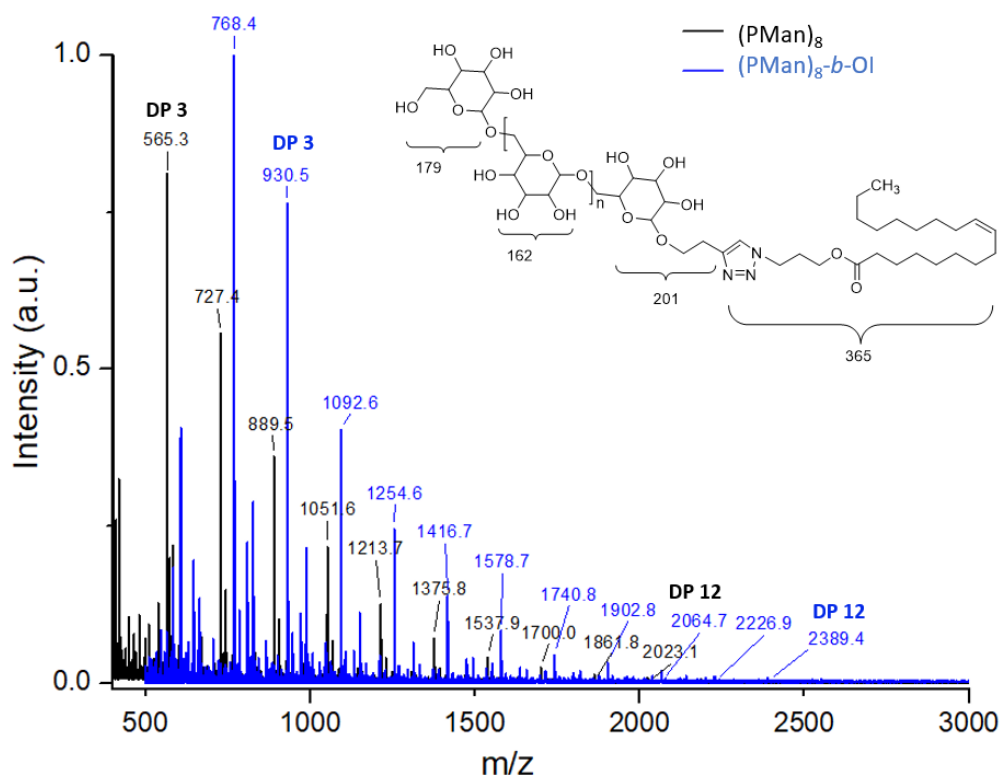


Figure 13. Plot of overlaid MALDI-TOF spectra of mannose-oligosaccharides $(PMan)_8$ (black plot) and amphiphile $(PMan)_8$ -*b*-OI (blue plot) after click reaction as $[M-Na]^+$ signals.

To further support this claim, MALDI-TOF spectroscopy was carried out (Figure 13). The overlay of the mass spectra of $(PMan)_8$ (black) before and $(PMan)_8$ -*b*-OI (blue) after click reaction, could show a clear shift in the molar mass. The series of the amphiphiles denoted a m/z higher than *ca.* 365 *u* compared to the mannose-oligomers, which corresponds to one azide-propyl oleate molecule. Together with the theoretical calculation of m/z , the successful click reaction between PMan and N₃OI was confirmed. As the series of $(PMan)_8$ -*b*-OI showed likewise the initial sugars DP up to 12, we proved that there was no depolymerization during the click reaction.

The Huisgen-cycloaddition, as demonstrated for the four selected amphiphiles (Scheme 3) was carried out at 30 °C for 24 h. A first experiment with mono equivalent amounts of FAE and $(PMan)_n$ could show, that the time was sufficient for a complete conversion of the fatty acid

with the disappearance of the N_3 vibration bond (2096 cm^{-1}) in the infrared spectrum (Figure 14).

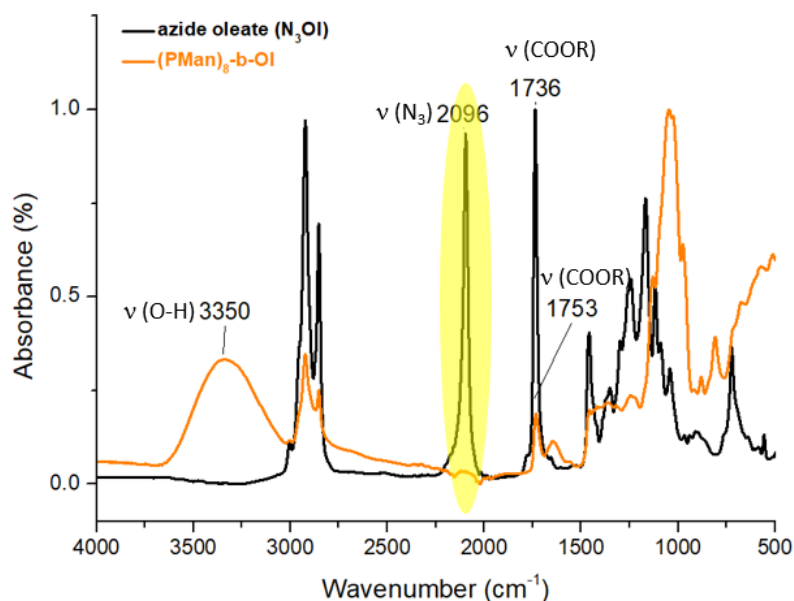


Figure 14. Plot of overlaid ATR-IR spectra of azide oleate (black) and amphiphile $(PMan)_8-b-OI$ (orange) after Click reaction with mono equivalent amounts of N_3OI and $(PMan)_8$.

For the reasons of purification, we increased the amount of fatty acid to 1.2 in the following experiments. The poor yield between 15 and 43 % was probably due to the final step of dialysis. The relatively low molar mass of the amphiphiles of 909 g/mol up to 1735 g/mol was susceptible to pass through the dialysis membrane. Different approaches were attempted to improve the yield, including the change of the solvent system, catalyst, reaction temperature and work-up procedure. However, the main hurdle presented the amphiphilic character of our product, which made it difficult to find a proper solvent for a precipitation or a washing procedure. The utilized excess of FAE allowed the simple removal of the latter with ethyl acetate, whereas the ascorbic acid remained still in the product. In order to avoid the dialysis step, ascorbic acid was tried to be removed through gel permeation separations using bio-bead column. These columns are composed of a porous styrenedivinylbenzene network. Small molecules of ascorbic acid should interact and dilute later as the larger mannose-derived amphiphile, affording a separation due to their sizes. Here, we changed the solvent to DMF, increased the temperature to $40\text{ }^{\circ}C$ and the reaction time to 48 - 84 h. The final product was obtained in up to 55 % yield, while DMF could only be completely removed after drying of the polymer under vacuum at $60\text{ }^{\circ}C$ for 2 - 3 d, or co-distillation with toluene. Altogether, the slightly improvement of the overall yield could not counterbalance the significant drawbacks of the high costs of the beads, the high temperatures and duration of the reaction and the low-volatile solvent. Therefore, the amphiphiles were prepared following the previous protocol in the following experiments.

The selective $^1\text{H-NMR}$ analysis of the sugar derivatives in D_2O and in CDCl_3 could give an initial insight into their amphiphilic nature. In D_2O (Figure 15, (1)), mainly the signals belonging to $(\text{PMan})_n$ are resolved, whereas in CDCl_3 (Figure 15, (2)), only the signals corresponding to the fatty esters are visible, respectively.

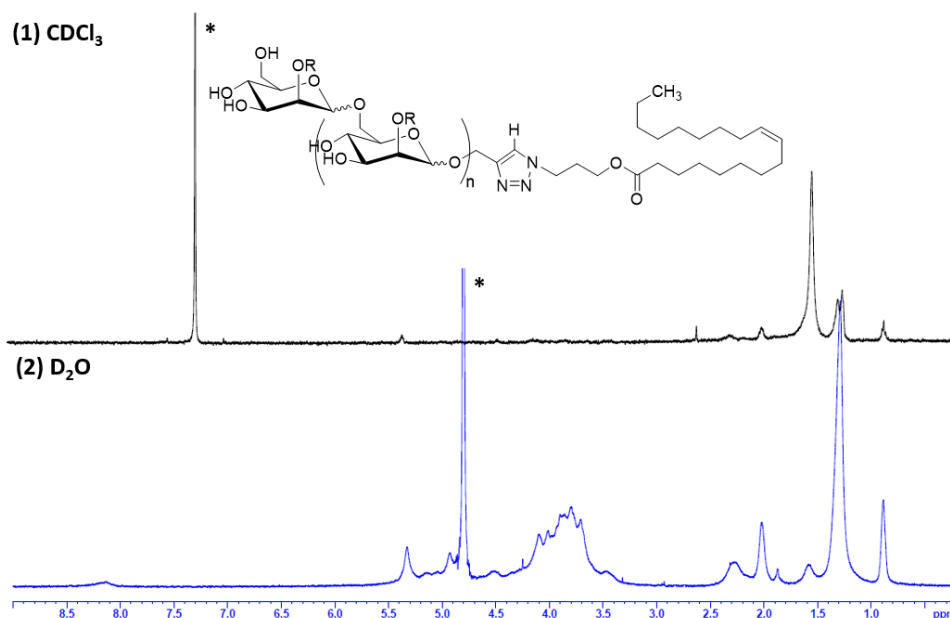


Figure 15. $^1\text{H-NMR}$ (400 MHz) spectra of the prepared sugar amphiphile in (1) deuterated chloroform and (2) deuterated water, resolving different domains of the compound.

The resulting self-assembly process and the surface properties of the amphiphiles are discussed in the following chapter. In order to obtain systematically comparable data to maintain structure-property trends, we prepared a library of amphiphiles (Table 2) with small ($\overline{DP}_n = 3$) and large ($\overline{DP}_n = 8$) sugar head groups, coupled each either with oleate or ricinoleate moiety. Moreover, the synthesized alkyne end-functional cellulose-oligosaccharide (COS-PGA) from chapter II B) were coupled with oleate ester to prepare glucose-based amphiphiles. The same protocol as for the mannose-oligomers was therefore followed and the obtained spectra and analytical characterizations are given in the experimental section. The larger azide-(oligo)-ricinoleate esters (7), however, were not used during this thesis due to the increased complexity of the amphiphilic system.

Table 2. Library of amphiphiles for the self-assembly study.

Number	Compound	\overline{M}_n (g/mol)	\overline{M}_n (g/mol)	\overline{D} ($\overline{M}_w/\overline{M}_n$)
		(NMR)	(SEC)	(SEC)
10	$(\text{PMan})_3$ - <i>b</i> -OI	909	479	1.6
11	$(\text{PMan})_8$ - <i>b</i> -OI	1719	598	1.6
12	$(\text{PMan})_3$ - <i>b</i> -Ric	924	678	1.3
13	$(\text{PMan})_8$ - <i>b</i> -Ric	1735	798	1.3

* measured against dextran-standard in DMSO at 80 °C.

3 Self-assembly

The four sugar-based amphiphiles (Table 2) were dissolved in distilled water and their interfacial behavior, colloidal properties and self-assembled structures were studied and described in the following.

3.1 Critical aggregation concentration (CAC)

When amphiphilic molecules, such as sugar-based surfactants, are dissolved in water, they show usually two specific behaviors: (1) adsorption at the interface and (2) self-aggregation. At very low concentration, the surface tension of the aqueous solution is close to that of pure water, but starts to reduce with increasing surfactant concentration. This behavior is generally analyzed by representing the evolution of the surface tension as a function of the natural logarithm of the concentration ($\ln C$). With further increase of the surfactant concentration, a critical limit is reached, where the surface tension remains almost constant, even though further surfactants are added. This point is called the critical aggregation concentration (CAC) and critical micelle concentration, CMC, when the formed aggregates are mainly micelles.^[12] We applied two different techniques in order to calculate the CAC of our sugar-based amphiphiles, namely the pendant drop method (PD) and the isothermal titration calorimetry (ITC).

3.1.1 Tensiometry: Pendant Drop (PD)

The pendant drop is one of the most robust and versatile method to measure surface and interfacial tension, consisting only of a fluid droplet suspended from a needle. The shape of an axisymmetric pendant drop, deformed by gravity, is thereby directly associated with the interfacial tension and fitted by the Young-Laplace equation (see experimental for more details). The latter relates the gravitational deformation of the droplet with the restorative interfacial tension γ . During the measurement, higher concentrations of the surfactant are subsequently added, more molecules are placed at the air/water interface and thus, γ decreases. Once the interface is completely saturated, new added amphiphiles aggregate in the bulk of the solution, maintaining the γ stable. The CAC is thus measured by plotting the decrease in surface tension against the concentration ($\ln C$), as shown in Figure 16. Here, the exemplarily curve is illustrated for sugar derivate (PMan)_s-*b*-OI, while the experiments of the other three amphiphiles are given in the appendix. From the obtained data, not only the CAC, but also other relevant physical and thermodynamic parameters can be deduced. The aggregation Gibbs energy (ΔG°) can be determined using the value of the CAC with $\Delta G^\circ = -RT * \ln CAC$ and subsequently A_{min} , the area per molecule at the air/water, with the following equation:

$$A_{min} = 1/(N_A * \Gamma) \quad (2)$$

Here, Γ is the surface excess $\Gamma = -\left(\frac{1}{RT}\right)\left(\frac{\delta\gamma}{\delta\ln C}\right)$ and N_A the Avogadro number. Γ indicates the relative amount of surfactant adsorbed at the interface, while A_{min} defines the minimum surface area, that is occupied by the latter (in two dimension). Consequently, a **lower** A_{min} indicates a **higher** adsorption of the surfactant molecules at the interface, reducing the interfacial tension (γ).

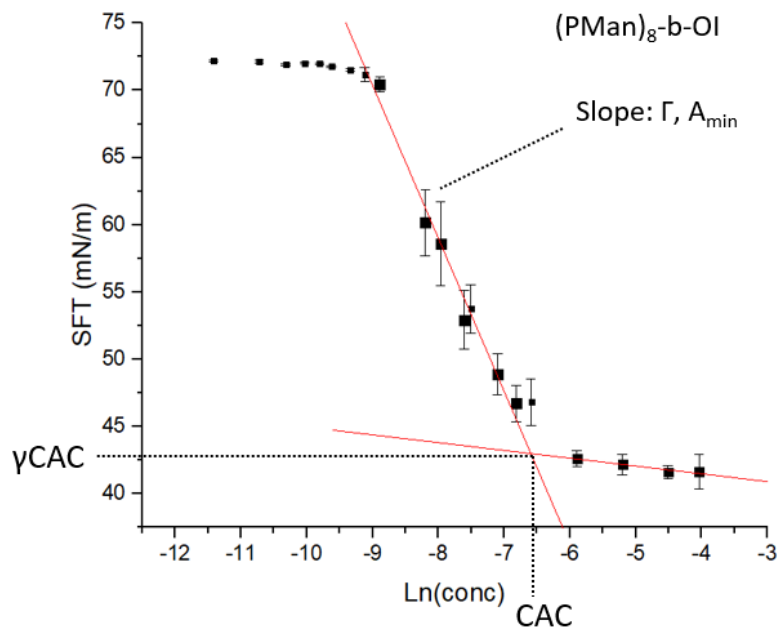


Figure 16. Plot of the surface tension against the concentration for $(PMan)_8-b-OI$.

Table 3. Surface tension data of the sugar derivatives obtained by pendant drop technique.

Structure	M_n (g/mol) (NMR)	HLB	CAC (mg/mL)	CAC (mM)	γ_{CAC} (mN/m)	ΔG° (kJ)	A_{min} (\AA^2)
$(PMan)_3-b-OI$	909	11.94	1.24	1.37	43.0	-16.1	35.6
$(PMan)_8-b-OI$	1719	15.75	0.99	0.58	48.4	-18.2	45.0
$(PMan)_3-b-Ric$	924	11.74	0.51	0.55	39.7	-18.3	48.5
$(PMan)_8-b-Ric$	1735	15.60	0.29	0.17	44.0	-21.1	62.4

With the data obtained from the pendant drop experiment (Table 3), some structure-property trends for the mannose-based amphiphiles could be postulated. Remarkable differences were observed according to the sugar degree of polymerization (\overline{DP}_n , size of the polar head group) and the presence of the hydroxyl group (OH) in the hydrophobic chain (in the case of ricinoleate).

Effect of the polar head group

Determine structure-property trends of sugar-based surfactants remains a very challenging enterprise. Due to the large structural diversity of the sugar components, there are less systematic studies available compared to other surfactants. Consequently, this is limiting the

access to general predictions. Nevertheless, Gaudin *et al.*^[12] proposed some ‘general trends’, collecting information of a large database of 659 sugar-based surfactants with 2626 property values. In their review (published in 2019) they claimed, that the influence of the polar head group of the sugar depends mainly on their size (\overline{DP}_n), the nature of the linker and the stereochemistry of the anomeric carbon. Usually, the increase of the polar region of a surfactant promotes the formation of hydrogen bonding with water and therefore a higher stabilization in the bulk media. The formation of aggregates by self-assembly is thus not favored, affording larger CAC values.^[13] For sugar derivatives, however, the situation is more complex, while most of the obtained interfacial behavior regarding micelle-formation was related to the steric hindrance of the bulky polar head.^[14] The size of the sugar was defined by different parameters such as (1) the type (pentose vs. hexose), (2) the number of repeating units (\overline{DP}_n) and (3) the degree of branching. Gaudin *et al.* reported a slight increase of the CAC with increasing size of the polar sugar head. The oligosaccharide head was supposed to disturb the micelle formation due to steric hindrance and higher hydrophilicity. However, other studies showed that this was not always the case, supported by systems for which a small \overline{DP}_n increase had either no impact, or even decreased the CAC.^[15] It was therefore suggested, that some sugar head groups may adapt favorable packing in the micelles, stabilized by H-bonding that thus compensated the additional steric hindrance. The interactions between the sugar molecules were claimed to be stronger and/or favored over the interactions with water.

In contrast, the surface tension at CAC (γ CAC) increased with higher numbers of sugars, a behavior in agreement with the general knowledge about sugar-based surfactants^[14]. Rosen^[14] explained this observation with the increased steric hindrance of larger polar sugar heads. The oligosaccharides occupy a larger area at the surface, leaving less space for the alkyl chains, so that the latter are less adsorbed at the air/water interface. Accordingly, γ CAC increases with larger polar head groups. Altogether, the CAC was claimed to be mainly influenced by the polarity of the sugar head, whereas for the γ CAC, the size of the sugar head (steric effects) was claimed to be decisive factor.

Table 4. General structure-property trends of sugar-based surfactants according to the literature (adapted by^[12]).

	Alkyl chain			Sugar
	length	branching	unsaturation	size
CAC	↓	↑	↑	↑
γ CAC	↓	↑	↑	↑

The data obtained during the pendant drop experiment showed, that the long chain polar head amphiphiles (PMan)_s-*b*-OI and (PMan)_s-*b*-Ric denoted a lower CAC (0.58 and 0.17 mM, respectively), compared to their short chain counterparts (PMan)₃-*b*-OI (1.37 mM) and (PMan)₃-*b*-Ric (0.55 mM). This atypical behavior was attributed to a stronger and preferred interaction among the mannose chains than with the surrounding water. The increase in number of mannose groups enhanced the interactions among them via H bonding. Thus, the

self-assembly process was promoted and the CAC decreased, respectively. The structural elucidation of our amphiphiles in the previous chapter showed that they consist of a linear chain of α -(1,6) linked mannose units with branching at the OH-2 position. Figure 17 shows a proposal of the inter and intra-molecular H-bonding. Note that the depicted H-bondings are hypotheses that would need analytical confirmation.

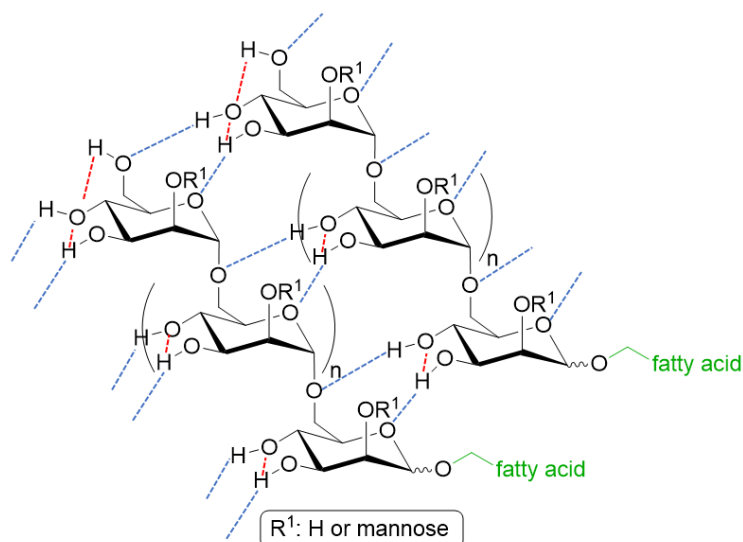


Figure 17. Proposed interactions between the mannose chains of the amphiphiles with intermolecular (blue) and intramolecular (red) H-bonding.

A direct increase in the surface tension at the CAC (γ_{CAC}) was also observed for longer PMan sugars (from 43.0 mN/m to 48.4 mN/m for oleate- and 39.7 mN/m to 44.0 mN/m for ricinoleate derivative, respectively). This behavior is in line with what is generally observed and reported in surfactants and more specifically in sugar-based ones.^[12] Bigger polar heads need more space at the air/water interface, leading to a decrease in the hydrophobic chain stacking and so their interfacial activity. Same packaging information could be obtained by analyzing the area per molecule (A_{min}) values. (PMan)₈ amphiphile denoted higher areas than (PMan)₃ derivatives at the air/water interface. While (PMan)₈-*b*-OI and (PMan)₈-*b*-Ric A_{min} values were *ca.* 45.0 and 62.4 Å², (PMan)₃-*b*-OI and (PMan)₃-*b*-Ric A_{min} decreased to *ca.* 35.6 and 48.5 Å², respectively. Note that sugar PDI values of *ca.* 2 make it impossible to analyze these A_{mins} as an absolute number, but as a general trend.

Finally, negative Gibbs free energy (ΔG°) values showed the thermodynamic favorable formation of self-assembled structures for all amphiphiles. Lower ΔG° values were observed for higher \overline{DP}_n polar derivatives ($\Delta G^\circ_{(PMan)8-b-OI} = -18.2$ kJ/mol, $\Delta G^\circ_{(PMan)8-b-Ric} = -21.1$ kJ/mol), compared to lower \overline{DP}_n ones ($\Delta G^\circ_{(PMan)3-b-OI} = -16.1$ kJ/mol, $\Delta G^\circ_{(PMan)3-b-Ric} = -18.2$ kJ/mol). This result supported the stabilizing effect of the H bonding between the mannose units that can compensate the additional sterical hindrance in the case of the larger polar head amphiphiles.

Effect of hydroxyl group (OH) in the hydrophobic tail

In the majority of the reported data of structure-property analysis of sugar based-surfactants^[12, 14], the main influence on the interfacial behavior is assigned to the hydrophobic alkyl chain. Table 4 summarizes the ‘general trends’ related to the length, branching and unsaturation of the alkyl chain to the critical aggregation concentration and the respective tension (CAC, γ CAC). For longer alky chains, an exponential decrease of the CAC was denoted, assigned to the entropy loss induced by water structuring around the chains (hydrophobic effect)^[16] that leads to a positive Gibbs energy. The formation of aggregates (micelles) is therefore thermodynamically advantageous to avoid the unfavorable water structuring. The phenomenon of chain entanglement (coiling) leads to the opposite behavior, however, remaining only to exceptions. The surface tension γ CAC decreases with increasing alkyl chain, since the surface, once saturated, is proposed to be more nonpolar due to a higher adsorption of the alkyl chains at the air/water interface.^[17] The branching in the alkyl chain is generally attributed to an increase in the CAC due to the unfavorable packing of the alkyl chains (into micelles). Note that thereby, the affinity for the surface was not affected, meaning that the γ CAC can be decreased more efficiently, even if the CAC is higher.^[18] In the case of an unsaturated double bond, as for oleyl chains (like in our structures), an increase in the CAC was observed. This observation was explained with the *cis*-character of the double bond, that leads to a non-linear, sterical more demanding and rigid alkyl chain, which is less easy to be packed in a micelle.^[14]

It is known that for simple saturated alkyl chains, the presence of OH disrupts the molecule packaging at the air/water interface due to the resulting steric hindrance. Moreover, the far away it is placed from the polar head group, the higher the A_{min} will be affected at low/mid interfacial pressure.^[15b] During the analysis of the four mannose-derived amphiphiles, we observed a clear decline in the A_{min} by the addition of a OH group. (PMan)₈-*b*-OI A_{min} denoted an A_{min} of *ca.* 48.4 Å² and increased to *ca.* 62.4 Å² for (PMan)₈-*b*-Ric. Same for (PMan)₃-*b*-OI, with A_{min} of *ca.* 35.6 Å², that raised to A_{min} of *ca.* 48.5 Å² for its counterpart (PMan)₃-*b*-Ric. Lower CAC and ΔG° results supported the faster self-assembly at the interface of (PMan)₃-*b*-Ric and (PMan)₈-*b*-Ric amphiphiles compared to their non-hydroxyl counterparts. (PMan)₃-*b*-OI (CAC = 1.37 mM, ΔG° = -16.1 kJ) and (PMan)₈-*b*-OI (CAC = 0.58 mM, ΔG° = -18.2 kJ) values decreased to (PMan)₃-*b*-Ric (CAC = 0.55 mM, ΔG° = -18.3 kJ) and (PMan)₈-*b*-OI (CAC = 0.17 mM, ΔG° = -21.1 kJ) ones, denoting their more thermodynamically favorable formation. On the basis of these results, we supposed the formation of H bonds between the OH group of the ricinoleate tail (Figure 18), explaining their increased stability.

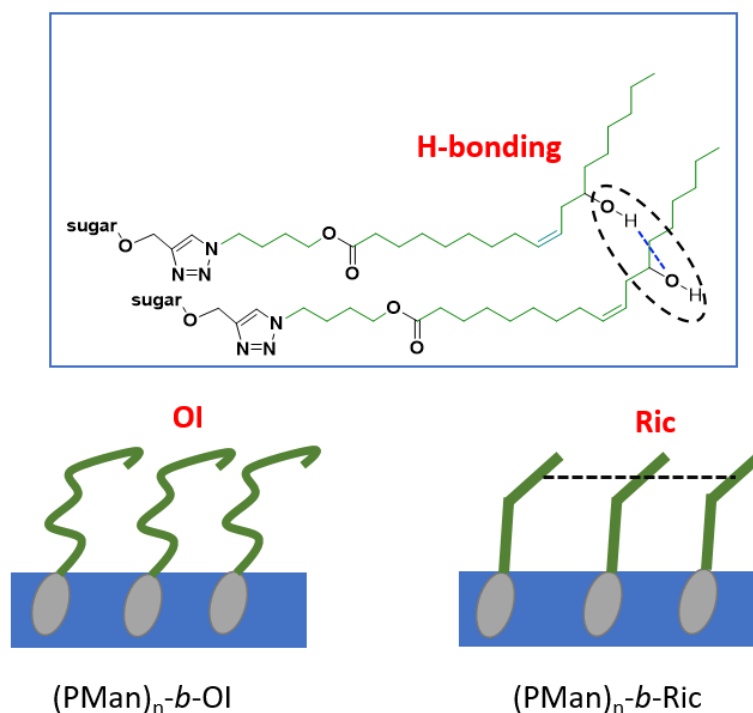


Figure 18. Schematic illustration of the oleate- (left) and ricinoleate (right) issued amphiphiles showing the proposed H-bonding between the OH group in the lipid tail of ricinoleate.

Altogether, the mannose-derived amphiphiles denoted surfactant properties according to the study at the air/water interface. A large polar head group ($\overline{DP}_n = 8$) favored the self-assembly process and the amphiphiles denoted lower CAC values than their smaller counterparts ($\overline{DP}_n = 3$). In contrast to what is expected for an increasing polar region, the H bonding among the mannose units was assumed to be stronger than to the surrounding water molecules. The final sugar self-assembled structures compensated the additional sterical hindrance and showed thermodynamically favorable systems. The obtained values for A_{min} and γ_{CAC} further supported the influence of the larger sugar head, that occupied more space at the air/water interface than the smaller derivatives, reducing the surface tension in a larger extend. The OH group at the hydrophobic region of the ricinoleate tail led to an increase in A_{min} and favored the self-assembly process. This was assumed to be due to the formation of H bonds between the OH group in the lipid tail. The collected structure-property trends are again summarized in Table 5.

Table 5. Summary of the obtained structure-property trends of the (PMan)_n-derived amphiphiles.

	higher \overline{DP}_n	+ OH
CAC	↓	↓
γ_{CA}	↑	↓
C		
A_{min}	↑	↑
ΔG^0	↓	↓

3.1.2 Isothermal Titration Calorimetry (ITC)

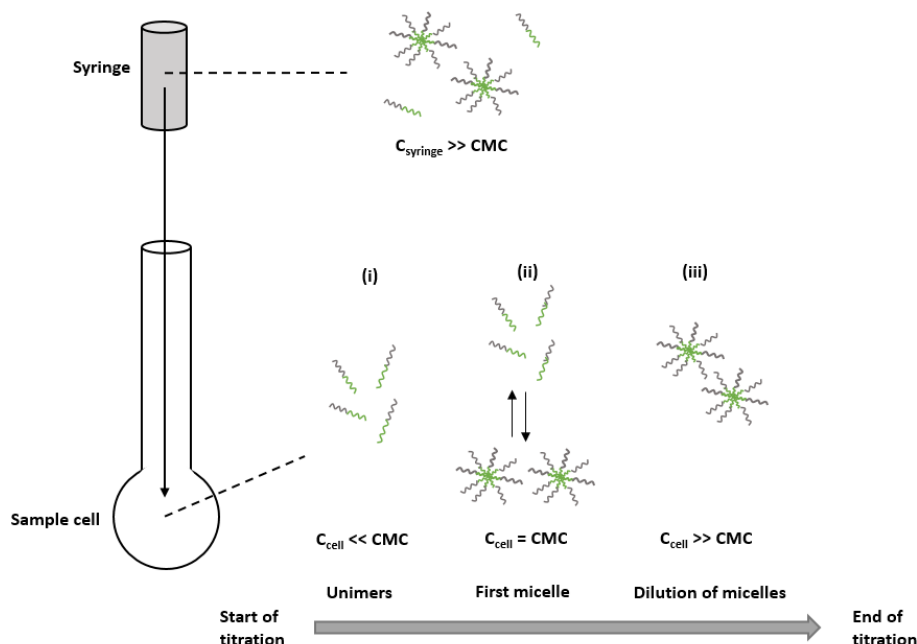


Figure 19. Schema of a typical ITC experiment (adapted from Bouchemal *et al.*, 2009)^[19]

Isothermal Titration Calorimetry (ITC) is a differential scanning calorimetry method to characterize the self-assembling process of surfactants into micelles in solution. During the experiment, small volumes of a micellar solution are consecutive injected into a sample cell containing pure water (isothermal titration), while the released heat during the dilution is detected and plotted. The heat flow is then integrated and plotted as the change of enthalpy ΔH_{mic} with respect to the temperature T . From these data, the thermodynamic parameters such as the free Gibbs Energy of micellization ΔG_{mic} , its Entropy ΔS_{mic} and the micellar aggregation number can be calculated. It is hence a method to determine the kinetic of the micellization process. Basically, the break of the micelles ('demicellation') is releasing the heat that is measured during the experiment until the CMC is reached. At that point, further addition of micellar solution led no longer to their break and the heat flow gets constant (Figure 19).

The enthalphograms (= thermograms) obtained by ITC can have various shapes. When a sigmoidal curve is obtained, the latter can be divided in three concentration regimes (indicated in Figure 19 by (i), (ii) and (iii)), while the CMC is determined by the maximum of the first derivate of the curve (Figure 20).

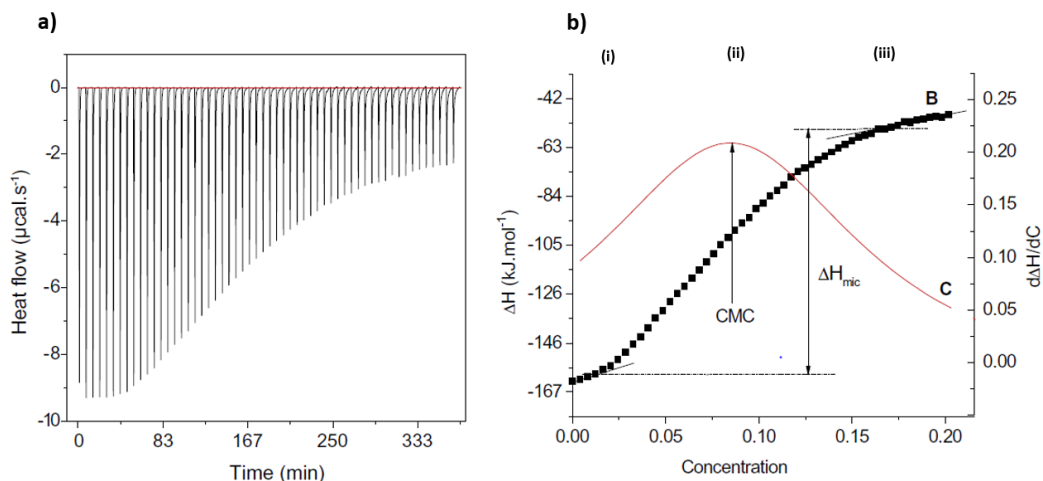


Figure 20. Typical data obtained from a ITC measurement, **a)** experimental curve of the released heat **b)** integrated heat data giving a sigmoidal micellization curve. (i) = heat generated by the dilution of the unimers, (ii) heat correspond directly to the enthalpy of the micellization, (iii) heat corresponds to the enthalpy of micelle dilution.^[19]

The enthalpy of the micellization process can then be calculated by the following equation

$$\Delta H_{(ii)} = \Delta H_{mic} = \Delta H_{observed} - \Delta H_{(i)} - \Delta H_{(iii)} \quad (3)$$

However, in some cases, the shape of the ITC curve shows not the ideal sigmoidal behavior and cannot be exploited in the same manner. Figure 21 shows an ITC curve, where no break in enthalpy versus concentration can be denoted and thus, the CMC can't be determined.

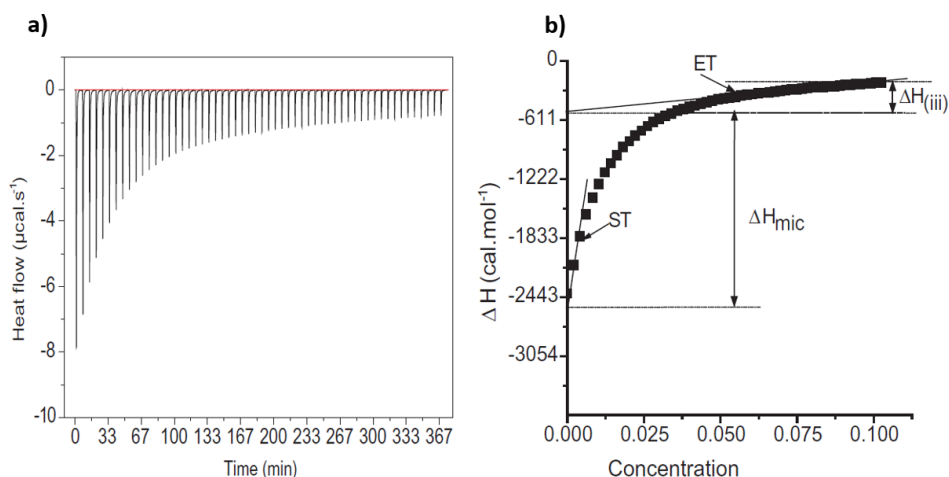


Figure 21. Typical data obtained from a ITC measurement in the case of a non-sigmoidal behavior; **a)** experimental curve of the released heat **b)** integrated heat data.^[19]

In the case of the non-sigmoidal ITC curve, the concentration from the start and end of the micellization process is calculated. Usually, a linear fit in the upper and lower concentration range is realized. The abscissa of the start- (ST) and the end (ET) of the transition are used to calculate ΔH_{mic} as shown in Figure 21.

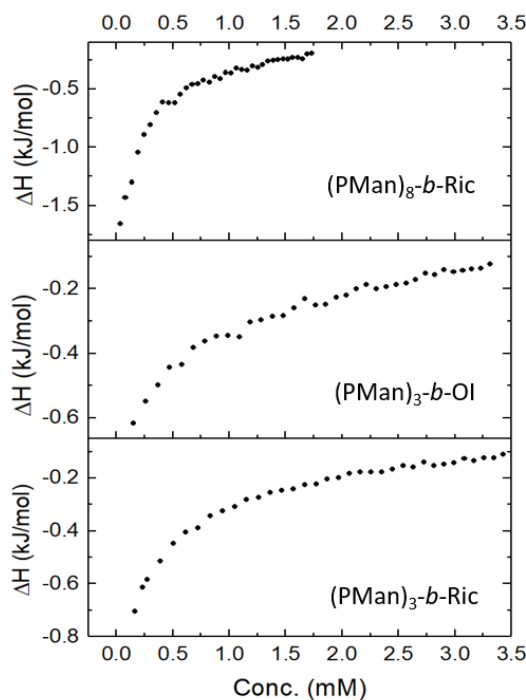


Figure 22. (PMan)₈-*b*-Ric, (PMan)₃-*b*-OI and (PMan)₃-*b*-Ric non-sigmoidal curves obtained from ITC measurements. (PMan)₈-*b*-OI is not shown due to high error/intensity ratios.

The ITC experiments of our sugar derivatives gave non-sigmoidal curves (Figure 22) and since we could not obtain values for very lower concentrations closer to the CMC, it was difficult to obtain proper information. The energy values could show, that the formation of the micelles was controlled by the enthalpy (exothermic), due to strong interaction between the sugar molecules (reminder: $\Delta G = \Delta H - T\Delta S$). This behavior was in line with the hypothesis made during the pendant drop experiment: the intermolecular interaction between the mannose chains was stronger than between mannose and water, favoring the formation of the micelles. Still, the absence of a developed data library from high \overline{DP}_n polysaccharide amphiphiles made it difficult to generalize this behavior. Further set of experiments with different structures and \overline{DP}_n are needed. Another strategy to exploit the ITC for a thermodynamic analysis of our amphiphiles might be a set of experiments at different temperatures. This method was described by Paula *et al.*^[20], who calculated the CMC from the resulting, temperature depending equation of van't Hoff $\Delta H_{mic}(T)$. However, these experiments could not be carried out during this thesis.

3.2 Direct Solubilization

Moving to their bulk study, using the Dynamic Light Scattering (DLS) technique, we observed how the sugar derivatives self-assembled in aqueous solution in different morphologies and sizes, depending on their molecular structure. We initiated the assembly process by the direct solubilization of the amphiphiles in an aqueous solution.

3.2.1 Dynamic light scattering (DLS)

For the direct solubilization, the amphiphiles were dissolved in ultrapure water and stirred at room temperature for 24 h. Then, the obtained solutions were filtrated to eliminate larger aggregates without losing a significant fraction of the sample, as attested by the minor change in scattered light intensity.

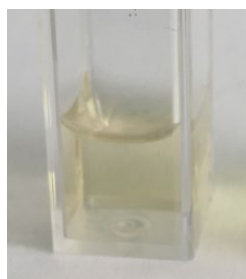


Figure 23. Obtained solution of the direct solubilization of $(\text{PMan})_8\text{-}b\text{-OI}$ (10 mg/mL).

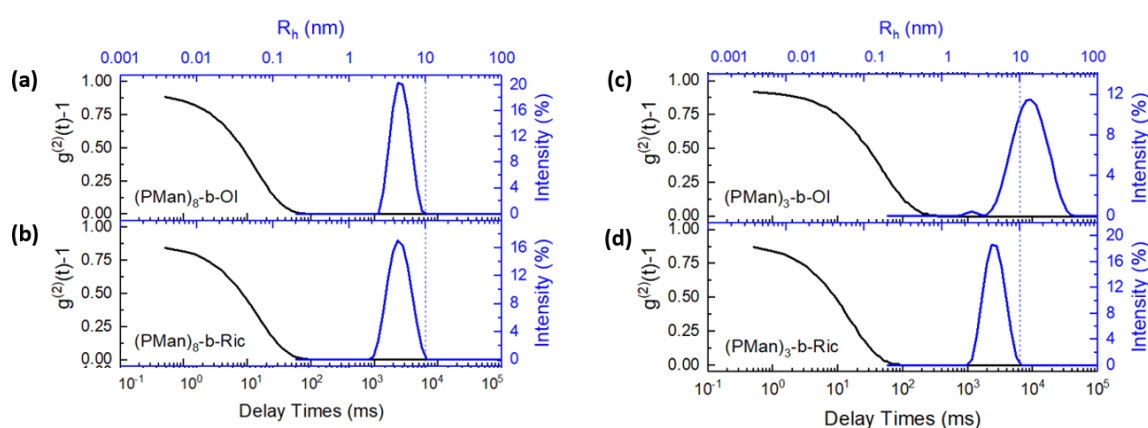


Figure 24. $(\text{PMan})_8\text{-}b\text{-OI}$ (a), $(\text{PMan})_8\text{-}b\text{-Ric}$ (b), $(\text{PMan})_3\text{-}b\text{-OI}$ (c) and $(\text{PMan})_8\text{-}b\text{-Ric}$ (d) DLS intensity autocorrelation (black) and size distribution (blue) function by Malvern at 173° (all samples were prepared in 10 mg/mL)

The obtained solutions (see above $(\text{PMan})_8\text{-}b\text{-OI}$ as illustrative example, Figure 23) were prepared at a concentration (10 mg/mL) far above the prior calculated CAC (Table 3) and showed a clear, transparent slightly yellowish colour. The analysis by light scattering at 173° (Malvern DLS, Figure 24) supported the formation of small, monodispersed systems with a hydrodynamic radius (R_h) of 4.6 nm and 4.3 nm with a polydispersity index (PDI) of 0.08 for the amphiphiles with large polar head groups $(\text{PMan})_8\text{-}b\text{-OI}$ and $(\text{PMan})_8\text{-}b\text{-Ric}$, respectively. Similar results were obtained for $(\text{PMan})_3\text{-}b\text{-Ric}$ with a slightly larger monomodal distribution of *ca.* 5.1 nm. These structures were tentatively attributed to spherical micelles, according to the theoretical packing parameters of the amphiphiles and size range. In all three cases, the polar head group volume was larger than the hydrophobic tail one, favoring the assembling of a spherical micelle, according to the high inherent molecular curvature. Smaller R_h values for $(\text{PMan})_8\text{-}b\text{-Ric}$ compared to its counterpart $(\text{PMan})_3\text{-}b\text{-Ric}$ suggested a more compacted sugar shell structure. This was in line with the previous assumed enhanced interactions among mannose *via* H bonding at the air/water interface.

A different behavior was observed for (PMan)₃-*b*-OI amphiphile, denoting self-assembled structures with a larger R_h of 13.5 nm and a PDI of 0.19. A deeper analysis of the obtained DLS spectra showed the formation of a second population with smaller sizes, albeit in small concentrations (Figure 24, c). Compared to (PMan)₃-*b*-Ric, the formation of larger (PMan)₃-*b*-OI structures could be explained by the absence of the hydroxyl group in the lipophilic tail, leading to a higher disorganized conformation in the core of the micelle. Such interpretations are in agreement with the previous 2D interfacial tensiometry, where the hydroxyl groups promoted their reorganization. H bonding interactions stabilize the core and promote more thermodynamically stable spherical micelles. Moreover, in line with Israelachvili packing parameter P (reminder $P = \frac{v_0}{(a_0 l_0)}$, with v_0 : volume of the tail, a_0 : head group area, l_0 : tail length), a decrease in the PMan polar head size as well as an increase in the volume of the hydrophobic tail due to its disorganization lead to higher P values. Higher P values are related to worm-like micelles, while smaller lead to spherical ones.^[21]

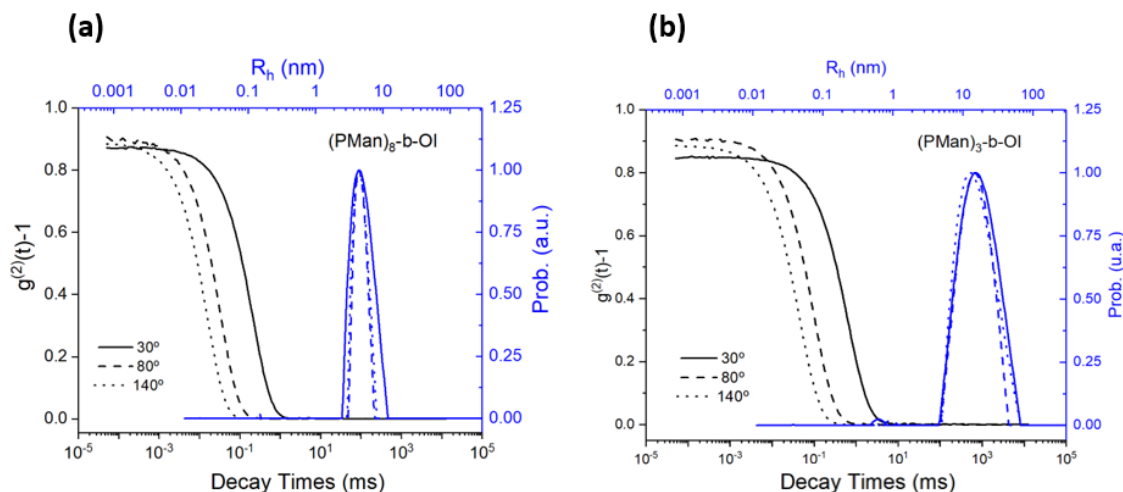


Figure 25. DLS intensity auto-correlation (black) and size distribution (blue) functions by ALV at high (dot line), mid (dash line) and low (solid line) angles of (a) (PMan)₈-*b*-OI and (b) (PMan)₃-*b*-OI.

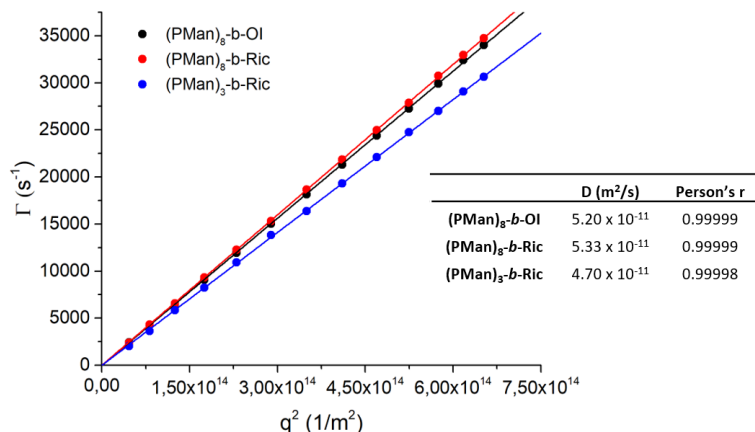


Figure 26. (PMan)₈-b-OI, (PMan)₈-b-Ric, (PMan)₃-b-OI and (PMan)₃-b-Ric ALV DLS cumulants coefficient Γ values obtained as a function of the square of the wave vector q^2 . Fitting values as final size distributions are also listed.

Multi-angle DLS experiments (using an ALV system) were carried out, measuring the scattered light at different angles from 30 to 150 °. Figure 25 shows the plot of the ALV DLS experiment for (PMan)₈-b-OI and (PMan)₃-b-OI as illustrative example (the spectra of the other amphiphiles are given in the appendix). In order to determine the exact hydrodynamic radius R_h from multi-angle DLS experiment, the measured normalized intensity of the second-order autocorrelation function $g^{(2)}(q, t)$ was related to the first-order function $g^{(1)}(q, t)$ through the Siegert relationship. The latter was then fitted using the Cumulant method, while the resulting cumulants coefficient Γ was directly related to the diffusion coefficient by the Fick relation. The cumulants coefficient Γ was then plotted as a function of the square of the wave vector q^2 (Figure 26), the slope of this plot denoted the diffusion coefficient D . From these plots, one can conclude that the scattering is purely diffusive, confirming the spherical shape of the nanoparticles, apart from (PMan)₃-b-OI for which two relaxation times are observed. Finally, the hydrodynamic radius R_h was calculated through the Stokes-Einstein equation using the determined D . The obtained values for the size of the aggregates at mono-angle (Malvern) were in line with the multi-angle ALV DLS ones and are summarized in Table 6.

Table 6. Size distribution of the sugar amphiphiles by Malvern- and ALV DLS experiments.

Sample	R_h (nm)	PDI	R_h (nm)
	(DLS, Malvern)	(DLS, Malvern)	(DLS, ALV)
(PMan) ₃ -b-OI	13.7	0.19	13.3
(PMan) ₈ -b-OI	4.6	0.08	4.7
(PMan) ₃ -b-Ric	5.1	0.07	5.2
(PMan) ₈ -b-Ric	4.3	0.08	4.6

Finally, time experiments were performed to follow the evolution and stability of the self-assembled structures during a time period of 15 days. Figure 27 shows the size-distribution in time of all the sugar derivatives synthesized. The times at 0, 7 and 15 days are noted in solid, dash and dot lines, respectively.

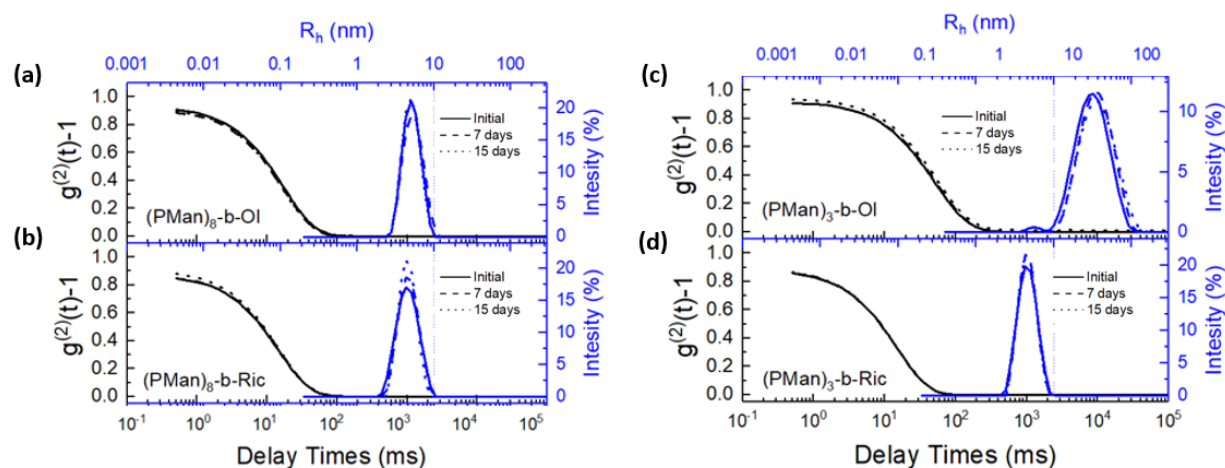


Figure 27. (PMan)₈-*b*-OI (a), (PMan)₈-*b*-Ric (b), (PMan)₃-*b*-OI (c) and (PMan)₃-*b*-Ric (d) DLS intensity autocorrelation (black) and size distribution (blue) function by Malvern at 173° in time (all samples were prepared in 10 mg/mL); 7 and 15-day stability times are denoted in solid, dash and dot lines, respectively.

For all samples, no change in the intensities was observed, confirming the stability of the self-assembled micelles. The repeating of the direct-solubilization process led to the same structures, further supporting their stability. We could conclude, that all the self-assembled structures formed by the direct solubilization process were thermodynamically stable and reproducible.

To obtain more in-depth information about the real shape of these structures, cryo-TEM images were measured, giving access to direct visualization of the self-assembled structures.

(PMan)₈-*b*-OI ($d_h = 9.22$ nm, DLS)

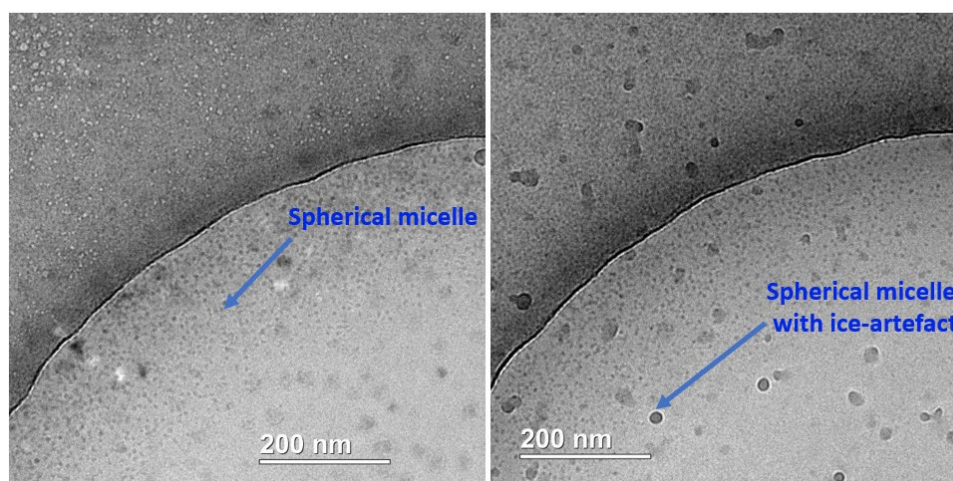
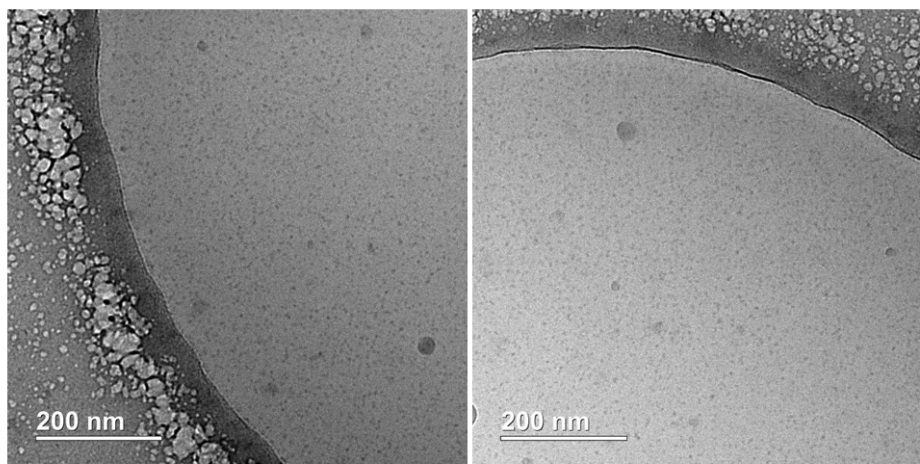
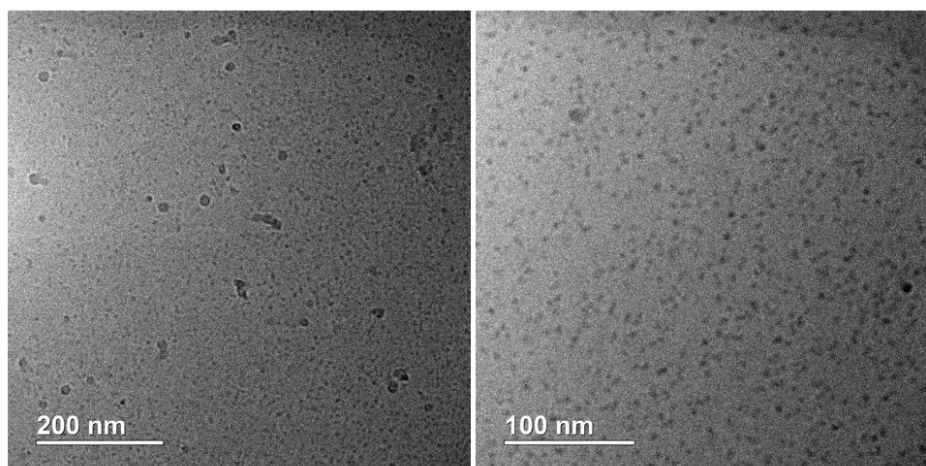


Figure 28. (PMan)₈-*b*-OI spherical micelle cryo-TEM images. Darker motives surrounded by a bright halo are ice aberrations produced during sample preparation. The value of the hydrodynamic diameter d_h given above the images was obtained by DLS.

(PMan)₈-*b*-Ric ($d_h = 8.65$ nm, DLS)Figure 29. (PMan)₈-*b*-Ric micelle cryo-TEM images.**(PMan)₃-*b*-Ric ($d_h = 9.14$ nm, DLS)**Figure 30. (PMan)₃-*b*-Ric micelle cryo-TEM images.

Micellar self-assembled structures were observed for (PMan)₈-*b*-OI (Figure 28), (PMan)₈-*b*-Ric (Figure 29) and (PMan)₃-*b*-Ric (Figure 30). The shape and the size range of the micelles in the cryo-TEM images were in agreement with the DLS results, supporting their structure. Note that the black dots surrounded by a bright halo are ice crystals produced during sample preparation and that the resolution could not be increased due to the small sizes of the aggregates. Previous measured transmission electron microscopy (TEM) experiment gave better resolved images. However, the sizes of the obtained structures were larger than in DLS experiments, arising from drying artefacts during sample preparation. The images are given in the appendix and not further discussed in this chapter.

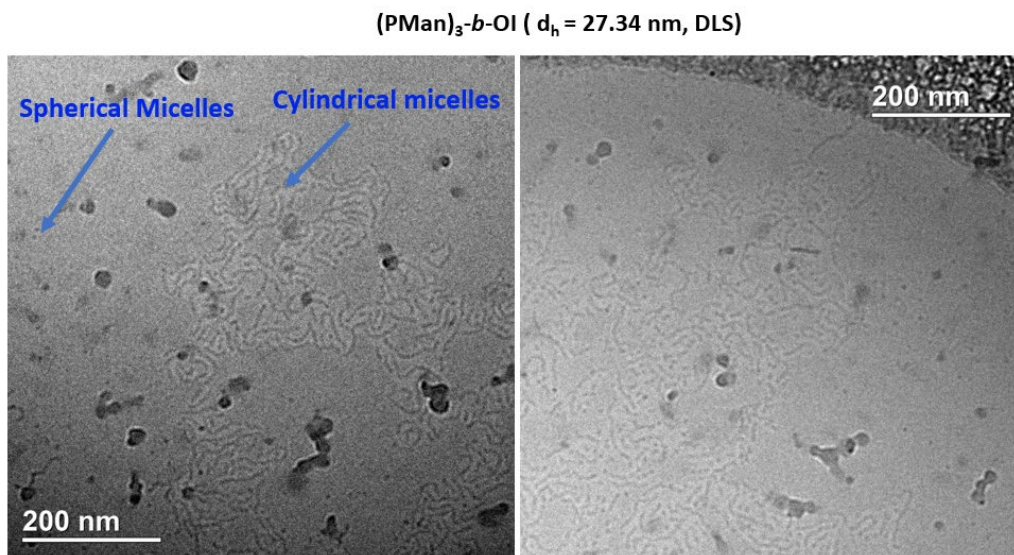


Figure 31. (PMan)₃-b-OI cryo-TEM images showing spherical and cylindrical micelles.

For the amphiphile (PMan)₃-b-OI, in contrast, the cryo-TEM images showed the self-assemble into clear flexible cylindrical structures, with the presence of a few small spherical micelles (Figure 31). The increased R_h and PDI during the DLS experiments could thus be explained by the formation of flexible cylindrical micelles with different lengths distribution. The measured wider length range was directly related to the variations at the R_h and thus the PDI. Usually, the spherical micelles are considered as the starting morphology, reported in various self-assembling processes in the literature.^[22] The cylindrical micelles could thereby be considered as the thermodynamic most stable structure, that is slowly formed from the spherical ones.

3.2.2 SAXS

In SAXS experiment, the size and shape of particles with typical dimensions in the range of 1-1000 nm can be determined. The measurement of small angle scattering of a well-collimated X-ray beam gives characteristic scattering curves for specific colloidal structures. The fitting of the experimental scattering curve with a model for the *assumed particle structure*, can finally denote the real structure. Figure 32 shows the plot of the scattering intensity $I(q)$ as a function of q for different types of structures. According to the Guinier law, the intensity at low q values is related to the radius of gyration R_g of the particles, whereas Fourier transformation of the integral over the scattering intensities taken over all values of the vector q , gives the particle distance distribution function (PDDF) $\rho(r)$.

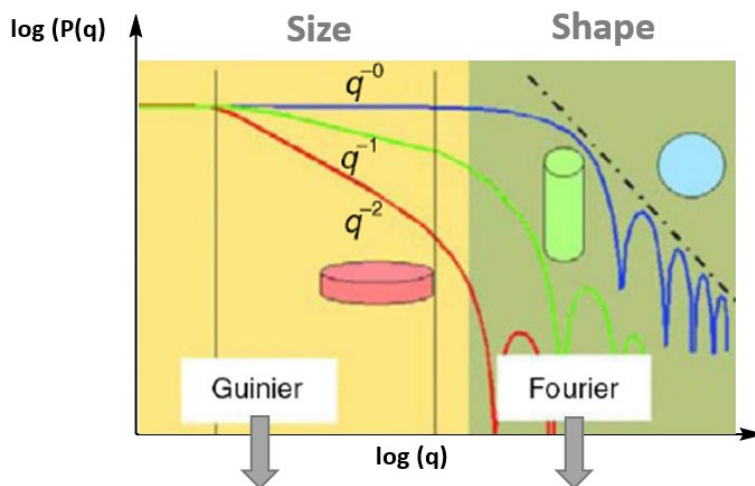


Figure 32. Reminder of the feasible information during SAXS experiments. The Guinier region gives the R_g and the Fourier region determines the pair distance distribution function (PDDF).^[23]

The experimental curves are adjusted with a theoretical scattering curve representing the form factor of the different structures in solution. The distance distribution function $\rho(r)$ is analyzed in the same manner, giving additional structural information due to the difference of the electron density of the core and shell region of the micelles. Furthermore, the relation between the hydrodynamic radius obtained prior by DLS and the radius of gyration R_g , is a well-known indicator for the architecture of the aggregate and can help to determine the structure.^[24]

Table 7. Structure prediction from the R_g/R_h ratio.

Structure	R_g/R_h
Spheres	0.77
Random coil	1.3
Rod like shape	2.33

The hydrodynamic radius R_h is defined as the radius of a hard sphere, that diffuses at the same rate as the molecule under observation. In solution, the latter is also interpreted as the ‘effective hydrated radius’, taking into account the apparent size due to the solvation. It can be referred to the Stokes radius of a polymer or a colloid, and is described by following equation

$$R_h = a = \frac{k_B T}{6\pi\eta D} \quad (4)$$

where k_B is the Boltzmann constant, η the liquid viscosity and D the diffusion constant. On the other hand, the radius of gyration R_g is defined as the root-mean-square distance of the polymer or particle parts from their center of mass. For nanoparticles, with R_g typically larger than 10 nm, the latter can be determined by multiangle light scattering. For smaller objects,

as it is the case for our sugar amphiphiles, R_g is preferably determined by small angle neutron scattering (SANS) or small angle x-ray scattering (SAXS).

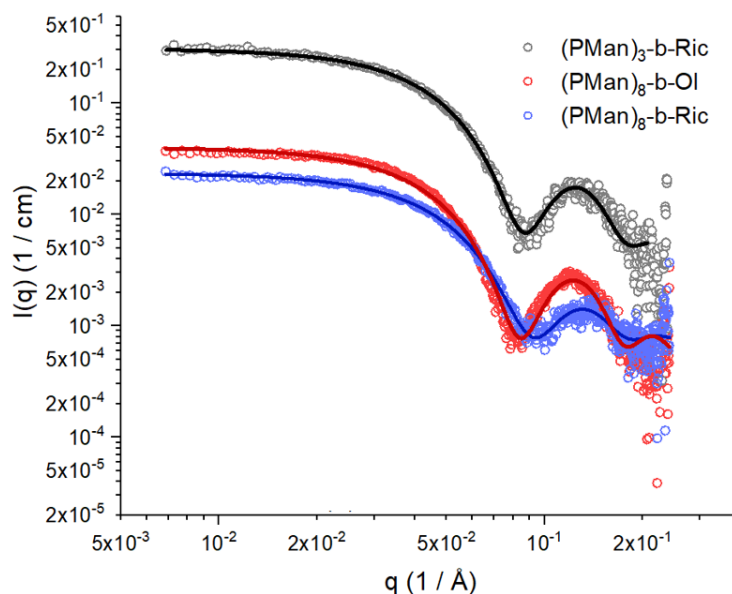


Figure 33. (PMan)₈-*b*-OI (red), (PMan)₈-*b*-Ric (blue) and (PMan)₃-*b*-Ric (black) small-angle X-ray scattering signal (dots) and their respective spherical core/shell fitting (solid line).

(PMan)₈-*b*-OI, (PMan)₈-*b*-Ric and (PMan)₃-*b*-Ric samples were analyzed by SAXS. The obtained experimental scattering curves (Figure 33) showed for all three compounds a similar trend, with a plateau of the scattered intensity $I(q)$ in the low q regime, followed by a decrease of $I(q)$ and an oscillation in the medium q region. The larger intensity of (PMan)₃-*b*-Ric compared to (PMan)₈-*b*-Ric and (PMan)₈-*b*-OI, was tentatively attributed to the difference in concentration of the samples during the experiments. From these experimental curves, we determined the R_g of our micelles in the low q regime according to the Guinier Law:

$$\ln I(q) = \ln I(0) - q^2 R_g^{2/3} \quad (5)$$

We then plotted $\ln I(q)$ as a function of q^2 in the low q region ($q_{max} < 1.3 \times R_g$) from which R_g was obtained from the slope of the obtained curve (Figure 34). We denoted R_g of 3.60 nm, 3.42 nm and 3.86 nm for (PMan)₈-*b*-OI, (PMan)₈-*b*-Ric and (PMan)₃-*b*-Ric, respectively. The R_g/R_h ratio was then determined and provided additional structural information. The ratio close to 0.77, found for all three amphiphiles, supported their close-to-ideal spherical shape (see literature values, Table 7). In Table 8, these values are again summarized together with the previous obtained hydrodynamic radii R_h from the DLS experiments.

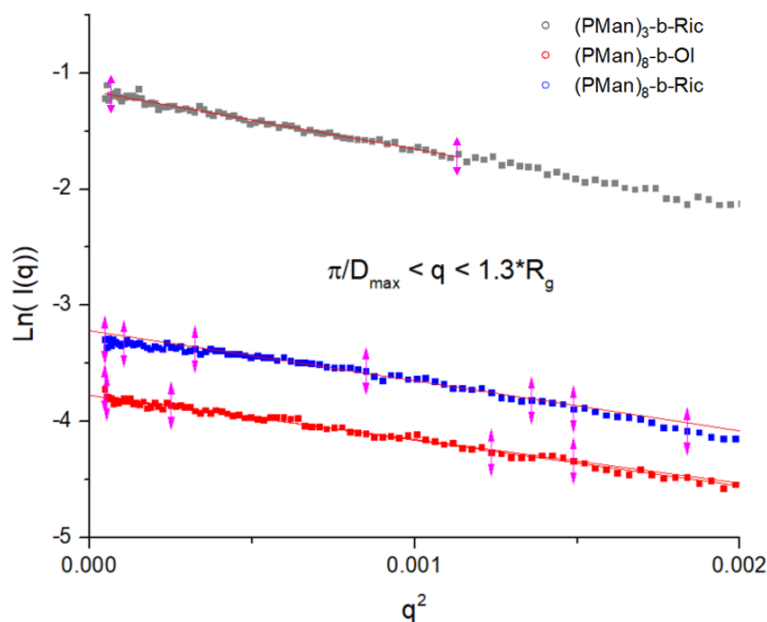


Figure 34. (PMan)_s-*b*-OI (red), (PMan)_s-*b*-Ric (blue) and (PMan)₃-*b*-Ric (black) Guinier plot of the linear fit to the natural log of the intensity $I(q)$ as a function of the square of the scattering vector q^2 .

Table 8. Self-assembled micellar structure hydrodynamic radius (R_h) and radius of gyration (R_g) comparison.

Sample	R_h (nm) (DLS)	R_g (nm) (SAXS)	R_g/R_h ratio	Predicted shape
(PMan) _s - <i>b</i> -OI	4.6	3.6	0.78	Spherical
(PMan) ₃ - <i>b</i> -Ric	5.1	3.9	0.76	Spherical
(PMan) _s - <i>b</i> -Ric	4.3	3.4	0.79	Spherical

These results clearly supported our previous assumptions. A compact mannose shell is surrounding a hydrophobic core formed by the amphiphiles tails in a spherical micellar shape. The obtained SAXS curves were then fitted with a spherical core-shell model (Figure 35), detailed in the experimental section. For the sugar derivatives, the core was composed of the fatty acid chain (lower electron density ρ_c) and the shell of the mannose-oligomers, including the triazole group (higher electron density, ρ_s).^[25] The accurate fit for all three amphiphiles (Figure 33, solid line), supported the self-assembled structures. It can be seen, that the curves were fitted with a minimal error.

Spherical core-shell sphere model

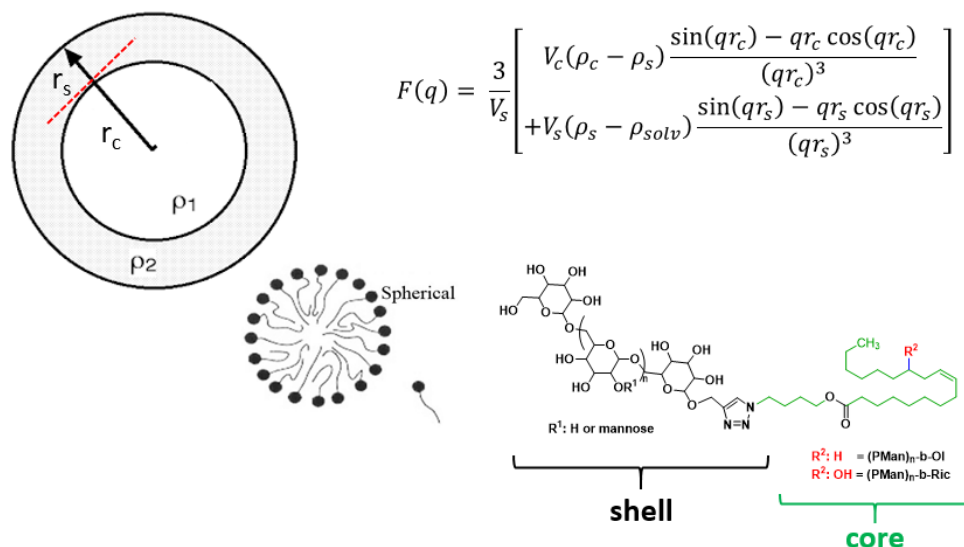
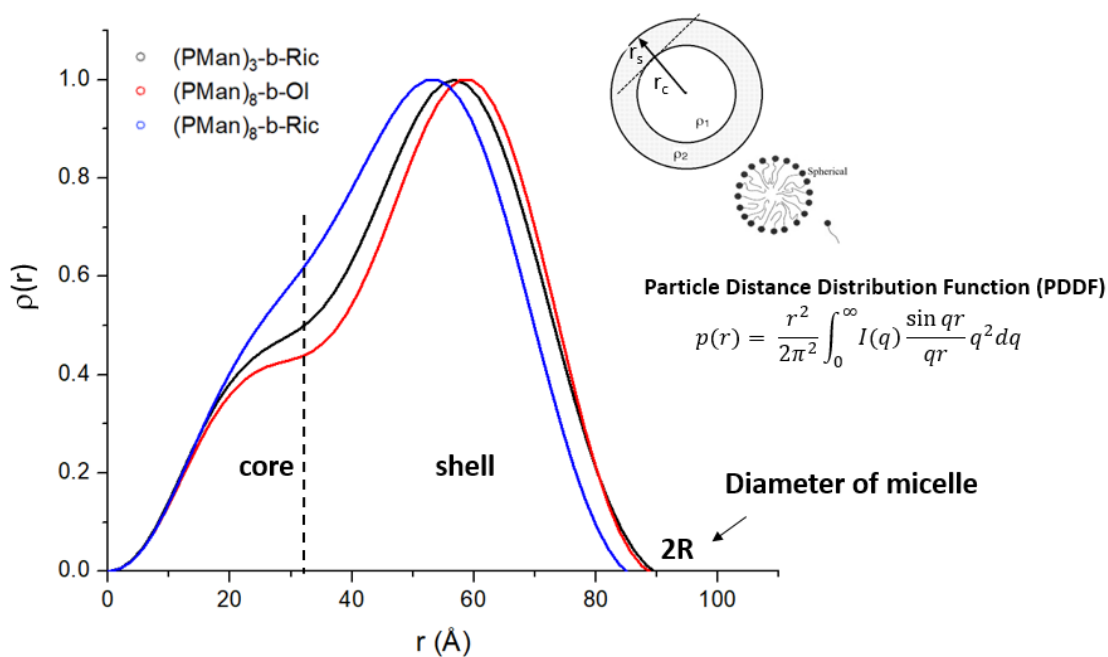


Figure 35. Scheme for the spherical core-shell model with the corresponding equation.

By using the inverse approach, the Pair Distance Distribution Functions (PDDFs) were calculated through Indirect Fourier Transformation (IFT) of the experimental form factor. The obtained functions $\rho(r)$ refer to the average distribution of the electron density over a radius r and are thus characteristic for specific structures. By assuming a spherical symmetry, the electron density difference became only a function of the radius r . Hence, the curve provided information about the size of the head group in the outer shell and the length of the chains in the inner shell.^[26]

Figure 36. (PMan)_s-b-OI (red), (PMan)_s-b-Ric (blue) and (PMan)₃-b-Ric (black) plot of the Pair Distance Distribution Functions (PDDF) determined from IFT as a function of q .

The obtained curves were characteristic for spherical micelles, which are expressed by a core-shell mode through a two-step function, showing pronounced side maxima (Figure 36).^[26] The electron density profile shows a larger electron density for the shell compared to the micellar core and the aqueous phase, according to the strong hydration of the sugars.^[25] From the obtained data, all micelles showed a *ca.* 3.1 nm hydrophobic core, with differences in their electron density transition. Due to the addition of the hydroxyl group at the hydrophobic (PMan)₈-*b*-Ric and (PMan)₃-*b*-Ric amphiphiles, the core-shell electron density difference is less marked. While still a core-shell structure, a closer approach to a solid sphere was observed, characterized by a single-step function. The intersection with the x-axis of the density function gave the diameter of the micelles and showed increasing radii from (PMan)₈-*b*-Ric (~ 8.5 nm) to (PMan)₈-*b*-OI (~ 8.8 nm) and (PMan)₃-*b*-Ric (~ 8.9 nm). All radii were in agreement with previous DLS results, confirming the size of the micelles. It can be inferred that the polar head organization is responsible of these size differences and a clear increase in the \overline{DP}_n , from 3 to 8, is not leading to a radius increase but a more compact interaction between the sugars, as it was previously concluded by DLS.

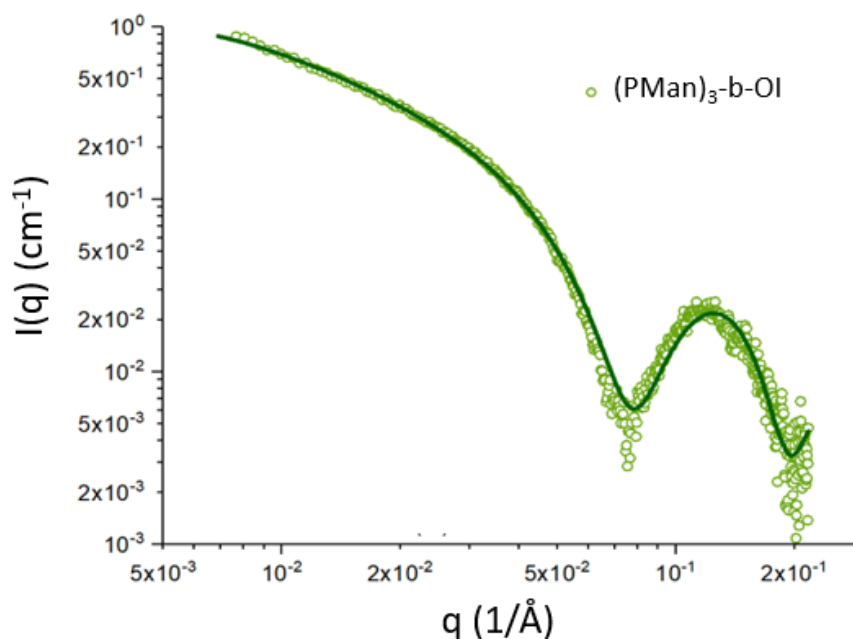


Figure 37. (PMan)₃-*b*-OI small-angle X-ray scattering signal (dots) and their respective spherical core/shell fitting (solid line).

Table 9. SAXS (PMan)₃-*b*-Ric cylindrical micelle values obtained after cylindrical core shell and mixed spherical-cylindrical core shell fitting.

Fitting used	Core R_g (nm)	Shell R_g (nm)	Length R_g (nm)	Cylindrical Ratio (%)
Cylindrical	2.17	1.13	283.7	100
Mixed	2.13	1.03	379.1	80

For amphiphile (PMan)₃-*b*-OI, for which the presence of spherical *and* cylindrical micellar structures was observed, a mixed cylindrical^[27] (Figure 38) and spherical (Figure 35) core-shell model was used. Due to the high cylindrical/spherical population ratio, close to no difference was obtained comparing the mixed and pure cylindrical fitting models (Table 9).

Cylindrical core-shell model

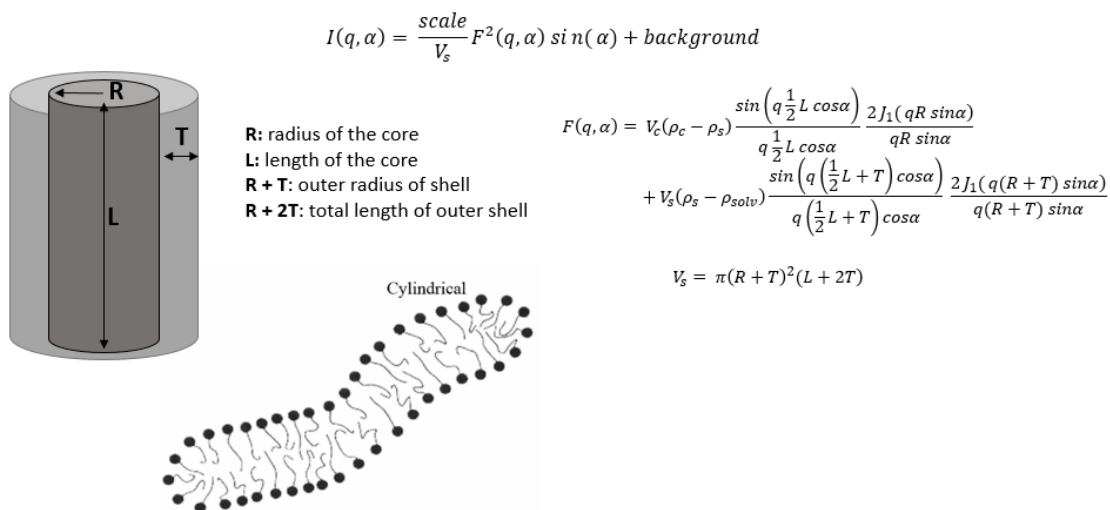


Figure 38. Scheme of the cylindrical core-shell model.

The PDDF plot, given in Figure 39, showed a first clear two-step model at *ca.* 3.2 nm supporting the same core-shell behavior of the spherical micelles. Moreover, a pronounced peak in the low-*r* regime and an extended tail in the high-*r* side exhibit a typical feature of cylindrical nanoparticles^[28]. A flexible behavior of the structure is also elucidated, characterized by a non-linear decay to high *r* values^[29]. Altogether, SAXS experiments could confirm the previous supported spherical- and cylindrical micellar structure obtained from the self-assembly of the mannose-derived amphiphiles.

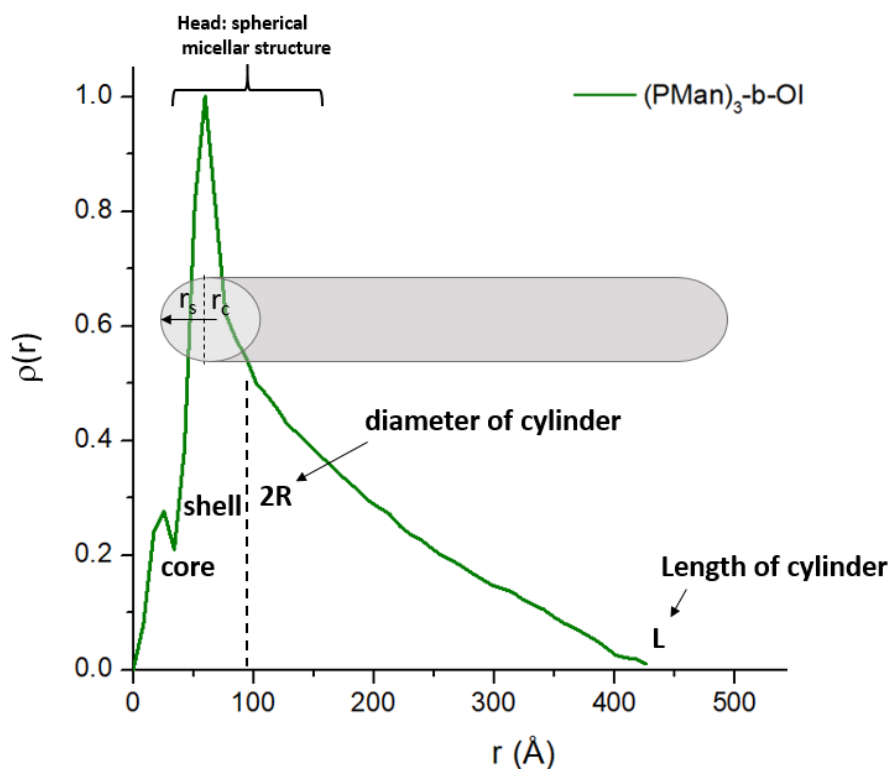


Figure 39. (PMan)₃-*b*-OI plot of the Pair Distance Distribution Functions (PDDF) determined from Indirect Fourier Transformation (IFT) as a function of q .

4 Conclusion

To the best of our knowledge, for the first time the behavior of high linear \overline{DP}_n mannose-derived amphiphiles were investigated at the air/water interface (2D) and aqueous media (3D). The systematic study performed on a small amphiphile library allowed us the establishment of structure-property relationships that could help designing amphiphilic sugars for self-assembly process. It was denoted how tiny tuning up changes in their structure could led to different self-assembly process and thus conformations.

We concluded that the sugar polar head, as well as the presence of a hydroxyl group at the hydrophobic chain was directly related to the final self-assembled structure. At the air/water interface, the amphiphiles with the larger polar sugar head occupied larger areas, along with higher interfacial tension. The critical aggregation concentration was also decreased with higher \overline{DP}_n . Inter- and intramolecular sugar-sugar interactions were promoted with the increase of the mannose polysaccharide length. We suggested the formation of hydrogen bonding *via* the OH group in the lipid tail of ricinoleate. These interactions led to a better packaging and the arrangement of the hydrophobic tail. (PMan)₈-*b*-OI and (PMan)₈-*b*-Ric high degree of polymerization mannose chains tended to form self-assembled spherical micellar structures, as shown by DLS, SAXS and cryo-TEM. While the addition of a hydroxyl group and final decrease in the non-polar region volume still formed spherical structures, as in (PMan)₃-*b*-Ric, (PMan)₃-*b*-OI short polar head group promoted a cylindrical micellar conformation. We tentatively attributed this observation to an initial (PMan)₃-*b*-OI self-

assembled spherical conformation that evolved to a more thermodynamically stable cylindrical one. All these results strongly denoted the surfactant properties of the mannose-derived amphiphiles, that are further exploited in the following chapter.

5 Appendix

NMR spectra.

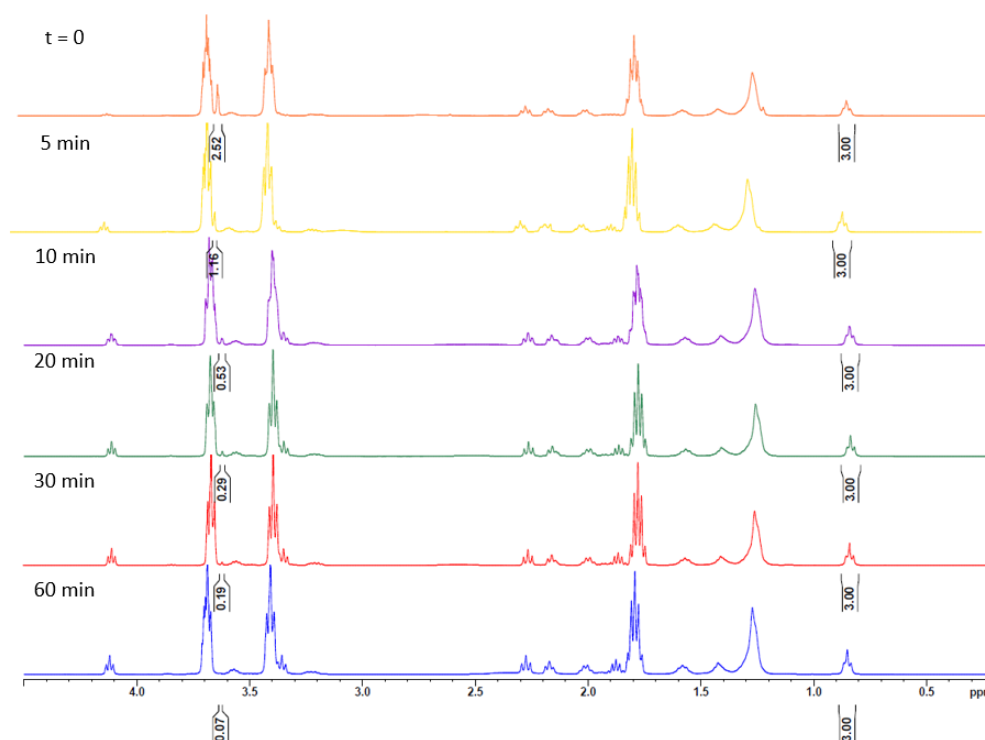


Figure 40. Overlaid ¹H-NMR (400 MHz, CDCl₃) spectra of the transesterification of methyl ricinoleate (**2**) with 3-azido-propanol (**4**) during step 1.

Pendant drop.

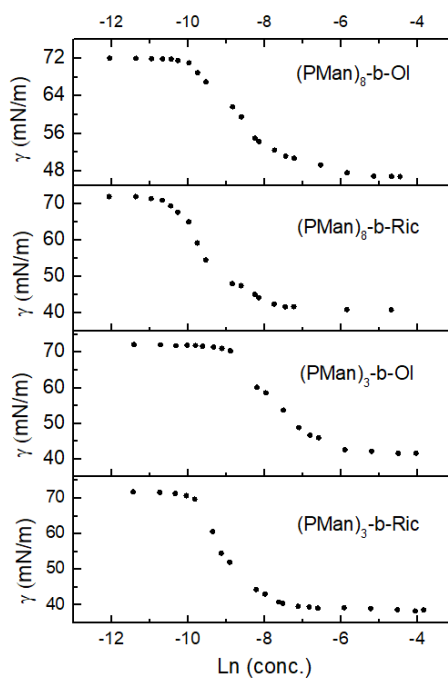


Figure 41. Surface tension versus concentration plot for (PMan)₈-b-OI, (PMan)₈-b-Ric, (PMan)₃-b-OI and (PMan)₃-b-Ric measured by pendant drop

ALV plots

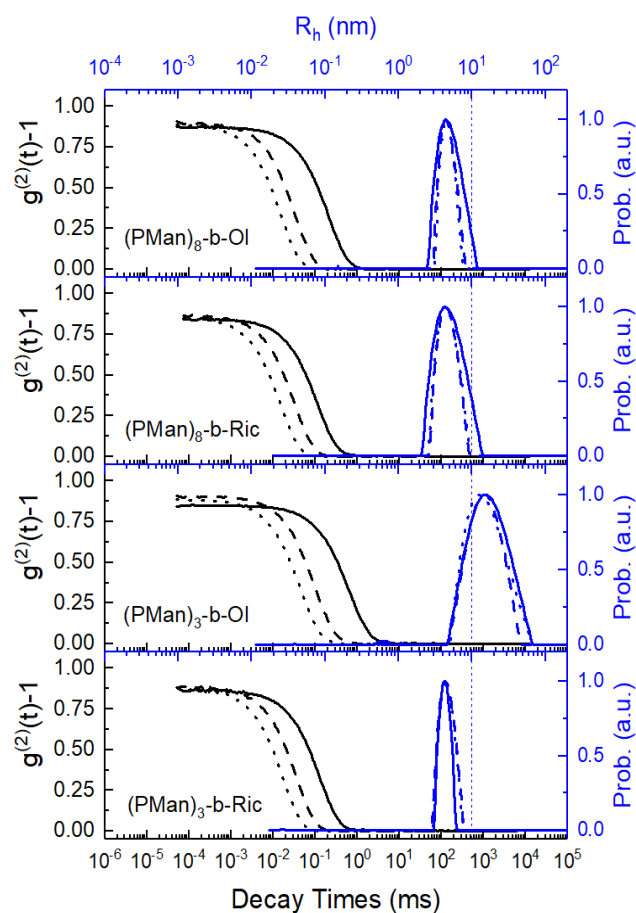
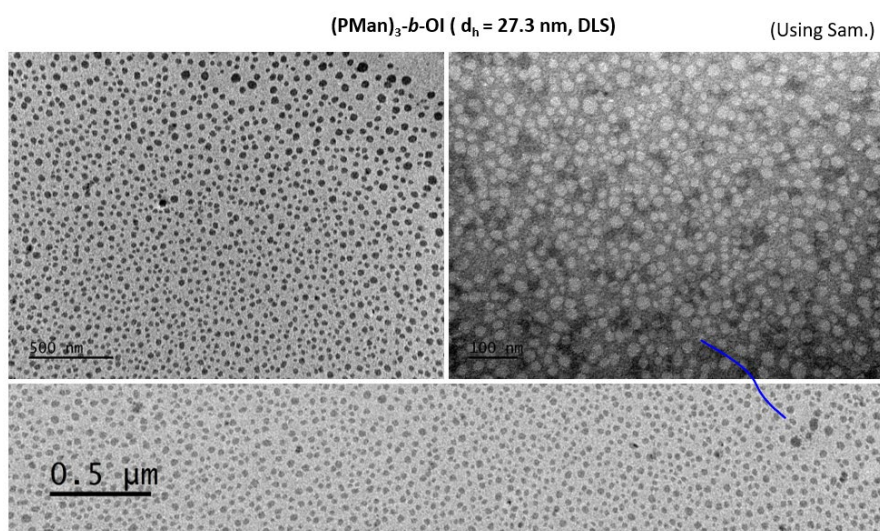
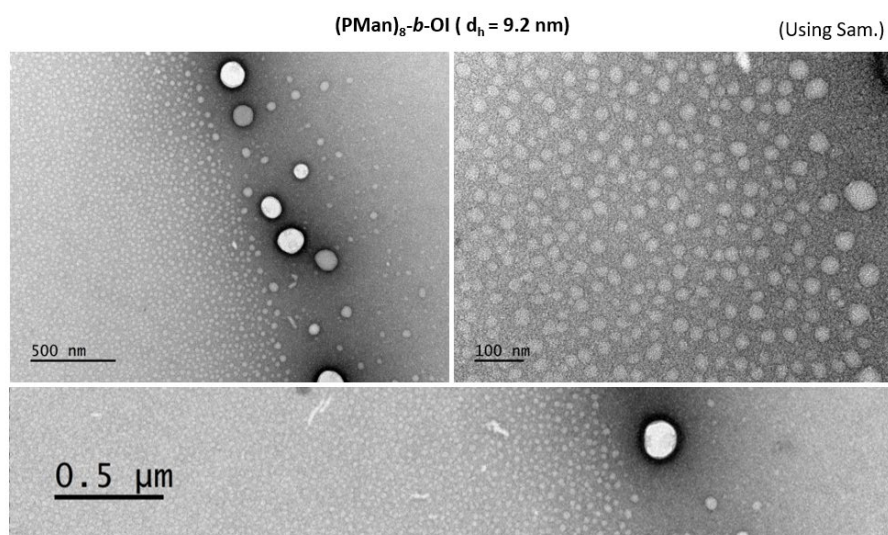
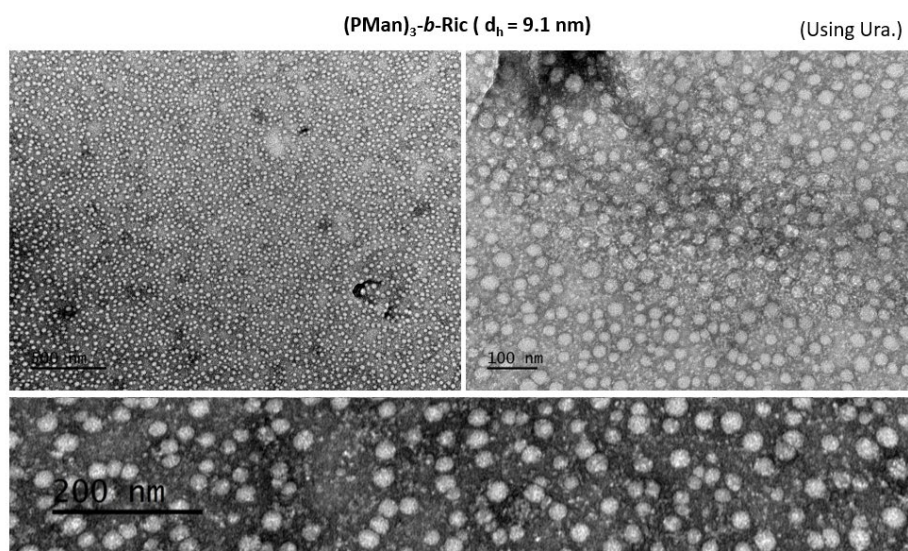
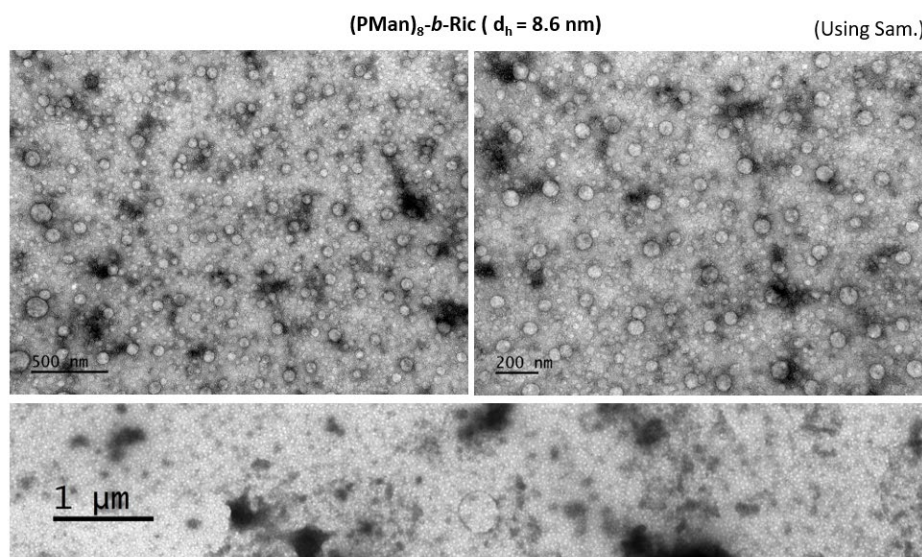


Figure 42. Examples of (PMan)₈-*b*-OI, (PMan)₈-*b*-Ric, (PMan)₃-*b*-OI and (PMan)₃-*b*-Ric DLS intensity auto-correlation (black) and size distribution (blue) functions by ALV at high (dot line), mid (dash line) and low (solid line) angles.

TEM-images

Figure 43. TEM image of (PMan)₃-*b*-OI.Figure 44. TEM image of (PMan)₈-*b*-OI.

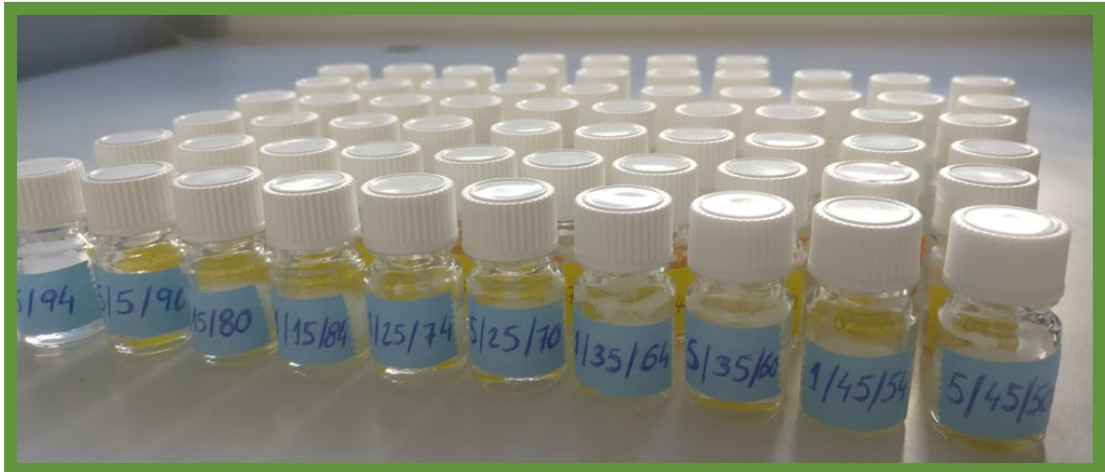
Figure 45. TEM image of (PMan)₃-*b*-Ric.Figure 46. TEM image of (PMan)₈-*b*-Ric.

Bibliography

- [1] C. Schatz, S. Lecommandoux, *Macromol Rapid Commun* **2010**, *31*, 1664-1684.
- [2] J. Rosselgong, M. Chemin, C. C. Almada, G. Hemery, J.-M. Guigner, G. Chollet, G. Labat, D. Da Silva Perez, F. Ham-Pichavant, E. Grau, S. Grelier, S. Lecommandoux, H. Cramail, *Biomacromolecules* **2019**, *20*, 118-129.
- [3] R. Huisgen, *Angewandte Chemie International Edition in English* **1963**, *2*, 565-598.
- [4] https://en.wikipedia.org/wiki/Oleic_acid.
- [5] https://en.wikipedia.org/wiki/Ricinoleic_acid.
- [6] M. A. R. Meier, J. O. Metzger, U. S. Schubert, *Chemical Society Reviews* **2007**, *36*, 1788.
- [7] T. Lebarbé, L. Maisonneuve, T. H. Nga Nguyen, B. Gadenne, C. Alfos, H. Cramail, *Polymer Chemistry* **2012**, *3*, 2842.
- [8] aZ. Li, L. Qu, W. Zhu, J. a. Liu, J.-Q. Chen, P. Sun, Y. Wu, Z. Liu, K. Zhang, *Polymer* **2018**, *137*, 54-62; bJ. G. Badiang, J. Aubé, *The Journal of Organic Chemistry* **1996**, *61*, 2484-2487; cD. Quémener, T. P. Davis, C. Barner-Kowollik, M. H. Stenzel, *Chemical communications* **2006**, 5051-5053.
- [9] F. Jérôme, G. Kharchafi, I. Adam, J. Barrault, *Green chemistry* **2004**, *6*, 72-74.
- [10] S. Dworakowska, C. Le Coz, G. Chollet, E. Grau, H. Cramail, *European Journal of Lipid Science and Technology* **2019**, *121*, 1900264.
- [11] A. Anastasaki, A. J. Haddleton, Q. Zhang, A. Simula, M. Driesbeke, P. Wilson, D. M. Haddleton, *Macromolecular rapid communications* **2014**, *35*, 965-970.
- [12] T. Gaudin, H. Lu, G. Fayet, A. Berthaud-Drelich, P. Rotureau, G. Pourceau, A. Wadouachi, E. Van Hecke, A. Nesterenko, I. Pezron, *Adv Colloid Interface Sci* **2019**, *270*, 87-100.
- [13] G. Milkereit, V. M. Garamus, K. Veermans, R. Willumeit, V. Vill, *Journal of Colloid and Interface Science* **2005**, *284*, 704-713.
- [14] M. J. Rosen, J. T. Kunjappu, *Surfactants and interfacial phenomena*, John Wiley & Sons, **2012**.
- [15] aB. Lu, M. Vayssade, Y. Miao, V. Chagnault, E. Grand, A. Wadouachi, D. Postel, A. Drelich, C. Egles, I. Pezron, *Colloids and Surfaces B: Biointerfaces* **2016**, *145*, 79-86; bG. Garofalakis, B. S. Murray, D. B. Sarney, *J Colloid Interface Sci* **2000**, *229*, 391-398.
- [16] C. Tanford, *Proceedings of the National Academy of Sciences* **1979**, *76*, 4175-4176.
- [17] J. Rumble, CRC Press/Taylor & Francis: Boca Raton, FL, USA, **2019**.
- [18] S. Matsumura, K. Imai, S. Yoshikawa, K. Kawada, T. Uchibori, *Journal of Japan Oil Chemists' Society* **1991**, *40*, 709-714.
- [19] K. Bouchemal, F. Agnely, A. Koffi, M. Djabourov, G. Ponchel, *J Mol Recognit* **2010**, *23*, 335-342.
- [20] S. Paula, W. Sues, J. Tuchtenhagen, A. Blume, *The Journal of Physical Chemistry* **1995**, *99*, 11742-11751.
- [21] J. N. Israelachvili, *Intermolecular and surface forces*, Academic press, **2011**.
- [22] Y. Mai, A. Eisenberg, *Chem Soc Rev* **2012**, *41*, 5969-5985.
- [23] L. Boldon, F. Laliberte, L. Liu, *Nano Rev* **2015**, *6*, 25661.
- [24] G. Gelardi, N. Sanson, G. Nagy, R. J. Flatt, *Polymers (Basel)* **2017**, *9*.
- [25] C. Bauer, P. Bauduin, L. Girard, O. Diat, T. Zemb, *Colloids and Surfaces A: Physicochemical and Engineering Aspects* **2012**, *413*, 92-100.
- [26] O. Glatter, in *Trends in colloid and interface science v*, Springer, **1991**, pp. 46-54.
- [27] C.-Y. Cheng, H. Oh, T.-Y. Wang, S. R. Raghavan, S.-H. Tung, *Langmuir* **2014**, *30*, 10221-10230.
- [28] L. K. Shrestha, S. C. Sharma, T. Sato, O. Glatter, K. Aramaki, *Journal of colloid and interface science* **2007**, *316*, 815-824.
- [29] B. Pérez, A. Coletta, J. N. Pedersen, S. V. Petersen, X. Periole, J. S. Pedersen, R. B. Sessions, Z. Guo, A. Perriman, B. Schiøtt, *Scientific reports* **2018**, *8*, 1-13.

Chapter IV:

Emulsions and molecular targeting



This work was carried out in collaboration with Dr. Pablo Gómez Argudo, to whom I want to address my grateful acknowledgement.

Contents

1	Introduction	227
2	O/W Emulsion: Castor oil	228
2.1	Surfactant/Castor oil/water	228
2.2	Surfactant/Castor oil/PBS	230
3	O/W Emulsion with different oils	234
3.1	Emulsions with different oils in water	234
3.1.1	Mineral Oil	235
3.1.2	Sunflower Oil.....	236
3.1.3	Olive Oil.....	237
3.1.4	Soybean Oil	238
3.2	Surfactant/PBS/Sunflower, - Soybean, - or Olive oil 37°C	240
3.3	Emulsions with mixtures of mannose- and glucose-based surfactants	241
3.3.1	Emulsions with glucose-based surfactants	242
3.3.2	Emulsion with mixtures of mannose- and glucose-based surfactants.....	243
4	Molecular targeting: Concanavalin A (ConA).....	243
5	Conclusion.....	250
6	Appendix.....	251
	Bibliography	254

1 Introduction

Oligosaccharides are known to serve as mediators in various biological processes. To name some of them: bacterial and viral infection, cell-cell recognition and adhesion, or the immunological recognition of tumor cells and pathogens.^[1] With the defined synthesis of glycoconjugates, the latter can be utilized to mimic terminal oligosaccharides to block the recognition and/or adhesion process in pharmaceutical issues.^[2] Therefore, it is of high interest to get more information about the interaction process between these biomolecules and their counterpart proteins. Phagocytosis, the internalization of pathogens by cells, is known to be triggered by specific receptors at the membrane. Among them, the mannose receptor family (MR) binds specifically to polysaccharide patterns with terminal mannose, fructose and N-acetylglucosamine. However, their role and ability to trigger the phagocytosis process remains unclear until date.^[3]

Here, O/W emulsions were prepared utilizing $(PMan)_8-b-OI$ as emulsifying agents. As hydrophobic phase, vegetable oils such as castor, sunflower, olive, and soybean as well as mineral oil were tested. The surfactant/oil/water weight ratios needed to reach stable emulsions were studied and the preparation protocol was optimized. The systems were then transposed to phosphate-buffered saline solution (PBS) to get close to biological conditions. Finally, the interaction and binding properties of our emulsions with concanavalin A (ConA), a glycoprotein that specifically binds to D-mannose and D-glucose, were studied. This lectin derivative was thereby used as a model to study the internalization of phagocytes. With the utilization of mannose-oligosaccharides with \overline{DP}_n of 8, larger “ConA-glycoside clusters” are expected due to the increasing active mannose-sides as shown in Figure 1, (II).

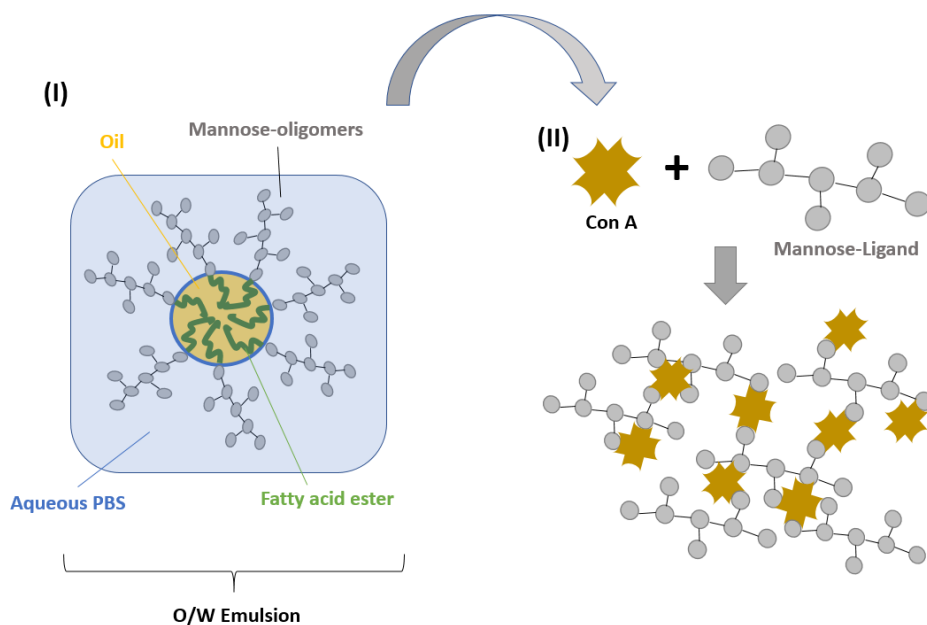


Figure 1. (I) Illustrative presentation of the O/W emulsion with $(PMan)_n-b-OI$ as surfactant; (II) Proposed multivalent binding between ConA and mannose forming large aggregates.

2 O/W Emulsion: Castor oil

Castor oil is a vegetable oil that is obtained from the castor beans as colorless to pale yellowish viscous liquid. It consists of different triglycerides with ricinoleate accounting up to 95 % (Table 1).

Table 1. Composition of Castor seed oil.^[4]

Acid	Percentage (%)
Ricinoleic acid	85 - 95
Oleic acid	2 - 6
Linoelic acid	1 - 5
α -Linolenic acid	0.5 - 1
Stearic acid	0.5 - 1
Palmitic acid	0.5 - 1
Dihydroxystearic acid	0.3 - 0.5
others	0.2 - 0.5

The HLB required of castor oil is 14 and thus matches to our sugar surfactant (PMan)₈-b-OI, for which we calculated the HLB to *ca.* 16. In the following we present the study of different ratios of surfactant/oil/water to prepare stable O/W emulsions. For synthetic reasons (purification, yield...), we selected exclusively the surfactant with oleic acid as hydrophobic segment.

2.1 Surfactant/Castor oil/water

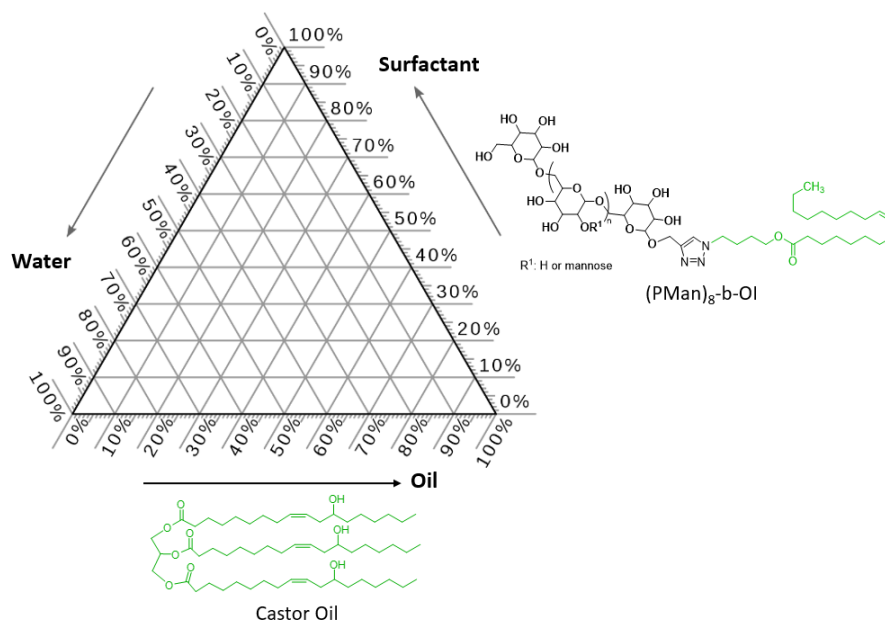


Figure 2. Pseudo-ternary phase diagram for O/W emulsion with (PMan)₈-b-OI and Castor oil.

We emulsified castor oil with surfactant (PMan)_s-*b*-OI using different surfactant/oil/water weight ratios (Figure 2). The composition of surfactant/oil/water affording stable- and no stable emulsions are listed in Table 2.

Table 2. Composition of stable and no stable emulsions between (PMan)_s-*b*-OI and castor oil in water.

(PMan) _s - <i>b</i> -OI (wt.%)	Oil (wt.%)	Water (wt.%)	Stability
0.5	5	94.5	stable
1	5	94	stable
1	15	84	stable
1	25	74	stable
1	50	49	no stable
1	70	29	no stable
3	5	92	stable
4	10	85	stable
4	24	72	stable
4	50	46	no stable
4	70	26	no stable
5	5	90	stable

Interestingly, (PMan)_s-*b*-OI could emulsify up to 25 wt.% castor oil in water, with concentration as low as 1 wt.% in the final emulsion. With increasing amount of the oil, the emulsions became unstable, even with larger surfactant concentration (5 wt.%). For higher amounts of oil, the system completely phase-separated. We could not observe a O/W to W/O phase inversion by further increasing the amount of the oil up to 70 wt.%. DLS (Cordouan) experiments at 135° gave average size distributions of the emulsions with dynamic radii of *ca.* 200 nm. All emulsions described in Table 2 were in the same size-range of *ca.* 150 - 212 nm (see more detail in appendix) with PDI distributions of *ca.* 0.1 - 0.2.

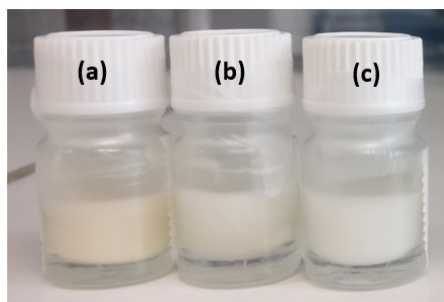


Figure 3. Illustrative examples of stable nano-emulsion of (PMan)_s-*b*-OI/castor oil/water: (a) 3-5-91, (b) 1-5-93, (c) 0.5-5-94.

The first emulsions were prepared by dissolving the surfactant in water and adding the oil after 30 minutes of stirring at 750 rpm. The nascent emulsion was then stirred (magnetically) at 750 rpm and the development of the size distribution was followed by DLS. Figure 4 (a) shows the size distribution after 24 h and 7 days of stirring. We denoted that the mean droplet size did not further changed after 7 days, assuming that the emulsion reached a stable state.

This stability was tested by allowing to let stand the emulsion during 7 days at room temperature. The DLS size distribution did not remarkably changed, supporting the stability of the emulsion. The increase of the stirring rate after the addition of the oil from 750 to 1400 rpm could improve the emulsification process. DLS experiments showed that the emulsion reached that stable state already after 24 h of stirring (Figure 4 (b)). This time, the as-obtained emulsion was allowed to stay for 15 days without stirring at R.T. and its stability could be confirmed (Figure 4 (b), blue line). We continued to observe the stability of the emulsion over 2 months (Figure 4 (b), black line) and denoted no significant changes in the DLS size distribution, supporting its stability. The so optimized emulsification protocol was maintained for the following experiments.

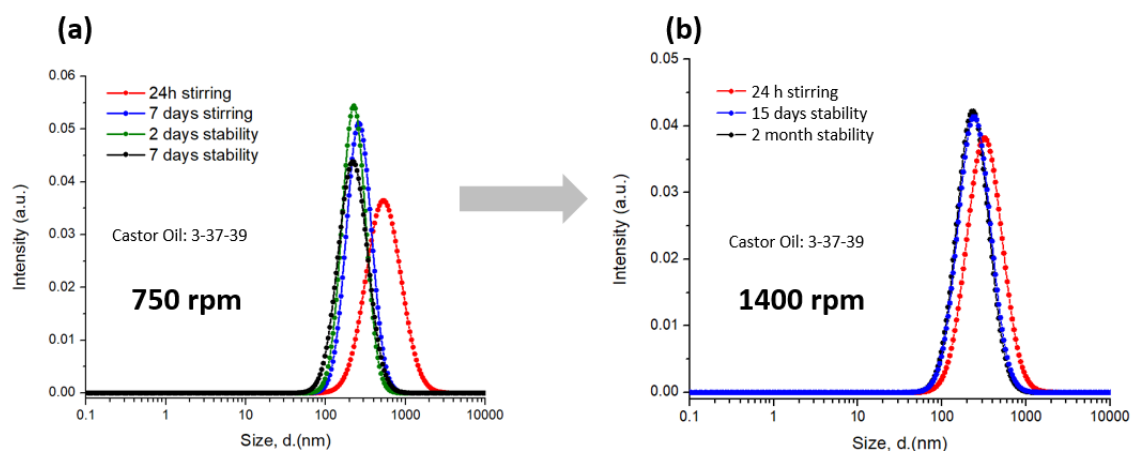


Figure 4. Emulsion $(\text{PMan})_8\text{-}b\text{-OI/Castor oil/water 3-37-39}$ DLS size distribution by Cordouan at 135° in time; the emulsion was prepared at (a) 750 rpm and (b) at 1400 rpm.

2.2 Surfactant/Castor oil/PBS

We next transposed the O/W emulsion between $(\text{PMan})_8\text{-}b\text{-OI}$ and castor oil to an aqueous solution of phosphate-buffered saline (PBS). This buffer is a water-salt-solution of disodium hydrogen phosphate, sodium chloride, potassium chloride and potassium dihydrogen phosphate. It is commonly used in biological systems since the pH-value and ion-concentrations are isotonic and non-toxic to most cells.^[5] In our case, we utilized a PBS solution from Sigma and adjusted the pH to 7.2 with the addition of 0.1 mM MnCl_2 and 0.1 mM CaCl_2 . This time, we denoted stable one-phase emulsions (Figure 5, (a)), but also emulsions with Winsor I regions (Figure 5, (b) and (c)).

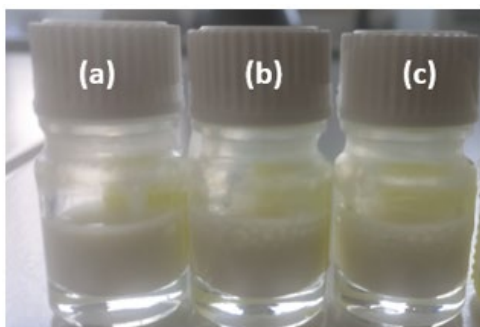


Figure 5. Illustrative examples of some nano-emulsion of (PMan)₈-*b*-OI/castor oil/PBS: (a) 1-15-84, (b) 4-35-61, (c) 4-45-51. Table 3. Composition of emulsions between (PMan)₈-*b*-OI and castor oil in PBS.

(PMan) ₈ - <i>b</i> -OI (wt.%)	Oil (wt.%)	PBS (wt.%)	Stability
1	15	84	stable
1	25	74	no stable
1	45	54	no stable
3	5	92	stable
4	15	81	stable
4	25	71	stable
4	35	61	Winsor I
4	45	51	Winsor I

We tested 9 different surfactant/castor oil/PBS ratios and could obtain four stable nano emulsions with average hydrodynamic radii of *ca.* 300 nm (Table 3) with 1,- 3,- and 4 wt.% of the lipid. The average size of the emulsion droplets obtained was 100 nm larger than in pure water, which we supposed to be due to presence of salts in PBS. It is indeed well known that salts do affect the solubility of organic compounds in water. Hofmeister^[6] classified them as “salting out” or “salting in”, depending whether they decrease or increase the solubility, respectively. He ordered them in the so-called “Hofmeister series” starting from the strongest ‘salting out’, to the strongest ‘salting in’ effect: $\text{SO}_4^{2-} > \text{HPO}_4^{2-} > \text{F}^- > \text{Cl}^- > \text{Br}^- > \text{NO}_3^- > \text{I}^- > \text{ClO}_4^- > \text{SCN}^-$. The effects of the salts are explained either by their ability to order, or disorder the structure of water, or their ad-, and desorption at the water-organic solute interface. Thereby, ‘salting out’ compounds are structure makers and ‘salting in’ ones are structure breakers, respectively. The salt effect on nonionic microemulsions was also reported in the literature^[7] and it was shown that lyotropic salts (NaCl) increases-, while hydrotropic salts (NaClO₄) decreases the polarity of water, respectively. A. Kabalnov *et al.*^[8] claimed that these effects are interfacial and due to the adsorption or depletion at the monolayer of the emulsion. Lyotropic salts led thereby to a depletion-, and hydrotropic salts to an enrichment of the emulsion phase. The addition of water soluble salts led them consequently enter into the water core of the emulsion droplets and modify their structure. Thereby, the size of the microemulsion droplet increases, which was supposed in the most reports due to the resulting hydration of the salts.^[9] In the case of our emulsion with (PMan)₈-*b*-OI, castor oil and PBS,

the additional salts consequently afforded an increase of the size of the emulsion droplets from *ca.* 200 nm in pure water to *ca.* 300 nm (Figure 6).

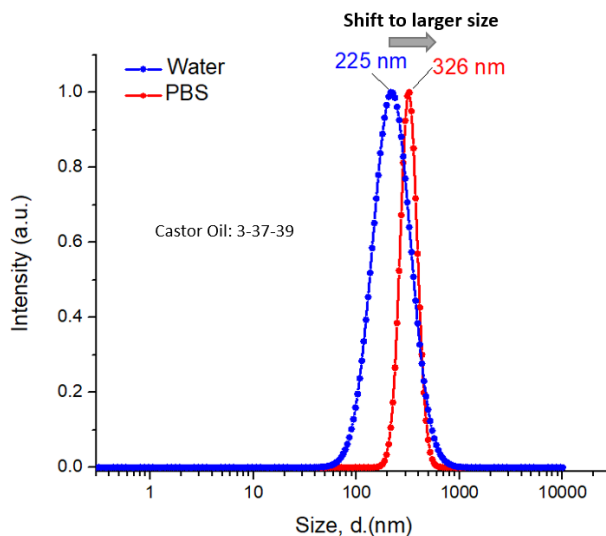


Figure 6. Emulsion (PMan)_s-*b*-OI/Castor oil/polar solvent 3-37-39 DLS size distribution in water (blue) and in PBS (red).

Moreover, the amount of oil that could be successfully emulsified in PBS was lower than in water, reaching a maximum of 15 wt.% for 1 wt.% of surfactant and up to 25 wt.% for 4 wt.% of surfactant, respectively. With increasing amount of oil for 4 wt.% of surfactant to 35-, and 45 wt.%, we observed the phenomena of Winsor I.

The behavior of microemulsions and their phase equilibria was described by Winsor^[10], who predicted four types of equilibria. He describes the ratio of the intermolecular attraction by following equation

$$R_0 = \frac{C_{LO}}{C_{HW}} \quad (1)$$

with L = lipophilic molecules, O = oil molecules, H = hydrophilic molecules and W = water. At the oil- and water interface, several interaction parameters are thus possible (Figure 7).

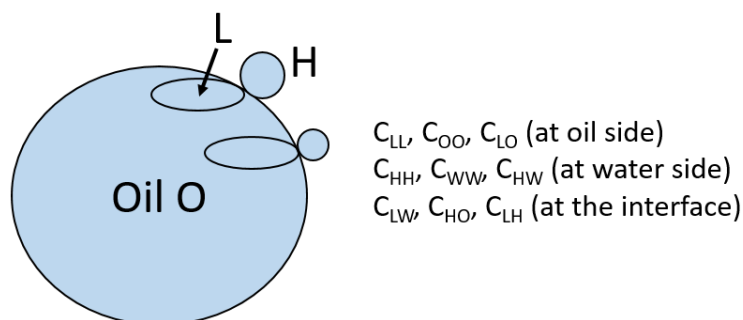


Figure 7. Interaction parameters at the oil and water phases^[10a]

The interactions between two lipophilic parts are described by C_{LL} , C_{OO} and L_{CO} , the interactions between two hydrophilic parts by C_{HH} , C_{WW} and C_{HW} and the interaction between the lipophilic and hydrophilic parts are described by C_{LW} , C_{HO} and C_{LH} , respectively. There are three different cases, corresponding to different values for R_0 . Winsor I ($R_0 < 1$): oil-in-water (O/W) emulsion, where the oil is solubilized in micelles in the aqueous phase. The affinity of the surfactant to the water phase is higher than to the oil phase. In the case of a two-phase system, an oil phase containing dissolved surfactant monomers consists above the emulsion phase. Winsor II ($R_0 > 1$): water-in-oil (W/O) emulsion, where the aqueous phase is solubilized in micelles in the oil phase. The affinity of the surfactant is higher to the oil-, than to the water phase. In the case of a two-phase system, a water phase containing dissolved surfactants coexists next to the W/O emulsion. Winsor III ($R_0 = 1$): three-phase system, where a surfactant-rich bicontinuous middle-phase coexists with the water-, and the oil phase. In this case, the surfactant affinity to the oil-, and water phase is balanced (Figure 8).^[10b]

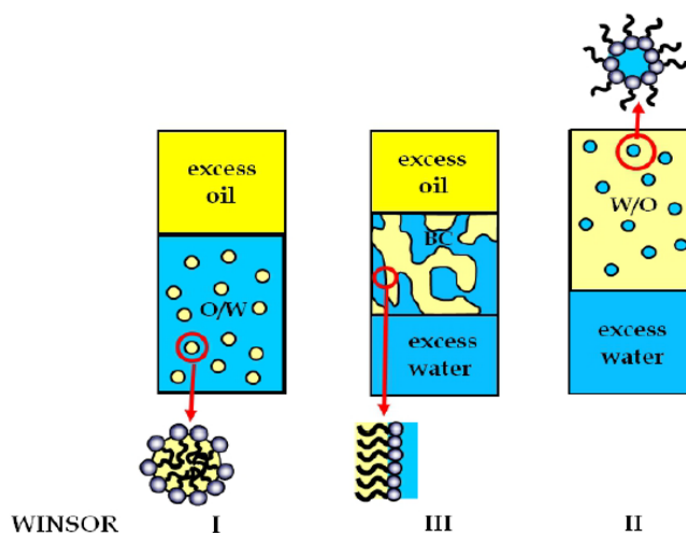


Figure 8. Schematic illustration of the different Winsor types I, II and II in microemulsions ^[10b]

Transitional phase inversions can be caused by the addition of electrolyte to an emulsion based on non-ionic surfactants. Different groups studied the effects of the addition of salts to nonionic microemulsion systems and found that the salting-in or salting-out effect increases or decreases the water solubilization of the latter.

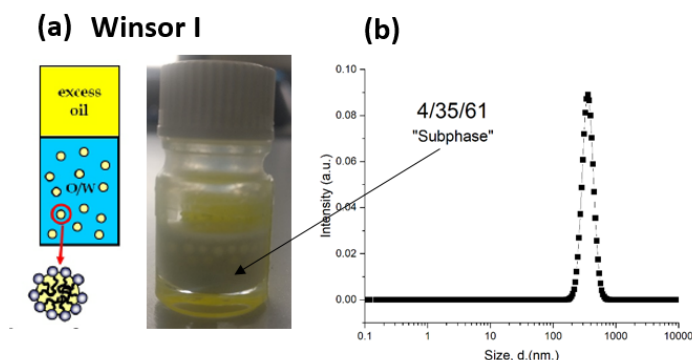


Figure 9. (a) Winsor I region of (PMan)₈-*b*-OI/Oil/PBS: 4/35/6; (b) corresponding DLS size distribution by DLS (Cordouan) at 135° from the “subphase”.

Figure 9 shows the emulsion between (PMan)₈-*b*-OI/castor oil/PBS with 4/35/6, where the Winsor I region was denoted. As described above, these type of systems shows an oil phase (bubbles in the image) above the O/W emulsion. The DLS experiment supported the existence of the O/W emulsion by measuring only the “subphase” with a hydrodynamic radius of *ca.* 300 nm.

3 O/W Emulsion with different oils

We next carried out a study of the emulsification capacity of our surfactant (PMan)₈-*b*-OI for different oils such as mineral-, soybean-, olive-, and sunflower oil in water. The HLB required of the oils ranged from 7 for soybean-, olive- and sunflower oil to 10 for mineral oil, respectively. The HLB of our surfactant was calculated to 16 and thus estimated to be more promising for the mineral oil than for the vegetable oils.

3.1 Emulsions with different oils in water

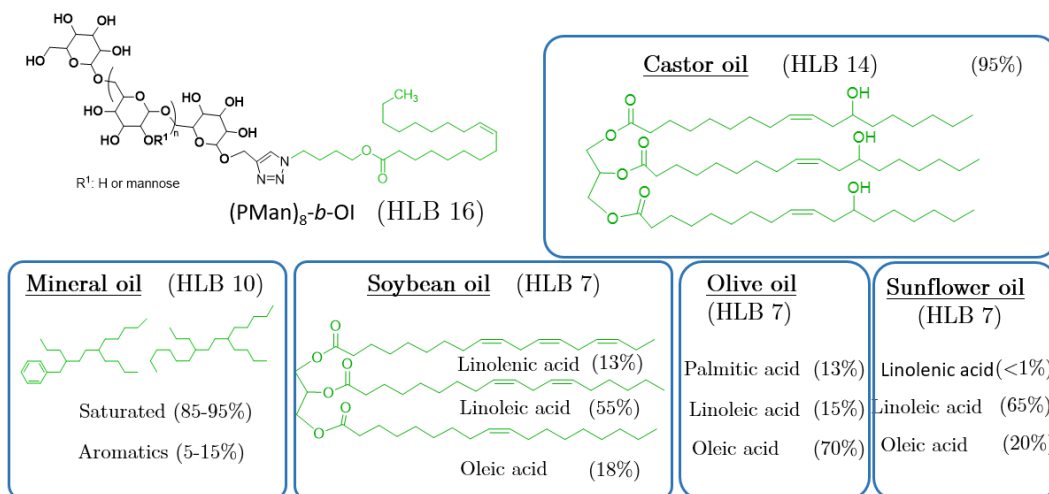


Figure 10. Study of the emulsification capacity of (PMan)₈-*b*-OI to castor-, mineral-, soybean-, olive-, and sunflower oil.

Table 4. Composition of the emulsion with the different oils.

Surfactant (wt.%)	Oil (wt.%)	Water (wt.%)
1	5	94
5	5	90
1	15	84
5	15	80
1	25	74
5	25	70
1	35	64
5	35	60
1	45	54
5	45	50

For this study, we increased the amount of the oil from 5 to 45 wt.%, while the amount of the surfactant was either fixed at 1-, or 5 wt.%. Thereby, 40 different emulsions were prepared following the same protocol, that was optimized for castor oil in water and PBS in the previous experiments (see subsection 2.1): First, the surfactant was dissolved in water and stirred (750 rpm) for 30 minutes at room temperature. Then, the oil was added and the mixture was stirred at 1400 rpm for 24 h.

3.1.1 Mineral Oil

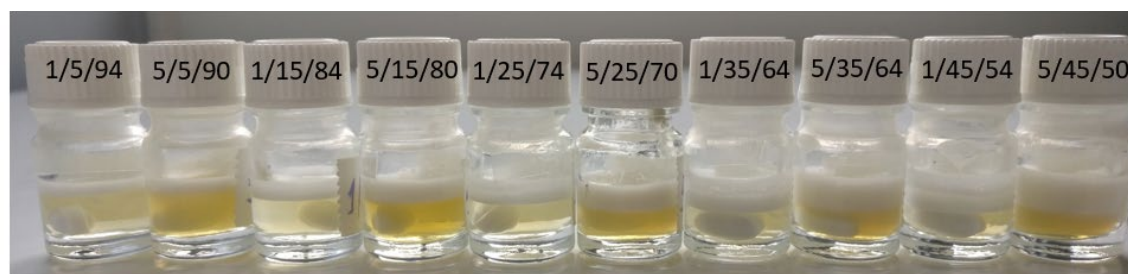


Figure 11. Emulsion of $(\text{PMan})_8\text{-}b\text{-OI}$ and mineral oil in water with the different ratios of surfactant/oil/water.

The mixtures of mineral oil in water with $(\text{PMan})_8\text{-}b\text{-OI}$ gave no stable emulsions for any surfactant/oil/water ratios. All samples showed two-phase systems containing a white foam as upper phase (Figure 11). DLS experiments supported that the sugar derivative could not emulsify the oil. Mineral oil is mainly composed of saturated higher alkanes and cycloalkanes with some aromatic compounds (*ca.* 5 - 15 %). The absence of any double bond was suggested to be one reason for the poor interaction with $(\text{PMan})_8\text{-}b\text{-OI}$. Besides, the preferred $\pi\text{-}\pi$ -stacking between the aromatic compounds in the mineral oil might hindered the interactions to the oleic chain of the surfactant (Figure 12). The HLB required of mineral oil (= 10) was too different to the HLB value of the surfactant (= 16), which explained further the poor interactions.

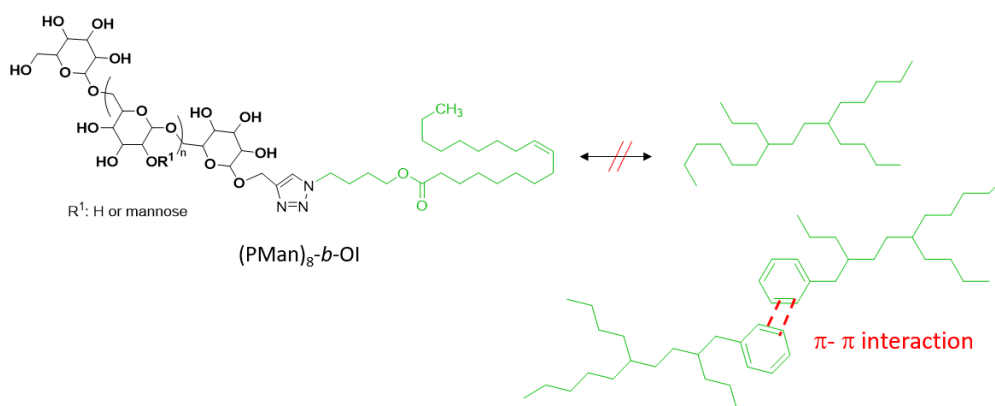


Figure 12. Poor interactions between mineral oil and surfactant $(\text{PMan})_8\text{-}b\text{-OI}$.

3.1.2 Sunflower Oil

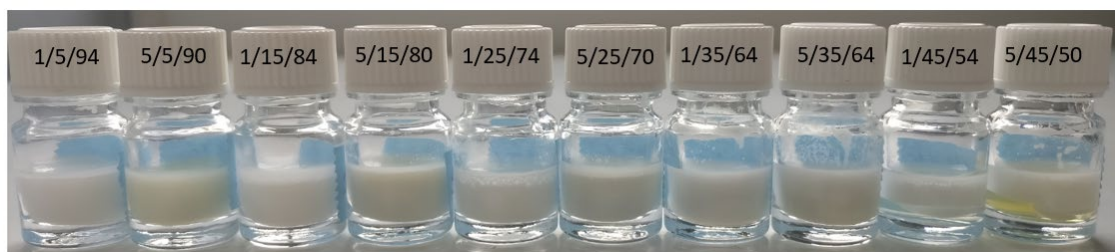


Figure 13. Emulsion of $(\text{PMan})_8\text{-}b\text{-OI}$ and sunflower oil in water with the different ratios of surfactant/oil/water.

The mixtures of sunflower oil and $(\text{PMan})_8\text{-}b\text{-OI}$ in water gave stable emulsions for 6 out of the 10 different surfactant/oil/water mixtures tested. Up to 25 wt.% of sunflower oil could be successfully emulsified giving one-phase systems (Figure 14). The average size measured by DLS at 135 ° gave dynamic radii from *ca.* 200 to *ca.* 300 nm with a dispersity of 0.08 - 0.17 (see table in the appendix).

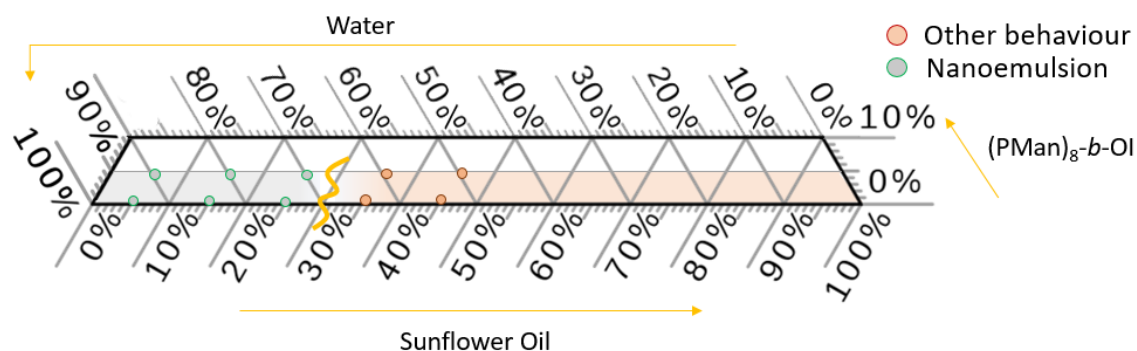


Figure 14. Extract of the pseudo-ternary phase diagram with the stable nanoemulsions in green and the non-stable in red for the system: sunflower oil/ $(\text{PMan})_8\text{-}b\text{-OI}$ /water.

The emulsions were then allowed to stand for 2 months at room temperature. The DLS experiments showed no change in the size distribution, supporting their stability. Figure 15

was selected as illustrative example with a $(\text{PMan})_s\text{-}b\text{-OI}$ /sunflower oil/water 1/5/94 ratio, while the remaining 5 stable emulsions described above showed the same behavior.

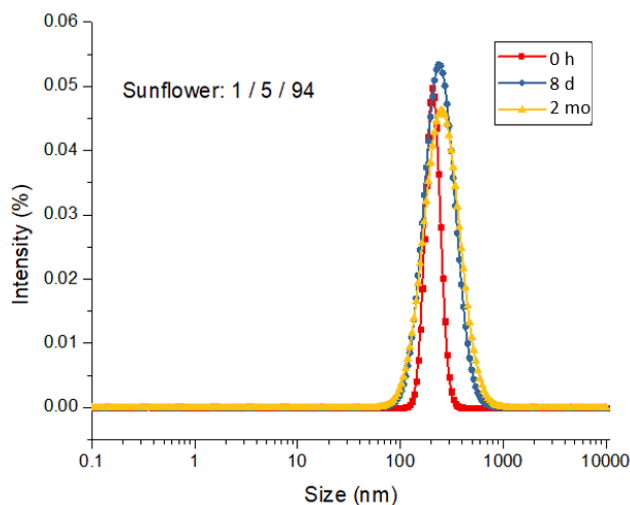


Figure 15. Plot of the size-distribution for the emulsion of $(\text{PMan})_s\text{-}b\text{-OI}$ /sunflower/water with the ratio 1/5/94 over a time period of 15 days.

3.1.3 Olive Oil

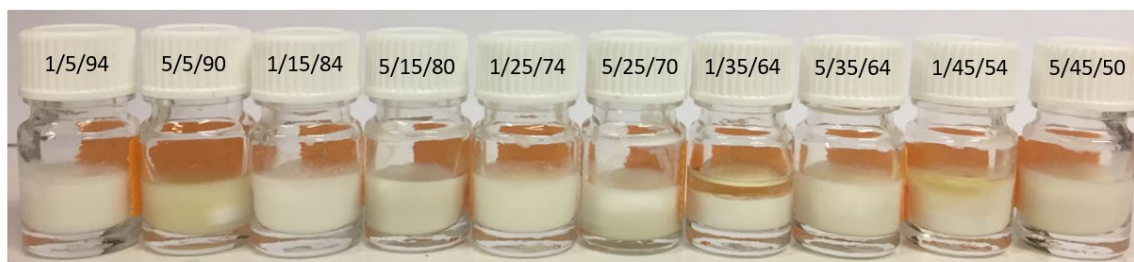


Figure 16. Emulsion of $(\text{PMan})_s\text{-}b\text{-OI}$ and olive oil in water with the different ratios of surfactant/oil/water.

Olive oil could be emulsified in water in up to 25 wt.% to give one-phase systems (Figure 16). The DLS experiments gave average size with dynamic radii from *ca.* 172 to *ca.* 433 nm with a dispersity of 0.04 - 0.23. The emulsions were stable for at least 2 months at room temperature. At higher amount of oil, from 35 to 45 wt.%, the solutions showed two phase behavior including Winsor regions.

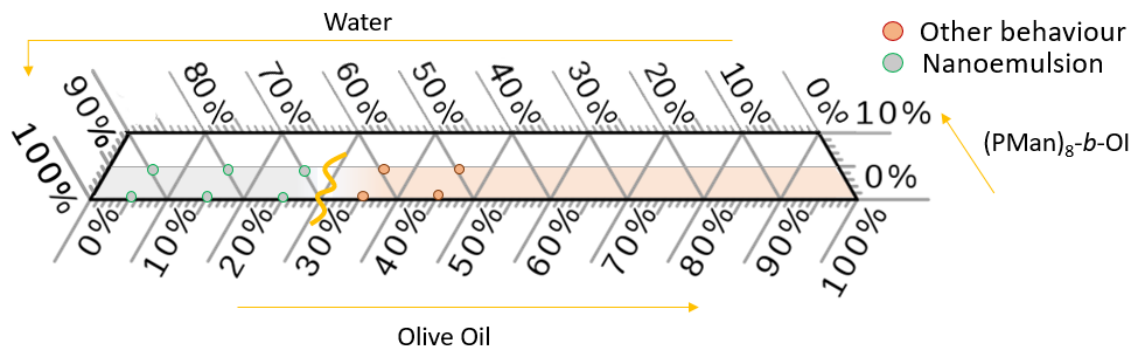


Figure 17. Extract of the pseudo-ternary phase diagram with the stable nanoemulsions in green and the non-stable in red for the system: olive oil/ $(\text{PMan})_s\text{-}b\text{-OI}$ /water.

3.1.4 Soybean Oil

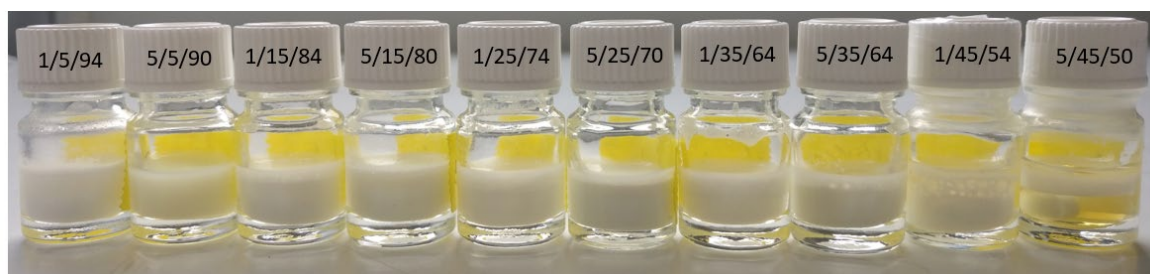


Figure 18. Emulsion of $(\text{PMan})_s\text{-}b\text{-OI}$ and soybean oil in water with the different ratios of surfactant/oil/water.

Soybean oil gave stable emulsions in water with up to 25 wt.% (Figure 18) with hydrodynamic radii from *ca.* 200 nm (1/35/64) to *ca.* 420 nm (1/25/74) and a dispersity of 0.02 - 0.19. The emulsions were stable for at least 2 months at room temperature. For higher amounts of oil, we denoted the formation of Winsor I and Winsor III regions (Figure 20). As already described for the emulsions of castor oil in PBS (chapter 2.2), we could find an oil phase above the emulsion for sample 1/35/64 and 1/45/54. We attributed this behavior to Winsor I regions since the measurement of the “subphase” by DLS confirmed the presence of an emulsion phase. For sample 5/45/50, we denoted the formation of three different phases: a water phase, a bicontinuous middle phase and an oil phase. This behavior was assigned to Winsor III regions.

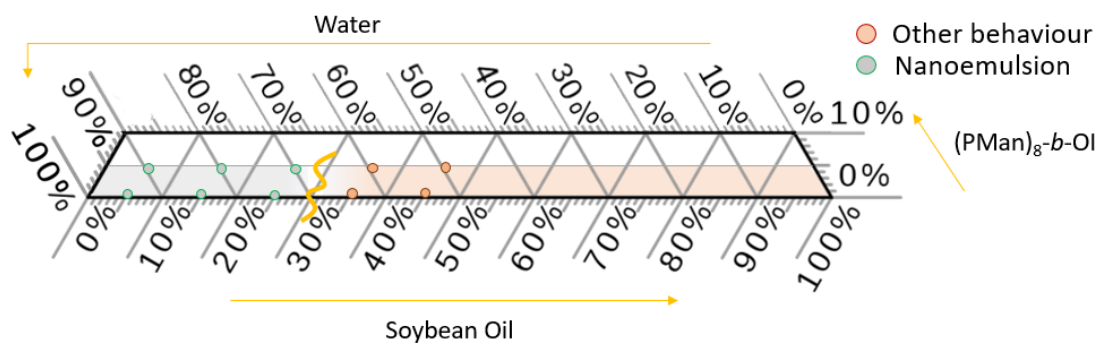


Figure 19. Extract of the pseudo-ternary phase diagram with the stable nanoemulsions in green and the non-stable in red for the system: soybean oil/(PMan)₈-*b*-OI/water.

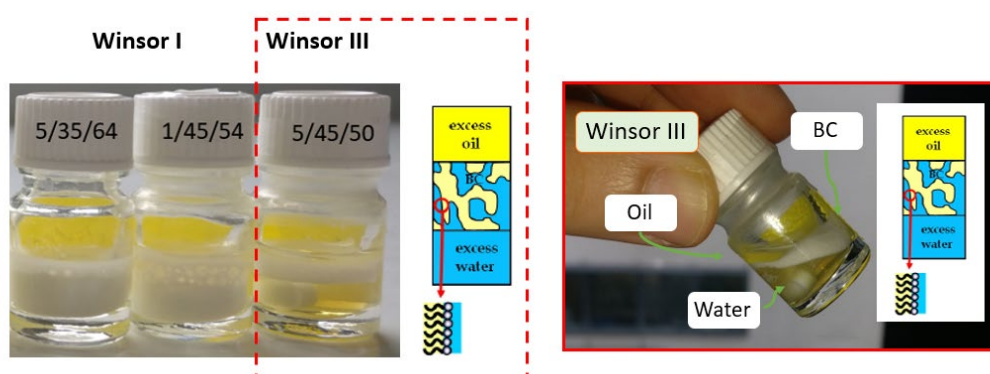


Figure 20. Winsor I and Winsor III phenomena for the systems of (PMan)₈-*b*-OI/soybean oil/water.

In summary, sunflower, - olive-, and soybean oil gave stable emulsions with up to 25 wt.% in water using 1 - 5 wt.% (PMan)₈-*b*-OI as surfactant. These emulsions were all stable at room temperature for up to 2 months. With increasing amount of oil, some of the emulsions showed a two-, respectively a three-phase system including Winsor I- and III regions. The average size of the emulsions was in the range of *ca.* 200 up to *ca.* 400 nm, while the largest droplets were found for soybean oil. The mixtures of our surfactant with mineral oil in water could not afford the formation of a one-phase stable emulsion.

3.2 Surfactant/PBS/Sunflower, - Soybean, - or Olive oil 37°C

We next transposed the emulsions of sunflower, - soybean- and olive oil from water to PBS at 37 ° to mimic biological conditions and prepare lectin-binding assays.

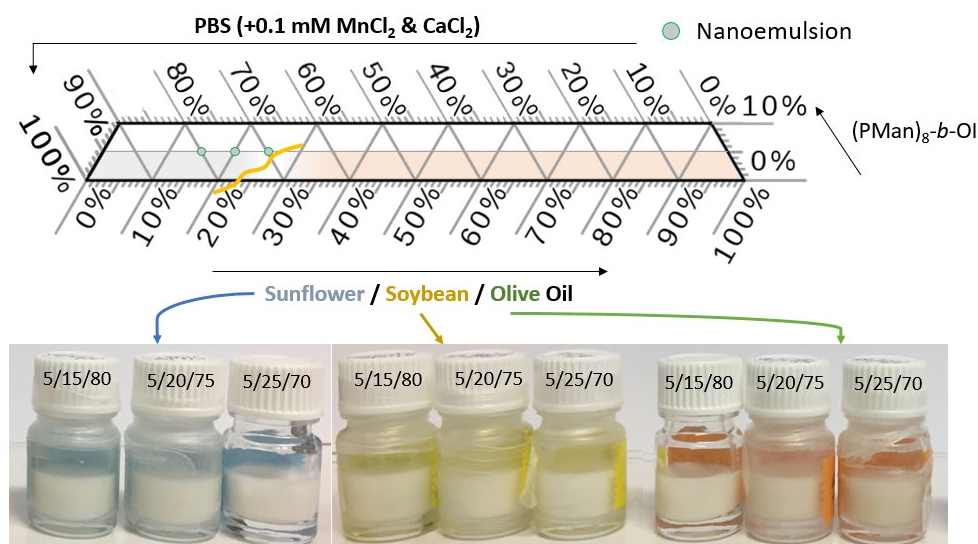


Figure 21. Stable emulsions of sunflower- (blue), soybean- (yellow-olive) and olive oil (orange) in PBS using $(PMan)_8-b-OI$ as surfactant.

As shown in Figure 21, we observed the formation of one-phase systems with all three oils with 15-, 20-, and 25 wt.% with 5 wt.% of $(PMan)_8-b-OI$ in PBS. The average size measured by DLS increased to *ca.* 300 - 500 nm, 300 - 640 nm and 310 - 620 nm for sunflower, - soybean, - and olive oil, respectively (Figure 22). The largest droplets were found in the samples with highest amount of oil: 5/25/70. The emulsions were found to be stable at least for 24 h.

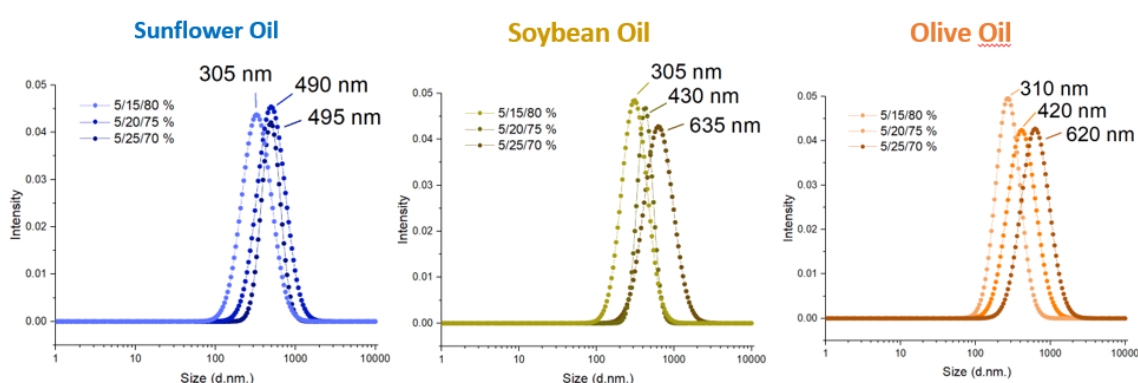


Figure 22. Plot of the size distribution of the emulsions by DLS at 135° of sunflower oil (blue), soybean oil (olive-green) and olive oil (orange).

In summary, we could obtain nanoemulsions of castor-, sunflower, - soybean, - and olive oil with $(PMan)_8-b-OI$ in water. The average size of these stable emulsions were in the range of *ca.* 200 - 380 nm. A general trend was denoted for increasing amount of oil in the emulsion. Higher weight percent oil emulsions gave larger d_H , while among them, soybean oil denoted

the largest size of the droplets with *ca.* 380 nm (Figure 23, (a)). The transpose of these systems to PBS gave stable nanoemulsions, while d_H increased to *ca.* 100 up to 300 nm. As for the emulsions in water, soybean oil showed the largest droplet size with up to *ca.* 640 nm. All of these nanoemulsions were stable for at least 15 days and were expected to be still one-phase systems after 1 month.

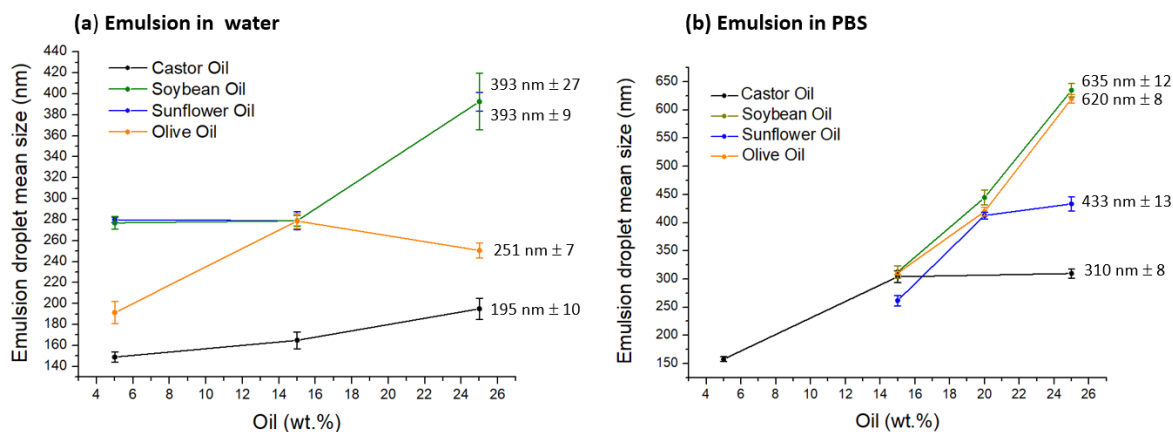


Figure 23. Plot of the droplet mean size of the emulsions from castor (black)-, soybean (olive-green)-, sunflower (blue)-, and olive oil (orange) as a function of the weight percent of the oil. For all emulsion, 5 wt.% (PMan)_s-*b*-OI was utilized as emulsifier.

3.3 Emulsions with mixtures of mannose- and glucose-based surfactants

We studied the emulsification capacity of glucose- and subsequently mixtures of glucose- and mannose- surfactants for soybean oil in PBS. For mannose, we selected the previous utilized (PMan)_s-*b*-OI derivative and for glucose, we chose COS-PGA(3)-*b*-OI obtained by ball-milling (chapter II B). The latter is a short chain of in average three glucose units linked via the β -(1,4)-glycosidic bond (Figure 24).

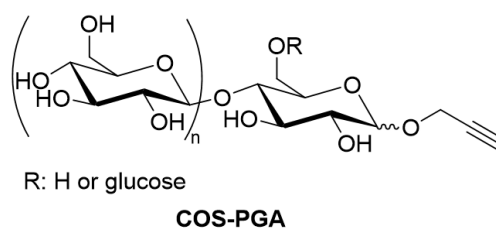


Figure 24. Structure of the glucose-based surfactants COS-PGA(3)-*b*-OI obtained from ball-milling and functionalization of cellulose (see Chapter II B).

3.3.1 Emulsions with glucose-based surfactants

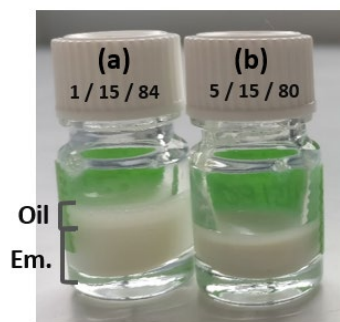


Figure 25. Emulsion of COS-PGA(3)-*b*-OI/soybean oil/PBS in the ratio (a) 1/15/84 and (b) 5/15/80. Experiment (a) gave a two-phase system (Winsor I region) with an oil phase above the emulsion phase.

We tested the emulsification of soybean oil (15 wt.%) in PBS with 1-, and 5 wt.% COS-PGA(3)-*b*-OI. Figure 25 supports the formation of emulsions for both compositions. For 1 wt.% of surfactant, we denoted a two-phase system with an extra oil phase above the emulsion one. The increase to 5 wt.% of surfactant gave a one-phase system that we measured by DLS (Figure 26). The average size of the droplets was *ca.* 350 nm after the preparation *ca.* 300 nm after 24 h and *ca.* 340 nm after 4 days. The same protocol as for the previous emulsions was also followed in this case.

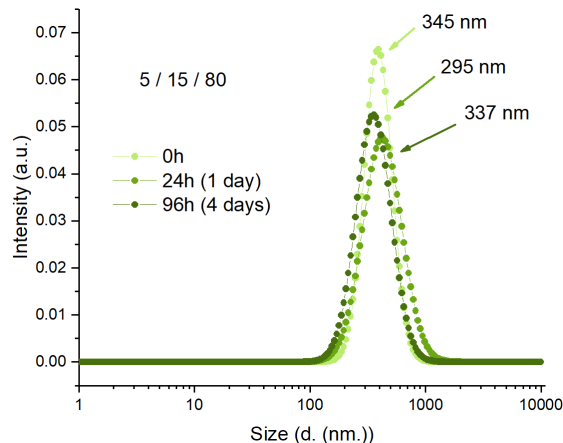


Figure 26. Plot of the size distribution of the emulsion COS-PGA(3)-*b*-OI/soybean oil/PBS with 5/15/80 over 4 days.

This experiment showed, that the COS-PGA(3)-*b*-OI retained less oil in emulsion than (PMan)₈-*b*-OI. We tentatively attributed this result to the decrease of the \overline{DP}_n from 8 of to 3 comparing the mannose with the glucose-based surfactant. We supposed that the stability of the droplet is due to the intermolecular interactions among the sugar molecules. These interactions are consequently lower for $\overline{DP}_n = 8$ than for $\overline{DP}_n = 3$ sugar surfactants, respectively. Furthermore, we assume that the glucose-based surfactants do not have the same air/water interface behavior than mannose.

3.3.2 Emulsion with mixtures of mannose- and glucose-based surfactants

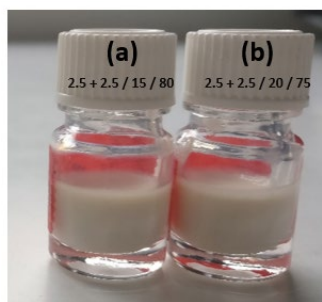


Figure 27. Emulsion COS-PGA(3)-*b*-OI + (PMan)_s-*b*-OI /soybean oil/PBS with (a) 2.5 + 2.5/15/80 and (b) 2.5 + 2.5/20/75.

Then, mixtures of mannose- and glucose-based surfactants were prepared (50:50 mixtures of (PMan)_s-*b*-OI and COS-PGA(3)-*b*-OI) and utilized to emulsify soybean oil in PBS. With a total amount of 5 wt.% of the surfactant solution, 15-, up to 20 wt.% of soybean oil could be successfully emulsified (Figure 27). The DLS experiments gave average size of *ca.* 330 nm and *ca.* 370 nm for 15-, respectively 20 wt.% soybean oil (Figure 28). Compared to the emulsion with pure mannose-, or glucose-based surfactants, no significant change in the size was denoted.

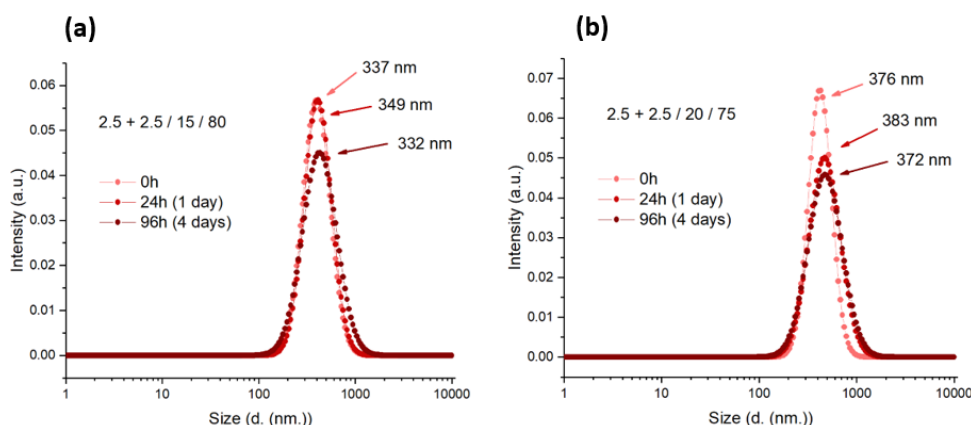


Figure 28. Plot of the size distribution of emulsion COS-PGA(3)-*b*-OI + (PMan)_s-*b*-OI /soybean oil/PBS with 0(a) 2.5 + 2.5/15/80 and (b) 2.5 + 2.5/20/75 over 4 days.

We could show here, that it was possible to obtain stable emulsions with mixtures of glucose- and mannose-based surfactants. Depending on further applications, the ratio between these sugars-derived emulsifiers can be adapted.

4 Molecular targeting: Concanavalin A (ConA)

Phagocytosis is defined as the internalization of objects larger than 0.5 microns by cells. This process is part of the innate immunity of phagocytes, consisting of the identification, ingestion and elimination of pathogens (= germ or more general any infectious microorganism such as

a virus, bacteria, fungi etc.). A phagocytosis is a special subset of cells, composed of two different species that form together the reticuloendothelial system, located in the reticular connective tissue. Among them, the macrophages fulfill the main task of the adaptive immune response. During the phagocytosis, the “target” bind to specific receptors that are localized at the surface of the phagocyte. From the various receptors existing, several have been identified to date. They differ each in their ingestion mechanism and signaling pathways, respectively. Among them, the Pattern Recognition Receptors recognize conserved pathogen-associated molecular patterns (PAMPs) on the surface of a bacteria. The Mannose Receptor (MR) and DC-SIGN belong both to these families. They are C-type lectin receptors for glycoconjugates, that can bind the latter in a Ca^{2+} dependent manner. While the MR recognize terminal mannose, fructose and N-acetylglucosamines, DC-SIGN detects terminal mannose groups like mannans. However, it is until today still unclear how they participate and trigger the phagocytosis process.

There are several ways to detect the macrophage activity. One is the indirect observation of a molecular fluorescent probe, that reports the pH acidification from the production of reactive oxygen species (ROS) inside the phagosome. Another method is the direct detection of the internalization by biosensors. Nano-, and micro particles have been used to build up biosensors in solid (silica- or polystyrene beads) or liquid form (liposomes or emulsions). Since liquid particles can mimic the mobility of the interfacial ligands of real cellular lipids, as they are fluid, they are preferred for phagocytosis targeting. Liposomes are by far the most applied biosensor for cell recognition of glycosylated structures. To them, O/W emulsions of vegetable oils present an attractive alternative. They can be prepared with narrow size distribution, ranging from nano- to micrometers and functionalized with biological-relevant adhesive molecules that interacts with the cell. Therefore, they are exploited as models for cell adhesion and are used in imaging or therapeutic applications.^[3a]

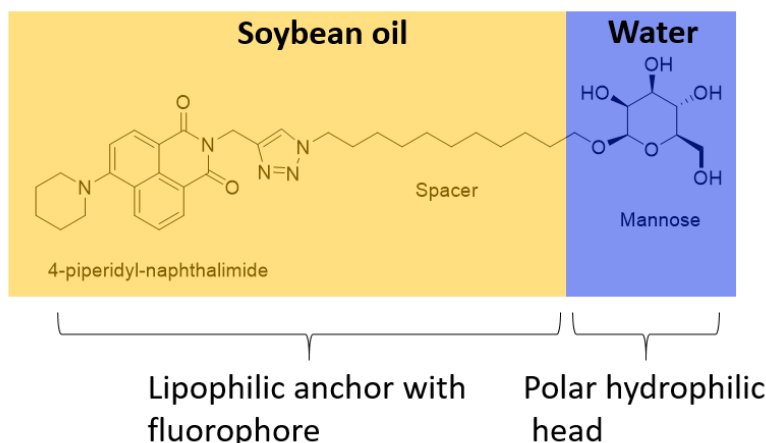


Figure 29. O/W emulsion of soybean oil, emulsified by the mannolipid from B. Dumat *et al.*^[3a], having a fluorescent dye attached.

The transformation of a O/W emulsion to an effective biosensor requires a controlled chemical surface functionalization. Towards this, B. Dumat *et al.*^[3a] developed a receptor out of a

micrometric O/W emulsion. They functionalized the emulsion droplet with a glycosylated fluorescent ligand to show the selective interaction with a model lectin protein concanavalin A (ConA). ConA is a tetravalent C-type lectin of the same type as the mannose receptors or the DC-SIGN. Among other glycosylated structures, it can bind to α -D-mannosyl residues in terminal positions of oligosaccharides. The amphiphilic ligand consisted of a single mannose unit as polar hydrophilic head, a C11 spacer and naphthalimide as fluorescence marker (Figure 29). Lectins are known to have a good binding to high-order glycan structures but low affinity for monosaccharide units. B. Dumat *et al.* demonstrated in their work that the ligand mobility at the surface of the droplet can improve the affinity of single monosaccharides. The multivalence of ConA led to the clustering of multiple monosaccharide-ligands. They compared their results to the interaction with isolated D-mannose and found an affinity 40 times higher for their mannose-coated droplets. With the help of the fluorescent dye, they could visualize the fate of the ligand and the clustering during cellular adhesion. Thereby, they concluded that the internalization of the macrophages was receptor-triggered and specific to mannose.

The specific mechanism of the binding of ConA with mannose was studied in more detail by I. Papp *et al.*^[3b] ConA is known to associate into tetramers at physiological pH and present thereby four binding sites.^[11] The approaches to study the carbohydrate interaction are usually based on the presentation of the ligand as ‘multivalent’. The specific binding affinity of the receptors depend on many factors such as the ligand flexibility, the spacer length and the amount of receptors inside the membrane. Papp and coll. synthesized hyperbranched polyglycerol (hPG) derivatives with different terminal linked mannose residues (10, 33 and 60 mannose molecules/hPG). They denoted that the polymers with the most mannose sides formed the largest clusters with ConA.

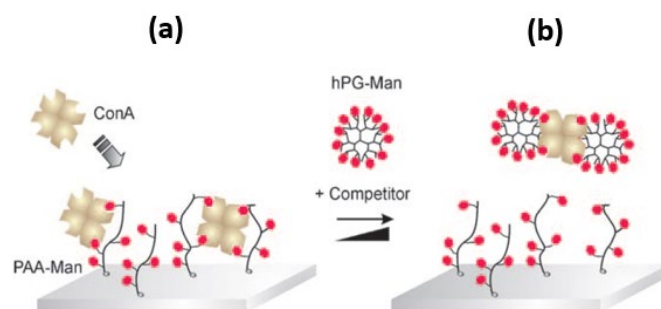


Figure 30. hPG-Man derivatives as inhibitors of Con A: **(a)** ConA bound to mannose residues of a polyacrylamide backbone (PAA-Man). **(b)** shielding of ConA by the addition of functionalized hPG compounds.^[3b]

The authors could also demonstrate that the hPG-Man conjugates inhibited ConA. When the hPG-mannose derivatives were given to polyacrylamide-Mannose (PAA-Man) coupled with ConA, the latter bound to the hPG polymers leaving the PAA-Man (Figure 30). Within this study, they denoted that the hPG-Man acted as multivalent ligands, which they referred to the “glycoside cluster effect”.^{[12],[13]} The highest binding affinity was amplified for the highest

number of mannose residues, supporting the multivalency of the ligands. These findings are in line with most reports on glycopolymer-interactions with ConA, mentioning the ability of mannose-ligands to cluster receptors.^[14]

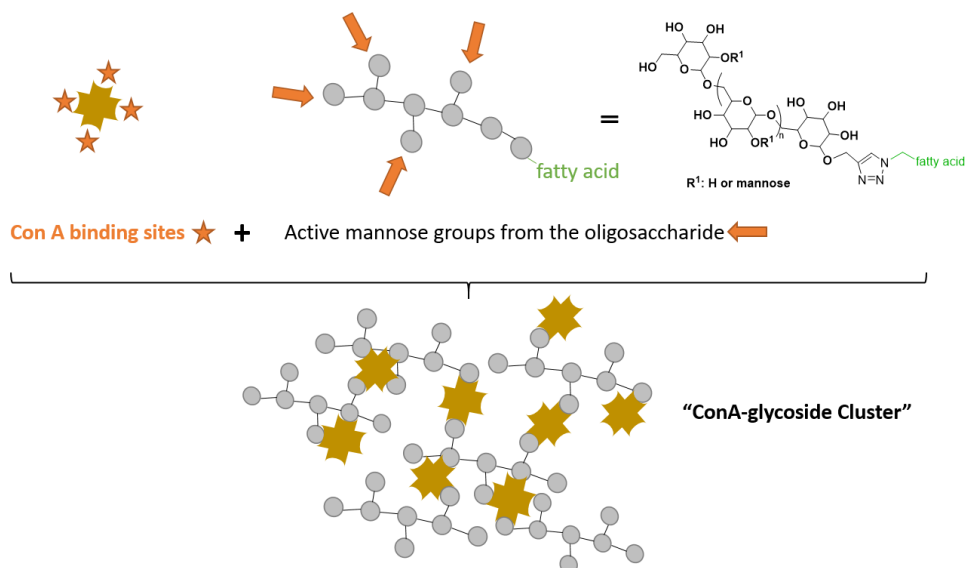


Figure 31. Illustrative presentation of the multivalent binding sites of ConA (stars) and the active mannose groups (arrows) from the surfactant (PMan)₈-b-OI and the proposed formation of complex “ConA-glycoside Clusters”.

Based on these studies, we analyzed the ‘glycoconjugate properties’ of the mannose-based surfactant (PMan)₈-b-OI, binding to ConA. The almost linear chain of mannose units with *ca.* 30 % branching pattern contains all sugar-units without any protecting groups. Consequently, the O/W emulsion stabilized with the mannose-derived surfactant is supposed to have an ‘active sugar surface’, that should bind multivalently to the numerous binding sites of ConA (Figure 31) forming a complex “ConA-glycoside cluster”. To support this hypothesis, the potential aggregation of (PMan)₈-b-OI stabilized emulsion in the presence of ConA has been elucidated by DLS, turbidity and microscopy experiments.

For the following experiments, O/W emulsions of (PMan)₈-b-OI/soybean oil/PBS (5/25/70) at 37 °C were prepared and diluted by 1:1000 in PBS. First, dynamic light scattering (DLS) was carried out to detect the formation of aggregates between ConA and the emulsion (= mannose-ligand). The correlation function from DLS measurement is directly related to the Brownian motion of objects in solution and provides therefore information of their size. While lower correlation time (τ) corresponds to smaller objects, higher values of τ give hindrance of bigger colloids in solution.

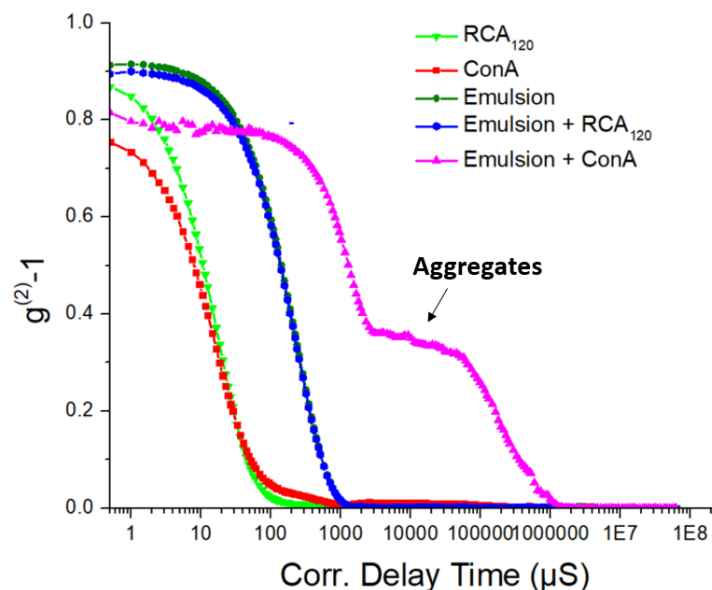


Figure 32. Correlation functions of $4.2\text{E-}5$ μM RCA₁₂₀ (green), $4.8\text{E-}5$ μM ConA (red), 0.75 μM Emulsion (olive), $4.16\text{E-}5$ μM RCA₁₂₀/ 0.75 μM Emulsion (blue) and $4.76\text{E-}5$ μM ConA/ 0.75 μM Emulsion (purple) at 25°C .

The correlation function for ConA (Figure 32, red) denoted small colloidal particles, while the diluted emulsion in PBS with the mannose-derive surfactant (Figure 32, olive-green) showed longer decay times due to their larger colloidal size. The obtained correlation function after the addition of the emulsion to ConA (Figure 32, purple) strongly supported the formation of aggregates. The shift to larger sizes and the appearance of a second population was denoted. These kind of experiments have already been carried out to prove the specific lectin-glycoconjugate binding between galactose and *ricinus communis agglutinin* (RCA₁₂₀).^[15] Anaya *et. al* could show, that RCA₁₂₀ binds specifically to galactose, but denoted no binding properties to glucose. As RCA₁₂₀ is not supposed to bind to mannose either^[16], we selected RCA₁₂₀ lectin as a negative control. This claim could be supported with the DLS results of the mixture of emulsion and RCA₁₂₀ (Figure 32, blue), denoting no binding and/or aggregation.

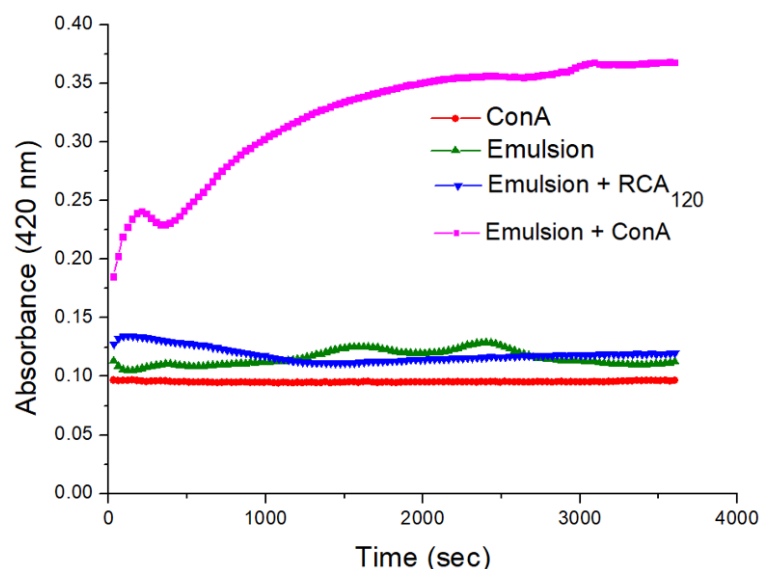


Figure 33. Overlaid plot of the absorbance at 420 nm of ConA (red, 1 mg/mL in PBS), Emulsion (green, 1:1000 dilution in PBS), 4.16×10^{-5} μM RCA₁₂₀/0.75 μM Emulsion (blue) and 4.76×10^{-5} μM ConA/0.75 μM Emulsion (purple) at 25°C.

To further confirm the specific binding of (PMan)₈-*b*-OI to ConA, we carried out turbidity assays, a common method to determine glycoside-lectin binding.^[17] The mannose-consistent emulsion was added (0.75 μM) into a solution of ConA in PBS (4.8×10^{-5} μM) and the absorbance was recorded for a time period of 60 min. every 30 sec. in a UV spectrometer. Figure 33 shows the obtained plot for a fixed wavelength at 420 nm. The absorbance of ConA after the addition of the emulsion denoted a clear increase from *ca.* 0.18 to *ca.* 0.36 a.u. (purple), supporting the formation of aggregates. The negative control with enzyme RCA₁₂₀ (blue) gave no binding signal, confirming the specific interaction of the mannose ligand exclusively with ConA. Note that the absorbance curves of ConA (red) and the emulsion (green) were also recorded for reasons of comparison. The first peak that was observed for the sample of ConA after the addition of the emulsion (purple, < 500 sec.) was supposed to be due to the experimental setup. Since the emulsion was added on top of the solution of ConA and no stirring was applied in the UV spectrometer, it took *ca.* 360 sec. to homogenize the system. However, these results were in line with what was observed *via* DLS and supported further the specific binding of ConA with our mannose-ligand.

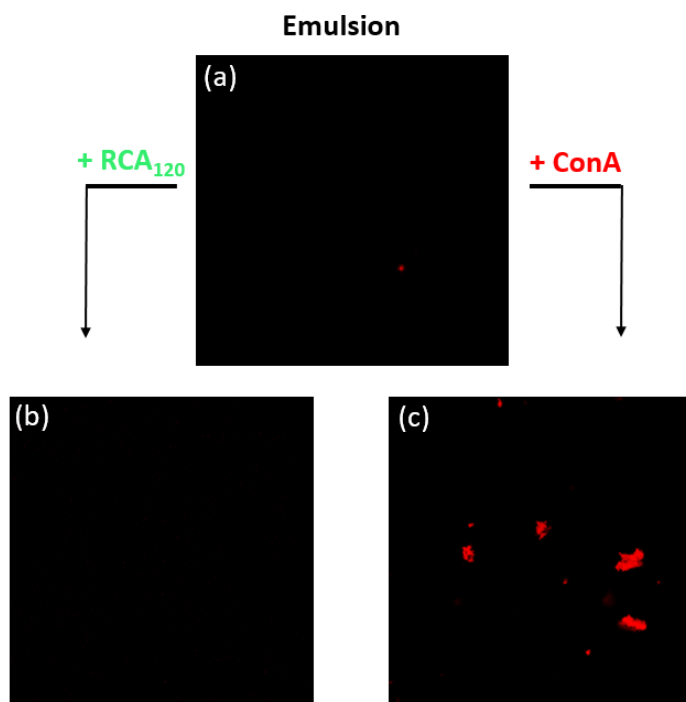


Figure 34. Laser scanning confocal microscope images of the emulsion before (a) and after the addition of (b) RCA₁₂₀ and (c) ConA. The emulsion was stained red using Nile red and excited at 561 nm and measured with the emission setting at 565 - 600 nm.

Finally, laser scanning confocal microscopy was used to gain more in-depth information about the formed aggregates. For visualization, Nile red was loaded into the emulsion and excited at 561 nm (Figure 34). The experiments showed that Nile Red could be incorporated in the O/W emulsion and did not disturb its stability. The images from the microscope denoted aggregates with a random- and clustered fashion in the μm -range after the addition of Nile Red to the emulsion (Figure 34 (c)). On the other hand, after addition of RCA₁₂₀ (Figure 34 (b)) no aggregates could be observed, showing the same image than the pure emulsion (Figure 34 (a)). These results additionally supported the specific binding of mannose to ConA. The large and random aggregates gave hindrance of a multivalent binding of (PMan)_s-*b*-OI to ConA, as suggested in Figure 31). The high \overline{DP}_n mannose ligands in our emulsion might have bound to several ConA binding sites, explaining the big aggregates. Despite the close packed micellar self-assembled structure of (PMan)_s-*b*-OI (see Chapter III), the combined results of DLS, turbidity and microscopy supported, that the surface of the mannose-based surfactant was still active for the binding, supporting its glycoconjugate properties.

5 Conclusion

Altogether, we showed that the mannose-derived surfactant (PMan)_s-*b*-OI could emulsify castor-, olive-, soybean-, and sunflower oil in water, as well as in aqueous PBS solution in up to 25 wt.% to give stable nanoemulsions. The amount of surfactant could be decreased to 1 wt.%, while the emulsions showed still excellent colloidal stability over several months. The nano-size emulsions could be prepared in a low energy-process by stirring (magnetically) at 1400 rpm for 24 h at room temperature. A general trend was denoted for increasing mean droplet sizes with larger amounts of oil. Among the vegetable oils applied, soybean oil gave the largest d_H followed by olive-, sunflower and castor oil. While with water, nanoemulsions in the range of *ca.* 150 to 390 nm were obtained, the transpose of the system to PBS gave droplet sizes from *ca.* 150 to 640 nm. We demonstrated that besides the mannose-based surfactants, also glucose-based surfactants could emulsify the vegetable oils in PBS. Due to the decrease in the sugar \overline{DP}_n from 8 ((PMan)_s-*b*-OI) to 3 (COS-PGA(3)-*b*-OI), the glucose-based surfactants retain less oil in the emulsion. Only after the addition of mannose-based surfactant to prepare 50:50 mixtures of both sugar-derivatives, the amount of oil could be increased. However, this result showed that it was possible to reduce the amount of mannose-derived surfactant with the addition of a second suitable emulsifier. This opens up further applications, for which the amount of mannose-, - respectively glucose- based surfactant can be adapted.

Finally, we showed that (PMan)_s-*b*-OI denoted glycoconjugate-properties due to the specific binding to lectin-derivative ConA. Complementary results of DLS, turbidity and microscopy supported the binding of the enzyme to the emulsion with the formation of aggregates in the μm -range. Due to the random and cluster-like conformation of the aggregates, we assumed that ConA was bound to several mannose groups of one polymer chain, that combined with other '(PMan)_s-*b*-OI-ConA' aggregates to a larger cluster. The negative control with enzyme RCA₁₂₀ confirmed the specific interaction of ConA to mannose. The incubating of Nile Red into the emulsion showed that the mannose-derived surfactants were able to transport lipophilic compounds *via* O/W emulsions. Despite their close packed self-assembly as spherical micelles (see chapter III), they maintained a bio-active surface, consisting of non-protected accessible mannose units. However, to confirm the multivalency of the binding process of (PMan)_s-*b*-OI and ConA, further quantitative studies need to be carried out.

6 Appendix

DLS experiments on Cordouan at 135°.

1) (PMan)₈-*b*-OI/Castor Oil/Water

Table 5. Average hydrodynamic radii and PDI of emulsion (PMan)₈-*b*-OI/Castor Oil/Water with different ratios; the spectra were measured 7 days after the preparation of the emulsion.

Surfactant/oil/water	d_H (nm)	PDI
	(Cordouan, 135°)	
0.5/5/94.5	196.62	0.10
1/5/94	199.76	0.12
1/15/84	184.16	0.20
1/25/74	186.13	0.14
3/5/92	211.57	0.12
4/10/86	165.57 ± 8.0	0.23
4/24/72	195.92 ± 10.1	0.23
5/5/90	149.31 ± 5.2	0.21

2) (PMan)₈-*b*-OI/Castor Oil/PBS

Table 6. Average hydrodynamic radii and PDI of emulsion (PMan)₈-*b*-OI/Castor Oil/PBS with different ratios; the spectra were measured 7 days after the preparation of the emulsion.

Surfactant/oil/water	d_H (nm)	PDI
	(Cordouan, 135°)	
1/15/84	211.41	0.18
3/5/92	158.93 ± 4	0.19
4/15/81	304.63 ± 10	0.04
4/25/71	310.45 ± 8	0.09

3) (PMan)₈-*b*-OI/Sunflower Oil/Water

Table 7. Average hydrodynamic radii and PDI of emulsion (PMan)₈-*b*-OI/Sunflower Oil/Water with different ratios; the spectra were measured 7 days after the preparation of the emulsion.

Surfactant/oil/water	d_H (nm)	PDI
	(Cordouan, 135°)	
1/5/94	198.44	0.17
1/15/84	195.16	0.10
1/25/74	220.65	0.08
1/35/64	218.4	0.13
5/5/90	269.99 ± 2.5	0.15
5/15/80	291.15 ± 8.4	0.12
5/25/70	341.27 ± 9.1	0.16
5/35/60	305.59	0.16

4) (PMan)₈-*b*-OI/Olive Oil/WaterTable 8. Average hydrodynamic radii and PDI of emulsion (PMan)₈-*b*-OI/Olive Oil/Water with different ratios; the spectra were measured 7 days after the preparation of the emulsion.

Surfactant/oil/water	d_H (nm) (Cordouan, 135°)	PDI
1/5/94	197.52	0.19
1/15/84	172.68	0.04
1/25/74	210.03	0.07
1/35/64	169.95	0.20
1/45/54	238.03	0.18
5/5/90	191.39 ± 10.7	0.23
5/15/80	274.05 ± 7.0	0.18
5/25/70	250.56 ± 7.3	0.12
5/35/60	432.81	0.19

5) (PMan)₈-*b*-OI/Soybean Oil/WaterTable 9. Average hydrodynamic radii and PDI of emulsion (PMan)₈-*b*-OI/Soybean Oil/Water with different ratios; the spectra were measured 7 days after the preparation of the emulsion.

Surfactant/oil/water	d_H (nm) (Cordouan, 135°)	PDI
1/5/94	223.12	0.02
1/15/84	226.83	0.16
1/25/74	423.46	0.19
1/35/64	213.19	0.18
5/5/90	279.89 ± 5.9	0.19
5/15/80	279.03 ± 5	0.12
5/25/70	392.55 ± 27	0.17
5/35/60	362.75	0.16

6) (PMan)₈-*b*-OI/Sunflower-, Soybean-, and Olive Oil/PBS at 37 °C

Table 10. Average hydrodynamic radii and PDI of emulsion (PMan)₈-*b*-OI/Sunflower-, Soybean-, and Olive Oil/PBS with different ratios at 37 °C; the spectra were measured 24 h after the preparation of the emulsion.

Oil	Surfactant/Oil/PBS	d _H (nm) (Cordouan, 135°)	PDI
Sunflower	5/15/80	304.5	0.19
Sunflower	5/20/75	490.0	0.14
Sunflower	5/25/70	494.8	0.13
Soybean	5/15/80	312.43	0.19
Soybean	5/20/75	443.7	0.17
Soybean	5/25/70	634.8	0.19
Olive	5/15/80	310.95	0.14
Olive	5/20/75	419.7	0.18
Olive	5/25/70	619.7	0.10

7) COS-PGA(3)-*b*-OI/Soybean Oil/PBS and COS-PGA(3)+(PMan)₈-*b*-OI/Soybean Oil/PBS at 37 °C

Table 11. Average hydrodynamic radii and PDI of emulsion COS-PGA(3)-*b*-OI and/or(PMan)₈-*b*-OI/ Soybean Oil/PBS at 37 °C; the spectra were measured 96 h after the preparation of the emulsion.

Surfactant	Surfactant/Oil/PBS	d _H (nm) (Cordouan, 135°)	PDI
COS-PGA(3)- <i>b</i> -OI	5/15/80	295.34	0.13
COS-PGA(3)- <i>b</i> -OI + (PMan) ₈ - <i>b</i> -OI (50:50)	5/15/80	332.05	0.18
COS-PGA(3)- <i>b</i> -OI + (PMan) ₈ - <i>b</i> -OI (50:50)	5/20/75	372.78	0.18

Bibliography

- [1] A. Varki, *Glycobiology* **1993**, *3*, 97-130; bA. Varki, R. D. Cummings, J. D. Esko, P. Stanley, G. W. Hart, M. Aebi, A. G. Darvill, T. Kinoshita, N. H. Packer, J. H. Prestegard, **2015**.
- [2] F. Baleux, L. Loureiro-Morais, Y. Hersant, P. Clayette, F. Arenzana-Seisdedos, D. Bonnaffé, H. Lortat-Jacob, *Nature chemical biology* **2009**, *5*, 743-748.
- [3] B. Dumat, L. Montel, L. Pinon, P. Matton, L. Cattiaux, J. Fattaccioli, J.-M. Mallet, *ACS Applied Bio Materials* **2019**, *2*, 5118-5126; bl. Papp, J. Dervedde, S. Enders, S. B. Riese, T. C. Shiao, R. Roy, R. Haag, *Chembiochem* **2011**, *12*, 1075-1083.
- [4] https://en.wikipedia.org/wiki/Castor_oil.
- [5] https://en.wikipedia.org/wiki/Phosphate-buffered_saline.
- [6] F. Hofmeister, *Archiv für experimentelle Pathologie und Pharmakologie* **1888**, *25*, 1-30.
- [7] M. Kahlweit, E. Lessner, R. Strey, *The Journal of Physical Chemistry* **1984**, *88*, 1937-1944; M. Kahlweit, R. Strey, D. Haase, *The Journal of Physical Chemistry* **1985**, *89*, 163-171.
- [8] A. Kabalnov, U. Olsson, H. Wennerstroem, *The Journal of Physical Chemistry* **1995**, *99*, 6220-6230.
- [9] Q. Jiang, D. Fan, D. Liu, X. Wang, Z. Chen, W. Shen, *Journal of Solution Chemistry* **2020**, *49*, 522-536.
- [10] aT. F. Tadros, *Emulsions: Formation, stability, industrial applications*, Walter de Gruyter GmbH & Co KG, **2016**; bM. Sanchez-Dominguez, C. Aubery, C. Solans, **2012**.
- [11] S. L. Mangold, M. J. Cloninger, *Organic & biomolecular chemistry* **2006**, *4*, 2458-2465.
- [12] aT. K. Dam, T. A. Gerken, C. F. Brewer, *Biochemistry* **2009**, *48*, 3822-3827; bJ. J. Lundquist, E. J. Toone, *Chemical reviews* **2002**, *102*, 555-578.
- [13] Y. C. Lee, R. T. Lee, *Accounts of chemical research* **1995**, *28*, 321-327.
- [14] aY. Gou, J. Geng, S. J. Richards, J. Burns, C. Remzi Becer, D. M. Haddleton, *J Polym Sci A Polym Chem* **2013**, *51*, 2588-2597; bC. W. Cairo, J. E. Gestwicki, M. Kanai, L. L. Kiessling, *Journal of the American Chemical Society* **2002**, *124*, 1615-1619; cJ. E. Gestwicki, C. W. Cairo, L. E. Strong, K. A. Oetjen, L. L. Kiessling, *Journal of the American Chemical Society* **2002**, *124*, 14922-14933.
- [15] L. M. B. Anaya, R. Petitdemange, M. Rosselin, E. Ibarboure, B. Garbay, E. Garanger, T. J. Deming, S. Lecommandoux, *Biomacromolecules* **2021**, *22*, 76-85.
- [16] Y. Wang, G. Yu, Z. Han, B. Yang, Y. Hu, X. Zhao, J. Wu, Y. Lv, W. Chai, *FEBS Letters* **2011**, *585*, 3927-3934.
- [17] aN. Vinson, Y. Gou, C. R. Becer, D. M. Haddleton, M. I. Gibson, *Polym. Chem.* **2011**, *2*, 107-113; bG. Yilmaz, V. Uzunova, M. Hartweg, V. Beyer, R. Napier, C. R. Becer, *Polymer Chemistry* **2018**, *9*, 611-618.

General Conclusion and Perspectives

One of the main challenges with respect to the synthesis of oligosaccharides today is the stereo- and regiochemical control of the glycosylation reaction. Due to the large number of reaction steps resulting from the utilized protecting groups, most researchers focus on expensive automated synthesis methods. As far as surfactants are concerned, for which the stereoselectivity is not crucial, unprotected and non-activated carbohydrates can be applied in a protecting group-free synthesis. Thereby, the classical Fischer-Glycosylation is one of the most reported reaction to synthesize sugar-based surfactants at an industrial scale. Among them, alkylpolyglycosides (APG) are forming the most widespread family. The latter are prepared *via* the acid-catalyzed reaction of a long chain fatty alcohol (C₅ – C₁₈) with an unprotected monosaccharide (glucose, mannose, galactose etc.). However, the release of stoichiometric amount of water during this reaction causes hydrolysis of the glycosidic bond of the *in situ* formed alkyl-(oligo)-glycosides, leading to a thermodynamic equilibrium in which APGs are composed, on average, of 1.5 to 2.1 sugar units per fatty chain. Another hurdle to increase the \overline{DP}_n of these surfactants is the low solubility of the monosaccharides in fatty alcohols. It is worth to be mentioned that the unwanted hydrolysis of the glycosidic bonds of the APGs can neither be prevented, when water is continuously distilled out during the reaction. Furthermore, at the end of the reaction, the removal of the excess of fatty alcohol by distillation is a very delicate step as it generally requires elevated temperatures, leading to the partial degradation of APGs.

During this work, we developed an alternative straightforward strategy based on the use of propargyl alcohol (PGA), which served not only as glycosyl acceptor but also as a linker to subsequently introduce the fatty chain to the oligosaccharide through a 100 % atom-economical copper-catalyzed Huisgen reaction. With the occurrence of the reaction into a two-step process, fully functionalized propargylated glycosides, (PMan)_n, with a \overline{DP}_n up to 8 in 88 % yield were obtained. The short alkyl chain alcohol, bearing an alkyne function, helped in the solubility of the sugar entities and enabled introducing a functionality (alkyne function) at the terminal end of the obtained oligosaccharides. In contrast to experimental conditions involving fatty alcohols, the propargyl alcohol can be conveniently separated by distillation at the end of the reaction, thus limiting the degradation of APGs. The key step for the oligomerization was (1) the distillation of water along with PGA in step 2 and (2) the consequent increasing probability of the reaction among PMan with other PMan or Man molecules, leading to an elongation of (PMan)_n. In contrast to the classical synthesis of APGs, the reaction medium was not neutralized prior to the distillation of the alcohol. We took advantage of the remaining active reaction medium, so that in our case, the distillation step initiated at the same time the oligomerization.

In another strategy, we explored to obtain oligosaccharides-based surfactants *via* the post-functionalization of larger oligosaccharides. These latter were obtained in our study by a mechanocatalytic depolymerization of cellulose. In the literature, end-functionalization are carried out mainly *via* reductive amination by ring-opening at the chain end of the respective saccharide. This method occurs within two-steps and was successfully applied to xylose-oligosaccharides in prior works in our group. However, this strategy demands several steps and long reaction times. To the best of our knowledge, the Fischer-Glycosylation has not been reported as efficient glycosylation of unprotected oligosaccharides. The acid conditions of the reaction lead to the cleavage of the inner glycosidic linkages, affording depolymerization. We faced similar problems, when we tried to synthesize end-functionalized glycosides from larger oligosaccharides. After the addition of PGA to cellulose-oligosaccharides (COS) in the presence of an acid-catalyst, we denoted a successful functionalization at the terminal end of the COS by PGA, but also a concomitant depolymerization of the COS chain. Under optimized conditions, COS were functionalized to ca. 80 %, while the \overline{DP}_n decreased from 4 to 3.

In summary, the glycosylation of monosaccharides with PGA and a subsequent oligomerization was the more promising strategy. We showed that this reaction could be applied to two different monosaccharides, mannose and glucose, and furthermore, that the \overline{DP}_n could be tuned *via* the variation of the reaction conditions (temperature, duration, PGA/mannose ratio). It might be of interest, in a future study, to use more environmentally friendly alcohols. Other short-chain alcohols bearing different functionalities could be reacted in the same manner with monosaccharides, circumventing the copper-catalyzed click reaction in the last step to prepare surfactants. Figure 1 compares the reaction method for the alkyne-functionalized oligo-glycosides with the classical industrial pathway of APG synthesis.

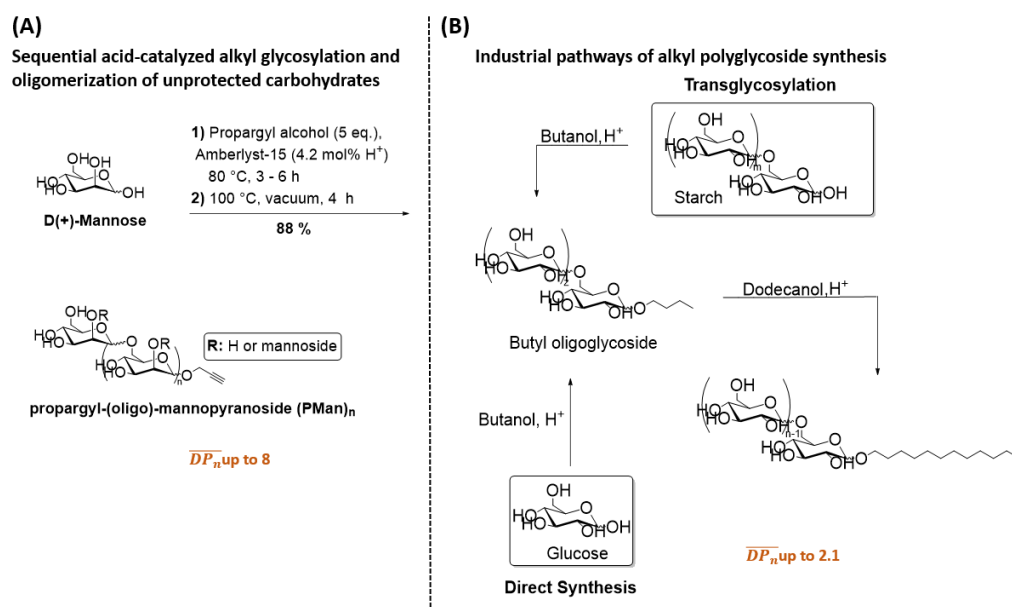


Figure 1. Comparison of the sequential acid-catalyzed alkyl glycosylation and oligomerization of mannose and glucose developed during this thesis and the classical (A) and the classical industrial pathway of APGs (B).

The sequential acid-catalyzed alkyl glycosylation and oligomerization of unprotected carbohydrates was further exploited to synthesize a small library of mannose-derived amphiphiles. Propargylated (PMan)_n with varying \overline{DP}_n were coupled with different types of fatty acids *via* azide-alkyne Huisgen cyclo-addition. The understanding of the 2D self-assembly of sugar-derived amphiphiles, as well as the analysis of their surfactant properties, is of high interest. Compared to commercially petrochemical-sourced surfactant, these biobased molecules possess lower environmental impact. However, there are to date few studies of large polar sugar head amphiphiles, containing only simple structures with one to four sugar units. First comprehensive studies of the surfactant properties and self-assembly behavior of high \overline{DP}_n sugar-based amphiphiles have been carried out by Chemin and Rosselgong in previous works in our group. A self-assembly of xylan-based amphiphiles to vesicles was observed, while other groups reported the aggregation of galactose- and glucose-based amphiphiles into micelles in aqueous media. Still, no further explanation of their final assembly was provided. The better comprehension of the interfacial behavior is a key parameter to design suitable amphiphiles.

In this contribution, we could provide further insights in the structure-behavior correlation with the four mannose-derived amphiphiles, focusing on the effect of the sugar \overline{DP}_n and the presence of a hydroxyl group at the hydrophobic tail. The analyses of the air/water interface behavior showed the surfactant properties and the self-assembled structures formed in aqueous media. A complete 3D characterization of the obtained aggregates could reveal how small-scale changes in the structure led to discrete self-assembled formations. In contrast to what is mainly observed for the hydrophilic part of amphiphiles, the larger sugar polar head amphiphiles ($\overline{DP}_n = 8$) promoted a decrease in the CAC compared to their smaller counterparts ($\overline{DP}_n = 3$). These results demonstrated the special and complex behavior of sugar-based amphiphiles, for which the strong inter- and intramolecular mannose-mannose interactions promoted the self-assembly process. The preparation method of the so-formed amphiphiles allowed us to keep the mannose units without any protecting group, assisting the strong intermolecular H-bonding. The intermolecular interactions also determined the final self-assembled structure of the sugar-derivatives. Amphiphiles (PMan)₈-*b*-OI, (PMan)₈-*b*-Ric and (PMan)₃-*b*-Ric assembled all in monodispersed spherical micellar structures with R_H of ca. 5 nm. In contrast, (PMan)₃-*b*-OI exhibited, as confirmed by cryo-TEM analyses, spherical and cylindrical micellar structures, with the later as main population. According to the Israelachvili packing parameters P ($P = \frac{v_0}{(a_0 l_0)}$, with v_0 : volume of the tail, a_0 : head group area, l_0 : tail length), a decrease in PMan polar head size as well as an increase in the volume of the hydrophobic tail led to higher P values and should consequently gave low interfacial curvature leading to worm-like micelles. While the decrease in volume of the polar head group from $\overline{DP}_n = 8$ to $\overline{DP}_n = 3$ still denoted spherical micellar structures as in (PMan)₃-*b*-Ric, its analogue (PMan)₃-*b*-OI assembled in cylindrical micelles. This feature pushed us to conclude that the OH group in ricinoleate tails generated hydrogen bondings, leading to a closer packing of the hydrophobic chains. The fatty acid chains were therefore ‘hold together’ and could not assemble as cylindrical micelles (Figure 2, A). In the case of (PMan)₃-*b*-OI, there were no such

a ‘hydrogen bonding stabilization’, so that cylindrical micelles are formed (Figure Figure 2, B).

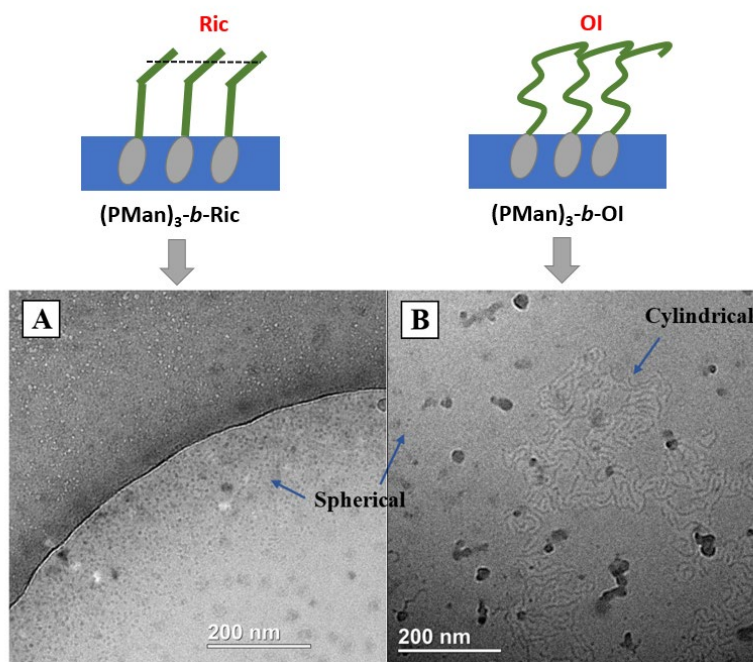


Figure 2. Self-assembly of $(\text{PMan})_3\text{-}b\text{-OI}$ into A cylindrical and spherical micelles and $(\text{PMan})_3\text{-}b\text{-Ric}$ in spherical micelles.

In a final study, the mannose-derived amphiphiles were applied as surfactants to prepare O/W emulsion using different vegetable oils. We could show that $(\text{PMan})_8\text{-}b\text{-OI}$ stabilized castor-, olive-, and sunflower oil in water, as well as in aqueous PBS solution at concentrations up to 25 wt.%. As nano-emulsions are usually challenging to prepare, we found, in an optimized protocol, that a low energy-process (magnetically stirring at 1400 rpm for 24 h at R.T.) was sufficient to emulsify the vegetable oils. Interestingly, the amount of surfactant could be decreased to 1 wt.%, while the emulsions showed excellent colloidal stability over several months.

The defined synthesis of APGs, also called glycoconjugates, is of high research interest since the latter can mimic terminal oligosaccharides in pharmaceutical issues. The so-formed mannose-derived surfactants consisted of an almost linear chain of free mannose-units with small amount of branching points. Despite the compact self-assembled structure due to the strong mannose-mannose interactions, the mannose-ligand in the emulsion denoted a bioactive surface. The specific binding of the lectin derivative concanavalin A (ConA) and mannose-oligosaccharides $(\text{PMan})_8\text{-}b\text{-OI}$ was supported *via* the complementary analysis of DLS, turbidity assays and confocal microscopy (Figure 3), supporting the glycoconjugate properties of the latter. We tentatively assumed that ConA was bound to several mannose groups of one polymer-chain, affording large random ordered clusters (Figure 3). Furthermore, the incubating of Nile Red into the emulsion for the visualization in the confocal microscopy experiments showed that the mannose-derived surfactants were appropriate carriers for lipophilic compounds. The presence of Nile Red was not affecting the stability of the emulsion.

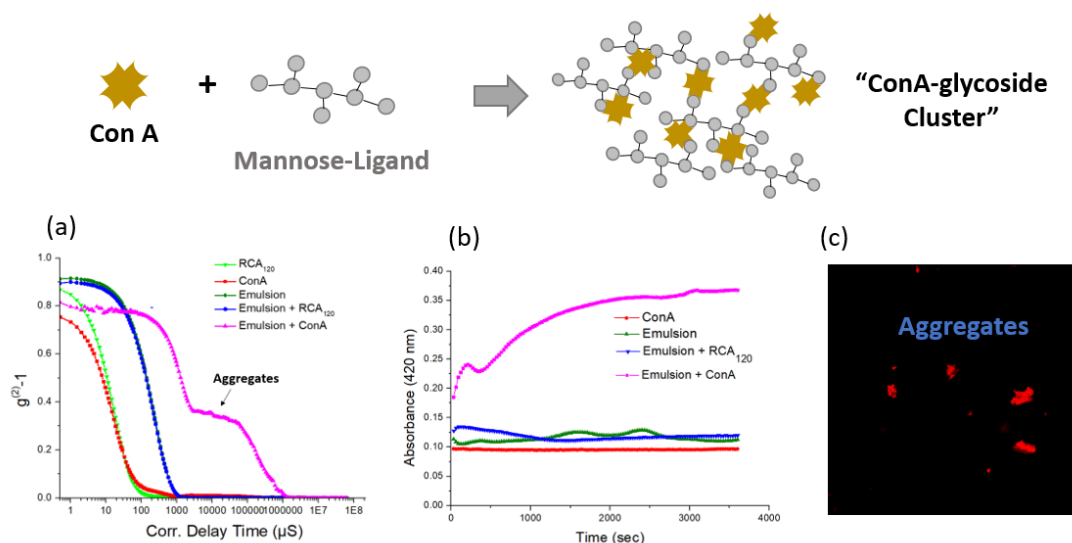


Figure 3. Binding of lectin ConA to mannose: (a) Plot of the DLS experiments, (b) Plot of the turbidity curves, (c) Laser scanning confocal microscope image.

It needs to be mentioned that the multivalent binding between the mannose-ligand and ConA requires more quantitative studies to be confirmed. The support of a quantitative turbidity assay to calculate the mannose/ConA ratio is crucial to get more information of the binding mechanism.

As a conclusion, an innovative synthetic strategy to prepare functionalized mannose- and glucose oligosaccharides was performed. The method allowed us to simultaneously tune the \overline{DP}_n of the glycosides and to bring an alkyne group at the terminal chain-end, opening the route to APGs by 'Click chemistry' *via* Huisgen coupling. A complete structure-property relationship of these APGs that self-assembled in water was discussed. Finally, these original mannose-based APGs could be applied as emulsifiers for vegetable oils in water, as carriers for lipophilic compounds and as glycoconjugates, denoting a bioactivity.

Chapter V: Experimental Section



Contents

1	Methods and Chemicals	264
1.1	Chemicals	264
1.2	Methods	264
2	Glycosylation of Sugars	277
3	Functionalization of Fatty Acids	278
4	Huisgen-Cycloaddition	281
5	Ball-milling protocol	283
6	Self-Assembly protocols	283
7	Emulsion protocols and molecular targeting	284
8	Calibration and Kinetic study	284
8.1	GC-Chromatography	284
8.1.1	Calibration of Mannose	286
8.1.2	Calibration of PMan	287
8.2	Size-exclusion-chromatography	288
8.2.1	Calibration of Mannose	288
8.2.2	Calibration of PMan	290
9	Calculation of <i>DP_n</i> and <i>M_n</i> by ¹H-NMR spectroscopy	292
10	Calculation of MW and DP by Mass spectroscopy	294
11	Appendix	297
	Bibliography	311

1 Methods and Chemicals

1.1 Chemicals

D-(+)-Mannose (from wood, $\geq 99\%$), D-(+)-Glucose ($\geq 99.5\%$) and Amberlyst-15 ($\geq 90\%$, 0.355 – 1.18 mm, 1.7 ml/L capacity) were purchased from Sigma Aldrich, and dried under vacuum before use. GC-FID standards propargyl α -D-mannopyranoside (PMan) and levomannosane (LVM) were purchased from Biosynth Carbosynth. Propargyl alcohol (99%), BSTFA (+ 1% TMCS), D-Sorbitol ($\geq 98\%$), 1,5,7-triazabicyclo[4.4.0]dec-5-ene (98%, TBD), sodium azide (reagent plus $\geq 99.5\%$), L-Ascorbic acid (99%) and 3-bromo-1-propanol (97%) were purchased from Sigma Aldrich and used without further purification. Methyl oleate (MeOI $\geq 99.9\%$) was obtained from Nuchekrep. Cuprisorb was purchased from Seachem and Copper(II) sulfate from ProLabo. Pure microcrystalline cellulose (Avicel PH200, FMC Biopolymer) was utilized for the ball-milling process. Aquivion PW98 was received from Solvay Specialty Polymers and used without further treatment. Acetone, tetrahydrofuran (THF), Acetonitrile, chloroform (CDCl_3), diethyl ether, dimethyl sulfoxide (DMSO), ethyl acetate, petroleum ether, pyridine and magnesium sulfate were purchased from Sigma Aldrich and used without further purification. Dialysis was operated using a Spectra/Por®6 MWCO 100-500 Da membrane. Ultrapure water used was produced by a Millipore Milli-Q unit, and pretreated by a Millipore reverse osmosis system ($>18.2\text{M}\Omega\text{ cm}^{-1}$). Olive Oil, Sunflower Oil, Soybean Oil, Castor Oil and Mineral Oil (all analytical standard) were purchased from Sigma Aldrich and utilized without further purification. Fluorescent dye Nile-Red (extra pure) was purchased from Roth and utilized without further modification. Concanavalin A, *canavalia ensiformis* and phosphate buffered saline (PBS) were purchased from Sigma-Aldrich, *Ricinus Communis Agglutinin* (RCA_{120}) from Vector Laboratories and used without further purification.

1.2 Methods

Nuclear Magnetic Resonance (NMR)

Analyses were performed at 298 K on a Bruker AVANCE III 400 (Bruker Scientific Instruments, Massachusetts, USA) equipment with a 5 mm probe operating at 400.2 MHz for ^1H . A 10-20 mg portion of material was dissolved/dispersed in 0.5 mL of deuterated solvent (D_2O , Eurisotop; 99.0 atom % D, CDCl_3 , Eurisotop; 99.5 atom % D, DMSO-d_6 , Eurisotop; 99.8 atom % D) and 128 up to 4096 scans were recorded for ^1H experiments and ^{13}C experiments, respectively. The spectra data were analyzed using TopSpin (v. 4.0.9). Automatic phase correction, and subsequently integration was applied. The following abbreviations were used for NMR: s: singlet, d: doublet, t: triplet, q: quartet, p: pentet, s: sextet, hept: heptet, m: multiplet, J: coupling constant, δ : chemical shift, H: number of protons depending on the integral of the spectra, ppm: parts per million.

Matrix Assisted Laser Desorption/Ionisation-Time of flight (MALDI-TOF)

MALDI-MS spectra were performed by the CESAMO (Bordeaux, France) on an autoflex maX TOF mass spectrometer (Bruker Daltonics, Germany) equipped with a frequency tripled

Nd:YAG laser emitting at 355 nm. Spectra were recorded in the positive-ion linear mode and with an accelerating voltage of 19 kV. All samples were dissolved at 20 mg/ml (water: acetonitrile 70/30 + trifluoroacetic acid (TFA, 10 vol.%). The 2,5-dihydroxybenzoic acid (DHB) matrix solution used was prepared in acetonitrile with a 10mg/ml final concentration. The solutions were combined in 10:1 v/v of matrix to sample. One to two microliters of the obtained solution were deposited onto the sample target and vacuum-dried.

Attenuated Total Reflectance Infrared Spectroscopy (ATR-IR)

Fourier transform infrared (FTIR) spectra were recorded on a Bruker VERTEX 70v (Bruker Daltonics, Germany) instrument. The detection conditions were 4 cm⁻¹ resolutions and 64 scans, carried out by a DLaTGS MIR (Bruker Daltonics, Germany). For the attenuated total reflectance (ATR) at room temperature measurements, the system is equipped with a diamond crystal plate GladiATR (Pike Technologies, Wisconsin, USA).

Size Exclusion Chromatography (SEC)

Oligosaccharides molar masses were determined by Size Exclusion Chromatography (SEC) using water as the eluent. Measurements in water were performed on an Ultimate 3000 system from ThermoScientific equipped with diode array detector DAD. The system also includes a multi-angle laser light scattering detector MALLS and differential refractive index detector dRI from Wyatt technology. Polymers were separated on two Shodex OH Pack 802.5 (8*300) columns (exclusion limits from 500 Da to 10 000 Da) at a flowrate of 0.6 mL/min. Columns temperature was held at 25 °C. Dextran from PSS was used as the standard.

The fatty acid ester derivatives were separated with G2000-, G3000- and G4000 TOSOH HXL gel columns (300 x 7.8 mm) with exclusion limits from 1000 to 400 000 Da at a flow rate of 1 mL/min. The column temperature was held at 40 °C with THF as eluent and polystyrene as standards.

The amphiphiles were separated on Tosoh TSK G3000HHR and G2000HHR (7.8*300) columns (exclusion limits from 200 Da to 60 000 Da) at a flowrate of 0.5 mL/min using dimethylsulfoxide (DMSO + lithium bromide LiBr 1g/L) as the eluent. Columns temperature was held at 80 °C. Dextran from PSS was used as the standard.

Gas Chromatography with Flame-Ionization Detection (GC-FID)

Gas chromatography analysis was conducted with a GC Trace 1300 Gas Chromatograph (ThermoScientific) equipped with a split/splitless injector and flame ionization detector (FID). A H₂ flow rate of 34 mL/min and an airflow rate at 350 mL/min were used. The flow rate of carrier gas (H₂) was set at 1.2 mL/min. The temperature of the injection port and detector were set at 250 °C and 320 °C. The oven temperature was programmed to initiate at 90 °C for 1 min, then the temperature was raised to 220 °C at a rate of 10 °C/min and finally increased to 320 °C at a rate of 40 °C/min and held there for 5 min. The injection volume was 1 µL in the split injection mode (15:1). Separation was performed on a capillary column TRB-5MS (30 m × 0.25 mm × 0.25 mm film thickness) from Teknokroma with matrix 95 % Dimethyl-(5 %) diphenyl polysiloxane.

Tensiometry

Surface tension (γ) measurements were performed on a Drop Shape Analyzer-DSA100 (Krüss GmbH, Germany) using a CF04 camera (320 fps at 1200×600 px), a high-power monochromatic LED ($\lambda = 470$ nm) illumination and a 0.72 mm diameter needle. All the samples were aqueous amphiphilic solutions at 20 ± 0.5 °C.

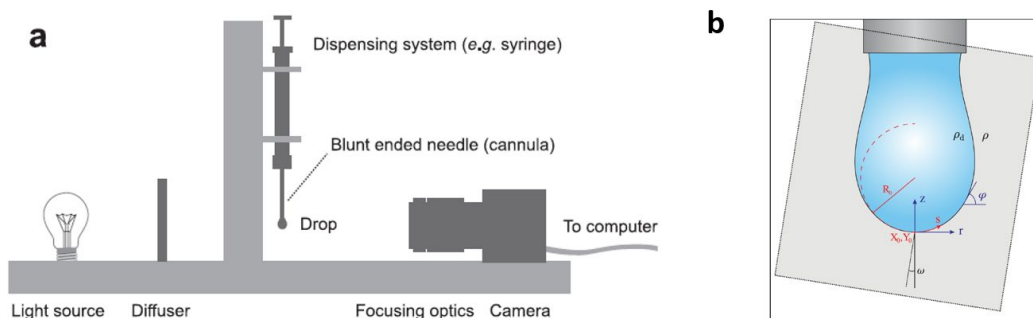


Figure 1. **a** Experimental setup for pendant drop tensiometry; **b** schematic pendant drop.^[1]

A pendant drop at equilibrium follows the Young–Laplace equation, which states the relationship between the Laplace pressure across an interface with its the curvature and γ (eq. 1). R_1 and R_2 are the radii of curvature, ΔP is the Laplace pressure across the interface and $\Delta\rho$ is the drop phase and continuous phase density. When the droplet profile is spherical, the Young–Laplace equation can be solved analytically. In this case, the shape of the pendant drop is dependent on a single dimensionless quantity, the Bond number, B_o (eq. 2), being R_o the droplet radius. If the B_o associated with a pendant drop together with R_o at the apex, the interfacial tension γ is then readily obtained. For accurate results, samples were measured at $B_o > 0.6$ ¹⁰. However, higher oscillations in the γ values were obtained close to the CAC values. Water evaporation during the measurement caused a local concentration rises inside the droplet, driving more surfactant to the interface and lowering the surface tension.

$$\gamma \left(\frac{1}{R_1} + \frac{1}{R_2} \right) = \Delta P \approx \Delta P_0 - \Delta\rho g z \quad (1)$$

$$B_o \approx \Delta\rho R_o^2 / \gamma \quad (2)$$

With the increase of the surfactant concentrations, more molecules are placed at the air/water interface and thus, the γ decreases. Usually, when the interface is completely saturated, new added amphiphiles aggregate in the bulk of the solution, maintaining the γ stable. The transition concentration when aggregates started to form is known as the Critical Aggregation Concentration (CAC). In case of forming only micelles, it is denoted as Critical Micelle Concentration (CMC). An estimated value of the area per molecule, A_{min} , can be obtained (eq. 3). Γ is the surface excess and can be calculated by the Gibbs adsorption isotherm (eq. 4). Also, the aggregates Gibbs energy formation, ΔG^o , can be deduced using the CAC (eq. 5).

$$A_{min} = 1/(N_A * \Gamma) \quad (3)$$

$$\Gamma = -\left(\frac{1}{RT}\right)\left(\frac{\delta\gamma}{\delta\ln C}\right) \quad (4)$$

$$\Delta G^0 = -RT * \ln CAC \quad (5)$$

Isothermal titration calorimetry (ITC)

Isothermal titration calorimetry experiments were performed on a GE Microcal iTC₂₀₀ (Malvern Panalytical Ltd., Malvern, UK) at 20 °C. In a typical experiment, small aliquots of concentrated amphiphile solution, the titrant solution, are injected into the sample cell initially containing milliQ water with stirring speed 750 rpm and 120s interval between titration steps. The concentration of the titrant solution should be high, at least 20 times the CAC so that the monomer concentration can be disregarded. Injections of 1µL on a 1mL water solution were carried out after an initial heat stabilization. Finally, thermodynamic data of micelle formation were deduced from the measured ITC curves, using the so-called phase-separation model¹¹. The Gibbs free energy of demicellation (ΔG°_{demic}) is defined by the chemical potential of the amphiphile in water and the amphiphile in micellar phase, which can also be obtained from the measured CAC' molar fractions (eq. 6). Demicellation enthalpy (ΔH°_{demic}) and demicellation entropy (ΔS°_{demic}) are obtained from ΔG°_{demic} according to the Gibbs–Helmholtz relation (eq. 7) knowing that the concentration of injected surfactant solution ($C_{syringe}$) is related to ΔH°_{demic} (eq. 8). An approximation where the concentration of the monomers remains constant is used above the CAC.

$$\Delta G^0_{demic} = -RT \cdot \ln CAC \quad (6)$$

$$\Delta G^{\circ}_{demic} = \Delta H^{\circ}_{demic} - T\Delta S \quad (7)$$

$$\Delta H^{\circ}_{demic} = \Delta_R H^{\circ}_{demic} \cdot C_{syringe} / (C_{syringe} - CAC) \quad (8)$$

Basics of radiation scattering

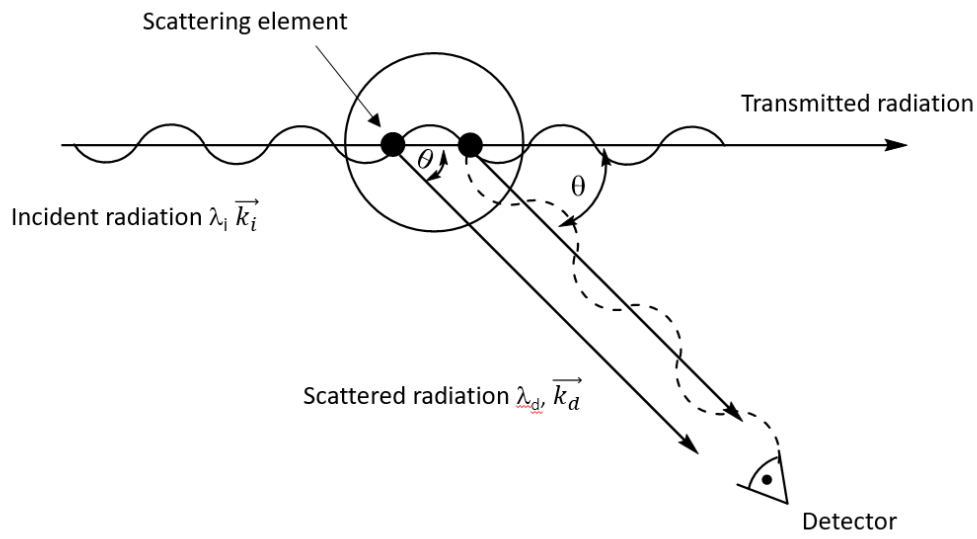
Radiation scattering provides information on the structure of matter. Radiation techniques are particularly used in polymer science for the characterization of large molar mass macromolecules. The interaction between matter and radiation leads to scattering, so that a radiation beam, which passes through a medium, gets reflected in all directions by contact with each volume element. In homogeneous medium, these waves recombine to reconstruct the incident beam. In inhomogeneous medium, however, this is not the case since the intensity of the scattered beam depends strongly on the geometry and interaction of the scattering elements.

There are three main scattering techniques, using different types of radiation: Light scattering, X-ray scattering and neutron scattering. The electromagnetic radiation (light and X-ray) is thereby scattered by the electrons of the material, whereas the neutron radiation interacts

with the nuclei of the atoms. Consequently, they differ also by the wavelength λ_i of the incident beam:

- ❖ Light scattering: $4000 \text{ \AA} < \lambda_i < 7000 \text{ \AA}$
- ❖ Neutron scattering: $1 \text{ \AA} < \lambda_i < 20 \text{ \AA}$
- ❖ X-ray scattering: $0.2 \text{ \AA} < \lambda_i < 2 \text{ \AA}$

Scheme 1 depicts a typical radiation scattering experiment, showing the interaction of a monochromatic incident beam of wavelength λ_i and wave vector \vec{k}_i with a scattering element to give the scattered radiation λ_d with the wave vector \vec{k}_d .



Scheme 1. Typical setup of a scattering experiment.

The incident- and the scattered wave vectors are defined with their absolute values as

$$|\vec{k}_i| = \frac{2\pi n}{\lambda_i} \quad (9)$$

and

$$|\vec{k}_d| = \frac{2\pi n}{\lambda_d} \quad (10)$$

with λ_i and λ_d the wavelength before and after diffusion and n , the refractive index of the medium. The intensity of the diffused radiation to a known direction is defined by a transfer wave vector \vec{q} , also called diffusion vector by

$$\vec{q} = \vec{k}_i - \vec{k}_d \quad (11)$$

In the case of an elastic diffusion (energy transfer), the wavelength of the incident- and diffused radiation are the same and the modulus of the wave vectors are equal $|\vec{k}_i| = |\vec{k}_d|$. We can

define the module of the diffusion vector as a function of the angle of diffusion θ , determining the direction of the observation (of the detector).

$$|\vec{q}| = \frac{4\pi n}{\lambda_i} \sin \frac{\theta}{2} \quad (12)$$

Equation (12) shows, that the diffusion vector is indirect proportional to λ_i and the possible values of q depend consequently on the type of radiation:

- ❖ Light scattering: $5 \cdot 10^{-5} \text{ \AA}^{-1} < q < 3 \cdot 10^{-3} \text{ \AA}^{-1}$
- ❖ Neutron and X-ray scattering: $2 \cdot 10^{-4} \text{ \AA}^{-1} < q < 5 \cdot 10^{-1} \text{ \AA}^{-1}$

The three diffusion techniques are thus complementary and their combination can give access to a domain of q which is large enough to characterize polymer samples in different spatial scales. However, for all radiation scattering experiments, a contrast is essential to differentiate the intensity scattered by the sample from that of the environment (e.g. solvent). Sharp images and reliable information are thus only obtained, when the contrast is well-defined and taken into account during the evaluation of the data. For each diffusion techniques, the contrast is defined differently as shown in Table 1.

Table 1. Contrast of the different diffusion methods.

Scattering method	Background
Light	Difference of the refractive index
X-Ray	Difference of the electron density
Neutrons	Difference of the length of the elastic scattering between the atoms

The intensity of the measured scattering during the experiment can be defined as

$$I_{theo.}(q) = background \times P(q) \times S(q), \quad (13)$$

with $P(q)$ as the form factor of the particles and $S(q)$ the structure factor. In the case of a diluted system, the structure factor is equal 1 and thus, the intensity of the measured scattering depends only on the form factor of the particles. We will now look at a diluted system of micelles, analyzed at different areas of q . The measured scattering (= form factor $P(q)$) is plotted against q in Figure 2, while the regions of the different methods are highlighted.

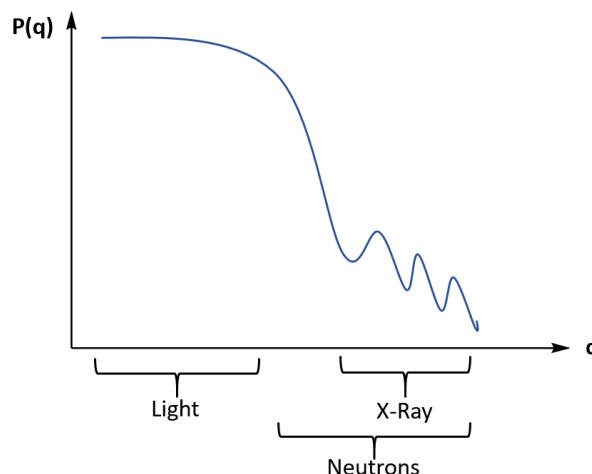


Figure 2. Typical plot of the form-factor P as a function of q from a diluted solution of micelles with the regions of q for the respective scattering methods.

For small values of q (light scattering), the scale of observation is very large, so that the separation of the micelles is poor, giving only points for each aggregate. Here, the number and molar mass of the aggregates can be obtained from the experimental data. For higher values of q (neutrons and X-Ray scattering), the micelles are now better resolved, enabling the measurement of the radius of gyration (R_g) and the hydrodynamic radius (R_H). At very large value of q , the internal structure of the micelle becomes observable, giving access to the radius of the core (R_c) and the thickness of the corona.

Light scattering

Dynamic light scattering (DLS)

The Brownian motion of particles dissolved in solutions causes a constantly varying distance between the them, leading to an either constructively or destructively interference of the scattered light, so that the scattering intensity fluctuates over time. Larger particles move slower and possess therefore lower diffusion coefficients than their lighter counterparts. The relation between particle size and velocity or the particles for hard spheres is given by the Stokes-Einstein equation:

$$D = \frac{k_B T}{6\pi\eta R_h} \quad (14)$$

(R_h : hydrodynamic radius of the particle, k_B : Boltzmann constant, T : temperature, η : viscosity of the dispersion, D : diffusion coefficient).

The fluctuations of the intensity have its origins in the Doppler effect, which described a change in frequency of a wave from an observer, if the emitting source moves with a certain speed relative to the observer:

$$\Delta\nu = \nu - \nu_0 \quad (15)$$

With ν the frequency of the observer and ν_0 the frequency emitted by the sources, leading to a Doppler-shift as following

$$\nu = \frac{\nu_0}{(1 - \nu)/c_0} \text{ or } \omega = \frac{\omega_0}{(1 - \omega)/c_0} \quad (16)$$

(c_0 : velocity of light, ω : angular frequency = $2\pi\nu$).

The Doppler effect causes a broadening of the frequency of the scattered light, while the half width $\Delta\omega$ of the scattered light is inverse proportional to the characteristic fluctuation time τ , describing the velocity of a particle as the following

$$\Delta\omega = \frac{1}{\tau} \quad (17)$$

The fluctuation time, and consequently the half width, are characteristic values and gives information about the size of a particle. The signal of the intensity fluctuation is correlated at a certain time $I(t+\tau)$ with the initial signal $I(t)$, resulting in the autocorrelation function:

$$g^2(t, t + \tau) = \frac{\langle I(t) \times I(t + \tau) \rangle}{\langle I(t) \rangle^2} \quad (18)$$

Where $\langle I(t) \times I(t + \tau) \rangle$ is the product of the signal intensities at different times and τ the correlation time.

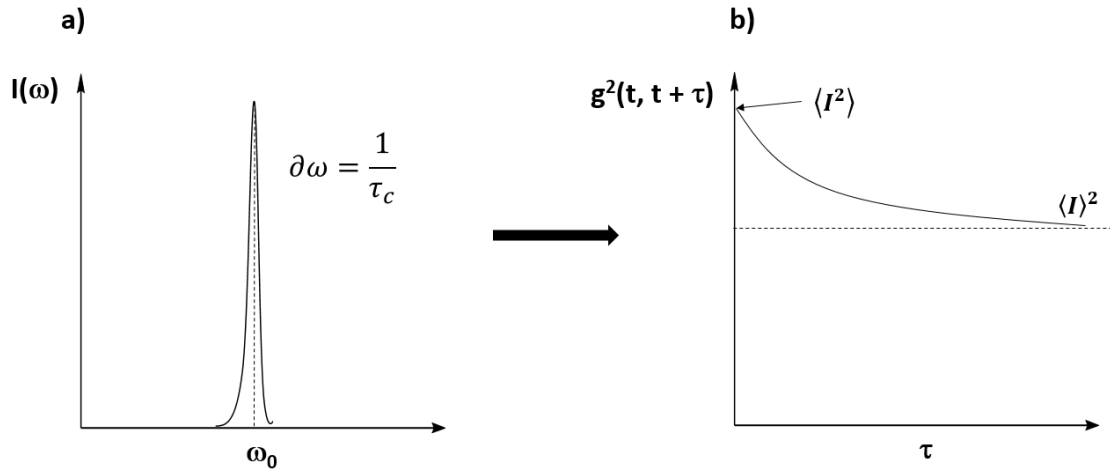


Figure 3. **a)** Plot of the spectrum of the scattered intensity as a function of the angular frequency; **b)** Correlation function.^[2]

The decay of the correlation function is exponential (Figure 3) and related to the movement of the particles and the diffusion coefficient, respectively. Larger particles move slower and exhibits therefore also slower fluctuations, leading to a slower decay of the correlation function compared to smaller particles. The auto-correlation function is then fitted using numerical

methods. First, the latter is normalized and converted to the autocorrelation of the electrical field $g^{(1)}$.

$$g^{(1)}(\tau) = e^{(-q^2 D \tau)} \quad (19)$$

where q is the wave vector with $q (= (4\pi n/\lambda) \sin(\theta/2))$, λ the incident laser wavelength, n the refractive index of the sample and θ : angle between detector and sample cell. The most common method is the cumulants fitting, which treats the deviation to a mono-exponential:

$$\ln(g^{(1)}(q, t))_{t \rightarrow 1} \approx \Gamma_0 - \Gamma_1 + \Gamma_2 \frac{t^2}{2!} + \dots \quad (20)$$

with the Γ coefficients as the cumulants. In the case of a monodispersed system, the development stops at the first linear term, while the first cumulant Γ_1 gives the mean value of the relaxation frequency and Γ_2 the standard derivation of the distribution of the relaxation frequency. The degree of dispersion can be obtained by the ratio Γ_2/Γ_1^2 . The width and the polydispersity can be calculated by

$$\bar{\Gamma} = q^2 D_z = q^2 \frac{k_B T}{6\pi\eta R_h} \quad (21)$$

$$width = \frac{\sqrt{q_t}}{\bar{\Gamma}} R_h \quad (22)$$

$$polydispersity\ index = \frac{q_2}{\bar{\Gamma}} \quad (23)$$

Finally, the diffusion coefficient can be calculated with the relation of Fick, who associates each relaxation time $\tau(1/\Gamma)$ with an apparent diffusion coefficient:

$$D = \frac{1}{\tau q^2} = \frac{\Gamma}{q^2} \quad (24)$$

The value of the self-diffusion coefficient D_0 is obtained with the dependence of D on the concentration (c) and the wave vector q as following

$$D = D_0(1 + Ac + \dots)(1 + Bq^2 + \dots) \quad (25)$$

where A and B are system dependent characteristic parameters. The self-diffusion coefficient D_0 is then measured by extrapolation at zero angle and zero concentration to be able to calculate the real hydrodynamic radius using the Stokes-Einstein equation (eq. 14).^[2]

Dynamic Light Scattering experiments were performed using a Zetasizer Nano ZS Instrument (Malvern Instruments Ltd., Malvern, UK). The DLS measurements were performed at 20 °C

using the red line (wavelength, $\lambda = 632$ nm) of a He-Ne laser in a quasi-backscattering configuration (scattering angle, $\theta = 173^\circ$). Moreover, to accurately corroborate the size distribution, multiangle light scattering analysis (ALV DLS) were also carried out using an ALV 22 mW linearly He-Ne polarized laser goniometer laser ($\lambda = 632$ nm) with an ALV-5000/EPP multiple tau digital correlator (initial sampling time 125 ns). Measurements were performed at 20 °C in an angle range from 30° to 150°. The emulsions were analyzed on a Cordouan Vasco particle size analyzer using 657 nm at 25 °C in an angle of 135°.

Small angle X-ray diffraction (SAXS)

SAXS measurements on the dilute aqueous micellar solutions were carried out on a Xeuss 2.0 (XENOCs, France) equipped with a Genix-3D Cu beam (K_α wavelength of 0.1542 nm) and a DECTRIS PILATUS-300k (DECTRIS, Switzerland) detector. The apparatus was operated at 40kV and 40mA. The sample to detector distance was 1.635 m. The sample holder used was a capillary made of quartz having inner diameter ~ 1.5 mm and 10 μ m thickness. Exposure time was 3 hours per sample. The scattered X-ray intensities were collected in a two-dimensional position sensitive imaging plate, and integrated over a linear profile to convert into one-dimensional ($I(q)$ vs. q) scattering data. Scattering data for the background, obtained under similar conditions, was subtracted from the sample data to obtain scattering just from the self-assembled structures. MilliQ water was used as reference/background matrix.

In SAXS experiments, the small-angle scattering of a monochromatic x-ray beam from the sample is measured. The size of the particles which can be analyzed by this method is in the range of 10 - 10000 Å. During SAXS, the scattered x-ray intensity $I(q)$ in a region of small angles is measured and plotted as a function of the wave factor $q (= 4\pi \sin\theta/\lambda)$, with λ as the wavelength of the incident X-ray beam and 2θ the scattering angle:

$$I(q) = 4\pi \int_0^\infty p(r) \frac{\sin qr}{qr} dr \quad (26)$$

Since the analyzed system contains many electrons, the amplitude of the secondary waves from the scattering are added with their phase differences in each direction. Eq. 26 presents thus the absolute square of the sum of these amplitudes and is also named generally ‘scattering curve’. Regardless the structure of the analyzed sample, SAXS gives always the mean square fluctuation of the electron density. The latter is defined in general terms as the number of electron moles per cubic centimeter. The integral over the scattering intensities taken over all values of the vector q gives then the particle distance distribution function (PDDF) $\rho(r)$ via Fourier transformation:

$$p(r) = \frac{r^2}{2\pi^2} \int_0^\infty I(q) \frac{\sin qr}{qr} q^2 dq \quad (27)$$

The scattering curve is characteristic for certain shapes (Figure 4), volumes and masses of the particles. Usually, a theoretical scattering curve for the *assumed particle structure* is calculated and compared to a fitted curve of the experimental scattering. The first model scattering curve is then optimized by trial-and-error variation until scattering equivalence is reached (calculated curve agrees with experimental).

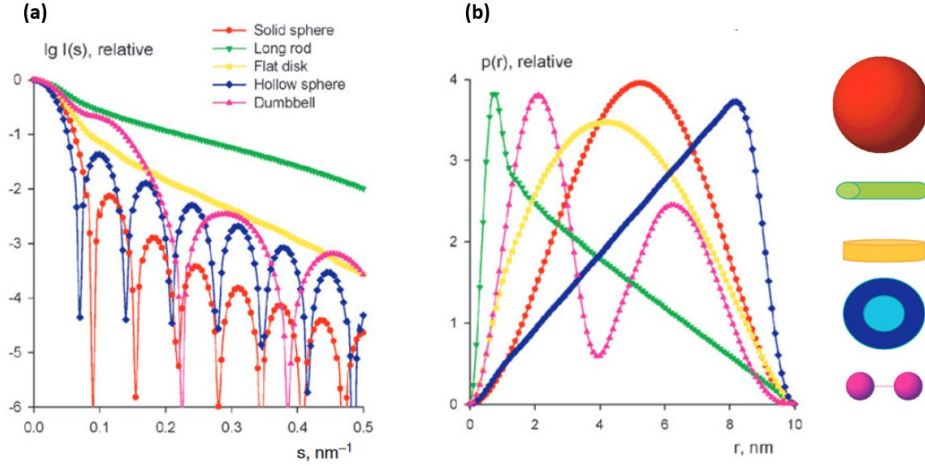


Figure 4. Typical (a) scattering curve and (b) particle distance distribution function for different particle structures in SAXS experiments.^[3]

Modeling of SAXS data was conducted using the SasView 5.0.3 analysis package software. Spherical micelles scattering was fitted using a core-shell sphere model. The form factor of core-shell spheres can be represented as:

$$P(q) = \frac{\text{scale}}{V} F^2(q) + \text{background} \quad (28)$$

where

$$F(q) = \frac{3}{V_s} \left[V_c (\rho_c - \rho_s) \frac{\sin(qr_c) - qr_c \cos(qr_c)}{(qr_c)^3} + V_s (\rho_s - \rho_{\text{solv}}) \frac{\sin(qr_s) - qr_s \cos(qr_s)}{(qr_s)^3} \right] \quad (29)$$

with V_s as the volume of the whole particle, V_c the volume of the core, r_s the total radius of the particle, r_c the radius of the core, ρ_c the scattering length density of the core, ρ_s the scattering length density of the shell and ρ_{solv} , the scattering length density of the solvent. For cylindrical micellar structures, a core-shell cylinder model was used. The intensity function of core-shell cylinders can be represented as:

$$I(q, \alpha) = \frac{\text{scale}}{V_s} F^2(q, \alpha) \sin(\alpha) + \text{background} \quad (30)$$

where

$$\begin{aligned}
F(q, \alpha) = & V_c(\rho_c - \rho_s) \frac{\sin(q \frac{1}{2} L \cos\alpha)}{q \frac{1}{2} L \cos\alpha} \frac{2J_1(qR \sin\alpha)}{qR \sin\alpha} \\
& + V_s(\rho_s - \rho_{solv}) \frac{\sin(q(\frac{1}{2}L + T) \cos\alpha)}{q(\frac{1}{2}L + T) \cos\alpha} \frac{2J_1(q(R + T) \sin\alpha)}{q(R + T) \sin\alpha}
\end{aligned} \tag{31}$$

and

$$V_s = \pi(R + T)^2(L + 2T) \tag{32}$$

where α is the angle between the axis of the cylinder and q , V_s the total volume (including both the core and the outer shell), V_c the volume of the core, L the length of the core, R the radius of the core, T the thickness of the shell, ρ_c the scattering length density of the core, ρ_s is the scattering length density of the shell, ρ_{solv} the scattering length density of the solvent and background level. The outer radius of the shell is given by $R + T$ and the total length of the outer shell is given by $L + 2 T$. J_l is the first order Bessel function.

With the scattering curve $I(q)$, the radius of gyration R_g and thus, the size of the particles can be determined. The radius of gyration is defined as the root-mean-square distance of all electrons from their center of gravity. For spherical monodisperse systems, the intensity can be expressed in function of the form factor $P(q)$ and structure factor $S(q)$. $P(q)$ is related to interparticle scattering contributions and $S(q)$ to interparticle interference scattering. In low concentrated systems, the $S(q)$ value is close to unity and the $I(q)$ can be given only in function of $P(q)$. In that conditions, according to the Guinier law, the intensity at low q values ($q_{max} < 1.3 \times R_g$) is related to the radius of gyration R_g of the particle, which can be then deduced by the slope of eq. 34.^{[13][4]}

$$I(q) = P(q)S(q) \tag{33}$$

$$\ln I(q) \cong -\frac{q^2 R_g^2}{3} + \ln I(0) \tag{34}$$

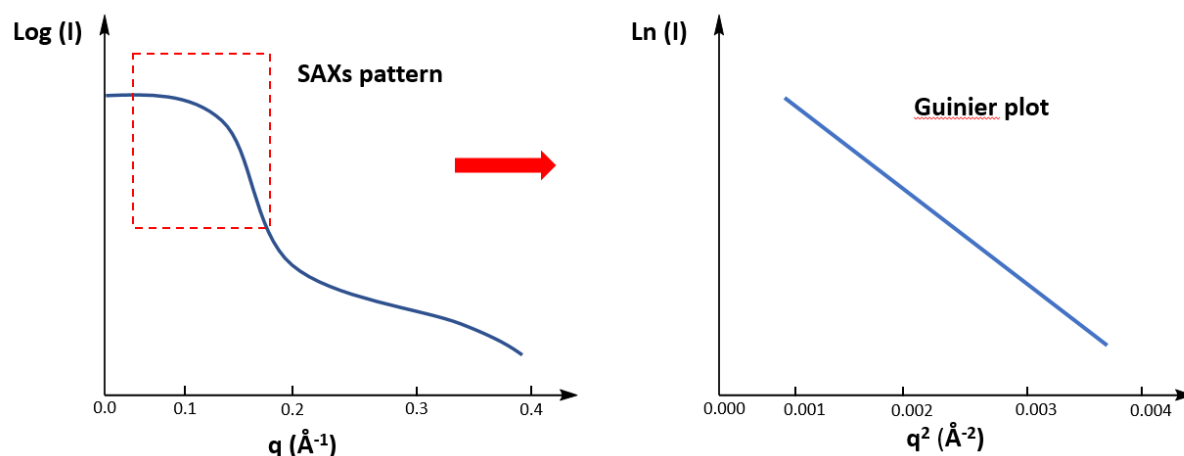


Figure 5. (a) Scattering curve with the low q values ($q_{max} < 1.3 \times R_g$) indicated in the red box and (b) the corresponding Guinier plot for that region of q .

Cryo-Transmission Electron Microscopy (cryo-TEM)

Cryo-TEM micrographs were obtained on a LaB6 JEOL 2100 (JEOL, Japan) cryo microscope operating at 200 kV with a JEOL low dose system (Minimum Dose System, MDS) to protect the thin ice film from any irradiation before imaging and reduce irradiation during image capture. An ultrascan 2k CCD camera (Gatan, USA) was used to record the images. Samples were prepared on a “quantifoil” (Quantifoil Micro Tools GmbH, Germany) carbon membrane. A droplet was directly deposited on the substrate and the excess of liquid on the membrane was absorbed with a filter paper. The membrane was quench-frozen quickly in liquid ethane to form a thin vitreous ice film. Once placed in a Gatan 626 cryo-holder cooled with liquid nitrogen, the samples were transferred to the microscope and observed at -180 °C.

Confocal microscope (LSCM)

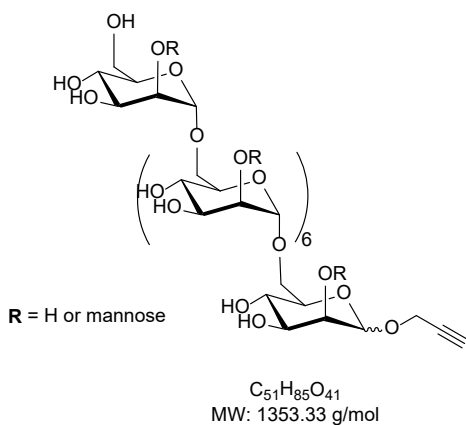
Laser Scanning Confocal Microscopy Images were acquired on an inverted Leica TCS SP5 microscope equipped with both PL APO 0.4 10x air objective and HCX PL APO 63x, NA 1.4 oil immersion objective. Samples (≈ 20 μ L) were injected in μ -slide (chambered coverslip) with uncoated 8 wells from Ibidi GmbH. The laser outputs are controlled via the Acousto-Optical Tunable Filter (AOTF) and the two collection windows using the Acousto-Optical Beam Splitter (AOBS) and photomultipliers (PMT) as follows: Nile Red was excited with a DPSS diode at 561 nm (15 %) and measured with emission setting at 565 - 600 nm, aggregates were excited with a Helium-Neon laser at 633 nm (10 %) in transmission mode. Images were collected using the microscope in sequential mode with a line average of 16 and a format of 512*512 pixels.

UV-VIS Spectrometer

Data were collected on a Cary 100 UV-Visible spectrophotometer equipped with a multi-cell temperature controller from Agilent Technologies. The solutions are placed in 1 cm quartz suprasil micro-cells (500 μ L). Scan: 200-500 nm. Kinetics: every 30 sec. during 60 min. at 420 nm.

2 Glycosylation of Sugars

Propargyl-manno-(oligo)-pyranoside (PMan)_n



General method of the Fischer glycosylation and oligomerization of mannose

- Step 1 -

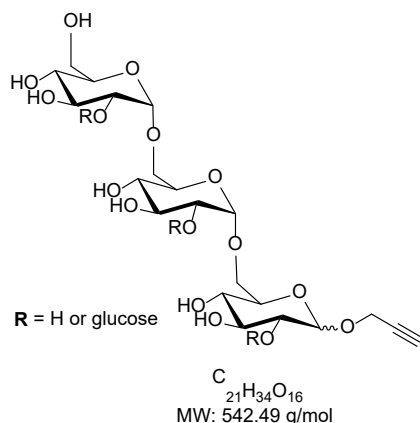
In a round-bottom flask, mannose (5 g, 27.75 mmol) was dispersed in an excess of propargyl alcohol (5 eq.) and stirred at 80 °C in the presence of amberlyst-15 (4.2 mol% H⁺) for 3 h. Then, the reaction was stopped and the obtained yellow/orange solution was separated by centrifugation from the catalyst. The as-recovered solution (pH 4) was used for the following step without further purification.

- Step 2 -

Oligomerization was attained by removing the excess of propargyl alcohol through heating of the mixture of step 1 at 100 °C for 4 h under vacuum. The obtained solid was dissolved in water and washed with chloroform to remove remaining traces of propargyl alcohol. The combined aqueous phase was freeze-dried to give a brown-beige solid.

yield: 4.3 g (3.2 mmol, 88 %); **¹H-NMR** (400 MHz, D₂O): δ = 5.32-5.08 (m, 1.66 H), 5.08-5.01 (db, 2 H), 4.97-4.90 (db, 3.23 H), 4.73 (d, 0.44 H), 4.41-4.32 (m, 6.56 H, CH₂), 4.15-3.53 (m, 49.86 H, α/β-H2 - α/β-H-6), 3.42-3.39 (tq, 0.74 H, β-H-5), 2.95 (tb, 1 H, alkyne); **¹³C-NMR** (100.4 MHz, D₂O): δ = 102.4, 102.4, 100.5, 99.5, 99.3, 99.0, 98.6, 97.0, 78.7, 78.3, 78.1, 76.2, 73.2, 72.9, 72.7, 71.29, 70.6, 70.5, 70.3, 69.9, 69.8, 66.7, 66.4, 65.4, 60.9, 54.7, 54.6; **PDI (SEC)** = 2.03; **ATR:** 2116 (C≡C str.) (s).

Propargyl-gluco-(oligo)-pyranoside (P_{Gluc})_n

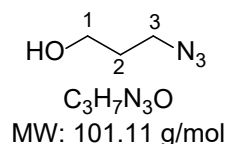


For the synthesis of propargyl-(oligo)glucosides, the same protocol as for (P_{Man})_n was followed.

yield: 4.2 g (7.7 mmol, 83 %); **¹H-NMR** (400 MHz, D₂O): δ = 5.39-5.35 (m, 0.44 H), 5.13-5.12 (d, 1 H, α-H-1), 4.98-4.97 (m, 0.51 H, α-(1,6)), 4.67-4.65 (d, 0.33 H, β-H-1), 4.50 (m, 0.64 H, β-CH₂), 4.37-4.35 (m, 2.17 H, α-CH₂), 4.33-3.2 m, (19.22 H, H-2 - H-6), 2.95-2.91 (m, 1 H, α/β-alkyne-H); **¹³C-NMR** (100.4 MHz, D₂O): 103.4, 79.6, 79.9, 76.6, 76.4, 73.6, 72.8, 72.5, 72.1, 71.6, 70.2, 70.0, 61.3, 60.9, 57.1, 55.6, 55.4.

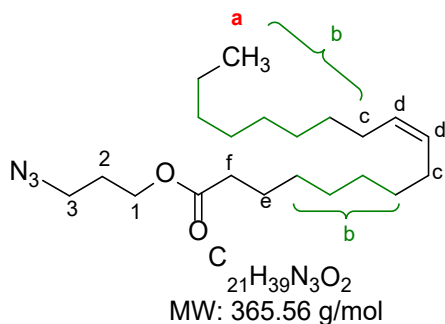
3 Functionalization of Fatty Acids

3-azido-1-propanol (4)



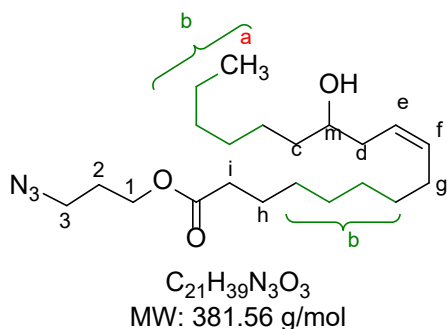
3-bromo-1-propanol (10 g, 71.94 mmol) and sodium azide (18.7 g, 287.79 mmol) were dissolved in a mixture of acetone/water (120/20 mL) and refluxed overnight. After removing acetone under reduced pressure, water (100 mL) was added and the mixture was extracted with diethyl ether (3x 100 mL). The combined organic layers were dried over MgSO₄ and the solvent was removed under vacuum to give a colorless oil.^[5]

yield: 6.24 g (61.7 mmol, 86 %); **¹H-NMR** (400 MHz, CDCl₃): δ = 3.74-3.71 (t, J = 6 Hz, 2H, H-1), 3.45-3.41 (t, J = 6.58 Hz, 2H, H-3), 2.06 (br, s, 1H, O-H), 1.84-1.78 (qi, J = 6.31, 2H, H-2); **¹³C-NMR** (100.4 MHz, CDCl₃): δ = 59.9 (C-1), 48.5 (C-3), 31.5 (C-2); **ATR:** 3330 cm⁻¹ (OH str) (br), 2089 cm⁻¹ (N₃ str) (s).

3-azido-1-propyl-oleate (N_3OI) (5)

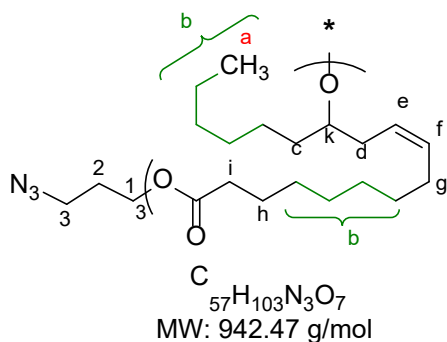
Methyl oleate (MeOI, 1 g, 3.37 mmol), azide-functionalized alcohol **4** (3-azido-1-propanol, 10 eq.) and catalyst 1,5,7-Triazabicyclo(4.4.0)dec-5-en (TBD, 0.1 eq.) were added in a schlenk-flask and stirred at 100 °C for 4 h under a gentle flux of nitrogen. The obtained dark solution was then placed for 4 h at 100 °C under vacuum to remove the excess of alcohol. After cooling to room temperature, the residue was dissolved in ethyl acetate (20 mL) and washed four times consecutive with distilled water (5 mL). The organic layer was dried over $MgSO_4$, filtrated and dried under vacuum to give an orange/yellow oil of azide-functionalized oleate (N_3OI). After purification via silica column chromatography (PE/EtOAc 9:1), a colorless oil was obtained.^[6]

yield 0.81 g (2.2 mmol, 65 %); **1H -NMR** (400 MHz, $CDCl_3$): δ = 5.34-5.31 (m, 2 H, H-d), 4.16-4.13 (t, J = 6.16 Hz, 2H, H-1), 3.39-3.36 (t, J = 6.7 Hz, 2 H, H-3), 2.30-2.26 (t, J = 7.54 Hz, 2 H, H-f), 2.0-1.99 (dd, 4 H, H-c), 1.93-1.86 (qi, 2 H, H-2), 1.62-1.59 (m, 2 H, H-e), 1.29-1.25 (d, br, 20 H, H-b), 0.88-0.85 (t, 3 H, CH_3 , H-a); **^{13}C -NMR** (100.4 MHz, $CDCl_3$): δ = 174.4 (C=O), 130.1 (C-d), 129.8 (C-d), 61.3 (C-1), 48.3 (C-3), 34.2 (C-f), 32.0 (C-b), 29.9 (C-b), 29.8 (C-b), 29.6 (C-b), 29.4 (C-b), 29.3 (C-b), 29.2 (C-b), 29.2 (C-b), 28.3 (C-2), 27.4 (C-c), 27.3 (C-b), 25.0 (C-e), 22.8 (C-b), 14.2 (C-a); **ATR-IR**: 2095 cm^{-1} (N_3 str.) (s), 1738 cm^{-1} (C=O str.) (s), 1655 cm^{-1} (C=C str.) (s); **SEC**: M_n = 506.9 g/mol.

3-azido-1-propyl-ricinoleate (N_3 Ric) (6)

Methyl ricinoleate (MeRic, 1 g, 3.2 mmol), azide-functionalized alcohol **4** (3-azido-1-propanol, 10 eq.) and catalyst 1,5,7-Triazabicyclo(4.4.0)dec-5-en (TBD, 0.1 eq.) were added in a schlenk-flask and stirred at 100 °C for 4 h under a gentle flux of nitrogen. The obtained dark solution was extracted with EtOAc (20 mL) and washed with water (3 x 5 mL). The combined organic layer was then dried over $MgSO_4$ and the excess of the alcohol was removed by heating under vacuum at 100 °C for 4 h to obtain an orange/yellow oil of azide-functionalized ricinoleate (N_3 Ric).

yield: 0.92 g (2.4 mmol, 75 %); **1H -NMR** (400 MHz, $CDCl_3$): δ = 5.54-5.51 (m, 1 H, H-f), 5.39-5.37 (m, 1 H, H-f), 4.15-4.12 (t, J = 6.1 Hz, 2 H, H-1), 3.60-3.57 (t, J = 5.45 Hz, 1 H, H-m), 3.38-3.35 (t, J = 6.63 Hz, 2 H, H-3), 2.30-2.26 (t, J = 7.53 Hz, 2 H, H-i), 2.20-2.17 (t, J = 6.73 Hz, 2 H, H-d), 2.03-2.02 (t, J = 6.67 Hz, 2 H, H-g), 1.90-1.87 (qi, J = 6.27 Hz, 2 H, H-2), 1.62-1.55 (m, 2 H, H-h), 1.46-1.39 (m, 2 H, H-c), 1.28 (s, br, 16 H, H-b), 0.88-0.84 (t, 3 H, H-a); **^{13}C -NMR** (100.4 MHz, $CDCl_3$): δ = 174.3 (C=O), 133.1 (C-e), 125.4 (C-f), 71.5 (C-m), 61.2 (C-1), 48.2 (C-3), 36.9 (C-c), 35.1 (C-d), 34.1 (C-i), 31.9, 29.6, 29.4, 29.1, 29.1, 25.7, 24.9 (C-b), 28.20(C-2), 27.4 (C-g), 22.6 (C-b), 14.1 (C-a); **ATR-IR:** 3425 cm^{-1} (O-H str.) (br), 2095 cm^{-1} (N_3 str.) (s), 1736 cm^{-1} (C=O str.) (s), 1655 cm^{-1} (C=C str.) (s); **SEC:** M_n = 555.9 g/mol.

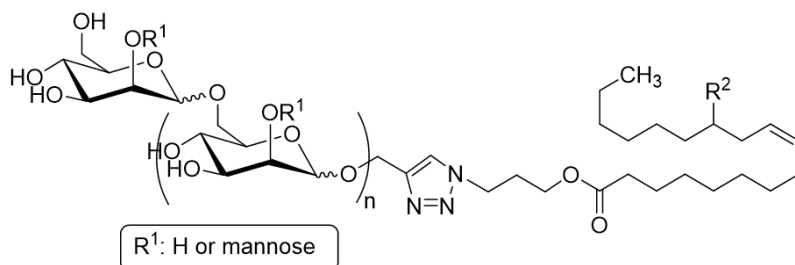
3-azido-1-propyl-(oligo)-ricinoleate (N_3 Ric) (7)

In a first step, methyl ricinoleate (MeRic, 12 g, 38.4 mmol), azide-functionalized alcohol **4** (3-azido-1-propanol, 10 eq.) and catalyst 1,5,7-Triazabicyclo(4.4.0)dec-5-en (TBD, 0.1 eq.) were added in a schlenk-flask and stirred at 100 °C for 2 h under a gentle flux of nitrogen. The oligomerization was then initiated by heating the mixture at 100 °C under vacuum for 4 h. After cooling to room temperature, the residue was dissolved in ethyl acetate (300 mL) and washed four times consecutive with distilled water (50 mL). The organic layer was dried over MgSO₄, filtrated and dried under vacuum to give an orange oil of azide-functionalized oligo-ricinoleate (N₃PRic).

yield: 11.4 g (12.1 mmol, 95 %); **¹H-NMR** (400 MHz, CDCl₃): δ = 5.43-5.32 (m, 5.48 H, H-f,e), 4.88-4.85 (t, 1.74 H, H-k), 4.15 (t, 2.16 H, H-l), 3.75 (m, 1.17 H, H-m), 3.44-3.36, t, 2 H, H-3), 2.28-2.25 (m, 9.76 H + 3.11 H, H-i,d), 2.03-2.01 (m, 6.12 H, H-g), 1.92-1.88 (t, 2 H, H-2), 1.84-1.51 (3 x m, 6.36 H, 7.37 H, H-h,c), 1.29 (s, br, 47.34 H, H-b), 0.87 (s, br, 9 H, H-a); **¹³C-NMR** (100.4 MHz, CDCl₃): δ = 173.8+173.9 (C=O), 133.4, 132.6 (C-f,e), 125.3+124.4 (C-k), 73.8 (C-k), 71.6 (C-m), 61.2 (C-l), 48.6, 48.4 (C-3), 36.9, 35.5, 34.8, 34.3, 33.8 (C-c,d), 32.1, 31.9, 31.9, 31.6 (C-i), 29.7-29.2 (C-b), 28.4 (C-2), 27.50, 27.5, 27.4 (C-g), 25.8-25.0 (C-h,C-b), 22.7, 22.7 (C-b), 14.2 (C-a).

4 Huisgen-Cycloaddition

(Propargyl-mannopyranosides)_n-*block*-fatty acid (PMan)_n-*b*-fatty acid (10-13)



(PMan)_n-*block*-fatty acid

- 10** = R²: H, n: 2 = (PMan)₃-*b*-OI, C₄₂H₇₃N₃O₁₈, MW: 908.05 g/mol
11 = R²: H, n: 7 = (PMan)₈-*b*-OI, C₇₂H₁₂₃N₃O₄₃, MW: 1718.75 g/mol
12 = R²: OH, n: 2 = (PMan)₃-*b*-Ric, C₄₂H₇₃N₃O₁₉, MW: 924.05 g/mol
13 = R²: OH, n: 7 = (PMan)₈-*b*-Ric, C₇₃H₁₂₅N₃O₄₃, MW: 1732.78 g/mol

General procedure:

In a typical Huisgen cycloaddition, 2.5 g of (PMan)_n was dissolved in DMSO and stirred at 30 °C overnight to ensure complete dissolution. Then, azide-fatty ester (N₃OI/N₃Ric) (1.2 eq.) was added and the mixture was stirred for 15 minutes. After that, sodium ascorbate (1 eq.) was added and after another 15 min, CuSO₄ (1 eq.) was introduced and the mixture was stirred for 24 h at 30 °C. The excess of fatty acid was removed by precipitation in ethyl acetate (EtOAc) and separated by centrifugation. The residue was dissolved in water and

Cuprisorb[®] (4 weight eq. of CuSO₄) was added to remove the copper during stirring overnight at room temperature. The cuprisorb-beads were then separated by filtration and the product was purified by dialysis (MWCO: 100-500 Da) against dist. water for 2 d. After freeze-drying for 2 d, a white powder was obtained.

(PMan)₃-*b*-OI (10)

yield: 1.2 g (1.3 mmol, 30 %); **¹H-NMR** (400 MHz, DMSO-d₆): δ = 8.12 (s, 1 H, triazole), 5.33-5.31 (t, 2 H), 5.12-4.30 (m, 19 H), 4.02-3.99 (t, 4 H), 3.8-3.36 (m, 19 H), 2.28-2.25 (t, 2 H), 2.15-2.12 (t, 2 H), 1.98-1.97 (m, 4 H), 1.5 (m, 2 H), 1.24 (s, br, 20 H), 0.86-0.83 (t, 3 H, CH₃).

(PMan)₈-*b*-OI (11)

yield: 1.3 g (0.7 mmol, 43 %); **¹H-NMR** (400 MHz, DMSO-d₆): δ = 8.12 (s, 1 H, triazole), 5.33-5.31 (t, 2 H), 5.12-4.30 (m, 26 H), 4.02-3.99 (t, 4 H), 3.8-3.36 (m, 30 H), 2.28-2.25 (t, 2 H), 2.15-2.12 (t, 2 H), 1.98-1.97 (m, 4 H), 1.5 (m, 2 H), 1.24 (s, br, 20 H), 0.86-0.83 (t, 3 H, CH₃).

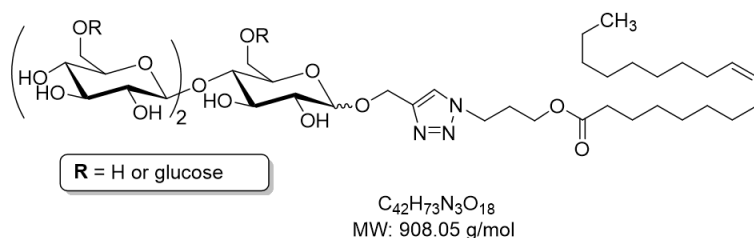
(PMan)₃-*b*-Ric (12)

yield: 0.6 g (0.6 mmol, 15 %); **¹H-NMR** (400 MHz, DMSO-d₆): δ = 8.12 (s, 1 H, triazole), 5.43-5.33 (m, 2 H), 5.14-4.28 (m, 25 H), 4.01-3.39 (4 H), 3.78-3.35 (m, 19 H), 2.29-2.25 (m, 2H), 2.15-2.06 (m, 4 H), 2.0-1.93 (m, 2 H), 1.54-1.45 (m, 2 H), 1.38-1.31 (m, 2 H), 1.31-1.82 (s, br, 16 H), 0.88-0.81 (t, 3 H, CH₃).

(PMan)₈-*b*-Ric (13)

yield: 0.5 g (0.28 mmol, 16 %); **¹H-NMR** (400 MHz, DMSO-d₆): δ = 8.12 (s, 1 H, triazole), 5.43-5.33 (m, 2 H), 5.14-4.28 (m, 37 H), 4.01-3.39 (4 H), 3.78-3.35 (m, 39 H), 2.29-2.25 (m, 2 H), 2.15-2.06 (m, 4 H), 2.0-1.93 (m, 2 H), 1.54-1.45 (m, 2 H), 1.38-1.31 (m, 2 H), 1.31-1.82 (s, br, 16 H), 0.88-0.81 (t, 3 H, CH₃).

(Propargyl-cellulose-oligosaccharides)₃-*block*-oleate (COS-PGA(3)-*b*-OI) (14)



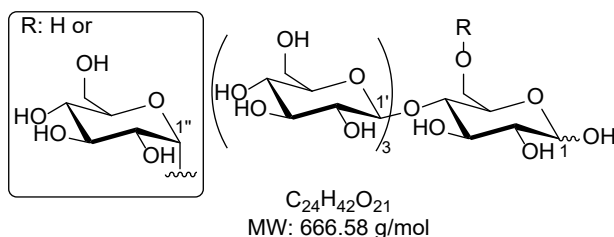
For the preparation of COS-PGA(3)-*b*-OI (14), the same protocol as described above was followed.

yield: 1.5 g (1.6 mmol, 36 %); **¹H-NMR** (400 MHz, DMSO-d6): δ = 8.12 (s, 1 H, triazole), 5.32 (m, 3 H), 5.14-4.2 (m, 21 H), 4.01 (m, 3 H), 3.8-3.5 (m, 10 H), 3.2-2.9 (m, 5 H) 2.29-2.25 (m, 2 H), 2.15-2.06 (m, 2 H), 2.0-1.93 (m, 4 H), 1.54-1.45 (m, 2 H), 1.38-1.31, 1.31-1.82 (s, br, 20 H), 0.88-0.81 (t, 3 H, CH₃).

5 Ball-milling protocol

Cellulose (microcrystalline cellulose AVICEL PH 200 (MCC)) (20g) was mixed with AQUIVION PW98 (2 g) and put into a planetary ball-mill (Retsch MP 100). The mixture of catalyst and cellulose were ground in a 125 mL bowl made of Zirconium Oxide, utilizing 20 of 10 mm balls made of the same material as the milling bowl. The milling process was carried out at 400 rpm during 24 h.

The milled mixture of cellulose and catalyst recovered after ball milling was dispersed in distilled water (20 mL water for 300 mg of solid mixture). The dispersion was stirred and left in an ultrasonic bath for 2 hours. The mixture was filtered through a 47 mm Millipore Pyrex Filter Holder (containing a PTFE filter with a pore size of 0.22 μ m). Then the filtrate was lyophilized to give the pure cellulose-oligosaccharide as a yellowish-white powder.



yield: 18 g (27 mmol, 90 %); **¹H-NMR** (400 MHz, D₂O): δ 5.18-5.17 (d, 1H, α -H-1), 4.95 (m, 1.4 H, H-1''), 4.63-4.58 (t, 2 H, β -H-1), 4.50-4.45 (t, 9 H, H-1'), 3.98-3.16 (m, H-2 - H-6); **¹³C-NMR** (100.4 MHz, D₂O): δ = 102.6, 102.4, 95.9, 95.8, 92.15, 91.8, 78.5, 78.4, 87.3, 76.0, 76.0, 75.8, 74.8, 74.2, 74.1, 73.9, 73.4, 69.7, 69.6, 69.5, 60.8, 60.6, 59.9.

6 Self-Assembly protocols

Pendant Drop

Tensiometry sugar-based amphiphiles samples were dispersed in filtered ultrapure water (using 0.22 μ m PTFE filter) at several concentrations, going from 0.01 to 20 mg/mL.

Direct solubilization

Samples were dispersed in filtered ultrapure water (using a 0.22 μ m PTFE filter) at a concentration of 10 mg/mL, concentration above the CAC. Solutions were magnetically stirred at 450 rpm for 24 h at room temperature. Finally, they were filtered prior analysis through a 0.45 μ m PTFE filter twice without a significant weight loss prior.

7 Emulsion protocols and molecular targeting

Preparation of the emulsions

The emulsions were prepared using ultrapure water (Milli-Q)/or PBS and a magnetically stirrer. In a glass vial, the respective surfactant was dissolved in water and stirred for 30 minutes at room temperature. Then, the oil was added and the mixture agitated at 1400 rpm at room temperature for another 24 h. For the stability test, the emulsions were allowed to stay at room temperature without stirring and analyzed in different time intervals.

Molecular targeting

Preformulated PBS from sigma was diluted before utilization by 10 and the pH was adjusted to 7.2 with the addition of 0.1 mM of MnCl_2 and CaCl_2 . The as-obtained buffer was filtrated (using a 0.1 μm PTFE filter) before utilization.

Centrifugation-precipitation assays

For the DLS experiments, the emulsion was diluted by 1:1000 in PBS, 200 μL were taken out and 5 μL of ConA (1 mg/mL in PBS) was added. The mixture was incubated at room temperature under shaking for 20 minutes. Then, the samples were incubated for another 20 minutes at 37 °C. Finally, the solutions were centrifuged at 10.000 g for 20 minutes at 40 °C. The supernatant solution was removed and the residue was dissolved with *ca.* 200 μL PBS solution. The washing process was repeated three times before the sample was measured by DLS.

Turbidity assays

For the turbidity experiments, to 300 μL of a diluted solution of ConA in PBS (0.016 mg/mL), 200 μL of the emulsion (diluted in PBS by 1:1000) was added into a quartz cuvette (0.5 mL, 10 mm path length) and placed in a UV spectrometer. The absorbance was quickly recorded at 420 nm for 60 minutes every 30 seconds.

8 Calibration and Kinetic study

8.1 GC-Chromatography

The composition of the mono- and disaccharide fraction was analyzed by GC-FID spectroscopy after the transformation of the sugar components into their corresponding per-O-trimethylsilyl (nonreducing sugars) or per-O-trimethylsilylated oxime (reducing sugars). The crude samples (in general 20-30 mg) were dissolved in 1 mL pyridine (containing 1 mg/mL sorbitol as internal standard). To 100 μL of the resulting solution was then added 200 μL of BSTFA (+1 % TMCS) and the mixture was stirred at r.t. for 2 h. During this operation, a white precipitate was observed, which was separated by filtration (0,45 μm , RC) before injection into the apparatus.^[7] By this procedure, the non-reducing sugars give single peaks in the chromatogram, whereas reducing

sugars afford two peaks for the corresponding syn- and anti TMS-oximes. The identification and the quantification were achieved by comparison with authentic standards for which the response factors were obtained from the corresponding calibration curves using sorbitol as internal standard. The standards with the corresponding retention times are shown in Figure 6.

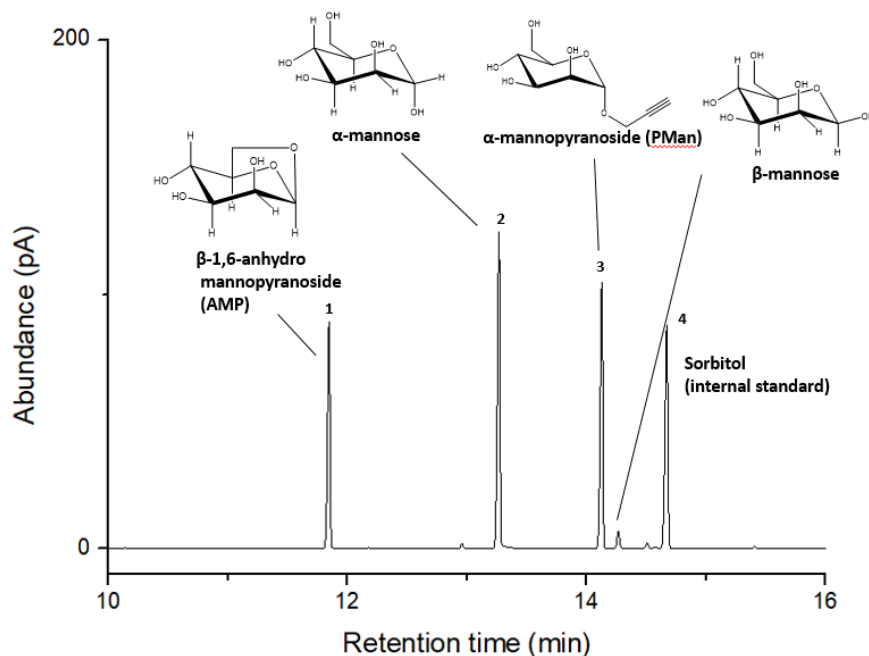


Figure 6. GC-FID spectrum of the sugar standards AMP, mannose, α -propargyl mannopyranoside and the internal standard sorbitol. Column: TRB-5MS (30 m \times 0.25 mm \times 0.25 mm film thickness) capillary column from Teknokroma with matrix 95 % Dimethyl- (5 %) diphenyl polysiloxane.

Table 2. Retention times in GC-FID of different sugar-standards.

Compound	Retention time (t_R) [min]
α -mannose	13.21
β -mannose	14.20
α -propargyl mannopyranoside	14.06
β -propargyl mannopyranoside	14.44
1,6-anhydro mannopyranoside	11.84
Sorbitol	14.59

8.1.1 Calibration of Mannose

Table 3. Surface Area (A) of the GC-FID signals for mannose and sorbitol at different concentration.

Concentration (mg/mL)	A (α -mannose)	A (β -mannose)	A ($\alpha+\beta$ mannose)	A (Sorbitol)
1.75	3.2325	3.3349	6.5674	2.6605
1.50	3.1608	3.1858	6.3466	3.0232
1.25	2.1498	1.5708	3.7206	2.7393
1.00	1.6731	1.2212	2.8943	2.7382
0.50	0.9075	0.6836	1.5911	3.009
0.25	0.4716	0.3458	0.8174	3.1245

The response factor (k) was calculated using following equation

$$Cx = \frac{A_x \times C_{is}}{A_{is} \times k} \quad (35)$$

where A_x is the surface area of the sample, A_{is} the surface area of the internal standard (here = sorbitol), C_{is} the concentration of the internal standard, C_x the concentration of the sample and k the response factor.

Table 4. Obtained values of C_x/C_{is} and A_x/A_{is} for the different mannose concentrations.

Concentration (mg/mL)	C_x/C_{is}	A_x/A_{is}
1.75	1.5	1.6200
1.50	1.5	1.3582
1.25	1.0	1.0570
1.00	0.5	0.5288
0.50	0.25	0.2616
0.25	1.5	1.6200

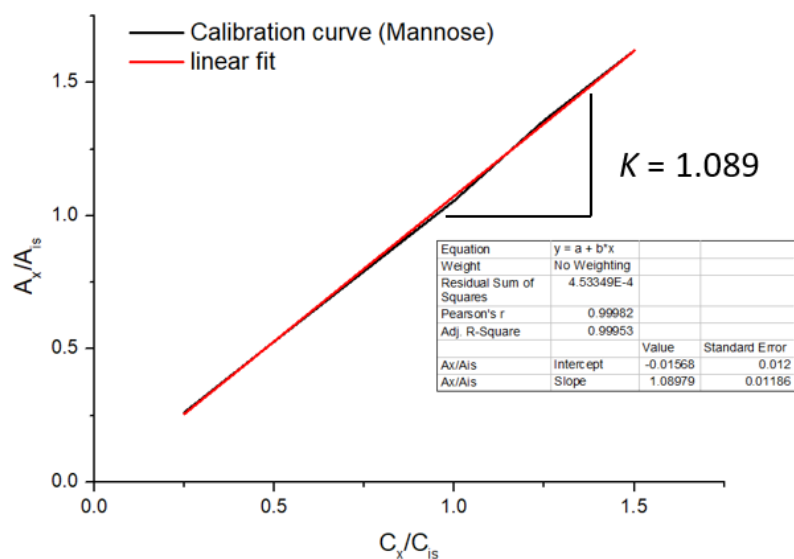


Figure 7. Calibration curve of mannose from the GC-FID with the corresponding linear fitting.

8.1.2 Calibration of PMan

Table 5. Surface Area (A) of the GC-FID signals for PMan and sorbitol at different concentration and the corresponding values of C_x/C_{is} and A_x/A_{is} .

Concentration (mg/mL)	A (α -PMan)	A (Sorbitol)	C_x/C_{is}	A_x/A_{is}
1.75	2.5367	2.6605	1.5	0.9883
1.50	2.6295	3.0232	1.25	0.8290
1.25	2.5063	2.7393	1.0	0.5728
1.00	1.5692	2.7382	0.5	0.4445
0.50	1.217	3.009	0.25	0.2204
0.25	0.6632	3.1245	1.5	0.1133

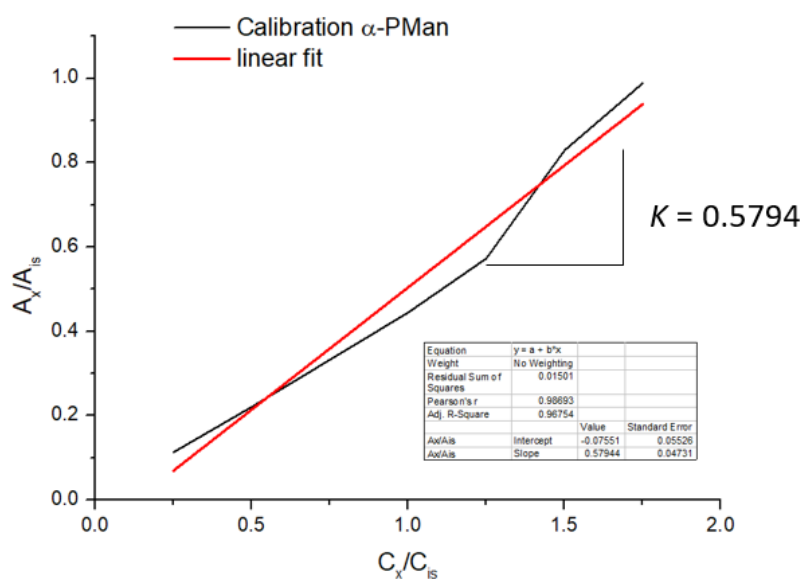


Figure 8. Calibration curve of PMan of the GC-FID with the corresponding linear fitting.

Protocol of the kinetic study for step 1 and step 2

In a round-bottom flask, 20 g mannose were dissolved in 50 mL propargyl alcohol and stirred in the presence of amberlyst-15 (4.2 mol%) at different temperatures (60 - 100 °C). The complete homogenous dissolved solution of the sugar was separated in 8 different vials, which were stirred under vigorous agitation and stopped after 1, 3, 6, 8, 10, 12, 24 and 48 h, respectively. The reaction was sampled overtime and each probe was dissolved in 1 mL pyridine (containing 1 mg/mL sorbitol as internal standard) and modified by BSTFA as described above prior to injection into the gas chromatogram. The yield of PMan was then calculated with the surface area of the GC signal, whereas the response factor k , determined for the α -anomer, was also used for its β -counterpart. The obtained values were then extrapolated to obtain the yield of the total batch.

8.2 Size-exclusion-chromatography

8.2.1 Calibration of Mannose

Different solutions of mannose in distilled water were prepared and injected into the SEC. The surface area of each concentration was calculated by integration of the peak from $R_t = 9$ -14 minutes. From the resulting data, a calibration curve was plotted using Origin.Pro 8.6.

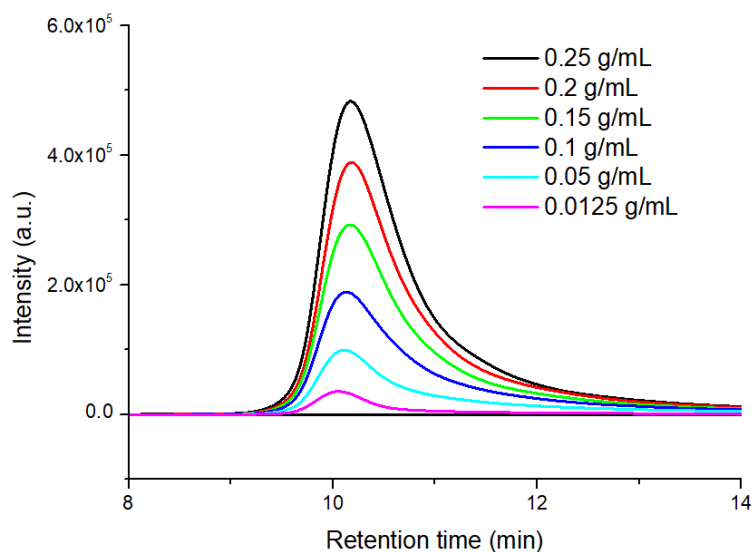


Figure 9. Plot of the overlaid SEC (measured against dextran standards in H₂O at 25 °C) traces of mannose in different concentration.

Table 6. Surface area of the mannose peak from the SEC spectra.

Concentration (g/mL)	Surface Area
0.25	554484.15
0.2	451273.16
0.15	345226.41
0.1	233407.20
0.05	118089.41
0.0125	31523.12
0.25	554484.15

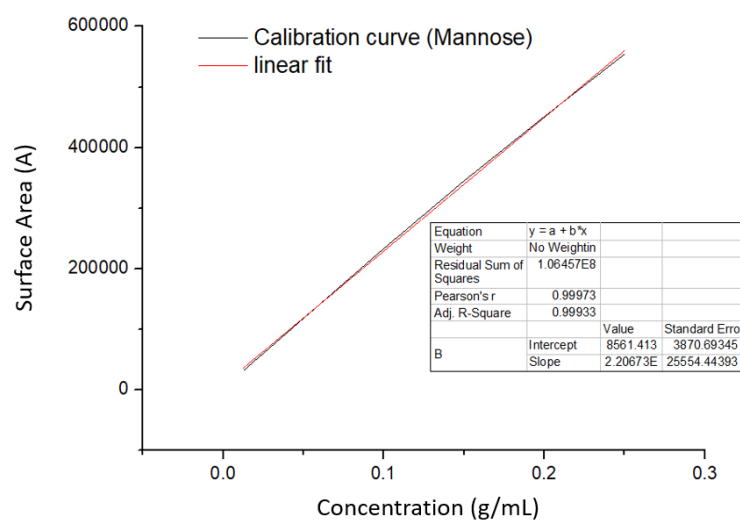


Figure 10. Calibration curve of mannose by SEC with the corresponding linear fitting.

Calibration curve: $y = 8561.41 + 2.20673E6*x$

General procedure for the kinetic study of the glycosylation reaction.

Table 7. General batch for the kinetic study of the glycosylation reaction.

compound	M (g/mol)	m (g)	V (mL)	n (mmol)	eq.
Mannose	180.16	2.5	-	13.87	1
Propargyl alcohol	56.06	-	6.25	117.55	8.47
Amberlyst-15	-	0.025	-	-	-

In a round-bottom flask, mannose was dispersed in propargyl alcohol in the presence of amberlyst-15 and stirred at 40 - 50 °C for 1 - 24 h. The obtained solution was filtrated, the remaining mannose collected and dissolved in 10 mL distilled water. Then, 1 mL of the sugar solution was injected to the SEC and the conversion rate was calculated via the surface area of the mannose peak (9-12 t_R).

8.2.2 Calibration of PMan

Different solutions of mannose in distilled water were prepared and injected into the SEC. The surface area of each concentration was calculated by integration of the peak from $R_t = 39.39 - 40.61$ minutes. With the resulted data, a calibration curve was plotted using Origin.Pro 8.6.

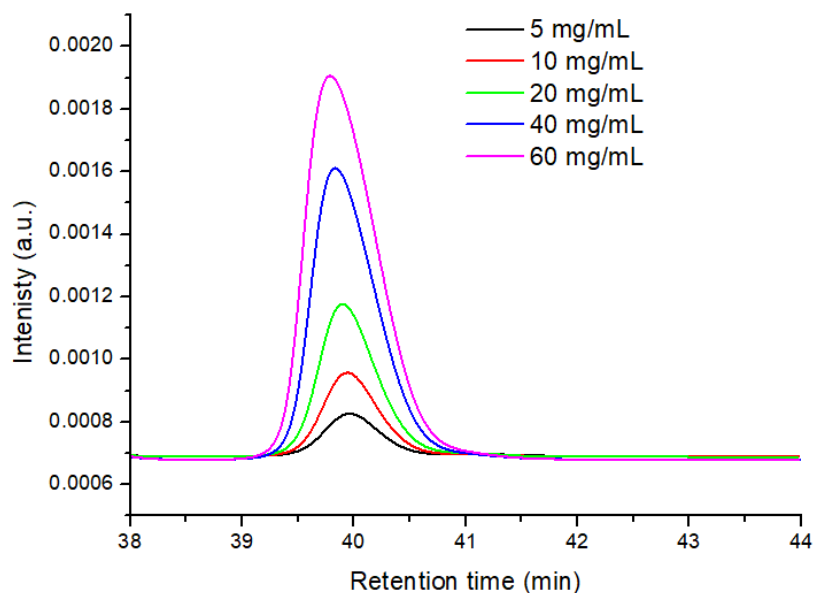


Figure 11. Plot of the overlaid SEC (measured against dextran-standards in H₂O at 25 °C) traces of PMan in different concentration.

Table 8. Surface area of the PMan peak from the SEC spectra.

Concentration (g/mL)	Surface Area
5	0.00008104
10	0.0001607
20	0.0002987
40	0.0006258
60	0.000891

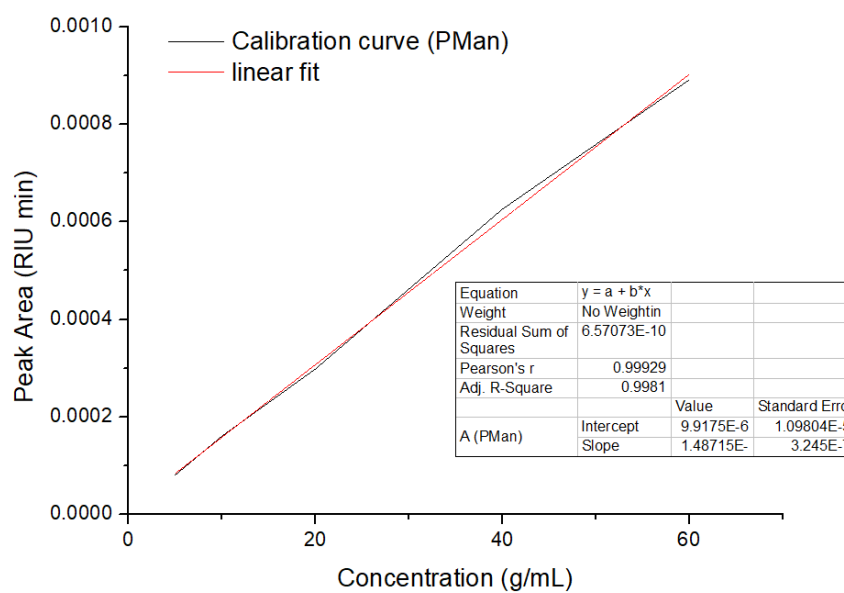


Figure 12. Calibration curve of PMane by SEC with the corresponding linear fitting.

Calibration curve: $y = 9.9175E-6 + 1.48715E-5*x$.

For the determination of the conversion rate of PMan during the oligomerization in step 2, the surface area of PMan from step 1 was set to $t = 0$. Each sample injected in the SEC was prepared in a concentration of 20 mg/mL.

9 Calculation of \overline{DP}_n and \overline{M}_n by $^1\text{H-NMR}$ spectroscopy

Step 1

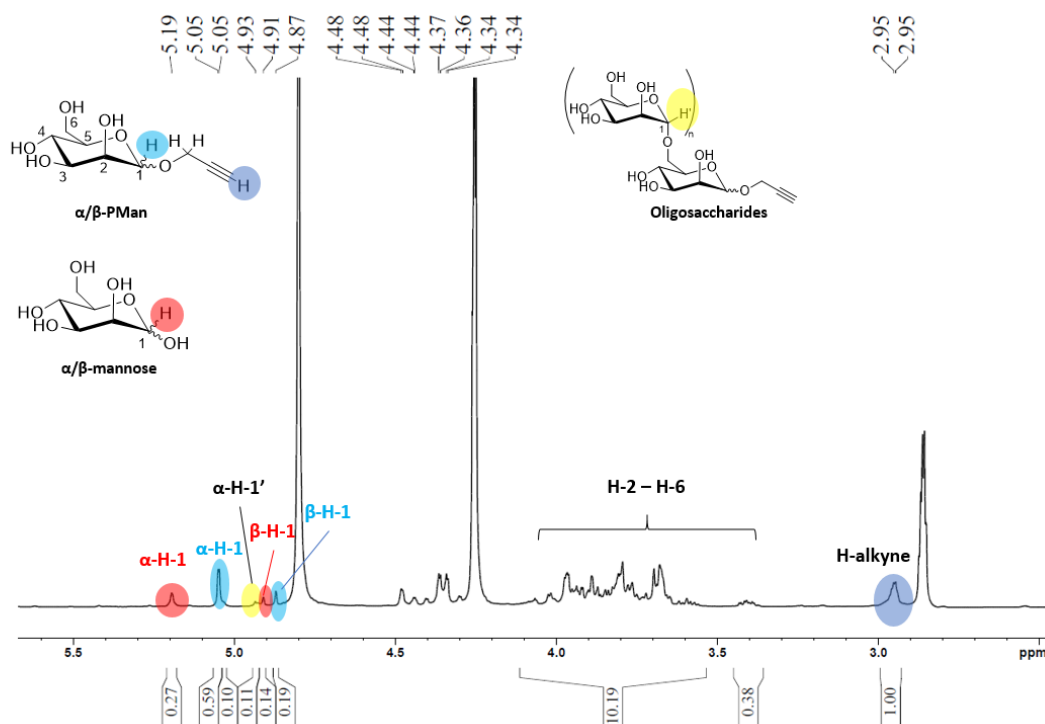


Figure 13. $^1\text{H-NMR}$ (400 MHz, D_2O) spectrum of $(\text{PMan})_n$ after 3 h of step 1.

The formation of oligosaccharides was studied by NMR spectroscopy over a time period of 48 h using the integrals of the arising signals in the anomeric region. Therefore, the relative proportions of the anomeric proton ($\alpha\text{-H-1}$) of α -propargyl mannopyranoside ($\alpha\text{-PMan}$), β -PMan, α - and β -mannose and oligosaccharides were calculated. For the oligosaccharides, the signal of the anomeric proton of the propargylated terminal end group (5.05 ppm) and the signal of the (1,6)-glycosidic linkage (4.93 ppm) should have the same value, when all oligomers are propargylated. However, since we could not determine the end-group of all oligosaccharides by NMR spectroscopy, only the integral of the (1,6)-glycosidic linkage was considered for the calculation of the proportion of the oligomers. Also all the other small signals in the anomeric region, that appeared during longer reaction times, were not taken into account. They were suggested to arise from other glycosidic linkages of the oligomers or side-products (furanosides, anhydro mannopyranoside, acyclic acetals, etc.), but considered as negligible for the kinetic study. Owing to the low field shift of the alkyne proton (2.95 ppm), the end-group method could be employed to calculate the degree of polymerization (\overline{DP}_n) and the molecular weight, respectively. For the reasons of simplification, the sugars were assumed to be completely functionalized. The next equation was then used:

$$\overline{DP}_n = \frac{(\text{H-2} + \text{H-3} + \text{H-4} + \text{H-5} + \text{H-6})}{6} \quad (36)$$

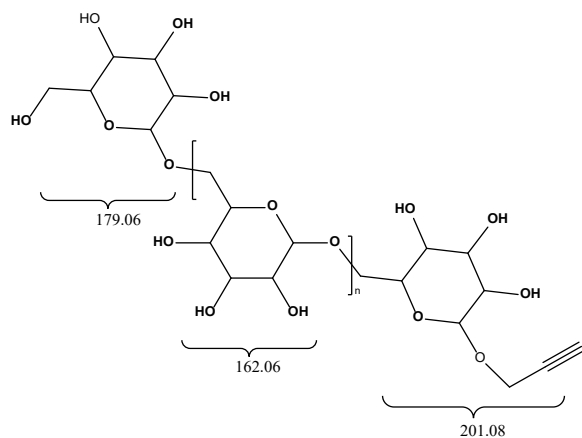
Note that the proportion of remaining free mannose molecules needed to be subtracted in order to calculate the \overline{DP}_n from only propargylated (PMan)_n. Therefore, we calculated the remaining amount of unreacted mannose by SEC and subtracted it from the integral of H-2 - H-6. For example, in Figure **13** the ¹H-NMR spectrum from step 1 is shown after 2 h of reaction. The integration of the ‘the protons H-2 - H-6’ gives 10.57, while the SEC experiment gave a remaining amount of mannose of *ca.* 40 %. After subtraction of the proportion of mannose, the value of the integral is reduced to 6.34. Using equation (42), the \overline{DP}_n of the sample was calculated to 1.1.

Step 2

For the kinetic study of the oligomerization reaction of PMan during step 2, the \overline{DP}_n was calculated using the end-group method. The alkyne proton (2.95 ppm) was calibrated and the oligosaccharides were assumed to be completely functionalized, so that the \overline{DP}_n could be calculated using equation (36).

10 Calculation of MW and DP by Mass spectroscopy

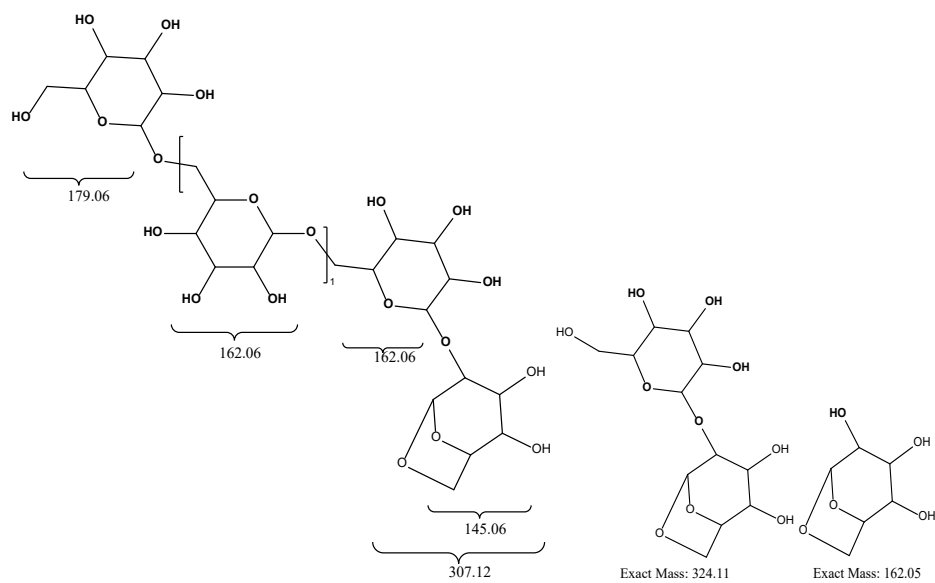
Propargyl-(oligo)-glycosides, (PMan)_n



$$M_w = 179.06 + 162.06 \cdot n + 201.08$$

Table 9. Calculated mass of propargyl-(oligo)-glycosides with different DP, that is expected by Mass spectroscopy analysis.

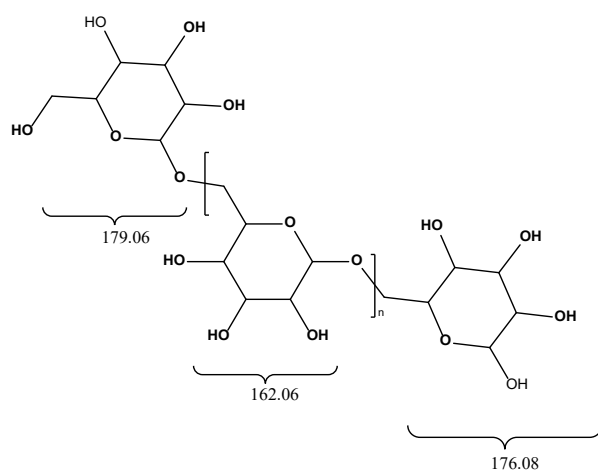
DP	n	MW	[M+Na] ⁺
1	-	218.08	241.08
2	-	380.14	403.14
3	1	542.2	565.2
4	2	704.26	727.26
5	3	866.32	889.32
6	4	1028.38	1051.38
7	5	1190.44	1213.44
8	6	1352.5	1375.5
9	7	1514.56	1537.56
10	8	1676.62	1699.62
11	9	1838.68	1861.68
12	10	2000.74	2023.74
13	11	2162.8	2185.8
14	12	2324.86	2347.86

Levomannosanes, (LVM)_n

$$\text{MW} = 179.08 + 162.08 \cdot n + 307.08$$

Table 10. Calculated mass of propargyl-(oligo)-levomannosanes with different DP, that is expected by Mass spectroscopy analysis.

DP	n	MW	[M+Na] ⁺
1	-	162.05	185.05
2	-	324.11	347.11
3	-	486.16	509.16
4	1	648.22	671.22
5	2	810.28	833.28
6	3	972.34	995.34
7	4	1134.4	1157.4
8	5	1296.46	1319.46
9	6	1458.52	1481.52
10	7	1620.58	1643.58
11	8	1782.64	1805.64
12	9	1944.7	1967.7
13	10	2106.76	2129.76
14	11	2268.82	2291.82

Terminal free glycosides, (Man)_n

$$M_w = 179.08 + 162.08 \cdot n + 163.08$$

Table 11. Calculated mass of terminal free oligo-glycosides with different DP, that is expected by Mass spectroscopy analysis.

DP	n	MW	[M+Na] ⁺
1	-	180.06	203.06
2	-	342.12	365.12
3	1	504.18	527.18
4	2	666.24	689.24
5	3	828.3	851.3
6	4	990.36	1013.36
7	5	1152.42	1175.42
8	6	1314.48	1337.48
9	7	1476.54	1499.54
10	8	1638.6	1661.6
11	9	1800.66	1823.66
12	10	1962.72	1985.72
13	11	2124.78	2147.78
14	12	2286.84	2309.84

11 Appendix

NMR + ATR-IR spectra

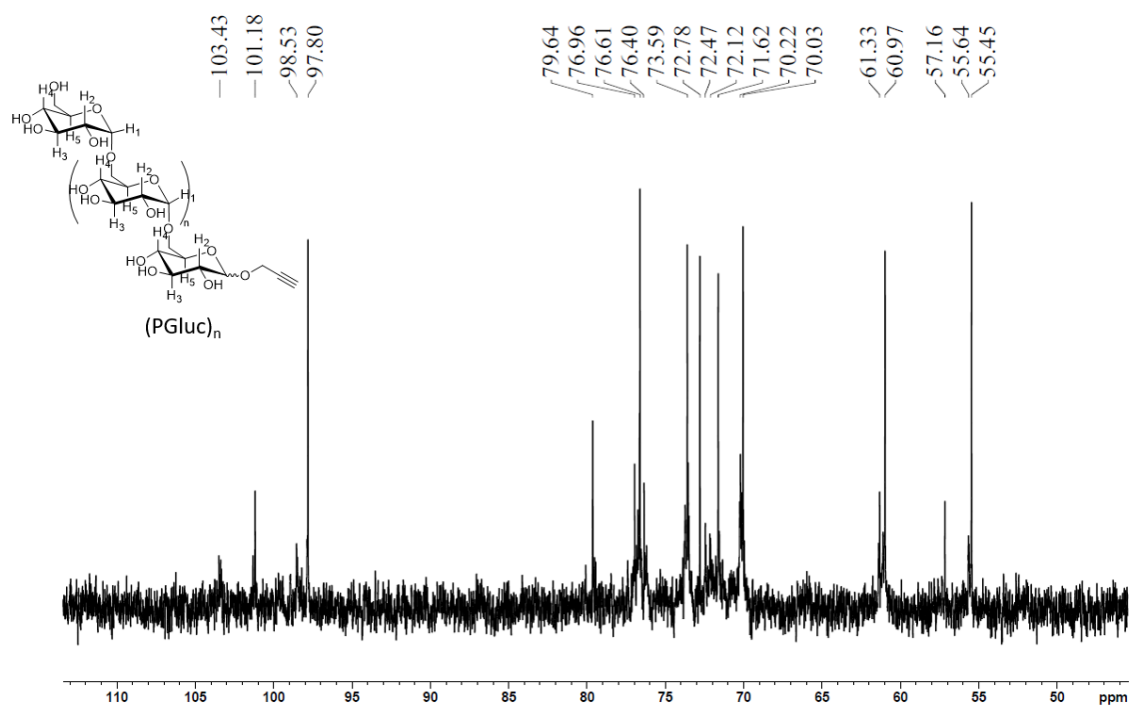


Figure 14. ¹³C-NMR (100.4 MHz, D₂O) spectrum of propargyl-(oligo)-glucoside, (PGLuc)_n.

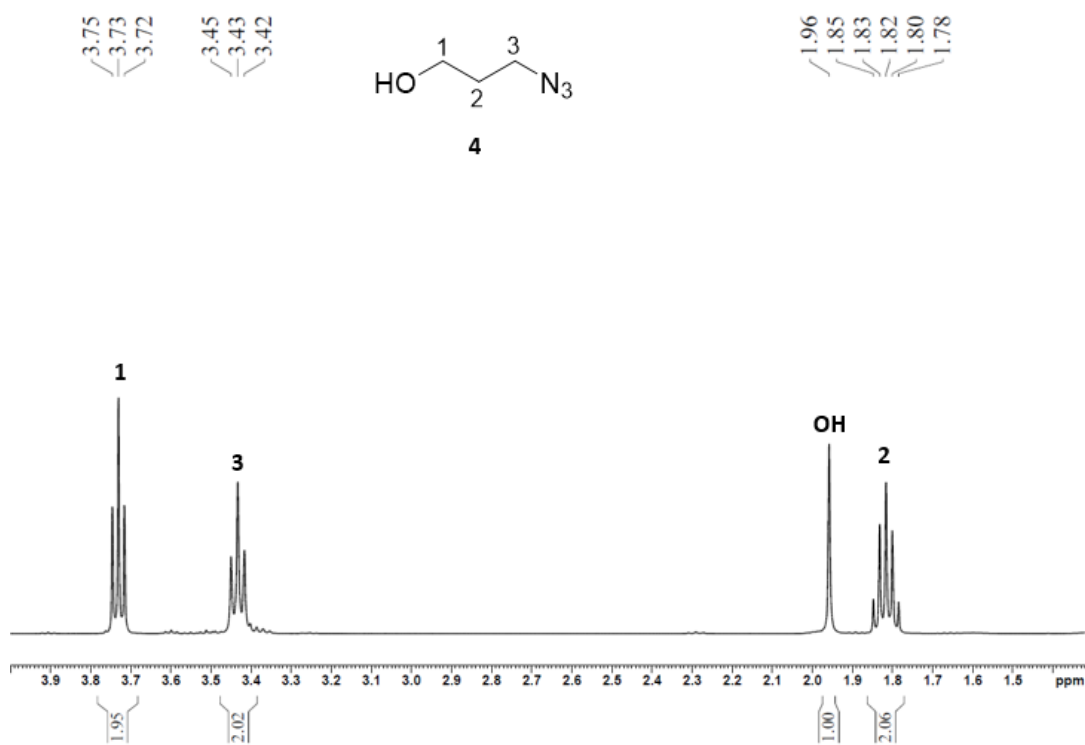


Figure 15. ¹H-NMR (400 MHz, CDCl₃) spectrum of 3-azido-1-propanol (4).

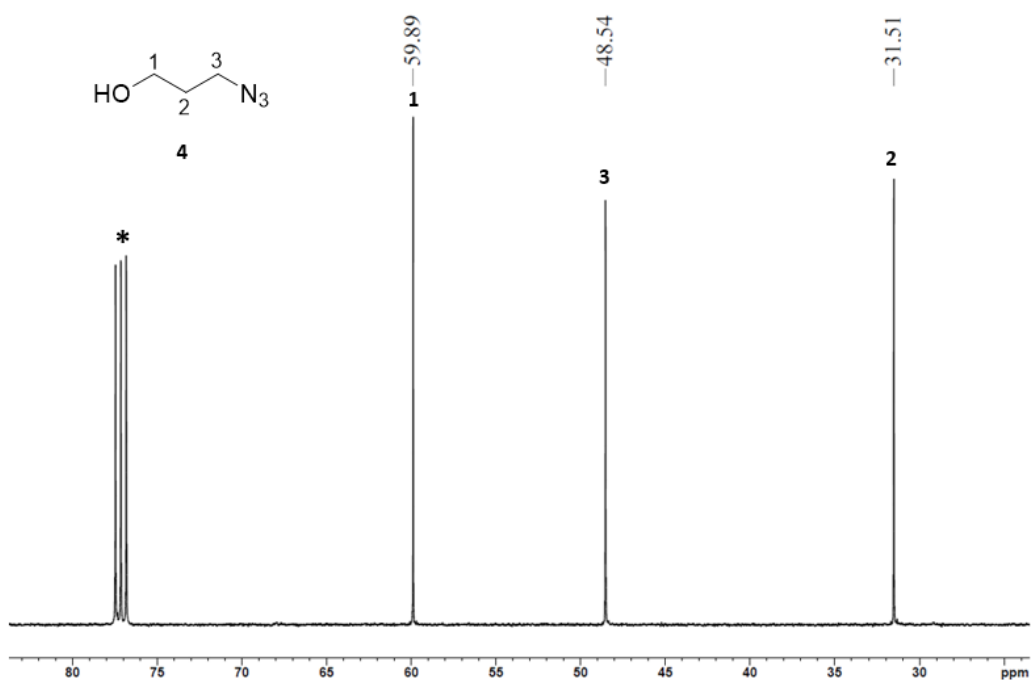
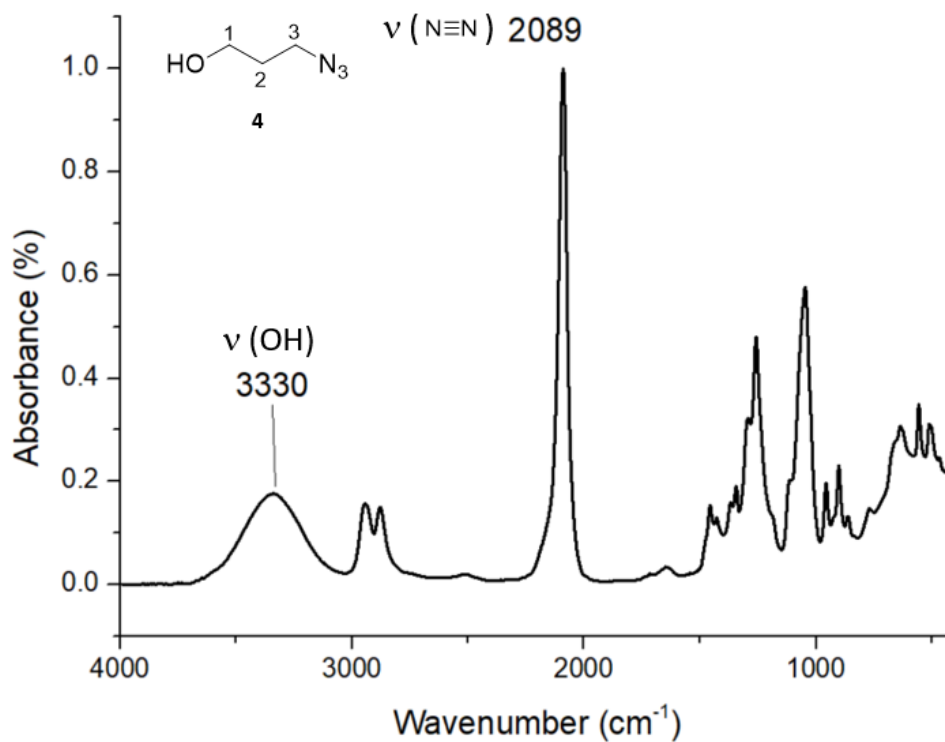
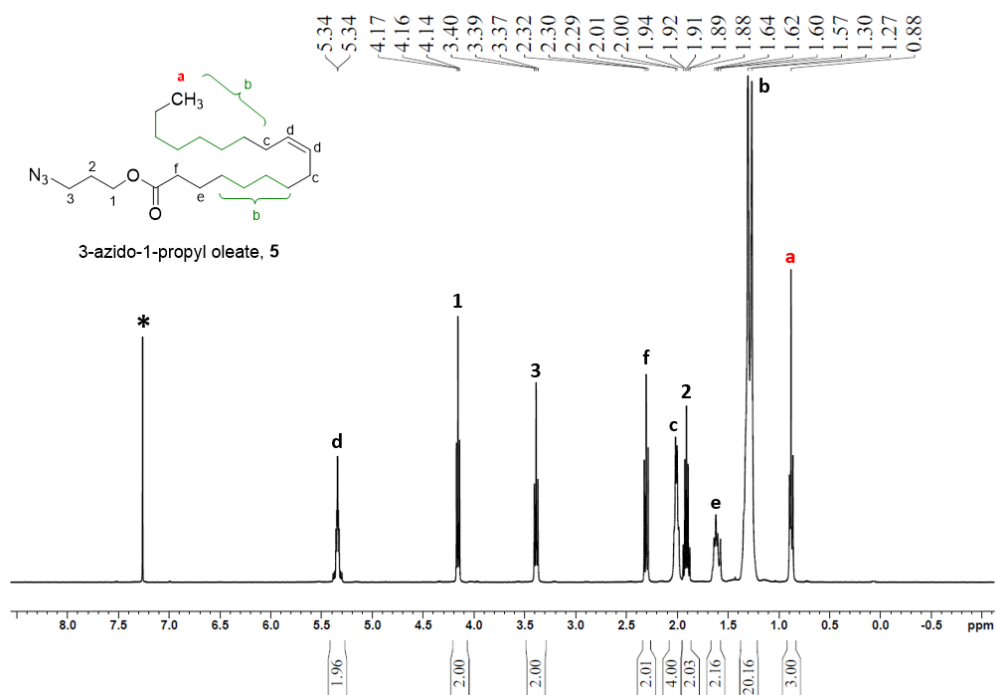
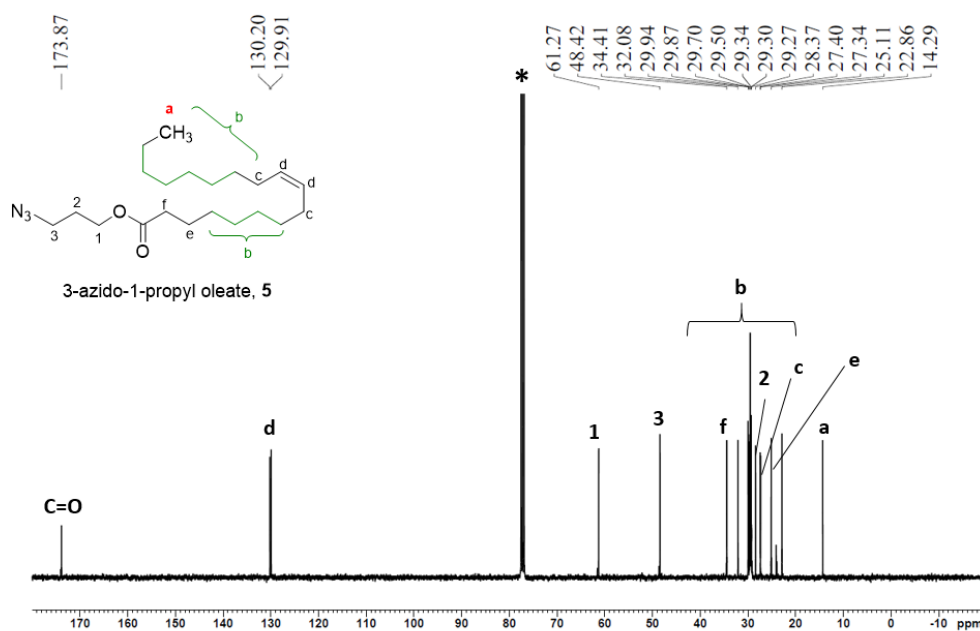
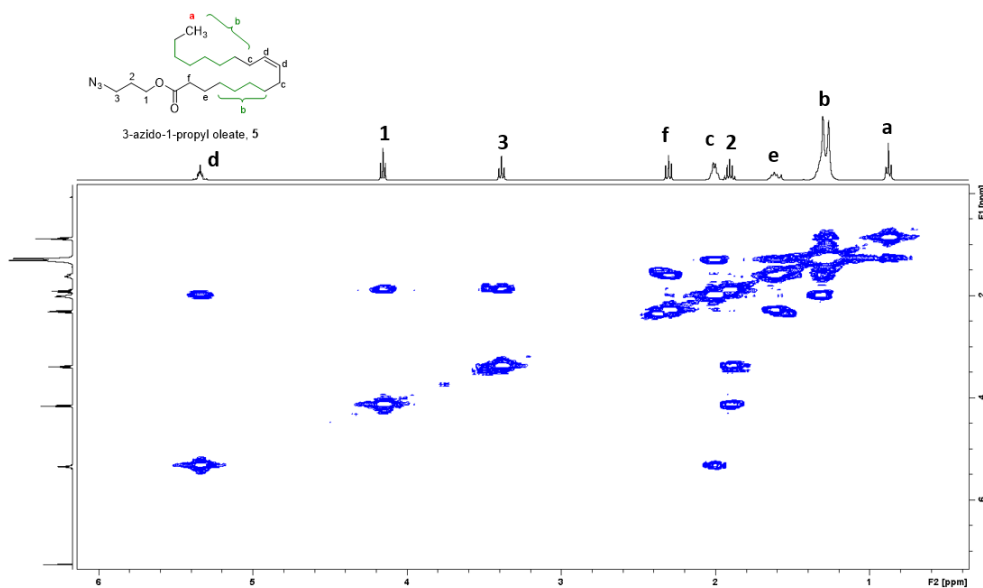
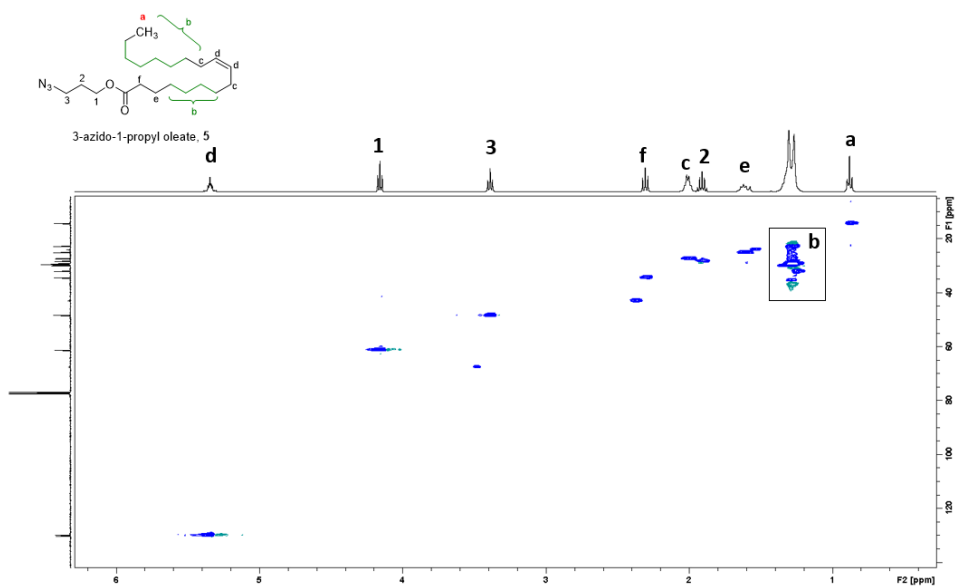
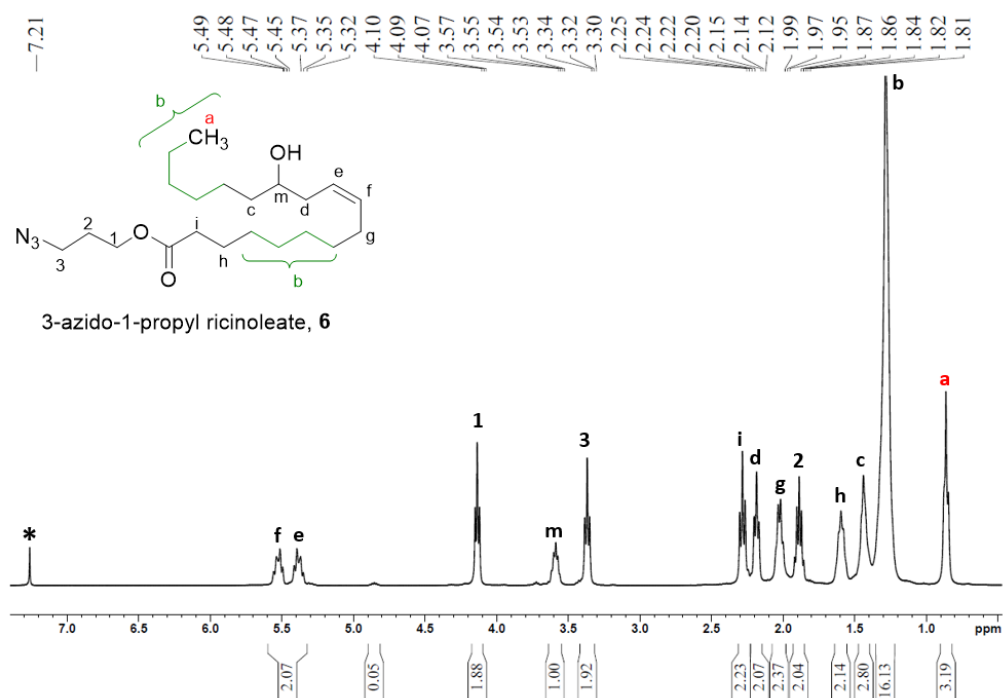
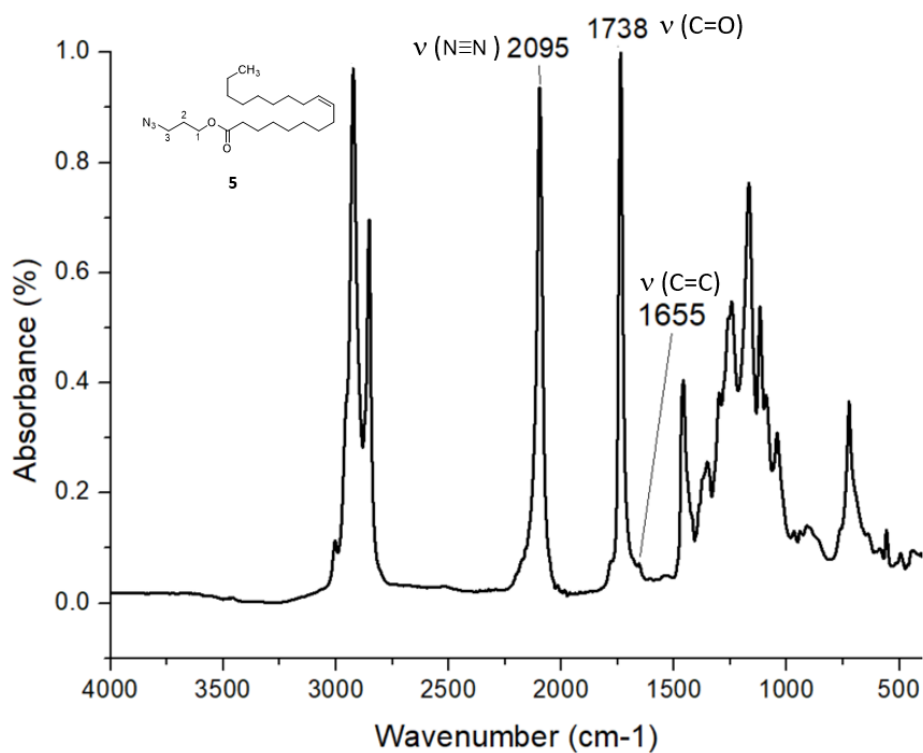
Figure 16. ^{13}C -NMR (100.4 MHz, CDCl_3) spectrum of 3-azido-1-propanol (4).

Figure 17. ATR-IR spectrum of 3-azido-1-propanol (4).

Figure 18. $^1\text{H-NMR}$ (400 MHz, CDCl_3) spectrum of 3-azido-1-propyl oleate (5).Figure 19. $^{13}\text{C-NMR}$ (100.4 MHz, CDCl_3) spectrum of 3-azido-1-propyl oleate (5).

Figure 20. ¹H-¹H COSY NMR spectrum of 3-azido-1-propyl oleate (5).Figure 21. ¹H-¹³C HSQC of 3-azido-1-propyl oleate (5).



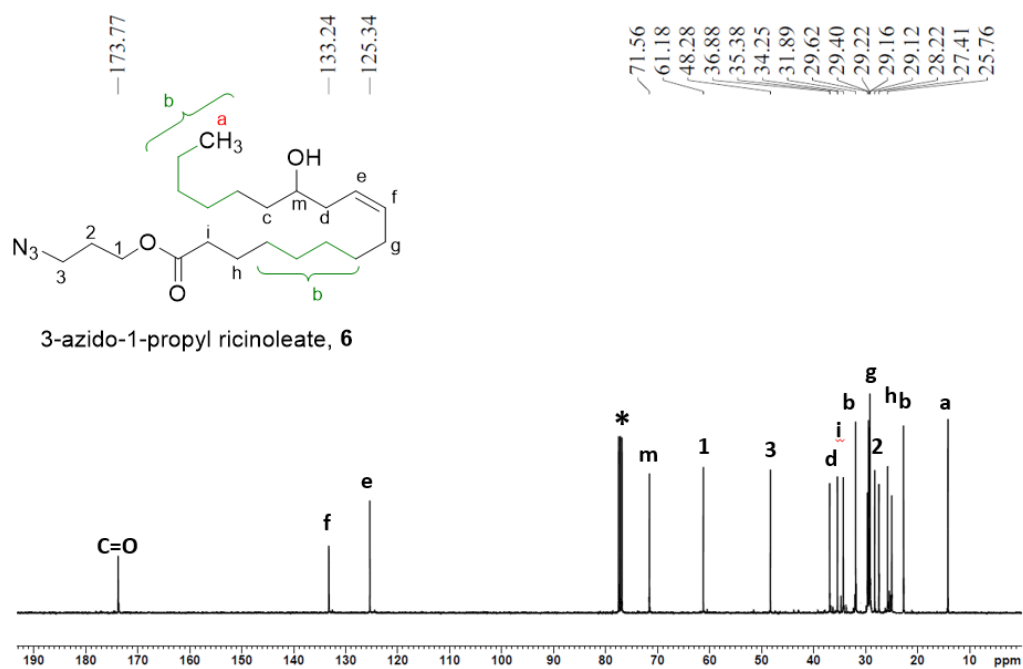


Figure 24. ^{13}C -NMR (100.4 MHz, CDCl_3) spectrum of 3-azido-1-propyl-ricinoleate (**6**).

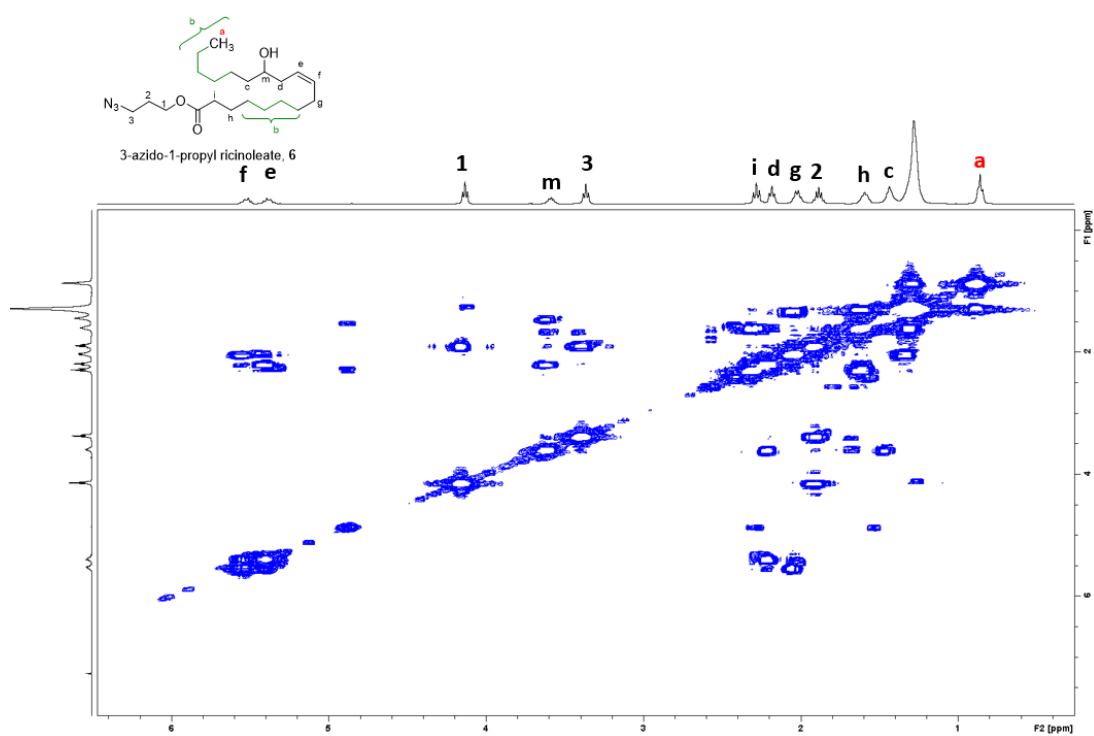


Figure 25. ^1H - ^1H COSY NMR of 3-azido-1-propyl-ricinoleate (**6**).

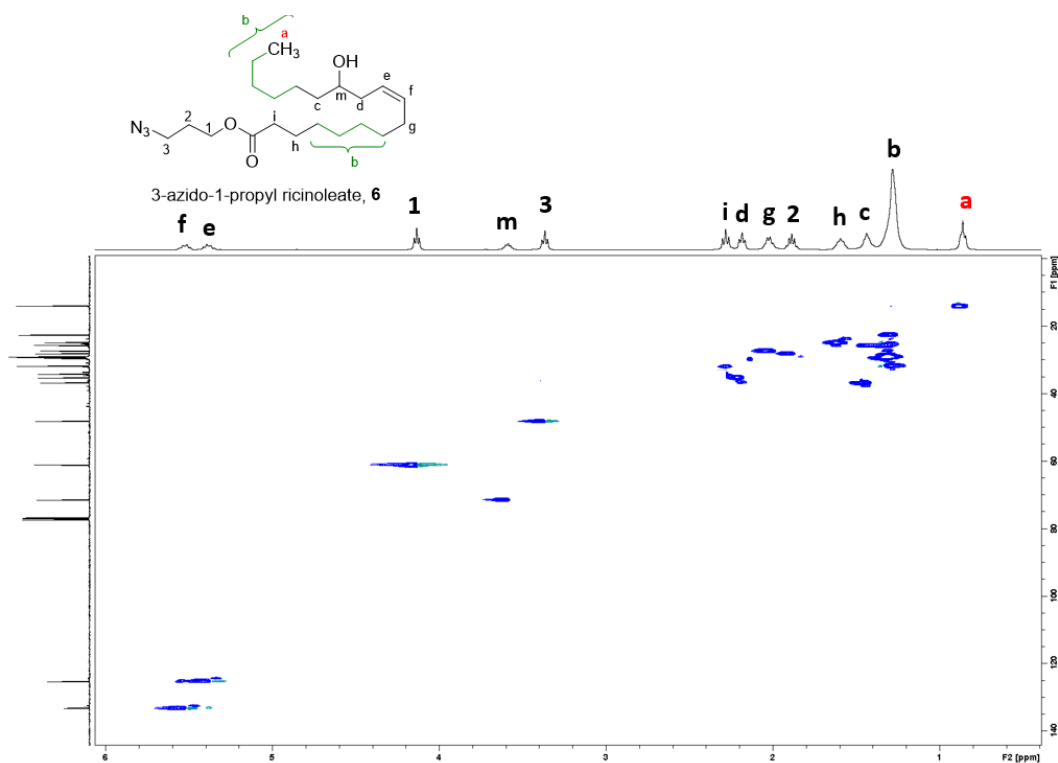


Figure 26. ^1H - ^{13}C HSQC NMR of 3-azido-1-propyl-ricinoleate (**6**).

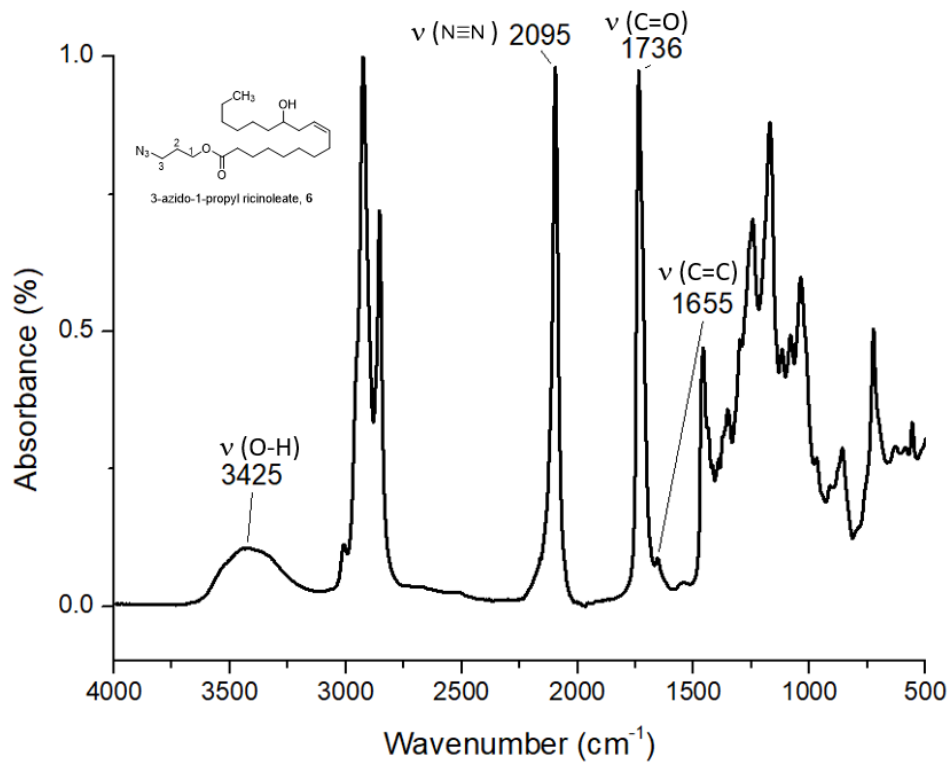


Figure 27. ATR-IR spectrum of 3-azido-1-propyl ricinoleate (**6**).

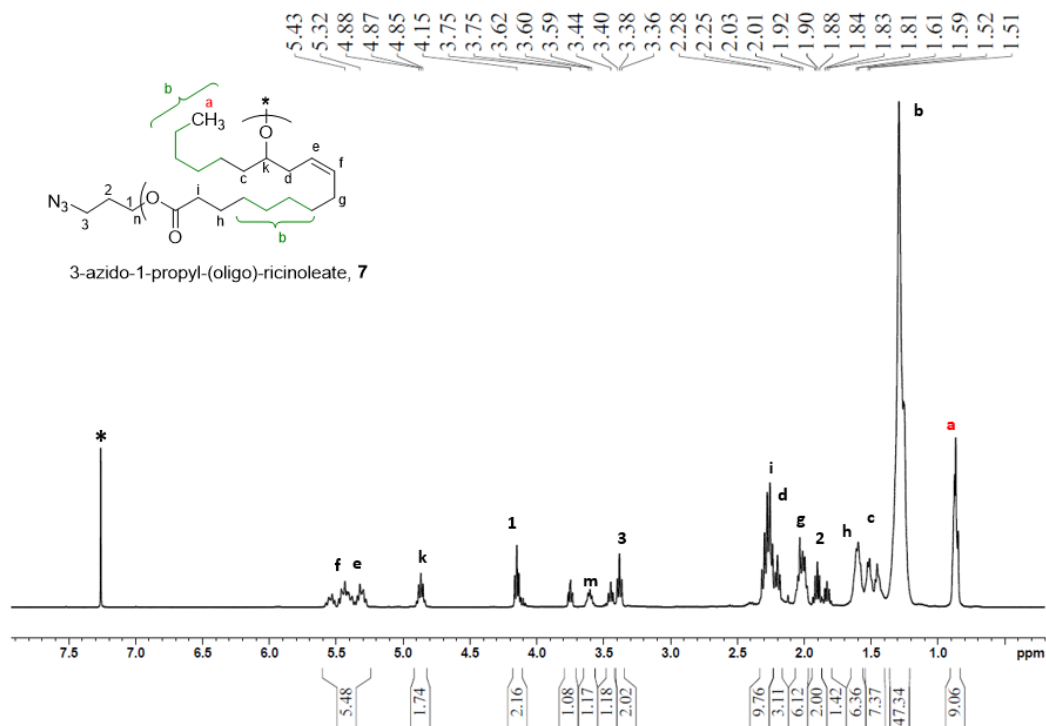


Figure 28. ¹H-NMR (400 MHz, CDCl₃) spectrum of 3-azido-1-propyl-(oligo)-ricinoleate (7).

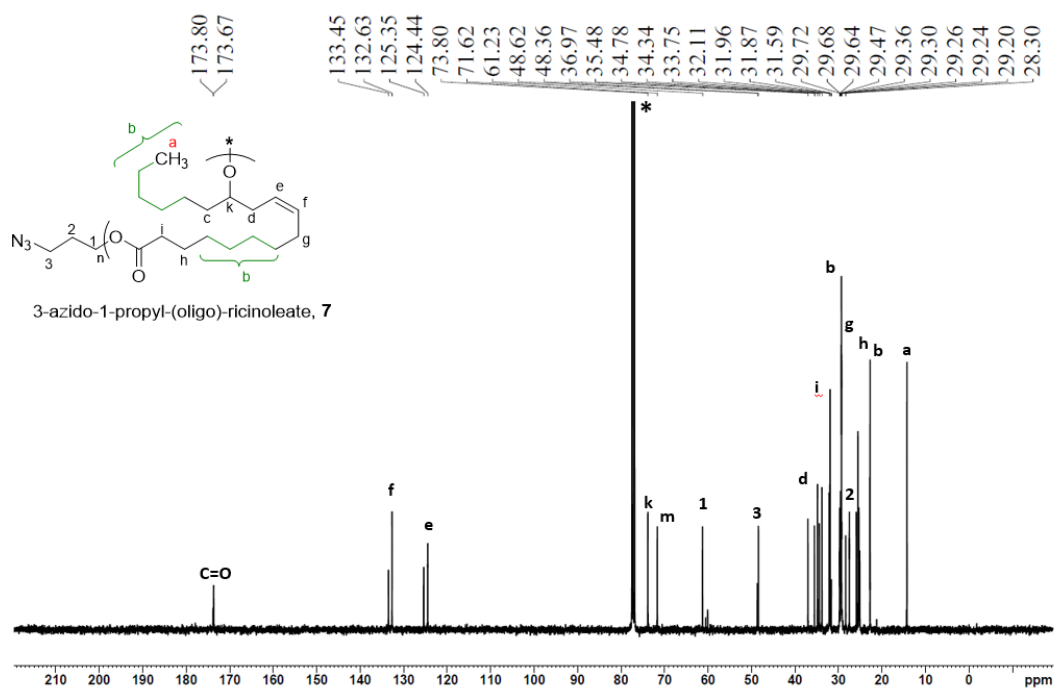
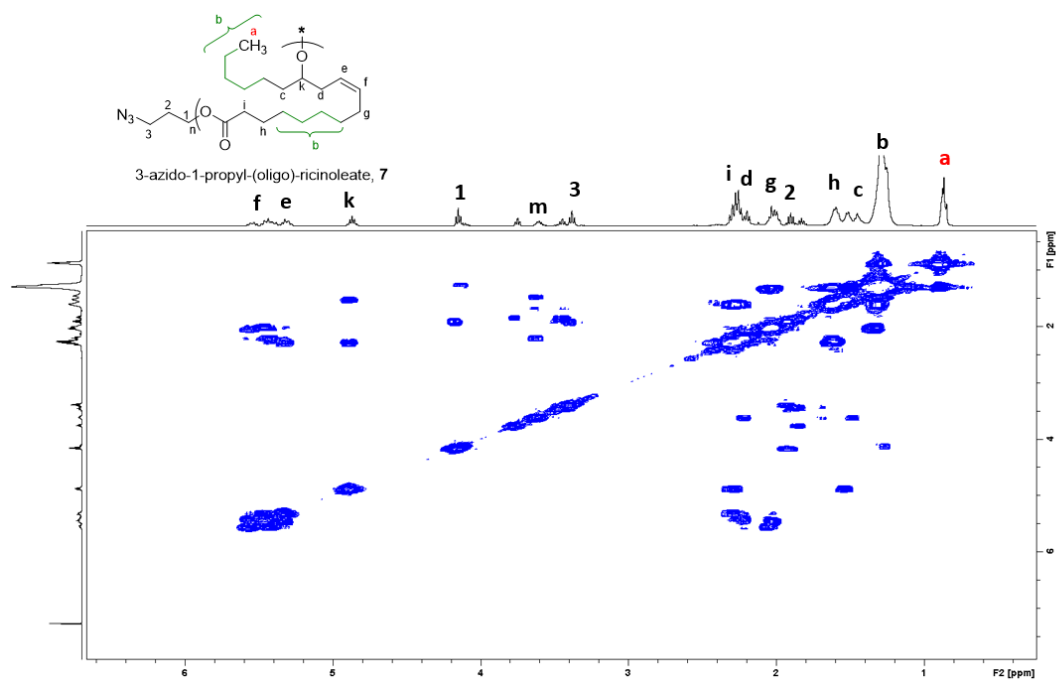
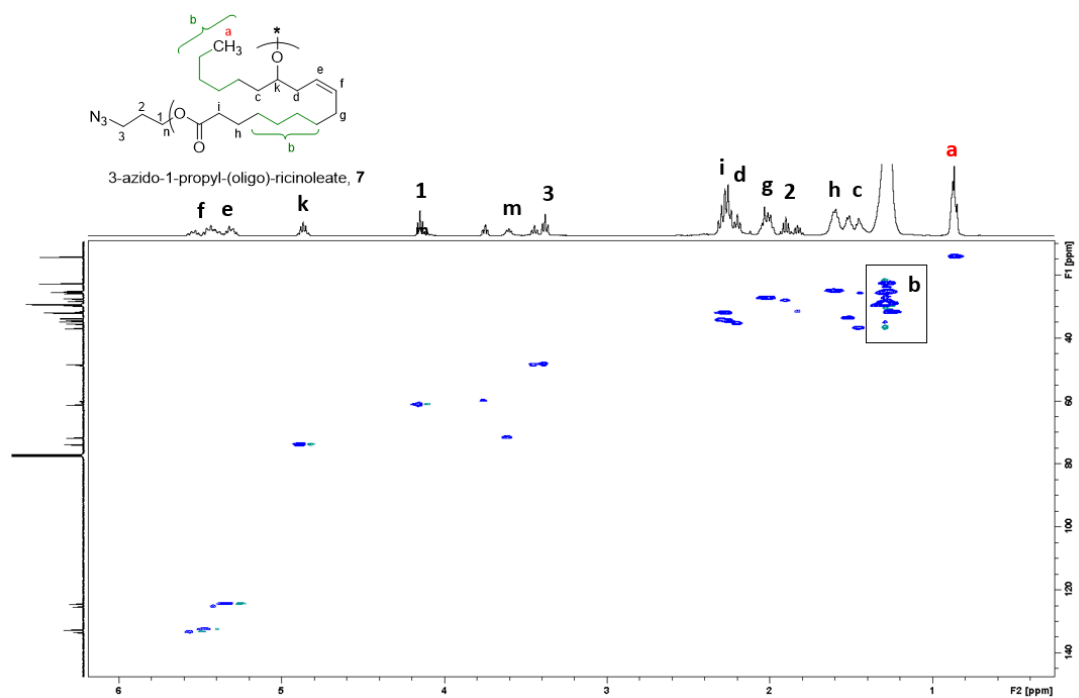
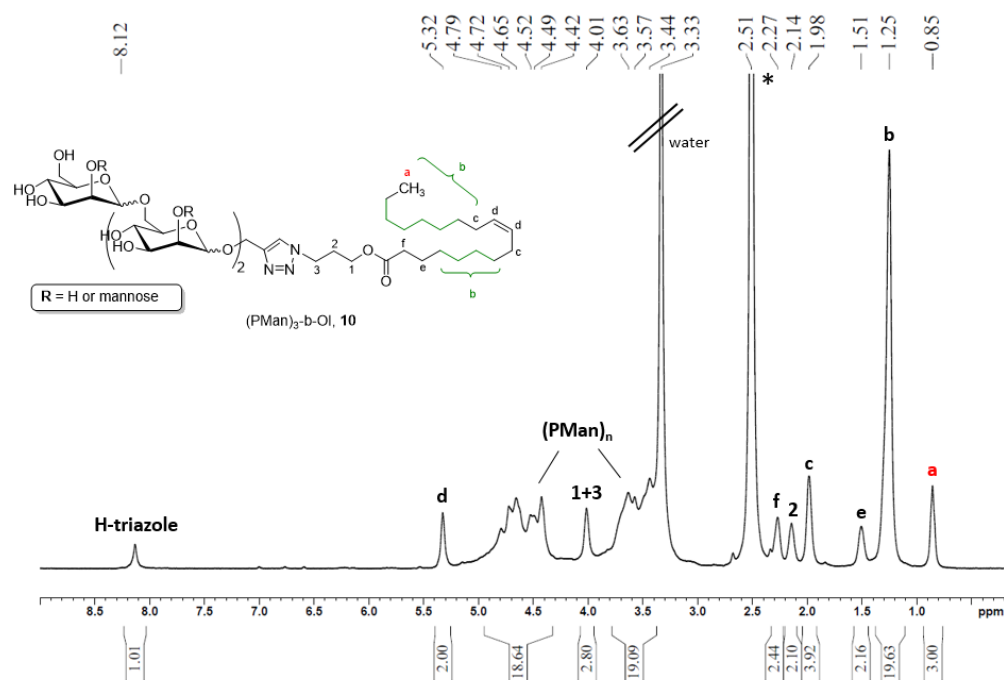
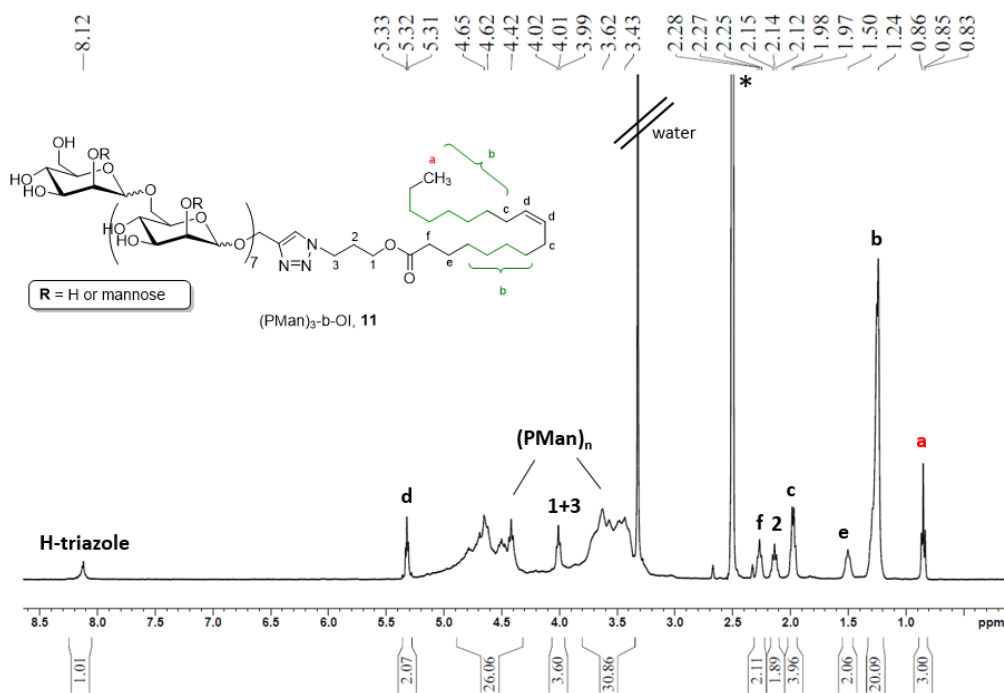


Figure 29. ¹³C-NMR (100.4 MHz, CDCl₃) spectrum of 3-azido-1-propyl-(oligo)-ricinoleate (7).

Figure 30. ^1H - ^1H COSY NMR of 3-azido-1-propyl-(oligo)-ricinoleate (7).Figure 31. ^1H - ^{13}C HSQC NMR of 3-azido-1-propyl-(oligo)-ricinoleate (7).

Figure 32. 1H -NMR (400 MHz, DMSO- d_6) spectrum of $(PMan)_3$ -b-OI (**10**).Figure 33. 1H -NMR (400 MHz, DMSO- d_6) spectrum of $(PMan)_8$ -b-OI (**11**).

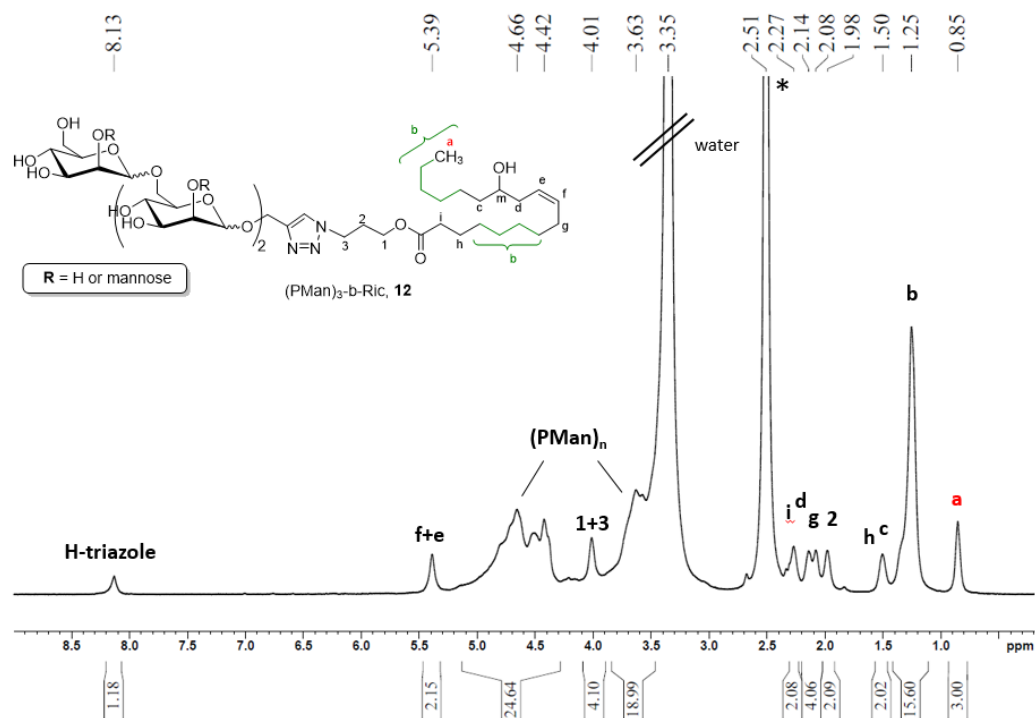


Figure 34. $^1\text{H-NMR}$ (400 MHz, DMSO-d_6) spectrum of $(\text{PMan})_3\text{-b-Ric}$ (**12**).

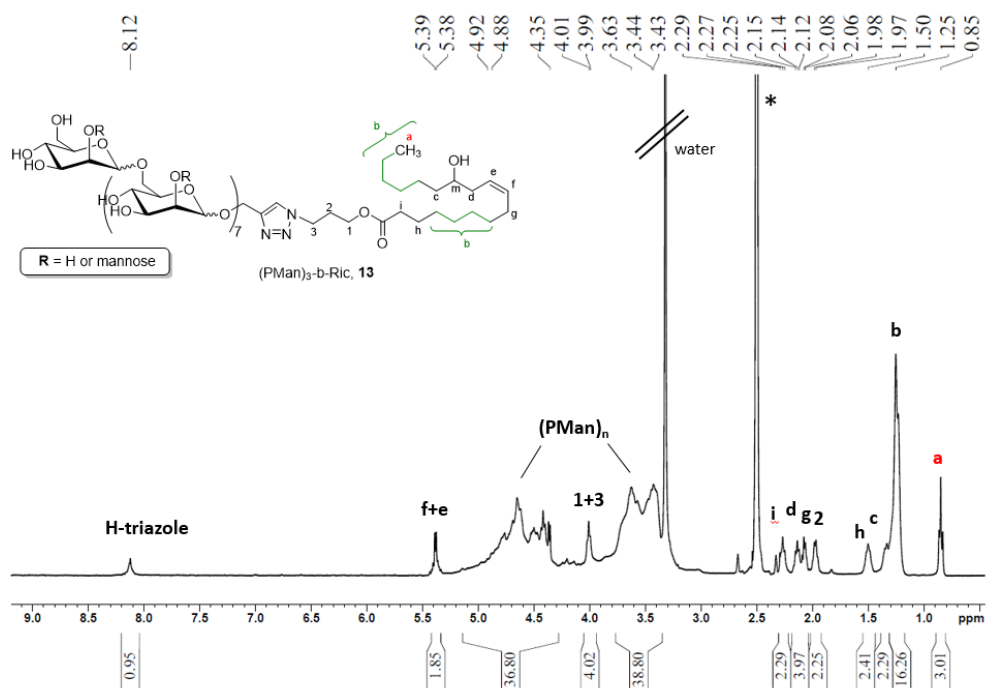


Figure 35. $^1\text{H-NMR}$ (400 MHz, DMSO-d_6) spectrum of $(\text{PMan})_8\text{-b-Ric}$ (**13**).

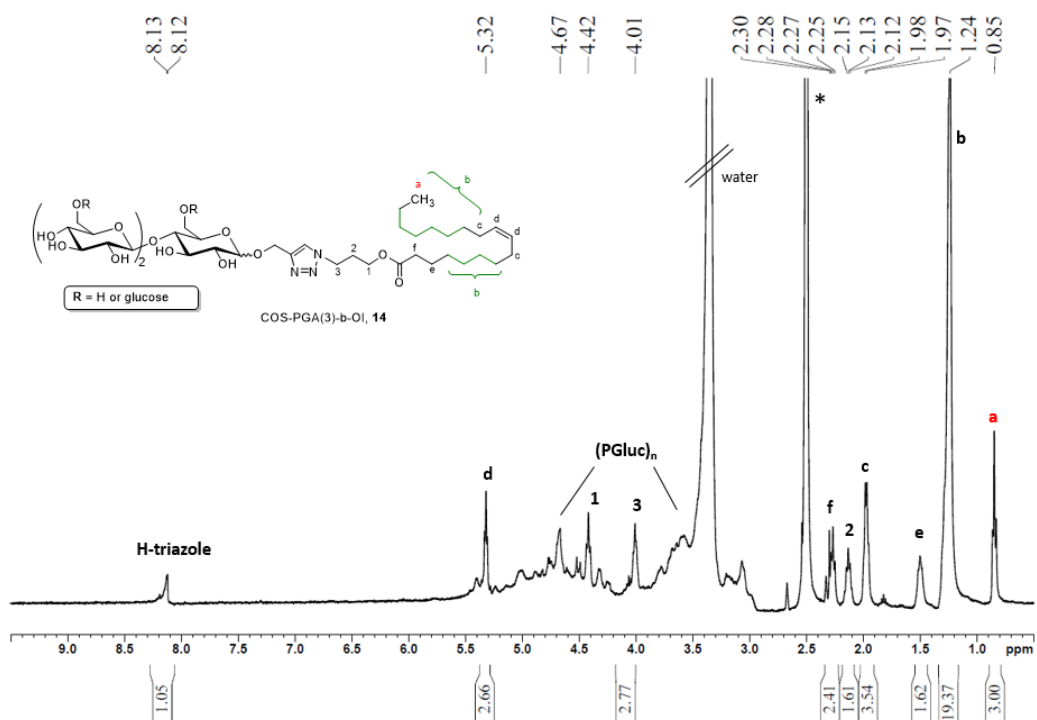


Figure 36. $^1\text{H-NMR}$ (400 MHz, DMSO-d_6) spectrum of COS-PGA(3)-*b*-OI (**14**).

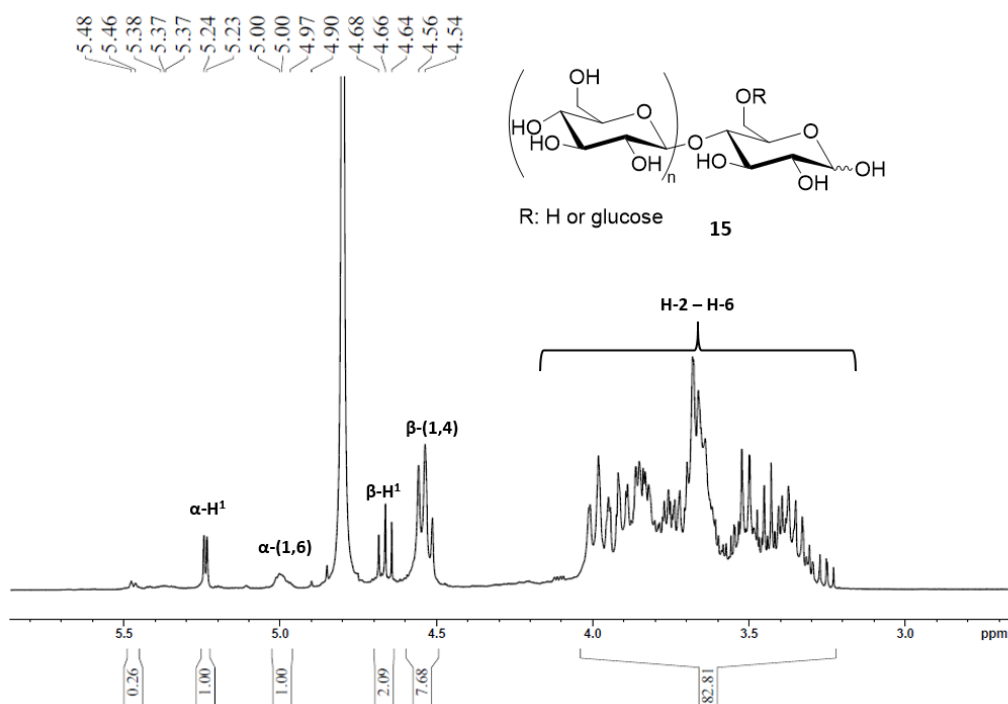


Figure 37. $^1\text{H-NMR}$ (400 MHz, D_2O) spectrum of cellulose-oligosaccharides **15**.

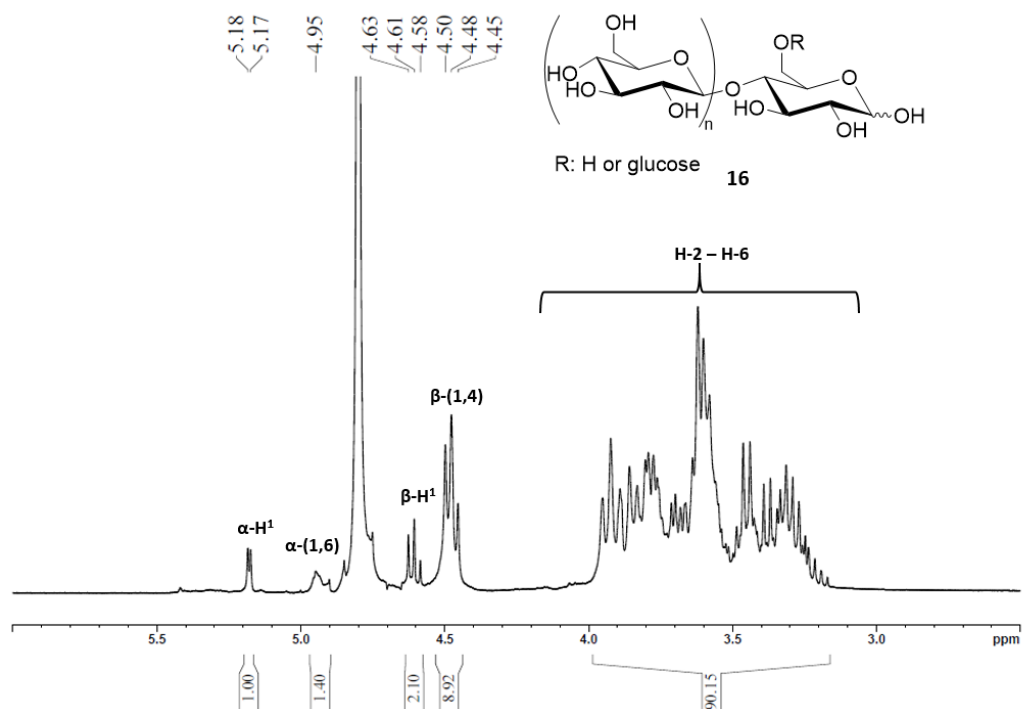


Figure 38. $^1\text{H-NMR}$ (400 MHz, D_2O) spectrum of cellulose-oligosaccharides **16**.

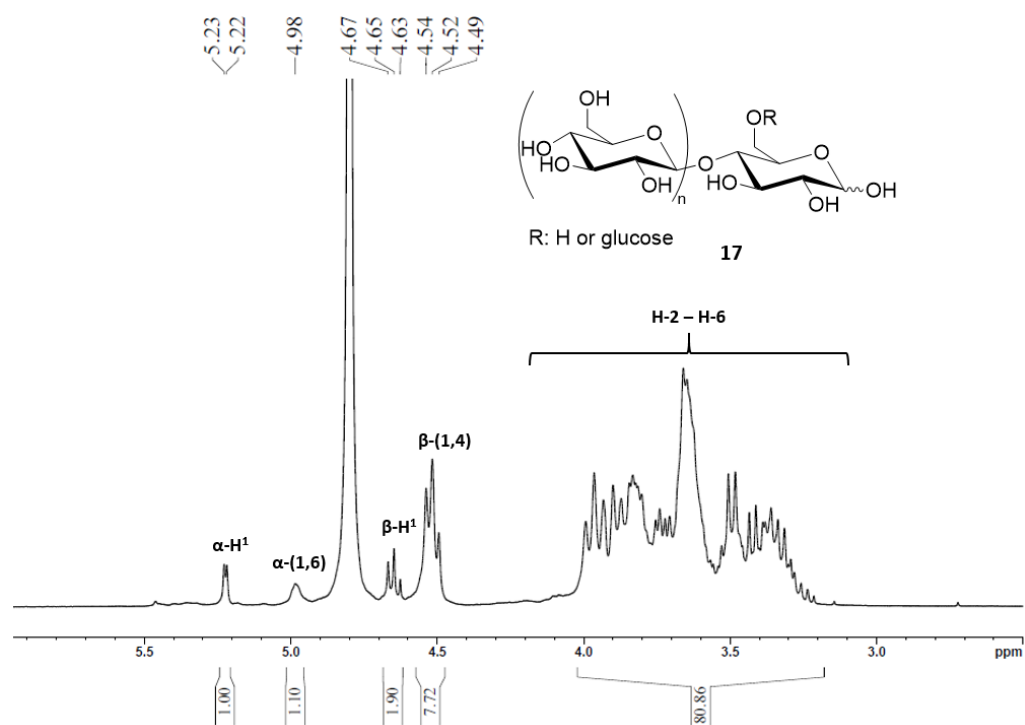
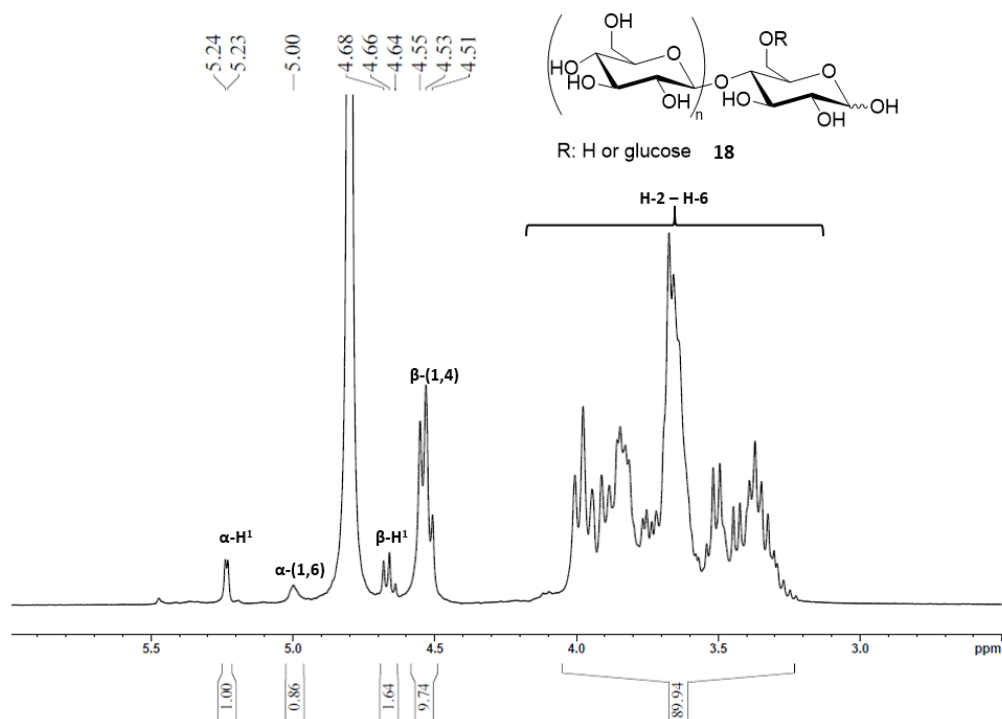
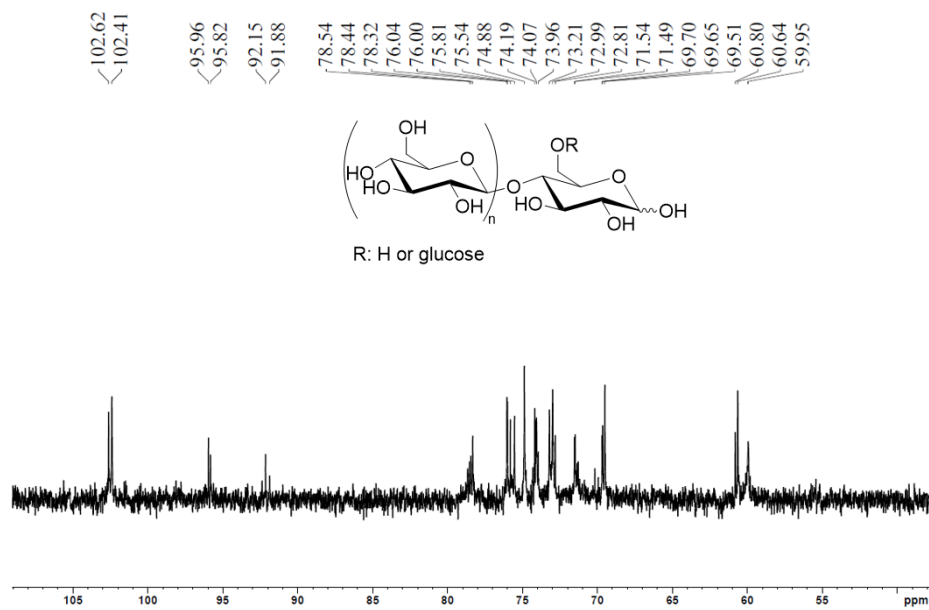


Figure 39. $^1\text{H-NMR}$ (400 MHz, D_2O) spectrum of cellulose-oligosaccharides **17**.

Figure 40. ^1H -NMR (400 MHz, D_2O) spectrum of cellulose-oligosaccharides **18**.Figure 41. ^{13}C -NMR (100.4 MHz, CDCl_3) spectrum of cellulose-oligosaccharides.

Bibliography

- [1] J. D. Berry, M. J. Neeson, R. R. Dagastine, D. Y. Chan, R. F. Tabor, *J Colloid Interface Sci* **2015**, *454*, 226-237.
- [2] H.-D. Dörfler, *Grenzflächen und kolloid-disperse Systeme: Physik und Chemie*, Springer, **2002**.
- [3] D. I. Svergun, M. H. J. Koch, *Reports on Progress in Physics* **2003**, *66*, 1735-1782.
- [4] aO. Kratky, P. Laggner, in *Encyclopedia of Physical Science and Technology (Third Edition)* (Ed.: R. A. Meyers), Academic Press, New York, **2003**, pp. 939-988; bL. Boldon, F. Laliberte, L. Liu, *Nano Rev* **2015**, *6*, 25661.
- [5] aC. Boyer, J. Liu, V. Bulmus, T. P. Davis, C. Barner-Kowollik, M. H. Stenzel, *Macromolecules* **2008**, *41*, 5641-5650; bZ. Li, L. Qu, W. Zhu, J. a. Liu, J.-Q. Chen, P. Sun, Y. Wu, Z. Liu, K. Zhang, *Polymer* **2018**, *137*, 54-62; cD. Quémener, T. P. Davis, C. Barner-Kowollik, M. H. Stenzel, *Chemical communications* **2006**, 5051-5053.
- [6] J. Rosselgong, M. Chemin, C. C. Almada, G. Hemery, J. M. Guigner, G. Chollet, G. Labat, D. Da Silva Perez, F. Ham-Pichavant, E. Grau, S. Grelier, S. Lecommandoux, H. Cramail, *Biomacromolecules* **2018**.
- [7] F. Orata, *Masinde Muliro University of Science and Technology*.

